International Journal of MECHANICAL SCIENCES

Volume 3, 1961

Vol. 3
1961

Editor-in-Chief

W. JOHNSON
(United Kingdom)

Regional Editors

W. RUPPERT
(Germany)

H. KUDO
(Japan)

PERGAMON PRESS

OXFORD • LONDON • NEW YORK • PARIS

INTERNATIONAL JOURNAL OF MECHANICAL SCIENCES

EDITORS

UNITED KINGDOM

W. Johnson (*Editor-in-Chief*), *Department of Mechanical Engineering, The Manchester College of Science and Technology, Manchester* 1, *England*

GERMANY

W. Ruppert, *Frankfurt a. M., Glaubergstrasse* 22, *Germany*

JAPAN

H. Kudo, *The Government Mechanical Laboratory*, 132 *Sumiyoshi, Suginami, Tokyo, Japan*

HONORARY EDITORIAL ADVISORY BOARD

C. B. Biezeno, *Delft*
P. F. Chenea, *Lafayette*
D. G. Christopherson, *London*
R. H. Evans, *Leeds*
G. Ford, *Alberta*
A. M. Freudenthal, *Columbia*
S. Fukui, *Tokyo*
A. J. Gould, *Natal*
R. Grammel, *Stuttgart*
A. S. Hall, *Purdue*
J. P. den Hartog, *M. I. T.*
R. M. Haythornthwaite, *Ann Arbor*
P. G. Hodge, *Illinois Inst. Tech.*
N. J. Hoff, *Stanford*
J. H. Horlock, *Liverpool*
G. A. Horvay, *Schenectady*
J. A. Hrones, *Case*
D. C. Johnson, *Cambridge*
C. F. Kettleborough, *Sydney*
J. Kolakowski, *Baghdad*
J. Marin, *Penn. State*
D. Mordell, *McGill*
E. Pestel, *Hanover*
H. C. Rothbart, *New Jersey*
B. W. Shaffer, *New York*
M. Shaw, *Queensland*
M. C. Shaw, *M. I. T.*
M. F. Spotts, *Northwestern*
W. T. Thomson, *UCLA*
L. C. Woods, *Oxford*

Sub-Editor: A. V. Oldham, *Journals Department, Pergamon Press Ltd., Headington Hill Hall, Oxford, England*

Publishing Offices: Headington Hill Hall, Oxford, England (Oxford 64881)

Published bi-monthly.

Annual subscriptions (including postage): (A) for libraries, government departments or industrial establishments, £14 0s. 0d. (U.S.A. $40.00); (B) for subscribers who write directly to the publisher certifying that the journal is for their personal use, £5 5s. 0d. (U.S.A. $15.00).

Single issues £2 10s. 0d. (U.S.A. $9.00) each.

Copyright © 1961 Pergamon Press Ltd.

PERGAMON PRESS LTD.

Headington Hill Hall, Oxford, England 122 East 55th Street, New York 22, N.Y.

LIST OF CONTENTS

Vol. 3
1961

Numbers 1/2

PAGE

J. B. MARTIN: On the elastic-plastic behaviour of certain bents under transverse loading 1

R. I. TANNER: The estimation of bearing loads using Galerkin's method 13

D. J. RYLEY: Phase equilibrium in low-pressure steam turbines 28

ENRICO VOLTERRA: Second approximation of method of internal constraints and its applications 47

P. L. B. OXLEY: A strain-hardening solution for the "shear angle" in orthogonal metal cutting 68

CHARLES W. BERT: Analysis of a nonlinear torsional coupling having dynamic links—I. Steady running and free oscillation 80

H. KUDO: Some analytical and experimental studies of axisymmetric cold forging and extrusion—II 91

M. G. SHARMA: Resonant strength of a vibrating member having two degrees of freedom, with hysteresis damping 118

W. MERCHANT and S. A. SAAFAN: Critical pressures and buckling modes of regular polygonal prismatic tubes 129

C. F. KETTLEBOROUGH: The effect of pressure on viscosity in hydraulic lock 137

Book Reviews:

Determination of the Mechanical and Technological Properties of Metals, by B. M. GLINER. (Reviewed by J. H. LAMBLE) 143

Field Computations in Engineering and Physics, by A. THOM and C. J. APELT. (Reviewed by A. P. HATTON) 143

Number 3

H. E. ENAHORO and P. L. B. OXLEY: An investigation of the transition from a continuous to a discontinuous chip in orthogonal machining 145

J. L. BOGDANOFF and P. F. CHENEA: Dynamics of some disordered linear systems 157

R. I. LEWIS and J. H. HORLOCK: Non-uniform three-dimensional and swirling flows through diverging ducts and turbo-machines 170

J. C. MALTBAEK: The influence of a concentrated mass on the free vibrations of a uniform beam 197

T. M. WANG, S. L. LEE and O. C. ZIENKIEWICZ: A numerical analysis of large deflections of beams 219

Number 4

PAGE

J. B. HADDOW and W. JOHNSON: Indenting with pyramids—I. Theory 229

W. JOHNSON: An analogy between upper-bound solutions for plane-strain metal working and minimum-weight two-dimensional frames 239

P. S. PELL, P. F. MCCARTHY and R. R. GARDNER: Fatigue of bitumen and bituminous mixes 247

D. F. WHITE: Turbine operation with nonsteady flow-analysis and experiments 268

A. O. GILCHRIST: The free oscillations of conservative quasilinear systems with two degrees of freedom 286

Book Reviews:

Increasing the Loading on Gearing and Decreasing its Weight, edited by M. M. SAVERIN. (Reviewed by D. C. JOHNSON) 312

Progress in Combustion Science and Technology, edited by J. DUCARME, M. GERSTEIN and A. H. LEFEBVRE. (Reviewed by G. S. CANTLE) 312

Stress Concentration around Holes, by G. N. SAVIN. (Reviewed by D. R. BLAND) 313

Mathematical Methods for Engineers and Technologists, by P. I. ROMANOVSKII. (Reviewed by J. K. ROYLE) 314

AUTHOR INDEX

(B.R. indicates a Book Review)

BERT C. W.		80	LEWIS R. I.		170
BLAND D. R.	(B.R.)	313	MALTBAEK J. C.		197
BOGDANOFF J. L.		157	MARTIN J. B.		1
CANTLE G. S.	(B.R.)	312	MCCARTHY P. F.		247
CHENEA P. F.		157	MERCHANT W.		129
ENAHORO H. E.		145	OXLEY P. L. B.		68, 145
GARDNER R. R.		247	PELL P. S.		247
GILCHRIST A. O.		286	ROYLE J. K.	(B.R.)	314
HADDOW J. B.		229	RYLEY D. J.		28
HATTON A. P.	(B.R.)	143	SAAFAN S. A.		129
HORLOCK J. H.		170	SHARMA M. G.		118
JOHNSON D. C.	(B.R.)	312	TANNER R. I.		13
JOHNSON W.		229, 239	VOLTERRA E.		43
KETTLEBOROUGH C. F.		137	WANG T. M.		219
KUDO H.		91	WHITE D. F.		268
LAMBLE J. H.	(B.R.)	143	ZIENKIEWICZ O. C.		219
LEE S. L.		219			

Int. J. Mech. Sci. Pergamon Press Ltd. 1961. Vol. 3, pp. 1–12. Printed in Great Britain

ON THE ELASTIC–PLASTIC BEHAVIOUR OF CERTAIN BENTS UNDER TRANSVERSE LOADING

J. B. MARTIN
Engineering Laboratory, Cambridge

(*Received* 3 *December* 1960)

Summary—The load–deflexion characteristics of two idealized elastic, perfectly plastic, right-angle bents under loading normal to the plane of the structure are obtained analytically, and it is shown that large plastic deformations may be initiated at a load significantly less than the rigid–plastic collapse load. Experimental evidence is given to illustrate the effect.

Vol. 3
1961

THE theorems of plasticity referring to the collapse of a structure depend primarily on the definition of collapse. The definition and its justification have been given in various forms, notably by Baker *et al.*[1], Greenberg and Prager[2] and Drucker *et al.*[3, 4] The following passage is quoted from Drucker *et al.*[4] as the most general example of the definition and its justification, assuming an elastic, perfectly plastic relation between stress and strain.

1. "*Collapse.* From the point of view of the practical engineer the term collapse implies that appreciable changes in the geometry of a structure will occur under *essentially constant loads.* [Present author's italics.] For the purpose of the following discussion however it is more convenient to use the term collapse to refer to conditions for which plastic flow would occur under constant loads *if the accompanying change in the geometry of the structure or body were disregarded.* In the discussion of this type of collapse the equilibrium conditions can be set up for the undeformed rather than the deformed body. This obviously represents a great simplification because the deformation occurring during collapse is not known beforehand but constitutes one of the unknowns of the collapse problem.

"To illustrate the relations between these two definitions of collapse consider first a hollow sphere of uniform wall thickness under gradually increasing interior pressure. The material at the interior surface reaches the yield limit first, but its plastic deformation is contained by the surrounding shell of still elastic material. As the pressure continues to increase, the boundary between the elastic and plastic regions moves towards the exterior surface; only when it has reached this surface does large plastic flow become possible. Let us now compare the simplified stress analysis, which neglects all changes of geometry during the loading process, to the complete analysis which takes account of these changes. Even in the elastic range, and also in the subsequent range of contained plastic deformation, the hollow sphere expands and its wall thickness diminishes somewhat. If those effects are taken into account the pressure for which the entire sphere becomes plastic is found somewhat smaller than when they are neglected. However, the difference between the two pressure

values is small *because the deformations up to the end of the range of contained plastic deformation are of the order of magnitude of the elastic deformations.* [Present author's italics.] Continuing the analysis into the subsequent range of unrestricted plastic flow we find that the simplified analysis predicts flow under constant interior pressure, whereas the complete analysis predicts flow under gradually decreasing pressure. In either case the sphere loses its usefulness as a pressure vessel. As far as this first example is concerned the two definitions of collapse are in substantial agreement as to the pressure under which collapse sets in."

A mathematical characterization of collapse may be given as follows. Let the surface tractions be denoted by T, the surface traction rates by $\dot{T}$, the body forces by F, the rate of change of body forces by $\dot{F}$ and the velocity field by V. Let the subscript c refer to collapse. From the definition given above it follows that, during collapse,

$$\int \dot{T}_c V_c \, ds = 0 \quad \text{and} \quad \dot{F}_c = 0 \quad \text{for some} \quad V_c \neq 0 \tag{1}$$

where the integration is extended over the surface s which bounds the considered body or assemblage of bodies. Since collapse is to occur under constant loads $\dot{F}_c$ must vanish throughout the volume: further either $\dot{T}_c$ or V_c must vanish at any point on the surface of the structure.

The principle of virtual velocities states that

$$\int Q\dot{q} \, dV = \int T V \, ds \tag{2}$$

where Q is the generalized stress at any point, q the generalized strain, and rates are indicated as before. The first integral is taken over the volume of the body and the second over the area. The same relation will be true for stress and surface traction rates: further the strain rate may be divided into elastic and plastic parts, denoted by $\dot{q}'$ and $\dot{q}''$ respectively.

Then
$$\int \dot{Q}\dot{q}' \, dV + \int \dot{Q}\dot{q}'' \, dV = \int \dot{T} V \, ds \tag{3}$$

It may be shown, for example Hodge[5], that

$$\int \dot{Q}\dot{q}'' \, dV = 0 \quad \text{always}$$

and
$$\int \dot{Q}\dot{q}' \, dV > 0 \quad \text{except for} \quad Q = 0$$

Hence it follows that $\dot{Q}$ vanishes during collapse, and also, since $\dot{q}'$ is proportional to $\dot{Q}$, that $\dot{q}'$ vanishes. The argument thus shows that the modulus of elasticity does not influence the collapse load, and may therefore be arbitrarily increased to any degree. The collapse load for an elastic, perfectly plastic body will therefore coincide with the collapse load of a corresponding rigid, perfectly plastic body, and the collapse theorems derived for a rigid–plastic material may be applied to the elastic–plastic material.

2. In their discussion on the justification of their definition of collapse, Drucker *et al.*[4] admit of a "region of contained plastic flow" where plastic strain will occur under increasing load and be limited to the order of the elastic strain, and also of a "region of unrestricted plastic flow" under constant load where the plastic strain is not restricted by the elastic parts of the system. Since immediately prior to collapse plastic strains are limited to the order of elastic strains it is justifiable to neglect changes in geometry.

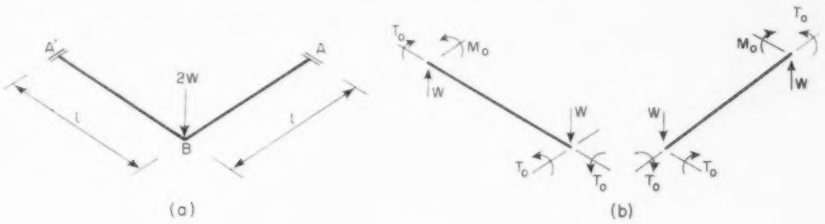

FIG. 1.

Drucker *et al.* do not admit, however, of the possibility of the existence of a transition region between that of contained plastic flow and that of unrestricted flow. Let us term such a region one of *restricted plastic flow*. In this region the plastic deformations will be only *partially* constrained by the elastic parts of the system: near the boundary between this region and that of contained flow the plastic deformations will be in the order of the elastic deformations. Progress through the region, caused by increasing load, will result in an increasing ratio of order of plastic strain to order of elastic strain: finally the region of unrestricted plastic flow is reached, where plastic deformation may increase without change in elastic deformation. There appears, in a perfectly general approach, *to be no justification in ignoring the possibility of the existence of such a region*. If such a region occurred during the loading history, the imminence of collapse (as defined in the definition of Drucker *et al.*) cannot be described by a condition of deformation in the order of the elastic deformation, *since the plastic strains may be large*. There are thus two possibilities to be considered: firstly that the deformations may be sufficiently large before collapse will have a significant effect on the equations of equilibrium, and secondly that the structure may become unserviceable at a load significantly less than the collapse load. The first factor will not be considered in the following discussion: examples will be chosen such that changes in geometry have negligible effect within the practical range of deflexion, and the effect on the equations of equilibrium will be ignored in analysis.

3. Consider first a right-angle bent loaded transversely at its tip (Fig. 1) with a load $2W$. Assume a flexural rigidity EI and a torsional rigidity which will be denoted by GJ. The equilibrium equation may be written

$$Wl = M_0 + T_0 \tag{4}$$

While the structure is completely elastic the compatibility equation is

$$\frac{l}{EI}\left[M_0 - \frac{Wl}{2}\right] = \frac{T_0 l}{GJ} \tag{5}$$

Vol. 3
1961

From these two equations the values of M_0 and T_0 may be obtained in terms of W.

Assume an elastic, perfectly plastic section: i.e. assume that under a given moment and torque any section behaves elastically until some limit is reached, and that thereafter the section is perfectly plastic. Let this yield limit be given by the equation

$$M^2+\alpha T^2 = M_p^2 \tag{6}$$

where M_p is the limit moment for a zero torque. When a section becomes plastic, bending rotation θ and twist ψ may take place at the section. According to the orthogonality condition (e.g. Hodge[5]), θ and ψ will be related by

$$\frac{d\psi}{d\theta} = \frac{\alpha T}{M} \tag{7}$$

Consideration of the example will show that plasticity will be first attained at the section at A, and that, owing to the shape of the bending moment diagram, plasticity will be confined to the section at A, forming a discrete hinge. As the load is increased, the hinges will deform, satisfying a revised compatibility equation

$$\frac{l}{EI}\left(M_0-\frac{Wl}{2}\right)+\theta = \frac{T_0 l}{GJ}+\psi \tag{8}$$

The values of M_0 and T_0 must satisfy equations (4) and (6): these may be solved for M_0 and T_0 in terms of W giving

$$T_0 = \frac{Wl-\sqrt{[(1+\alpha)M_p^2-\alpha W^2 l^2]}}{(1+\alpha)}$$

$$M_0 = \frac{\alpha Wl+\sqrt{[(1+\alpha)M_p^2-\alpha W^2 l^2]}}{(1+\alpha)} \tag{9}$$

Substituting these values in the orthogonality condition (7) we obtain

$$\frac{d\psi}{d\theta} = \frac{\alpha Wl-\alpha\sqrt{[(1+\alpha)M_p^2-\alpha W^2 l^2]}}{\alpha Wl+\sqrt{[(1+\alpha)M_p^2-\alpha W^2 l^2]}} \tag{10}$$

Differentiation of the revised compatibility equation (8) with respect to θ gives

$$\frac{d\psi}{d\theta} = 1-\frac{(1+R)}{EI(1+\alpha)}\frac{\alpha Wl^3}{\sqrt{[(1+\alpha)M_p^2-\alpha W^2 l^2]}}\frac{dW}{d\theta}-\frac{(1-\alpha+2R)}{EI}l^2\frac{dW}{d\theta} \tag{11}$$

where

$$R = \frac{EI}{GJ}$$

Elimination of $d\psi/d\theta$ from equations (10) and (11) gives a differential equation relating θ and W. Solving this equation by integrating with respect to W gives

$$\frac{EI\theta}{M_p l} = \frac{(1+\alpha+3\alpha R+2R-\alpha^2)}{(1+\alpha)^2}\frac{Wl}{M_p}+\frac{1}{2(1+\alpha)}\sqrt{\left(\frac{\alpha}{1+\alpha}\right)}\log\left\{\frac{\sqrt{[(1+\alpha)/\alpha]}+(Wl/M_p)}{\sqrt{[(1+\alpha)/\alpha]}-(Wl/M_p)}\right\}$$
$$-\frac{(2+3R-2\alpha R-\alpha^2)}{(1+\alpha)}\sqrt{\left[(1+\alpha)-\frac{\alpha W^2 l^2}{M_p^2}\right]}+C \tag{12}$$

The constant C may be evaluated by putting $\theta = 0$ at the elastic limit. Using virtual work methods, for example Heyman[6], the deflexion of the load point may be written as

$$\frac{EI\Delta}{M_p l^2} = \frac{EI\theta}{M_p l} + \left(\frac{M_0}{3M_p} - \frac{T_0}{2M_p}\right) \tag{13}$$

The values of the parameters $EI\theta/M_p l$ and $EI\Delta/M_p l$ have been calculated in terms of Wl/M_p, arbitrarily assigning $\alpha = 1$ and $R = 4/3$. The resulting curves are shown in Fig. 2. It may be seen that the rotation and deflexion increase rapidly after the formation of the hinges and that the load parameter tends to a limit of 1·414 at infinitely large deflexion. This limiting load is the rigid–plastic collapse load, and may be obtained directly by the application of the rigid–plastic collapse theorems (Heyman[7]).

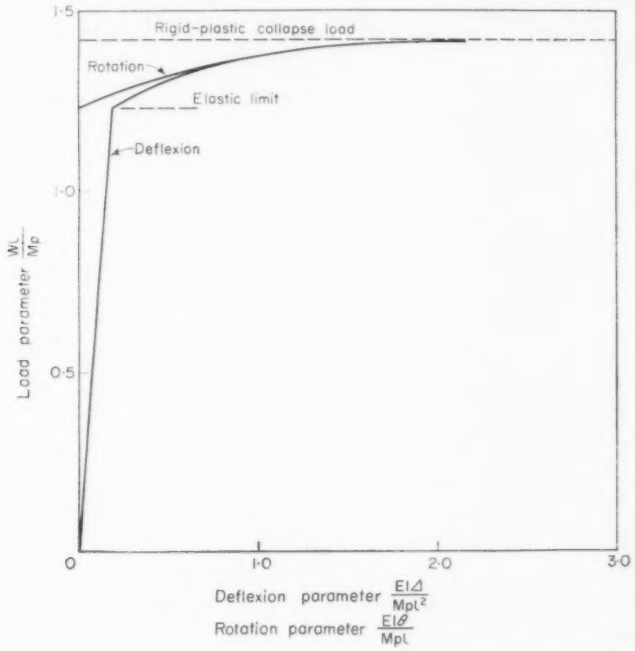

FIG. 2. Theoretical curves of deflexion–load and rotation–load for right-angle bent loaded at end, neglecting changes of geometry.

A better physical picture of the behaviour of the structure may be obtained from regarding the development of the rotations in the following manner. Plot the moment M_0 and torque T_0 at the hinge as a stress point on an interaction diagram (Fig. 3). The yield condition (6), equilibrium condition (4), and the elastic compatibility equation (5) may also be plotted on this diagram. As the load W is increased from zero the stress point will move up the elastic line, with plasticity occurring when it reaches the yield circle at point L. If the load is increased beyond this value the stress point must leave the elastic line and pass along the yield circle to the right. Since the elastic compatibility equation

(5) is satisfied only on the elastic line, deformation must take place at the hinge so that the revised compatibility equation (8) is satisfied. Disregarding for the present the orthogonality condition (7), the revised compatibility equation may be satisfied by assigning a value to the quantity $(\theta - \psi)$. Choose ψ as zero, and use a differential form of the equation so that a quantity $d\theta$ may be found which satisfies the compatibility requirements for an increase in load $d(Wl)$. The orthogonality condition must now be satisfied. This may be achieved by adding a suitable component to $d\theta$. The selection of a strain vector with components $d\theta_1$, $d\psi_1$ such that $(d\theta_1 - d\psi_1)$ is zero will not affect the compatibility equation. The quantities $d\theta_1$, $d\psi_1$ must be chosen so that the final strain rate vector $(\mathbf{d\theta} + \mathbf{d\theta_1}, \mathbf{d\psi_1})$ satisfies the orthogonality condition. This is shown diagrammatically in Fig. 4. A part of the yield circle is shown, and bending

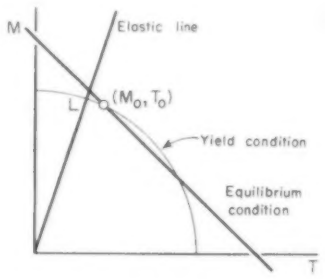

FIG. 3.

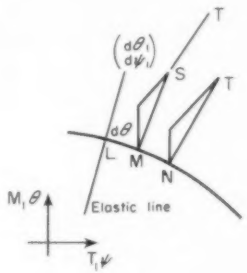

FIG. 4.

rotations θ are plotted in the direction of the M_0 axis, twists ψ in the direction of the T_0 axis. The orthogonality condition is satisfied when the strain vector is normal to the yield circle. Thus if a change in load $d(Wl)$ requires the stress point to move from L to M, the compatibility requirements demand a vector $\mathbf{d\theta}$ plotted with the point M as origin. The neutral vector $\mathbf{d\theta_1}$, $\mathbf{d\psi_1}$ is added to this such that the final strain vector **MS** is normal to the yield curve. A further incremental increase in load resulting in a movement of the stress point to N will, by the same mechanism, result in an increase in deformation shown by the vector **NT**. The total deformation at the hinge so far will thus be given by **MST**. It will be seen that as the stress point moves around the circle the angle between the orthogonal final increment vector and the neutral vector will become increasingly smaller, and hence the final vector and the neutral vector will become increasingly larger. The limit to the process occurs when the stress point reaches its furthest distance from the origin, measured in a direction normal to the equilibrium line. Under the assumption of neglect in changes in geometry this represents the largest load the structure may carry and is the rigid–plastic collapse load.

Consideration of the neutral vector will show that it is in fact a rotation of the structure about an axis passing through the supports, and, since it coincides with the deformation vector at the limiting load, is therefore a finite movement of the mechanism forecast by the rigid–plastic analysis. A mechanism motion may thus be regarded as having been initiated at the elastic limit, but is

restrained to a finite value by the elastic part of the system. The choice of ψ zero in satisfying the revised compatibility equation was prompted by the fact that it leads to the smallest positive required strain vector: the choice of any positive vector would lead to similar conclusions.

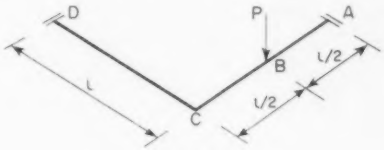

FIG. 5.

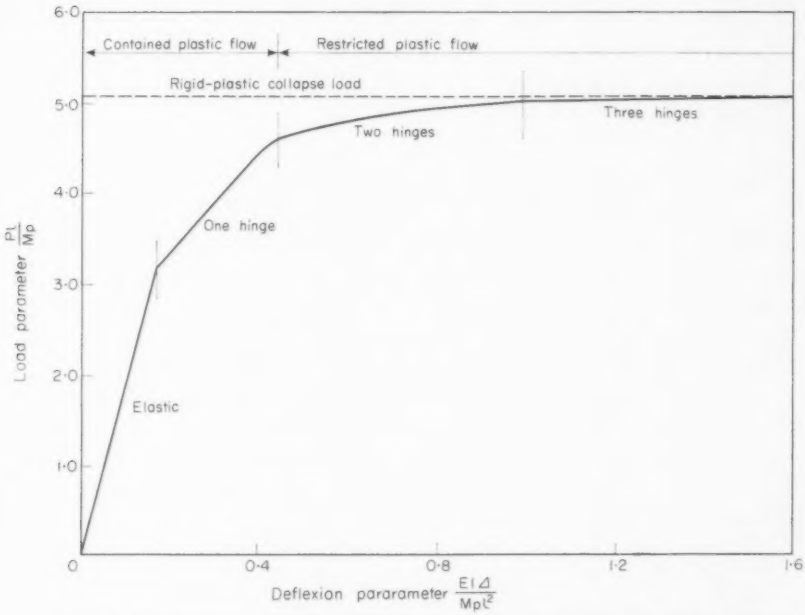

FIG. 6. Theoretical load–deflexion curve for right-angle bent loaded in centre of one leg, neglecting change in geometry.

Under the same basic assumptions a complete analysis of the same structure loaded in the centre of one leg has been made, as shown in Fig. 5. Rigid–plastic analysis (Heyman[7]) predicts collapse with three hinges, at A, B and D for $\alpha = 1$. The analysis was carried out incrementally, with hinges forming first at A, second at D and finally at B. The resulting load–deflexion curve is shown in Fig. 6. It may be seen that deflexions remain small while there is one hinge, but increase rapidly after the formation of the second hinge. In this case the existence of two hinges may be said to allow a finite deformation in a primitive mechanism: primitive in the sense that an additional hinge must be formed before limiting conditions are reached. The transition from contained to restricted flow takes place at the formation of the second hinge, or at the point where a primitive mechanism becomes possible.

Vol. 3
1961

4. The load–deflexion characteristics of both the examples given above exhibit a large and clearly defined change of slope at the boundary between the region of contained plastic flow and the region of restricted plastic flow. Term the load at which this transition takes place the *yield load*. A region of large deflexions is thus defined, with the yield load as a lower bound and the rigid–plastic collapse load as an upper bound.

The previous discussion has been limited to elastic, perfectly plastic section behaviour. Provided only discrete hinges are formed the argument may be justifiably extended to cover elastic, perfectly plastic stress–strain behaviour. Since the magnitude of the stress depends on the magnitude of the strain the deformations in the plastic part of the section will be limited to small order as long as any part of the section remains elastic. This will be less true as the elastic core of the section becomes very small: the effect of these elastic stresses on the stress resultant will, however, decrease rapidly as the elastic region becomes small, so that the section will behave substantially as if it were wholly plastic. Thus although the deflexions at the yield load will be increased, the yield load will not be substantially decreased.

As an indication of the relevance of the yield load and the region of large deflexions the observed load–deflexion curves obtained in two tests on model rectangular portal frames are presented in Figs. 7 and 8. The models were of rectangular section, approximately 0·300 in. by 0·250 in., and of approximately 9·5 in. height and span. Horizontal loads were applied, one in the plane of the frame in the line of the beam, and another transverse to the plane of the frame, in the centre of the beam. Theoretical calculations were made on the basis of an ultimate bending moment obtained from simply supported beam tests on specimens cut from the frame after testing. The value of α in the interaction equation (equation 6) was obtained theoretically. The rigid–plastic collapse and yield loads calculated on this basis are superimposed on the observed load–deflexion curves in the figures.

Tests carried out by Boulton and Boonsukha[8] on circular-arc bow girders also exhibit the characteristics described above. The load–deflexion curves from two of these tests are shown in Figs. 9 and 10. The first of these girders was of "H" section, and the second of square section. The rigid–plastic collapse load and the load at which a mechanism movement becomes possible (i.e. the yield load) were calculated by Boulton and Boonsukha: further details may be obtained by reference to the paper.

It may be seen from these curves that the yield load is successful in predicting the initiation of a region of large deflexions. The examples are such that within the range of deflexions recorded in the tests, changes in geometry have little effect on the rigid–plastic collapse load, and may be disregarded. Owing to the large plastic strains required before the limiting load is attained strain hardening must inevitably occur: this effect will be counterbalanced to some extent by the fact that the hinges are not confined to an infinitely thin section as assumed in the theoretical examples, but spread along the beam. The load–deflexion curve can thus be expected to flatten off considerably at or slightly above the rigid–plastic collapse load. Deflexions will, however, be large at this apparent limit.

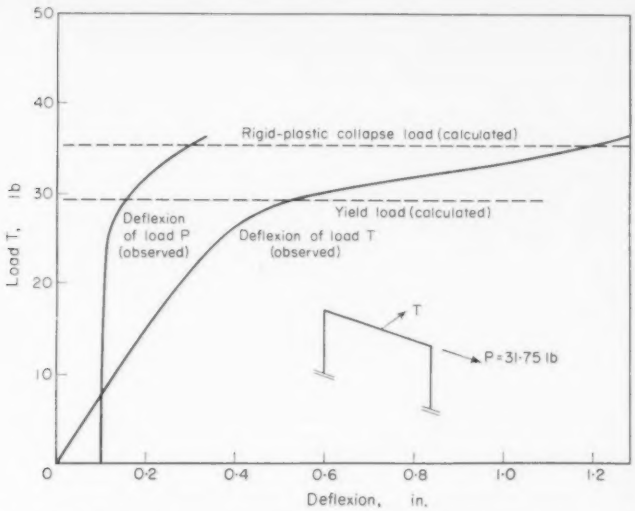

FIG. 7. Load–deflexion curve for portal frame loaded in and out of plane. Test B3.

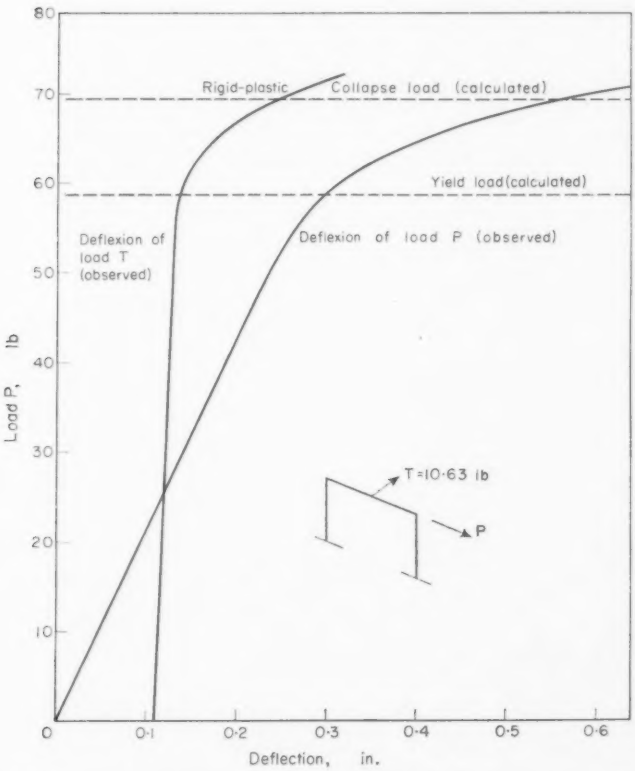

FIG. 8. Load–deflexion curve for portal frame loaded in and out of plane. Test B7.

Vol. 3
1961

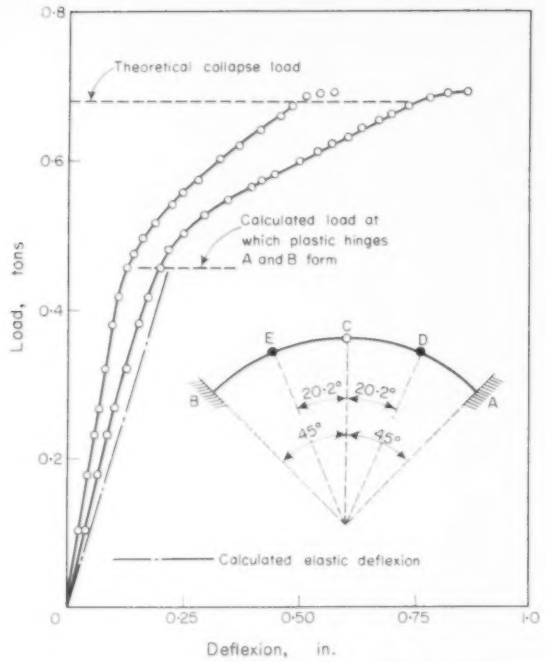

FIG. 9. Observed load–deflexion curves for bow girder H1 with central load. (After Boulton and Boonsukha[8].)

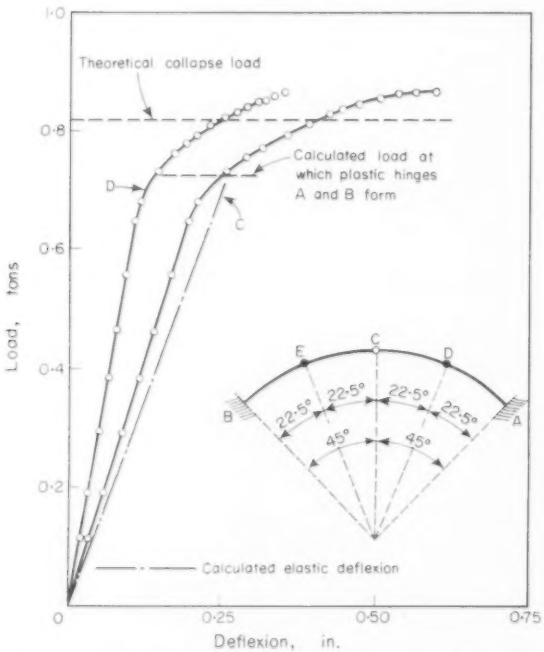

FIG. 10. Observed load–deflexion curves for bow girder S1 with central load. (After Boulton and Boonsukha[8].)

5. The phenomenon of restricted flow has been noted by Hill *et al.*[9] in connexion with the analysis of the elastic–plastic behaviour of a long thick tube under internal pressure, and by Lee[10] who discussed the phenomenon in relation to the limit load theorems of Drucker *et al.*[4] The case considered by Lee was the influence of lateral stresses introduced into a bar subject to tensile force. It is shown that full plasticity (corresponding to the initiation of restricted flow) occurs at a load approximately 2·6 per cent less than the limit load, and that the tensile force is within 0·1 per cent of the limiting value at a strain 2·5 times the strain at the elastic limit. These figures are used to justify the general accuracy of the collapse concept quoted at the beginning of this paper. In the first example given in Section 3 of this paper, restricted flow is initiated at a load 86·9 per cent of the limit load, and at a strain 2·5 times the elastic limit strain the load is about 91·5 per cent of the limit load. These quantities are considered significant: it is possible to obtain a yield load which is a much smaller proportion of the limit load. Further, the idealized elastic–plastic behaviour discussed is an upper bound on the behaviour of a structure with an elastic–plastic stress–strain characteristic.

Vol. 3
1961

The most general criterion of failure of a structure is that of unserviceability due to excessive deformation. This excessive deformation may occur in the elastic or contained flow regions: an example of such a case is in the design of pitch-roof portal frames. It is, however, more likely that it will occur due to restricted or unrestricted flow. The limit and yield loads become in general upper and lower bounds respectively on a zone of collapse. The limit load must be regarded as an upper bound: it is not justifiable to generalize the collapse concept of unrestricted plastic flow following contained flow. The yield load, as a lower bound on the zone of collapse, and the deflexion at the yield load become more significant as design tools.

In many cases the yield load is not significantly less than the limit load: particularly when the effect of one stress resultant acting at a hinge dominates the others. It may be shown that when there is only one stress resultant acting on the section the yield load and the limit or rigid–plastic collapse load will always coincide. More precise definition of the yield load and its relation to the general behaviour of the elastic–plastic structure will form the subject of a further paper.

Acknowledgements—The author is indebted to Professor N. S. Boulton for permission to use the test results presented in Figs. 9 and 10, and to Dr. J. Heyman for his valuable criticism and advice in the preparation of his paper.

Note added in proof

It has recently been brought to the notice of the author that similar work has been carried out by R. M. Haythornthwaite in an M.Sc. Thesis, Brown University, Graduate Division of Applied Mathematics, 1953 (unpublished).

REFERENCES

1. J. F. Baker, M. R. Horne and J. Heyman, *The Steel Skeleton* Vol. 2, p. 118 ff. Cambridge University Press (1956).
2. H. J. Greenberg and W. Prager, *Trans. Amer. Soc. Civ. Engrs.* **117**, 447 (1950).
3. D. C. Drucker, H. J. Greenberg and W. Prager, *J. Appl. Mech.* **18**, 371 (1951).

4. D. C. DRUCKER, H. J. GREENBERG and W. PRAGER, *Quart. Appl. Math.* **9**, 381 (1957).
5. P. G. HODGE, *Plastic Analysis of Structures* p. 195. McGraw Hill, New York (1960).
6. J. HEYMAN, On the estimation of deflexions in elastic–plastic framed structures. *Proc. Inst. Civ. Engrs.* To be published.
7. J. HEYMAN, *J. Appl. Mech.* **18**, 157 (1951).
8. N. S. BOULTON and B. BOONSUKHA, *Proc. Inst. Civ. Engrs.* **13**, 161 (1959).
9. R. HILL, E. H. LEE and S. J. TUPPER, *Proc. Roy. Soc.* **A191**, 278 (1947).
10. E. H. LEE, *Phil. Mag.* **43**, 549 (1952).

Vol.
196

Int. J. Mech. Sci. Pergamon Press Ltd. 1961. Vol. 3, pp. 13–27. Printed in Great Britain

THE ESTIMATION OF BEARING LOADS USING GALERKIN'S METHOD

R. I. TANNER
Department of Mechanical Engineering, University of Manchester

(*Received* 14 *November* 1960)

Summary—In the paper it is shown that the prediction of bearing loads and friction in hydrodynamic lubrication is a problem which may be effectively tackled by variational methods. Using the Galerkin method with an extrapolation procedure several examples are worked out to show how load estimates within a few per cent of the true value may be obtained with little labour on a desk machine.

It is shown that for a tilted flat pad of any shape the approximate load values obtained form a lower-bound sequence always less than the true load. Certain other load integrals are also bounded, and it is shown that the approximate values of the work input to the bearing are also a lower-bound sequence.

The advantage of the method over relaxation, for example, is that it involves no special knowledge other than the ability to differentiate and integrate polynomials and trigonometric expressions. Being a semi-analytical procedure a whole range of bearing width/length ratios can be worked out together up to the final stage, giving a great economy in effort.

NOTATION

h	film thickness
p	pressure
x, y, z	co-ordinates
η	viscosity
U_1, U_0	x-
V_1, V_0	y- components of velocity of planes $z = h$, $z = 0$, respectively
X, Y	non-dimensional co-ordinates
c	slope of Michell pad
P	non-dimensional pressure
P^+	non-dimensional pressure not satisfying Reynolds' equation
$a_1, a_2, \ldots$	disposable constants
N	bearing load
l, R	bearing dimensions
h_0	oil film thickness at origin
F_i	surface tractions
f	$\equiv \frac{\partial}{\partial x}\{h(U_1+U_0)\}+\frac{\partial}{\partial y}\{h(V_1+V_0)\}$
e	eccentricity
P_H, P_V, N^*, F	non-dimensional horizontal load component, vertical load component, total load and friction load respectively

Other symbols are defined in the text.

INTRODUCTION

DESPITE the large array of charts and tables now available for the estimation of bearing loads in hydrodynamic lubrication it is unlikely that the characteristics of every shape which may be considered in a design will be at hand.

Given a bearing problem with side leakage not covered by a design chart, it is usually safe to assume that the Reynolds equation[1] for the pressure distribution

$$\frac{\partial}{\partial x}\left(h^3\frac{\partial p}{\partial x}\right)+\frac{\partial}{\partial y}\left(h^3\frac{\partial p}{\partial y}\right)=6\eta\left[\frac{\partial}{\partial x}\{h(U_1+U_0)\}+\frac{\partial}{\partial y}\{h(V_1+V_0)\}\right] \tag{1}$$

is not solvable in closed form, and an approximate method for finding the loads must be found.

Various methods of load estimation are given in the literature. Gümbel[2], in the journal-bearing problem, approximates the pressure distribution by considering it to be parabolic across the bearing and to have the same form as the infinite width bearing around the shaft. Vogelpohl[3] refined this method by giving an optimum series development for the distribution across the bearing. Boswall[4] gives examples in which he assumes the pressure distribution is of the form $f(x)g(y)$; he then takes a simple form for $g(y)$ and solves the resulting differential equation for $f(x)$. Ocvirk[5] has given a useful treatment for narrow bearings.

The above methods generally involve the solution of more or less complicated ordinary differential equations or the introduction of errors which may be large. More precise methods for the solution of equation (1) have been given by Kingsbury[6], who used an electrical analogy, and by Christopherson[7], who used relaxation methods. Recently many authors have used digital computers in the solution of bearing problems. These techniques all need some special skill or experimental facility for their effective application to a new configuration, and may not always be rapidly applicable.

It is surprising that so little mention has been made of variational methods of "solving" equation (1). No less an authority than Courant[8] has re-emphasized their power in a recent lecture. Only four papers applying variational methods to lubrication analysis have been found by the author.

Chein[9] showed in 1949 that the prediction of the pressure distribution can be reduced to a variational problem. Starting from the Navier–Stokes equations he shows that the Reynolds equation is a first approximation in terms of the Reynolds number and a second approximation in terms of a film-thickness parameter. For a plane slider of infinite width he shows that the variational solution is the same as the exact solution. For finite-width sliders he takes a crude solution of the form

$$P=a_1x(1-x)\,y(k-y)/h_m^2 \tag{2}$$

where k = width/length of the pad.

Comparison with the work of Muskat *et al.*[10] shows that the friction is close to the true value. This is not surprising as the friction is frequently almost independent of the pressure distribution.

Wang[11] has apparently used the Rayleigh–Ritz method to solve plane slider and finite full-journal bearing problems. He thus avoids the solution of differential equations. Weber[12], in the solution of the finite journal bearing, assumes $p = f(\theta)g(y)$ and finds a differential equation for f, which he solves numerically. The author believes that the necessity for solving the differential equation detracts from the value of the method.

Hays[13] in a recent paper sets up the variational problem directly, starting from Helmholtz' theorem[14] on minimal energy dissipation. He then solves the finite full-journal bearing problem, but does not use the boundary outlet condition, $dp/d\theta = 0$, $p = 0$, usually associated with this problem. He uses a large number of terms in the variational solution and solves the resulting 20×20 or 40×40 matrices by digital computation.

While the methods of Hays[13] and Weber[12] give good results (with a correspondingly large amount of labour) for the pressure distribution this is normally not of much interest in bearing problems, the integrated load and friction being usually all that is required. (This is to be contrasted with stress problems, for example, where the magnitude of the largest stress is the important quantity.) Therefore, a highly approximate pressure distribution containing a few disposable parameters may be expected to give an exceedingly close estimate for the load and an even better percentage estimate for the friction. In view of the assumptions, such as that of isoviscosity, made in deriving the Reynolds equation, a good approximation to the true load is all that should be expected from the solution of the equation in any case.

The optimum values of the disposable constants may be chosen by the Rayleigh–Ritz method or the more direct but less well-known Galerkin[15] method. For these methods no special mathematical knowledge is required.

In this paper it is shown how the latter method may be used to give underestimates of the friction drag on a bearing, and how, for certain configurations, one is able to prove that the approximate load capacity calculated is also definitely less than the true value. This gives, of course, an estimate on the safe side.

The paper is concerned only with cases in which the zero-pressure boundary is given. Some slight modification of the direct procedure given here would be necessary for problems in which the boundary of zero pressure is not known beforehand, and it is not yet known if the procedure is much more convenient than relaxation in these cases. Therefore no discussion of this type of problem is given.

THE GALERKIN METHOD

An excellent account of this method is now readily available in English;[15] only a brief summary is given here.

If the Reynolds equation is written in the form given in equation (1), then it is shown[15] that the Galerkin and Ritz methods give the same approximate results, but the former is a little more direct. In order to make use of the maximum-work principle (see Appendix I) it is necessary to write the lubrication equation as in equation (1), which is fortunately the natural form in which it occurs.

Vol. 3
1961

Write the Reynolds equation for brevity as

$$L(p) = 0 \tag{3}$$

An approximate solution is sought of the form

$$p^+ = \sum_{i=1}^{n} a_i \phi_i(x, y) \tag{4}$$

where all the ϕ_i are functions chosen to satisfy the boundary conditions on p. a_i are constants to be determined. Obviously the ϕ_i do not satisfy equation (3).

In the Galerkin procedure the ϕ_i are made orthogonal to $L(p^+)$. That is, one puts

$$\iint_S L(p^+)\,\phi_i\,dx\,dy = \iint_S \left(\sum_{j=1}^{n} a_j \phi_j\right) \phi_i\,dx\,dy \tag{5}$$

where $i = 1 \ldots n$.

If p^+ were the exact solution then equation (5) would automatically be satisfied. In the approximate procedure, equation (5) leads to n simultaneous equations for the a_i, which are then solved.

The ϕ_i are usually chosen to be simple polynomials or trigonometric series. This has the great advantage that the process consists mainly of manipulation of these simple functions.

THE MICHELL PAD

To assess the value of the method the classic problem first worked out by Michell[16] in 1905 was attempted. The co-ordinate system given in Fig. 1 was used, the pad being square and the inlet film thickness twice that of the outlet.

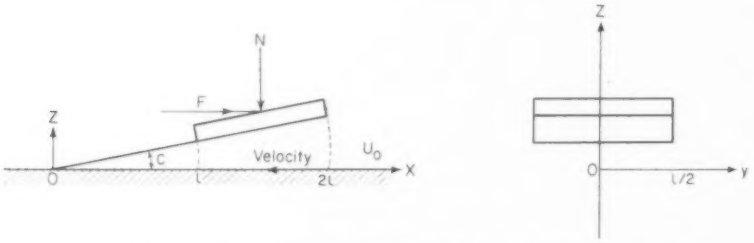

FIG. 1. Co-ordinates for Michell pad problem.

Written in non-dimensional form, the Reynolds equation becomes, with $h = cx$,

$$X^3 \frac{\partial^2 P}{\partial X^2} + 3X^2 \frac{\partial P}{\partial X} + X^3 \frac{\partial^2 P}{\partial Y^2} + 1 = 0 \tag{6}$$

where $P = pc^2 l/6\eta |U_0|$, $x = lX$, $y = lY$.

The boundary conditions are that

$$P = 0 \quad \text{when} \quad \begin{cases} X = 1, 2 \\ Y = \pm \frac{1}{2} \end{cases} \tag{7}$$

A simple set of functions for P^+ will be

$$P^+ = (X-1)(X-2)(Y^2 - \tfrac{1}{4})(a_1 + a_2 X + a_4 X^2 + a_6 Y^2 + a_7 X^3 + a_9 X Y^2 + \ldots) \tag{8}$$

where all the constants in odd powers of Y have been put equal to zero because of the symmetry about the X-axis.

Working with the first two constants only, $L(P^+)$ turns out to be

$$L(P^+) = 1 + 4a_1 X^3 + (4a_2 - 6a_1) X^4 + (2a_1 - 6a_2) X^5 + 2a_2 X^6 + (Y^2 - \tfrac{1}{4})[(6a_2 - 9a_1) X^2 + (8a_1 - 24a_2) X^3 + 15a_2 X^4] \quad (9)$$

This is to be multiplied by ϕ_1 and ϕ_2 in turn. ϕ_1 is $(X-1)(X-2)(Y^2-\frac{1}{4})$ and ϕ_2 is $X(X-1)(X-2)(Y^2-\frac{1}{4})$. Upon integrating over the pad area, two simultaneous equations for a_1 and a_2 emerge

$$\left.\begin{aligned} 2{\cdot}52857a_1 + 4{\cdot}10635a_2 &= 0{\cdot}83333 \\ 4{\cdot}10635a_1 + 6{\cdot}87262a_2 &= 1{\cdot}25 \end{aligned}\right\} \quad (10)$$

It will be noticed that the coefficient of a_1 in the second equation is the same as the coefficient of a_2 in the first equation. In fact, it turns out that the coefficients of the equations always form a matrix symmetrical about the leading diagonal when the equation is of the form (1). If, for example, one divides equation (1) through by h^3, then this will no longer be so.

The symmetry of the coefficients can either be used to save labour or to provide a partial check on the work.

Solution of the equations (10) gives $a_1 = 1{\cdot}1521$, $a_2 = -0{\cdot}0565$; integration of p^+ over the pad area gives the following result for the load:

$$N = 0{\cdot}0654\eta |U_0| l/c^2 \quad (11)$$

The value given by Michell[16, 17] is

$$N = 0{\cdot}0669\eta |U_0| l/c^2 \quad (12).$$

Further terms were taken to get a closer approximation and the values obtained are given below, including a figure based on Refs. 1 and 10, which appears to be tolerably correct.

Table 1. Square Michell pad loads

Source	Value of $Nc^2/\eta \lvert U_0 \rvert l$	Error (%)
Muskat *et al.*[10]; Fuller[1]	(about) 0·0698	—
Michell[16, 17]	0·0669	−4·1
Extrapolated value (see Appendix II)	0·0694	−0·7
First-term approximation	0·0549	−21·3
First-two-term approximation	0·0654	−6·3
First-three-term approximation	0·0683	−2·1
First-four-term application	0·0687	−1·6

While the author wishes in no way to detract from Michell's pioneering work it seems that the sheer numerical problem of evaluating "exact" solutions may lead to inaccurate values for the loads.

Vol. 3
1961

Exactly the same process can be applied to a pad of any shape, the boundary of which is describable by an algebraic relation. As a simple example, a Michell pad of circular plan (radius R) and inclination c was chosen. The co-ordinate axes were located from the pad centre, where the thickness of the oil film is h_0.

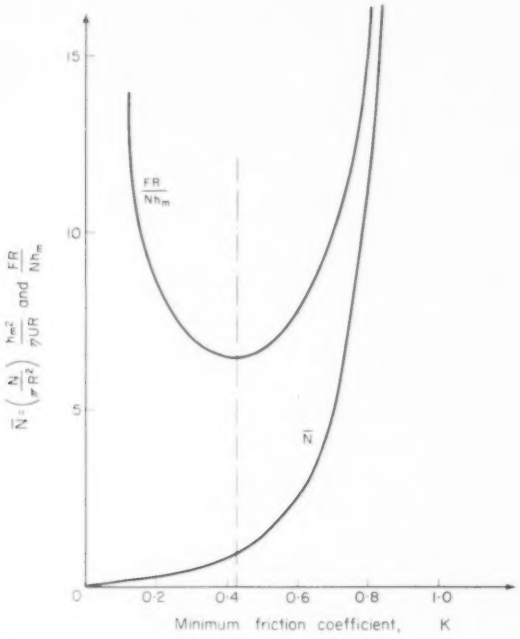

FIG. 2. Friction coefficient and load factors for circular Michell pad for given minimum film thicknesses h_m.

Putting
$$X = Rx$$
$$Y = Ry$$
$$K = Rc/h_0$$
and
$$P = ph_0^3/6\eta UR^2 c$$

the Reynolds equation may be rewritten

$$\frac{\partial}{\partial X}\left[(1+KX)^3\frac{\partial P}{\partial X}\right]+\frac{\partial}{\partial Y}\left[(1+KX)^3\frac{\partial P}{\partial Y}\right]+1=0 \tag{13}$$

Assume $P=(1-X^2-Y^2)(a_1+a_2X+\ldots)$, using only the first two terms. After integration of the $L(p)\phi_i$ over the pad area, two equations are obtained for a_1 and a_2

$$\left.\begin{aligned} a_1(1+K^2)+a_2\left(\frac{3K}{4}+\frac{5K^3}{32}\right)&=\tfrac{1}{4}\\ a_1\left(\frac{3K}{4}+\frac{5K^3}{32}\right)+a_2\left(\frac{1}{3}+\frac{7K^2}{16}\right)&=0\end{aligned}\right\} \tag{14}$$

In this case a_2 contributes nothing to the load, $a_2\phi_2$ being asymmetric with respect to the pad centre. Solving for a_1 gives

$$a_1 = \frac{16(16+21K^2)}{64(1+K^2)(16+21K^2) - K^2(24K+5K^2)^2} \tag{15}$$

which may rapidly be tabulated for various values of K.

Using only one term gives

$$a_1 = \tfrac{1}{4}(1+K^2) \tag{16}$$

For $K = \frac{1}{3}$, which corresponds to the case of the square pad previously worked out, one finds that the first two estimates for the load are

$$Nc/2\eta UR = 0{\cdot}0393, 0{\cdot}0414$$

The approximate load function and coefficient of friction are shown in Fig. 2. They are plotted in terms of the trailing-edge film thickness, h_m. The minimum-friction coefficient occurs when K is about 0·43, i.e. inlet film thickness is about $2{\cdot}5h_m$. This is the same result as that for the square pad.

Vol. 3
1961

THE APPROXIMATE LOAD—A LOWER BOUND IN CERTAIN CASES

For the square Michell pad it was seen that the approximate load calculation appeared to approach the true load from below. This can be easily proved for this configuration, starting from the result for the drag given in Appendix I.

This may be written, after transforming the first two terms on the right-hand side of equation (40) using Green's theorem and cancelling the constant term,

$$\iint_S F_i V_i \, dS = \iint_S pL(p)\, dS - \iint_S pf\, dS \geqslant \iint_S p^+ L(p^+)\, dS - \iint_S p^+ f\, dS \tag{17}$$

where

$$f \equiv \frac{\partial}{\partial x}[h(U_1+U_0)] + \frac{\partial}{\partial y}[h(V_1+V_0)] \tag{18}$$

This obviously reduces to

$$-\iint_S pf\, dS \geqslant -\iint_S p^+ f\, dS \tag{19}$$

For the Michell pad $f = -(\partial/\partial x)(cxU) = -Uc$. Hence the result is obtained

$$N = \iint_S p\, dS \geqslant \iint_S p^+\, dS = N^+ \tag{20}$$

and the approximate load is a lower bound. If the equation is divided by h^3 before applying the Galerkin method, the first approximation to the load will be $0{\cdot}0736\eta Ul/c^2$ which is greater than the true load. Unfortunately, it seems that such definite results cannot be obtained for all configurations. Only when it is needed to calculate a constant $\times \iint pf\, dS$ will a definite bound be furnished. Fortunately, the method appears to converge so rapidly that this is not a great disadvantage.

THE FINITE FITTED PARTIAL-JOURNAL BEARING— THE USE OF TRIGONOMETRIC SERIES

The solution to this problem has been computed recently.[18] It illustrates the difficulties which may be present unless a computer of the largest size is available. In Ref. 18 moderate accuracy has been achieved from considerable machine time; the results are presented to 2-figure accuracy only, which means a possible error of nearly ± 5 per cent in certain cases. Such an accuracy, which is probably all that can be justified for practical calculations, can readily be obtained with a few terms in a variational method.

The configuration shown in Fig. 3 was used to define the co-ordinate system. The film thickness $h = e\cos\theta$. The pressure is assumed zero at $y = \pm lR$, $\theta = 0$ and $\theta = \pi/K$ $(K > 2)$, although a slight modification would allow the positive pressure to begin at any angle.

Putting $P = pe^2/6\eta UR$, $Y = y/R$, the Reynolds equation becomes

$$\frac{\partial}{\partial\theta}\left(\cos^3\theta\frac{\partial P}{\partial\theta}\right)+\frac{\partial}{\partial Y}\left(\cos^3\theta\frac{\partial P}{\partial Y}\right)+\sin\theta = 0 \tag{21}$$

Assume a double trigonometric series for p^+,

$$p^+ = \sum_{m=1,3\ldots}^{\infty}\sum_{n=1}^{\infty} p_{m,n} = \sum_{m=1,3\ldots}^{\infty}\sum_{n=1}^{\infty} a_{mn}\cos\frac{m\pi Y}{2l}\sin nK\theta \tag{22}$$

Each term satisfies the boundary conditions. A polynomial could have been chosen for the Y-variation, or indeed for the θ-variation, but since trigonometric functions occur in $L(P)$ it is possible to simplify the integration by choosing a double trigonometric series for P^+.

Forming $\phi_{q,r}\,L(p_{m,n})$ and integrating over the y-positive half of the bearing gives the following result, upon writing $(n-r)K = a$, $(n+r)K = b$

$$\begin{aligned}
&\int_0^l\int_0^{\pi/K}\phi_{q,r}[L(p_{m,n})-\sin\theta]\,d\theta\,dY = 0 \quad (m\neq q)\\
&\quad = -\frac{a_{mn}}{32}\,l\left(n^2K^2+\frac{m^2\pi^2}{4l^2}\right)\left[\frac{3\sin(a+1)\theta}{a+1}+\frac{3\sin(a-1)\theta}{a-1}-\frac{3\sin(b+1)\theta}{b+1}\right.\\
&\qquad\left.-\frac{3\sin(b-1)\theta}{b-1}+\frac{\sin(a+3)\theta}{a+3}+\frac{\sin(a-3)\theta}{a-3}-\frac{\sin(b+3)\theta}{b+3}-\frac{\sin(b-3)\theta}{b-3}\right]_0^{\pi/K}\\
&\qquad-\frac{3a_{mn}}{32}\,nkl\left[\frac{\sin(b-1)\theta}{b-1}-\frac{\sin(b+1)\theta}{b+1}+\frac{\sin(a+1)\theta}{a+1}-\frac{\sin(a-1)\theta}{a-1}\right.\\
&\qquad\left.+\frac{\sin(b-3)\theta}{b-3}-\frac{\sin(b+3)\theta}{b+3}+\frac{\sin(a+3)\theta}{a+3}-\frac{\sin(a-3)\theta}{a-3}\right]_0^{\pi/K} \quad (m=q)
\end{aligned} \tag{23}$$

Also

$$\int_0^l\int_0^{\pi/K}\phi_{m,r}\sin\theta\,d\theta\,dY = (-1)^{(m-1)/2}\frac{l}{\pi m}\left[\frac{\sin(rk-1)\theta}{rk-1}-\frac{\sin(rk+1)\theta}{rk+1}\right]_0^{\pi/K} \tag{24}$$

As an example consider a bearing whose width is equal to the shaft radius $(l = \frac{1}{2})$ and which extends from $\theta = 0$ to $\theta = 60$ degrees. Thus $K = 3$. As an approximate solution put $m = 1$ (cosine distribution across the bearing) and take $n, r = 1$, 2 and 3.

Substituting these numbers in the above equations gives three simultaneous equations for a_{11}, a_{12} and a_{13}. Only nine coefficients need be calculated because of the symmetry of the equations. Solving gives the following values for a_{11}, a_{12} and a_{13}.

$$a_{11} = 0{\cdot}08597,\ a_{12} = -0{\cdot}03641,\ a_{13} = 0{\cdot}01378$$

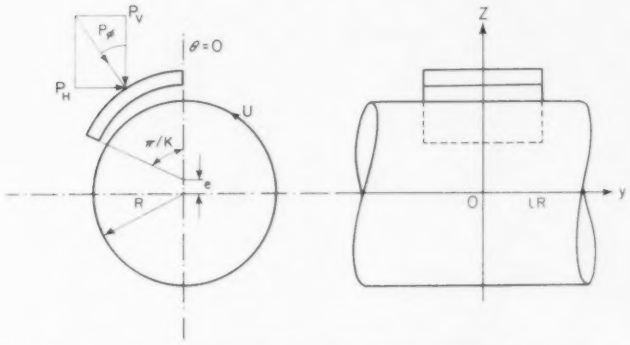

FIG. 3. Co-ordinates for partial fitted-bearing problem.

The values of P, $P\cos\theta$ and $P\sin\theta$ for the one-, two- and three-term approximations and for the computed solution are shown in Figs. 4, 5 and 6. The values of

$$P_H \equiv 2\int_0^l\int_0^{\pi/3} P\sin\theta\,d\theta\,dY,\quad P_V \equiv 2\int_0^l\int_0^{\pi/3} P\cos\theta\,d\theta\,dY,\quad N^* \equiv \sqrt{(P_H^2+P_V^2)},$$

$$\phi \equiv \tan^{-1}(P_H/P_V)\quad\text{and}\quad F \equiv 2\int_0^l\int_0^{\pi/3}\left[\sec\theta+3\cos\theta\frac{\partial P}{\partial\theta}\right]d\theta\,dY$$

are given below in Table 2.

TABLE 2. LOADS ON SECTOR BEARING

Source	P_H	P_V	N^*	ϕ (degrees)	F
One-term approximation	0·014	0·024	0·028	30	1·40
Two-term approximation	0·020	0·028	0·034	35	1·43
Three-term approximation	0·022	0·030	0·037	36	1·43
Extrapolation (see Appendix II)	0·025	0·033	0·041	37	1·44
Computed solution[18]	0·024	0·032	0·040	37	1·22

Thus the three-term plus extrapolation (see Appendix II) "solution" appears to be almost as accurate as the computed solution in this case. The computed friction value must be in error.

For this geometry it can be proved that P_H is a lower bound, but the author has been unable to prove this for P_V, and hence for N^*. It appears from the table that these loads do approach the true values from below.

Vol. 3
1961

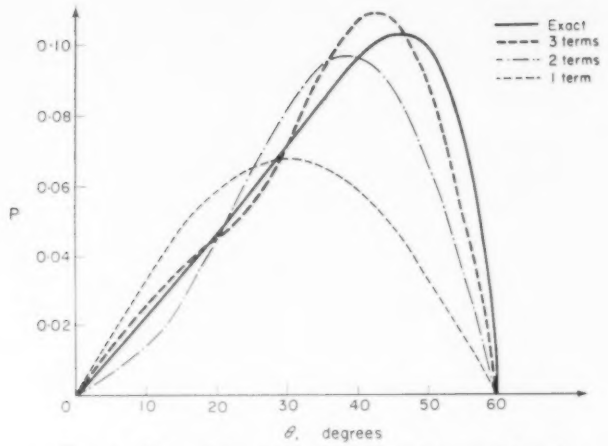

FIG. 4. P vs. θ for 60° partial fitted journal bearing.

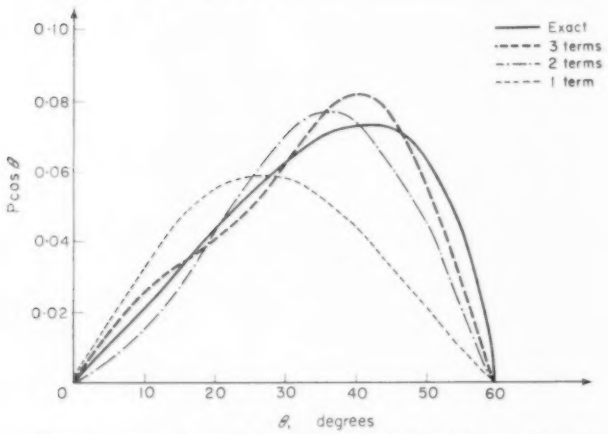

FIG. 5. $P \cos \theta$ vs. θ for 60° partial fitted journal bearing.

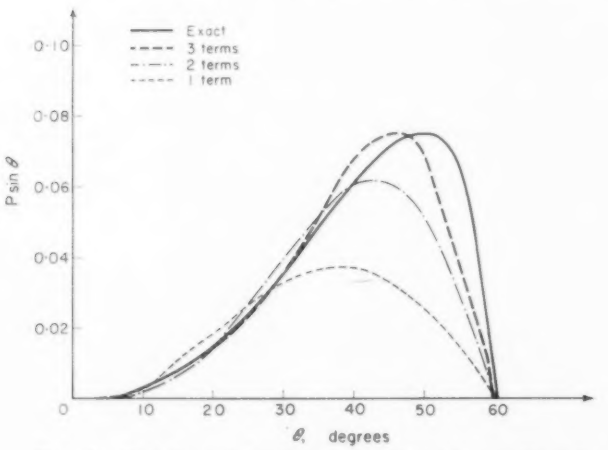

FIG. 6. $P \sin \theta$ vs. θ for 60° partial fitted journal bearing.

CONCLUSIONS

The method presented gives results of adequate accuracy for relatively little labour. Although no useful direct estimate of the final error can be given, the rate of convergence when one extra term in each variable is included gives a good indication of the distance from the true solution. For example, in the square Michell pad problem, after the first two estimates, an extra term in X improves the solution by 4 per cent but the extra Y term improves the load estimate by only 0·5 per cent. Therefore one can be tolerably certain that the load estimate is within at least 4 per cent of the true value. Three terms seem to give a reasonably accurate estimate; only two terms barely suffice. The fitted bearing gives less-accurate results with the same number of terms. Here the "exact" estimate is too hazy to make it worth while computing further values.

The advantage of the semi-analytical procedure is shown here; all the possible configurations have a large number of common steps. The same remark applies to the circular Michell pad problem.

It has been estimated[19] that the circular Michell pad problem would take about five times as long at least by hand relaxation methods. The actual machine time in digital computation is, of course, a matter of minutes. However, it is the author's observation that even with fairly experienced programmers the time required to solve a problem can sometimes run into weeks or months.

It is not the contention of the author that the Galerkin procedure solves the Reynolds equation. A glance at Figs. 4, 5 and 6 shows that the first few estimates bear little relation to the true profile. In fact, depending on the choice of the ϕ_i functions, many first approximations can be constructed, so that it is incorrect to claim that variational methods used in the above manner solve the Reynolds equation. However, they do provide a very economical method of solving the engineering problem of load prediction.

APPENDIX I

Proof that the frictional work is a maximum for the exact solution of the lubrication problem

The equations of inertialess incompressible viscous flow derive from the equilibrium equations with the inertia terms omitted, which may be written

$$\frac{\partial p_{ik}}{\partial x^k} = \frac{\partial p}{\partial x^i} \tag{25}$$

and the linear relation between deviatoric stress tensor p_{ik} and the flow tensor (or deformation-rate tensor) d_{ik}

$$p_{ik} = 2\eta\, d_{ik} \tag{26}$$

The continuity equation gives a third equation. The linearity of the above equations enables one to adapt directly the extremum principle proof given for a linear elastic body, which may be found in many books; for example Ref. 20.

In general, the velocities will be prescribed over part of the surface of the fluid volume (say on S_v), and on the remainder the stresses are prescribed (say on S_s).

If the p, p_{ik}, d_{ik} satisfy equations (25) and (26), the continuity equation and all the boundary conditions, then p, p_{ik}, d_{ik} give the true solution of the problem. Let p^+, p^+_{ik}, d^+_{ik} be any other state satisfying equations (25), (26) and the boundary conditions but not the continuity equation.

By exactly similar considerations to the elastic case one can prove that

$$(p^+_{ik}d^+_{ik} - p_{ik}d_{ik}) \geqslant 2(p^+_{ik} - p_{ik})d_{ik} \tag{27}$$

where the equality only holds if $p^+_{ik} = p_{ik}$. The quantities on the left-hand side of equation (27) represent local rates of energy dissipation per unit volume. Therefore, unless $p^+_{ik} = p_{ik}$ everywhere,

$$\iiint_V (p^+_{ik}d^+_{ik} - p_{ik}d_{ik})\,dV > 2\iiint_V (p^+_{ik} - p_{ik})d_{ik}\,dV \tag{28}$$

and by the use of Green's theorem and the equilibrium equations, it can be shown that

$$\iiint_V (p^+_{ik}d^+_{ik} - p_{ik}d_{ik})\,dV > 2\iint_{S_V} (F^+_i - F_i)V_i\,dS \tag{29}$$

where F_i are the tractions on the ports of the boundary where the velocities (V_i) are specified.

For the type of problem considered in this paper the stresses over S_s are zero, and, therefore, by equating work input to dissipation rate, one has

$$\iint_{S_V} F_i V_i\,dS = \iiint_V p_{ik}d_{ik}\,dV \tag{30}$$

Hence (28) becomes

$$\iint_S F_i V_i\,dS > 2\iint_S F^+_i V_i\,dS - \iiint_V p^+_{ik}d^+_{ik}\,dV \tag{31}$$

In the application to lubrication theory it is of interest to note that since the Reynolds equation itself is an approximation, frictional loads calculated from it will be slightly higher than the true solution of the creeping-flow equations.

In view of the approximation made in the Reynolds equation it seems necessary to investigate the extremal principles directly from the lubrication equations. To do this use is made of the proposition that the solution u of the equation

$$\frac{\partial}{\partial x}\left(a\frac{\partial u}{\partial x}\right) + \frac{\partial}{\partial y}\left(b\frac{\partial u}{\partial y}\right) = f \tag{32}$$

minimizes the integral

$$\iint_D \left[a\left(\frac{\partial u}{\partial x}\right)^2 + b\left(\frac{\partial u}{\partial y}\right)^2 + 2fu\right] dx\,dy \tag{33}$$

The proof is given in Ref. 15.

Let us investigate the rate of dissipation, D, minus twice rate of working by surface forces, $2\iint F_i V_i \, dS$, on the assumption that the only velocities are u and v, given by

$$\frac{\partial u}{\partial z} = \frac{1}{2\eta}\frac{\partial p}{\partial x}(2z-h) + \frac{U_1 - U_0}{h} \tag{34}$$

and a similar expression for v.

The local value of the dissipation is given by $\eta[(\partial u/\partial z)^2 + (\partial v/\partial z)^2]$.

Integration throughout the volume gives

$$D = \iint_S \frac{h^3}{12\eta}\left\{\left(\frac{\partial p}{\partial x}\right)^2 + \left(\frac{\partial p}{\partial y}\right)^2\right\} dx\,dy + \iint_S \frac{\eta}{h}\{(U_1-U_0)^2 + (V_1-V_0)^2\}\,dx\,dy \tag{35}$$

Subtraction of twice the rate of working over the surface S gives

$$\begin{aligned} D - 2\iint_S F_i V_i \, dS \equiv \iint_S \frac{h^3}{12\eta}\left\{\left(\frac{\partial p}{\partial x}\right)^2 + \left(\frac{\partial p}{\partial y}\right)^2\right\} dx\,dy \\ - \iint_S h\left\{\frac{\partial p}{\partial x}(U_1+U_0) + \frac{\partial p}{\partial y}(V_1+V_0)\right\} dx\,dy \\ - \iint_S \frac{\eta}{h}\{(U_1-U_0)^2 + (V_1-V_0)^2\}\,dx\,dy \end{aligned} \tag{36}$$

Application of Green's theorem to the last term but one gives

$$\begin{aligned} 2\iint_S F_i V_i \, dS \equiv \int_C \{h(U_1+U_0)\,p\,dy - h(V_1+V_0)\,p\,dx\} - 2\iint_S pf\,dS \\ + 2\eta \iint_S \frac{(U_1-U_0)^2 + (V_1-V_0)^2}{h}\,dS \end{aligned} \tag{37}$$

where

$$2f \equiv \frac{\partial}{\partial x}\{h(U_1+U_0)\} + \frac{\partial}{\partial y}\{h(V_1+V_0)\} \tag{38}$$

The line integral is zero, p being zero on the boundary. Hence the expression (36) becomes

$$\iint_S \left[\frac{h^3}{12\eta}\left\{\left(\frac{\partial p}{\partial x}\right)^2 + \left(\frac{\partial p}{\partial y}\right)^2\right\} + 2pf\right] dx\,dy - \text{constant} \tag{39}$$

the constant being

$$\iint_S \frac{\eta}{h}\{(U_1-U_0)^2 + (V_1-V_0)^2\}\,dS$$

Using equations (32) and (33) it can be seen that this expression takes a minimum when p satisfies the Reynolds equation.

Hence, since the dissipation $D = \iint F_i V_i \, dS$ in the lubrication case, another application of Green's theorem and the fact that $\iint p^+ L(p^+)\,dS = 0$ with the Galerkin method give the result

$$\iint_S F_i V_i \, dS > \iint_S F_i^+ V_i \, dS \tag{40}$$

Vol. 3
1961

Equation (40) states that, under the conditions of the theory of lubrication, of all the pressure distributions possible in a bearing, that which satisfies the Reynolds equation involves the maximum work input. This is the result used in the paper.

APPENDIX II

Extrapolation procedure

From the Galerkin method a series of estimates $E_1, E_2, E_3, \ldots, E_n$, etc., will be obtained which approach the true value E more and more closely as more of the ϕ_i are introduced into the calculation.

To take more than four or five terms results in considerable labour, and it will be found that much less work is involved for a given accuracy if use is made of an extrapolation procedure. This method is always used in digital-computer programming to estimate the limit of a sequence E_n as n approaches infinity.

In the present paper an extrapolation method[21] due to Richardson has been used, being the simplest of the suitable ones investigated.

Use of this will give a closer estimate of E, but it will no longer be possible to state whether it is a lower bound or not.

In this method, the nth term of the sequence E_n is assumed to be of the form

$$E_n = A + \frac{B}{n^2} + \frac{C}{n^4} + \ldots \tag{41}$$

The desired limit is then A. The above formula works better (in the cases the author has investigated) than one like

$$E_n = E + \frac{B}{n} + \frac{C}{n^2} + \ldots \tag{42}$$

because it takes less account of the inaccurate values of the beginning terms.

For example, considering two estimates E_1 and E_2 only, formula (1) gives

$$A = \frac{4E_2 - E_1}{3} \tag{43}$$

whereas formula (2) gives

$$A = 2E_2 - E_1 \tag{44}$$

For three terms formula (1) gives

$$A = \frac{81}{40}E_3 - \frac{14}{15}E_2 - \frac{11}{120}E_1 \tag{45}$$

Formulae (43) and (45) have been used in the paper to estimate the limit of the load and friction sequences.

REFERENCES

1. D. D. FULLER, *Theory and Practice of Lubrication for Engineers* p. 176. John Wiley, New York (1956).
2. L. GÜMBEL, *Mitt. berl. BezVer. dtsch. Ing.* No. 5, 109 (1914).
3. G. VOGELPOHL, *Ing. Arch.* XIV, **3**, 192 (1943).
4. R. O. BOSWALL, *The Theory of Film Lubrication* p. 206. Longmans Green, London (1926).

5. F. W. Ocvirk, *Short-bearing Approximation for Full Journal Bearings.* NACA TN 2808 (1952).
6. A. Kingsbury, *Trans. Amer. Soc. Mech. Engrs.* **53**, 59 (1931).
7. D. G. Christopherson, *Proc. Inst. Mech. Engrs.* **146**, 126 (1941).
8. R. Courant, *Boundary Problems in Differential Equations* (Edited by R. E. Langer) p. 273. The University of Wisconsin Press, Madison, Wisconsin (1960).
9. W. Z. Chein, *Chin. J. Phys.* **7**, 278 (1949).
10. M. Muskat, F. Morgan and M. W. Meres, *J. Appl. Phys.* **11**, 208 (1940).
11. T. T. Wang, *Engng. Rep. Tsing Hua Univ.* **4**, 2, 96 (1950).
12. C. Weber, *Z. angew. Math. Mech.* **30**, 112 (1950).
13. D. F. Hays, *Trans. Amer. Soc. Mech. Engrs.* (*J. Basic Engng.*) **81**D, 13 (1959).
14. H. Lamb, *Hydrodynamics* (6th Ed.) p. 617. Dover, New York (1945).
15. L. V. Kantorovich and V. I. Krylov (translated by C. D. Benster), *Approximate Methods of Higher Analysis* p. 241. Noordhoff, Groningen (1958).
16. A. G. M. Michell, *Z. Math.* **53**, 123 (1905).
17. A. G. M. Michell, *Lubrication* p. 122. Blackie, London (1950).
18. M. Jacobson and E. Saibel, A.S.L.E. Preprint No. 59 AM 4A–1. Chicago, Ill. (1959).
19. B. H. Baines, Private communication (1960).
20. R. Hill, *The Mathematical Theory of Plasticity* p. 60. Clarendon Press, Oxford (1950).
21. Sir Harold Jeffreys and B. Swirles, *Methods of Mathematical Physics* p. 288. Cambridge University Press (1956).

Vol. 3
1961

Int. J. Mech. Sci. Pergamon Press Ltd. 1961. Vol. 3, pp. 28–46. Printed in Great Britain

PHASE EQUILIBRIUM IN LOW-PRESSURE STEAM TURBINES

D. J. RYLEY
Department of Mechanical Engineering, University of Liverpool

(*Received* 3 *October* 1960)

Summary—Experimental measurements of the weight discharge of steam passed by converging elementary nozzles suggest that rapidly expanding steam will supersaturate even if it is wet saturated at entry. A step-by-step method is described for calculating the growth of water droplets in an experimental converging nozzle receiving steam at 95 p.s.i.a., dryness fraction 0·96 and upwards, expanding to a sub-critical back pressure. Calculations indicate that supersaturation cannot be prevented by condensation on existing droplets unless the entry liquid is subdivided to an unrealistically fine degree—approximately 0·1 μ. Similar calculations on a representative commercial turbine nozzle support this view, and other possible agencies which may promote reversion are briefly indicated.

NOTATION

A aggregate surface
A_G specific aggregate surface of droplets
C_v specific heat at constant volume of undercooled steam
J mechanical equivalent of heat
K mass diffusivity
k thermal conductivity
L enthalpy change: liquid–vapour
M maximum precipitation for full reversion
m actual precipitation
N number of droplets
N_g specific number of droplets
p static pressure in vapour remote from interface
p_e static pressure in equilibrium expansion
p_s saturation pressure corresponding to temperature T
q dryness fraction
R characteristic gas constant
$r = d/2$ droplet radius
S supersaturation ratio
T absolute temperature in vapour remote from interface
T_0 absolute temperature at liquid–vapour interface
t time
V velocity
x fractional reversion
ρ_w saturated liquid density
ρ vapour density
γ isentropic index

Additional subscripts

1 beginning of section
2 end of section
i beginning of entry section

1 ft = 30·5 cm = $30{\cdot}5 \times 10^4$ μ
1 $\mu \simeq 3{\cdot}3 \times 10^{-6}$ ft

INTRODUCTION

THE capacity of expanding steam to supersaturate within nozzles has long been known, and during the past sixty years extensive experiments have been conducted by many workers[1–4] to determine the position of the so-called Wilson Line, and to try to relate it to the rapidity of the expansion, etc. Various experimental techniques have been devised for indicating the position within the expansion at which self-nucleation occurs,[5,6] and the effects of nozzle wall or search tube roughness have been superficially investigated.[3] It is fair to claim that the interest in supersaturation has been mainly academic; the phenomenon has a distinct attraction for the scholar and experimenter. The results obtained and the knowledge accumulated have been of only marginal interest to the more recent generation of steam turbine designers and the position of contemporary thought remains much the same as that stated by Guy[7] some twenty years ago: "Although supersaturation occurs in turbine nozzles, yet there is little evidence of it in the stages themselves and a turbine in which the effects of supersaturation are ignored evidently behaves as well as one for which allowance is made for supersaturation. This is probably due to the fact that, while supersaturation reduces the heat drop it at the same time reduces wetness and causes the volume to contract thereby causing a considerable reduction in the terminal loss at the turbine exhaust since this loss depends upon the square of the specific volume. The slightly increased reheat with supersaturated flow will also have an influence, but it is more probable that the empirical coefficients employed in the design of turbines automatically allow for the total effect of the various influences." Although this remains true, it is also the case that the advent of the medium pressure low temperature steam cycle for the nuclear reactor has revived interest in all phenomena associated with steam wetness, and a study of the equilibrium wet condition cannot be divorced from considerations of the metastable condition that preceded it. The view is widely held that supersaturation is restricted to that part of the total expansion immediately following a condition of dry saturation, and that once relief has been gained by the expanding steam in the form of self-nucleation, no further undercooling will occur. This is a thoroughly plausible belief based on the recognition that the presence of any liquid within a supersaturated vapour makes the mixture unstable thermodynamically and promotes active restoration of full equilibrium. What is not recognized, however, is that such condensation takes a finite time to occur however rapid it may appear to be, and that the time so occupied may be commensurate in magnitude with the time taken for further expansion to occur with the promotion of new supersaturation. The question of whether supersaturation persists or recurs is thus

Vol. 3
1961

only capable of being answered if a careful study of the comparative rates of the two processes is undertaken. It is thus necessary, in general, to compare the rate at which supersaturation may be relieved by any known relieving agency with the concurrent rate at which it would otherwise increase during expansion.

EARLIER STUDIES ON THE RELIEF OF SUPERSATURATION

For steam expanding from a condition of superheat there is no internal surface available within the vapour, in the absence of foreign matter, upon which droplets may grow, and in all normal nozzle expansions the supersaturation will increase almost unrelieved until self-nucleation enforces a sudden reversion to conditions of equilibrium. For steam which is initially wet, it is to be expected that expansion will still promote supersaturation within the dry saturated content, but that the entrained liquid will provide internal surface upon which condensation may proceed. The relief of supersaturation afforded by the liquid present will depend upon the extent of the subdivision of the liquid, because the greater the subdivision, the greater the specific surface, i.e. the greater the interfacial surface for a given mass of liquid. In an earlier paper,[8] the present writer presented the results of simple calculations which supported the view that with a given degree of atomization the growth of entrained droplets in an experimental converging nozzle was of the correct order to promote a value of exit section reversion which agreed with experimental measurements; reversion is defined as the ratio of the actual liquid precipitated to that appropriate to full equilibrium. These measurements were made by discharging wet steam of known initial quality through the nozzle and using the weighed values of discharge as data for a new theory of partly reverted flow which enabled a value of exit reversion to be obtained. It was recognized, however, that the drop growth theory there employed was at best only approximate as it was based entirely on heat transfer by conduction and did not accommodate the progressive relief of supersaturation as reversion proceeds. More seriously, the validity of the conclusions reached rested upon the assumption that a specified degree of atomization occurred in the entrained liquid upon entry to the nozzle, and the relief of supersaturation was found to be very sensitive to the degree of atomization. Caution was accordingly enjoined upon the reader. It was assumed that the abrupt rise in steam velocity in the radiused entry to the nozzle atomized the entrained liquid into globules having a size order 5×10^{-7} to 5×10^{-6} ft (0·15–1·5 μ) radius.

Further investigations have suggested that this estimate was too optimistic, and that the liquid was not, in fact, atomized so finely. In order, therefore, to pursue this whole subject further and thus to throw light upon the stability of the steam expanding in low pressure turbines the writer has recalculated the rate of droplet growth for several values of inlet atomization and the calculations have been considerably refined by employing a step-by-step method through the nozzle and recognizing the continuous relief of supersaturation. The ensuing paragraphs discuss, firstly, the mechanism of droplet growth and, secondly, its application to the present problem.

THE CALCULATION OF DROPLET GROWTH

Condensation takes place upon any suitable internal surface provided it is hydrophilic. For a given degree of supersaturation the Kelvin–Helmholtz equation defines the size of a critical sphere or "cluster" which is capable of forming a suitable nucleation centre for continued growth. Several forms of this equation have been defined. The simplest and best known is that for an uncharged homogeneous nucleus, but modifications have been devised to cater for the case where the nucleus is electrically charged, and for the case of an alien nucleus soluble in the condensed liquid. If the nucleus is other than a homogeneous assembly of molecules of the condensing vapour, e.g. an aerosol particle of an alien substance, the nucleation is said to be "heterogeneous". These equations, although employing concepts such as surface tension, pressure, etc., which are essentially macroscopic to assemblages as small as thirty molecules, are generally believed to be accurate.

For a critical cluster to grow it is necessary that the latent heat liberated by condensing liquid at its surface shall be removed into the body of the vapour and that concurrently mass shall be transported to the cluster. The removal of latent heat from the interfacial surface probably takes place partly by conduction and partly by convection, but as the latter is dependent on the local mass transport it is customary to think in terms of conduction only. Heat transfer processes within the liquid drop itself are usually neglected, it being assumed that the significant processes are those occurring at the interface. Proceeding from the respective laws of Fick and Fourier and employing the Clausius–Clapeyron equation Mason[9] derives the following differential equation for droplet growth:

$$S-1=\left(\frac{\rho_w RT}{2Kp_s}+\frac{L^2\rho_w J}{2kRT^2}\right)\frac{dr^2}{dt} \tag{1}$$

To enable this equation to be employed for values of r much less than 5×10^{-4} cm (5 μ) it is necessary to replace K and k by compensated coefficients numerically smaller which recognize that the dimensions of the droplet are commensurate with that of the mean free path. These coefficients are not known and thus equation (1) has a lower limit of useful accuracy at, say, 1 μ.

Alternative equations may be devised from considerations of molecular statistics, and the following, due to Oswatitsch[10], has been successfully applied by him to the experimental results of Binnie and Woods[4] and of Yellot[1].

$$\frac{dr}{dt}=\frac{3p}{8L\rho_w}\sqrt{\left(\frac{3R}{T}\right)}(T_0-T) \tag{2}$$

where (T_0-T) is the effective undercooling.

According to Oswatitsch equation (2) overestimates the growth rate at diameters larger than 2×10^{-4} cm (2 μ), and he proposes the following equation when $d>2\mu$:

$$\frac{dr^2}{dt}=\frac{2k(T_0-T)}{L\rho_w} \tag{3}$$

which equation must not be used for $d < 2\mu$ as it is then stated to underestimate the growth rate.

To employ equations (1) and (3) it is necessary to know both K, the diffusion coefficient, and k, the thermal conductivity, for supersaturated steam. No direct experimental values exist or can be found, but suitable values may be obtained for k by extrapolating known values. Thus extrapolation of the appropriate pressure parameter on a k–T diagram, such as that due to Timrot and Vargaftik[11], is permissible since $(\partial^2 k/\partial T^2)_p$ is very small in the low pressure region. The diffusion coefficient, K, may then be obtained from

$$K = \frac{k}{\rho C_v} \tag{4}$$

a relation derived from the kinetic theory of gases. The values of k and K thus found are only approximate, but the accuracy is the best at present possible and is acceptable for the present purpose.

AVAILABLE INTERNAL SURFACE

Suppose that unit mass of liquid is atomized into fragments of uniform size. Owing to surface tension these fragments, if small, will assume a spherical shape and become a spray monodisperse in size for which the specific number is given by

$$N_g = \frac{3}{4\pi r^3 \rho_w} \tag{5}$$

and the specific surface by

$$A_g = \frac{3}{r\rho_w} \tag{6}$$

The respective variations of A_g and N_g with droplet radius r is shown on Fig. 1. If the spray is polydisperse in size distribution having, in general, N globules of diameter d, then the effective representative diameter, from the point of view of available surface, is the so-called Sauter Mean Diameter defined by

$$d_{sv} = \frac{\epsilon N d^3}{\epsilon N d^2} \tag{7}$$

To facilitate calculation it will be assumed that the liquid entering an expansion passage entrained in dry steam is atomized and monodisperse in droplet size. It is then possible to treat the growth of a single droplet. It is usual to define the quality of entry steam to a nozzle, etc., in terms of a nominal dryness fraction, q. In such a case the number of uniform droplets of radius r for unit mass of wet steam will be

$$N = \frac{3(1-q)}{4\pi r^3 \rho_w} \tag{8}$$

and their aggregate surface is

$$A = \frac{3(1-q)}{r\rho_w} \tag{9}$$

Values of N and A for representative values of q are also shown on Fig. 1.

For a given weight of steam expanding in full equilibrium a certain maximum weight of liquid is precipitated at every point in the expansion, i.e. there is an increasing wetness fraction which can be calculated as the expansion proceeds. If the internal available aggregate surface is adequate full reversion is preserved during expansion, but the extent of the droplet growth will, in general, be inhibited. On the other hand, if the surface is inadequate the growth is unhindered and proceeds as rapidly as the prevailing physical conditions admit, and in the limiting case of no internal surface the familiar type of almost wholly unrelieved metastable expansion occurs.

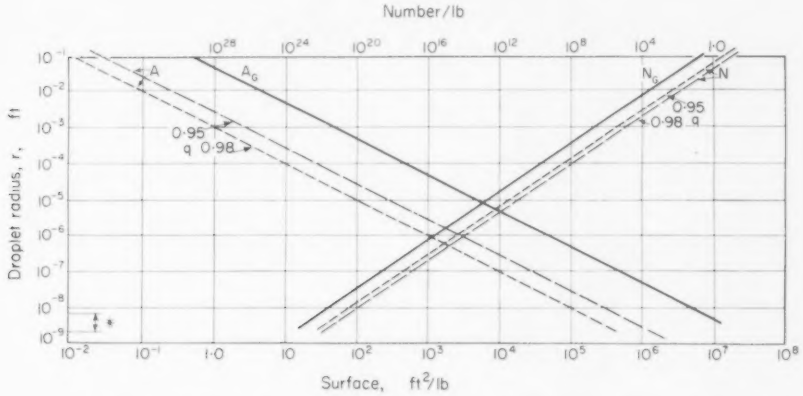

FIG. 1. Variation of aggregate surface and droplet number with droplet radius for monodisperse subdivision.

A_G Specific surface per pound of liquid.
A Specific surface per pound of mixture of dryness fraction q.
N_G Specific number per pound of liquid.
N Specific number per pound of mixture of dryness fraction q.
* Normal size range for critical nuclei.

STEP-BY-STEP CALCULATIONS OF DROPLET GROWTH

It is clear from an examination of equations (1) and (2), and bearing in mind the possibility of inhibited growth just described, that it is impracticable to relate functionally all the relevant variables for solution as a single equation and it is necessary to resort to a step-by-step method of solution. The method will now be described in detail.

(1) As a preliminary it is necessary to work out the distribution of pressure through the expansion passage (the general title "nozzle" will henceforward be used) and this itself incurs difficulty as the variation of pressure is functionally related to the reversion. It is found, however, that the respective pressure distributions for the extreme conditions of full supersaturation and of equilibrium are generally closely similar and either curve is acceptable for the calculations. Fig. 2 illustrates this point for the writer's experimental nozzle and conditions. Indeed, but for this near coincidence it might be possible to assess the local value of reversion directly from static pressure measurements.

The distribution of velocity is also needed in order to find the transit time of the steam through a given section, and it is assumed that all droplets move everywhere at the speed of the surrounding steam. Determination of velocity distribution incurs the same difficulty as pressure distribution, but it is found in this case also that the distribution is insensitive to the degree of reversion. The insensitivity of section pressure and velocity to the degree of reversion is fortunate in so far that it obviates the need for iterative calculations with estimated values. The distribution of equilibrium wetness is also required.

Vol. 3
1961

(2) The nozzle is divided into sections, the number of which must be adequate to secure the degree of refinement required. These sections will not normally be of equal length, but the length will be chosen arbitrarily and should diminish as property changes become more rapid.

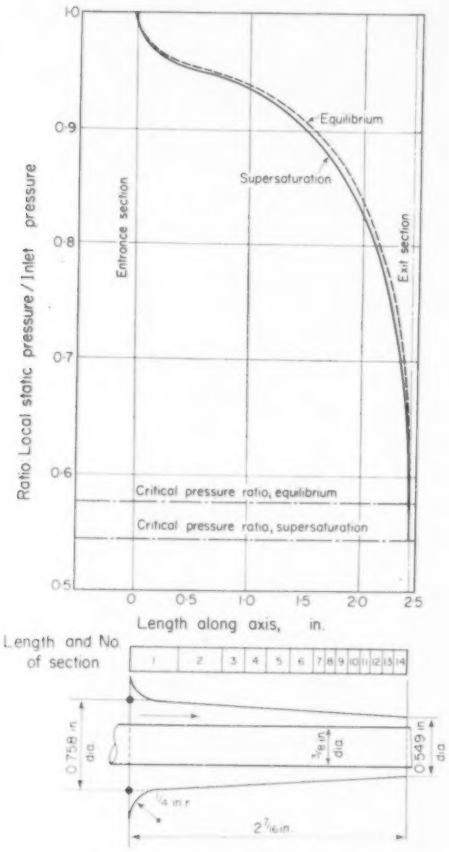

FIG. 2. Distribution of static pressure ratio for experimental nozzle for extreme types of isentropic flow.

Referring to Fig. 3, let the starting point of the expansion be at pressure A, or absolute temperature F. Let AB be the static pressure distribution for full supersaturation and AC that for full reversion and let FD and FE be the respective corresponding temperature curves. The separation of the curves in each pair has been exaggerated for the purpose of clarifying the figure. For the end of Section 1 and for the positions as lettered on Fig. 3

$$T_G = T_F\left(\frac{p_J}{p_A}\right)^{(\gamma-1)/\gamma} \tag{10}$$

The sectional expansion is assumed to be isentropic and the index γ has the value which is appropriate for the conditions. The maximum value of the sectional undercooling is

$$T_H - T_G = T_0 - T \tag{11}$$

(3) The time of transit, δt, of the steam through the section may be obtained and the appropriate growth equation, whether (1), (2) or (3), employed to find δr^2 or δr. It is then necessary to decide the extent of the subdivision of the entry liquid to the nozzle. Clearly

there is no means of knowing this and in the results to be discussed various values of entry radius, r_i, have been assumed. The number of discrete globules, N, may be obtained from equation (8). In general, at the end of a section, the final radius as calculated will be

$$r_2 = (r_1 + \delta r) \tag{12}$$

and the total calculated precipitation will be

$$m = \frac{4}{3}\pi\rho_w(r_2^3 - r_i^3)\,N \tag{13}$$

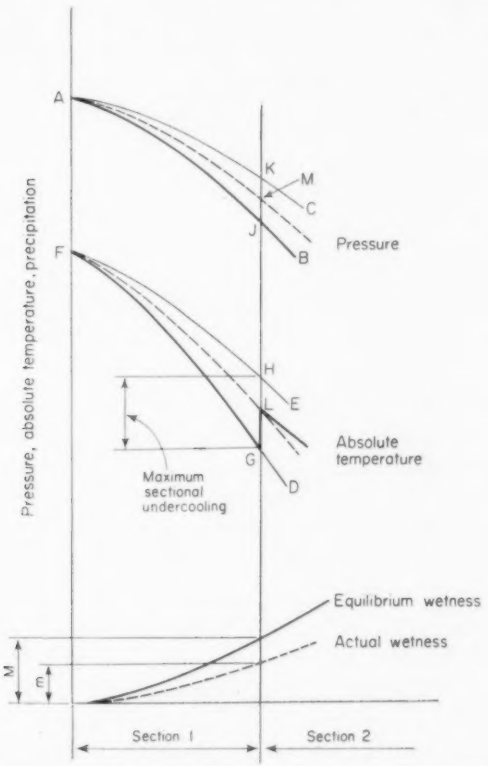

FIG. 3. Diagram explaining the step-by-step method of calculating droplet growth; broken line shows the actual trend of property.

The value of m thus found can be compared with the theoretically possible value M for full reversion. If $m > M$ growth is inhibited, and the droplets will only grow to the maximum radius r_2' sufficient for full reversion where

$$r_2' = \left\{\frac{3M}{4\pi\rho_w N} + r_i^3\right\}^{1/3} \tag{14}$$

If, on the other hand, $m < M$, the growth is uninhibited and equations (12) and (13) are valid. In such a case, the fractional reversion, x, is given by

$$x = \frac{m}{M} \tag{15}$$

(4) The reversion thus found is now used to correct the temperature for the section considered in preparation for the succeeding section for which this corrected temperature becomes the entry temperature. Thus, referring to Fig. 3,

$$T_L = T_G + x(T_H - T_G) \tag{16}$$

(5) It will have been observed that the value of δr was calculated on the full extent of the sectional undercooling, not on the reduced value which will in fact prevail if $x > 0$. By assuming a smaller value of undercooling, corresponding to a predicted value of reversion one may calculate the drop growth and check the harmony of the reversion so calculated with that assumed, and by repetition obtain iteratively a converging value of x. If, however, the section is short in length the enhanced accuracy so gained contributes little improvement to the over-all results. It may also be observed that the maximum sectional undercooling is based on the supposition that if full reversion took place it would raise the temperature to the value appropriate to equilibrium expansion to that point. This is substantially, but not strictly, true, inasmuch that any completed history of undercooling will displace slightly the subsequent equilibrium expansion temperature curve from the locus it would occupy in the absence of such history.

(6) The section end pressure is not needed for calculation purposes, but can be obtained with acceptable accuracy from

$$p_M = p_J \frac{T_L}{T_G} \tag{17}$$

(7) The prevailing supersaturation ratio is

$$S = \frac{p_M}{p_{s_M}} \tag{18}$$

EXPERIMENTAL NOZZLE. COMPARISON OF EXPERIMENTAL AND THEORETICAL RESULTS

The profile of the experimental nozzle is shown in Fig. 2 together with the length and numbering of the sections employed for theoretical calculations of droplet growth. The nozzle is penetrated by a $\frac{3}{8}$-in. diameter rod which may either have a smooth outline as shown, or a $\frac{1}{32}$-in. square thread with a full diameter of $\frac{3}{8}$ in. The function of the latter is to encourage reversion and its action is more fully described in Ref. 8. The steam was supplied to the nozzle at 95·7 p.s.i.a., and calculations are based on this inlet pressure. The back pressure was subcritical and the wetness fraction varied up to a maximum of 0·04 beyond which the action of the throttling calorimeter was unsatisfactory. Accordingly, calculations for values of wetness fraction 0·01, 0·02, 0·03 and 0·04 were undertaken for each of the following values of droplet radius at inlet: 5×10^{-9} ft, 5×10^{-8} ft, 5×10^{-7} ft, 5×10^{-6} ft and 5×10^{-5} ft. Equation (2) was employed for inlet radii 5×10^{-9} ft, 5×10^{-8} ft and 5×10^{-7} ft. For the inlet radius 5×10^{-6} ft both equations (1) and (2) were employed, and for radius 5×10^{-5} ft equation (1) only. It was assumed in all cases that the entry steam was in a state of wet saturation (i.e. in equilibrium) and that the entrained liquid was uniformly subdivided as in equation (8). In applying equations (1) and (2) constant representative values of R, k and ρ_w may legitimately be taken but the respective variations of all other properties were recognized.

Figs. 4 and 5 show respectively the drop growth and reversion curves for entry droplets having initial radii 5×10^{-9} ft and 5×10^{-7} ft respectively. It will be observed that corresponding curves are similar and they are similar also to the corresponding curves for the initial radius 5×10^{-8} ft, which are not exhibited. It is seen, therefore, that a wetness fraction of 1 per cent is adequate to relieve completely the supersaturation and promote full reversion throughout the expansion provided the inlet radius does not exceed 5×10^{-7} ft (0·15 μ). If more liquid is present in the same degree of size dispersion, reversion is, of

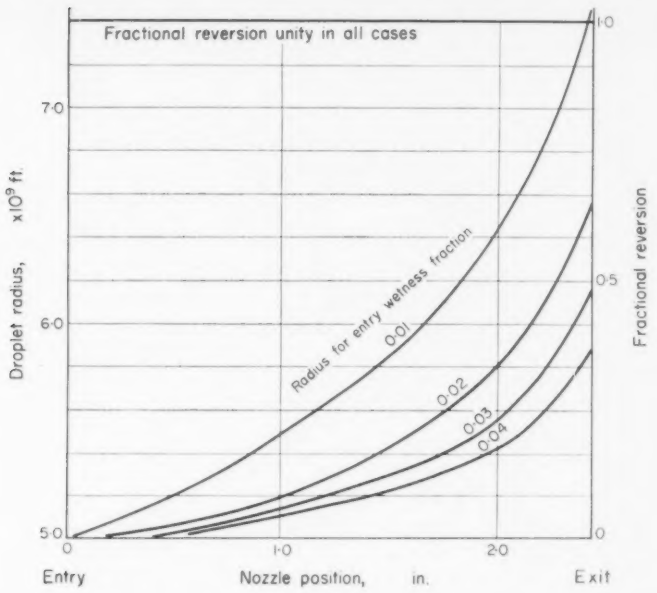

FIG. 4. Droplet growth and reversion curves for experimental nozzle. Initial radius of droplet 5×10^{-9} ft.

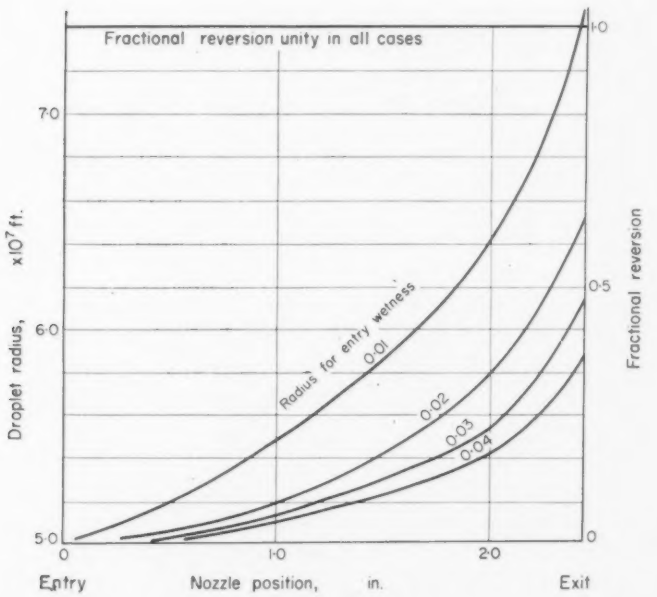

FIG. 5. Droplet growth and reversion curves for experimental nozzle. Initial radius of droplet 5×10^{-7} ft.

course, still complete, but the droplets cannot achieve the same growth since a greater number are sharing the available precipitation. Clearly there is a minimum wetness fraction for each of these degrees of atomization and the first indication of failure in relief would appear at the exit, where, for this nozzle, the expansion is most rapid. These results illustrate the manner in which self-nucleation, which produces critical nuclei of the magnitude $2\text{–}6 \times 10^{-9}$ ft radius, is able to relieve with great rapidity a critical degree of supersaturation.

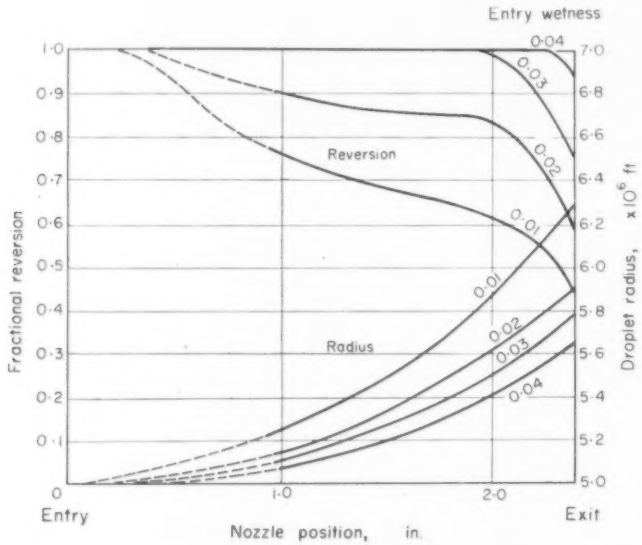

FIG. 6. Droplet growth and reversion curves for experimental nozzle. Initial radius of droplet 5×10^{-6} ft.

The case where the entry radius is 5×10^{-6} ft (1·5 μ) presents difficulties as it is at the transition size between molecular and macroscopic treatment. Fig. 6 shows the results obtained with the equation (3) and Fig. 7 shows the comparative results for $(1-q) = 0{\cdot}02$ using equations (1) and (3). Since Oswatitsch advises against the use of equation (2) for droplets greater in radius than 2 μ ($6{\cdot}6 \times 10^{-6}$ ft) equation (3) must be employed, but it is being used at the lower limit of its validity and is stated to underestimate the growth rate. Similarly, regarding equation (1) Mason states a limiting lower diameter of 5 μ ($16{\cdot}5 \times 10^{-6}$ ft) for uncompensated coefficients K and k, and it is, therefore, also being employed at the lower limit of its validity. As, however, equation (1) recognizes the processes of both mass diffusion and thermal conductivity, and equation (3) only the latter, it is probable that the results obtained by equation (1) are more nearly correct than those obtained by equation (3).

With droplets having an entry radius as large as 5×10^{-5} ft (15 μ) no considerable relief is given to the supersaturation at any wetness fraction up to and including 0·04.

In spite of the uncertainty in detail in the value of growth for a droplet of entry radius 5×10^{-6} ft it is quite clear that this is a critical order of size for the relief of supersaturation in the present nozzle experiments. The question then arises as to what degree of subdivision can reasonably be expected in practice at the nozzle entry. Whilst this question cannot be directly answered, it devolves upon what maximum degree of atomization is possible as a consequence either of rapid pressure changes within the flow or of impact upon a solid surface. A great many experimental data are available in the extensive literature on atomization particularly in the context of water and of fuel oils.

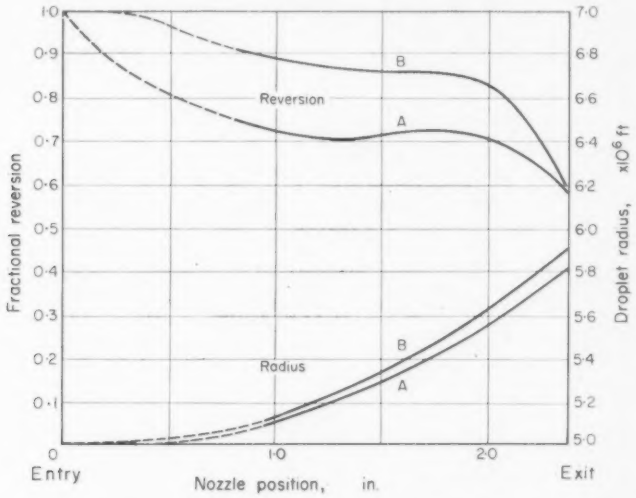

FIG. 7. Comparison of rate of droplet growth and of reversion in experimental nozzle by two theories. Entry wetness 0·02. Initial radius of droplet 5×10^{-6} ft. Curves A: Equation (1). Curves B: Equation (3).

A search reveals that a representative lower limit of size consequent upon subdivision from larger liquid bodies is about 3×10^{-5} ft ($10\,\mu$) irrespective of the liquid or mode of fracture, though occasional smaller droplets are found. Neither aerodynamic nor mechanical agencies appear capable of producing a spray with any considerable number of globules below this modal size.

The above theory would suggest therefore that, for the present conditions, unless the initial wetness fraction is much higher than 0·04, or unless unidentified agencies are promoting extremely effective subdivision at the nozzle entry, very little relief will be afforded to supersaturation.

It is now necessary to see how these conclusions are supported by experiment. A long series of careful measurements were made of the weight of steam actually discharged under the above conditions and the results are shown in Figs. 8 and 9, which reproduce the essential information of Figs. 9 and 10 in Ref. 8. The trend of experimental exit fractional reversion can be calculated from the dotted part of the curve lying in the region of initial wetness, i.e. to the left of the diagrams, and the method employed to do this is fully discussed in

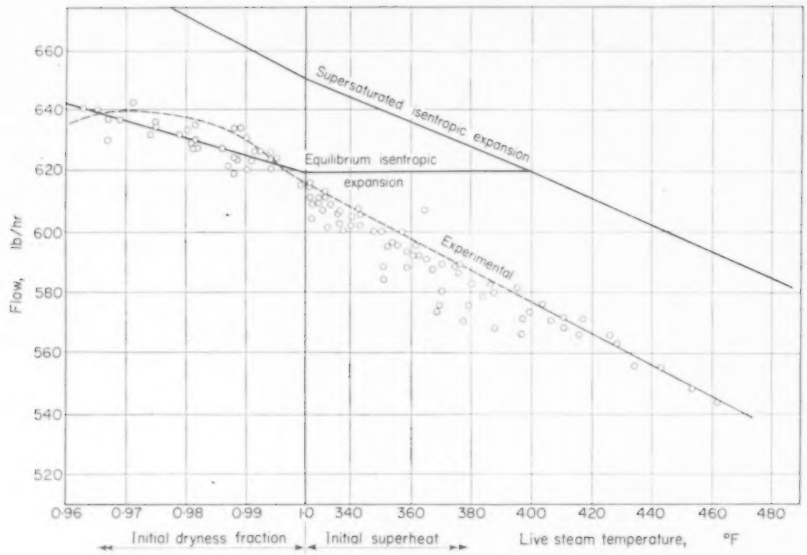

FIG. 8. Variation of experimental discharge with initial quality of steam. Experimental nozzle with smooth rod in penetration.

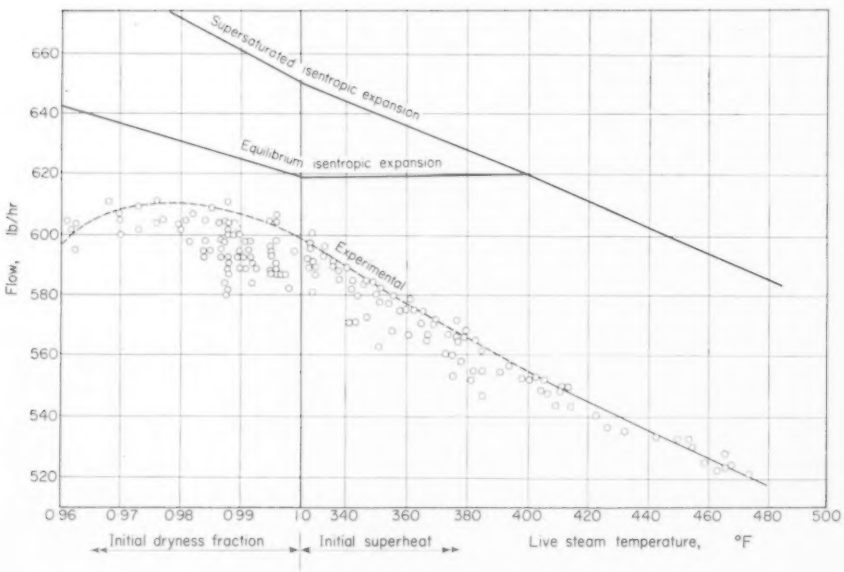

FIG. 9. Variation of experimental discharge with initial quality of steam. Experimental nozzle with rough rod in penetration.

Ref. 8. Such a procedure yields the curves A and B on Fig. 10 which may be compared with those obtained in the foregoing calculations, also displayed on Fig. 10. It is evident that the inlet radius of the droplets must lie between 5×10^{-5} ft and 5×10^{-6} ft, say about $\frac{1}{3}\ \mu$, to promote the observed degree of reversion. Bearing in mind that this size is much smaller than can apparently be obtained in practice the problem immediately arises as to whether droplets of $\frac{1}{3}\ \mu$ radius are, in fact, present, or in the event of their absence, how the reversion is promoted.

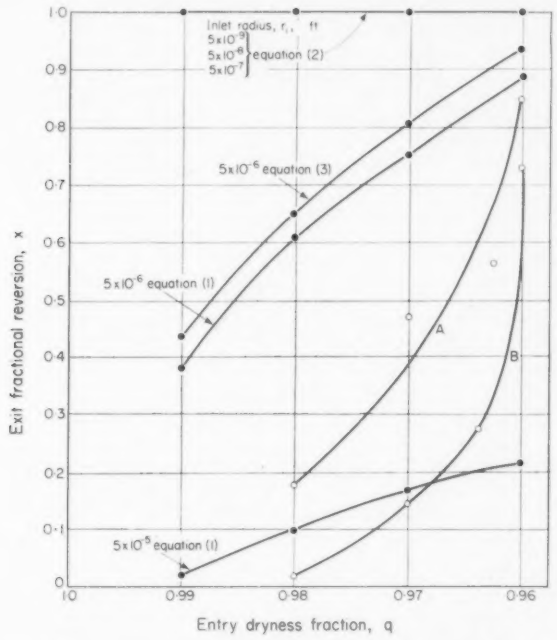

FIG. 10. Comparison of calculated and measured values of reversion for experimental nozzle. Curves A and B are experimentally measured reversion. Curve A: Rough rod in penetration. Curve B: Smooth rod in penetration.

The discussion on this anomaly will be deferred to a later paragraph. In the meantime the objection must be met that the above experimental nozzle with its straight axis, high initial pressure and critical pressure drop is not representative of L.P. turbine practice. The typical L.P. turbine nozzle will have a curved axis, a longer flow path and deal with a low inlet pressure and a smaller expansion pressure ratio, and would seem to be better able to avoid undercooling.

CALCULATED REVERSION FOR LOW PRESSURE TURBINE NOZZLE PASSAGE

A typical L.P. turbine nozzle, as used in a large commercial set, is shown in Fig. 11, which displays both the essential dimensions and the normal operating conditions. Using the nozzle axis to define the position of a given section for

Vol. 3
1961

application of the one-dimensional flow theory, curves may be obtained as shown in Fig. 12 in which the variation of pressure, p_e, velocity, V, equilibrium precipitation, M and area, A, are presented. The three first-named are based on equilibrium expansion.

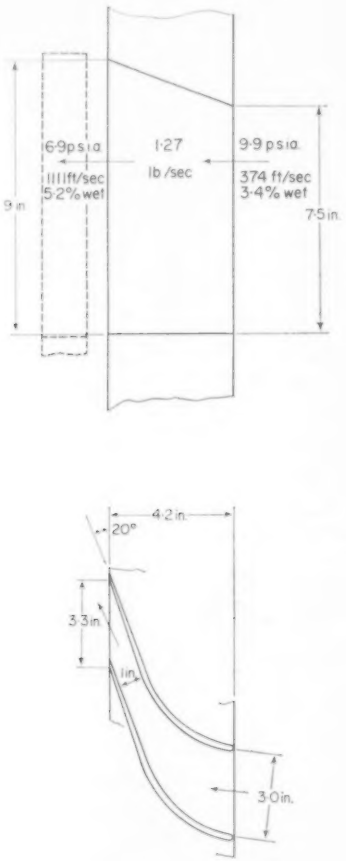

FIG. 11. Dimensions and operating conditions of commercial low pressure turbine nozzle.

The flow path may be divided into sections in the manner shown in Fig. 12 and it was considered that eight such sections gave the necessary degree of refinement. The 3·4 per cent entry liquid was assumed to be subdivided into droplets having a radius at entry of 1 μ ($3{\cdot}3 \times 10^{-6}$ ft). Step-by-step calculations were then undertaken employing equation (1). For this purpose R was taken to be constant at 85 ft-lb/lb °F, k at 0·013 B.t.u./hr ft °F and γ at 1·3. The calculated axial distribution of reversion, x, supersaturation ratio, S, and droplet radius r are shown in Fig. 13 and it is evident that only very limited relief is given to the supersaturation by condensation on the existing subdivided liquid. Certainly the method employed takes no cognizance of forced convective

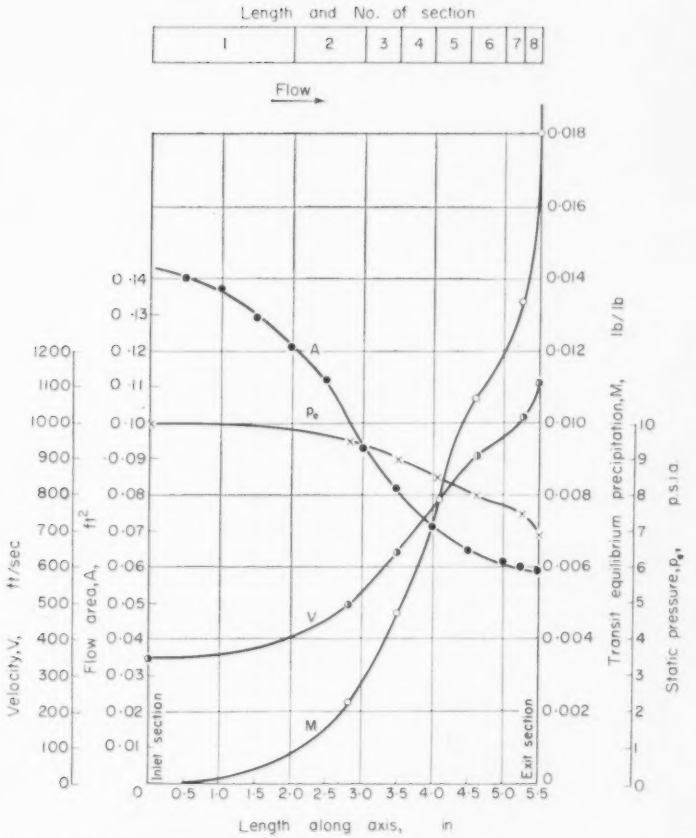

FIG. 12. Variation of flow area, velocity, equilibrium static pressure and equilibrium precipitation in low pressure turbine nozzle.

effects at the interface of the condensing droplet, and it incurs some inaccuracy in so far as equation (1) is being used somewhat below the recommended lower limiting size with gross values of K and k, but there is no reason to doubt the principal conclusions. Accepting, therefore, the essential accuracy of the calculations it would appear that neither in the case of the experimental nozzle nor in the case of the commercial turbine nozzle is the condensation process materially assisted by the entrained liquid during the brief duration of the expansion.

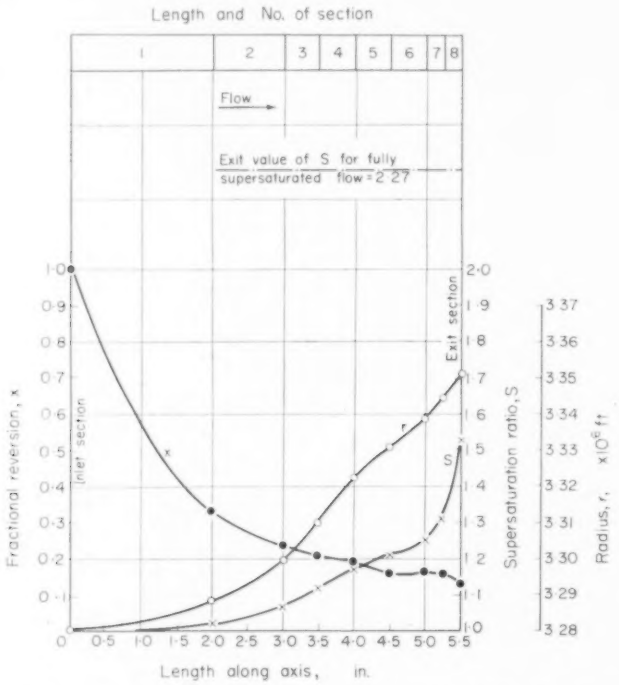

FIG. 13. Variation of fractional reversion, droplet radius and supersaturation ratio for low pressure turbine nozzle.

DISCUSSION OF ALTERNATIVE FACTORS ENCOURAGING REVERSION

The belief that supersaturation is largely absent from L.P. turbines is widely held. It would be more correct to accept the position stated by Guy, namely, that it does not betray itself by external evidence owing to the mutual cancellation of certain effects. Internal evidence is difficult to obtain since attempts to measure static temperature in those regions where it is likely to be significantly different from the equilibrium value incur the usual difficulties associated with this problem, with the added difficulty that the presence of the measuring device may disturb the metastability of the steam. If the steam is indeed substantially in equilibrium throughout the earlier part of the "wet" expansion, then it is necessary to seek agencies other than the dispersed liquid which may be capable of promoting reversion. Three such agencies, which may act singly or in concert, may be distinguished.

(a) *Heterogeneous nucleation upon ions*

It has been shown that ions can act as nucleation centres, and condensation occurs in a cloud chamber at lower values of supersaturation than otherwise when they are present. Attempts have been made to encourage condensation in flowing steam by causing the steam to pass through an electrical discharge,[1, 12] but the results were inconclusive and the subject not pursued.

(b) *Heterogeneous nucleation upon foreign nuclei*

Despite efforts to obtain the utmost purity in the steam entering a turbine there are always residual traces of alien substances. These may be traces of silica or salts of sodium which have entered the turbine either with the steam or as a consequence of "aquaglobejection" or priming, together with traces of gases, carbon dioxide and ammonia. Any acidity in the steam renders possible chemical attack on steam-swept surfaces. The efficacy of foreign substances as centres of nucleation is largely unknown in this context, though some work has been done with cloud chambers.

Vol. 3
1961

(c) *Agitation of the steam*

There is a great deal of scattered information supporting the view that supersaturated steam is incapable of withstanding any considerable degree of agitation or shock without reversion. Thus Kerr *et al.*[6] found that a plane shock in a supersonic nozzle was capable of destroying the metastable state. The present writer has shown[8] that a roughened axial rod in penetration of a nozzle tends to encourage reversion as indicated on Fig. 10. The corresponding effect for supercooled water[13] is well known: its metastability is highly sensitive to agitation. It is fully plausible to suggest that whereas steam may supersaturate whilst expanding rapidly in a nozzle the agitation inseparable from flow across the ensuing gap and through the following blade may restore equilibrium before further expansion occurs.

CONCLUSIONS

Assuming the accuracy of the drop growth calculations and of the method for obtaining experimental values of reversion, the foregoing studies suggest that the liquid content present within rapidly expanding steam is incapable of relieving the undercooling when subject to a realistic degree of subdivision. If such relief is gained for relatively low values of wetness fraction, and this has never been conclusively proved, there would appear to be other agencies acting independently of or conjointly with the liquid present. The respective contributions of these several factors cannot yet be assessed.

REFERENCES

1. J. I. Yellot, *Trans. Amer. Soc. Mech. Engrs.* **56**, 411 (1934a); **137**, 303 (1934b).
2. J. I. Yellot and C. K. Holland, *Trans. Amer. Soc. Mech. Engrs.* **59**, 171 (1937).
3. J. T. Rettaliata, *Trans. Amer. Soc. Mech. Engrs.* **58**, 599 (1936).
4. A. M. Binnie and M. W. Woods, *Proc. Inst. Mech. Engng.* **138**, 299 (1938).
5. A. M. Binnie and J. R. Green, *Proc. Roy. Soc.* A **181**, 134 (1943).

6. W. KERR, A. W. SCOTT and M. SOROUR, *General Discussion on Heat Transfer* 1951, p. 69. Institute of Mechanical Engineers and American Society of Mechanical Engineers.
7. H. L. GUY. Quoted by D. A. WRANGHAM, *Theory and Practice of Heat Engines* p. 359. Cambridge University Press (1942).
8. D. J. RYLEY, *Engineer, Lond.* **203**, 708 (1957).
9. B. J. MASON, *Proc. Phys. Soc.* B**64**, 773 (1951).
10. K. OSWATITSCH, *Z. angew. Math. Mech.* **22**, 1 (1942).
11. D. L. TIMROT and N. B. VARGAFTIK, *Trans. 4th World Power Conf.* Vol. III, p. 1647. Lund-Humphries, London (1952).
12. C. A. PARSONS, *Heaton Works J.* **4**, 24, 223 (1947).
13. N. E. DORSEY, *J. Res. Nat. Bur. Stand.* **20**, 799 (1938).

Vol.
196

Int. J. Mech. Sci. Pergamon Press Ltd. 1961. Vol. 3, pp. 47–67. Printed in Great Britain

Vol. 3
1961

SECOND APPROXIMATION OF METHOD OF INTERNAL CONSTRAINTS AND ITS APPLICATIONS*

ENRICO VOLTERRA
Austin, Texas

(*Received* 5 *May* 1960)

Summary—The present paper complements previous papers in which the first approximation of the method of internal constraints was applied to problems of vibration and of wave propagation in straight, curved and twisted and curved bars and in cylindrical shells and plates.

Problems of vibration of plates and of straight rods are discussed by introducing higher-order terms in the equations of constraints. These new parameters are determined as functions of the coefficients of the linear terms by the condition that the normal stresses acting on the free surfaces of the rods and of the plates must be zero. By expressing the potential and kinetic energies of the bars and plates in terms of unknown functions which are reduced to the linear terms only, the equations of motion and the boundary conditions are derived by the application of Hamilton's principle.

The equations of motion and the boundary conditions of this second-approximation method have the same mathematical simplicity as those of the first-approximation method. Moreover, this second-approximation method presents the advantage that it leads to a greater accuracy in the numerical results.

1. INTRODUCTION

THE present paper complements previous papers published in *Ingenieur-Archiv* and in other scientific and technical magazines in which the method of internal constraints has been applied to problems of vibration and wave propagation in straight, twisted and curved, and curved bars and in cylindrical shells and plates taking into account the effects of shear and of rotatory inertia.

In the case of bars the equation of constraints was expressed by the following vector equation:

$$\mathbf{V}(x, y, z; t) = \mathbf{v}(x; t) + y\boldsymbol{\lambda}(x; t) + z\boldsymbol{\mu}(x; t) \tag{1}$$

whereas in the case of plates or shells by

$$\mathbf{V}(x, y, z; t) = \mathbf{v}(x, y; t) + z\boldsymbol{\mu}(x, y; t) \tag{2}$$

The vector $\mathbf{V}$ in equations (1) and (2) represents the elastic displacement vector. In equation (1) $\mathbf{v}$, $\boldsymbol{\lambda}$ and $\boldsymbol{\mu}$ represent three unknown vectors, functions of the variable x and of the time t. In equation (2) $\mathbf{v}$ and $\boldsymbol{\mu}$ represent two unknown vectors, functions of the variables x, y and of the time t. In the case of an elongated bar [equation (1)] the axes of reference are respectively the axis of the bar (X axis), the normal (Y axis) and the binormal (Z axis) to the axis X see [Fig. 1(b)]. In the case of the plate [equation (2)], the XY surface coincides with the middle surface of the plate [see Fig. 1(a)].

* The material presented in this paper is based on an investigation which is being conducted under the sponsorship of The National Science Foundation, Washington 25, D.C., and is presented with the permission of The National Science Foundation.

In the present paper problems of vibration of plates and of straight rods will be discussed by introducing, in the equations of constraints, higher-order terms of y and of z in the case of rods and of z in the case of plates. The new parameters, which are introduced in the equations of constraints, are *a priori* unknown functions of the variables x and t, in the case of bars, and of the variables x, y and t, in the case of plates. They are, however, determined, as

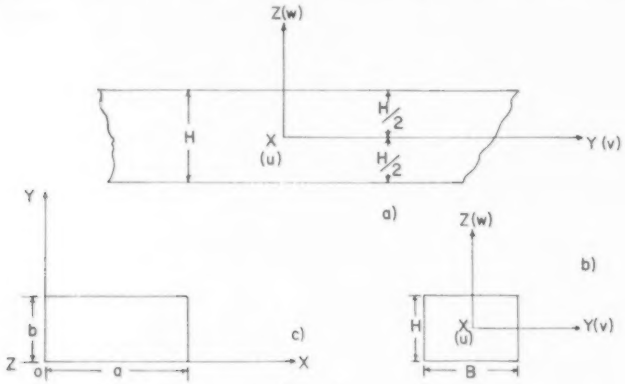

FIG. 1.

functions of the coefficients of the linear terms by the condition that the normal stresses acting on the free surfaces of the rods and of the plates must be zero. Expressing the potential and kinetic energies of the bars and plates in terms of unknown functions, which are reduced to the coefficients of the linear terms only, the equations of motion and the boundary conditions of the problem are derived by the application of the Hamilton principle.

In the text of this paper the equations of motion and boundary conditions derived by applying equations (1) and (2) will be referred to as the first approximation of the method of internal constraints whereas equations of motion and boundary conditions derived by using the higher-order terms in the equations of constraints will be referred to as the second or higher approximation of the method of internal constraints.

It should be pointed out here that a similar method, in which terms in the equations of constraints of a higher order than those given by equations (1) and (2), was already used by Zachmanoglou and the author to discuss problems of dispersion of longitudinal waves in cylindrical rods[1] and in elastic plates[2]. However, the method which will be discussed in this paper presents the advantage that, although the approximation is greatly increased as compared with the first approximation method, the equations of motion and corresponding boundary conditions have the same mathematical simplicity as in the first approximation. In fact the present approximation changes not the form but the numerical coefficients of the equations of motion. Thus the frequency equations and modal functions of a vibrating straight bar can be derived by properly changing the constants in the equations given in a previous paper.[3,4]

In comparing the results obtained by the use of the first and second approximation of the method of internal constraints as well as by other engineering

theories in problems of wave propagation in plates and rods in cases in which the exact solutions furnished by the application of the Mathematical Theory of Elasticity are known, it is possible to show how this second approximation increases the accuracy of the results.

The method will be applied first to the discussion of flexural vibrations of rectangular thin plates. The equations of motion and proper boundary conditions will be derived for this case. These equations of motion coincide with the equations of motion derived by Mindlin[5] from the three-dimensional equations of elasticity. However, the present equations are obtained in a much more straightforward way.

These equations reduce in the static case to equations which are very similar to those obtained by Reissner[6] in his theory of bending of thin elastic plates by taking into account the transverse-shear deformation of the plate and by an application of Castigliano's theorem of minimum energy. Reissner's equations were reobtained directly from the stress equations of equilibrium and the stress–strain relations by Green[7], Schaefer[8] and Timoshenko and Woinowsky-Krieger[9]. Reissner, in his important work, showed how his equations satisfy three boundary conditions along the edges of the plate instead of the two boundary conditions established by Kirchhoff in his classical theory.[10] Moreover, Reissner by use of his equations was able to solve problems of practical importance such as the problem of bending and twisting of an infinite plate with a circular hole and the bending of a cantilever plate due to terminal transverse loads. For such problems the classical theory leads to results which are not in accordance with experiment, whereas Reissner's equations, which take transverse shear deformation into account, lead to results which are substantially in agreement with experiment. Moreover, Reissner's equations have been used to discuss the problem of the determination of the reactions along the edges of a square plate simply supported under a uniformly distributed load.[11]

Another topic to be discussed in this paper is the vibration of elongated straight rods. The equations of motion and the boundary conditions for flexural vibrations will be derived first. It will be shown that these equations reduce in the plane–stress case to the well-known Timoshenko beam equation.

Finally, a second approximation of the method of internal constraints will be applied to derive the equations of motion and the boundary conditions for longitudinal vibrations of elongated rods.

2. EQUATIONS OF MOTION AND BOUNDARY CONDITIONS FOR RECTANGULAR PLATES

Let the components of the elastic displacement in the X, Y and Z directions of the rectangular plate of sides a and b [see Fig. 1(a) and 1(c)] be

$$\left.\begin{aligned} u(x,y,z;t) &= z\mu_x(x,y;t) \\ v(x,y,z;t) &= z\mu_y(x,y;t) \\ w(x,y,z;t) &= v_z(x,y;t)+\frac{z^2}{2}f(x,y;t) \end{aligned}\right\} \tag{3}$$

Vol. 3
1961

The corresponding components of strain computed from equations (3) are

$$\epsilon_x = \frac{\partial u}{\partial x} = z\frac{\partial \mu_x}{\partial x}; \quad \gamma_{xy} = \frac{\partial u}{\partial y} + \frac{\partial v}{\partial x} = z\left(\frac{\partial \mu_x}{\partial y} + \frac{\partial \mu_y}{\partial x}\right)$$

$$\epsilon_y = \frac{\partial v}{\partial y} = z\frac{\partial \mu_y}{\partial y}; \quad \gamma_{yz} = \frac{\partial v}{\partial z} + \frac{\partial w}{\partial y} = \left(\mu_y + \frac{\partial v_z}{\partial y} + \tfrac{1}{2}z^2\frac{\partial f}{\partial y}\right)$$

$$\epsilon_z = \frac{\partial w}{\partial z} = zf; \qquad \gamma_{zx} = \frac{\partial w}{\partial x} + \frac{\partial u}{\partial z} = \left(\mu_x + \frac{\partial v_z}{\partial x} + \tfrac{1}{2}z^2\frac{\partial f}{\partial x}\right)$$

$$e = \epsilon_x + \epsilon_y + \epsilon_z = z\left(\frac{\partial \mu_x}{\partial x} + \frac{\partial \mu_y}{\partial y} + f\right)$$

The normal stress σ_z is given by:

$$\sigma_z = \lambda e + 2G\epsilon_z = \lambda z\left(\frac{\partial \mu_x}{\partial x} + \frac{\partial \mu_y}{\partial y} + f\right) + 2Gzf \tag{4}$$

where λ (Lamé's constant) and G (modulus of rigidity) are connected to Young's modulus E and to Poisson's ratio ν of the material of the plate by the well-known relationships

$$\lambda = \frac{\nu E}{(1+\nu)(1-2\nu)}; \quad G = \frac{E}{2(1+\nu)}$$

By satisfying the requirement that $\sigma_z = 0$ one obtains from equation (4) the following relationship for the unknown function $f(x, y; t)$:

$$f(x, y; t) = -\frac{\nu}{(1-\nu)}\left(\frac{\partial \mu_x(x, y; t)}{\partial x} + \frac{\partial \mu_y(x, y; t)}{\partial y}\right) \tag{5}$$

The terms containing second-order powers z^2 in the expressions for the components of strain and particle velocities will be neglected in comparison with linear terms. The components of strain and particle velocities according to the above assumptions and in view of equation (5) are reduced to the following expressions:

$$\left.\begin{aligned} \epsilon_x &= z\frac{\partial \mu_x}{\partial x}; & \gamma_{xy} &= z\left(\frac{\partial \mu_x}{\partial y} + \frac{\partial \mu_y}{\partial x}\right) \\ \epsilon_y &= z\frac{\partial \mu_y}{\partial y}; & \gamma_{yz} &= \mu_y + \frac{\partial v_z}{\partial y} \\ \epsilon_z &= -\frac{\nu}{(1-\nu)}z\left(\frac{\partial \mu_x}{\partial x} + \frac{\partial \mu_y}{\partial y}\right); & \gamma_{zx} &= \mu_x + \frac{\partial v_z}{\partial x} \end{aligned}\right\} \tag{6}$$

$$e = \frac{1-2\nu}{1-\nu}z\left(\frac{\partial \mu_x}{\partial x} + \frac{\partial \mu_y}{\partial y}\right)$$

$$\left.\begin{aligned} \frac{\partial u}{\partial t} &= z\frac{\partial \mu_x}{\partial t} \\ \frac{\partial v}{\partial t} &= z\frac{\partial \mu_y}{\partial t} \\ \frac{\partial w}{\partial t} &= \frac{\partial v_z}{\partial t} \end{aligned}\right\} \tag{7}$$

The potential energy of the plate U is given by the expression

$$U = \frac{1}{2}\int_V (\sigma_x \epsilon_x + \sigma_y \epsilon_y + \sigma_z \epsilon_z + \tau_{xy}\gamma_{xy} + \tau_{yz}\gamma_{yz} + \tau_{zx}\gamma_{zx})\, dx\, dy\, dz$$

or by the expression

$$U = \int_V \left[\tfrac{1}{2}\lambda e^2 + G(\epsilon_x^2 + \epsilon_y^2 + \epsilon_z^2) + \frac{G}{2}(\gamma_{xy}^2 + K\gamma_{yz}^2 + K\gamma_{zx}^2)\right] dx\, dy\, dz \tag{8}$$

In equation (8) V is the volume of the plate. The factor K is introduced into equation (8) to take into account the non-linear distribution of shear-stresses over the cross-section of the plate. It has the same significance as that of the well-known Timoshenko shear-coefficient. The kinetic energy will be computed from the expression

$$T = \frac{\rho}{2}\int_V \left[\left(\frac{\partial u}{\partial t}\right)^2 + \left(\frac{\partial v}{\partial t}\right)^2 + \left(\frac{\partial w}{\partial t}\right)^2\right] dx\, dy\, dz \tag{9}$$

where ρ is the density of the material of the plate. By substituting into equations (8) and (9) equations (6) and (7), and by integrating with respect to z, the potential and kinetic energies are expressed by the following integrals:

$$\left.\begin{aligned} U = \int_A \Bigg\{ & \frac{E}{2(1-\nu^2)}\left[I\left(\frac{\partial \mu_x}{\partial x}\right)^2 + I\left(\frac{\partial \mu_y}{\partial y}\right)^2\right] + \frac{\nu E}{(1-\nu^2)} I \frac{\partial \mu_x}{\partial x}\frac{\partial \mu_y}{\partial y} \\ & + \frac{E}{4(1+\nu)}\left[I\left(\frac{\partial \mu_x}{\partial y}\right)^2 + I\left(\frac{\partial \mu_y}{\partial x}\right)^2 + 2I\frac{\partial \mu_x}{\partial y}\frac{\partial \mu_y}{\partial x} + KH(\mu_y)^2\right. \\ & + KH\left(\frac{\partial v_z}{\partial y}\right)^2 + 2KH\mu_y\frac{\partial v_z}{\partial y} + KH(\mu_x)^2 + KH\left(\frac{\partial v_z}{\partial x}\right)^2 \\ & \left. + 2KH\mu_x\frac{\partial v_z}{\partial x}\right]\Bigg\}\, dx\, dy \end{aligned}\right\} \tag{10}$$

$$T = \frac{\rho}{2}\int_A \left[I\left(\frac{\partial \mu_x}{\partial t}\right)^2 + I\left(\frac{\partial \mu_y}{\partial t}\right)^2 + H\left(\frac{\partial v_z}{\partial t}\right)^2\right] dx\, dy \tag{11}$$

In equations (10) and (11)

$$I = \int_{-H/2}^{H/2} z^2 \cdot 1\, dz = \frac{H^3}{12}$$

where H is the constant thickness of the plate, and A is the area of the surface of the plate. Hereafter the function v_z, which represents the vertical displacement of the middle surface of the plate, will be indicated with the letter w_0.

The work done by the external distributed force $p(x, y; t)$ acting on the middle surface of the plate in a virtual displacement is given by the following expression:

$$\delta L = \int_A p(x, y; t)\, \delta w_0\, dx\, dy$$

Vol. 3
1961

By applying Hamilton's principle the following equations of motion:

$$\left.\begin{aligned} D\frac{\partial^2\mu_x}{\partial x^2}+\frac{1+\nu}{2}D\frac{\partial^2\mu_y}{\partial x\,\partial y}+\frac{1-\nu}{2}D\frac{\partial^2\mu_x}{\partial y^2}-\frac{EHK}{2(1+\nu)}\frac{\partial w_0}{\partial x} \\ -\frac{EHK}{2(1+\nu)}\mu_x=\frac{\rho H^3}{12}\frac{\partial^2\mu_x}{\partial t^2} \\ D\frac{\partial^2\mu_y}{\partial y^2}+\frac{1+\nu}{2}D\frac{\partial^2\mu_x}{\partial x\,\partial y}+\frac{1-\nu}{2}D\frac{\partial^2\mu_y}{\partial x^2}-\frac{EHK}{2(1+\nu)}\frac{\partial w_0}{\partial y} \\ -\frac{EHK}{2(1+\nu)}\mu_y=\frac{\rho H^3}{12}\frac{\partial^2\mu_y}{\partial t^2} \\ \frac{EHK}{2(1+\nu)}\Delta w_0+\frac{EHK}{2(1+\nu)}\left(\frac{\partial\mu_x}{\partial x}+\frac{\partial\mu_y}{\partial y}\right)=\rho H\frac{\partial^2 w_0}{\partial t^2}-p(x,y;t) \end{aligned}\right\} \tag{12}$$

and the following boundary conditions:

$$\left.\begin{aligned} x=\begin{cases}=0\\=a\end{cases}\quad 0\leqslant y\leqslant b;\quad 0\leqslant x\leqslant a\quad y=\begin{cases}=0\\=b\end{cases} \\ D\left(\frac{\partial\mu_x}{\partial x}+\nu\frac{\partial\mu_y}{\partial y}\right)\delta\mu_x=0;\quad \frac{1-\nu}{2}D\left(\frac{\partial\mu_y}{\partial x}+\frac{\partial\mu_x}{\partial y}\right)\delta\mu_x=0 \\ \frac{1-\nu}{2}D\left(\frac{\partial\mu_x}{\partial y}+\frac{\partial\mu_y}{\partial x}\right)\delta\mu_y=0;\qquad D\left(\frac{\partial\mu_y}{\partial y}+\nu\frac{\partial\mu_x}{\partial x}\right)\delta\mu_y=0 \\ \frac{EKH}{2(1+\nu)}\left(\frac{\partial w_0}{\partial x}+\mu_x\right)\delta w_0=0;\quad \frac{EKH}{2(1+\nu)}\left(\frac{\partial w_0}{\partial y}+\mu_y\right)\delta w_0=0 \end{aligned}\right\} \tag{13}$$

are derived.

In equations (12) and (13) $D=EH^3/12(1-\nu^2)$, and $\Delta=[(\partial^2/\partial x^2)+(\partial^2/\partial y^2)]$ is Laplace's two-dimensional operator. The shear forces T_x and T_y, the bending moments M_x and M_y, the twisting moments M_{xy} and M_{yx} per unit length of the plate (see Fig. 2) are defined by the following expressions:

$$\left.\begin{aligned} T_x=\int_{-H/2}^{H/2}\tau_{xz}\,1\,dz=\int_{-H/2}^{H/2}GK\gamma_{xz}\,1\,dz=\frac{EKH}{2(1+\nu)}\left(\frac{\partial w_0}{\partial x}+\mu_x\right) \\ T_y=\int_{-H/2}^{H/2}\tau_{yz}\,1\,dz=\int_{-H/2}^{H/2}GK\gamma_{yz}\,1\,dz=\frac{EKH}{2(1+\nu)}\left(\frac{\partial w_0}{\partial y}+\mu_y\right) \end{aligned}\right\} \tag{14}$$

$$\left.\begin{aligned} M_x=\int_{-H/2}^{H/2}\sigma_x z1\,dz=D\left(\frac{\partial\mu_x}{\partial x}+\nu\frac{\partial\mu_y}{\partial y}\right) \\ M_y=\int_{-H/2}^{H/2}\sigma_y z1\,dz=D\left(\frac{\partial\mu_y}{\partial y}+\nu\frac{\partial\mu_x}{\partial x}\right) \end{aligned}\right\} \tag{15}$$

$$M_{xy}=M_{yx}=\int_{-H/2}^{H/2}\tau_{xy}z1\,dz=\int_{-H/2}^{H/2}G\gamma_{xy}z1\,dz=\frac{1-\nu}{2}D\left(\frac{\partial\mu_x}{\partial y}+\frac{\partial\mu_y}{\partial x}\right) \tag{16}$$

In view of equations (14), (15) and (16), equations (12) can be written

$$\left.\begin{aligned} \frac{\partial M_x}{\partial x}+\frac{\partial M_{xy}}{\partial y}-T_x &= \frac{\rho H^3}{12}\frac{\partial^2 \mu_x}{\partial t^2} \\ \frac{\partial M_{yx}}{\partial x}+\frac{\partial M_y}{\partial y}-T_y &= \frac{\rho H^3}{12}\frac{\partial^2 \mu_y}{\partial t^2} \\ \frac{\partial T_x}{\partial x}+\frac{\partial T_y}{\partial y}+p &= \rho H\frac{\partial^2 w_0}{\partial t^2} \end{aligned}\right\} \tag{17}$$

The terms on the right of the first two equations (17) represent the terms due to rotatory inertia.

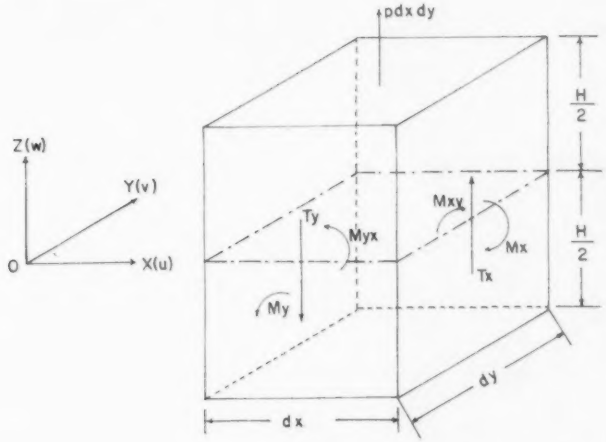

FIG. 2.

Equations (17) are the same equations as those obtained in 1951 in a completely different way by Mindlin[5]. By differentiating the first of equations (12) with respect to x, the second with respect to y and adding them together, one obtains the following equation:

$$\left[D\Delta-\frac{EHK}{2(1+\nu)}-\frac{\rho H^2}{12}\frac{\partial^2}{\partial t^2}\right]\left(\frac{\partial \mu_x}{\partial x}+\frac{\partial \mu_y}{\partial y}\right)=\frac{EHK}{2(1+\nu)}\Delta w_0 \tag{18}$$

By eliminating the term $[(\partial \mu_x/\partial x)+(\partial \mu_y/\partial y)]$ between equation (18) and the third of equations (12), one obtains

$$\left.\begin{aligned} &\left[\Delta-\frac{2\rho(1+\nu)}{EK}\frac{\partial^2}{\partial t^2}\right]\left[D\Delta-\frac{\rho H^3}{12}\frac{\partial^2}{\partial t^2}\right]w_0(x,y;t)+\rho H\frac{\partial^2 w_0(x,y;t)}{\partial t^2} \\ &\qquad=\left[1-\frac{H^2}{6(1-\nu)K}\Delta+\frac{\rho H^2(1+\nu)}{6EK}\right]p(x,y;t) \end{aligned}\right\} \tag{19}$$

If in equation (19) the terms due to shear are neglected equation (19) becomes

$$\left[D\Delta-\frac{\rho H^3}{12}\frac{\partial^2}{\partial t^2}\right]\Delta w_0(x,y;t)+\rho H\frac{\partial^2 w_0(x,y;t)}{\partial t^2}=p(x,y;t) \tag{20}$$

Vol. 3
1961

If in equation (19) the terms due to rotatory inertia are neglected equation (19) becomes

$$D\left[\Delta-\frac{2\rho(1+\nu)}{EK}\frac{\partial^2}{\partial t^2}\right]\Delta w_0(x,y;t)+\rho H\frac{\partial^2 w_0(x,y;t)}{\partial t^2}=\left[1-\frac{H^2}{6(1-\nu)K}\Delta\right]p(x,y;t) \tag{21}$$

If finally in equation (19) terms due to rotatory inertia and to shear are neglected at the same time, equation (19) reduces to the classic plate equation

$$D\Delta\Delta w_0(w,y;t)+\rho H\frac{\partial^2 w_0(x,y;t)}{\partial t^2}=p(x,y;t) \tag{22}$$

If in the components of the elastic displacement one considers only the first approximation terms in accordance with equation (2) (see Ref. 12):

$$\left.\begin{aligned} u(x,y,z;t)&=z\mu_x(x,y;t)\\ v(x,y,z;t)&=z\mu_y(x,y;t)\\ w(x,y,z;t)&=v_z(x,y;t)\end{aligned}\right\} \tag{2'}$$

the following equation of motion is obtained in final form

$$\left.\begin{aligned}\left[\Delta-\frac{2\rho(1+\nu)}{E}\frac{\partial^2}{\partial t^2}\right]\left[\frac{D(1-\nu^2)}{(1-2\nu)}\Delta-\frac{\rho H^3}{12}\frac{\partial^2}{\partial t^2}\right]w_0(x,y;t)+\rho H\frac{\partial^2 w_0(x,y;t)}{\partial t^2}\\ =\left[1-\frac{H^2}{6(1-2\nu)}\Delta+\frac{\rho H^2(1+\nu)}{6E}\frac{\partial^2}{\partial t^2}\right]p(x,y;t)\end{aligned}\right\} \tag{23}$$

3. PROPAGATION OF FLEXURAL WAVES IN PLATES

Let

$$w_0(x;t)=C\exp\left[i\gamma(x-ct)\right] \tag{24}$$

where C is a constant, $i=\sqrt{-1}$, $\gamma=2\pi/L$, L the wavelength and c the phase velocity. By substituting equation (24) into equations (19), (20), (21), (22) and (23) after expressing that $p=0$, one obtains the following dispersion equations:

From the elementary theory [equation (22)]

$$\frac{c}{c_0}=\frac{H}{L}\frac{\pi}{\sqrt{[3(1-\nu^2)]}} \tag{25}$$

From equation (19) one obtains

$$\left(\frac{H}{L}\right)^2=\frac{3}{\pi^2}\frac{K}{2(1+\nu)}\frac{(c/c_0)^2}{[(c/c_0)^2-K/2(1+\nu)]\,[(c/c_0)^2-1/(1-\nu^2)]} \tag{26}$$

From equations (20), (21) and (24) respectively one obtains

$$\left(\frac{H}{L}\right)^2=\frac{3}{\pi^2}\frac{(c/c_0)^2}{1/(1-\nu^2)-(c/c_0)^2} \tag{27}$$

$$\left(\frac{H}{L}\right)^2=\frac{3K(1-\nu)}{2\pi^2}\frac{(c/c_0)^2}{K/2(1+\nu)-(c/c_0)^2} \tag{28}$$

$$\left(\frac{H}{L}\right)^2=\frac{3}{2\pi^2(1+\nu)}\frac{(c/c_0)^2}{[(c/c_0)^2-1/2(1+\nu)]\,[(c/c_0)^2-(1-\nu)/(1+\nu)\,(1-2\nu)]} \tag{29}$$

Instead the theory given by Lamb[13] which will be referred to in our text as the "exact theory" gives the following frequency equation in the case of flexural waves:

$$\frac{\tanh[n(H/2)]}{\tanh[m(H/2)]} = \frac{(\gamma^2+n^2)^2}{4\gamma^2 mn} \tag{30}$$

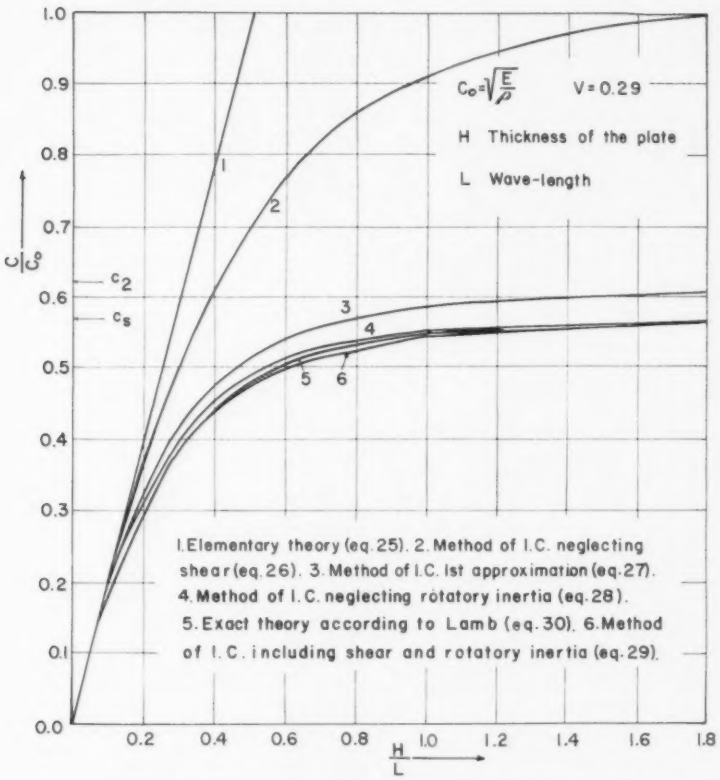

FIG. 3. Phase velocity of flexural waves in a thin plate.

In equation (30)

$$m = \gamma\sqrt{\left(1-\frac{c^2}{c_1^2}\right)}$$

$$n = \gamma\sqrt{\left(1-\frac{c^2}{c_2^2}\right)}$$

$$\gamma = \frac{2\pi}{L} \qquad \text{wavenumber}$$

with

$$c_1 = \sqrt{\left[\frac{E(1-\nu)}{(1+\nu)(1-2\nu)\rho}\right]} \qquad \text{velocity of waves of dilatation}$$

$$c_2 = \sqrt{\left[\frac{E}{2(1+\nu)\rho}\right]} \qquad \text{velocity of waves of distortion}$$

In the case of long waves (i.e. $L \gg H$) equation (30) reduces to equation (25) of the elementary theory, as Lamb has shown, whereas in the case of short waves (i.e. $L \ll H$) equation (30) can be written under the following form:

$$\left(\frac{c_s^2}{c_2^2}\right)^3 - 8\left(\frac{c_s^2}{c_2^2}\right)^2 + \left(\frac{c_s^2}{c_2^2}\right)\left(24 - 16\frac{c_2^2}{c_1^2}\right) - 16\left(1 - \frac{c_2^2}{c_1^2}\right) = 0 \tag{31}$$

Equation (31) is the equation of the Rayleigh surface waves.[14] In the case of $\nu = 0{\cdot}29$ the only solution of equation (31) is

$$c_s = 0{\cdot}9238\, c_2 \quad \text{or} \quad c_s = 0{\cdot}5763\, c_0$$

In Fig. 3 the curves c/c_0 against H/L according to equations (25), (26), (27), (28), (29) and (30) are given. The value for the constant K in equations (26) and (28) is equal to 0·857 which is the value of the ratio between the velocities of the Rayleigh surface waves and the waves of dilatation in an infinite medium for $\nu = 0{\cdot}29$ (Steel).

4. REDUCTION TO THE STATIC CASE

In the static case equations (12) become

$$\left.\begin{aligned} D\frac{\partial^2 \mu_x}{\partial x^2} + \frac{1+\nu}{2} D\frac{\partial^2 \mu_y}{\partial x\, \partial y} + \frac{1-\nu}{2} D\frac{\partial^2 \mu_x}{\partial y^2} \\ - \frac{EHK}{2(1+\nu)}\frac{\partial w_0}{\partial x} - \frac{EHK}{2(1+\nu)}\mu_x = 0 \\ D\frac{\partial^2 \mu_y}{\partial y^2} + \frac{1+\nu}{2} D\frac{\partial^2 \mu_x}{\partial x\, \partial y} + \frac{1-\nu}{2} D\frac{\partial^2 \mu_y}{\partial x^2} \\ - \frac{EHK}{2(1+\nu)}\frac{\partial w_0}{\partial y} - \frac{EHK}{2(1+\nu)}\mu_y = 0 \\ \frac{EHK}{2(1+\nu)}\Delta w_0 + \frac{EHK}{2(1+\nu)}\left(\frac{\partial \mu_x}{\partial x} + \frac{\partial \mu_y}{\partial y}\right) = -p(x,y) \end{aligned}\right\} \tag{32}$$

whereas the equations for the boundary conditions remain the same [equations (13)].

Equations (17) become in the static case

$$\left.\begin{aligned} \frac{\partial M_x}{\partial x} + \frac{\partial M_{xy}}{\partial y} = T_x \\ \frac{\partial M_{yx}}{\partial x} + \frac{\partial M_y}{\partial y} = T_y \\ \frac{\partial T_x}{\partial x} + \frac{\partial T_y}{\partial y} = -p(x,y) \end{aligned}\right\} \tag{33}$$

while equation (19) becomes

$$D\Delta\Delta w_0(x,y) = \left[1 - \frac{H^2}{6(1-\nu)K}\Delta\right] p(x,y) \tag{34}$$

From equations (14) and (15) one obtains

$$\frac{EH}{2(1+\nu)}\mu_x = \frac{T_x}{K} - \frac{EH}{2(1+\nu)}\frac{\partial w_0}{\partial x}$$

$$\frac{EH}{2(1+\nu)}\mu_y = \frac{T_y}{K} - \frac{EH}{2(1+\nu)}\frac{\partial w_0}{\partial y}$$

$$M_x = D\left(\frac{\partial \mu_x}{\partial x} + \nu\frac{\partial \mu_y}{\partial y}\right) = \frac{H^2}{6(1-\nu)}\left[\frac{1}{K}\left(\frac{\partial T_x}{\partial x} + \nu\frac{\partial T_y}{\partial y}\right) - D\left(\frac{\partial^2 w_0}{\partial x^2} + \nu\frac{\partial^2 w_0}{\partial y^2}\right)\right]$$

or
$$M_x - \frac{H^2}{6K}\frac{\partial T_x}{\partial x} - \frac{\nu H^2}{6(1-\nu)K}\left(\frac{\partial T_x}{\partial x} + \frac{\partial T_y}{\partial y}\right) = -D\left(\frac{\partial^2 w_0}{\partial x^2} + \nu\frac{\partial^2 w_0}{\partial y^2}\right)$$

and in view of the last of equations (33) one obtains

$$M_x - \frac{H^2}{6K}\frac{\partial T_x}{\partial x} + \frac{\nu H^2}{6(1-\nu)K}p = -D\left(\frac{\partial^2 w_0}{\partial x^2} + \nu\frac{\partial^2 w_0}{\partial y^2}\right) \tag{35}$$

In the same way one obtains for

$$M_y - \frac{H^2}{6K}\frac{\partial T_y}{\partial y} + \frac{\nu H^2}{6(1-\nu)K}p = -D\left(\frac{\partial^2 w_0}{\partial y^2} + \nu\frac{\partial^2 w_0}{\partial x^2}\right) \tag{36}$$

By combining equations (14) and (16) one obtains

$$M_{xy} = M_{yx} = \frac{1-\nu}{2}D\left(\frac{\partial \mu_x}{\partial y} + \frac{\partial \mu_y}{\partial x}\right) = \frac{H^2}{12}\left[\frac{1}{K}\left(\frac{\partial T_x}{\partial y} + \frac{\partial T_y}{\partial x}\right) - \frac{EH^3}{12(1+\nu)}\frac{\partial^2 w_0}{\partial x\,\partial y}\right]$$

and finally

$$M_{xy} - \frac{H^2}{12K}\left(\frac{\partial T_x}{\partial y} + \frac{\partial T_y}{\partial x}\right) = -(1-\nu)D\frac{\partial^2 w_0}{\partial x\,\partial y} \tag{37}$$

By substituting for M_x and M_y in the first of equations (33) the values given by equations (35) and (37), and, in view of the last of equations (33), one obtains

$$T_x - \frac{H^2}{12K}\Delta T_x + \frac{H^2}{12(1-\nu)K}\frac{\partial p}{\partial x} = -D\frac{\partial}{\partial x}\Delta w_0 \tag{38}$$

In the same way for T_y one obtains

$$T_y - \frac{H^2}{12K}\Delta T_y + \frac{H^2}{12(1-\nu)K}\frac{\partial p}{\partial y} = -D\frac{\partial}{\partial y}\Delta w_0 \tag{39}$$

In the static case the value of the shear coefficient K should be

$$K = 1/1{\cdot}2 = 0{\cdot}833 \quad \text{(See Ref. 15.)}$$

Vol. 3
1961

In the case of a very thin plate ($H \to 0$), the above equations then reduce to the following

$$D\Delta\Delta w_0 = p(x,y) \tag{34'}$$

$$M_x = -D\left[\frac{\partial^2 w_0}{\partial x^2} + \nu\frac{\partial^2 w_0}{\partial y^2}\right] \tag{35'}$$

$$M_y = -D\left[\frac{\partial^2 w_0}{\partial y^2} + \nu\frac{\partial^2 w_0}{\partial x^2}\right] \tag{36'}$$

$$M_{xy} = M_{yx} = -(1-\nu)\,D\frac{\partial^2 w_0}{\partial x\,\partial y} \tag{37'}$$

$$T_x = -D\frac{\partial}{\partial x}(\Delta w_0) \tag{38'}$$

$$T_y = -D\frac{\partial}{\partial y}(\Delta w_0) \tag{39'}$$

of the classical theory.

Equations (34), (35), (36), (37), (38) and (39) correspond to the following equations of Reissner's theory:[6,8]

$$D\Delta\Delta w_0 = \left(1 - \frac{H^2}{10}\frac{2-\nu}{1-\nu}\right)p \tag{34''}$$

$$M_x - \frac{H^2}{5}\frac{\partial T_x}{\partial x} - \frac{H^2}{10}\frac{\nu}{(1-\nu)}p = -D\left(\frac{\partial^2 w_0}{\partial x^2} + \nu\frac{\partial^2 w_0}{\partial y^2}\right) \tag{35''}$$

$$M_y - \frac{H^2}{5}\frac{\partial T_y}{\partial y} - \frac{H^2}{10}\frac{\nu}{(1-\nu)}p = -D\left(\frac{\partial^2 w_0}{\partial y^2} + \nu\frac{\partial^2 w_0}{\partial x^2}\right) \tag{36''}$$

$$M_{xy} - \frac{H^2}{10}\left(\frac{\partial T_x}{\partial y} + \frac{\partial T_y}{\partial x}\right) = -(1-\nu)\,D\frac{\partial^2 w_0}{\partial x\,\partial y} \tag{37''}$$

$$T_x - \frac{H^2}{10}\Delta T_x + \frac{H^2}{10(1-\nu)}\frac{\partial p}{\partial x} = -D\frac{\partial}{\partial x}(\Delta w_0) \tag{38''}$$

$$T_y - \frac{H^2}{10}\Delta T_y + \frac{H^2}{10(1-\nu)}\frac{\partial p}{\partial y} = -D\frac{\partial}{\partial y}(\Delta w_0) \tag{39''}$$

In Reissner's theory appropriate and rational assumptions are made regarding the variation of the stresses across the thickness of the plate: i.e. the bending stresses vary linearly while the transverse shear-stresses vary parabolically, and the normal stress σ_z is different from zero. However, the theory which we have presented and which is based on the second approximation of the method of internal constraints leads almost to the same numerical results as those derived by the more elaborate theory.

5. FLEXURAL VIBRATIONS OF STRAIGHT ELASTIC BARS

In the case of flexural vibrations the components of displacement u, v, w, in the direction of the axes X, Y and Z will be assumed to be

$$\left.\begin{aligned} u(x,y,z;t) &= y\lambda_x(x;t) \\ v(x,y,z;t) &= v_y(x;t) + \tfrac{1}{2}y^2 f_1(x;t) \\ w(x,y,z;t) &= yzf_2(x;t) \end{aligned}\right\} \tag{40}$$

The axis X coincides with the axis of the bar while the Y and Z axes coincide with the principal axes of inertia of the cross-section of the bar. This cross-section will be at first supposed to be a rectangle of sides H and B [see Fig. 1(b)].

From equations (40) one finds for the normal stresses σ_y and σ_z the expressions

$$\left.\begin{aligned}\sigma_y &= (\lambda+2G)\,yf_1+\lambda yf_2+\lambda y\frac{\partial\lambda_x}{\partial x}\\ \sigma_z &= (\lambda+2G)\,yf_2+\lambda yf_1+\lambda y\frac{\partial\lambda_x}{\partial x}\end{aligned}\right\} \tag{41}$$

Equations (41) show that in order to satisfy the conditions that

$$\sigma_y=\sigma_z=0$$

the following relationships must be verified:

$$f_1=f_2=-\nu\frac{\partial\lambda_x}{\partial x} \tag{42}$$

From equations (40) and (42) the following expressions are obtained for the potential and kinetic energies of the bar:

$$U=\int_0^l\left\{\frac{E}{2}I_z\left[1+K\frac{\nu^2}{2(1+\nu)}\frac{I_y}{I_z}\right]\left(\frac{\partial\lambda_x}{\partial x}\right)^2+\frac{KE}{4(1+\nu)}A\left[(\lambda_x)^2+\left(\frac{\partial v_y}{\partial x}\right)^2+2\lambda_x\frac{\partial v_y}{\partial x}\right]\right\}dx \tag{43}$$

$$T=\frac{\rho}{2}\int_0^l\left\{I_z\left(\frac{\partial\lambda_x}{\partial t}\right)^2+A\left(\frac{\partial v_y}{\partial t}\right)^2\right\}dx \tag{44}$$

In deriving equations (43) and (44) terms containing y^2 and yz have been neglected in the expressions for the components of strain and particle velocities in comparison with linear terms. l represents the length of the bar, I_y and I_z the moments of inertia of its cross-section with respect to the Y and Z axes, A the area of the cross-section. The factor K (shear-coefficient) was introduced as in the previous case of the plate to take into account the non-linear distribution of shear over the cross-section of the bar. On the assumption that no external forces (body and surface forces) are applied to the bar, using the Hamilton principle, the following equations of motion:

$$\begin{aligned}EI_z(1+\epsilon)\frac{\partial^2\lambda_x}{\partial x^2}-KGA\lambda_x-KGA\frac{\partial v_y}{\partial x}&=\rho I_z\frac{\partial^2\lambda_x}{\partial t^2}\\ KGA\frac{\partial^2 v_y}{\partial x^2}+KGA\frac{\partial\lambda_x}{\partial x}&=\rho A\frac{\partial^2 v_y}{\partial t^2}\end{aligned} \tag{45}$$

and boundary conditions:

$$\text{for}\quad x=0;\quad x=l\qquad\left[\frac{\partial\lambda_x}{\partial x}\right]\delta\lambda_x=0,\quad\left[\frac{\partial v_y}{\partial x}+\lambda_x\right]\delta v_y=0 \tag{46}$$

with $\epsilon=K\dfrac{\nu^2}{2(1+\nu)}\dfrac{I_y}{I_z}$ are obtained.

Vol. 3
1961

It should be pointed out that the validity of equations (45) and (46) is not limited to a bar of rectangular cross-section. In fact the only parameter related to the shape of the cross-section is the ratio of the moments of inertia I_y/I_z, so that equations (45) and (46) are valid for a bar of any cross-section.

If one compares equations (45) and (46) with the equations for flexural vibrations of bars which were derived in previous papers by using the first approximation of the method of internal constraints[3, 16] one sees that from a mathematical point of view they are exactly the same equations except that the numerical coefficients have changed. However, the approximation given by the newly derived equations is much improved. This is clearly shown by comparing the dispersion curves of flexural vibrations of straight bars as will be shown later.

Equations (45) can be written under the following form:

$$\frac{E}{\rho} r_z^2(1+\epsilon)\frac{\partial^4 w_0}{\partial x^4} - r_z^2\left[(1+\epsilon)+\frac{2(1+\nu)}{K}\right]\frac{\partial^4 w_0}{\partial x^2\,\partial t^2} + \frac{2(1+\nu)}{EK}\rho r_z^2\frac{\partial^4 w_0}{\partial t^4} + \frac{\partial^2 w_0}{\partial t^2} = 0 \tag{47}$$

where $w_0 = v_y$ and $r_z = \sqrt{(I_z/A)}$.

In the case of plain strain the ratio I_y/I_z becomes zero and equation (47) reduces to the well-known Timoshenko equation

$$\frac{E}{\rho} r^2\frac{\partial^4 w_0}{\partial x^4} - r^2\left[1+\frac{2(1+\nu)}{K}\right]\frac{\partial^4 w_0}{\partial x^2\,\partial t^2} + \frac{2(1+\nu)}{EK}\rho r^2\frac{\partial^4 w_0}{\partial t^4} + \frac{\partial^2 w_0}{\partial t^2} = 0 \tag{48}$$

If in equation (48) the terms due to shear are neglected, the differential equation is modified to the form usually attributed to Rayleigh (Rayleigh theory):

$$\frac{E}{\rho} r^2\frac{\partial^4 w_0}{\partial x^4} - r^2\frac{\partial^4 w_0}{\partial x^2\,\partial t^2} + \frac{\partial^2 w_0}{\partial t^2} = 0 \tag{49}$$

If in equation (48) terms due to rotatory inertia and to shear are neglected the equation reduces to the equation

$$\frac{E}{\rho} r^2\frac{\partial^4 w_0}{\partial x^4} + \frac{\partial^2 w_0}{\partial t^2} = 0 \tag{50}$$

of the elementary theory.

If in the components of the elastic displacement one considers only the first approximation, in accordance with equation (1) the following equation of motion is obtained:

$$\frac{E}{\rho}\frac{(1-\nu)}{(1+\nu)(1-2\nu)} r^2\frac{\partial^4 w_0}{\partial x^4} - r^2\left(\frac{3-4\nu}{1-2\nu}\right)\frac{\partial^4 w_0}{\partial x^2\,\partial t^2} + \frac{2(1+\nu)}{E} r^2\rho\frac{\partial^4 w_0}{\partial t^4} + \frac{\partial^2 w_0}{\partial t^2} = 0 \tag{51}$$

From equation (47) the following dispersion equation is derived:

$$\left[\frac{r_z}{L}\right]^2 = \frac{1}{4\pi^2}\frac{K}{2(1+\nu)}\frac{(c/c_0)^2}{[(c/c_0)^2 - K/2(1+\nu)]\,[(c/c_0)^2 - (1+\epsilon)]} \tag{52}$$

In Fig. 4 phase velocities of flexural waves in cylindrical bars according to the elementary theory, the Rayleigh theory, the Timoshenko theory, the exact Pochhammer theory,[17] and the method of internal constraints (first and second approximation) are compared.

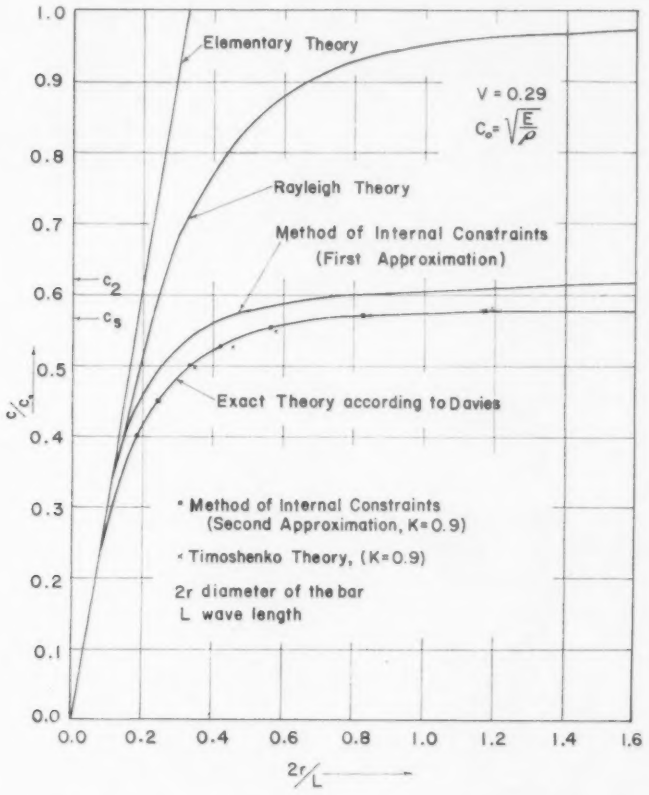

FIG. 4. Phase velocity of flexural waves in cylindrical bars.

6. LONGITUDINAL VIBRATIONS OF STRAIGHT ELASTIC BARS

In the case of longitudinal vibrations in a bar of rectangular cross-section [see Fig. 1(b)] the components of the elastic displacement will be assumed to be

$$\left.\begin{aligned} u(x,y,z;t) &= v_x(x;t) \\ v(x,y,z;t) &= y\lambda_y(x;t)+y^3f_1(x;t)+yz^2f_2(x;t) \\ w(x,y,z;t) &= z\lambda_z(x;t)+z^3f_3(x;t)+zy^2f_4(x;t) \end{aligned}\right\} \tag{53}$$

The functions f_1, f_2, f_3 and f_4 are determined in terms of the unknown functions v_x, λ_y and λ_z from the condition that the free surfaces of the bar are free from normal stresses.

In fact if

$$\sigma_y = 0 \quad \text{for} \quad y = \pm H/2$$

$$\sigma_z = 0 \quad \text{for} \quad z = \pm B/2$$

the following two equations are obtained:

$$(\lambda+2G)\left[\lambda_y+\frac{3H^2}{4}f_1+z^2 f_2\right]+\lambda\left[\frac{\partial v_x}{\partial x}+\lambda_z+3z^2 f_3+\frac{H^2}{4}f_4\right]=0$$

$$(\lambda+2G)\left[\lambda_z+\frac{3B^2}{4}f_3+y^2 f_4\right]+\lambda\left[\frac{\partial v_x}{\partial x}+\lambda_y+3y^2 f_1+\frac{B^2}{4}f_2\right]=0$$

Since the above two equations have to be satisfied identically for any value of the variables y and z, they are equivalent to the following four equations:

$$\left.\begin{aligned}
f_1 &= -\frac{1}{3H^2}\frac{\lambda+2G}{G(\lambda+G)}\left[\lambda\frac{\partial v_x}{\partial x}+\lambda\lambda_z+(\lambda+2G)\lambda_y\right]\\
f_2 &= \frac{1}{B^2}\frac{\lambda}{G(\lambda+G)}\left[\lambda\frac{\partial v_x}{\partial x}+\lambda\lambda_y+(\lambda+2G)\lambda_z\right]\\
f_3 &= -\frac{1}{3B^2}\frac{\lambda+2G}{G(\lambda+G)}\left[\lambda\frac{\partial v_x}{\partial x}+\lambda\lambda_y+(\lambda+2G)\lambda_z\right]\\
f_4 &= \frac{1}{H^2}\frac{\lambda}{G(\lambda+G)}\left[\lambda\frac{\partial v_x}{\partial x}+\lambda\lambda_z+(\lambda+2G)\lambda_y\right]
\end{aligned}\right\} \tag{54}$$

In the evaluation of the potential and kinetic energies of the bar the terms containing y^4, z^4 and y^2z^2 are neglected in comparison with second-degree terms. After integration with respect to the variables y and z the following expressions are obtained:

$$\left.\begin{aligned}
U = BH\int_0^l \Bigg\{ &\left(\frac{\lambda}{2}+G\right)\left[\left(1-\frac{4}{3}\frac{\nu^2}{(1-\nu)}\right)\left(\frac{\partial v_x}{\partial x}\right)^2+\tfrac{1}{3}(\lambda_y)^2+\tfrac{1}{3}(\lambda_z)^2\right.\\
&\left.+\frac{2}{3}\frac{\nu}{1-\nu}\left(\frac{\partial v_x}{\partial x}\lambda_y+\frac{\partial v_x}{\partial x}\lambda_z+\lambda_y\lambda_z\right)\right]\\
&+\frac{KG}{2}\left[\frac{H^2}{12}\left(\frac{\partial\lambda_y}{\partial x}\right)^2+\frac{B^2}{12}\left(\frac{\partial\lambda_z}{\partial x}\right)^2\right]\Bigg\}dx
\end{aligned}\right\} \tag{55}$$

$$T = \frac{BH\rho}{2}\int_0^l\left\{\left(\frac{\partial v_x}{\partial t}\right)^2+\frac{H^2}{12}\left(\frac{\partial\lambda_y}{\partial t}\right)^2+\frac{B^2}{12}\left(\frac{\partial\lambda_z}{\partial t}\right)^2\right\}dx \tag{56}$$

In the absence of body and surface forces, applying the Hamilton principle, the following equations of motion

$$\left.\begin{aligned}
&(\lambda+2G)\left(1-\frac{4}{3}\frac{\nu^2}{1-\nu}\right)\frac{\partial^2 v_x}{\partial x^2}+\tfrac{1}{3}\lambda\frac{\partial\lambda_y}{\partial x}+\tfrac{1}{3}\lambda\frac{\partial\lambda_z}{\partial x}=\rho\frac{\partial^2 v_x}{\partial t^2}\\
&KG\frac{H^2}{12}\frac{\partial^2\lambda_y}{\partial x^2}-\tfrac{1}{3}(\lambda+2G)\lambda_y-\tfrac{1}{3}\lambda\frac{\partial v_x}{\partial x}-\tfrac{1}{3}\lambda\lambda_z=\rho\frac{H^2}{12}\frac{\partial^2\lambda_y}{\partial t^2}\\
&KG\frac{B^2}{12}\frac{\partial^2\lambda_z}{\partial x^2}-\tfrac{1}{3}(\lambda+2G)\lambda_z-\tfrac{1}{3}\lambda\frac{\partial v_x}{\partial x}-\tfrac{1}{3}\lambda\lambda_y=\rho\frac{B^2}{12}\frac{\partial^2\lambda_z}{\partial t^2}
\end{aligned}\right\} \tag{57}$$

and boundary conditions at $x = 0; \quad x = l$

$$\left.\begin{aligned}\left[(\lambda+2G)\left(1-\frac{4}{3}\frac{\nu^2}{1-\nu}\right)\frac{\partial v_x}{\partial x}+\tfrac{1}{3}\lambda\lambda_y+\tfrac{1}{3}\lambda\lambda_z\right]\delta v_x = 0\\ \left[\frac{\partial\lambda_y}{\partial x}\right]\delta\lambda_y = 0\\ \left[\frac{\partial\lambda_z}{\partial x}\right]\delta\lambda_z = 0\end{aligned}\right\} \tag{58}$$

are derived.

If one compares equations (57) and (58) with the equations (37) and (41) of the previous paper[16] (where the equations of motion and boundary conditions for longitudinal vibrations of a straight bar were derived by applying the first approximation of the method of internal constraints) one sees that, in the case of longitudinal vibrations also, the second approximation does not change the form *but changes only* the constants of the equations of motion. Thus the frequency equations and modal functions of a longitudinally vibrating bar can be derived by properly changing the constants of the equations given in a previous paper.[3]

Vol. 3
1961

The equations of motion and corresponding boundary conditions for the plane stress case are obtained from the previous equations (57) and (58). In fact, by letting B approach zero the third of equations (57) becomes

$$\lambda_z = -\frac{\lambda}{\lambda+2G}\left[\frac{\partial v_x}{\partial x}+\lambda_y\right]$$

Substituting this value of λ_z in the two other equations (57) and (58) the equations of motion and boundary conditions for the case of plane stress are obtained under the following form. For the equations of motion:

$$\left.\begin{aligned}\frac{E}{(1-\nu^2)}(1-\tfrac{2}{3}\nu^2)\frac{\partial^2 v_x}{\partial x^2}+\frac{1}{3}\frac{E\nu}{1-\nu^2}\frac{\partial\lambda_y}{\partial x} = \rho\frac{\partial^2 v_x}{\partial t^2}\\ K\frac{E}{2(1+\nu)}\frac{H^2}{12}\frac{\partial^2\lambda_y}{\partial x^2}-\frac{1}{3}\frac{E}{1-\nu^2}\lambda_y-\frac{1}{3}\frac{E\nu}{1-\nu^2}\frac{\partial v_x}{\partial x} = \rho\frac{H^2}{12}\frac{\partial^2\lambda_y}{\partial t^2}\end{aligned}\right\} \tag{59}$$

For the boundary conditions at $x = 0; \quad x = l$

$$\left.\begin{aligned}\left[(1-\tfrac{2}{3}\nu^2)\frac{\partial v_x}{\partial x}+\frac{\nu}{3}\lambda_y\right]\delta v_x = 0\\ \left[\frac{\partial\lambda_y}{\partial x}\right]\delta\lambda_y = 0\end{aligned}\right\} \tag{60}$$

From equations (57) the dispersion equation for longitudinal waves is derived under the following form:

$$\begin{aligned}&\left(\frac{H}{L}\right)^4\pi^4\beta^2\left[\left(\frac{c}{c_0}\right)^2-\frac{(1-\nu)}{(1+\nu)(1-2\nu)}\left(1-\frac{4}{3}\frac{\nu^2}{(1-\nu)}\right)\right]\left[\left(\frac{c}{c_0}\right)^2-\frac{K}{2(1+\nu)}\right]^2\\ &-\left(\frac{H}{L}\right)^2\pi^2(1+\beta^2)\frac{(1-\nu)}{(1+\nu)(1-2\nu)}\left[\left(\frac{c}{c_0}\right)^2-\frac{K}{2(1+\nu)}\right]\left[\left(\frac{c}{c_0}\right)^2-\frac{1}{(1-\nu^2)}(1-\tfrac{2}{3}\nu^2)\right]\\ &+\frac{(c/c_0)^2-1}{(1+\nu)^2(1-2\nu)} = 0\end{aligned} \tag{61}$$

The constant β in equation (61) represents the ratio of the sides B/H of the beam. If $\beta \to 0$ in equation (61) the dispersion equation for the case of plane stress is obtained under the form

$$\left(\frac{H}{L}\right)^2 = \frac{1}{\pi^2}\frac{1}{(1-\nu^2)}\frac{(c/c_0)^2-1}{[(c/c_0)^2-K/2(1+\nu)]\{(c/c_0)^2-[1/(1-\nu^2)](1-\frac{2}{3}\nu^2)\}} \tag{62}$$

The lowest root, c/c_0, of equation (61) is plotted against the ratio r/L in Fig. 5 for the case of a bar of square cross-section ($\beta = 1$). These results are

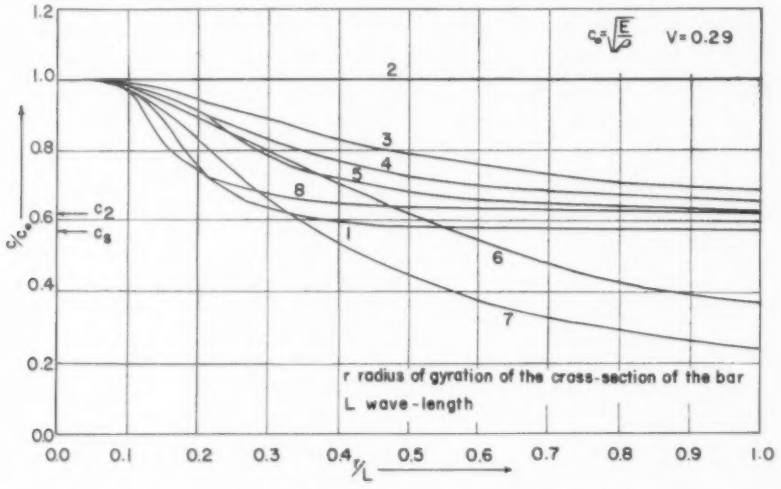

FIG. 5. Phase velocity of longitudinal waves in a bar of square cross-section: 1—Exact theory (according to Davies for cylindrical bars); 2—Elementary theory; 3—Bishop theory; 4—Bishop improved theory; 5—Method of I.C. (first approx.); 6—Love theory; 7—Love theory improved by Bishop; 8—Method of I.C. (second approx.).

compared with the results given by use of other engineering theories of longitudinal wave propagation and with the results obtained for a cylindrical bar from use of the exact theory by Davies[17]. It is possible to make this comparison between the results for bars of circular cross-section and square cross-section because, according to experiments made by Morse[18], the dispersion curve for a bar of square cross-section is very close to the one obtained for a bar of circular cross-section if the ratio of the diameter to the side of the square cross-section is 1·13.

The engineering theories, results of which are compared in Fig. 5 with the results given by the second approximation of the method of internal constraints, are the elementary theory[14], Love's theory[17], Bishop's theory, Bishop's improved theory, Love's theory improved by Bishop[20] and the method of internal constraints (first approximation). Since the frequency equations of all the above-mentioned engineering theories were derived and their implications discussed by the author in a previous paper,[21] they will not be discussed here.

In a Report of the Office of Ordnance Research[4] Zachmanoglou and the author applied the second approximation of the method of internal constraints to the problem of longitudinal vibrations in the plane-strain case and in the case of a bar of circular cross-section.

In the case of plane strain the assumed components of displacement are

$$\left.\begin{aligned} u(x,y;\,t) &= v_x(x;\,t) \\ v(x,y;\,t) &= y\lambda_y(x;\,t)+y^3 f(x;\,t) \\ w(x,y;\,t) &= 0 \end{aligned}\right\} \tag{63}$$

The condition that σ_y vanishes at the surface $y = \pm H/2$ implies

$$f = -\frac{4}{3H^2}\left[\lambda_y + \frac{\nu}{(1-\nu)}\frac{\partial v_x}{\partial x}\right]$$

In the same order of approximation as used in the previous cases the following equations of motion:

$$\left.\begin{aligned} (\lambda+2G)\left[1-\frac{2}{3}\left(\frac{\nu}{1-\nu}\right)^2\right]\frac{\partial^2 v_x}{\partial x^2}+\tfrac{1}{3}\lambda\frac{\partial \lambda_y}{\partial x} &= \rho\frac{\partial^2 v_x}{\partial t^2} \\ KG\frac{H^2}{12}\frac{\partial^2\lambda_y}{\partial x^2}-\tfrac{1}{3}(\lambda+2G)-\tfrac{1}{3}\lambda\frac{\partial v_x}{\partial x} &= \rho\frac{H^2}{12}\frac{\partial^2\lambda_y}{\partial t^2} \end{aligned}\right\} \tag{64}$$

and boundary conditions at $x = 0, \quad x = l$:

$$\left.\begin{aligned} \left[\left(1-\frac{2}{3}\frac{\nu^2}{(1-\nu)^2}\right)\frac{\partial v_x}{\partial x}+\frac{1}{3}\frac{\nu}{(1-\nu)}\lambda_y\right]\delta v_x &= 0 \\ \left(\frac{\partial\lambda_y}{\partial x}\right)\delta\lambda_y &= 0 \end{aligned}\right\} \tag{65}$$

are derived.

From equation (64) the dispersion equation

$$\left(\frac{H}{L}\right)^2 = \frac{1}{\pi^2}\frac{1-\nu}{(1+\nu)(1-2\nu)}\frac{(c/c_0)^2-[1/(1-\nu^2)]}{[(c/c_0)^2-K/2(1+\nu)]\{(c/c_0)^2-[(1-\nu)/(1+\nu)(1-2\nu)][1-\frac{2}{3}\nu^2(1-\nu)^2]\}} \tag{66}$$

is obtained.

In the case of the bar of circular cross-section the assumed components of displacement in polar co-ordinates are

$$\left.\begin{aligned} u_x(x,r,\theta;\,t) &= v_x(x;\,t) \\ u_r(x,r,\theta;\,t) &= r\lambda_r(x;\,t)+r^3 f(x;\,t) \\ u_\theta(x,r,\theta;\,t) &= 0 \end{aligned}\right\} \tag{67}$$

Vol. 3
1961

The condition that the normal stress σ_r vanishes on the surface $r = a$ of the bar implies

$$f = -\frac{1}{a^2}\frac{1}{(3-2\nu)}\left[\lambda_r + \nu\frac{\partial v_x}{\partial x}\right]$$

After performing the integration with respect to the variables r and θ, neglecting fourth powers of r, the following expressions are obtained:

For the potential energy

$$U = \pi a^2 \int_0^l \left\{ \frac{E(1-\nu)}{(1+\nu)(1-2\nu)} \left[\left(1 - \frac{4\nu^2}{(1-\nu)(3-2\nu)}\right)\left(\frac{\partial v_x}{\partial x}\right)^2 + \frac{2(1-2\nu)}{(1-\nu)(3-2\nu)}\left(\lambda_r^2 + 2\nu\lambda_r\frac{\partial v_x}{\partial x}\right)\right] + K\frac{G}{2}\frac{a^2}{2}\left(\frac{\partial \lambda_r}{\partial x}\right)^2 \right\} dx \tag{68}$$

For the kinetic energy

$$T = \pi a^2 \frac{\rho}{2}\int_0^l \left\{ \left(\frac{\partial v_x}{\partial t}\right)^2 + \frac{a^2}{2}\left(\frac{\partial \lambda_r}{\partial t}\right)^2 \right\} dx \tag{69}$$

In the absence of surface and body forces the following equations of motion:

$$\left.\begin{aligned} \frac{E(1-\nu)}{(1+\nu)(1-2\nu)}\left(1 - \frac{4\nu^2}{(1+\nu)(3-2\nu)}\right)\frac{\partial^2 v_x}{\partial x^2} + \frac{2\nu E}{(1+\nu)(3-2\nu)}\frac{\partial \lambda_r}{\partial x} &= \rho\frac{\partial^2 v_x}{\partial t^2} \\ KG\frac{a^2}{4}\frac{\partial^2 \lambda_r}{\partial x^2} - \frac{E}{(1+\nu)(3-2\nu)}\lambda_r - \frac{E\nu}{(1+\nu)(3-2\nu)}\frac{\partial v_x}{\partial x} &= \rho\frac{a^2}{4}\frac{\partial^2 \lambda_r}{\partial t^2} \end{aligned}\right\} \tag{70}$$

and boundary conditions at $x = 0, \quad x = l$

$$\left.\begin{aligned} \left[\frac{1-\nu}{1-2\nu}\left(1 - \frac{4\nu^2}{(1+\nu)(3-2\nu)}\right)\frac{\partial v_x}{\partial x} + \frac{2\nu}{3-2\nu}\lambda_r\right]\delta v_x = 0 \\ \left[\frac{\partial \lambda_r}{\partial x}\right]\delta\lambda_r = 0 \end{aligned}\right\} \tag{71}$$

are obtained.

From equation (70) the dispersion equation

$$\left(\frac{a}{L}\right)^2 = \frac{1}{\pi^2(1+\nu)(3-2\nu)} \frac{(c/c_0)^2 - 1}{[(c/c_0)^2 - K/2(1+\nu)]\{(c/c_0)^2 - (1-\nu)/(1+\nu)(1-2\nu)[1 - 4\nu^2/(1-\nu)(3-2\nu)]\}} \tag{72}$$

is derived.

In this particular case the first approximation of the method of internal constraints coincides, as already pointed out in a previous paper,[22] with the one-dimensional theory of compressional waves in an elastic rod presented by Mindlin and Herrmann[23].

Acknowledgement—Much of the material presented in Sections 5 and 6 above appeared in an Office of Ordnance Research Report by E. C. Zachmanoglou and the author[4]. Mr. E. C. Zachmanoglou did the computational work under the supervision of the author.

Vol. 196

Vol. 3
1961

REFERENCES

1. E. C. Zachmanoglou and E. Volterra, *Proc. 3rd U.S. Nat. Congr. Appl. Mech., Brown University, Providence, June* 1958, p. 239. The American Society of Mechanical Engineers, New York.
2. E. Volterra and E. C. Zachmanoglou, *J. Engng. Mech. Div.* Paper 1896; *Proc. Amer. Soc. Civil Engrs.* **85**, 33 (1959).
3. E. Volterra and E. C. Zachmanoglou, *Ing.-Arch.* **25**, 424 (1957).
4. E. C. Zachmanoglou and E. Volterra, Tech. Rep. No. 6. Office of Ordnance Research Contract No. DA–30–155–ORD–709 (May 1957).
5. R. D. Mindlin, *J. Appl. Mech.* **18**, 31 (1951).
6. E. Reissner, *J. Math. Phys.* **23**, 184 (1944); *J. Appl. Mech.* **12**A, 68 (1945); *Quart. Appl. Math.* **5**, 55 (1947).
7. A. E. Green, *Quart. Appl. Math.* **7**, 223 (1949).
8. M. Schaefer, *Z. angew. Math. Mech.* **32**, 161 (1952).
9. S. Timoshenko and S. Woinowsky-Krieger, *Theory of Plates and Shells* p. 165. McGraw-Hill, New York (1959).
10. K. O. Friedrichs, *Proc. Symp. Appl. Math.* 1949 Vol. 1, p. 188; *Reissner Anniversary Volume* p. 197. Edwards, Ann Arbor, Michigan (1949).
11. A. Kromm, *Ing.-Arch.* **21**, 266 (1955); *Z. angew. Math. Mech.* **35**, 231 (1955); M. Schaefer, *Ibid.* **32**, 161 (1952); S. Timoshenko and S. Woinowsky-Krieger, *Theory of Plates and Shells* p. 173. McGraw-Hill, New York (1959).
12. E. Volterra, *G. Gen. Civ.* Nos. 7 and 8 (1958).
13. H. Lamb, *Proc. Roy. Soc.* A **93**, 119 (1917).
14. H. Kolsky, *Stress Waves in Solids.* Clarendon Press, Oxford (1953).
15. L. Bolle, *Bull. Tech. Suisse Romande* No. 21 (11 October 1947) and No. 22 (25 October 1947).
16. E. Volterra, *Ing.-Arch.* **23**, 402 (1955).
17. R. M. Davies, *Trans. Roy. Soc.* A **240**, 375 (1948).
18. R. W. Morse, *J. Acoust. Soc. Amer.* **20**, 833 (1948); **22**, 219 (1950).
19. A. E. H. Love, *The Mathematical Theory of Elasticity.* University Press, Cambridge (1934).
20. R. E. D. Bishop, *Aeronaut. Quart.* **3**, 280 (1952).
21. E. Volterra, *J. Engng. Mech. Div. Proc. Amer. Soc. Civil Engrs.* **83**, 1 (1957).
22. E. Volterra, *Proc. September* 1955 *Madrid Colloq. Int. Un. Theoret. Appl. Mech. Deform. Flow Solids* p. 236. Springer, Berlin (1956).
23. R. D. Mindlin and G. Herrmann, *Proc. 1st Nat. Congr. Appl. Mech. Chicago* (1951) p. 187; *Proc. 2nd Nat. Congr. Appl. Mech. Ann. Arbor* (1954) p. 233. The American Society of Mechanical Engineers, New York.

Int. J. Mech. Sci. Pergamon Press Ltd. 1961. Vol. 3, pp. 68–79. Printed in Great Britain

A STRAIN-HARDENING SOLUTION FOR THE "SHEAR ANGLE" IN ORTHOGONAL METAL CUTTING

P. L. B. OXLEY

Department of Mechanical Engineering
Manchester College of Science and Technology

(*Received* 3 *September* 1960)

Summary—A new method of calculating the shear angle in orthogonal metal cutting is derived by allowing the normal stress along the shear plane to vary. Good agreement is shown with experimental results.

NOTATION

t	depth of cut
α	tool rake angle
T	chip thickness
ϕ	shear angle
λ	angle of tool–chip interface friction
K	slope of curve of shear strength against compressive stress
p	mean normal or hydrostatic stress
k	maximum shear yield stress
ψ	orientation of slip-lines
η	size of built-up edge or deviation of shear plane from direction of maximum shear stress
s_1 and s_2	distances along slip-lines of each family
p_A, p_B	hydrostatic stresses at A and B
θ	angle made by resultant cutting force with shear plane
σ_n	normal stress on tool face

INTRODUCTION

IN ORTHOGONAL cutting the cutting edge of the tool is parallel to the work surface and perpendicular to the direction of cutting, and if the depth of cut is small compared to its width the process is essentially one of plane strain. Following the well-known Ernst[1] definition the removed metal chip can be discontinuous, i.e. in which fracture occurs and the chip is made up of segments; continuous, i.e. formed by continuous plastic deformation; or continuous but with a "built-up edge" which builds-up and breaks-down in a cyclic fashion. Only with the second type of chip can the process be considered as a steady motion problem, and it is therefore not surprising that analytical work has usually been limited to machining with this type of chip.

From the evidence of photomicrographs most workers have assumed that continuous chip formation can be represented as shown in Fig. 1, with the chip formed by simple shear across a shear plane AB. For a given depth of cut t and tool rake angle α the geometry of Fig. 1 is not completely specified unless

either the chip thickness T or the angle of inclination of the shear plane with the direction of cutting ϕ is known.

Various solutions for the shear angle ϕ have been proposed. Merchant[2], by assuming the angle ϕ would be such as to make the expenditure of work in cutting a minimum, derived the equation

$$\phi = \pi/4 + \alpha/2 - \lambda/2 \tag{1}$$

where λ is the angle of friction between the chip and tool (assumed constant over the contact area). On finding this expression in poor agreement with

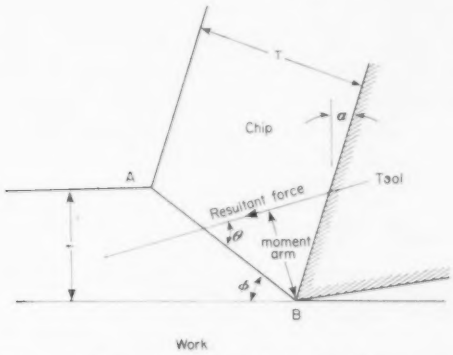

FIG. 1. Shear plane model of chip formation.

experimental observations Merchant introduced the concept of the dependence of the shear strength of the work material on the normal compressive stress on the shear plane. Thus he obtained the equation

$$2\phi = \cot^{-1} K + \alpha - \lambda \tag{2}$$

where K is the slope of the graph of shear strength plotted against normal stress. The value of K required to satisfy cutting data has not been supported by independent tests.

In terms of ideal slip-line theory the shear plane AB, which is a velocity discontinuity, is a slip-line, i.e. a plane of maximum shear stress and maximum shear strain-rate, and the variation of mean normal (hydrostatic) stress p along it is given by an equation of the form

$$p + 2k\psi = \text{const} \tag{3}$$

where k is the maximum shear yield stress (assumed constant in ideal slip-line theory) and ψ is the orientation of the slip-line to some datum direction. As ψ is constant for a straight slip-line the stress p according to equation (3) will be constant along the shear plane and the resultant cutting force will pass through the centre of AB. Although this constant stress distribution and position of resultant cutting force are implicit in all shear plane solutions it is not usual to check either.

Lee and Schaffer[3] applied ideal slip-line theory to metal cutting. They still assumed that all the deformation occurred across AB but that a triangular

plastic zone existed above AB with its apex at A and with slip-lines parallel and normal to AB. The plastic zone was therefore one of constant stress and moved as a rigid body although in a state of incipient plasticity. It was further assumed that the full cutting force was transmitted over the base of the plastic zone in contact with the tool. It follows from these assumptions that the hydrostatic stress p will equal the maximum shear stress k at all points in the plastic zone and, therefore, that the resultant cutting force will be inclined at an angle of $\pi/4$ with the shear plane. Hence, from simple geometry,

$$\phi = \pi/4 + \alpha - \lambda \tag{4}$$

For certain cutting conditions Lee and Schaffer observed that the resultant cutting force was inclined at an angle greater than $\pi/4$ and assumed that a small stable built-up edge was responsible for this apparent discrepancy with equation (4). Taking this into account they obtained the equation

$$\phi = \pi/4 + \alpha + \eta - \lambda \tag{5}$$

where η measures the size of built-up edge.

In satisfying experimental results over a wide range of cutting conditions η would have to assume negative as well as positive values, and a negative value would be meaningless in terms of built-up edge. Shaw *et al.*[4] suggested an equation identical in form to equation (5) but in which the η term measured not the size of built-up edge but the deviation of the shear plane from the direction of maximum shear stress [which they assumed was given by equation (4)] and this they argued could have positive or negative values. Equation (5) can then by its very nature be fitted to experimental results, but since it lacks an independent measurement of the deviation of the shear plane from the direction of maximum shear stress it is of no real practical significance.

Of the shear angle equations considered only equations (1) and (4) do not contain terms which, lacking independent measurement, allow satisfaction of experimental results, and unfortunately both are in poor agreement with observation when a wide range of cutting conditions is considered.

Recent investigators[5, 6, 7] have criticized the shear plane model of chip formation and the assumption of a constant normal stress along the shear plane. By observing the deformation during actual slow-speed cutting Palmer and Oxley[6] found that the plastic zone was of substantial width and roughly triangular in shape as shown in Fig. 2, with the streamlines of flow following smooth curves from the work into the chip. The streamlines in the chip were found to be circular arcs which could be drawn from a common centre. From this it was assumed that the distortion of the chip by the tool was essentially elastic in character with local elastic flattening of the chip by the tool and with the resultant cutting force passing through the centre of contact (Fig. 2). Calculation of the tool–chip contact zone by applying the Hertzian result for a cylinder on a plane showed that, with elastic contact, contact would not extend down to the cutting edge, and it was suggested that a gap existed between the chip and tool in the region of the cutting edge.

In order to obtain internal consistency of stress within the plastic zone and agreement between the resultant cutting force direction calculated by integrating the stresses along the boundary slip-line AB (Fig. 2) and the observed direction, it was found necessary to introduce strain-hardening into the slip-line theory. In strain-hardening slip-line theory[5, 6, 7] the slip-lines are still assumed to

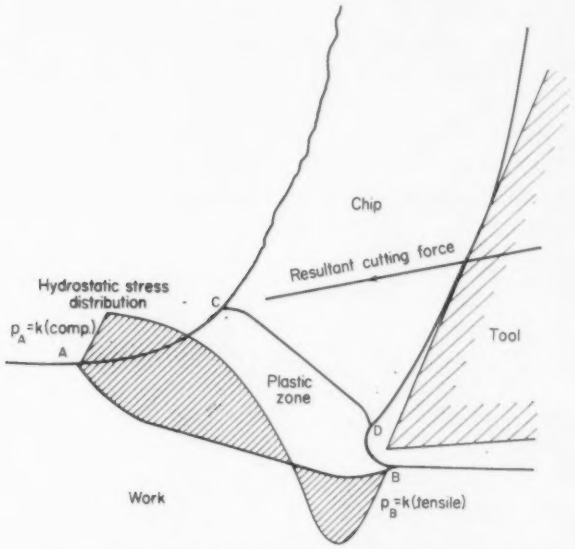

FIG. 2. Strain-hardening model of chip formation.

represent the directions of maximum shear stress and shear strain rate, with the material incompressible in the plastic state. The maximum shear yield stress k is, however, no longer assumed constant. Allowing a variable k equation (3) becomes

$$p + 2k\psi + \int \frac{\partial k}{\partial s_1} \delta s_2 = \text{const.} \tag{6}$$

where $\partial k/\partial s_1$ represents the rate of change of k normal to the considered slip-line, and δs_2 is measured along the slip-line. The variation of the hydrostatic stress p along a slip-line now depends not only on the change in ψ but also on the rate of change of k normal to the slip-line. In practice k may vary because of temperature, rate of strain, etc., but in the investigations considered[5, 6, 7] cutting was at the low speed of 0·5 in/min and the variation in k was assumed to result entirely from strain-hardening.

Palmer and Oxley showed that the conflicting curvatures of the boundary slip-lines AB and CD (Fig. 2), which are slip-lines of the same family and which therefore violate the well-known Hencky–Prandtl theorems of ideal theory, could be satisfied using strain-hardening theory. The most striking feature of their analysis was the calculated distribution of hydrostatic stress along AB which was shown to vary from compression at A (where, from the free surface condition, p equals k and on physical grounds is compressive) to tension at B

(the change in ψ on passing from A to B giving a compressive increment to p, while the strain-hardening term gives a tensile increment which becomes increasingly large as the cutting edge is approached). This stress distribution gave a cutting force direction which agreed well with the observed direction, and by taking moments of the stresses about the cutting edge they showed that the force acted approximately through their assumed centre of elastic flattening. They concluded that the chip was formed by combined bending and shearing as opposed to the simple shear of the shear plane model of chip formation.

More recent work[7] suggests that the cutting force acts nearer the cutting edge than is given by assuming elastic flattening, and that the chip and tool are in contact at the cutting edge with a plastic state of stress in the chip along the tool–chip interface. The main findings regarding the shape of the plastic zone and the idea that the chip is formed by combined bending and shearing were, however, confirmed.

By carrying out cutting tests on a high rate of strain-hardening material and a relatively low rate of strain-hardening material Oxley *et al.*[7] found that, for such external parameters of the process as cutting force, angle of tool–chip interface friction, chip thickness ratio and chip curvature, no significant difference existed between the two materials. Externally, therefore, the difference in strain-hardening properties was not reflected in the cutting process. The plastic zones on the other hand were found to have a marked difference, and for similar cutting conditions the plastic zone was always far wider, measured from work to chip, for the high rate of strain-hardening material than for the low rate of strain-hardening material.

These two observations, the similarity between the external parameters on the one hand and the difference in plastic zones on the other, were shown to be entirely consistent with the strain-hardening slip-line theory. The strain as measured by say the chip thickness ratio was approximately the same for both materials and, therefore, the change in maximum shear stress (∂k) from the work to chip was far greater for the high rate of strain-hardening material. Had the width of the plastic zone (∂s_1) been approximately the same in each case the strain-hardening term in equation (6) would have been much greater for the high rate of strain-hardening material. The hydrostatic stress would then have become tensile far more quickly (on passing from A to B) for this material and the cutting force directions would have been very different. However, this was not the case and the greater width of the plastic zone for the high rate of strain-hardening material gave a strain-hardening term which was of similar magnitude for each material. The stress distributions and hence the cutting force directions were, therefore, sensibly the same.

In conclusion, direct observation of the plastic zone during actual cutting and the introduction of strain-hardening into the slip-line theory has led to a physically consistent model of chip formation which is very different from the shear plane model and which appears to offer a new starting point for analysis of the process. At high cutting speeds and hence high rates of straining it can be expected and is in fact observed that the width of the plastic zone decreases and approaches the shear plane so often assumed in previous work. However,

the work reported in Ref. 7 shows that there is no justification in assuming that the normal stress is constant along the shear plane. In other words, although at high rates of straining the change in maximum shear stress (∂k) will decrease, the width of the plastic zone (∂s_1) may well decrease proportionally and give a strain-hardening term of the same order of magnitude as at low rates of straining. In the present paper new equations are derived which take into account this possible variation in normal stress at high cutting speeds and which enable the calculation of the shear angle ϕ given only the tool rake angle α and angle of tool–chip interface friction λ. Finally, the new equations are shown to be in good agreement with experimental observations.

THEORY

The present analysis is limited to cutting at speeds where the deformation can be approximated to a shear plane deformation. At very low speeds[5, 6, 7] the plastic zone is wide and the analysis does not apply.

Vol. 3
1961

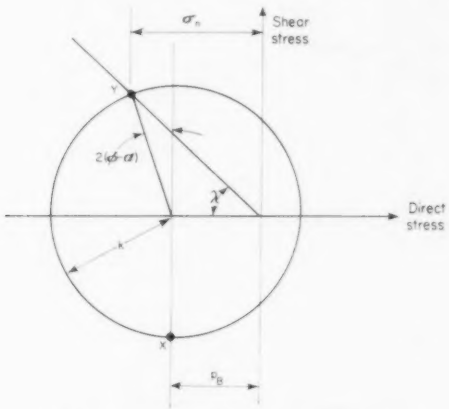

FIG. 3. Stress circle for point B.

Palmer and Oxley showed that the hydrostatic stress in the region of the free surface AC (Fig. 2) could be estimated most reliably from the boundary condition at A, as the boundary in the region of C was always observed to be cracked and therefore irregular. When the plastic zone reduces in width and approaches the shear plane (Fig. 1) it would appear reasonable that this still applies. Let us assume that the shear plane AB (Fig. 1) bends to meet this free surface condition but does so in a negligible distance. The angle turned through then determines by virtue of equation (3) the hydrostatic stress at A

$$p_A = k\{1 + 2(\pi/4 - \phi)\} \tag{7}$$

where k is the shear stress along AB.

If the chip and tool are in contact at the cutting edge, the hydrostatic stress at B (Fig. 1) can be determined by considering the state of stress at the tool–chip interface. Assuming the angle of friction λ along the interface is constant the stresses at B can be represented by the Mohr's stress circle shown in Fig. 3.

Point 'X' represents the shear plane AB and point 'Y' the tool–chip interface. The hydrostatic stress at B is then given by

$$p_B = k\left\{\frac{\cos 2(\phi-\alpha)}{\tan\lambda} - \sin 2(\phi-\alpha)\right\} \tag{8}$$

Therefore, for given values of α, λ and ϕ, p_A and p_B are uniquely determined by equations (7) and (8).

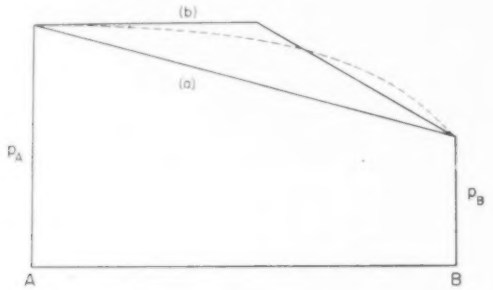

FIG. 4. Hydrostatic stress along shear plane.

Following previous work[5, 6, 7] the most probable shape of the hydrostatic stress curve between A and B would be that shown dotted in Fig. 4, i.e. with the change in stress increasing as the cutting edge is approached. However, to a first approximation let us assume a linear stress distribution [i.e. (a) in Fig. 4]. The angle θ made by the resultant cutting force with AB is then given by

$$\tan\theta = \frac{p_A + p_B}{2k} \tag{9}$$

Also from geometry

$$\theta = \phi + \lambda - \alpha \tag{10}$$

For given values of λ and α, equations (7), (8), (9) and (10) determine ϕ uniquely.

Consider the position of the resultant cutting force. By taking moments of the stresses acting on AB about B, we obtain the moment arm (Fig. 1) of the resultant

$$\text{moment arm} = \frac{2t\sin\theta}{\sin\phi}\left(\frac{\frac{1}{3}p_A + \frac{1}{6}p_B}{p_A + p_B}\right) \tag{11}$$

The moment arm can also be calculated by considering the stresses at the tool–chip interface. Assuming a constant state of plastic[7] stress along the interface, i.e. the simplest stress distribution consistent with the assumed constant friction, the contact length between chip and tool can be found by dividing the force component normal to the tool face by the normal stress σ_n (Fig. 3) on this face, where

$$\sigma_n = \frac{k\cos 2(\phi-\alpha)}{\tan\lambda} \tag{12}$$

The resultant cutting force should then pass through the centre of this contact, its moment arm being

$$\text{moment arm} = \frac{tk\cos^2\lambda}{2\sigma_n \sin\phi\cos\theta} \tag{13}$$

RESULTS AND DISCUSSION

In view of the very large number of experimental results for orthogonal metal cutting available in the literature further tests were not made. The results chosen to check the new theory were those of Merchant[2] and Thomsen

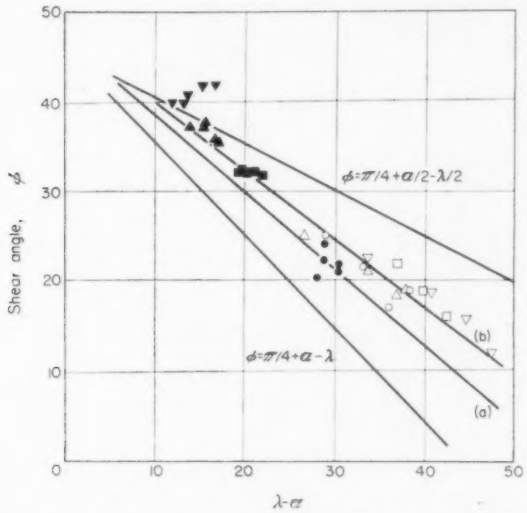

FIG. 5. Comparison between observed and theoretical values of shear angle.

Merchant[2]

Variable speed	$\alpha = 10°$	○
Variable speed	$\alpha = -10°$	□
Variable depth of cut	$\alpha = 10°$	△
Variable depth of cut	$\alpha = -10°$	▽

Thomsen *et al.*[8]

Variable depth of cut	$\alpha = 25°$	●
Variable depth of cut	$\alpha = 35°$	■
Variable depth of cut	$\alpha = 40°$	▲
Variable depth of cut	$\alpha = 45°$	▼

et al.[8] These cover a wide range of rake angles ($-10°$ to $45°$), depths of cut (0·00109 to 0·0085 in.) and cutting speeds (197 to 1186 ft/min) and are given in Tables 1 and 2 (Appendix).

In selecting values of ϕ which would satisfy equations (7–10) for given values of λ and α it was found that if the selected value of ϕ was too small the value of θ given by equation (9) was greater than given by equation (10), and conversely if ϕ was too large. The values of ϕ found in this way are given in the Appendix, and plotted as line (a) in Fig. 5. The experimentally observed values of ϕ are also plotted in Fig. 5 together with the lines representing equations (1) (Merchant) and (4) (Lee and Schaffer).

Vol. 3
1961

Equations (11) and (13) were used to calculate the moment arm of the resultant for calculated values of ϕ, and these are given in Fig. 6. The average values of the hydrostatic stresses, p_A and p_B, and normal stress to tool face σ_n found in the analysis are plotted in Fig. 7 (actual values in the Appendix).

The agreement between the calculated and observed values of ϕ is good; in all cases better than the Lee and Schaffer result and in the majority of cases better than the Merchant result. The results which deviate most widely from the present theory are those for the 45° rake angle tool. However, as previously reported[5, 6] the very high values of friction associated with large positive rakes may be misleading and result from an upward force on the base of the tool.

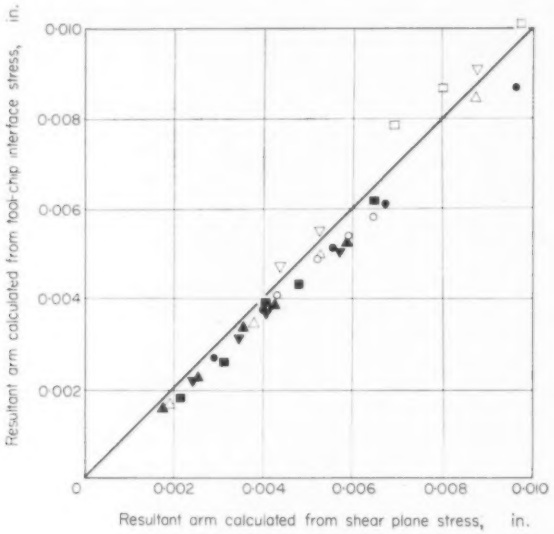

FIG. 6. Comparison of moment arms.

The values of λ for the 45° angle tool (Appendix) which are excessively large appear to confirm this, and it is therefore not surprising that these results fall above the theoretical line.

The moment arms calculated independently from the shear plane and interface stresses (Fig. 6) are in good agreement, thus supporting the assumed stress distributions. The interface stresses are important in determining tool life and an interesting feature of the present analysis is the possibility of determining the mean normal stress on the tool face for given values of λ and α, i.e. without having to make cutting tests to measure the contact length. For the considered results this stress was shown to decrease with increasing positive rake angle (Fig. 7).

The hydrostatic stress at A had in all cases a much higher compressive value than the corresponding value at B (Fig. 7). The general change in stress was therefore the same as for the strain-hardening stress distribution at low cutting speeds, and in accounting for this change reference must be made to the strain-hardening term in equation (6).

It is of considerable interest that if λ is accepted as a true material constant then the present solution is successful in predicting ϕ without taking into account the actual physical properties and in particular the actual strain-hardening properties of the work material. That is, although strain-hardening considerations allow the hydrostatic stress to vary along a straight slip-line in the way that it does and probably determine the shape of the stress curve between A and B (Fig. 4) the actual values of stress at A and B are determined by the respective boundary conditions. The plastic zone must therefore adjust its width, in a way similar to that reported in Ref. 7, to give a rate of change of k which will in turn give the required change in stress along AB.

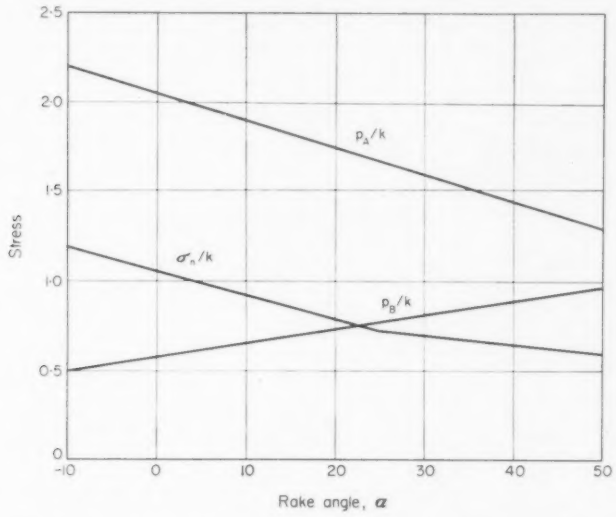

FIG. 7. Hydrostatic stresses at A and B, and normal stress to tool face.

If a different shape of stress curve is assumed between A and B the present solution will be modified. Let us assume as a nearer approximation to the distribution suggested by earlier work the two straight lines (b) in Fig. 4, i.e. with the stress constant to the mid point of AB and then changing rapidly to the cutting edge. Equations (7), (8) and (10) are unchanged but equation (9) becomes

$$\tan\theta = \frac{3p_A + p_B}{4k} \tag{14}$$

Values of ϕ calculated using equations (7), (8), (10) and (14) are plotted as line (b) in Fig. 5 and are in excellent agreement with experimental results.

REFERENCES

1. H. ERNST, *Trans. Amer. Soc. Metals.* Symposium on Machining of Metals—I. Physics of Metal Cutting, p. 24 (1938).
2. M. E. MERCHANT, *J. Appl. Phys.* **16**, 267, 318 (1945).
3. F. A. LEE and B. W. SCHAFFER, *J. Appl. Mech.* **18**, 405 (1951).
4. M. C. SHAW, N. H. COOK and I. FINNIE, *Trans. Amer. Soc. Mech. Engrs.* **75**, 273 (1953).

5. D. G. CHRISTOPHERSON, P. L. B. OXLEY and W. B. PALMER, *Engineering, Lond.* **186**, 113 (1958).
6. W. B. PALMER and P. L. B. OXLEY, *Proc. Inst. Mech. Engrs.* **173**, 623 (1959).
7. P. L. B. OXLEY, A. G. HUMPHREYS and A. LARIZADEH. *Proc. Inst. Mech. Engrs.* To be published.
8. E. G. THOMSEN, J. T. LAPSLEY and R. C. GRASSIE, *Trans. Amer. Soc. Mech. Engrs.* **75**, 591 (1958).

APPENDIX—ORTHOGONAL METAL CUTTING RESULTS

TABLE 1. MERCHANT[8]: WORK MATERIAL—NE 9445 STEEL; TOOL MATERIAL SINTERED CARBIDE; WIDTH OF CUT—0·25 in.

$\alpha = 10°$ $t = 0{\cdot}0037$ (const.)

Cutting speed (ft/min)	λ	ϕ_{obs}	ϕ_{cal}	p_A/k	p_B/k	σ_n/k
197	46·5	17·0	17·0	1·99	0·69	0·93
400	48·0	19·0	16·0	2·01	0·67	0·88
642	43·5	21·5	19·0	1·91	0·70	1·01
1186	39·0	25·0	23·0	1·77	0·70	1·14

$\alpha = -10°$ $t = 0{\cdot}0037$ (const.)

Cutting speed (ft/min)	λ	ϕ_{obs}	ϕ_{cal}	p_A/k	p_B/k	σ_n/k
400	33·0	16·5	11·0	2·18	0·49	1·16
637	30·0	19·0	13·0	2·12	0·47	1·19
1160	27·0	22·0	15·0	2·04	0·49	1·16

$\alpha = 10°$ cutting speed = 542 ft/min (const.)

t (in.)	λ	ϕ_{obs}	ϕ_{cal}	p_A/k	p_B/k	σ_n/k
0·00109	48·0	19·0	16·0	2·01	0·66	0·87
0·00234	47·0	18·5	17·0	1·98	0·66	0·90
0·00370	44·0	21·5	19·0	1·91	0·68	0·99
0·00788	37·0	25·0	24·0	1·73	0·69	1·16

$\alpha = -10°$ cutting speed = 542 ft/min (const.)

t (in.)	λ	ϕ_{obs}	ϕ_{cal}	p_A/k	p_B/k	σ_n/k
0·00109	38·0	12·5	7·0	2·32	0·50	1·06
0·00234	35·0	16·0	9·0	2·26	0·51	1·13
0·00370	31·0	19·0	12·0	2·15	0·51	1·20
0·00788	24·5	22·5	17·0	1·98	0·47	1·28

TABLE 2. THOMSEN *et al.*[8]: WORK MATERIAL—SHELBY TUBING 6 in. o.d.; TOOL MATERIAL HSS; WIDTH OF CUT—0·475 in.

Cutting speed = 90·0 ft/min (const.)

α	t(in.)	λ°	$\phi_{obs}{}^\circ$	$\phi_{cal}{}^\circ$	p_A/k	p_B/k	σ_n/k
25·0°	0·0025	55·5	20·9	22·0	1·80	0·77	0·67
	0·0035	55·5	21·5	22·0	1·80	0·77	0·67
	0·0050	54·0	24·0	23·0	1·77	0·79	0·72
	0·0080	53·5	20·1	23·0	1·77	0·80	0·73
	0·0085	54·0	22·4	23·0	1·77	0·79	0·72
35·0°	0·0025	57·0	31·6	28·5	1·58	0·88	0·65
	0·0035	57·0	31·9	28·5	1·58	0·88	0·65
	0·0050	56·0	32·0	29·0	1·56	0·87	0·66
	0·0060	55·0	32·2	30·0	1·52	0·87	0·70
	0·0085	54·5	32·0	30·5	1·51	0·87	0·71
40·0°	0·0025	56·0	35·7	33·0	1·42	0·90	0·66
	0·0035	56·5	35·4	32·5	1·44	0·90	0·64
	0·0050	55·5	37·5	33·5	1·40	0·90	0·67
	0·0060	55·0	37·2	34·0	1·38	0·89	0·68
	0·0085	53·5	37·2	35·0	1·35	0·90	0·73
45·0°	0·0025	61·5	41·9	33·0	1·42	0·91	0·50
	0·0035	60·0	41·9	34·0	1·39	0·91	0·54
	0·0050	58·5	40·2	35·0	1·36	0·92	0·58
	0·0060	58·0	39·6	35·5	1·33	0·91	0·58
	0·0085	56·5	39·9	36·5	1·30	0·93	0·64

Vol. 3
1961

Int. J. Mech. Sci. Pergamon Press Ltd. 1961. Vol. 3, pp. 80–90. Printed in Great Britain

ANALYSIS OF A NONLINEAR TORSIONAL COUPLING HAVING DYNAMIC LINKS—I

STEADY RUNNING AND FREE OSCILLATION

CHARLES W. BERT
Department of Engineering Mechanics
The Ohio State University, Columbus, Ohio

(*Received* 14 *September* 1960)

Summary—A torsional coupling, consisting of a number of masses connected by means of simple links to both the driving member and the load member, has been found to be effective in suppressing torsional oscillations of the load while transmitting a large mean torque to the load.

Under the assumptions stated in the paper the equations of motion are derived by means of the Lagrangian method. These equations are used to obtain the quasi-static performance, that is, the torque vs. relative angular displacement at constant rotational velocity. An exact solution is also found for the phase-plane representation* for motion under steady torque. This is analogous to the usual phase-plane representation for free oscillation, since this system seeks an equilibrium position which is dependent upon the mean torque transmitted.

The results show clearly that this coupling can be designed to have a wide variety of nonlinearities in the restoring torque, depending upon a geometrical parameter. Curves are presented which show the effects of the various parameters upon the phase-plane characteristics, and a tabulation shows the effects of these same parameters on the fluctuation in output velocity for a given input-velocity fluctuation.

INTRODUCTION

ALTHOUGH reciprocating- and turbine-type engines can be designed so as to avoid harmful torsional critical speeds under normal operation, it is often impossible to avoid harmful critical speeds under all conditions of operation. Thus, there has been a great need for an effective, reliable and inexpensive means of suppressing torsional oscillations in engine-driven machinery. Basically, there have been three avenues of approach to this problem: (1) viscous dampers, such as the Lanchester damper, (2) centrifugal-pendulum dynamic absorbers and (3) torsionally flexible couplings.

Attention will be focused on the last approach. There have been three main types of torsional couplings: (1) elastic couplings, such as those using curved flexural elements or rubber in shear, (2) hydraulic couplings and (3) electrical slip couplings. The latter two types have the desirable feature of having a very low effective spring rate, but they are large and expensive. The elastic couplings are relatively simple and inexpensive but they cannot be designed to achieve both a low spring rate and a long service life, since they are highly limited by the fatigue characteristics of the elastic material.

* The phase plane refers to velocity plotted vs. the corresponding displacement.

Recently, an entirely new type of torsional coupling has been described by Dorton[1]. This coupling utilizes dynamic forces acting on a number of masses connected via simple links to the driver and to the load member. The advantages of this coupling are: (1) it can be designed to have a lower spring rate and longer life than an elastic coupling of the same capacity and (2) it is much more simple and inexpensive than hydraulic or electrical couplings of the same capacity. Furthermore, it has the unusual characteristic that its spring rate and torque capacity both increase as the square of the rotational speed. This makes it ideal for driving centrifugal machines, such as centrifugal pumps and compressors, as well as airplane and ship propellers.

Although experimental verification of the effectiveness of this new coupling in isolating torsional oscillations has been obtained for several specific configurations,[1] the only analysis of the dynamic characteristics of this system, so far as is known, utilized an approximate method of analysis.[2]

Vol. 3
1961

EQUATIONS OF MOTION

The coupling is shown schematically in Fig. 1. The system consists of a driver A, connected via a number of pinned links B to the same number of masses C, which in turn are connected to the driven member D via similar links E. In operation the driver leads the load so that torque is transmitted as tension in the links, this being necessary for stability of the linkage system. As will be seen, centrifugal action on the masses provides the restoring torque.

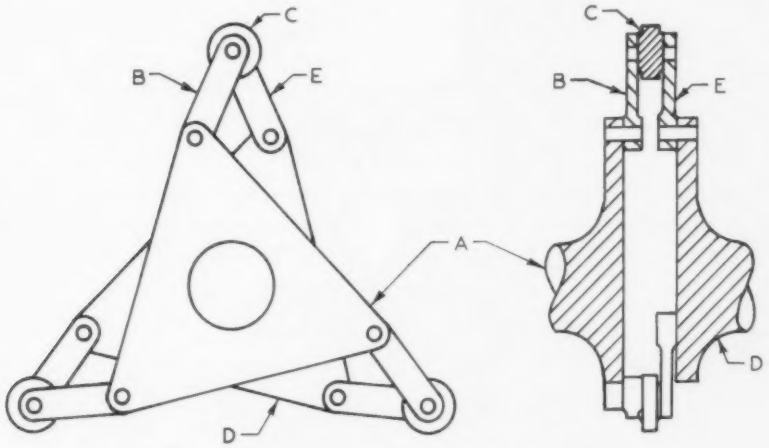

FIG. 1. Schematic diagram of the coupling.

As is usual in engineering analyses of physical systems, it is advisable to make some mathematical idealizations. In this analysis the following assumptions, which are believed to be reasonable, are made:

(1) The masses of the links (B and E) are negligible in comparison with their attached masses (C).

(2) Each attached coupling mass (C) is assumed to be concentrated at a point.

(3) All members are rigid.

(4) The rotational velocity is sufficiently high so that the centrifugal-force field is considerably larger than the gravitational-force field, thus enabling the latter to be neglected.

(5) The rotational dynamic characteristics of the driver and of the load can be represented by their respective constant moments of inertia I_1 and I_2.

(6) All frictional effects are negligible.

(7) All of the coupling masses, and all of the links and the radii at which the links are attached, are assumed to be identical. Then the effect of a single mass having a mass m, equal to the total mass of all of the actual masses, is equivalent to their total effect.

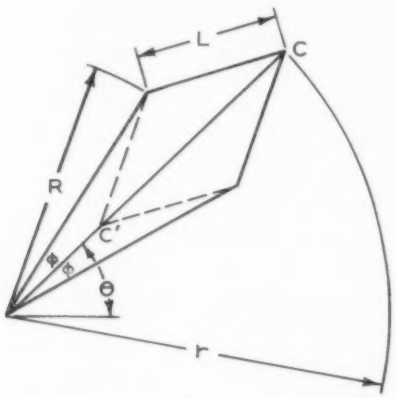

FIG. 2. Link geometry. Normal position of coupling mass is C; innermost position of coupling mass, which is possible only at very low speeds, is C′.

The Lagrangian method is used here to derive the equations of motion. Letting r, θ denote the polar co-ordinates of one of the coupling masses, its velocity is

$$(\dot{r}^2 + r^2\dot{\theta}^2)^{\frac{1}{2}} \tag{1}$$

where dots represent derivatives with respect to time.

The kinetic energy T of the system can be expressed as

$$T = \tfrac{1}{2}I_1(\dot{\theta}+\dot{\phi})^2 + \tfrac{1}{2}m(\dot{r}^2 + r^2\dot{\theta}^2) + \tfrac{1}{2}I_2(\dot{\theta}-\dot{\phi})^2 \tag{2}$$

where $(\theta+\phi)$ is the angular position of the driver, and $(\theta-\phi)$ is the angular position of the load (see Fig. 2).

The virtual work accomplished by the driving torque M_1 and the load torque M_2 during virtual displacement $d\theta$ and $d\phi$ of the generalized co-ordinates θ and ϕ is

$$M_1(d\theta + d\phi) - M_2(d\theta - d\phi) = (M_1 - M_2)\,d\theta + (M_1 + M_2)\,d\phi \tag{3}$$

so that the generalized forces associated with the θ and ϕ co-ordinates, respectively, are

$$Q_\theta = M_1 - M_2; \quad Q_\phi = M_1 + M_2 \tag{4}$$

In view of the fourth assumption listed above the potential energy is negligible. Thus, the Lagrangian equation reduces to

$$\frac{d}{dt}\left(\frac{\partial T}{\partial \dot{q}}\right) - \frac{\partial T}{\partial q} = Q_q \tag{5}$$

where q represents a generalized co-ordinate (θ or ϕ) and t denotes time. Applying equations (5), the following equations of motion, corresponding respectively to the θ and ϕ co-ordinates, are obtained:

$$\left.\begin{aligned} I_1(\ddot{\theta}+\ddot{\phi}) + I_2(\ddot{\theta}-\ddot{\phi}) + m\frac{d}{dt}(r^2\dot{\theta}) &= M_1 - M_2 \\ I_1(\ddot{\theta}+\ddot{\phi}) - I_2(\ddot{\theta}-\ddot{\phi}) + m\ddot{r}\frac{d\dot{r}}{d\dot{\phi}} - mr^2\dot{\theta}^2\frac{dr}{d\dot{\phi}} &= M_1 + M_2 \end{aligned}\right\} \tag{6}$$

By noting that $d\dot{r}/d\dot{\phi} = dr/d\phi$ and letting $A \equiv I_1 + I_2$ and $B \equiv I_1 - I_2$, equations (6) can be simplified to the following form:

$$\left.\begin{aligned} A\ddot{\theta} + B\ddot{\phi} + m\frac{d}{dt}(r^2\dot{\theta}) &= M_1 - M_2 \\ B\ddot{\theta} + A\ddot{\phi} + m(\ddot{r} - r\dot{\theta}^2)\frac{dr}{d\phi} &= M_1 + M_2 \end{aligned}\right\} \tag{7}$$

PERFORMANCE AT CONSTANT ROTATIONAL VELOCITY

Under steady running conditions all of the accelerations and all of the relative velocities of one part of the system with respect to another are zero. Then the only non-zero velocity appearing in the equations of motion is the rotational velocity $\dot{\theta}$, which in this case is the rotational velocity of all parts of the system. Thus the equations of motion, equations (7), reduce to the following expression for the torque transmitted $M(= M_1 = M_2)$:

$$M = -\tfrac{1}{2}mr\dot{\theta}^2\frac{dr}{d\phi} \tag{8}$$

In order for a positive torque to be transmitted $dr/d\phi$ obviously must be negative.

From the geometry of Fig. 2, it can be seen that

$$\frac{r}{R} = \cos\phi + \frac{L}{R}\sqrt{\left(1 - \frac{R^2}{L^2}\sin^2\phi\right)} \tag{9}$$

Here the sign in front of the square root has been taken as positive, since under normal operating conditions centrifugal force carries the coupling masses to their outermost positions (fourth assumption). Only when the system is started or stopped is the rotational velocity too small to overcome gravitational force and allow the coupling masses to vibrate between their outermost positions (solid lines in Fig. 2) and their innermost positions (dotted lines in Fig. 2) once each revolution of the shaft.

Differentiating equation (9) with respect to ϕ and substituting this result into equation (8) results in the following expression for the transmitted torque

Vol. 3
1961

in dimensionless form:

$$\frac{M}{\frac{1}{2}mR^2\dot{\theta}^2} = \sin 2\phi + \frac{(R/L)\sin\phi\cos^2\phi}{[1-(R^2/L^2)\sin^2\phi]^{\frac{1}{2}}} + (L/R)\sin\phi[1-(R^2/L^2)\sin^2\phi]^{\frac{1}{2}} \quad (10)$$

It is interesting to note that this method of determining the quasi-static constant-velocity performance is considerably shorter and less tedious than using Newton's second law directly in conjunction with the geometry of the system. The latter method was outlined by Dorton[1] and carried out by Balzhi and Esin[2], who obtained a result mathematically identical to equation (10).

Fig. 3 gives dimensionless torque plotted vs. relative angular position ϕ for various values of the ratio of link length L to link-attachment radius R.

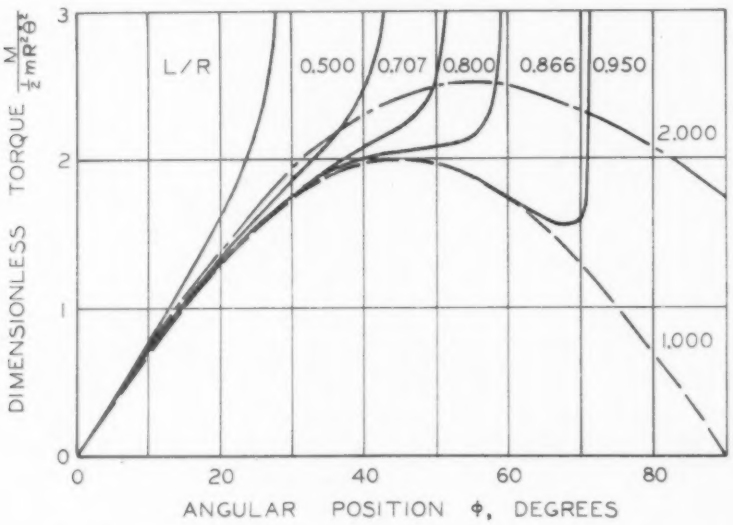

FIG. 3. Dimensionless curves of torque vs. angular displacement at constant rotational velocity for various values of the coupling geometrical parameter.

It should be noted that when the ratio L/R is less than unity the torque vs. displacement curve approaches a vertical asymptote. The physical explanation for this is that as the links approach a position in which they lie in a straight line, the ratio of force in the links (and thus the torque) to the centrifugal force increases without limit. Thus, for any L/R ratio less than or equal to unity, in order for the mechanism to remain connected together, the angle ϕ cannot exceed a maximum value given by

$$\phi_{\text{stop}} = \arcsin\frac{L}{R} \quad \left(\frac{L}{R} \leqq 1\right) \quad (11)$$

This angle-limiting effect has been called a "soft stop"[1] because it has an effect equivalent to a mechanical stop made of a material having a force-displacement curve analogous to that of a "soft" (low spring rate) spring which gradually "hardens" as displacement is increased (i.e. curves concave upward). At least

two factors not taken into consideration in this analysis help keep the actual forces in the link from increasing without limit; elasticity of the links and clearance in the joints. Thus this inherent "soft-stop" effect appears to be advantageous over a conventional stop.

For L/R ratios greater than unity, there is no limitation on the angle ϕ, i.e. there is no stop effect present. For such L/R ratios the motion of the coupling masses is demagnified so that such configurations would not be expected to be as effective as those having smaller L/R ratios.

It is interesting to note that for an L/R ratio exactly equal to unity the torque-displacement curve degenerates to the positive portion of a perfect sine curve. Although there is a maximum limitation on displacement of 90°, as given by equation (11), the curve does not have an infinite positive slope as in the case of L/R ratios less than one.

Vol. 3
1961

EXACT SOLUTION FOR MOTION UNDER STEADY TORQUE

In the preceding Section it was assumed that the system was operating at constant rotational velocity; thus, the transmitted torque also did not fluctuate and there were no nonsteady dynamic effects, only quasi-static effects. In the analysis in this section considerably different conditions will be assumed. With the system operating under steady-torque conditions

$$(M_1 = M_2 = M = \text{constant})$$

it will be assumed that some relative displacement ϕ (or some velocity $\dot{\phi}$) is suddenly applied. Then it is desired to determine the effect of ϕ (or $\dot{\phi}$) on $\dot{\phi}$ (or on ϕ), i.e. the phase plane for the co-ordinate ϕ.

Under these conditions, the equations of motion, equations (7), become

$$\left.\begin{aligned} A\ddot{\theta} + B\ddot{\phi} + m\frac{d}{dt}(r^2\dot{\theta}) &= 0 \\ B\ddot{\theta} + A\ddot{\phi} + m(\ddot{r} - r\dot{\theta}^2)\frac{\dot{r}}{\dot{\phi}} &= 2M \end{aligned}\right\} \tag{12}$$

Since the first of equations (12) is cyclic in both θ and ϕ it can be integrated directly to give

$$A\dot{\theta} + B\dot{\phi} + mr^2\dot{\theta} = C \tag{13}$$

Multiplying the second of equations (12) by $\dot{\phi}$ and substituting $\dot{\phi}$ from equation (13) into it to remove the mixed products gives the following relation:

$$C\ddot{\theta} - A\dot{\theta}\ddot{\theta} + A\dot{\phi}\ddot{\phi} + m\dot{r}\ddot{r} - m(r^2\dot{\theta}\ddot{\theta} + r\dot{r}\dot{\theta}^2) = 2M\dot{\phi} \tag{14}$$

Now equation (14) is also a perfect differential and can be integrated immediately to obtain

$$C\dot{\theta} - \tfrac{1}{2}A\dot{\theta}^2 + \tfrac{1}{2}A\dot{\phi}^2 + \tfrac{1}{2}m\dot{r}^2 - \tfrac{1}{2}mr^2\dot{\theta}^2 = D + 2M\phi \tag{15}$$

Note that equation (13) expresses the constancy of the angular momentum of the system. Substituting the expression for C given by equation (13) into

equation (15), using the definitions of A and B in terms of I_1 and I_2 and employing equation (2) it can be shown that equation (15) can be rewritten as

$$T - 2M\phi = D \tag{16}$$

Obviously, this equation expresses the constancy of the total energy of the system. Thus, under the assumptions made, the system is a conservative one.

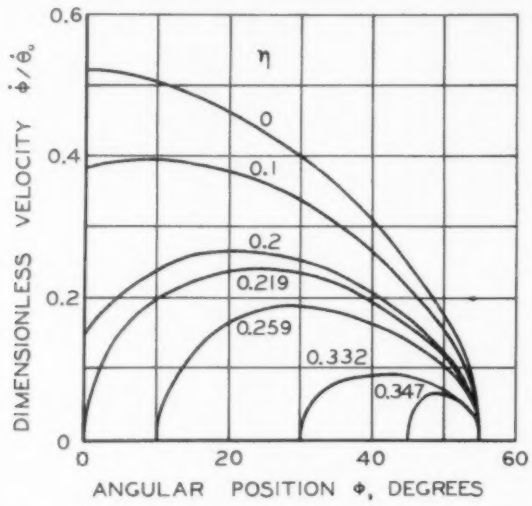

FIG. 4. Effect of steady torque on the phase-plane diagram for $I_2/I_1 = 1/3$, $\mu = 0{\cdot}1$, $L/R = 0{\cdot}866$ and $\phi_{max} = 55°$.

In order to determine the phase-plane plot for any desired system the integration constants C and D must first be evaluated in terms of the system parameters. There are three convenient choices of conditions for which the constants can be evaluated: $\dot{\phi} = \dot{\phi}_{max}$, $\phi = \phi_{min}$, or $\phi = \phi_{max}$. Using the last condition, it is noted that when $\phi = \phi_{max}$, then $r = r_{min}$, $\dot{\phi} = 0$, $\dot{r} = 0$ and $\dot{\theta} = \dot{\theta}_0$.* (Since θ does not appear in the equations its value is unimportant.) Then from equations (13) and (15) the constants are found to be

$$C = (A + mr_{min}^2)\,\dot{\theta}_0; \quad D = \tfrac{1}{2}(A + mr_{min}^2)\,\dot{\theta}_0^2 - 2M\phi_{max} \tag{17}$$

Substituting $\dot{\theta}$ from equation (13) into equation (15) and using equation (17) results in the following dimensionless expression for the phase-plane curve corresponding to co-ordinate ϕ:

$$\frac{\dot{\phi}}{\dot{\theta}_0} = \pm \left\{ \frac{\mu(\rho^2 - \rho_{min}^2)\,(1 + \mu\rho_{min}^2) - \eta(1 + \mu\rho^2)\,[1 - (\phi/\phi_{max})]}{(1 + \mu\rho^2)\,[1 + \mu(d\rho/d\phi)^2] - (B^2/A^2)} \right\}^{\frac{1}{2}} \tag{18}$$

where $\rho \equiv r/R$, $\mu \equiv mR^2/A$ and $\eta \equiv 4M\phi_{max}/A\dot{\theta}_0^2$. The effects of the five parameters involved in equation (18) are shown in Figs. 4–8.

Since the θ co-ordinate is cyclic or ignorable the phase plane corresponding to this co-ordinate is meaningless.

* For a wide range of practical values of the parameters involved $\dot{\theta}_0$ is equal to approximately $0{\cdot}98\,\dot{\theta}_{max}$.

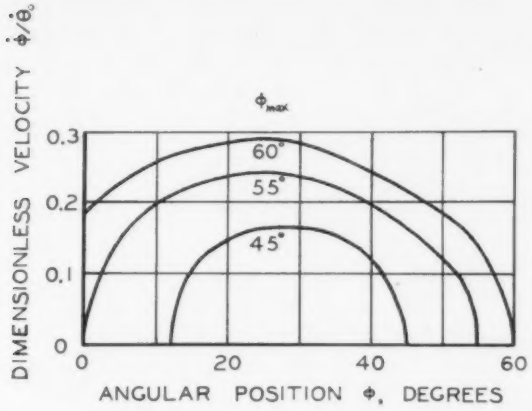

FIG. 5. Effect of maximum displacement on the phase-plane diagram for $I_2/I_1 = 1/3$, $\mu = 0{\cdot}1$, $L/R = 0{\cdot}866$ and $\eta = 0{\cdot}219$.

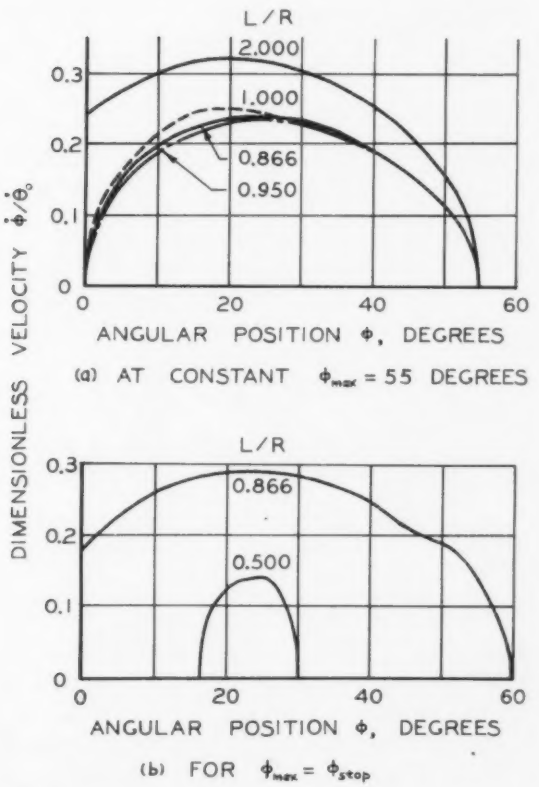

FIG. 6. Effect of the coupling geometrical parameter L/R on the phase-plane diagram for $I_2/I_1 = 1/3$, $\mu = 0{\cdot}1$ and $\eta = 0{\cdot}219$.

In view of the ease with which the phase-plane curve can be changed by varying one or more of the five parameters involved the question is raised as to what kind of curve is most desirable. This question will be considered in the

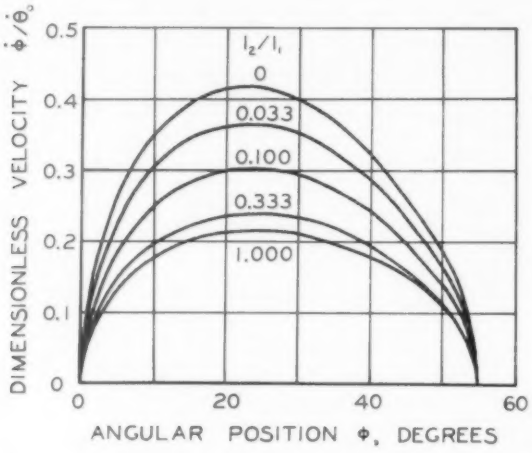

FIG. 7. Effect of load inertia on the phase-plane diagram for $\mu = 0{\cdot}1$, $L/R = 0{\cdot}866$, $\phi_{max} = 55°$ and $\eta = 0{\cdot}219$.

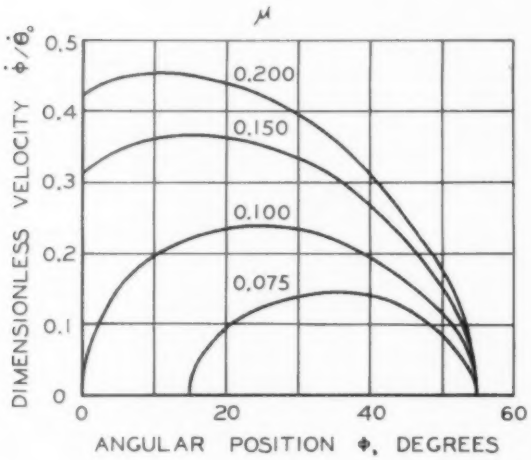

FIG. 8. Effect of coupling mass on the phase-plane diagram for $I_2/I_1 = 1/3$, $L/R = 0{\cdot}866$, $\phi_{max} = 55°$ and $\eta = 0{\cdot}219$.

light of two criteria: orbital or phase-plane stability; and minimization of output-velocity fluctuation for a given fluctuation of input velocity.

It is well known that if closed phase-plane curves cross the displacement axis perpendicularly, the system is stable in the orbital sense. As can be seen in Figs. 4–8 all of the curves shown are stable. However, there is one degenerate case which is known to be unstable. This instability occurs only in the case of an L/R ratio equal to one, with no load torque (i.e. $\eta = 0$), and then

only when $\phi_{max} = \phi_{stop}$, which is 90° in this instance (see Fig. 9). Due to the soft-stop effect described previously, this condition cannot be achieved physically. Therefore, under all conditions physically possible all variations of this system possess inherent stability.

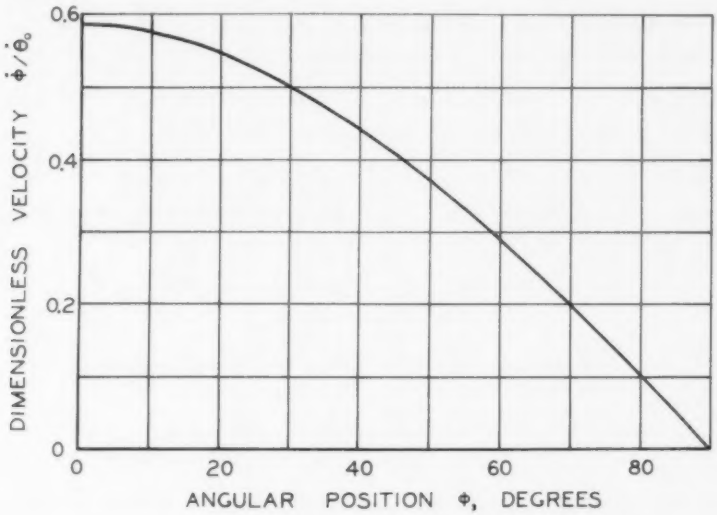

FIG. 9. The phase-plane for the only conditions under which this coupling configuration lacks orbital stability: for $L/R = 1{\cdot}000$, $\eta = 0$ and $\phi_{max} = 90°$. (Shown for $I_2/I_1 = 1/3$ and $\mu = 0{\cdot}1$; curves corresponding to other values of these parameters are similar.)

In order to determine the effect of small input-velocity fluctuations, it is first necessary to introduce the following expression for the generalized velocity $\dot{\theta}$, readily obtained from equation (13):

$$\frac{\dot{\theta}}{\dot{\theta}_0} = \frac{(1+\mu\rho_{min}^2) - (B/A)\,(\dot{\phi}/\dot{\theta}_0)}{1+\mu\rho^2} \tag{19}$$

Now the input- and output-velocity fluctuations Δ_1 and Δ_2 will be defined as the differences between the maximum and minimum values of the input and output velocities, respectively. Thus

$$\Delta_1 \equiv (\dot{\theta}+\dot{\phi})_{max} - (\dot{\theta}+\dot{\phi})_{min}; \quad \Delta_2 \equiv (\dot{\theta}-\dot{\phi})_{max} - (\dot{\theta}-\dot{\phi})_{min} \tag{20}$$

It is desirable to minimize the fluctuation ratio Δ_2/Δ_1. This ratio can readily be calculated by substituting the extremal values of $\dot{\theta}$ and $\dot{\phi}$ into the appropriate equation (20). To study the effects of the five parameters involved, the fluctuation ratios corresponding to the phase-plane plots of Figs. 4–8 were calculated. The results are as follows:

(1) Increasing steady torque increases the fluctuation ratio (under the conditions of Fig. 4):

$$\Delta_2/\Delta_1 = \begin{cases} 0{\cdot}46 \text{ for } \eta = 0{\cdot}00 \\ 0{\cdot}51 \text{ for } \eta = 0{\cdot}219 \end{cases}$$

Vol. 3
1961

(2) Increasing maximum displacement has little effect on the fluctuation ratio (under the conditions of Fig. 5):

$$\Delta_2/\Delta_1 = \begin{cases} 0{\cdot}52 \text{ for } \phi_{\max} = 45^\circ \\ 0{\cdot}51 \text{ for } \phi_{\max} = 55^\circ \text{ and } 60^\circ \end{cases}$$

(3a) Increasing L/R ratio (at constant $\phi_{\max} = 55^\circ$) first increases the fluctuation ratio, then decreases it [under the conditions of Fig. 6(a)]:

$$\Delta_2/\Delta_1 = \begin{cases} 0{\cdot}51 \text{ for } L/R = 0{\cdot}866 \text{ and } 0{\cdot}950 \\ 0{\cdot}52 \text{ for } L/R = 1{\cdot}000 \\ 0{\cdot}45 \text{ for } L/R = 2{\cdot}000 \end{cases}$$

(3b) Increasing L/R ratio (for $\phi_{\max} = \phi_{\text{stop}}$, which depends upon L/R) increases the fluctuation ratio [under the conditions of Fig. 6(b)]:

$$\Delta_2/\Delta_1 = \begin{cases} 0{\cdot}43 \text{ for } L/R = 0{\cdot}500 \ (\phi_{\max} = 30^\circ) \\ 0{\cdot}46 \text{ for } L/R = 0{\cdot}866 \ (\phi_{\max} = 60^\circ) \end{cases}$$

(4) Increasing load inertia increases the fluctuation ratio (under the conditions of Fig. 7):

$$\Delta_2/\Delta_1 = \begin{cases} 0{\cdot}20 \text{ for } I_2/I_1 = 0 \\ 0{\cdot}51 \text{ for } I_2/I_1 = \frac{1}{3} \end{cases}$$

(5) Increasing coupling mass decreases the fluctuation ratio (under the conditions of Fig. 8):

$$\Delta_2/\Delta_1 = \begin{cases} 0{\cdot}56 \text{ for } \mu = 0{\cdot}075 \\ 0{\cdot}51 \text{ for } \mu = 0{\cdot}100 \end{cases}$$

In the second part of the paper the system performance under forced oscillation and the selection of design parameters, as affected by steady-running, transient and steady-state oscillation requirements, will be considered.

Acknowledgement—The author wishes to acknowledge the helpful advice and encouragement of his adviser, Professor C. T. West.

REFERENCES

1. G. A. DORTON, *Amer. Soc. Mech. Engrs.* Paper No. 59–OGP–8 (1959).
2. M. F. BALZHI and G. D. ESIN, *Mach. Ind. Bull., Moscow* **40**, 31 (1960). For an English abstract of this paper see *Engrs.' Dig.* **21**, 98 (1960).

Int. J. Mech. Sci. Pergamon Press Ltd. 1961. Vol. 3, pp. 91–117. Printed in Great Britain

SOME ANALYTICAL AND EXPERIMENTAL STUDIES OF AXI-SYMMETRIC COLD FORGING AND EXTRUSION—II

H. KUDO
The Government Mechanical Laboratory, Suginami, Tokyo, Japan

(*Received* 10 *February* 1960)

Summary—The results obtained from several forging and extrusion tests at room temperature and low speed are compared with theoretical results, and the following conclusions emerge.

(1) The working pressures for the compression of soft aluminium cylinders between rough flat dies, for the compression of soft aluminium annuli in a container between lubricated or rough dies and for the steady-state lubricated extrusion and piercing of hard aluminium and copper cylindrical billets, are 10–20 per cent below the calculated upper bound.

(2) Calculated upper bounds agree qualitatively with the working pressures obtained during some non-steady extrusions and piercings of soft aluminium, hard aluminium, copper and soft brass.

(3) The steady pressures divided by the mean yield stress in combined bar and tube extrusions from cylindrical billets and in tube extrusions from hollow billets, together with those in ordinary extrusion and piercing, were found to be almost entirely a function of the total reduction in area, when the tools are lubricated.

(4) The working pressure in opposed extrusion–piercing-forging is considerably lower than that for a one-way extrusion-forging.

The working pressures in opposed extrusion-forging with two dies and in opposed piercing-forging with two punches were lower than that in corresponding one-way working, using a die or punch of the larger orifice when the length of billet is moderate. In symmetrically opposed working, the pressure exceeds that in one-way working when the billet length becomes very small.

When the material flow through one orifice is interrupted midway in an opposed forging, the working pressure thence follows that of the corresponding one-way working.

(5) The deformation of hard aluminium and copper annuli compressed between lubricated flat dies was as predicted from the most suitable velocity field.

The speed of efflux of material through two separate orifices was affected by the frictional resistances acting on the material rather than by the difference in the areas of the orifices when the billet length was moderate. But, as the length was reduced, the speed from the wider orifice tended to increase. These results were in qualitative accordance with those derived from plane-strain analysis.

(6) The internal flow pattern observed on the meridian section of a lead billet as photographed through a glass plate was in qualitative agreement with the corresponding most suitable velocity field and was very similar to that of the comparable plane-strain working.

(7) The main types of defect found in the various extruded and extrusion-forged products were skin inclusion, cavity formation and internal cracking. They were predicted quantitatively and qualitatively from the velocity field of the least upper bound.

The inclusion was prevented by using a rough die in contact with the material surface from which the skin was unfolded.

Cavity formation and internal cracking was thought to be prevented by restraining the material flow through the orifices. The onset of the latter defects was retarded by intermediate annealing.

Vol. 3
1961

(8) The internal pressure acting on the container during extrusion-forging and coining was found to be lower than the mean working pressure within the range of conditions tested. The pressure acting on the projection of the coining die was in excess of the mean working pressure, the difference being larger for higher projections and for thinner slug thicknesses. The residual pressure between the material and the container after extrusion or closed-die coining was found to be nearly equal to the uniaxial yield stress of the material.

1. EXPERIMENTAL MATERIALS

FOR the measurement of working load and the observation of external deformation and internal defects, 99·6 per cent pure aluminium, pure copper and 30 per cent zinc–brass were used. In almost all cases, the aluminium and the copper were cold-upset by about 60 per cent before testing, to try to ensure their having a constant yield stress; it was later found that this aim was not completely achieved. In other cases, the materials were soft annealed. For the observation of internal flow patterns pure lead was used.

To determine the yield stresses of the materials used for the experiments, compression tests were performed. The cylindrical specimens used were originally of 30 mm outside diameter and 45 mm in height for the soft aluminium (V.P.H. 22 ~ 23), 19 mm × 33 mm for soft copper (V.P.H. 43 ~ 44) and 15 mm × 26 mm for brass (V.P.H. 56 ~ 57). The test procedure consisted of the repeated application of Johnson Wax 111 for lubrication purposes, small load increments or decrements, the taking out of the specimen and measuring its height with a micrometer followed by re-lubrication, to minimize friction.

The first stage of compression continued until the specimen height was reduced to about 60 per cent of its initial value. The specimen was then turned down to a height–diameter ratio of 1·2–1·4 and compressed again. The same procedure was repeated until a final logarithmic compressive strain of 2·4 for the aluminium and copper, and of 1·8 for the brass, was achieved.

Yield stress (Y)–logarithmic-strain (ϵ) relations as calculated from the compression tests are shown in Fig. 1(a).

To examine the effect of change in the direction of compression, several specimens were compressed to a particular strain, following the procedure described above, and then turned to cylindrical specimens whose axes were perpendicular to their original axes. The compression tests were then continued in the new direction. Such changes in the direction of compression of material elements are actually considered to occur in deformation of an extrusion type. The test results are shown in Fig. 1(a). Remarkable decreases in the yield stresses (about 10 per cent), due to the change in the direction of compression, are seen. But these yield-stress curves converge on the curves obtained by simple continued uniaxial compression. The yield stress of material during a deformation of extrusion type, therefore, was taken to be 95 per cent of that obtained in the ordinary compression test.

In extrusion-forging, the material attains a total logarithmic strain of as much as 7–10, and, as no material of such dimensions as to facilitate the compression test down to such a large strain was available, the yield stresses at very large strains were evaluated by extrapolation, see Fig. 1(b). In Fig. 1(b) is indicated the 95 per cent yield-stress curves as obtained by extrapolation.

Vol. 3
1961

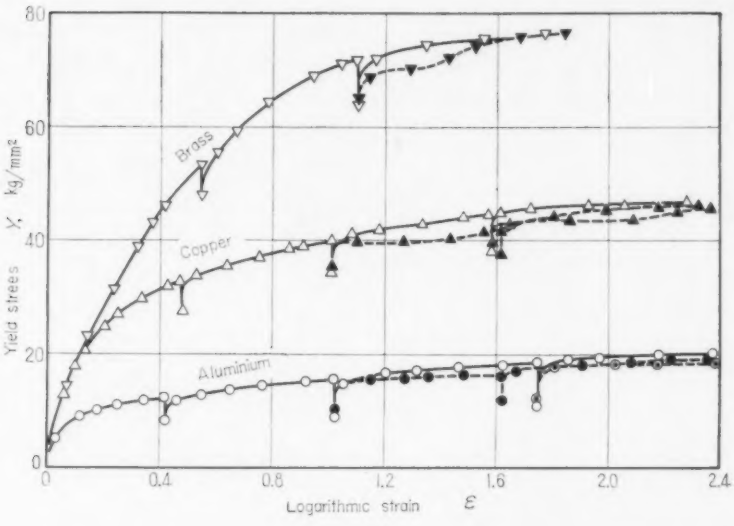

(a)

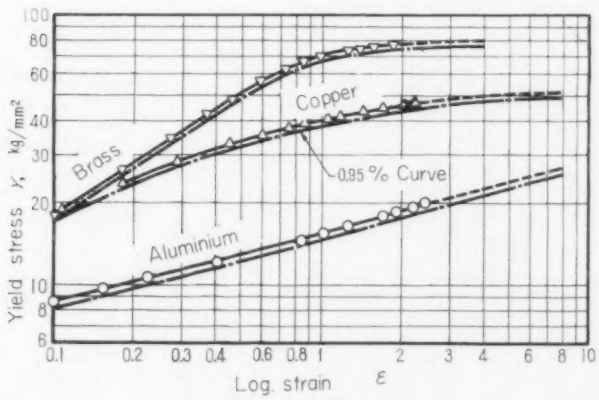

(b)

FIG. 1. Yield-stress curves of test materials. (a) Yield stress–log compressive strain: ——— unidirectional compression with intermediate re-turning; – – – compression perpendicular to previous direction of compression. (b) Log yield stress–log log compressive strain: ——— obtained from unidirectional compression; – – – extrapolated curve; — — — assumed yield-stress curve for extrusion; 95% of unidirectional compression. ○ ● △ ▲ ▽ ▼ Experimental results.

2. COMPRESSION

(i) *Compression of a cylinder between rough dies*

Cylindrical specimens of soft aluminium having various initial height–diameter ratios $(T/D_0)_0$ were compressed between two flat and roughened dies, these being guided in a cylindrical sub-press; both the specimen and dies were degreased with benzine and trichlorethylene before commencing. The instantaneous height of the specimen during a test was measured using two dial gauges, allowance being made for the elastic deformation of the apparatus which was obtained from an unloading curve.

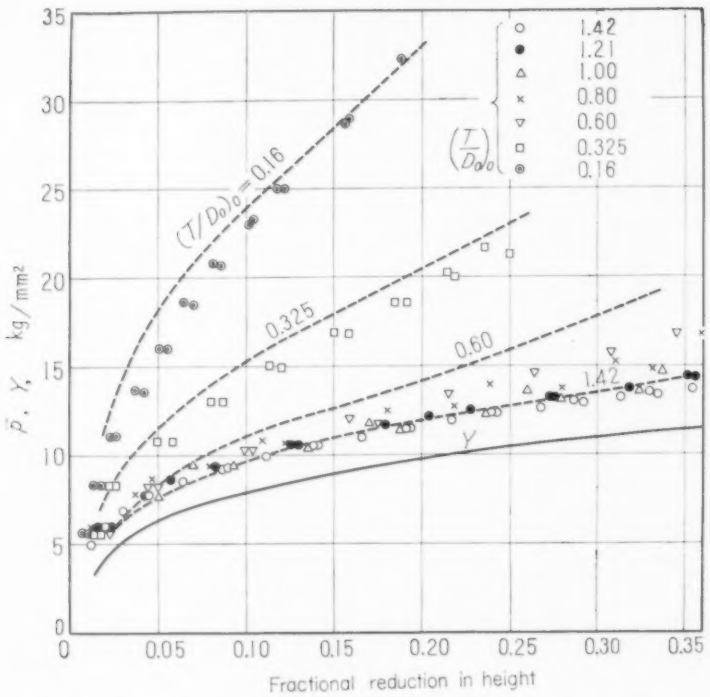

FIG. 2. Compression of soft aluminium cylinders between parallel rough dies: ——— yield-stress curve; – – – upper bound for mean working pressure; ○ ● △ × ▽ □ ○ experimental results.

Bulging of the specimen usually occurred during the test. For simplicity, however, the true pressure and the mean fractional reduction in height were calculated on the assumption that the specimen maintained a cylindrical form. The results obtained are shown in Fig. 2.

The theoretical working pressure, that is the upper bound for compression pressure, is calculated using Fig. 10 and equation (10) of Part I,[1] and incorporating the yield-stress curve of Fig. 2. The theoretical results, see Fig. 2, show fairly good agreement with the experimental results. The over-estimation of the working pressure can be attributed to the character of the upper-bound

Vol. 3
1961

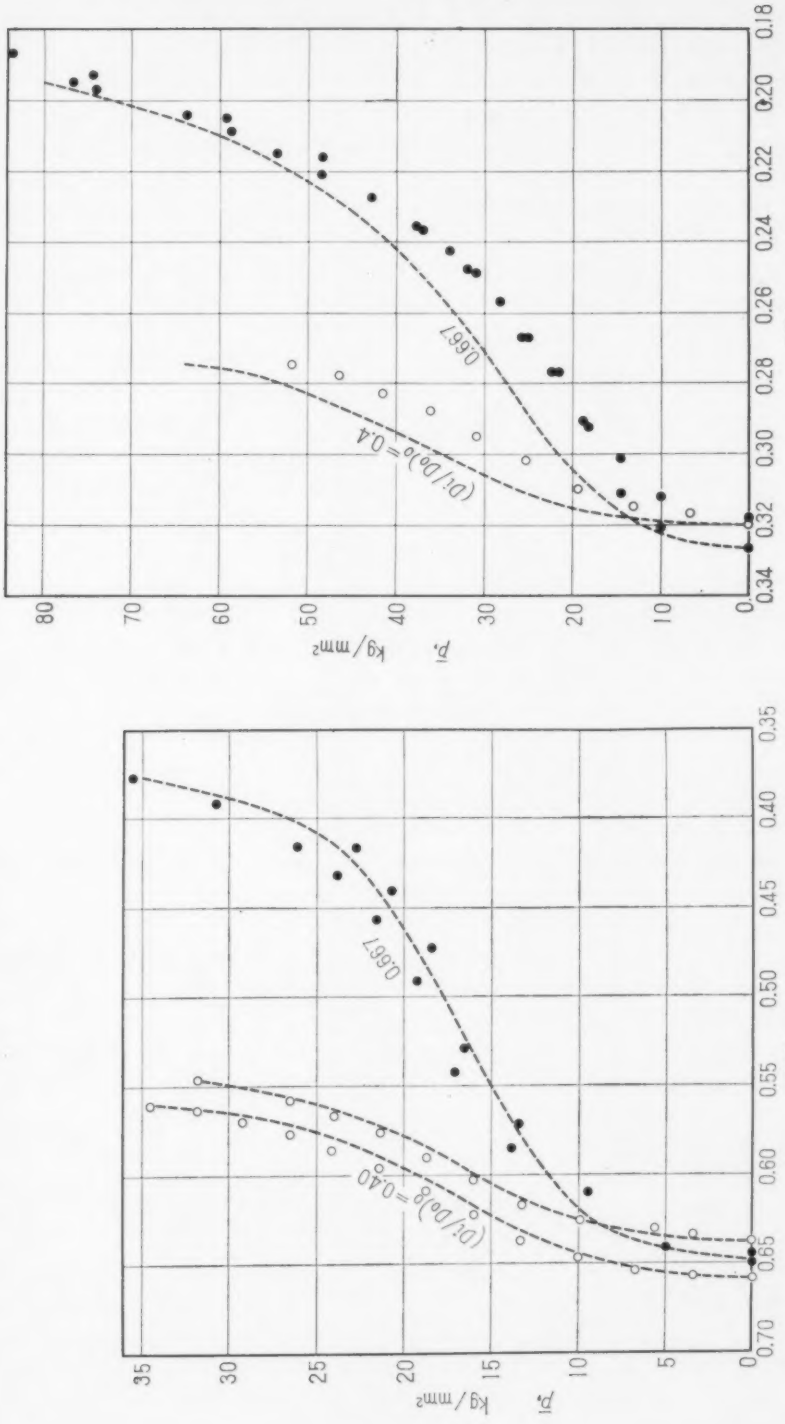

(a) $2T_0/D_0 \simeq 0{\cdot}65$. (b) $2T_0/D_0 \simeq 0{\cdot}32$.

FIG. 3. Compression of soft aluminium annuli in container: – – – – upper bound for mean working pressure; ○ ● experimental results.

solution itself, and to some inevitable contamination of the contact surfaces between the specimen and the dies.

By predicting the working pressure with the method used here, an over-estimate of $\bar{p}_n/Y$ for non-hardening materials leads to an over-estimate of mean yield stress for hardening materials, thus resulting in an over-estimation twice over. Thus the good agreement between the predicted and experimental results is rather surprising. The discrepancies between the experimental and analytical results, as reported by Schroeder and Webster[2] and Kobayashi *et al.*[3], can to some extent be reduced if the analytical method used here is employed.

(ii) *The compression of an annulus in a container between flat dies*

Test specimens of soft aluminium, having an outer diameter $D_0 = 15$ mm, an inner diameter $D_i = 6$ or 10 mm and a height $T_0 = 2{\cdot}4$ and $4{\cdot}9$ mm, were compressed between two flat dies in a container of internal diameter 15 mm. Two frictional conditions were examined, one corresponding to a degreased case and the other to a lubricated case. In the former, the bottom die and the container were fixed together whilst the top die descended. In the latter case, the specimens were etched with caustic soda solution to increase the affinity and the surface area for the lubricant.

The test procedure and the method of calculating experimental and analytical pressure were the same as above (Fig. 12, Part I). For the lubricated case, an upper-bound solution was derived from equation (21), Part I, using a value of $\mu = 0{\cdot}05$ as determined by the experiments described below.

The results are compared in Fig. 3 and again a satisfactory agreement is seen.

(iii) *Compression of annulus between flat dies*

To determine the coefficients of friction between the material and the tools in the present forging and extrusion experiments, compression tests on hard aluminium and copper annuli (2 mm thick) were performed with Johnson Wax 111 as lubricant. The dimensions of the test specimens are tabulated in Table 1.

The compression was effected by two flat dies supported and guided by a sub-press having two guide pillars. The bottom die contains a small hole leading from the centre of the lower compression surface to a manometer. This device enabled the change in the internal volume of the annulus between the dies to be measured as the compression proceeded.

From the various measurements, the coefficients of friction were calculated with the aid of Fig. 13, Part I, and are listed in Table 1. Consistent values of coefficient of friction are seen except for the cases of $D_i/D_0 = 0{\cdot}818$. These values are 0·046–0·057 for aluminium and 0·039–0·048 for copper, showing good agreement with those obtained in sheet-drawing tests.[4]

The reasons for the considerable scatter in the measured coefficients of friction for the case of $D_i/D_0 = 0{\cdot}818$, especially when the diameter of the specimen is large, are considered to be the flatness of the ρ/R_i versus $\mu D_i/2T$ curve in Fig. 13, Part I, on the one hand, and the effect of elastic deformation of the compression disks on the other.

The mean value of the measured coefficient of friction 0·05 has been adopted for all calculations of the working pressures throughout this paper.

TABLE 1. FRICTION COEFFICIENT DERIVED FROM COMPRESSION TEST OF ANNULAR SPECIMEN BETWEEN PARALLEL DIES

Specimen		Derived friction coefficient	
Outer diameter D_0 (mm)	Inner diameter D_i (mm)	Hard copper	Hard aluminium
10	5	0·047	0·047
9·8	8	0·048	0·062
15·8	5	0·046	0·057
20	10	0·043	0·053
31·8	26	0·026	0·033
19·6	16	0·044	0·046
32	16	0·039	0·046
31·6	10	—	0·047

Vol. 3
1961

3. EXTRUSION, PIERCING- AND EXTRUSION-FORGING IN ONE DIRECTION

(i) *Experimental apparatus, tools and procedure*

A drawing of the axi-symmetrical extrusion apparatus which was made in hardened tool steel is shown in Fig. 4. It was designed to extrude specimens originally of 15 mm

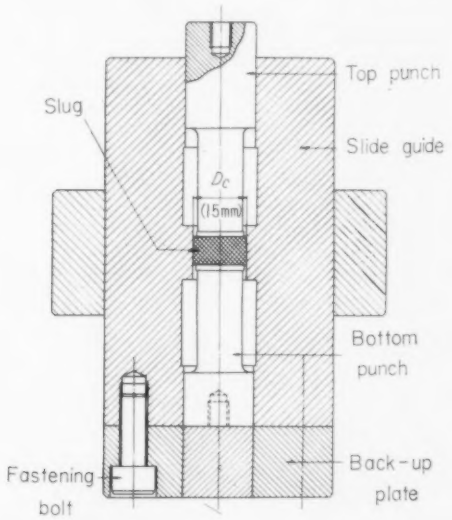

FIG. 4. Tool assembly for extrusion and piercing test.

diameter and length 14 mm. The container is a compound shrink-fitted cylinder, the upper and bottom parts of its inner face serving as guides for the sliding die and punch. By changing the dies, various types of direct extrusion, piercing- and extrusion-forging [Fig. 5 (a, c, e–g)] from solid and hollow billets, could be effected. Opposed extrusions could also be performed, see Fig. 5 (b, d, h–j).

This container was used also to produce work-hardened specimens by upsetting material of small diameter. The V.P.H., after upsetting, was $43 \sim 46$ for aluminium and $115 \sim 118$ for copper. Some of these were also annealed and used as the soft specimens. In order to put these specimens easily into the container again before testing, and to retain sufficient lubricant on their surfaces, they were etched in caustic soda or sulphuric acid solution, thus reducing their diameters and making the surfaces rough and clean.

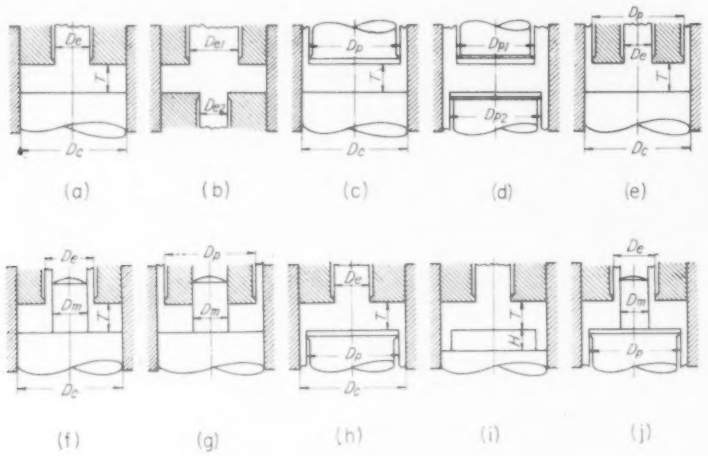

FIG. 5. Various die combinations for extrusion and piercing test.

In most cases, the wax was used as lubricant. The tests were carried out in a 30-ton testing machine at a speed of 0·01 mm/sec. The travel of the sliding die was measured by two dial gauges in the same way as described in the preceding section. Backward extrusion or piercing was usually performed but when lubrication was applied, no significant difference in the working pressure was found between forward and backward working.

Photographs of the internal flow patterns of material made through a thick glass plate throughout the forming process when lead is used have been obtained by Kudo[5].

(ii) *Autographic diagrams*

Several autographic diagrams, which indicate the variations in the mean working pressure $\bar{p}$ over the cross-sectional area of the billet against the remaining billet length T divided by the inner radius of the container, are illustrated in Figs. 6 and 7.

Theoretical upper bounds to the working pressures in bar and shell extrusion or piercing, and extrusion-forging as obtained from solid cylindrical billets, are obtained as follows.

In Figs. 25(c) and 28(c), Part I, the upper bounds, $\bar{p}_u/Y$, are given by curves I as functions of $2T/D_c$ for a non-hardening material with a coefficient of friction $\mu = 0{\cdot}05$. When the billet is long, the initial part of an autographic diagram is calculated using equation (31), Part I, and by reference to the yield-stress curve, Fig. 1. The subsequent steady state is calculated using Hill's suggestion regarding a mean yield stress.

To obtain the transition point from the steady to the non-steady state an equivalent mean total logarithmic strain $\bar{\epsilon}'_m$ for the steady deformation

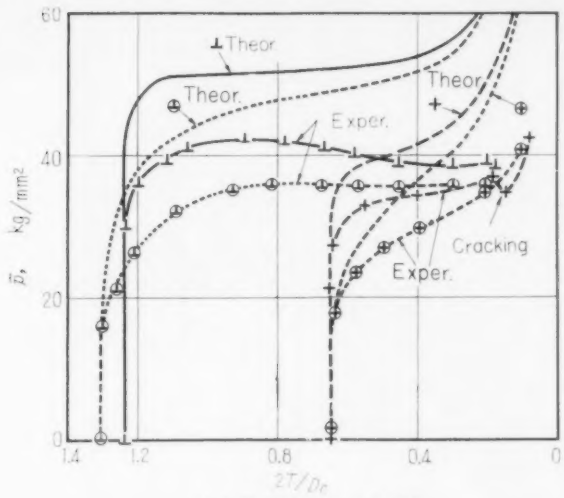

(a) $R_e, R_{e1}, R_{e2} = 0{\cdot}716$.

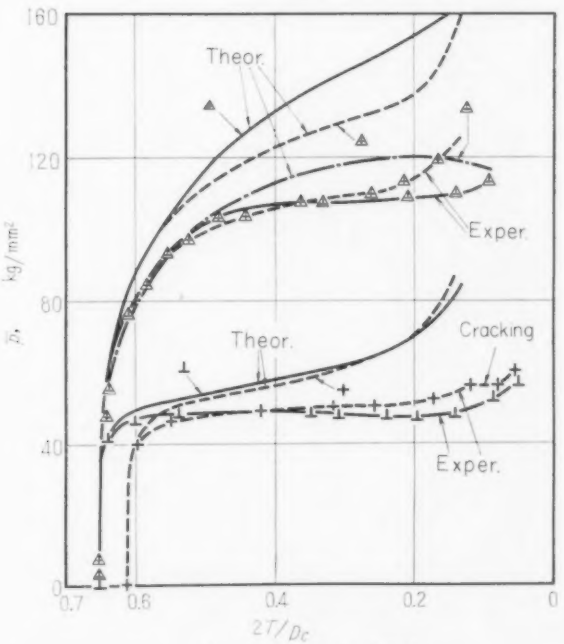

(b) $R_e, R_{e1}, R_{e2} = 0{\cdot}840$.

FIG. 6. Mean working pressure during extrusion and symmetrically opposed extrusion: ——— and – – – – upper-bound curve for $\mu = 0{\cdot}05$; — – — upper-bound curve for $\mu = 0$;

Experimental data

⊥⊕▲ Extrusion [Fig. 5(a)]
+⊕▲ Opposed extrusion [Fig. 5 (b), $D_{e1} = D_{e2}$]
⊥+ Hard aluminium
●⊕ Soft aluminium
▲▲ Hard copper

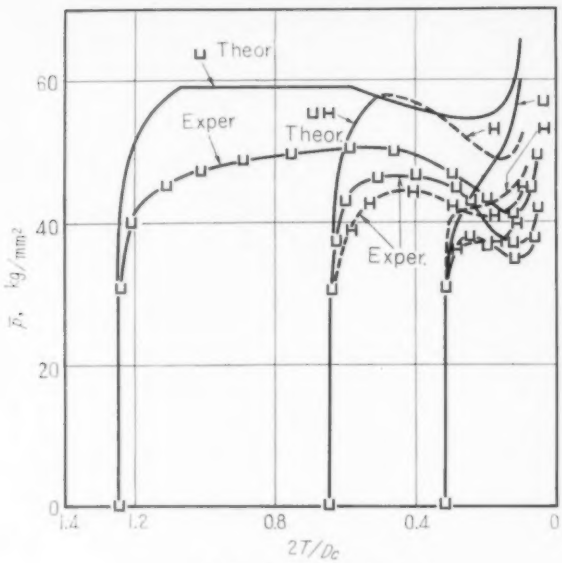

(a) $R_p, R_{p1}, R_{p2} = 0{\cdot}798$.

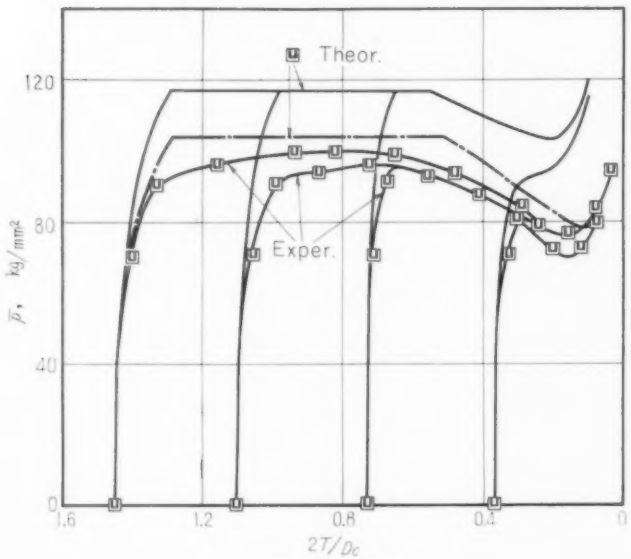

(b) $R_p = 0{\cdot}70$.

FIG. 7. Mean working pressure during piercing and symmetrically opposed piercing: ——— and – – – upper-bound curve for $\mu = 0{\cdot}05$, — – — upper-bound curve for $\mu = 0$

Experimental data

⊔□	Piercing [Fig. 5 (c)]
H	Opposed piercing [Fig. 5 (d), $D_{p1} = D_{p2}$]
⊔H	Hard aluminium
□	Hard copper

zone is determined from the yield-stress curve using Hill's mean yield stress Y_m. On changing to the non-steady extrusion-forging phase, $\bar{\epsilon}'_m$ is conceived as being distributed uniformly throughout the whole of the material in the container. For the final stage, equation (29), Part I, is used. The mean total equivalent logarithmic strain during the extrusion-forging stage is then given by

$$\bar{\epsilon}_m = \frac{G\bar{\epsilon}'_m}{T_l} + \int_{T_t}^{T} \left(\frac{\bar{p}_n}{Y}\right) \frac{(-dT)}{T} \tag{1}$$

where G is the depth of the steadily deforming region and T_l the residual length of billet at the transition point.

Using this method, the transition in a work-hardening material is found to occur at an earlier stage than in a non-hardening material, thus resulting in a lower upper bound. Upper-bound curves for non-hardening material are therefore required for values of $2T/D_c$, in excess of that prevailing at the transition point for non-hardening materials and are calculated and shown in Figs. 25(c) and 28(c) of Part I.

The predicted autographic diagrams obtained in this way are illustrated in Figs. 6 and 7. Comparisons with experimental results show them to be good in respect of tendency, but providing considerable over-estimates of theoretical values, especially when $2T/D_c$ is small. These discrepancies can be attributed to the following factors.

(a) Upper-bound solutions over-estimate the actual pressure to some extent. This is especially the case for the present axi-symmetric problems where upper-bound solutions are calculated from velocity fields which are simple when compared with those used in the plane-strain problems.[6,7]

(b) Over-estimates of the effect of work-hardening—the method of estimating the effect of work-hardening of material on the working pressure proposed in the present study results in an over-estimate, because the non-uniformity of strain distribution in the deforming material and the convexity of the yield-stress curve are not taken into consideration and because the whole of the work done by Coulomb friction is assumed to be transformed into plastic work. The assumed values of yield stress of the materials are likely to be much higher than the mean yield stresses operative during a deformation of extrusion type. This seems to be suggested by the Vickers pyramid hardness numbers of the extruded materials[8] which, on dividing by $2{\cdot}9 \sim 3{\cdot}0$ following Tabor, approximate their yield stresses.

(c) Over-estimates of the effect of Coulomb friction—the method of estimating the effect of Coulomb friction described above leads to a considerable over-estimate (Fig. 6, Part I), especially when $2T/D_c$ is small. However, the assumed values of $\mu = 0{\cdot}05$ taken from the annulus compression test is also very doubtful.

In extrusion, the applied lubricant should be contained between tools and material, and tangential stresses on the contact surface are not likely to increase

Vol. 3
1961

in proportion to the normal pressure especially when the lubricant is a solid wax such as that used here.

The upper-bound curves calculated on the assumption that $\mu = 0$ and shown in Fig. 7 indicate that either or both of the reasons (a) and (b) are true.

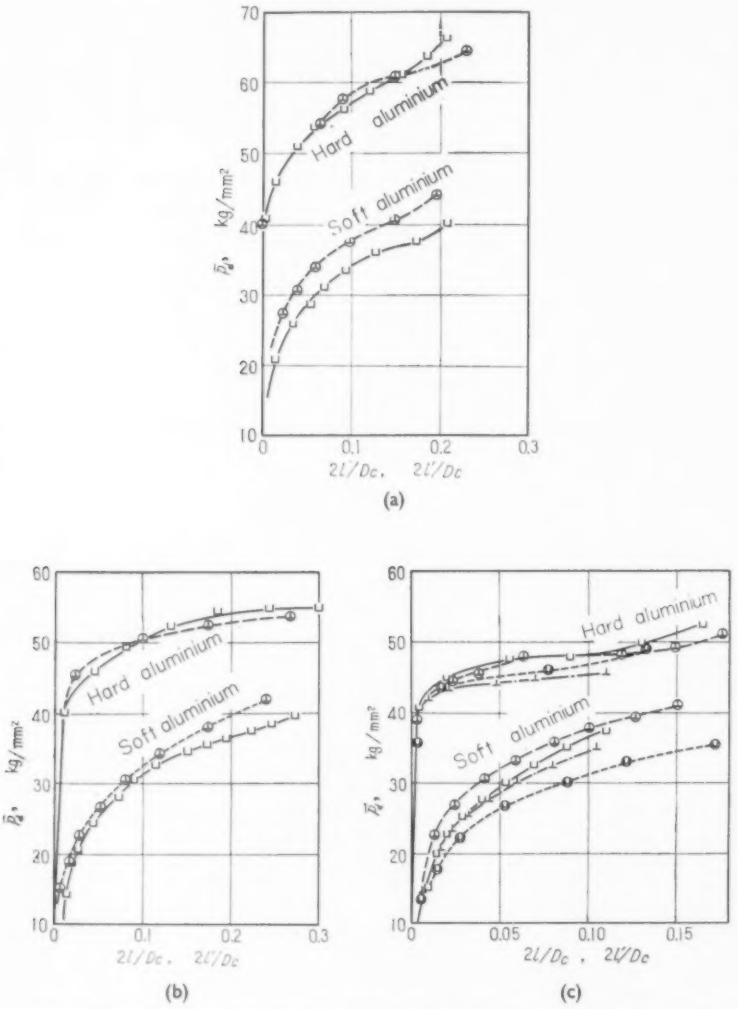

FIG. 8. Mean die and punch pressure during early stage of extrusion and piercing, respectively, with low reduction in area: $2T_0/D_c = 1$;

⊥Φ Extrusion [Fig. 5 (a)]
⌊Θ Piercing [Fig. 5 (c)]

(a) $D_p/D_c = D_e/D_c = 0.25$
(b) $D_p/D_c = D_e/D_c = 0.40$
(c) ⊥⊔ $D_p/D_c = D_e/D_c = 0.80$
ΦΘ $D_p/D_c = D_e/D_c = 0.60$

Vol. 3
1961

Although the theoretical method does not give quantitatively very satisfactory predictions, it will facilitate predictions with the aid of experimental results. Compare, for instance, the initial non-steady stages in the autographic diagrams for an extrusion and piercing of long billets of a work-hardening material, where there is a relation $D_e = D_p$ or $R_e = 1 - R_p$.

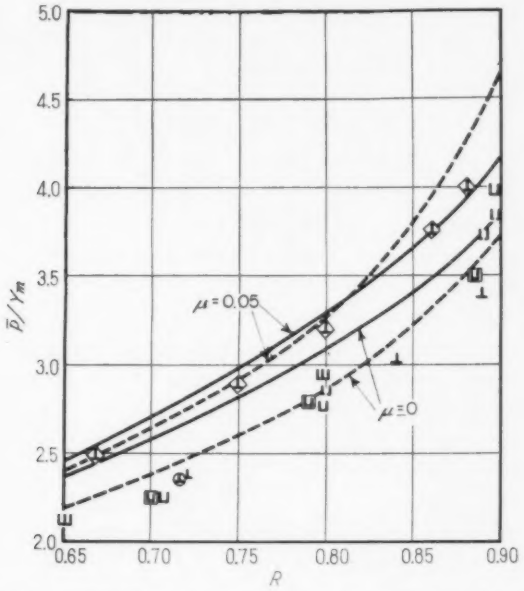

FIG. 9. Mean steady extrusion and piercing pressure vs. reduction in area:

Upper bound { —— Extrusion
- - - Piercing

Experimental data

⊥	Fig. 5 (a)	Hard aluminium
⊔	Fig. 5 (c)	
⊔	Fig. 5 (g)	
⊔	Fig. 5 (e)	
⊕	Fig. 5 (a)	Soft aluminium
⊡	Fig. 5 (c)	Hard copper
◈	Fig. 5 (a)	Lead [after Johnson *et al*]

The similarity between extrusion and piercing has been pointed out in Part I of the present paper, and the upper bounds for the die and punch pressures as well as the most suitable velocity fields in steady-state working, using a non-hardening material, were found identical when both the die and the punch were rough and $D_e = D_p$. If this is assumed to hold also for the initial stage of lubricated extrusion and piercing, then, from equation (30), Part I, the mean yield stress of the deforming material after a punch travel of l in piercing is seen to be equal to that after a die travel of $l' = D_e^2 l/(D_c^2 - D_e^2)$ in the extrusion.

The piercing punch pressure and the extrusion die pressures for soft and hard aluminiums, plotted against l and l' respectively in Fig. 8, show very

good agreement when $D_p = D_e$ and for $0{\cdot}25 < D_p/D_e < 0{\cdot}8$. This indicates that the piercing pressure of a material can be predicted fairly exactly from a corresponding extrusion pressure for the same material when the extrusion die and the punch have the same shape, the container being commonly used.

(iii) *Steady-state pressure*

The experimental steady-state pressures in various types of extrusion and piercing of hard aluminium and copper divided by the mean yield stresses are shown in Fig. 9 against fractional reduction in area. The solid and broken lines in the figure refer to the upper-bound solutions with $\mu = 0$ and $0{\cdot}05$ for the bar extrusion and the shell piercing respectively.

For these steady-state pressures, the agreement between theory and experiment is within 15 per cent, probably because the over-estimate of the effects of work-hardening and friction are not serious in this case. It is interesting to see that the steady-state lubricated extrusion pressures are a simple function only of reduction and regardless of type of extrusion. This is to be expected from the fact that the upper bounds for extrusion and piercing are nearly the same when $\mu = 0$ and from plane-strain considerations made concerning the multi-hole extrusions,[1, 10, 11] The same conclusion has been drawn by Dodeja and Johnson[12] and Frisch and Thomsen[13] in their lubricated multi-hole extrusions.

The experimental results by Johnson[14] and Dodeja and Johnson[12] with non-hardening pure lead are also shown in Fig. 9. Their agreement with the present upper-bound solution is surprisingly good. On the other hand, the results with aluminium by the same investigators fall above the theoretical curves, contrary to the present experimental results. The reason for this is not clear.

(iv) *Deformation*

The flow patterns observed on meridian sections of a lead billet are illustrated and contrasted with that predicted by calculations from the most suitable velocity field in Figs. 11–13. The concordance in general character is seen to be good. However, detailed examination indicates considerable difference between them, and this is caused by the simplified velocity fields used for the analysis, by the existence of friction between the material and tools and by the non-ideal mechanical properties of lead.

In Fig. 10, the lengths of the extruded material from the two orifices during the combined extrusion [Fig. 5(e)] are illustrated. Recalling the observations made concerning three-orifice extrusion in plane-strain,[7] together with the fact that the steady-state bar-extrusion and shell-piercing pressures are almost the same for a given reduction, leads to the conclusion that the lengths of the extruded material should be nearly equal if $\mu = 0$. In Fig. 10, however, the bar is seen to be extruded somewhat faster than the shell is. This will be caused by the friction whose effect is larger for the shell, because it has a larger surface area than that of the bar material.

(v) *Extrusion defects*

Various types of extrusion defect have been observed. Fig. 14(a) shows a defect caused by an inclusion of surface skin along the conical surface of the

dead metal underlying the extrusion die;[15] the reduction was 0·716. A degreased die and a lubricated container were used. The most suitable velocity field which gave the least upper bound under the present conditions is shown in Fig. 14(b) and (c). The black circles in the figure represent the particles of surface skin of the billet and, with this velocity field, it becomes included in the billet body as the process proceeds, going along the boundary surface between the dead metal and the flowing material until it emerges on the external surface of the extruded bar.

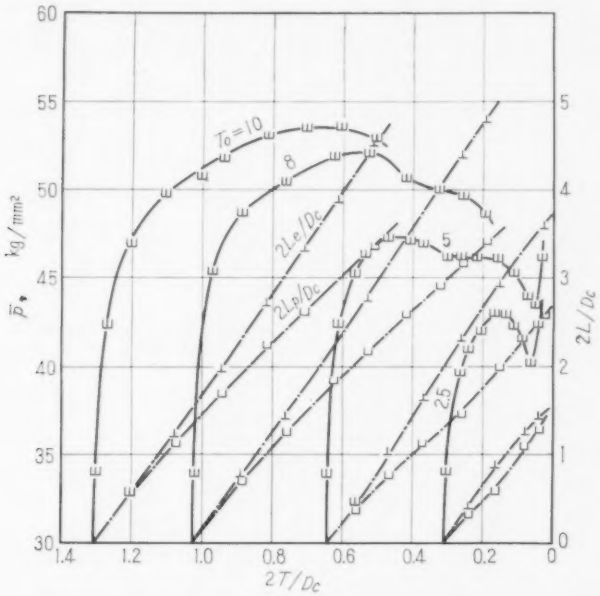

FIG. 10. Mean working pressure and extruded length during extrusion of Fig. 5(e) for hard aluminium:

$R_e = 0{\cdot}889$, $R_p = 0{\cdot}909$, $R_t = R_e + R_p - 1 = 0{\cdot}798$;

— · — ⊥ · — extruded length of bar; — · — ⊔ · — extruded length of shell.

If the dead metal is not perfectly rigid and gradually flows out through the orifice, the included surface skin will lie just beneath the surface of the extruded bar. Such a defect is often observed in practice. The type of defect of Fig. 14(b) was not seen in the products extruded with higher reductions. This is to be expected according to the most suitable velocity field shown in Fig. 14(d) which requires no dead-metal region.

On the sections of the extruded products shown in the upper part of Fig. 15, another type of defect caused by the skin inclusion is seen. This has already been observed experimentally[15, 16] and explained, with the upper-bound approach method, by Kudo[7] and Johnson[17] for the case of plane strain. In the axi-symmetric extrusion with lubricated tools, the most suitable velocity field in the non-steady-state phase is that shown in Fig. 16(a) (see Part I).

Vol. 3
1961

The skin of the bottom surface of the billet starts to move towards the centre as the non-steady stage begins, until it is included into the body of the billet along the centre axis. Experiments with copper and aluminium done immediately after etching resulted again in the same defect, indicating that no welding has occurred.

The prevention of this kind of defect is to be anticipated if a rough bottom die is used, because the transition point is retarded in such cases [see Fig. 25(a) and (b), Part I] and the inward movement of the skin resisted. In fact, no inclusion is seen on the meridian sections of parts extruded with a rough bottom die (Fig. 15).

However, if a thick surface layer covers the bottom surface, represented by hollow circles in Fig. 16(c), it will be enfolded in the billet along a surface of dead metal at the bottom centre and will form a tubular inclusion because the dead metal at the bottom centre shrinks as the deformation proceeds. Such a defect has been reported already.[15]

The third type of defect is seen as a cavity at the bottom centre of the extruded products (Fig. 15). The remaining length of the billet at the beginning of this cavity formation has been predicted in Part I of the present paper, using the velocity field shown in Fig. 16(b), as $0{\cdot}36D_e$ for a smooth bottom die and $0{\cdot}44D_e$ for a rough bottom die. Comparison of these critical lengths as predicted and observed is made in Table 2 and indicates good agreement.

TABLE 2. COMPARISON OF PREDICTED AND OBSERVED VALUE OF $2T/D_e$ FOR INITIATION OF NON-STEADY PHASE OR SKIN INCLUSION AND CAVITY FORMATION DURING EXTRUSION OF HARD ALUMINIUM

Reduction in area R	Lubrication	Transition or inclusion point $2T/D_e$		Cavity point $2T/D_e$	
		Predicted	Observed	Predicted	Observed
0·716	Lubricated	0·75	0·66	0·39	0·36
0·837	Lubricated	0·81	0·60	0·29	0·25
0·837	Lubricated except bottom die	0·48	—	0·35	0·36
0·906	Lubricated	0·75	0·57	0·22	0·25
0·906	Lubricated except bottom die	0·43	—	0·26	0·24
0·936	Lubricated	0·71	0·51	0·18	0·15

In this table, the theoretical length of the billet at the steady–non-steady transition point and the experimental value of the billet length at which the skin inclusion has started are compared. The visible skin inclusion seems to begin considerably later than predicted. This will be due in part to the work-hardening property of the actual material.

The cavity formation is prevented to some extent by increasing the resistance to flow of the material through the die orifice. This is done, for instance, by increasing the length of the cylindrical die orifice or by using a conical die orifice.

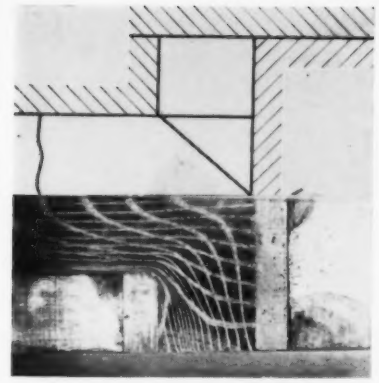

(c)

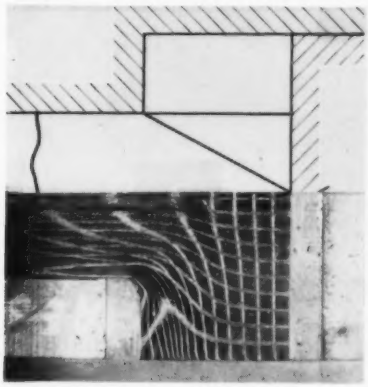

(b)

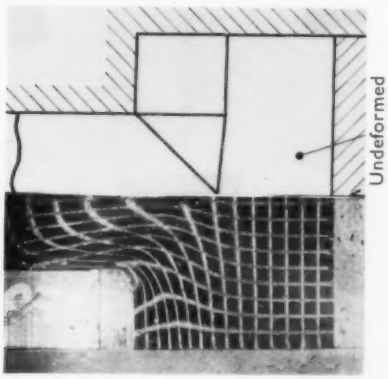

Undeformed

(a)

FIG. 11.

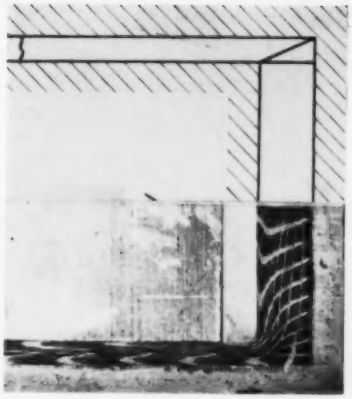

(c)

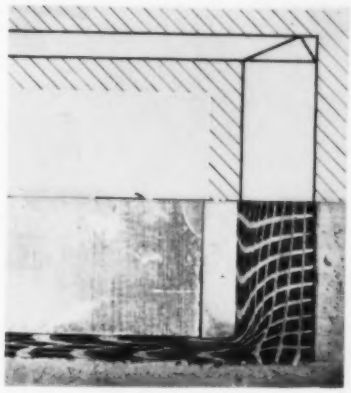

(b)

Deforming

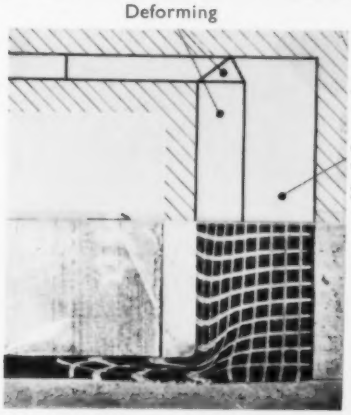

Undeformed

(a)

FIG. 12.

FIG. 11. Flow pattern of lead specimen and least-energy-dissipation field during extrusion with $R_e = 0{\cdot}75$.

FIG. 12. Flow pattern of lead specimen and least-energy-dissipation field during piercing with $R_p = 0{\cdot}75$.

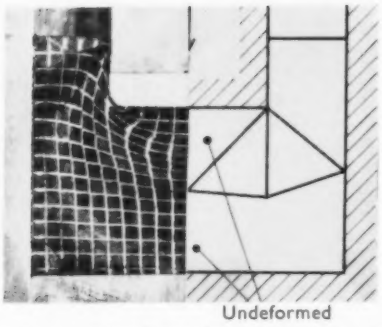

FIG. 13. Flow pattern of lead specimen and least-energy-dissipation field during piercing with $R_p = 0{\cdot}25$.

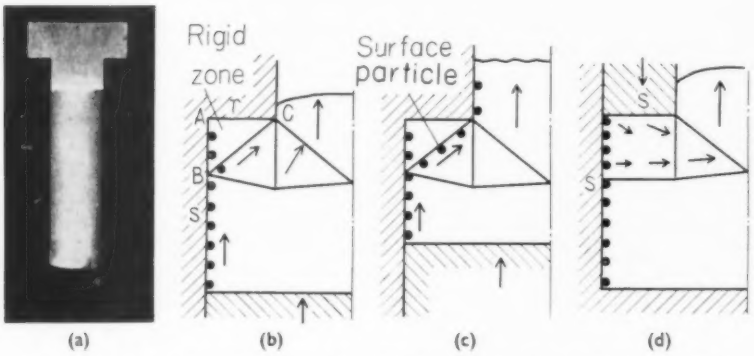

FIG. 14. Extrusion defect at the shoulder. (a) Aluminium extruded from lubricated container with degreased die of $R_e = 0{\cdot}716$. (b, c) Least-energy-dissipation field for the above conditions and skin inclusion. (d) Least-energy-dissipation field for larger reduction or lubricated die.

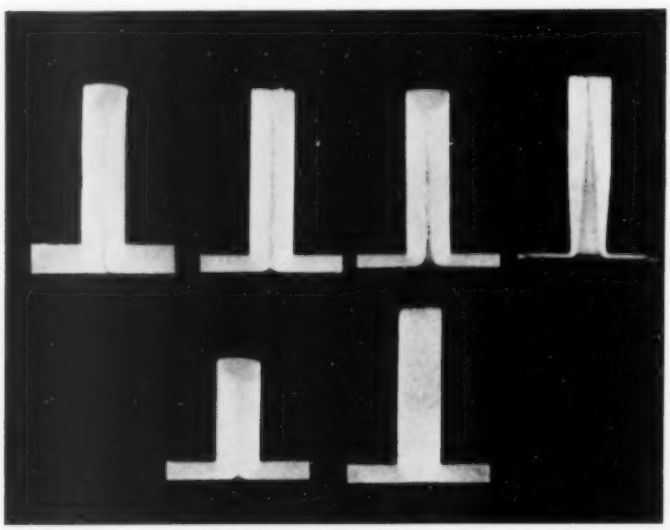

FIG. 15. Defects on the section of extruded hard aluminium: $R_e = 0{\cdot}906$.

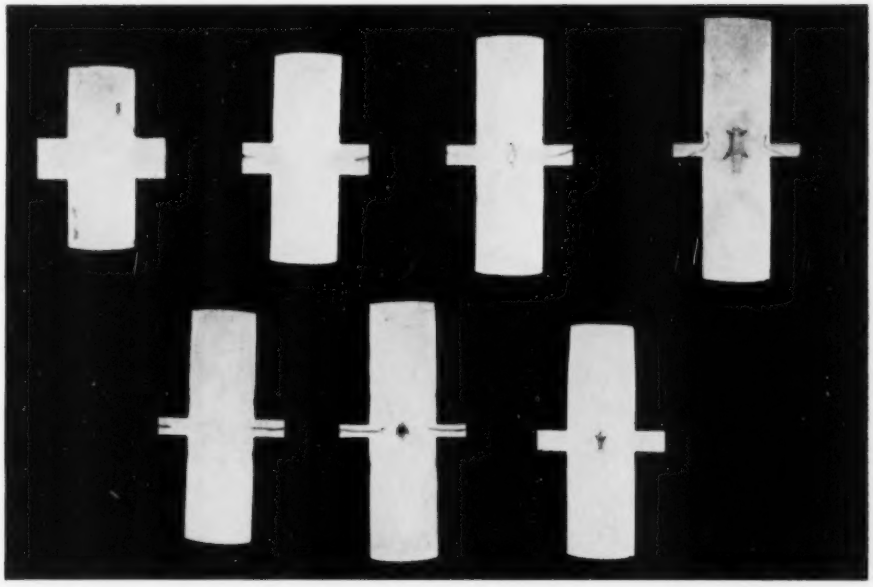

FIG. 17. Defects on the section of aluminium specimen extruded symmetrically in two opposed directions [Fig. 5(b), $D_{e1} = D_{e2}$].

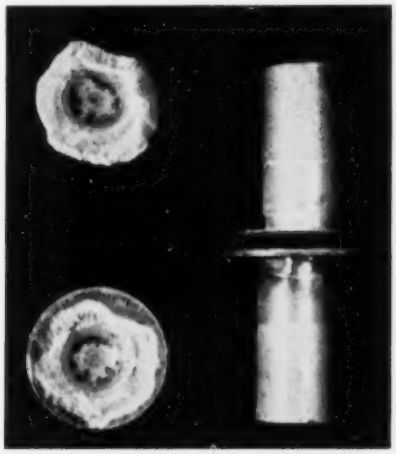

FIG. 19. Separation of two-way extrusion; hard aluminium.

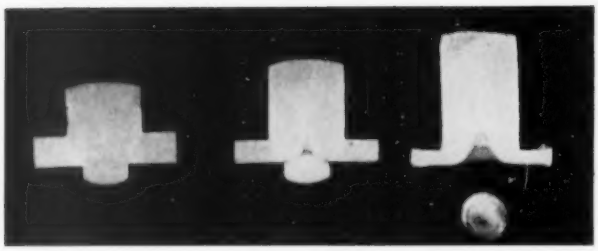

FIG. 21. Defects during unsymmetrically opposed extrusion of hard aluminium.

(a) (b)

FIG. 22. Defects and deformation during unsymmetrically opposed piercing [Fig. 5(d)].

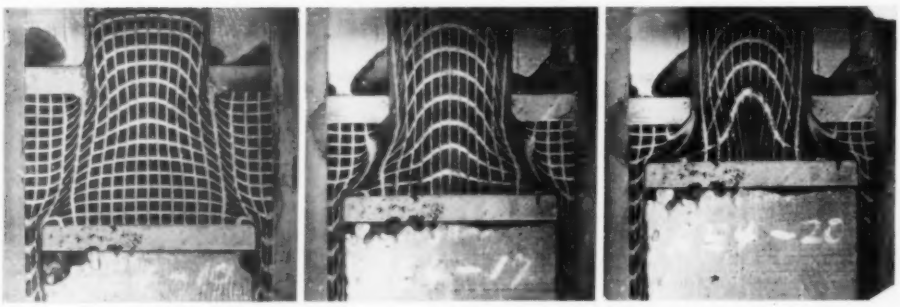

(a) (b) (c)

FIG. 24. Internal flow pattern during opposed extrusion-piercing of lead: $R_e = R_p = 0{\cdot}75$.

The effect of the increase in the efflux resistance is formulated as follows: Let us consider, for simplicity, a plane-strain case having unit thickness perpendicular to the paper, Fig. 16(b). The material underlying the extrusion orifice is assumed to be pressed laterally with a speed of unity. The surface 13 is a surface of velocity discontinuity, the region 123 and the region above

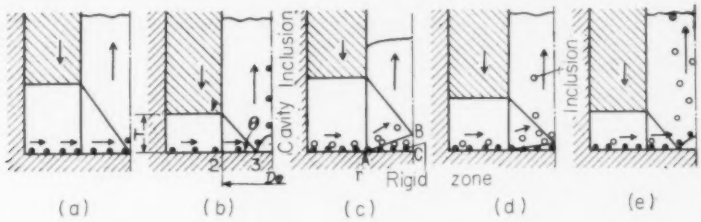

FIG. 16. Least-energy-dissipation field and defect formation during later stage of extrusion.

the surface 13 being considered rigid. The latter region is assumed to be acted on by a mean resisting pressure q. The rate of internal energy dissipation is then

$$\dot{E} = kT \sec\theta \operatorname{cosec}\theta + \frac{qD_e}{2}\tan\theta$$

for a smooth bottom die.

The value of θ which makes $\dot{E}$ a minimum is

$$\tan\ \theta_e = 1\Big/\sqrt{\left(1+\frac{qD_e}{2kT}\right)}$$

The condition of cavity formation, that is $\tan\theta_e \geqslant 2T/D_e$, is then

$$\left(\frac{2T}{D_e}\right)_e = \left\{-\frac{q}{k}+\sqrt{\left[\left(\frac{q}{k}\right)^2+4\right]}\right\}\Big/2$$

This relation indicates how the critical thickness is decreased by the action of q.

Through the sections of the extremely thin flanges shown in Fig. 15, top right, oblique cracks are found. It is not clear whether they were developed by the skin inclusion or merely by the embrittlement of the material.

On the other hand, practically no defect was found in the pierced shells having thin walls. The skin of the billet bottom goes out along the outer-side surface of the shell. The lifting-up of the bottom corner of the shell [Fig. 23(b), Part I] is prevented by a relatively high frictional resistance acting on the surface of the thin wall.

4. OPPOSED EXTRUSION- AND PIERCING-FORGINGS

(i) *Symmetrically opposed extrusion- and piercing-forgings*

The autographic diagrams of the symmetrically opposed extrusion- [Fig. 5(b) $D_{e1} = D_{e2}$] and piercing-forgings [Fig. 5(d), $D_{p1} = D_{p2}$] are illustrated in Figs. 6 and 7. The corresponding upper-bound solutions obtained with the use of Figs. 25(c) and 28(c), Part I, are given by broken lines. For comparison with

Vol. 3
1961

the extrusion- and piercing-forgings in one direction, the remaining lengths of billet in the present problems were taken as $2T$.

When $2T/D_c$ is not very small, the working pressures measured in the opposed cases are seen to be lower than those for the one-way extrusions or piercing-forgings, as is to be expected from theory. However, this is reversed as $2T/D_c$ decreases. This reversal appears in the upper-bound solutions when μ is assumed to be, say, 0·02, showing that there should be an over-estimate of the effect of friction in the calculation of the effect of friction.

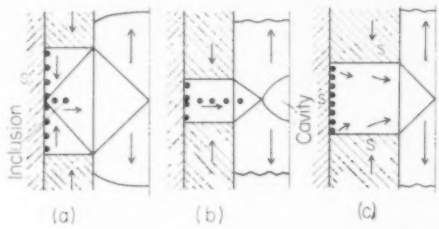

FIG. 18. Least-energy-dissipation field to explain defects of Fig. 17.

Physically speaking, the differences between unidirectional and opposed extrusions with tools of identical dimensions exist because there is no friction on the boundary between the two opposed extrusion regions, whilst, in the former case, the billet bottom is acted on by the friction; cavity formation does not occur as easily in the latter case as in the former.

However, cavities were found in the centre of hard and soft aluminium and soft copper parts extruded in opposite directions (Fig. 17, top), as has been predicted in Section 7(iii), Part I. In the autographic diagrams, this is detected by a slight drop in the working pressure [Fig. 6(a)]. One half of the length of the billet T at the time of cracking was estimated from the experiments to be $0{\cdot}18D_c$ when $R = 0{\cdot}716$, and $0{\cdot}25D_c$ when $R = 0{\cdot}899$, these being much less than the values of T at the cavity formation in one-way extrusion. This fact indicates that a certain amount of energy is required to produce a cavity within the metal.

Several aluminium specimens were extruded in opposed directions with $R = 0{\cdot}716$, down to a stage just before the cracking point. They were then annealed and worked in the same tools. Fig. 17, bottom-left and -centre, shows sections of the part extruded after the annealing. The effect of an intermediate anneal is evident and the crack is considered to have been initiated when $T \simeq 0{\cdot}1D_c$.

As has been suggested in the preceding section, increasing the efflux resistance is also a preventive measure against cracking.

Another type of defect is seen in the flanges of the extruded part in opposed directions with $R = 0{\cdot}716$ (Fig. 17). This was caused again by the inclusion of the skin of the billet side and is well explained by the most suitable velocity field shown in Fig. 18(a) in which the dead-metal regions are formed on the top and bottom die faces.

As working proceeds, the included skin is drawn towards the billet centre until it joins with the central crack [Figs. 18(b) and 19] when the extrusion load drops suddenly with a resounding bang. This inclusion is again mitigated when a degreased container is used (Fig. 17, bottom-right). When the reduction is large, the corresponding velocity field is as shown in Fig. 18(c), this causing no skin inclusion. In fact, no defect is found in the flanges of the parts extruded with $R = 0{\cdot}899$ except when the flange has been reduced to an extremely small thickness.

Defects in symmetrically opposed piercing-forged parts are very rare. Only a circumferential groove round the outer-side surface was found on a very thick-walled and thin-bottomed cylinder. This groove is not a crack but a contraction, and is likely to be formed following Johnson's[18] velocity field.

(ii) *Unsymmetrically opposed extrusion- and piercing-forgings*

An example of autographic diagrams for the unsymmetrically opposed extrusion-forging [Fig. 5(b), $D_{e1} > D_{e2}$] of hard aluminium is shown in Fig. 20,

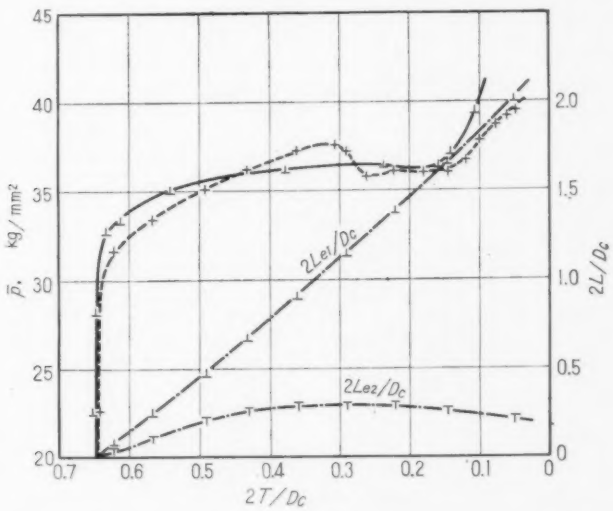

FIG. 20. Working pressure and extruded length during the unsymmetrically opposed extrusion of hard aluminium: + Fig. 5(b), $R_{e1} = 0{\cdot}716$, $R_{e2} = 0{\cdot}889$; —·⊥—· extruded length from larger orifice; —·⊤—· extruded length from smaller orifice; ⊥ Fig. 5(a), $R_e = 0{\cdot}716$.

together with that for an ordinary extrusion-forging with an orifice diameter D_{e1}. In the figure, the lengths of extruded bar in the upward and downward directions are also shown. The variation in the working pressure during this process is well understood with the aid of sections of the extruded parts (Fig. 21). According to these, the material is first extruded from two orifices—thus resulting in a lower pressure compared with the one-way extrusion. The material then ceases to flow out of the smaller orifice, and the skin of the bottom

surface begins to be enfolded into the material from the root of the bottom projection. At this stage, the pressure required for working should be higher than that for the ordinary lubricated extrusion-forging because the bottom projection resists the inward flow of the material.

A cavity inside the material is next developed until it joins with the enfolded skin, and the bottom projection separates off. After this, the process proceeds in the same manner as the ordinary extrusion-forging.

In unsymmetrical piercing-forging [Fig. 5(d), $D_{p1} < D_{p2}$], the separation of the thinner wall from the material body was again observed (Fig. 22). This was caused by the skin inclusion from the root of the thinner wall. This separation was also found when piercing with opposed punches (where $D_{p1} = D_{p2}$); the flow of the extruded material from one orifice was stopped by a punch shoulder. In such a case, however, when degreased punches were used, the separation was prevented.

(iii) *Opposed extrusion–piercing-forging*

Several forging tests were performed using an extrusion die on one side and a piercing punch on the other [Fig. 5(h–j)]. Typical autographic diagrams are shown in Fig. 23.

In these figures, autographic diagrams are also shown for one-way extrusions and piercing-forgings, using respectively the die and the punch used in the opposed forging, and they indicate how the working pressures are greatly reduced by adding a second orifice.

The upper bound for working pressure during the opposed extrusion–piercing-forging of non-hardening material in plane-strain has already been given by Kudo[7] and it has been shown to be much lower than the corresponding one-way extrusion. The forging flow patterns, Fig. 24, will also be seen to be very similar to those predicted analytically and observed experimentally[21] in plane-strain problems.

According to plane-strain analysis, the efflux velocities of material from the two orifices are equal when the billet length is not small and provided the container is smooth. As the billet length reduces, the velocity at the wider orifice tends to increase. These velocities, as obtained in the present experiments, are shown in Fig. 23. Again a qualitative agreement is found between them and those predicted from the plane-strain analysis. The general tendency for the bar to flow out faster than the shell is attributable to the different degrees of frictional resistance acting on the bar and the shell.

An autographic diagram during an opposed extrusion–piercing-forging, using a punch with a shoulder [Fig. 5(i)], is shown in Fig. 23(b). At the start, the working pressure varies in the usual manner of opposed forging, being followed by a cessation in the shell extrusion, the pressure rising suddenly until it alters in the typical manner of a one-way extrusion-forging.

The only defects found in the products of the extrusion–piercing-forging were the cavity formations on the sides of the slug opposite to the bar and the shell wall, which are inherent to the extrusion- and piercing-forging respectively.

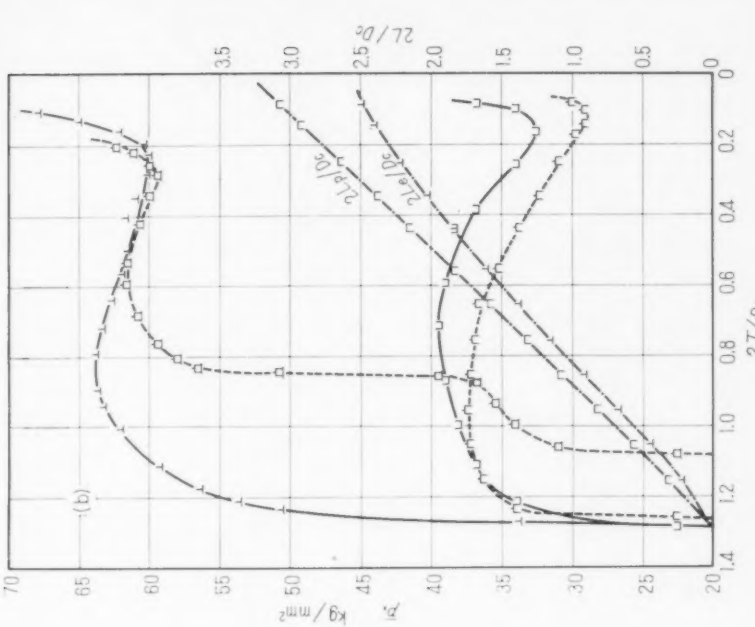

(b) – – ⊓ – – Fig. 5(b), $R_e = 0{\cdot}889$, $R_p = 0{\cdot}706$; – – □ – – Fig. 5(i), $R_e = 0{\cdot}889$, $R_p = 0{\cdot}706$; – ⊥ – Fig. 5(a), $R_e = 0{\cdot}889$; – □ – Fig. 5(c), $R_p = 0{\cdot}706$.

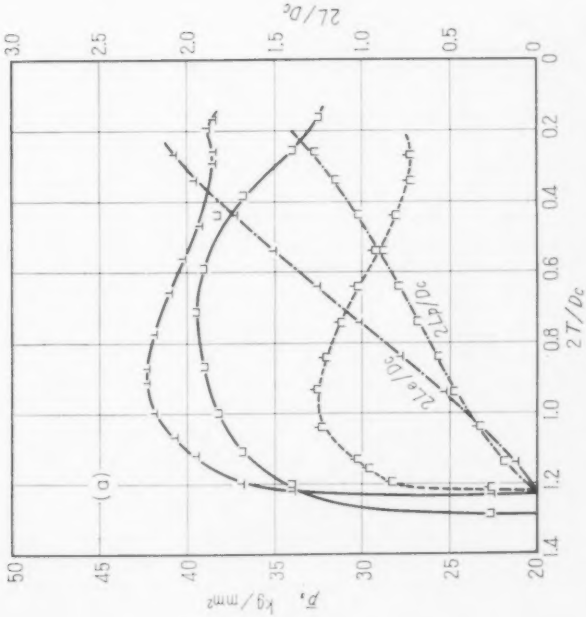

(a) – – ⊓ – – Fig. 5(b), $R_e = 0{\cdot}716$, $R_p = 0{\cdot}706$; – · – ⊥ – · – length of extruded bar; – · – ⊓ – · – length of extruded shell; – ⊥ – Fig. 5(a), $R_e = 0{\cdot}716$; – □ – Fig. 5(c), $R_p = 0{\cdot}706$.

FIG. 23. Working pressure and extruded length during opposed extrusion–piercing of hard aluminium.

5. SOME MEASUREMENTS OF TOOL PRESSURE

(i) *Experimental apparatus and material*

An experimental apparatus depicted in Fig. 25 was constructed to measure the average internal pressure on the container and the average normal pressure on the die projection during an extrusion-forging or coining.

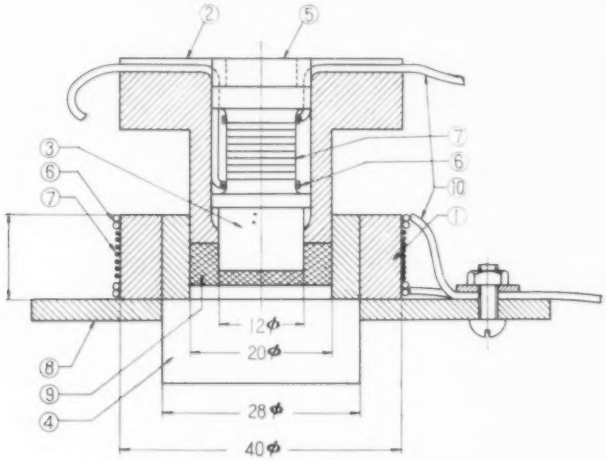

FIG. 25. Experimental tool assembly for measurement of pressure in extrusion and coining: (1) Container ring, (2) top die, (3) top die core, (4) bottom die, (5) distance disk, (6) phosphor-bronze wire, (7) constantan wire, (8) Bakelite plate, (9) specimen.

The container ring is made of hardened tool steel shrink-fitted and of a compound type having outer and inner diameters 40 and 20 mm, respectively, and a height 10 mm. Its outer surface is phosphate-coated and insulated by Araldite. A 0·05-mm thick wire having an electric resistance of 120 Ω was wound round this surface, the terminals being fixed to two bands of phosphor-bronze wire.

The longitudinal position of the 12-mm diameter core which forms a portion of the top die can be adjusted by means of backing disks. This core is also a pick-up made in the same manner as described above.

The changes in the electric resistances of these pick-ups are amplified in the usual circuits for strain-gauge measurement and tests were made using an oscilloscope.

The total pressing load was read from the indicator of the 30-ton testing machine.

ii) *Calibration*

The calibration of the container pick-up was done using a lead disk as a medium of pressure transmission. To carry out measurements up to 10,000 atm, the corners of the lead disk were covered with 0·3-mm thick brass bands, and these prevented the lead from flashing between the pressure pad and the container.

The readings of mean vertical pressure during loading and unloading for disks of heights 4·59 and 7·92 mm are shown in Fig. 26. It exhibits a loop, the main part of which is two parallel straight lines. Their distance corresponds to $5 \sim 6$ kg/mm^2.

This loop is well interpreted with reference to Fig. 27. The container pressure on loading should be less than the mean vertical pressure $\bar{p}$ by the yield stress Y, while on unloading it should be $(\bar{p}+Y)$. Therefore, the difference between the loading and unloading curves is considered to be $2Y$ in accordance with the experimental observation (Fig. 26).

The slopes of the straight lines for the two disks are proportional to their thicknesses. This indicates that the response of this pick-up depends only on the total internal side force.

From the above considerations, the reading of the internal hydrostatic-pressure curve for this pick-up is seen to be represented by a straight line through the origin and parallel to the straight parts of the reading of the vertical pressure loop. The accuracy of this calibration curve was considered to be ±3 per cent on measuring a pressure of some tens of kg/mm².

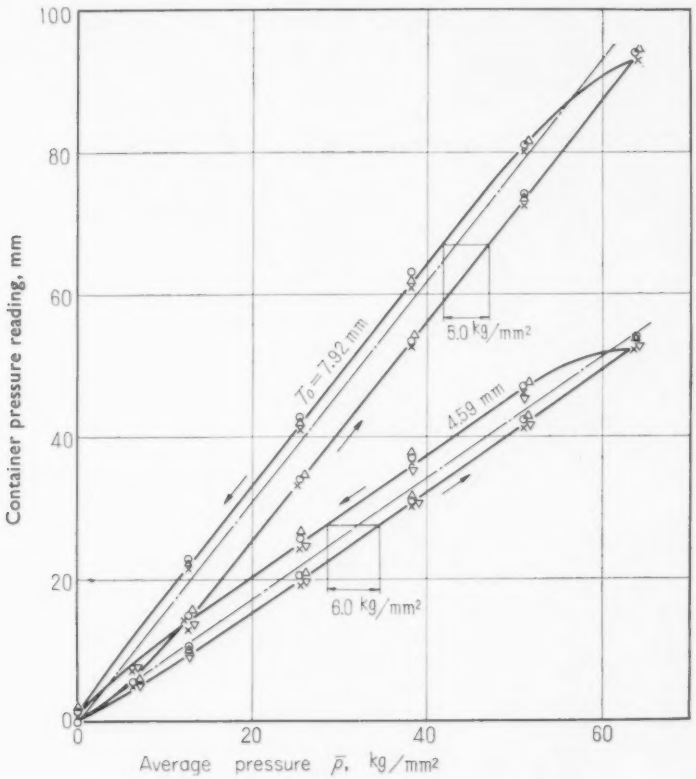

FIG. 26. Calibration curve for container-wall pressure gauge with the use of lead disk.

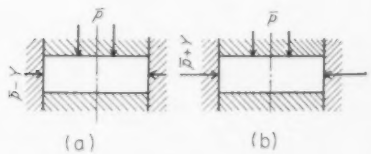

FIG. 27. Mean pressure $\bar{p}$ and container-wall pressure during loading and unloading of lead disk.

(iii) *Experimental results and discussion*

A hard aluminium disk of 20 mm diameter was coined between two flat dies, one of which contained the core pick-up. The end face of the core pick-up projected from the die face by 0·05 mm when no load was applied.

The readings for the container and the core are shown in Fig. 28, making loops. Two straight parts of the loop of the internal-pressure curve are again parallel to each other, their distance being 25 kg/mm² which is about double the yield stress of hard aluminium. This indicates that the residual pressure between container and material after forging is nearly equal to Y.

The core pressure in Fig. 28 is slightly higher than and parallel to the mean pressing pressure. This is because the core end was not in the same plane as the top die surface.

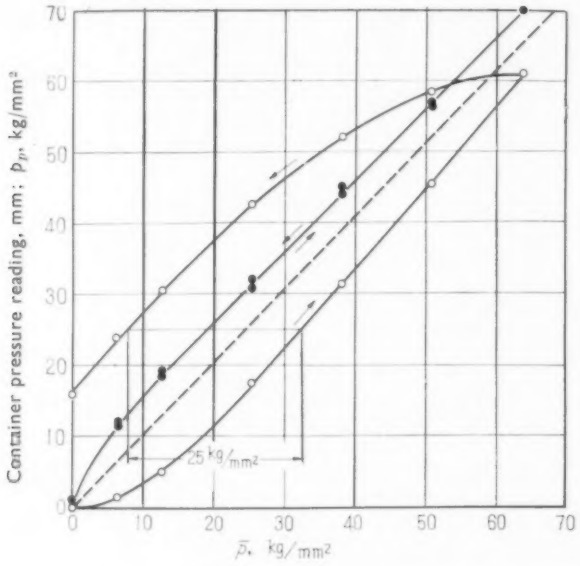

FIG. 28. Container-wall pressure $\bar{p}_c$ (○) and top-die core pressure $\bar{p}_p$ (●) during compression and unloading of hard aluminium disk.

Twenty-millimetre diameter hard aluminium disks with thicknesses of 6 and 8 mm were extruded through an orifice having a diameter of 6 or 8 mm ($R = 0{\cdot}91$ or $0{\cdot}84$) and the container pressure was measured. Typical measurements are shown in Fig. 29. The mean extrusion pressures $\bar{p}$ in these experiments were nearly constant throughout a test. The reading of the container pressure decreased as the extrusion-forging proceeded. However, the normal pressure $\bar{p}_c$ per unit area of the contact surface between the container and the material is again nearly constant and is approximately equal to $\bar{p}$ in all experiments. The difference between the mean die pressure $\bar{p}_d$ and $\bar{p}_c$ shows an initial peak of 12 to 15 kg/mm² followed by a constant value of 5 to 10 kg/mm².

If an annular region under the extrusion die face is assumed to be compressed, first under a uniform pressure $\bar{p}_d$, Fig. 30(a), the mean container pressure will be about $(\bar{p}_d - Y)$ in accordance with the previous discussion. The die pressure will not be uniform over the die surface after flow begins; it is greatest at the container wall. Then $(\bar{p}_d - \bar{p}_c) < Y$. The $(\bar{p}_d - \bar{p}_c)$ curve in Fig. 29 can thus be interpreted.

The present discussion indicates that it is possible for $\bar{p}_c$ to be larger than $\bar{p}$ if the reduction in area is very low in an extrusion-forging, since $\bar{p}_d \gg \bar{p}$.

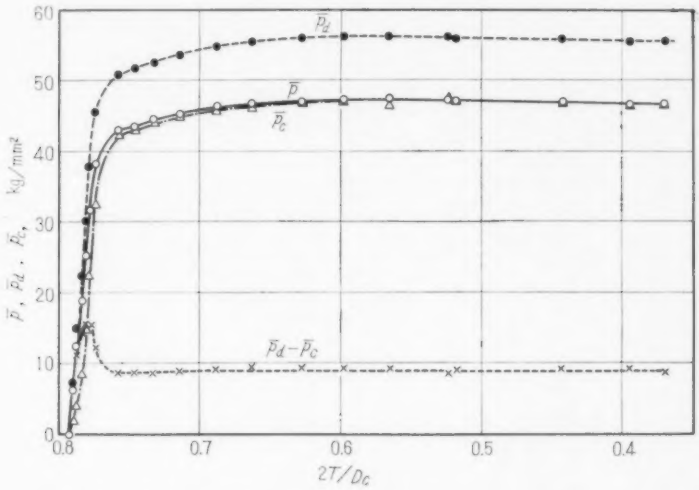

FIG. 29. Mean working pressure $\bar{p}$ (○), mean container pressure $\bar{p}_c$ (△) and mean extrusion-die pressure $\bar{p}_d$ (●) during extrusion of hard aluminium disk: $R_e = 0{\cdot}84$.

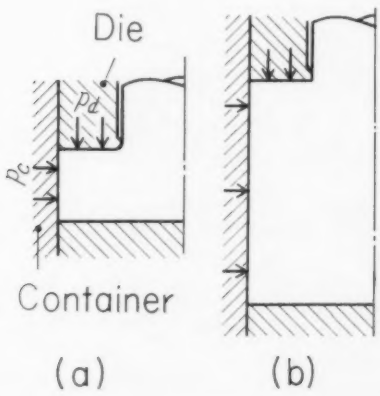

FIG. 30. Relation between container-wall pressure and die pressure in extrusion.

On the other hand, when the billet length is very large and the container is smooth, $\bar{p}_c$ should be nearly equal to $(\bar{p} - Y)$.

These considerations and experimental results lead to the conclusion that the average container pressure is less than the mean extrusion pressure when the reduction is high or when the billet is long. This is in agreement with the findings of Frisch and Thomsen[19] and Thomsen[20].

Fig. 31 illustrates the variations in the container pressure and the projection pressure with applied load during the closed-die coining of hard aluminium (see Fig. 25). For the container pressure, the readings taken from the meter are directly plotted because the instantaneous contact area between the material and the container is not known. The instantaneous thickness of the specimen is also shown.

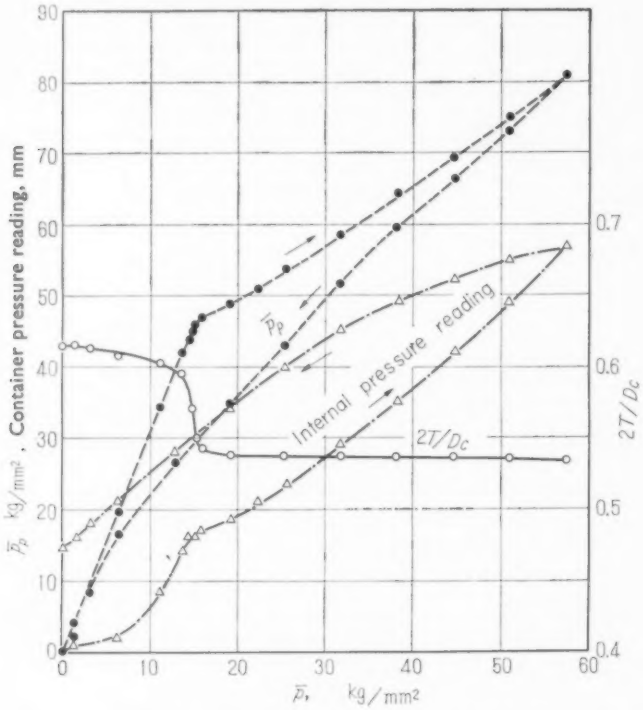

FIG. 31. Mean working pressure $\bar{p}$, working stroke (○), top-die projection pressure (●) and container-wall pressure (△) during coining of aluminium.

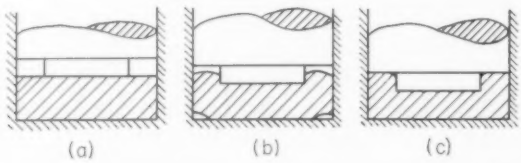

FIG. 32. Deformation of disk specimen during coining.

The hesitation in the container pressure curve corresponds to the bending of the unsupported part of the specimen around the indentation punch (Fig. 32). After this, the loading and unloading curves are similar to those of Fig. 28.

The projection pressure increases linearly with the applied load during the indentation period, and then rather slowly.

For the experimental conditions tested, $\bar{p} > \bar{p}_c$ at the final stage of coining. The mean projection pressure $\bar{p}_p$ exceeds $\bar{p}$ by an amount which increases as the height of the projection increases and the thickness of the specimen decreases.

The residual radial pressures after unloading are again nearly equal to the yield stress of the material.

Acknowledgements—The author wishes to thank Professor S. Fukui, of the University of Tokyo, for his helpful advice and encouragement throughout the work. He also wishes to thank Mr. J. Seino and Mr. I. Takita, of the Institute of Aeronautical Research at the University of Tokyo, and Mr. M. Kametani, of Iwisaki Communication Apparatus Co. Ltd., for their kind assistance in making of experimental apparatus and with the experiments, calculations and the preparation of the manuscript. Acknowledgement is also made to Professor W. Johnson of the University of Manchester for his kind help in preparing the paper for publication.

This work was supported by the Fund for Scientific Research provided through the Ministry of Education, Japan.

Vol. 3
1961

REFERENCES

1. H. Kudo, *Int. J. Mech. Sci.* **2**, 102 (1960).
2. W. Schroeder and D. A. Webster, *J. Appl. Mech.* **16**, 289 (1949).
3. S. Kobayashi, R. Herzog, J. T. Lapsley and E. G. Thomsen, *Trans. Amer. Soc. Mech. Engrs.* B**81**, 228 (1959).
4. S. Fukui, H. Kudo and I. Takita, *The Coefficient of Friction in Sheet Drawing.* Unpublished work (1957).
5. H. Kudo, *Rep. Inst. Sci. Tech., Tokyo Univ.* **11**, 147 (1957).
6. H. Kudo, *Int. J. Mech. Sci.* **1**, 57 (1960).
7. H. Kudo, *Int. J. Mech. Sci.* **1**, 229 (1960).
8. S. Fukui, H. Kudo and J. Seino, *Rep. Inst. Sci. Tech., Tokyo Univ.* **11**, 91 (1957).
9. D. Tabor, *The Hardness of Metals.* Clarendon Press, Oxford (1951).
10. L. C. Dodeja and W. Johnson, *J. Mech. Phys. Solids* **5**, 267 (1957).
11. W. Johnson, P. B. Mellor and D. B. Woo, *J. Mech. Phys. Solids* **6**, 203 (1958).
12. L. C. Dodeja and W. Johnson, *J. Mech. Phys. Solids* **5**, 281 (1957).
13. J. Frisch and E. G. Thomsen, *Trans. Amer. Soc. Mech. Engrs.* B**81**, 207 (1959).
14. W. Johnson, *J. Inst. Met.* **85**, 403 (1956).
15. E. Pearson, *The Extrusion of Metals.* Chapman and Hall, London (1953).
16. W. Johnson, *J. Mech. Phys. Solids* **4**, 269 (1956).
17. W. Johnson, *Appl. Sci. Res., Hague* A**8**, 228 (1959).
18. W. Johnson, *Appl. Sci. Res., Hague* A**8**, 52 (1959).
19. J. Frisch and E. G. Thomsen, *Trans. Amer. Soc. Mech. Engrs.* **76**, 599 (1954).
20. E. G. Thomsen, *Trans. Amer. Soc. Mech. Engrs.* **75**, 515 (1955).
21. H. Kudo, *Int. J. Mech. Sci.* **1**, 393 (1960).

Int. J. Mech. Sci. Pergamon Press Ltd. 1961. Vol. 3, pp. 118–128. Printed in Great Britain

RESONANT STRENGTH OF A VIBRATING MEMBER HAVING TWO DEGREES OF FREEDOM, WITH HYSTERESIS DAMPING

M. G. SHARMA

Department of Engineering Mechanics, The Pennsylvania State University
University Park, Pa.

(*Received* 7 *September* 1960)

Summary—Vibrating members frequently undergo resonance during their useful life. For the durability of members it is very necessary to limit the large induced stresses at resonance to the fatigue strength of the material. Amplification in induced stresses at resonance depends on the inherent damping present in the vibrating system. Different types of damping are known to exist in a vibrating system. This paper considers only material damping. The specific problem considered in this investigation is of a shaft fixed at one end and free at the other, with a pulley and subjected to a fluctuating load. The fluctuating load induces combined fluctuating stresses which become critical when resonance takes place in either of the co-ordinates of the vibrating system. A fatigue-strength damping criterion has been developed for this problem which makes it possible to evaluate the resonant load from the distortion theory for fatigue under combined stresses and the material-damping characteristics of the material. A numerical example is worked out to show how this method could be applied to a practical problem. Curves are drawn for various materials showing the variation of resonant load with natural frequency ratios.

INTRODUCTION

VIBRATING members experience resonance when one of their natural frequencies coincides with the frequency of the impressed force or any disturbing force in the vicinity of the members. Severe stresses are induced in a member at resonance owing to the magnification of amplitude of the vibrating member. These stresses are usually much larger than the stresses that would occur under normal static-loading condition. For the durability of a vibrating part, these resonant-induced stresses must be kept below a safe limit so that failure may not occur due to fatigue. It is well known that the magnification of amplitude at resonance is influenced by the inherent damping in the vibrating system. Several types of damping have been known to exist in a vibrating system, such as structural or slip damping, damping due to extraneous effects and material damping. In many applications material damping is small compared to other sources of energy dissipation and is viewed as supplementary to other types of damping. There are certain cases, however, where hysteresis or material damping provides the only effective source of energy dissipation. For example, in turbine and compressor blade vibrations material damping plays an important role in suppressing dangerous amplitudes at resonance. Unlike the design of a vibrating member at off-resonance frequencies the design of a resonant member requires the simultaneous knowledge of stiffness, fatigue and damping characteristics of the material used. A fatigue-strength damping

criterion of the design of a resonant cantilever beam subjected to simple fluctuating stresses was originally suggested by Marin and Stulen[1]. Recently, the same criterion was extended to various types of members subjected to simple and combined fluctuating stresses at normal and elevated temperatures by Marin and Sharma[2]. The present paper extends the criterion to a vibrating member subjected to combined fluctuating stresses and having two degrees of freedom. In order to illustrate the application of the method a numerical example has been worked out. The result is shown in terms of curves relating resonant load and ratios of natural frequencies.

Vol. 3
1961

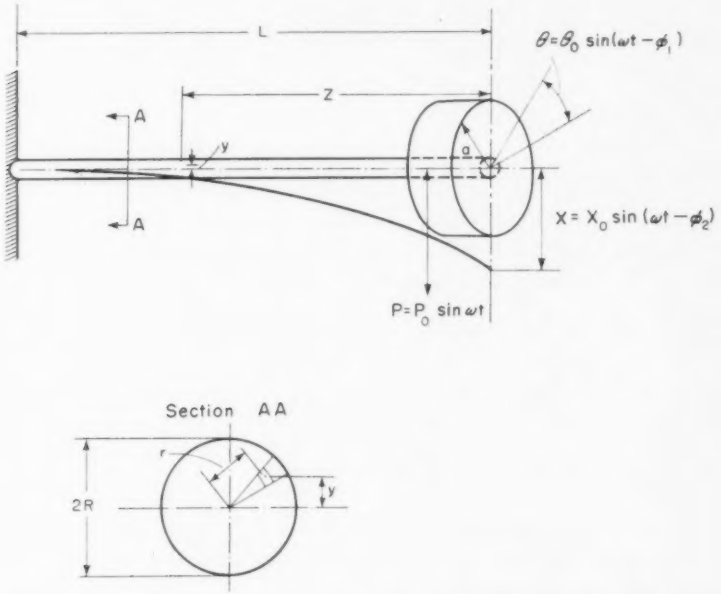

FIG. 1. A circular shaft subjected to a fluctuating load $P = P_0 \sin \omega t$.

BASIC EQUATIONS OF MOTION

Consider a pulley–shaft combination shown in Fig. 1 subjected to a fluctuating load varying sinusoidally

$$P = P_0 \sin \omega t \tag{1}$$

where P = load at any instant
P_0 = amplitude of load
ω = circular frequency of fluctuation of the load
t = time

The vibrating system has two degrees of freedom and therefore has two generalized co-ordinates θ and x.

The equations of motion for this system can be written as

$$\left.\begin{aligned} J\ddot{\theta} + K(1+i\mu_1^*)\theta &= P_0 a \exp(i\omega t) \\ M\ddot{x} + k(1+i\mu_2^*)x &= P_0 \exp(i\omega t) \end{aligned}\right\} \tag{2}$$

where
J = mass moment of inertia of the pulley
M = mass of the pulley
K = torsional stiffness
k = bending stiffness
μ_1 = damping coefficient in θ-co-ordinate
μ_2 = damping coefficient in x-co-ordinate
a = radius of the pulley

The steady-state solutions for equations (2) are

$$\left.\begin{aligned} \theta &= \theta_0 \sin(\omega t - \phi_1) \\ x &= x_0 \sin(\omega t - \phi_2) \end{aligned}\right\} \tag{3}$$

where

θ_0, x_0 are the amplitudes in θ- and x-co-ordinates respectively
ϕ_1, ϕ_2 phase angles between the impressed load and the displacements in θ- and x-co-ordinates respectively

In equations (3) the amplitudes θ_0, x_0 can be shown to be

$$\left.\begin{aligned} \theta_0 &= \frac{\theta_s}{\{[1-(\omega/\omega_1)^2]^2 + \mu_1^2\}^{1/2}} = M_\theta \theta_s \\ x_0 &= \frac{x_s}{\{[1-(\omega/\omega_2)^2]^2 + \mu_2^2\}^{1/2}} = M_x x_s \end{aligned}\right\} \tag{4}$$

where
ω_1 = natural circular frequency of vibration in θ-co-ordinate
ω_2 = natural circular frequency of vibration in x-co-ordinate
μ_1 = material damping constant in shear
μ_2 = material damping constant in tension
θ_s = static rotation $(P_0 a/K)$
x_s = static deflection (P_0/k)
M_x = magnification factor in x-co-ordinate
M_θ = magnification factor in θ-co-ordinate

ENERGY DISSIPATED IN INTERNAL FRICTION

An expression for the energy dissipated in internal friction for direct stressed members has been experimentally determined by Lazan[3] and Podnieks and Lazan[4]. The experimental evidence proves that for uniaxial stress case the specific damping energy is a power function of stress, i.e.

$$u = C_D \sigma^n \tag{5}$$

where u = specific damping energy (energy dissipated in material damping per

* μ_1 and μ_2 are obtained on the basis of assumption that the specific damping energy is proportional to the square of the amplitudes θ_0 and x_0.

unit volume per cycle), σ = amplitude of stress and n = damping exponent (usually lies between 2 and 3 for most materials, below a certain stress level usually termed cyclic stress sensitivity limit). Experiments of Robertson and Yorgiadis[5] indicate that the specific damping energy under normal and shear stress conditions are different. Comparing the damping coefficients experimentally determined for various materials under normal and shear stress

TABLE 1. COMPARISON OF EXPERIMENTAL AND THEORETICAL DAMPING COEFFICIENT IN SHEAR FOR VARIOUS MATERIALS

(Data after Robertson and Yorgiadis[5])

Material	Experimental		Theoretical*	Deviation (%)
	Tension $C_D \times 10^{12}$	Torsion $C'_D \times 10^{12}$	$C'_D = C_D\, 3^{3/2}$	
Magnesium alloy M (tubing)	1·0	5·196	9·20	56
Magnesium alloy J–1 (extruded)	0·55	2·86	3·90	27
Monel metal ($\frac{3}{4}$ in. dia. tubing)	0·05	0·26	0·27	4
Monel metal ($\frac{1}{2}$ in. dia. tubing)	0·03	0·156	0·19	18
SAE 1020 steel	0·05	0·26	0·4	35
SAE 4130 steel	0·043	0·223	0·2	12

* Based on equation (6).

conditions in Table 1, it is evident that the specific damping energy approximately follows the distortion-energy criterion. Therefore, the specific damping energy under combined states of stress can be expressed as a function of significant stress $\bar{\sigma}$, i.e.

$$u = C_D \bar{\sigma}^n \tag{6}$$

and $$\bar{\sigma} = [\sigma_x^2 + \sigma_y^2 + \sigma_z^2 - (\sigma_x \sigma_y + \sigma_y \sigma_z + \sigma_z \sigma_x) + 3(\tau_{xy}^2 + \tau_{yz}^2 + \tau_{zx}^2)]^{1/2}$$

σ_x, σ_y, σ_z are the normal stresses in x, y, z directions and τ_{xy}, τ_{yz}, τ_{zx} are the shear stresses.

Using equation (6) the expression for specific damping energy in terms of stress components for the vibrating system considered can be written as

$$u = C_D[M_x^2 \sigma^2 + 3M_\theta^2 \tau_r^2]^{n/2} \tag{7}$$

σ = axial stress due to a static moment $P_0 z$ on any element at a distance "y" from the neutral axis and at a distance "z" from the free end

τ_r = shear stress on any cross-section at any radius "r" from the center of the cross-section due to a static torque $P_0 a$

M_x = magnification factor in "x"-co-ordinate

M_θ = magnification factor in "θ"-co-ordinate

DERIVATION FOR RESONANT STRENGTH

Resonance takes place in either θ- or x-co-ordinate depending upon whether the frequency of the impressed force ω coincides with either ω_1 or ω_2.

Case (i). *Resonance takes place in θ-co-ordinate*

Energy input per cycle

$$\Delta W_e = \int_0^{2\pi/\omega} Pa\,d\theta + \int_0^{2\pi/\omega} P\,dx$$

Substituting the values of P, θ and x from equations (1) and (3) and integrating

$$\Delta W_e = \pi P_0 a\theta_0 \sin\phi_1 + \pi P_0 x_0 \sin\phi_2 \tag{8}$$

If resonance takes place in θ-co-ordinate

$$\left.\begin{aligned} \phi_1 &= \pi/2 \\ \phi_2 &= \tan^{-1}\left[\frac{\mu_2}{1-(\omega_1/\omega_2)^2}\right] \end{aligned}\right\} \tag{9}$$

Substituting the values of ϕ_1, ϕ_2 from the equation (9) in equation (8) and changing θ to θ_R and x_0 to $x_{\theta R}$

$$\Delta W_e = \pi P_0 a\theta_R + \pi P_0 x_{\theta R} \frac{\mu_2}{\{[1-(\omega_1/\omega_2)^2]^2+\mu_2^2\}^{1/2}} \tag{10}$$

where θ_R = amplitude in "θ"-co-ordinate at resonance

$x_{\theta R}$ = amplitude in "x"-co-ordinate when resonance takes place in "θ"-co-ordinate

Replacing $$x_{\theta R} = \frac{x_s}{\{[1-(\omega_1/\omega_2)^2]^2+\mu_2^2\}^{1/2}}$$

in equation (10)

$$\Delta W_e = \pi P_0 a\theta_R + \pi P_0 x_s \frac{\mu_2}{[1-(\omega_1/\omega_2)^2]^2+\mu_2^2} \tag{11}$$

Changing M_x to $M_{x\theta}$ and $M_\theta^2\tau_r^2$ to τ_S^2 in equation (7) and integrating over the volume

$$\Delta W_i = \int^V C_D[M_{x\theta}^2\sigma^2 + 3\tau_S^2]^{n/2}\,dv \tag{12}$$

where τ_S = shear stress amplitude on any fiber at a distance "r" from the center at resonance in "θ" co-ordinate (see Fig. 1)

ΔW_i = energy dissipated in internal friction per cycle

Substituting in equation (12),

$$\sigma = \frac{P_0 zy}{I}, \quad \tau_S = \tau_{RS}\left(\frac{r}{R}\right)$$

where τ_{RS} = shear stress amplitude on the outermost fiber and I = moment of inertia of the section about the diameter

$$\Delta W_i = 2\int_0^L\int_0^R\int_0^\pi C_D\left[M_{x\theta}^2\left(\frac{P_0 zy}{I}\right)^2 + 3\tau_{RS}^2\left(\frac{r}{R}\right)^2\right]^{n/2} r\,d\theta\,dr\,dz \tag{13}$$

Assuming $n = 2$ and solving the above integral by putting $y = r\sin\theta$

$$\Delta W_i = 2C_D\left[\frac{M_{x\theta}^2 P_0^2 L^3 R^4 \pi}{24 I^2} + \frac{3\pi R^2 L}{4}\tau_{RS}^2\right] \tag{14}$$

At resonance, energy input is equal to energy dissipated in internal friction or

$$\Delta W_e = \Delta W_i$$

Substituting in the above equation values of ΔW_e and ΔW_i from equations (11) and (14) respectively

$$\pi P_0 a\theta_R + \pi P_0 x_s \mu_2 M_{x\theta}^2 = 2C_D\left[\frac{\pi M_{x\theta}^2 L^3 R^4 P_0^2}{24I^2} + \frac{3\pi R^2 L}{4}\tau_{RS}^2\right] \tag{15}$$

At resonance the maximum induced stress should not exceed the fatigue-failure stress for combined-stress condition if fracture is to be averted. By the distortion-energy theory for fatigue failure under combined stresses,[6]

$$\sigma_e^2 = [\sigma_m^2 + 3\tau_{RS}^2] = \left[M_{x\theta}^2\left(\frac{P_0 LR}{I}\right)^2 + 3\tau_{RS}^2\right] \tag{16}$$

Vol. 3
1961

where σ_m = maximum normal stress in bending and σ_e = fatigue strength of the material.

Solving equation (16) for τ_{RS}

$$\tau_{RS}^2 = \frac{1}{3}\left[\sigma_e^2 - M_{x\theta}^2\left(\frac{P_0 LR}{I}\right)^2\right] \tag{17}$$

Substituting the value of τ_{RS} from equation (17) in equation (15) and noting

$$\theta_R = \frac{\tau_{RS} L}{RG}$$

$$x_s = \frac{P_0 L^3}{3EI}$$

equation (15) becomes

$$X^2 - AX + B = 0 \tag{18}$$

where

$$\left.\begin{aligned} X &= \left[\left(\frac{\sigma_e}{P_0}\right)^2 - \left(\frac{M_{x\theta} LR}{I}\right)^2\right]^{1/2} \\ A &= \frac{2}{\sqrt{3}}\frac{a}{C_D R^3 G} \\ B &= \frac{8}{3}\frac{L^2 M_{x\theta}^2}{\pi R^6}\left[\frac{1}{\pi} - \frac{\mu_2}{EC_D}\right] \end{aligned}\right\} \tag{19}$$

It can be shown[2] that $\mu_2 = C_D E/\pi$.

Substituting the above value of μ_2 in the expression for B in equations (19)

$$B = 0$$

Substituting this value of B in equation (18)

$$X^2 - AX = 0 \tag{20}$$

The roots of equation (20) are

$$\left.\begin{aligned} X &= 0 \\ X &= A \end{aligned}\right\} \tag{21}$$

Substituting the values of X and A from equations (19) in equations (21) and solving the resonant load P_0

$$P_0 = \frac{\sigma_e I}{M_{x\theta} LR} \tag{22}$$

or
$$P_0 = \frac{\sigma_e}{\sqrt{[A^2 + (M_{x\theta} LR/I)^2]}}$$

i.e.
$$P_0 = \frac{\sigma_e}{\sqrt{\{[(2/\sqrt{3})(a/C_D R^3 G)]^2 + (M_{x\theta} LR/I)^2\}}} \tag{23}$$

Equations (22) and (23) represent the expressions for resonant loads corresponding to the roots (equation 21) of the quadratic equation (20) for the case of resonance in θ-co-ordinate.

Case (ii). *Resonance in x-co-ordinate*

By equation (8), energy input per cycle

$$\Delta W_e = \pi P_0 a\theta_0 \sin\phi_1 + \pi P_0 x_0 \sin\phi_2 \tag{24}$$

At resonance in x-co-ordinate

$$\phi_1 = \tan^{-1}\left(\frac{\mu_1}{1 - [\omega_2/\omega_1]^2}\right) \quad \text{and} \quad \phi_2 = \pi/2$$

After substituting the above values of ϕ_1, ϕ_2 in equation (24) and changing θ_0 to θ_{xR} and x_0 to x_R

$$\Delta W_e = \pi P_0 a\theta_{xR} \frac{\mu_1}{\{[1 - (\omega_2/\omega_1)^2]^2 + \mu_1^2\}^{1/2}} + \pi P_0 x_R \tag{25}$$

where

θ_{xR} = amplitude in θ-co-ordinate when resonance takes place in x-co-ordinate

x_R = amplitude at resonance in x-co-ordinate

Substituting ω_2 for ω in equation (4)

$$\theta_{xR} = \frac{\theta_s}{\{[1 - (\omega_2/\omega_1)^2]^2 + \mu_1^2\}^{1/2}} \tag{26}$$

Substituting the value of θ_{xR} from equation (26) in equation (25) and noting

$$M_{\theta x} = \frac{1}{\{[1 - (\omega_2/\omega_1)^2]^2 + \mu_1^2\}^{1/2}}$$

the energy input per cycle becomes

$$\Delta W_e = \pi P_0 a\theta_s \mu_1 M_{\theta x}^2 + \pi P_0 x_R \tag{27}$$

where $M_{\theta x}$ = magnification factor in "θ"-co-ordinate when resonance takes place in "x"-co-ordinate.

By equation (7) the energy dissipated in internal friction per cycle becomes

$$\Delta W_i = \int^V u\, dv = \int [M_x \sigma^2 + 3M_{\theta x}^2 \tau_r^2]^{n/2} dv \tag{28}$$

Substituting $$\sigma = \sigma_{mR}\left(\frac{Z}{L}\right)\left(\frac{y}{R}\right)$$

and $$\tau_r = \tau_R\left(\frac{r}{R}\right) \quad \text{in equation (28)}$$

$$\Delta W_i = 2C_D\int_0^L\int_0^R\int_0^\pi\left[\sigma_{mR}^2\left(\frac{Z}{L}\right)^2\left(\frac{y}{R}\right)^2 + 3M_{\theta x}^2\tau_R^2\left(\frac{r}{R}\right)^2\right]^{n/2} r\,d\theta\,dr\,dz \tag{29}$$

where σ_{mR} = maximum normal stress in the shaft at resonance
τ_R = maximum shear stress due to static torque $T = P_0 a$

Integrating equation (29) for a value of $n = 2$,

$$\Delta W_i = \frac{\pi R^2 L}{12}C_D\sigma_{mR}^2 + \tfrac{3}{2}C_D M_{\theta x}^2\tau_R^2\pi R^2 L \tag{30}$$

At resonance, to prevent failure from fatigue, by distortion-energy theory for combined-stress fatigue,[6] the stresses must be related as follows:

$$\sigma_e^2 = \sigma_{mR}^2 + 3M_{\theta x}^2\tau_R^2 \tag{31}$$

Solving equation (31) for σ_{mR}

$$\sigma_{mR}^2 = \sigma_e^2 - 3M_{\theta x}^2\tau_R^2 = \sigma_e^2 - 3M_{\theta x}^2\left(\frac{2P_0 a}{\pi R^3}\right)^2 \tag{32}$$

Substituting the values of σ_{mR} from equation (32) and $\tau_R = 2P_0 a/\pi R^3$ in equation (30)

$$\Delta W_i = C_D\frac{\pi R^2 L}{12}\left[\sigma_e^2 - 12M_{\theta x}^2\left(\frac{P_0 a}{\pi R^3}\right)^2\right] + 6C_D M_{\theta x}^2\pi R^2 L\left(\frac{P_0 a}{\pi R^3}\right)^2 \tag{33}$$

Equating the energy input per cycle (equation 27) to energy dissipated per cycle (equation 33) and noting

$$\theta_S = \left(\frac{2P_0 aL}{G\pi R^4}\right), \quad x_R = \frac{P_0 L^3}{3EI} = \frac{\sigma_{mR} I}{R}\left(\frac{L^2}{3EI}\right)$$

and $$\sigma_{mR}^2 = \sigma_e^2 - 3M_{\theta x}^2\left(\frac{2P_0 a}{\pi R^3}\right)^2,$$

$$\frac{2P_0^2 a^2\mu_1 LM_{\theta x}^2}{GR^4} + \pi P_0\left[\sigma_e^2 - 12M_{\theta x}^2\left(\frac{P_0 a}{\pi R^3}\right)^2\right]^{1/2}\frac{L^2}{3ER}$$
$$= C_D\frac{\pi R^2 L}{12}\left[\sigma_e^2 - 12M_{\theta x}^2\left(\frac{P_0 a}{\pi R^3}\right)^2\right] + 6C_D M_{\theta x}^2\pi R^2 L\left(\frac{P_0 a}{\pi R^3}\right)^2 \tag{34}$$

Rewriting equation (34)

$$X^2 - AX + B = 0 \tag{35}$$

where

$$X^2 = \left(\frac{\sigma_e}{P_0}\right)^2 - 12\left(\frac{a}{\pi R^3}\right)^2 M_{\theta x}^2$$

$$A = 4L/R^3 C_D E$$

$$B = \frac{24M_{\theta x}^2 a^2}{\pi R^6}\left[\frac{3}{\pi} - \frac{\mu_1}{GC_D}\right]$$

Vol. 3
1961

The roots of the quadratic equation (35) are

$$X = \frac{A}{2} \pm \sqrt{\left(\frac{A^2}{4} - B\right)} \tag{36}$$

Solving equation (36) for resonant load P_0

$$P_0 = \frac{\sigma_e}{\{(A^2/2) \pm A[(A^2/4) - B]^{1/2} - B + 12(a/\pi R^3)^2 M_{\theta x}^2\}^{1/2}} \tag{37}$$

Equation (37) represents two values of resonant loads corresponding to two roots of the quadratic equation (35).

NUMERICAL EXAMPLE

In order to obtain numerically the value of the resonant load and determine the combined effects of hysteresis damping, fatigue characteristics and stiffness on the resonance response of the vibrating member the following values are assumed

$$R = 1''$$

$$a = 5''$$

$$L = 20''$$

Various materials chosen for comparison of their resonant strengths are given in Table 2.

TABLE 2. MATERIAL DAMPING CONSTANTS
(Data after Lazan[7])

Material	Damping coefficient $C_D \times 10^{12}$	Damping exponent n	Fatigue strength 2×10^7 cycles (lb/in^2)	Modulus of elasticity $\times 10^{-6}$ (lb/in^2)
Aluminum 24 ST–4	780	2	27,000	10·6
J–1 magnesium	1560	2	17,000	6·5
SAE 1020 steel	500	2	35,500	29·4
Titanium RC–130 B	274	2	86,000	16·9
Titanium RC–55 A	278	2	41,000	13·8

TABLE 3. RESONANT LOAD P_0 CORRESPONDING TO RESONANCE IN x-CO-ORDINATE
(Equation 37)

Material	Resonant load P_0 (lb)
Aluminum 24 ST–4	2·8
J–1 magnesium	2·2
SAE 1020 steel	6·5
Titanium RC–130B	2·0
Titanium RC–55A	5·0

Using equations (22) and (23), curves relating resonant load to material frequency ratio ω_1/ω_2 are plotted in Figs. 2 and 3 for various materials shown

in Table 2. The resonant load corresponding to resonance in x-co-ordinates (equation 37) does not seem to be influenced by the frequency ratio ω_1/ω_2. The constant resonant load for various materials calculated from equation (37) is shown in Table 3.

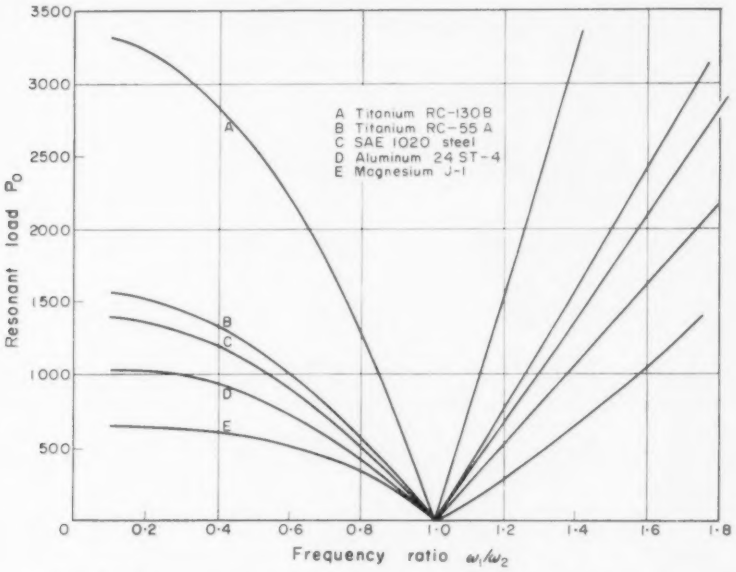

FIG. 2. Resonant-load variation with natural circular-frequency ratio (equation 22).

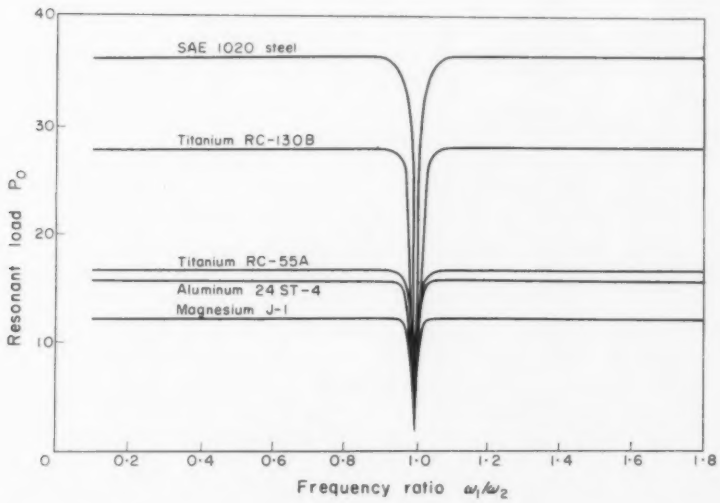

FIG. 3. Resonant-load variation with natural circular-frequency ratio (equation 23).

Vol. 3
1961

CONCLUSION

When designing a member to withstand periodic loads it is very important to study the resonance response of the vibrating system to which the member belongs. Severe stresses induced in a member due to a resonant condition can be avoided by providing a suitable damping in the vibrating system. There are many applications where material damping provides the only effective source of energy dissipation at resonance. For such cases the designer must consider not only the stiffness and the fatigue characteristics but also the damping properties of the material.

Acknowledgements—The author wishes to thank Dr. Marin for his guidance throughout this work. This study represents a part of the Ph.D. thesis submitted to the Pennsylvania State University in January 1960 by the author.

REFERENCES

1. J. MARIN and F. B. STULEN, *Trans. Amer. Soc. Mech. Engrs.* **68**, A-209 (1947).
2. J. MARIN and M. G. SHARMA, Paper presented at a *Colloquium on Structural Damping*, ASME Annual Meeting, Atlantic City, N.J., 1959.
3. B. J. LAZAN, *J. Appl. Mech.* **20**, 201 (1953).
4. E. R. PODNIEKS and B. J. LAZAN, WADC Technical Note 55–284 (1955).
5. J. M. ROBERTSON and A. J. YORGIADIS, *J. Appl. Mech.* **13**, A173 (1946).
6. J. MARIN, *Engineering Materials* p. 201, Prentice Hall, New York (1956).
7. B. J. LAZAN, Report 54–1, ONR Contract N8–ONR–66207 (1954).

Int. J. Mech. Sci. Pergamon Press Ltd. 1961. Vol. 3, pp. 129–136. Printed in Great Britain

CRITICAL PRESSURES AND BUCKLING MODES OF REGULAR POLYGONAL PRISMATIC TUBES

W. MERCHANT and S. A. SAAFAN
Department of Structural Engineering
Manchester College of Science and Technology, Manchester

(*Received* 20 *October* 1960)

Summary—The critical pressures and buckling modes of regular polygonal prismatic tubes of 3, 4 and 5 sides under uniform external pressures are determined in this paper.

Vol. 3
1961

INTRODUCTION

THIS paper shows how stability functions which have been tabulated[1] for frame problems may be used to determine the critical pressures and buckling modes of regular polygonal prismatic tubes under external pressure.

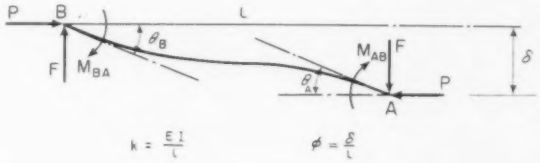

FIG. 1.

The functions used are defined as follows: consider a member of length l and flexural rigidity EI. We define forces F, P, moments M_{AB}, M_{BA} and displacements θ_A, θ_B, ϕ as shown in Fig. 1.

Then

$$\left.\begin{aligned} M_{AB} &= k[s\theta_A + sc\theta_B - s(1+c)\phi] \\ Fl &= s(1+c)k\left[\frac{2\phi}{m} - \theta_A - \theta_B\right] \end{aligned}\right\} \tag{1}$$

If $\theta_B = \phi = 0$ (i.e. end B encastered and no sway displacements) then

$$M_{AB} = sk\theta_A$$
$$M_{BA} = csk\theta_A$$

Hence s is a non-dimensional stiffness factor showing the dependence of the stiffness of a member on its axial load. Similarly c is a non-dimensional carry-over factor.

If $\theta_A = \theta_B = 0$ (i.e. pure sway) then

$$M_{AB} = M_{BA} = -s(1+c)k\phi$$
$$Fl = \frac{2s(1+c)k\phi}{m} = -\frac{(M_{AB}+M_{BA})}{m}$$

Hence m is a magnification factor showing how much greater the end moments for a sway force are compared with the no-stability case ($m = 1$) due to the axial load in the member. Reference 1 gives tables of s, c and m in terms of the ratio of the axial load in a member to its Euler Load, i.e. $\rho = P/P_E$.

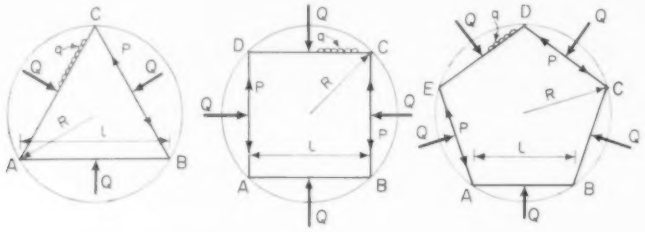

FIG. 2.

Consider the prismatic tubes shown in cross-section in Fig. 2. Buckling is treated as a plane problem and calculations are done for unit lengths of the tubes. The tubes are supposed to have sufficient constraints to prevent movement as a whole by being pinned at A and having a roller support at B two adjacent corners.

The distributed normal loading q causes local bending of the sides but this does not affect the stability problem which depends solely on the axial forces in the sides. Supposing all the tubes to be inscribed in a circle of radius R and with notation as in Fig. 2, the axial loads P in the sides are related to the normal pressure as shown in Table 1.

TABLE 1

Tube cross-section	Triangle	Square	Pentagon
l/R	$\sqrt{3}$	$\sqrt{2}$	1·176
P/qR	$\frac{1}{2}$	$1/\sqrt{2}$	0·809
ρ_c	1·51	0·55	0·28
$\dfrac{q_c R^3}{\pi^2 EI}$	1·01	0·389	0·251

The method of solution is to impose an arbitrary distortion on an otherwise undistorted tube. The external moments and forces required for such a distortion are given by equations (1). At a critical load, no external moments or forces are required to maintain the distorted shape.

TRIANGULAR TUBE

Rotations at A, B, C are possible, but no sway displacements.
Hence

$$\begin{vmatrix} M_A \\ M_B \\ M_C \end{vmatrix} = sk \begin{vmatrix} 2 & c & c \\ c & 2 & c \\ c & c & 2 \end{vmatrix} \begin{vmatrix} \theta_A \\ \theta_B \\ \theta_C \end{vmatrix}$$

and at a critical load the determinant

$$\begin{vmatrix} 2 & c & c \\ c & 2 & c \\ c & c & 2 \end{vmatrix} = 0$$

i.e.

$$(1+c)(2-c)^2 = 0$$

$$c = 2, \quad \rho = 1{\cdot}51, \quad q = 1{\cdot}01\frac{\pi^2 EI}{R^3} \quad \text{and} \quad \theta_B = \theta_C = -\tfrac{1}{2}\theta_A$$

$$c = 1, \quad \rho = 4{\cdot}0, \quad 2 = 2{\cdot}68\frac{\pi^2 EI}{R^3} \quad \text{and} \quad \theta_B = \theta_C = \theta_A$$

The buckling modes are shown in Fig. 3.

Vol. 3
1961

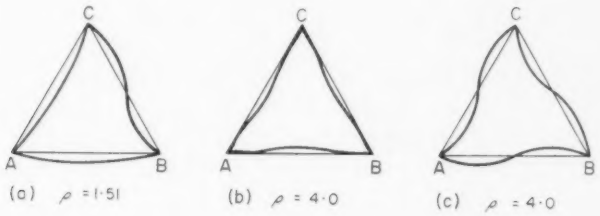

FIG. 3. Buckling modes for triangular tubes.

For $\rho = 4{\cdot}0$ two cases are shown and any mixture of the two is also possible. This circumstance also holds for regular tubes of any number of sides and will not be referred to again in the subsequent examples.

SQUARE TUBES

Here, in addition to rotations θ_A, θ_B, θ_C, θ_D, we have to allow for one sway distortion of the type shown in Fig. 4.

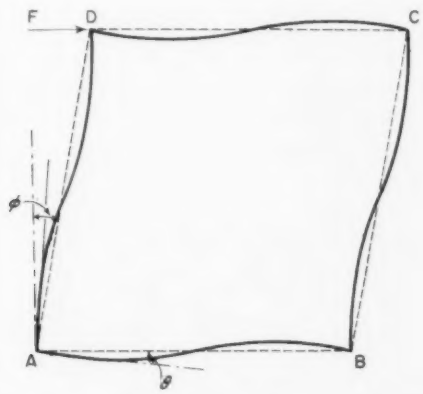

FIG. 4. Buckling mode for square tubes.

Then

$$\begin{vmatrix} M_A \\ M_B \\ M_C \\ M_D \\ F \end{vmatrix} = sk \begin{vmatrix} 2 & c & 0 & c & -(1+c) \\ c & 2 & c & 0 & -(1+c) \\ 0 & c & 2 & c & -(1+c) \\ c & 0 & c & 2 & -(1+c) \\ -(1+c) & -(1+c) & -(1+c) & -(1+c) & \frac{4}{m}(1+c) \end{vmatrix} \begin{vmatrix} \theta_A \\ \theta_B \\ \theta_C \\ \theta_D \\ \phi \end{vmatrix}$$

Again the critical load is given by the vanishing of the determinant. To determine the critical modes we have

$$\begin{vmatrix} 2 & c & 0 & c \\ c & 2 & c & 0 \\ 0 & c & 2 & c \\ c & 0 & c & 2 \end{vmatrix} \begin{vmatrix} \theta_A \\ \theta_B \\ \theta_C \\ \theta_D \end{vmatrix} = (1+c)\phi$$

which from symmetry has the solution

$$\theta_A = \theta_B = \theta_C = \theta_D = \frac{\phi}{2} \qquad (c^2 \neq 1)$$

Substituting in the equation for F

$$-2\phi(1+c) + \frac{4}{m}(1+c)\phi = 0$$

i.e.

$$m = 2$$

$$m = 2, \quad \rho = 0{\cdot}55, \quad q = 0{\cdot}389\frac{\pi^2 EI}{R^3}$$

$$\theta_A = \theta_B = \theta_C = \theta_D = \frac{\phi}{2}$$

The buckling mode is shown in Fig. 4.

PENTAGONAL TUBES

In the first place, to keep the maximum symmetry in our equations, assume that each side can have its own sway angle. We shall afterwards investigate what sways are in fact possible.

Then from the joint equations of equilibrium, we have at a critical load

$$\begin{vmatrix} 2 & c & 0 & 0 & c \\ c & 2 & c & 0 & 0 \\ 0 & c & 2 & c & 0 \\ 0 & 0 & c & 2 & c \\ c & 0 & 0 & c & 2 \end{vmatrix} \begin{vmatrix} \theta_A \\ \theta_B \\ \theta_C \\ \theta_D \\ \theta_E \end{vmatrix} = \begin{vmatrix} +(1+c) & & & & +(1+c) \\ +(1+c) & +(1+c) & & & \\ & +(1+c) & +(1+c) & & \\ & & +(1+c) & +(1+c) & \\ & & & +(1+c) & +(1+c) \end{vmatrix} \begin{vmatrix} \phi_{AB} \\ \phi_{BC} \\ \phi_{CD} \\ \phi_{DE} \\ \phi_{EA} \end{vmatrix}$$

Consider the case when $\phi_{BC} = \phi_{CD} = \phi_{DE} = \phi_{EA} = 0$.

From symmetry we will look for a solution with $\theta_A = \theta_B$ and $\theta_C = \theta_E$. Then

$$\begin{vmatrix} 2+c & c & 0 \\ c & 2 & c \\ 0 & 2c & 2 \end{vmatrix} \begin{vmatrix} \theta_A \\ \theta_C \\ \theta_D \end{vmatrix} = \begin{vmatrix} 1+c \\ 0 \\ 0 \end{vmatrix} \phi_{AB}$$

which gives

$$\theta_A = \theta_B = (2-c^2)\lambda\phi_{AB}$$
$$\theta_C = \theta_E = -c\lambda\phi_{AB}$$
$$\theta_D = c^2\lambda\phi_{AB}$$

where

$$\lambda = \frac{1+c}{4+2c-3c^2-c^3}$$

The solution for any other ϕ can now be written down by inspection. In fact only two sway patterns need be considered. They are shown in Fig. 5.

Vol. 3
1961

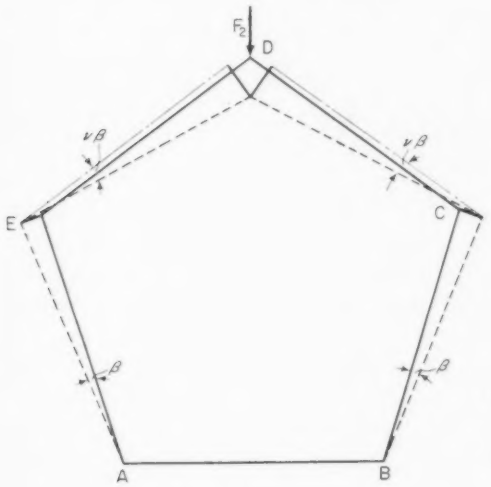

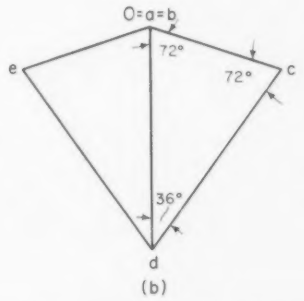

(b)

Williot diagram for vertical displacements

FIG. 5(a). Sway buckling mode.

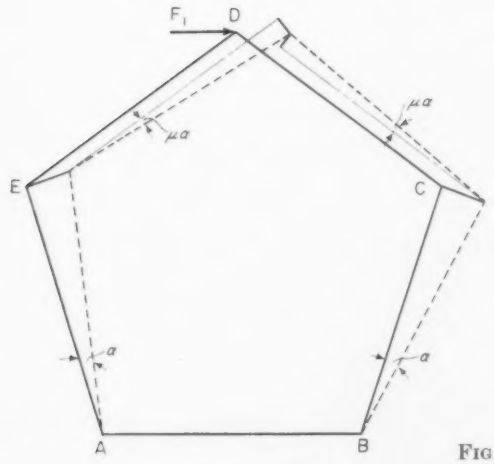

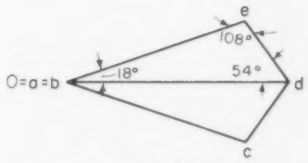

(a)

Williot diagram for sway displacements

FIG. 5(b). Vertical buckling mode.

For type I	and	*For type II*
$\phi_{AB} = 0$		0
$\phi_{BC} = \alpha$		β
$\phi_{CD} = \mu\alpha$		$-\nu\beta$
$\phi_{DE} = \mu\alpha$		$+\nu\beta$
$\phi_{EA} = \alpha$		$-\beta$

where $$\mu = \frac{\sin 18}{\sin 54} \quad \text{and} \quad \nu = \frac{\sin 72}{\sin 36}$$

By applying virtual sway displacements as shown in Fig. 5 we have the two sway equations of equilibrium:

$$F_1 l \frac{\sin 72}{\sin 54}\alpha = (F_{BC} + F_{EA})\, l\alpha + (F_{CD} + F_{DE})\, l\mu\alpha$$

$$F_2 l \frac{\sin 72}{\sin 36}\beta = (F_{BC} - F_{EA})\, l\beta - (F_{CD} - F_{DE})\, l\nu\beta$$

These virtual sway displacements involve no change in length of members or rotations of joints. Therefore no axial force or moment terms appear in the equilibrium equation. Also the external forces are in equilibrium with the axial forces and therefore also do no work and do not appear in the equation.

The complete set of equations for the constraints M_A, M_B, M_C, M_D, M_E, F_1 and F_2 is written down as shown opposite so that the reciprocal check of the coefficients may be exhibited.

We have, however, already used the first five equations in determining the θ's in terms of α and β at a critical load. Substituting for the θ's in the last two equations we have for the two types of sway

$$(1+c)\left[\lambda\{(1+3\mu^2)c^2 + (1+4\mu+\mu^2)c - 2(2+2\mu+3\mu^2)\} + \frac{2}{m}(1+\mu^2)\right]\alpha = 0$$

i.e. $$\rho = 0{\cdot}28, \quad q = 0{\cdot}251\frac{\pi^2 EI}{R^3}$$

and

$$(1+c)\left[\lambda\{(2-3\nu+\nu^2)c^2 - (1+\nu^2)c - (3-3\nu+2\nu^2)\} + \frac{2}{m}(1+\nu^2)\right]\beta = 0$$

i.e. $$\rho = 0{\cdot}63, \quad q = 0{\cdot}562\frac{\pi^2 EI}{R^3}$$

These buckling modes are shown in Fig. 6. The critical pressures for the three types of tube are also shown in Table 1.

M_A								θ_A	θ_B	θ_C	θ_D	θ_E	α	β
2	c	0	0	c		$-(1+c)$		$+(1+c)$						
c	2	c	0	0		$-(1+c)$			$-(1+c)$					
0	c	2	c	0		$-(1+c)(1+\mu)$				$-(1+c)(1-\nu)$				
0	0	c	2	c		$-2(1+c)\mu$				0				
c	0	0	c	2		$-(1+c)(1+\mu)$				$+(1+c)(1-\nu)$				
$= sk$													α	β
$-(1+c)$	$-(1+c)$	$-(1+c)(1+\mu)$	$-2(1+c)\mu$	$-(1+c)(1+\mu)$	$\frac{4}{m}(1+c)(1+\mu^2)$								0	
$+(1+c)$	$-(1+c)$	$-(1+c)(1-\nu)$	0	$(1+c)(1-\nu)$	0									$\frac{4}{m}(1+c)(1-\nu^2)$

$F_1 l \frac{\sin 72}{\sin 54}$

$F_2 l \frac{\sin 72}{\sin 36}$

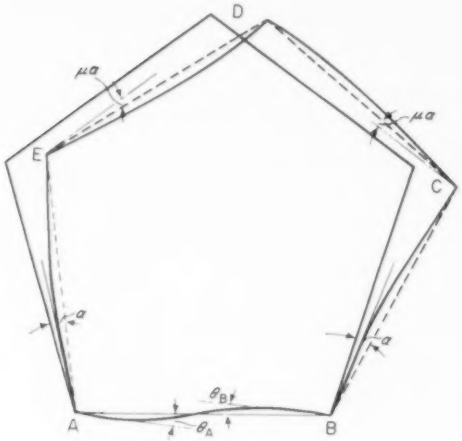

FIG. 6(a). Sway buckling mode.

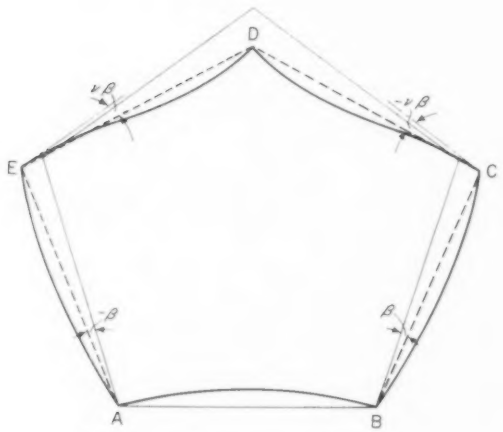

FIG. 6(b). Vertical buckling mode.

REFERENCE

1. R. K. LIVESLEY and D. B. CHANDLER, *Stability Functions for Structural Frameworks*. Manchester University Press (1956).

Int. J. Mech. Sci. Pergamon Press Ltd. 1961. Vol. 3, pp. 137–142. Printed in Great Britain

THE EFFECT OF PRESSURE ON VISCOSITY IN HYDRAULIC LOCK

C. F. KETTLEBOROUGH*
University of Auckland, New Zealand

(*Received* 22 *November* 1960)

Summary—The solution of Reynolds' equation for hydraulic lock is given when the viscosity is a known function of pressure. This leads to the evaluation of an integral which is solved numerically on a digital computer. The results show that as a result of the pressure–viscosity effect the hydraulic-lock forces can be considerably increased.

Vol. 3
1961

INTRODUCTION

HYDRAULIC lock is encountered in piston-type control valves governing the supply of high-pressure oil to mechanical equipment. Investigations in Refs. 1–4 show that true hydraulic lock is essentially a hydrodynamic effect because of asymmetric pressure distribution in the clearance space between piston and cylinder. Oil pressures of several thousands lb/in^2 are normally used. At these pressures the increase in viscosity can be considerable, e.g. for a typical SAE 30 motor oil the increase in viscosity at 5000 lb/in^2 over the viscosity at ambient atmospheric pressure would be three times. At higher pressures the viscosity is further increased; ultimately many lubricants become plastic solids. Previous analysis of the side thrust due to hydraulic lock have neglected the increase of viscosity due to pressure although its effect has been questioned on several occasions.

This paper presents a solution for the hydraulic-lock problem when the variation of viscosity with pressure is taken into account.

THEORY

The basic equation for the pressure distribution in the clearance space between a hydraulic piston and cylinder is Reynolds' equation[5] for incompressible fluid flow†

$$\frac{\partial}{\partial x}\left(\frac{h^3}{\mu}\frac{\partial p}{\partial x}\right)+\frac{\partial}{\partial y}\left(\frac{h^3}{\mu}\frac{\partial p}{\partial y}\right)=6U\frac{\partial h}{\partial x} \tag{1}$$

This equation has been the starting point for all subsequent theoretical investigations in hydrodynamic lubrication. In the case of hydraulic lock the relative velocity U is very small or zero and hence equation (1) reduces to

$$\frac{\partial}{\partial x}\left(\frac{h^3}{\mu}\frac{\partial p}{\partial x}\right)+\frac{\partial}{\partial y}\left(\frac{h^3}{\mu}\frac{\partial p}{\partial y}\right)=0 \tag{2}$$

* Now at Department of Mechanical Engineering, University of N.S.W., Kensington, Sydney, Australia.

† p denotes fluid pressure and μ viscosity. The meaning of other symbols will be clear upon referring to Figs. 1 and 2.

For the case where the piston and cylinder are each constant in diameter and are parallel the pressure is a linear function of the axial distance only, and hence in any plane normal to the cylinder axis the pressure in the clearance space is uniform and no resultant transverse force exists on the piston.

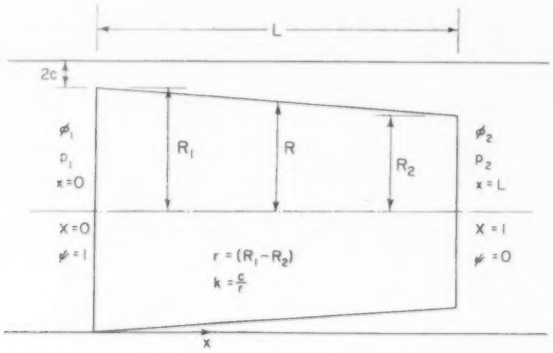

FIG. 1. Piston and cylinder.

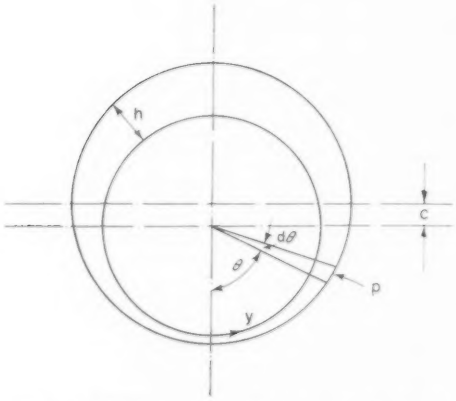

FIG. 2. Cross-section of piston and cylinder.

The case when a taper exists between the piston and cylinder (Fig. 1) has been investigated by Manhajm and Sweeney[3] for the case of constant viscosity with side leakage neglected. In this case the side thrust is

$$F = \frac{(p_1 - p_2) R_1 L r \pi}{2c} \left[1 - \frac{r + 2c}{(r^2 + 4cr)^{\frac{1}{2}}} \right] \tag{3}$$

When $r = 0$ (i.e. for parallel piston and cylinders) the side thrust is zero as discussed above.

The viscosity–pressure effect in bearings has been discussed in Refs. 6–8. The work of Hersey and Shore[6] gave quantitative results which lead to an empirical expression

$$\mu = \mu_0 \exp(\alpha p) \tag{4}$$

This result has since been derived theoretically.[9]

Neglecting side leakage or any circumferential flow, equation (2) reduces to

$$\frac{d}{dx}\left(\frac{h^3}{\mu}\frac{dp}{dx}\right) = 0 \tag{5}$$

Substituting $\mu = \mu_0 \exp(\alpha p)$

$$\frac{d}{dx}\left(\frac{h^3}{\exp(\alpha p)}\frac{dp}{dx}\right) = 0 \tag{6}$$

Changing the variable to ϕ by the substitution

$$\frac{dp}{d\phi} = \exp(\alpha p) \tag{7}$$

equation (6) simplifies to

$$\frac{d}{dx}\left(h^3\frac{d\phi}{dx}\right) = 0 \tag{8}$$

From equation (7)

$$\phi_p - \phi_0 = \int_0^p \frac{dp}{\exp(\alpha p)} \tag{9}$$

With the provision that $\phi_0 = 0$, the solution of (9) is

$$p = -\frac{1}{\alpha}\log_e(1-\alpha\phi) \tag{10}$$

Before solving, equation (8) is converted to non-dimensional terms by the substitutions

$$\left.\begin{aligned} x &= XL \\ \phi &= \phi_2 + (\phi_1 - \phi_2)\psi \\ h &= [X + (c/r)(1-\cos\theta)]r \end{aligned}\right\} \tag{11}$$

Some manipulation gives

$$\frac{d^2\psi}{dX^2} + \frac{3}{X + (c/r)(1-\cos\theta)}\cdot\frac{d\psi}{dX} = 0 \tag{12}$$

from which

$$\psi = A + \frac{B}{[X + k(1-\cos\theta)]^2} \tag{13}$$

The boundary conditions

$$X = 0, \quad \psi = 1$$

$$X = 1, \quad \psi = 0$$

yield

$$A = -\frac{[k(1-\cos\theta)]^2}{[1 + 2k(1-\cos\theta)]} \tag{14}$$

$$B = \frac{[1 + k(1-\cos\theta)]^2\,[k(1-\cos\theta)]^2}{[1 + 2k(1-\cos\theta)]} \tag{15}$$

Vol. 3
1961

Hence the pressure p is given by

$$p = -\frac{1}{\alpha}\log_e\left[(1-\alpha\phi_2)-\alpha(\phi_1-\phi_2)\left\{A+\frac{B}{[X+k(1-\cos\theta)]^2}\right\}\right] \tag{16}$$

The radial force $p\delta A$ (Fig. 2) has two components. Due to symmetry about the vertical centre line the components in the horizontal direction balance. The vertical components produce a resultant out-of-balance force or side thrust.

Side thrust
$$T = \int\int p\cos\theta\, dA \tag{17}$$

$$= \int_0^{2\pi}\int_0^1 LRp\cos\theta\, d\theta\, dX \tag{18}$$

Substituting for p from (16)

$$T = -\frac{R_1 L}{\alpha}\int_0^{2\pi}\int_0^1 \ln\left\{G+\frac{H}{[X+k(1-\cos\theta)]^2}\right\}\cos\theta\, d\theta\, dX \tag{19}$$

where
$$G = (1-\alpha\phi_2)-\alpha(\phi_1-\phi_2)A \tag{20}$$

and
$$H = -\alpha(\phi_1-\phi_2)B \tag{21}$$

Integrating (19) with respect to X

$$\begin{aligned} T = -\frac{R_1 L}{\alpha}\int_0^{2\pi}\Bigg(&\ln\left\{G+\frac{H}{[1+k(1-\cos\theta)]^2}\right\}+\left[k(1-\cos\theta)\ln\left\{G+\frac{H}{[1+k(1-\cos\theta)]^2}\right\}\right.\\ &\left.-k(1-\cos\theta)\ln\left\{G+\frac{H}{[k(1-\cos\theta)]^2}\right\}\right]\\ &+2\sqrt{\left(\frac{H}{G}\right)}\left[\tan^{-1}\frac{1+k(1-\cos\theta)}{\sqrt{(H/G)}}-\tan^{-1}\frac{k(1-\cos\theta)}{\sqrt{(H/G)}}\right]\Bigg)\cos\theta\, d\theta \end{aligned} \tag{22}$$

Integrating with respect to θ the first term of the integrand reduces to zero whilst the second term simplifies to

$$\frac{\pi R_1 LC}{r}[p_1-p_2] \tag{23}$$

The third term does not appear to have a closed solution; the value of the function and the integral has been obtained numerically using the SILLIAC digital computer of the University of Sydney. The Runge–Kutta technique was used to perform the integrations.

NUMERICAL RESULTS

The integral was computed for the following given values:

$$p_1 = 4000 \text{ lb/in}^2 \quad p_2 = 6000 \text{ lb/in}^2$$

$$\alpha = 15\times 10^{-5}$$

From equation (10)

$$\phi_1 = 3008 \quad \text{and} \quad \phi_2 = 3956$$

Equations (20) and (21) give

$$G = 0{\cdot}4066 + 0{\cdot}1422\,A$$

$$H = 0{\cdot}1422\,B$$

The required integral

$$I = \int_0^{2\pi} \sqrt{\left(\frac{H}{G}\right)}\left[\tan^{-1}\frac{1+k(1-\cos\theta)}{\sqrt{(H/G)}} - \tan^{-1}\frac{k(1-\cos\theta)}{\sqrt{(H/G)}}\right]\cos\theta\,d\theta \qquad (24)$$

is tabulated below for several values of k.

TABLE 1

k	$\frac{1}{16}$	$\frac{1}{8}$	$\frac{1}{4}$	$\frac{1}{2}$	1	$1\frac{1}{2}$	2	3
I	−0·02766	−0·05070	−0·08988	−0·1570	−0·2787	−0·3966	−0·5136	−0·7474
$T_1/\pi R_1 L$	112	168	244	309	342	342	333	313
$T_2/\pi R_1 L$	111	181	263	333	366	366	360	350
Per cent increase		7·7	7·8	7·8	7·0	7·0	8·1	11·8

T_1 = Side-thrust with constant viscosity.

T_2 = Side-thrust with viscosity a function of pressure.

For higher pressure the pressure–viscosity effect is greater, e.g.

$p_1 = 8000$ lb/in^2 $\qquad$ $p_2 = 12{,}000$ lb/in^2

$\phi_1 = 4659$ $\qquad$ $\phi_2 = 5565$

$G = 0{\cdot}1653 + 0{\cdot}1359\,A$ $\qquad$ $H = 0{\cdot}1359\,B$

Typical values are given in Table 2.

TABLE 2

k	$\frac{1}{16}$	$\frac{1}{8}$	$\frac{1}{4}$	$\frac{1}{2}$	1
$T_1/\pi R_1 L$	224	336	488	618	684
$T_2/\pi R_1 L$	239	390	560	698	760
Per cent increase	6·7	16·1	14·7	12·9	11·1

Note that for large values of k, G becomes negative. Integral (24) then takes the form

$$\int_0^{2\pi} \sqrt{\left(\frac{H}{|G|}\right)}\left[\ln\left|\frac{\sqrt{(H/|G|)}+1+k(1-\cos\theta)}{\sqrt{(H/|G|)}-1-k(1-\cos\theta)}\right| - \ln\left|\frac{\sqrt{(H/|G|)}+k(1-\cos\theta)}{\sqrt{(H/|G|)}-k(1-\cos\theta)}\right|\right]\cos\theta\,d\theta \qquad (25)$$

Extension of Tables 1 and 2 involve this integral.

Vol. 3
1961

CONCLUSIONS

The typical figures computed show that the effect of the pressure on viscosity can be quite considerable. However, other factors will modify these values; these include the compressibility of the oil, the deflexion of the cylinder and the compression of the piston.

REFERENCES

1. D. C. SWEENEY, *Engineering* **172**, 513 (1951).
2. J. F. BLACKBURN, *Trans. Amer. Soc. Mech. Engrs.* **75**, 1175 (1953).
3. J. MANHAJM and D. C. SWEENEY, *Proc. Inst. Mech. Engrs.* **169**, 865 (1955).
4. J. MANNAM, *Proc. Inst. Mech. Engrs.* **173**, 699 (1960).
5. O. REYNOLDS, *Phil. Trans.* Part 1, **177**, 157 (1886).
6. M. D. HERSEY and H. SHORE, *Mech. Engng.* **50**, 221 (1928).
7. S. J. NEEDS, *Trans. Amer. Soc. Mech. Engrs.* **60**, 347 (1938).
8. M. MUSKAT and H. H. EVINGER, *J. Appl. Phys.* **11**, 739 (1940).
9. S. GLASSTONE, K. LAIDIER and H. EYRING, *The Theory of Rate Processes.* McGraw-Hill, New York (1941).

Int. J. Mech. Sci. Pergamon Press Ltd. 1961. Vol. 3, pp. 143–144. Printed in Great Britain

BOOK REVIEWS

B. M. GLINER: **Determination of the Mechanical and Technological Properties of Metals** (translated from the Russian—2nd Ed.). Pergamon Press, London, 1960. 160 pp., 50s.

THE English translation of this Russian handbook will be found well worthwhile by Testing Laboratories, Designers and Students, for in it an excellent summary is given of the mechanical testing methods in general use in the Soviet Union together with the standard tests carried out on metals for the determination of their suitability for engineering purposes. The work is divided into three parts and in the first of these the more usual tension, compression, torsion, shear, bend, impact and hardness tests are dealt with. Micro-mechanical tests, endurance tests and elevated temperature tests then follow in turn. For each there are brief descriptions of the types of machines and instruments which are in use, the properties measured being defined and the accuracy of measurement discussed. It is to be regretted that this part suffers from poor choice of terminology in translation, examples of this being the use of *arbitrary* for nominal stress, *relative* for percentage elongation, *absolute residual* for total elongation, *tensometer* for extensometer, *prism blade* for knife edge, *properly centred* for axial loaded, *moment of resistance* for section modulus, *angular indices* for movements, *imprint* for impression, and so on.

It is of interest to note the emphasis placed on autographic diagrams in tests where these may be obtained, and also of the importance given to torsion testing (including the determination of proof stress) in contrast to its almost non-appearance in the B.S. specifications. The author draws attention to the use of vibration methods in the determination of the elastic constants for materials without mentioning the factors which limit the scope and accuracy of such methods. In endurance testing the nomenclature of the I.S.O. is adopted, although this is by no means as expressive as that in more common use in the United Kingdom or the U.S.A. Considerable importance is attached to elevated temperature tests, distinction being made between creep, rupture strength and relaxation.

The second part of the book is given over to the treatment of the testing of welds and welded joints of various types. The tests appear to be more extensive than those called for under existing British Standards.

In Part III there is an interesting treatment of "technological properties" of metals, and these are given as machinability, hardenability, weldability, cold drawing, bending (both hot and cold), repeated bending, flattening of tube specimens. Some new ideas are shown in dealing with these which give food for further thought.

Apart from the earlier criticism the work is an excellent one, and the translators could have added to its value by quoting comparative British Standards in footnotes. For any Laboratory interested in mechanical testing, this is a book which should appear on their reference shelves. It is not one to be wholeheartedly recommended to students because of the looseness of the translation, but it does offer considerable scope for senior students who may be encouraged to investigate differences between British Standard and Soviet tests.

J. H. LAMBLE

A. THOM and C. J. APELT: **Field Computations in Engineering and Physics.** Von Nostrand, New York, 1961. 165 pp., 30s.

THIS book is concerned with numerical methods of solution of partial differential equations of the elliptic type. The equations of Laplace and Poisson, the Biharmonic equation and the Navier–Stokes equations fall into this class.

The method, originally called the method of squares because a square computation mesh is used, has been developed by Professor Thom since the 1920's. The use of a square mesh, however, is only of minor importance and the main feature of the method is the use

of differences to accelerate convergence to the solution. A further important feature is that the mesh calculations are carried out in a systematic manner, say, for example, working row by row from top to bottom. This makes it particularly suitable for Digital Computer programming and most of the examples discussed have been programmed for such a machine.

The well-known Relaxation methods are alternatives to some of the techniques described. With Relaxation it is nearly always best to operate on the largest residuals, which usually means moving about the mesh in a haphazard manner, a procedure which is not yet practicable for a digital computer. A systematic progress, such as described by the authors, is much more suitable for programming, but whether the method of squares is the best computer method for dealing with large-scale problems is another question. There is no doubt that the Band matrix methods currently being developed are extremely powerful and enable a greater number of mesh points to be dealt with for a given machine capacity.

Solution of partial differential equations by any mesh method is carried out by first obtaining a rough approximation using a large size of grid and using this to advance to a more accurate solution. A choice may be made between using a finer mesh with simple numerical approximation to the functions (the simple averaging procedure being almost always used for Laplace's equation) or retaining a fairly coarse mesh and employing more accurate approximations to the functions. It is the second alternative which the authors have developed and which they claim gives a less laborious convergence to the solution.

The early chapters are devoted to developing the numerical formulae used, particularly the "large molecule" formulae which give function values in terms of values at up to sixteen surrounding points. Later chapters deal with applications to Laplace's equation in regions bounded by straight lines and circles, examples being a tube in a square passage and rows of tubes. The authors choose to discuss these regions in terms of ideal inviscid fluid flow which is of little practical significance. Nevertheless, the solutions are of great value when considered in terms of heat conduction, the circle in square boundary being a configuration used for graphite reactor bricks and the rows of cylinders corresponding to cooling passages in a large solid such as a reactor core.

Fourth-order equations, Navier–Stokes equations and compressible-flow equations are discussed in later chapters.

It should be borne in mind that the facility of the digital computer does not reduce the value of such books as this. A digital computer must be instructed at all stages on the method it is to use, and it will produce results only as good as the numerical techniques it has been instructed to apply. For this reason intense study of numerical methods in general is proceeding at the present time and this book is a summary of patient work in this field by Professor Thom and others over a long period.

The book will be of interest and value to those working in computing and, in particular, in the numerical solution of partial differential equations using electronic computers or pencil and paper methods.

A. P. Hatton

Int. J. Mech. Sci. Pergamon Press Ltd. 1961. Vol. 3, pp. 145–156. Printed in Great Britain

AN INVESTIGATION OF THE TRANSITION FROM A CONTINUOUS TO A DISCONTINUOUS CHIP IN ORTHOGONAL MACHINING

H. E. Enahoro and P. L. B. Oxley
Manchester College of Science and Technology, Manchester

(*Received* 20 *December* 1960)

Summary—Various depths of cut were taken with all other cutting conditions constant and within this range continuous and discontinuous chips were obtained. Ciné pictures of the deformation were taken through a microscope and an analysis made using strain-hardening slip-line theory. The hydrostatic stress-distribution in the plastic zone was shown to vary from compression at the outer free surface to tension near the cutting edge, and the magnitude of the tensile stress was shown to be important in determining whether or not the chip became discontinuous.

Vol. 3
1961

NOTATION

α	tool rake angle
ϕ	shear-plane angle
t	depth of cut
ϵ_{eff}	effective natural strain
p	hydrostatic stress (tensile positive)
k	shear yield stress of material
s_1, s_2	distance along slip-lines of each family
ψ	orientation of slip-lines (anti-clockwise positive)
m	slope of stress–strain curve
ϵ	shear strain of chip
ϵ_0	shear strain of metal at rupture for zero compressive stress
K	slope of shear strain (at rupture)–compressive normal stress curve
p_m	average normal stress on shear plane
p_A, p_B	normal stress on shear plane at A and B respectively
λ	mean angle of tool–chip interface friction

1. INTRODUCTION

In metal-cutting research it is usual to limit attention to the relatively simple process of orthogonal cutting. In orthogonal cutting the tool moves with a relative motion parallel to the machined surface and perpendicular to its own cutting edge, and in doing so cuts a parallel layer of material from the work-piece which after removal is termed the chip (Fig. 1). The type of chip produced depends upon the cutting conditions and the properties of the cut material, and it is usual to distinguish between continuous-type chips (Fig. 2) in which the chip is produced by continuous plastic deformation and discontinuous-type chips (Fig. 3) in which fracture occurs. It is well known that when machining

a ductile material such as mild steel quite small changes in the cutting conditions, for example, a decrease in the tool rake angle (α in Fig. 1) or an increase in the depth of cut (t in Fig. 1), can bring about a transition from a continuous to a discontinuous chip.

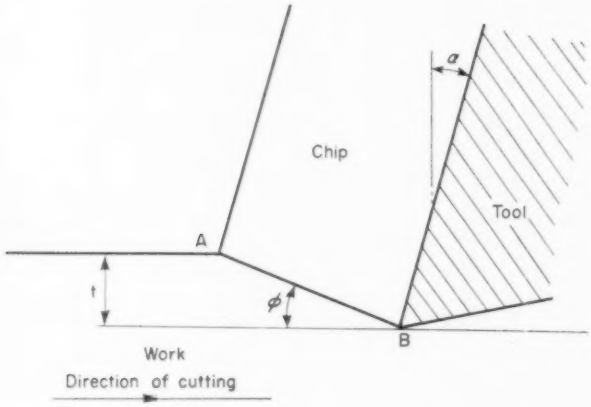

Fig. 1. Shear-plane model of chip formation.

This transition is extremely difficult to understand within the framework of the usually assumed shear-plane model of continuous-chip formation shown in Fig. 1, where the chip is assumed to be formed by a process of simple shear across a narrow shear plane AB with the normal stress along AB constant. A notable attempt to explain this transition was made by Field and Merchant[1], who observed that at the start of cutting the shear-plane angle ϕ, that is, the angle made by AB with the direction of cutting, decreased. A decrease in ϕ indicated an increase in the strain imparted to the chip and Field and Merchant suggested that at a critical value of strain, the exact value depending on the mean normal stress on AB which under all normal cutting conditions will be compressive, the chip would crack. They then reasoned that if the steady-state value of ϕ is greater than the value giving critical strain, a continuous chip will result, whereas if ϕ falls to this value the chip will be discontinuous. Although qualitatively this argument is sound enough, the actual results predicated by this analysis were in poor agreement with experimental observations.

In a recent paper (Palmer and Oxley[2]), it was suggested that the assumption of a shear-plane model of chip formation together with the associated constant normal stress were too far removed from reality to allow a successful understanding of the machining process. By taking ciné films through a microscope of the deformation during actual cutting they arrived at the picture of cutting shown in Fig. 4, with the plastic zone of finite width and roughly triangular in shape. The chip was shown to be "born" curled in the plastic zone and it was assumed that the contact between chip and tool was elastic flattening with the resultant cutting force passing through the centre of flattening. For all cutting conditions considered it was found that the line of action of the resultant

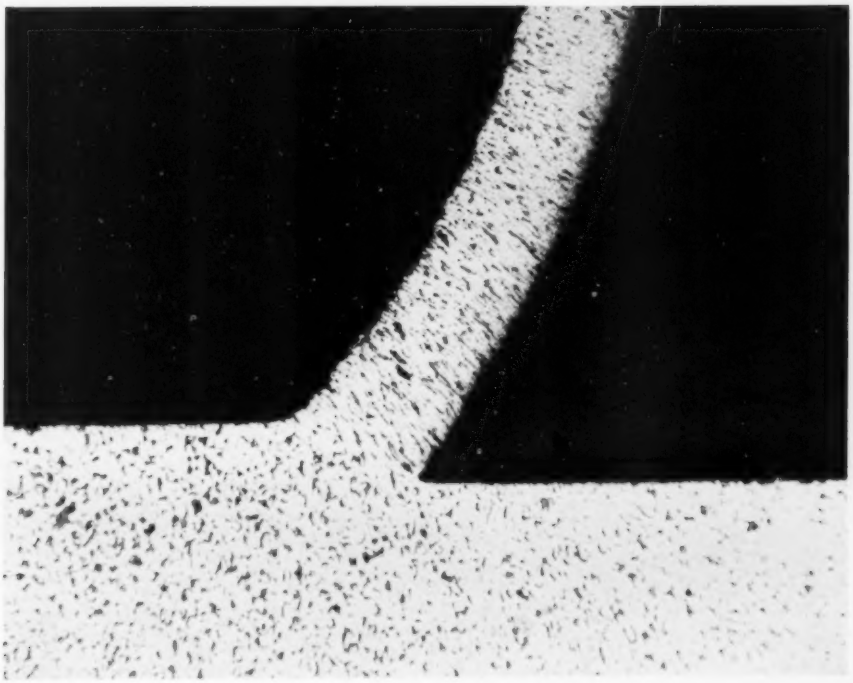

FIG. 2. Continuous-type chip.

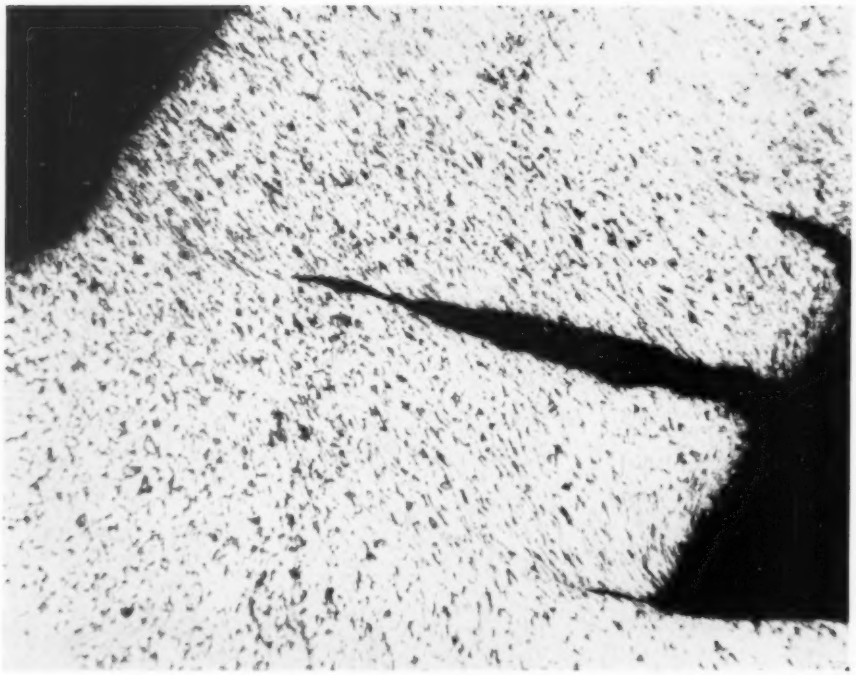

FIG. 3. Discontinuous-type chip.

determined in this way passed approximately through the point A of the plastic zone and was therefore applying a bending moment to the chip.

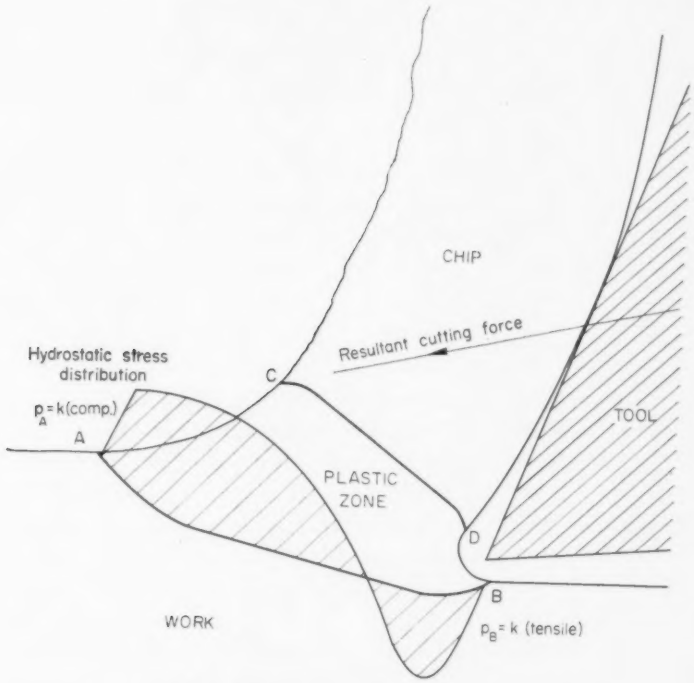

FIG. 4. Strain-hardening model of chip formation.

In their slip-line analysis of the plastic zone Palmer and Oxley found that internal consistency in stress and velocity could only be obtained if the slip-line theory, in which a non-strain-hardening material is usually assumed and in which the variation in hydrostatic stress along a slip-line depends only on the change in direction of the slip-line, was modified to allow for the variation in flow stress due to strain hardening. The variation in hydrostatic stress then depends not only on the change in direction of the slip-line but also on the change of flow stress normal to the slip-line. The most striking feature of this "strain-hardening" analysis was the predicted distribution of hydrostatic stress, which varied from compression at A to tension at B (Fig. 4). This type of stress-distribution was consistent with the position of the cutting force given by assuming elastic flattening and it was concluded that the chip was formed by combined bending and shearing as opposed to the simple shear of the shear-plane model of chip formation. Finally, it was suggested that the value of the tensile stress at the cutting edge could be important in determining the type of chip produced, and that the higher this stress, the greater would be the likelihood of a discontinuous chip. However, no conclusive evidence regarding this point was put forward.

Vol. 3
1961

The present work was undertaken to determine if the magnitude of the hydrostatic stress at the cutting edge is important in determining whether or not the chip will crack. Various depths of cut were taken with all other cutting conditions constant and within this range of cuts continuous and discontinuous chips were obtained. Ciné pictures of the deformation were taken through a microscope, cutting forces recorded and an analysis carried out using the modified slip-line theory. Attention was limited to orthogonal machining under approximately plane-strain conditions.

2. EXPERIMENTAL WORK

The object of the experimental work was to obtain records of the cutting forces and of the geometry of deformation for a range of depths of cut in which continuous and discontinuous chips were produced.

The apparatus and experimental technique have been described in detail elsewhere (Refs. 2 and 3) but can be briefly summarized as follows. A microscope was focused on the sides of the work, chip and tool, and ciné films taken through the microscope during actual cutting. The viewed side of the work was polished and etched and on subsequent projection of the films (over-all magnification 357) individual crystal grains could be identified and their paths plotted. In this way streamlines of the flow were obtained in the work, plastic zone and chip. From the projected pictures it was also possible to sketch the outline of the chip, the newly and previously machined surfaces, and the boundary between the undeformed work and plastic zone. Fig. 8 shows a typical plot obtained in this way.

The cutting machine used was basically a planer with the tool held in a dynamometer which was rigidly fixed to the machine and which measured the cutting forces in the direction of cutting and normal to the machined surface. Special fixtures provided locations for the microscope and ciné camera.

It was found from preliminary cutting tests that with a 35° rake-angle tool the spread (i.e. deviation from plane strain) of the viewed side of the work was small and also that a suitable range of continuous (up to 0·007 in. depth of cut) and discontinuous chips could be obtained at the slow speed of cutting (0·54 in./min) used. For larger rake angles discontinuous chips were produced only with depths of cut which were considered too large for the present investigation, and with smaller rake angles the side spread was too large. Attention was therefore limited to this one rake angle (35°) at one slow cutting speed with the realization that further cutting tests under widely different conditions would be necessary in order to confirm or deny any findings resulting from the present work.

In all the cutting tests steady cutting conditions as indicated by the cutting forces were first established before any readings or films were taken. In the case of discontinuous chips the cutting forces were not steady and in such cases "steady conditions" were assumed to have been attained when the forces had reached a maximum mean value.

The work material used was cold-rolled mild steel which had a small randomly orientated grain structure and which was, therefore, consistent with

the isotropic material normally assumed in plasticity theory. A plastic stress–strain curve of the material, obtained from a compression test as in Refs. 2 and 3, is given in Fig. 5.

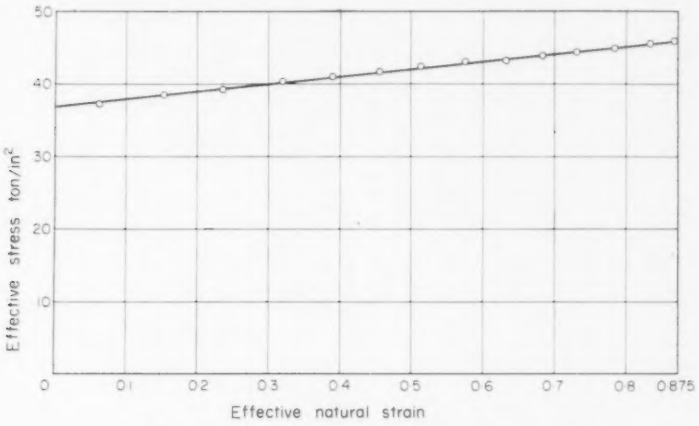

FIG. 5. Stress–strain curve for work material.

3. RESULTS

In the cutting tests the depths of cut ranged from 0·0036 to 0·0207 in. in increments of approximately 0·001 in. The cutting speed was 0·54 in./min and the width of cut 0·25 in.

Horizontal (i.e. in the direction of cutting) and vertical (i.e. normal to the machined surface) cutting forces, mean angle of friction at the tool–chip interface, chip-thickness ratio (defined in the present work as the ratio of mean chip velocity to work velocity) and chip curvature are plotted in Figs. 6 and 7. The friction angles were calculated from the observed cutting forces and all other values measured from the plots. At the higher depths of cut the chip became discontinuous and the cutting forces became unsteady (± 2 per cent for the horizontal force, ± 12 per cent for the vertical force). The mean values are recorded.

In the tests it was observed that the chip was continuous (i.e. free of cracks) up to a depth of cut of approximately 0·007 in., at which stage slight cracks occurred in the face of the chip in contact with the tool. An increase in depth of cut above this value gave deeper cracks and with depths of cut of the order of 0·020 in. (Fig. 3) the cracks extended far into the chip and in some cases the chip was completely fractured.

From the Field and Merchant[1] shear-plane analysis the chip would be expected to be either completely continuous (i.e. no fracture) or completely discontinuous (i.e. complete fracture), that is, because of the assumed constant stress–strain state across the shear plane. The observation that this is not necessarily the case and that cracks can be limited to part of the chip suggests that the stress–strain state in the plastic zone is not constant, and supports the suggestion[2] that the magnitude of the hydrostatic stress near the cutting

Vol. 3
1961

edge is important in determining whether or not the chip will crack. The next Section considers the calculation of this stress.

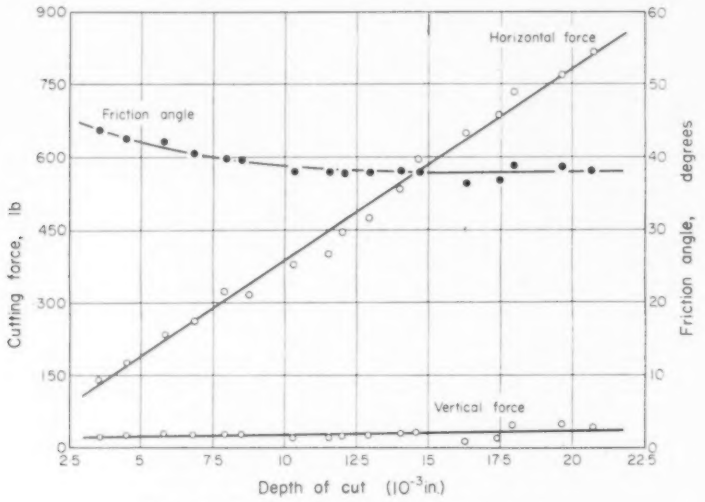

FIG. 6. Cutting forces and friction angle.

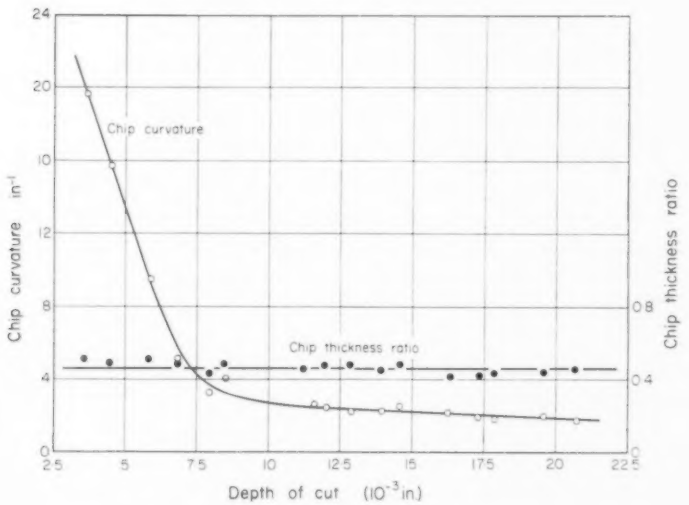

FIG. 7. Chip-thickness ratio and chip curvature.

4. CALCULATION OF STRESSES IN PLASTIC ZONE

Detailed plots of the plastic zone were prepared for depths of cut in the range 0·0036–0·0144 in. For greater depths the cracks extended too far into the chip to enable a worth-while analysis.

Figure 8 shows a typical plot of the plastic zone. The boundary AB between the plastic zone and the undeformed work had already been approximately

sketched in but was further checked by noting the points of departure of the streamlines of flow from the direction of the horizontal streamlines in the undeformed work. The end of plastic flow on each streamline and hence the boundary CD between the plastic zone and chip were determined by noting the points where the flow began to follow the streamlines of constant curvature in the chip. From Fig. 8 it can be seen, as previously reported,[2] that the plastic zone is roughly triangular in shape with its apex near the cutting edge and that the streamlines of flow in the plastic zone are smooth curves.

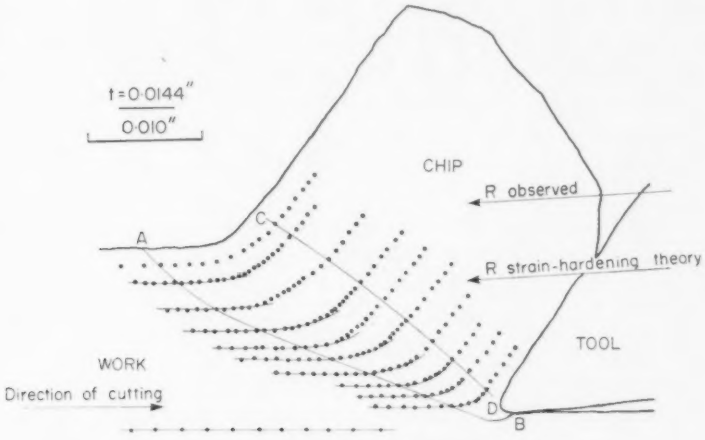

FIG. 8. Typical plot of plastic zone.

It was shown[2] that a slip-line analysis of the full plastic zone is extremely laborious. Fortunately, from the point of view of the present work, the partial analysis used by Oxley *et al.*[3] is particularly suitable as it enables the calculation of the stress near the cutting edge. This analysis is based on the boundary AB of the plastic zone which as a boundary between plastic and rigid material is a slip-line.

Neglecting any upthrust on the base of the tool the slip-line AB will transmit the resultant cutting force. From the free surface condition at A it is known that the hydrostatic stress at this point is equal in magnitude to the maximum shear stress and from physical considerations will be compressive. The distribution of hydrostatic stress along AB can, therefore, be calculated by starting from A and applying the relevant slip-line equation. In this way and bearing in mind that a slip-line represents a plane of maximum shear stress, the force transmitted by AB can be calculated and compared with the resultant cutting force obtained from the dynamometer readings.

As drawn in Fig. 8, AB is a II slip-line (see Ref. 2 or 3 for derivation of the slip-line equations and sign convention). The equilibrium equation governing the hydrostatic stress variation along such a slip-line is

$$p + 2k\psi + \int \frac{dk}{ds_1}\delta s_2 = \text{constant} \qquad (1)$$

where p is the hydrostatic stress (i.e. acting normal to the slip-line), k is the maximum shear stress (i.e. acting along the slip-line), ψ is the angle of inclination of the slip-line relative to some datum direction and s_1 and s_2 are distances along the I and II slip-lines respectively.

The value of dk/ds_1 must first be determined before the above equation can be used to calculate the hydrostatic stress along AB. dk/ds_1 is the rate of change of maximum shear stress k in a direction normal to AB, and at the slow cutting speed used in the present work can be assumed to be entirely due to strain hardening. The method used to calculate this "strain-hardening" term is described in detail in Ref. 3 but was briefly as follows.

Velocities of flow in the plastic zone region adjacent to AB were measured using the hodograph technique. Effective rates of strain were then determined from these velocities and integrated with respect to time along streamlines of flow to give the effective strain. The effective stress and hence maximum shear stress at a given distance from AB were then found using an effective stress–effective strain curve.

In Ref. 3 definitions of effective stress and effective strain are given and following these definitions the stress–strain curve given in Fig. 5 is an effective stress–effective strain curve. However, this was not used directly to find the change in k. Instead an effective stress–strain curve of slope m (where $m = [1/k][dk/d\epsilon_{\text{eff}}]$) was assumed and the change of k expressed in terms of m. The equilibrium equation was then applied to calculate the hydrostatic stress-distribution along AB. The change of slope of the slip-line (i.e. the change in ψ) in passing from A to B gives a compressive increment to the hydrostatic stress, while the strain-hardening term gives a tensile increment. The value of m was finally selected to give a hydrostatic stress-distribution which in turn gave a calculated resultant cutting-force direction coinciding with the observed direction. (As previously mentioned, the cutting force became unsteady with the deeper cuts. However, the variation was small and gave only small changes in the direction of the resultant cutting force. The mean direction was therefore used in selecting m.) It was considered that this procedure would allow for probable rate of strain effect and would give a calculated stress distribution similar to the actual distribution.

The value of maximum shear stress k along AB was similarly not found directly from Fig. 5 but instead calculated by equating the observed and calculated (in terms of k) resultant cutting-force magnitudes. The values of m and k found in this way are given in Table 1.

Examples of the finally calculated hydrostatic stress distributions are given in Fig. 9. In the immediate region of B the flow could not be plotted with sufficient accuracy to enable the calculation of stress in this region. The stress curves had therefore to be extrapolated to B. As in Ref. 2, the hydrostatic stress at B was found to be tensile. It was further suggested in Ref. 2 that its magnitude should be equal to that of the maximum shear stress at B. Although the sketched-in form of AB appeared to confirm this free surface condition, i.e. made an angle of approximately $\pi/4$ with the surface, it was decided not to extrapolate the curves to this value at B but to make them smooth, continuous

curves. The magnitudes of the tensile stress at B found in this way are given in Fig. 10.

TABLE 1

Depth of cut t (in.)	Slope m	Shear stress k on AB (ton/in^2)
0·0036	0·24	22·6
0·0045	0·27	22·0
0·0058	0·22	21·5
0·0068	0·33	19·6
0·0079	0·22	23·0
0·0085	0·21	18·9
0·0116	0·16	22·1
0·0120	0·18	21·4
0·0129	0·22	21·1
0·0144	0·16	21·4

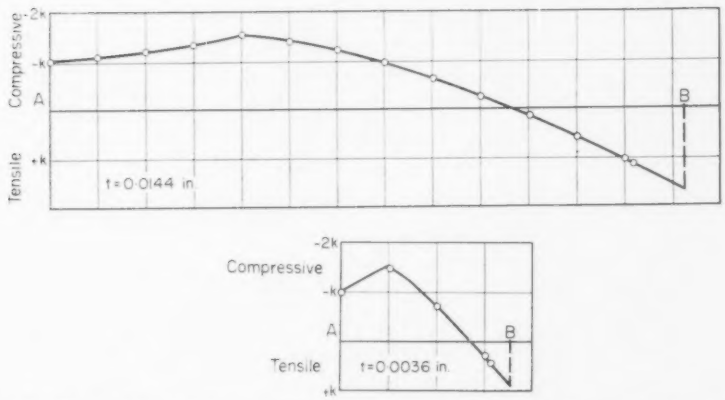

FIG. 9. Typical hydrostatic stress curves for a small and a large depth of cut.

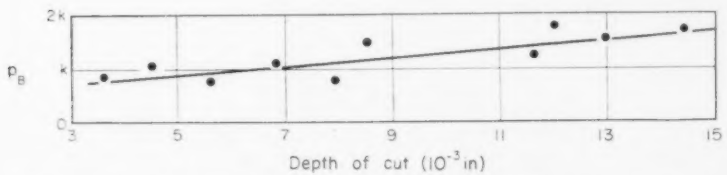

FIG. 10. Graph showing increase in hydrostatic tensile stress at B with increase in depth of cut.

5. DISCUSSION

Before drawing any conclusions regarding the relationship between the value of the hydrostatic stress adjacent to the cutting edge of the tool and the occurrence of a discontinuous chip it is necessary to first consider the validity of the method used in calculating this stress.

From Table 1 it can be seen that although there is some scatter in the values of slope m (apparently mainly due to finding the exact position of AB)

Vol. 3
1961

the average value compares well with the slope of Fig. 5, namely 0·22 compared to 0·27. The higher rate of strain in the cutting tests (approximately 8 per sec) compared to that used in obtaining the "static" stress–strain curve could account for this difference. The average value of maximum shear stress k along AB is 21·4 ton/in^2 and this compares well with the initial yield stress given by Fig. 5, namely 21·4 ton/in^2 (i.e. $37/\sqrt{3}$) shear-strain energy criterion, and 18·5 ton/in^2 (i.e. 37/2) maximum shear-stress criterion.

The agreement between the values of m and k obtained in the analysis of the plastic zone and the corresponding values measured from an independent test (Fig. 5) is most striking and clearly justifies the strain-hardening analysis used. The ideal slip-line theory, in which m is assumed to be zero, gives a hydrostatic stress-distribution which is compressive from A to B and which is totally incompatible with the observed cutting-force direction.

It has already been mentioned that in drawing the hydrostatic stress curves (Fig. 9) in the region of B the curves had to be extrapolated. From the values of stress obtained in this region it seems quite possible that the actual value of hydrostatic stress at B was consistent with a free surface condition, i.e. tensile and equal to k. However, the values of stress at B given in Fig. 10 should give a good indication of the order of magnitude of stress in this region even if the actual stress curves had a sharp change in curvature (in this region) to meet the free surface condition at B. It was, therefore, considered that the values of stress given in Fig. 10 could be used to compare the magnitudes of stress in this region for the various depths of cut.

It was not possible from the observations made to say exactly at what stage of the deformation and hence stress–strain state the material cracked. (On passing from B to D (Fig. 8) the strain of the bulk of the chip increases and the tensile hydrostatic stress decreases.) However, as the total strain of the chip, as measured by say chip-thickness ratio (Fig. 7), was approximately constant for all depths of cut and the hydrostatic tensile stress in the region of B (Fig. 10) increased with increasing depth of cut, it appears reasonable to conclude that the chip cracked with the deeper cuts because of the increase in the tensile stress. Although, for the reasons given above, too great a significance should not be attached to the actual values of the calculated hydrostatic stresses in relation to cracking it is of interest that cracks first occurred at a depth of cut of approximately 0·007 in. which corresponds to a tensile hydrostatic stress equal in magnitude to k (Fig. 10), i.e. the maximum tensile stress was $2k$.

The observation that the chip curvature (Fig. 7) changes rapidly up to a depth of cut of approximately 0·007 in. and then remains more or less constant suggests a correlation between chip curvature and the transition from a continuous to a discontinuous chip. There does not, however, appear to be any immediate simple explanation for this.

The calculated position of the resultant cutting force, found by taking moments of the stresses on AB about B (Fig. 8), in all cases passed approximately midway between the cutting edge and the centre of "elastic flattening".[2] (In Fig. 8 the observed force is shown acting through the centre of "elastic flattening".) This is in agreement with recent work[3] where it was shown that

the contact between chip and tool was essentially plastic and that contact extended from near the cutting edge to the point where the chip curled away from the tool.

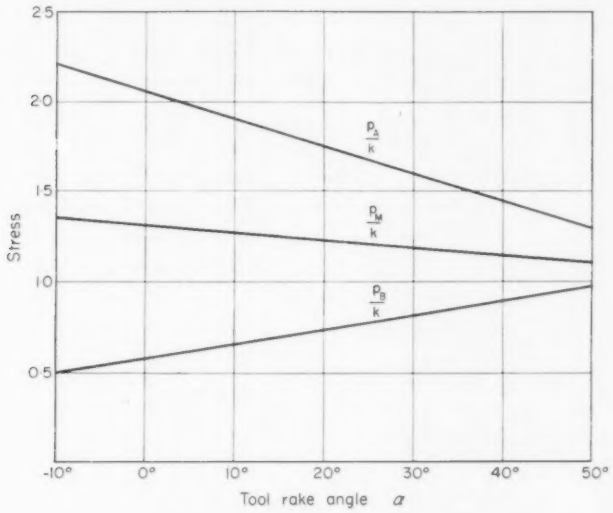

FIG. 11. Normal stresses on shear plane.

At commercial cutting speeds, which are high compared to the speed used in the present tests, it is to be expected from strain-hardening considerations[3] —and is in fact observed—that the width of the plastic zone will decrease and approximate to a shear plane. Following Merchant[4] the shear strain for such a deformation is given by

$$\epsilon = \cot\phi + \tan(\phi - \alpha) \tag{2}$$

In their analysis Field and Merchant[1] reasoned that the chip would rupture when this strain was equal to a certain critical value, the latter depending upon the magnitude of the normal stress on the shear plane which they assumed was constant from A to B (Fig. 1). Thus, they obtained the rupture condition

$$\cot\phi + \tan(\phi - \alpha) \geq \epsilon_0 + K p_m \tag{3}$$

where ϵ_0 is the shearing strain at rupture for zero compressive stress, K is the slope of the shear strain (at rupture)–compressive normal stress curve and p_m is the average normal stress on the shear plane.

However, in the present work it has been shown that in order to explain the observed cracking account must be taken of the variation in hydrostatic stress across the plastic zone. In view of this the use of the average value of stress p_m in equation (3) must be questioned. Recent work[5] has in fact shown that even at high cutting speeds with the deformation approximating to a shear plane the value of the normal (hydrostatic) stress on the shear plane varies and

Vol. 3
1961

has a smaller compressive value at B (Fig. 1) than at A—the values being given by

$$p_A = k\{1 + 2(\pi/4 - \phi)\} \tag{4}$$

$$p_B = k\left\{\frac{\cos 2(\phi - \alpha)}{\tan \lambda} - \sin 2(\phi - \alpha)\right\} \tag{5}$$

where λ is the mean angle of friction at the tool–chip interface. Therefore, as p_B has a smaller compressive value than p_m equation (3) should be rewritten with p_B in place of p_m.

Figure 11 shows the general variation of p_A, p_B and p_m (all compressive) with change in tool rake angle calculated from the results (cutting with a continuous chip) of Merchant[4] and Thomsen *et al.*[6] It can be seen that although the compressive value of p_m increases slightly with decrease in rake angle (a decrease in rake angle being one of the changes in cutting conditions which can give a transition from a continuous to a discontinuous chip), the compressive value of p_B decreases significantly.

Acknowledgements—The authors wish to express their thanks to Professor W. Johnson and Dr. M. M. Barash for their help and encouragement. They also wish to thank Mr. N. Whitworth and Mr. G. Robinson for their help with the experimental work and in constructing the apparatus.

REFERENCES

1. M. Field and M. E. Merchant, *Trans. Amer. Soc. Mech. Engrs.* **71**, 421 (1949).
2. W. B. Palmer and P. L. B. Oxley, *Proc. Inst. Mech. Engrs., Lond.* **173**, 623 (1959).
3. P. L. B. Oxley, A. G. Humphreys and A. Larizadeh, *Proc. Inst. Mech. Engrs., Lond.* To be published.
4. M. E. Merchant, *J. Appl. Phys.* **16**, 267 (1945).
5. P. L. B. Oxley, *Int. J. Mech. Sci.* **3**, 68 (1961).
6. E. G. Thomsen, J. T. Lapsley and R. C. Grassie, *Trans. Amer. Soc. Mech. Engrs.* **75**, 591 (1953).

Int. J. Mech. Sci. Pergamon Press Ltd. 1961. Vol. 3, pp. 157–169. Printed in Great Britain

DYNAMICS OF SOME DISORDERED LINEAR SYSTEMS*

J. L. BOGDANOFF† and P. F. CHENEA‡

(*Received* 23 *September* 1960)

Summary—Numerical and theoretical results are presented on the statistics of the dynamical behavior of some linear systems when the parameters which define the system are considered as random variables. Considerable dispersion in frequency response, impedance and impulsive admittance is encountered with relatively small dispersion in parameters. The significance of the results presented on the selection of component tolerance to achieve a specified system tolerance is commented upon.

Vol. 3
1961

I. INTRODUCTION

IN THE present paper we shall present some results on the statistical behavior of the dynamics of a simple physical system when the parameters which define the system are regarded as random variables. Statistically defined systems are familiar to the physicist in connection, for example, with the determination of the probability that a given energy is allowed or forbidden in a random mixed lattice.[1] However, the consideration by engineers of such systems is relatively recent. The need for a discussion of systems defined in a probabilistic sense from the engineering point of view becomes clear when it is recalled that the engineer's ability to define the constants which specify his system is often subject to considerable uncertainty and he must know how these uncertainties effect the accuracy of his prediction of their dynamical behavior. We propose to examine certain aspects of the dynamics of some statistically defined systems so as to enhance the engineer's general understanding of the significance of stochastic parameters on the behavior of engineering systems. The frequency response, impedance and impulsive admittance are good vehicles to generate this understanding and hence were selected for study.

The results presented here deal with a damped linear oscillator when the spring constant K, the mass M and the damping constant C are assumed to be random variables. New numerical results on impedance and frequency response and on the mean and variance of the impulsive admittance are included. We also solve the partial differential equation for the joint density function of the impulsive admittance in terms of displacement x, velocity v and the system parameter. However, deductions of an engineering nature are difficult to draw from this function.

II. BACKGROUND

Born[2] has pointed out the need to introduce probabilistic considerations into the formulation of problems in classical mechanics. In particular, he determined

* Sponsored in part by a National Sciences Foundation Grant (NSFG 10853) to Purdue University.

† Professor of Aeronautical and Engineering Sciences, Purdue University, Indiana.
‡ Professor and Head of Mechanical Engineering, Purdue University, Indiana.

the time development of the joint probability density function $P(x, v, t)$ (in his notation) for a one-dimensional one-particle gas moving on a straight line between two points ($x = 0$, $x = l$) where it is elastically reflected, assuming that at $t = 0$ the joint probability density function of initial position x_0 and initial velocity v_0 is given. For sufficiently large times the position of the particle becomes completely undetermined as long as the initial position and velocity are not known with mathematical precision. Brillouin[3] discussed by means of phase plane diagrams some statistical consequences of experimental errors in specifying the initial configuration of a number of simple systems; in one case he also considered a system with a probabilistically defined system parameter. Brillouin emphasized that experimental errors in determining initial configurations and system parameters are inevitable and to ignore such errors in the formulation of problems in classical physics is unrealistic.

It is interesting to note that Wilson[4] in 1909 developed some thermodynamic analogies for a simple dynamical system (Chinese dinner-gong) of n degrees of freedom using a function of one of the system parameters (length of the uppermost string) as an external coordinate of the system. However, Wilson confined his attention to statistical equilibrium and on that basis evaluated average properties of the system behavior in terms of the external coordinate.

Recently[5] we presented results on the mean and variance of the impedances and one of the frequency responses of a damped linear one-degree of freedom system where spring constant, mass and damping constant are considered as random variables. For reasonably lightly damped systems such as are encountered in structural dynamics considerable dispersion as well as deviation between mean and deterministic values were encountered in the neighborhood of resonance. Our results were mainly of a numerical nature.

Kozin[6] developed the partial differential equation satisfied by the joint density function of the displacement and velocity of an undamped simple harmonic oscillator when the spring constant and initial conditions are regarded as random variables. Under certain initial conditions, he was able to solve the equation for this density function and draw conclusions about the mean motion.

III. NUMERICAL RESULTS

The two arrangements of the damped linear oscillator considered in this paper are shown in Fig. 1.

It will be recalled that the differential equation of motion of the system in Fig. 1(a) is

$$m\ddot{x} + c\dot{x} + kx = F_0 \exp(i\omega t)$$

The substitution of the equation

$$x(t) = X \exp(i\omega t)$$

permits the dimensional frequency response to be written as follows:

$$Y(i\omega) \equiv \frac{X}{\delta_{st}} = (K - Mr^2 + i2\bar{\zeta}rC)^{-1} \tag{1}$$

where the mean values of the spring, mass and damper are, respectively, $\bar{k}$, $\bar{m}$, $\bar{c}$; K, M, and C are random variables with unity for mean value;

$$k = \bar{k}K, \quad m = \bar{m}M, \quad c = \bar{c}C$$

and

$$r = \omega/\omega_0, \quad \omega_0^2 = \bar{k}/\bar{m}, \quad 2\bar{\zeta}\omega_0 = \bar{c}/\bar{m}, \quad \delta_{st} = F_0/\bar{k}$$

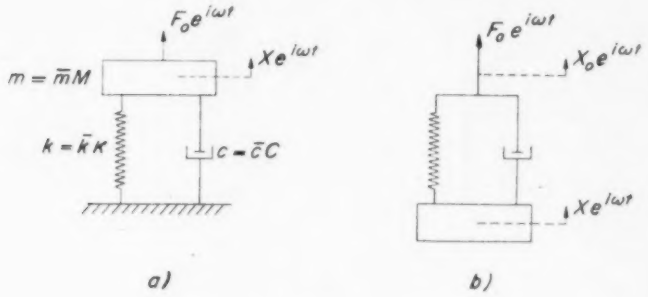

FIG. 1. Damped linear oscillators.

For the system shown in Fig. 1(b) the equation of motion is

$$m(\ddot{x} - \ddot{x}_0) + c(\dot{x} - \dot{x}_0) + k(x - x_0) = -m\ddot{x}_0$$

and the force at the top is given by the formula

$$f_0 = k(x_0 - x) + c(\dot{x}_0 - \dot{x})$$

The substitution of the expression $x = X\exp(i\omega t)$, $x_0 = X_0\exp(i\omega t)$ and $f_0 = F_0\exp(i\omega t)$ into these equations and the use of a little algebra yield the impedance of the second system:

$$Z(i\omega) \equiv \frac{F_0}{x_0} = -\bar{k}\,\frac{r^2 M(K + i2\bar{\zeta}rC)}{K - r^2 M + i2\bar{\zeta}rC} \tag{2}$$

We shall assume that K, M and C are independent and have the same distribution. The distribution assumed is a discrete one approximating a one-dimensional normal distribution; the probabilities of taking the values $1 \pm 3\Delta_0$, $1 \pm 2\Delta_0$, $1 \pm \Delta_0$ and 1 are, respectively, 0·0060, 0·0606, 0·2417 and 0·3834. The mean is unity and the standard deviation is 0·052 with $\Delta_0 = 0{\cdot}050$.

Figs. 2–6 pertain to statistical aspects of $Y(i\omega)$. Fig. 2 gives curves of the absolute value of $E\{Y(i\omega)\}$ vs. r for three values of mean critical damping; Figs. 3 and 4 provide the corresponding curves of the phase angle Φ of $E\{Y(i\omega)\}$ and the square root σ_Y of the variance of $Y(i\omega)$. For $\bar{\zeta}$ equal to 1, it is easy to show that deterministic and mean values nearly coincide with little or no dispersion. This observation suggests that in certain electrical systems which are fairly heavily damped, high accuracy of components is not necessary to insure that system performance be close in the mean sense with little dispersion to the performance of the mean or design system. For many structural systems which are lightly damped this is not the case. Not only does $|EY|$ at $r = 1$ differ from the mean system values (10 for $\bar{\zeta} = 0{\cdot}050$ and 20 for $\bar{\zeta} = 0{\cdot}025$)

Vol. 3
1961

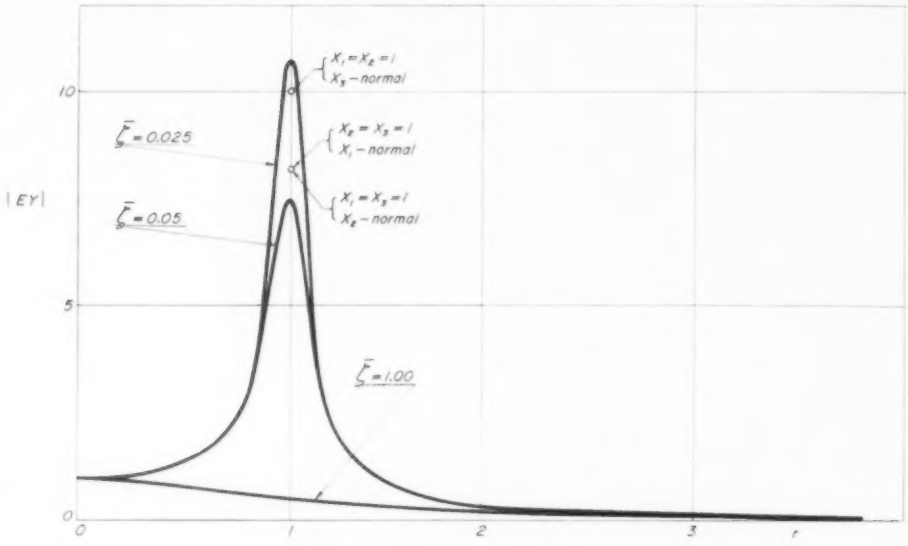
10
5
0
|EY|
$\bar{\zeta}$ = 0.025
$\bar{\zeta}$ = 0.05
$\bar{\zeta}$ = 1.00
$X_1 = X_2 = 1$
X_3 – normal
$X_2 = X_3 = 1$
X_1 – normal
$X_1 = X_3 = 1$
X_2 – normal
0
1
2
3
r

FIG. 2.

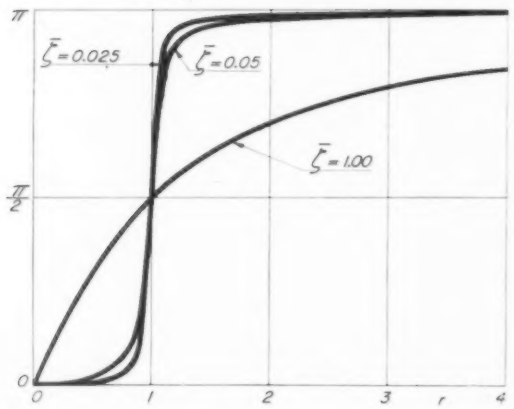
π
π/2
0
$\bar{\zeta}$ = 0.025
$\bar{\zeta}$ = 0.05
$\bar{\zeta}$ = 1.00
0
1
2
3
r
4

FIG. 3.

Vol. 3
1961

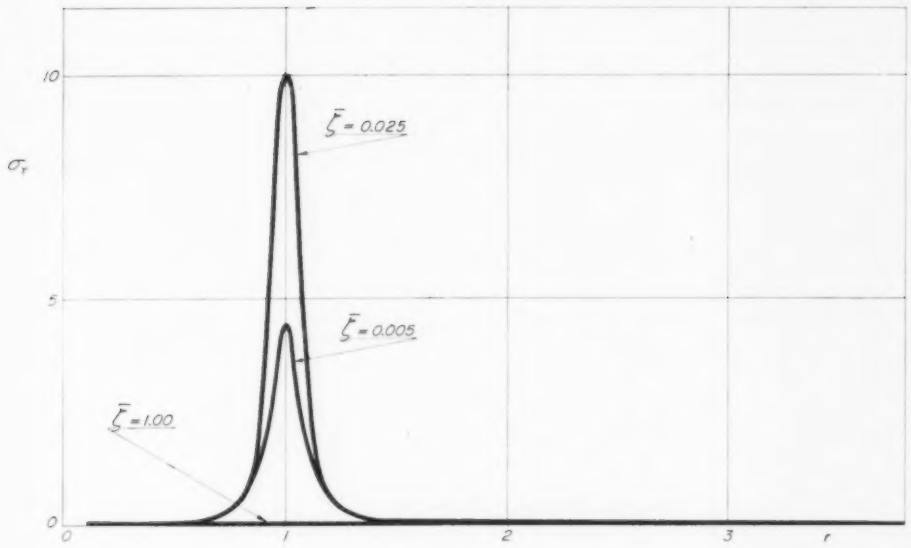

FIG. 4.

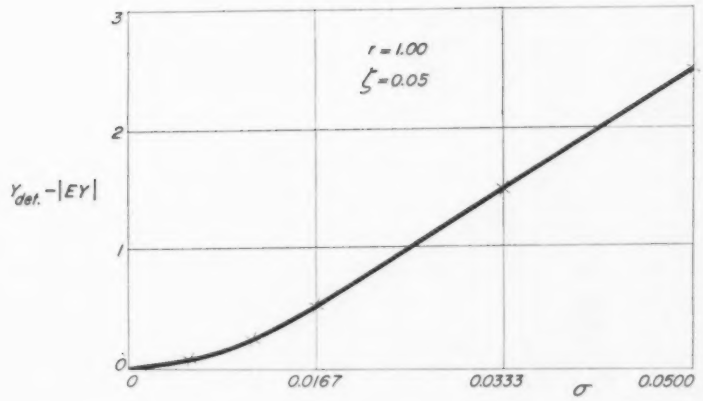

FIG. 5.

but the dispersion as measured by the standard deviation σ_Y is substantial. The difference between the absolute value of the mean system frequency response and $E\{Y(i\omega)\}$ for different values of Δ_0 with $r = 1$ and $\bar{\zeta} = 0{\cdot}050$ is shown in Fig. 5, this difference amounting to approximately 5 per cent of the mean system frequency response (absolute value) where $\Delta_0 = 0{\cdot}0167$.

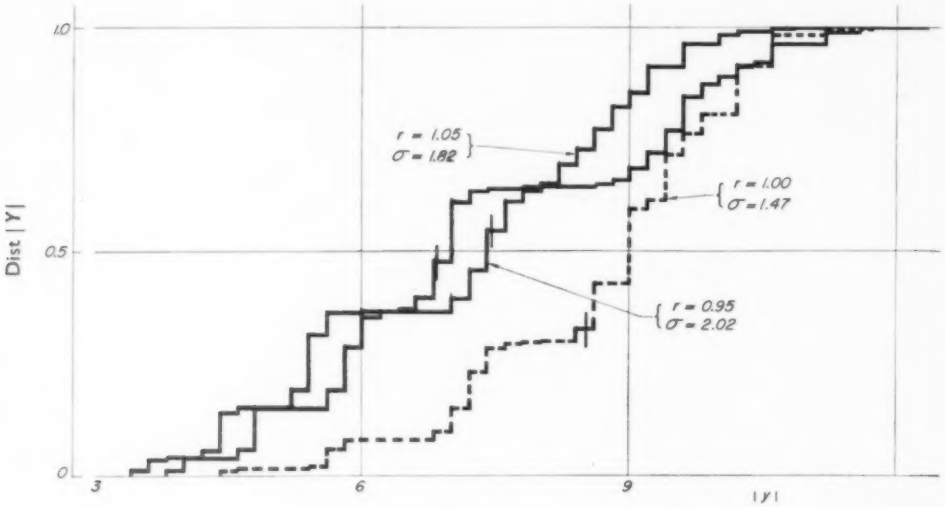

FIG. 6.

We have also shown on Fig. 2 at $r = 1$ and $\bar{\zeta} = 0{\cdot}05$ the separate influence of each of the three random variables or $|E\{Y(i\omega)\}|$. As one would expect, the variables which influence undamped natural frequency have the more pronounced influence, these being K and M. C causes no difference between the deterministic value and $|E\{Y(i\omega)\}|$.

Fig. 6 gives the distribution function of $|Y(i\omega)|$ at $r = 0{\cdot}95$, $r = 1{\cdot}00$ and $r = 1{\cdot}05$ for $\bar{\zeta} = 0{\cdot}050$.

Figs. 7–10 present results on statistical properties of $Z(i\omega)/(-k)$. The results given in this sequence of figures and the observations which may be drawn from them are quite similar to those for $Y(i\omega)$; hence we shall not repeat the observations again. We shall refer to some of these results in the next Section. The phase angle of $E\{Z(i\omega)/(-k)\}$ is denoted by Ψ to distinguish it from the phase angle of $E\{Y(i\omega)\}$.

The impulsive admittance of the system of Fig. 1(a) may be obtained from its equation of motion when it is excited at time $t = 0$ by the impulse $m\delta(t)$, where $\delta(t)$ is the Dirac delta function. The appropriate equation is

$$m\ddot{x} + c\dot{x} + kx = m\delta(t)$$

We find the solution for $x(t)$ is

$$x(t) \equiv H(t) = \frac{\exp[-\bar{\zeta}\omega_0 t(C/M)] \sin\{\omega_0 t\sqrt{[(K/M) - \bar{\zeta}^2(C^2/M^2)]}\}}{\omega_0\sqrt{[(K/M) - \bar{\zeta}^2(C^2/M^2)]}} \qquad (3)$$

and the impulsive admittance of the mean system is

$$h(t) = \frac{\exp(-\bar{\zeta}\omega_0 t)\sin[\omega_0 t\sqrt{(1-\bar{\zeta}^2)}]}{\omega_0\sqrt{(1-\bar{\zeta}^2)}} \tag{4}$$

Clearly
$$E\{H(t)\} \neq h(t) \tag{5}$$

and
$$\left.\begin{aligned} H(0) = 0, \quad \dot{H}(0) = 1 \\ h(0) = 0, \quad \dot{h}(0) = 1 \end{aligned}\right\} \tag{6}$$

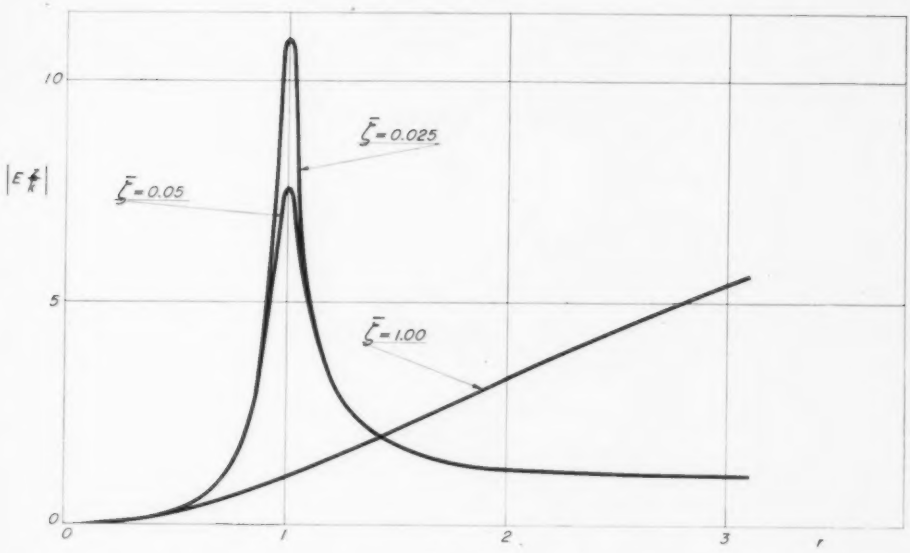

FIG. 7.

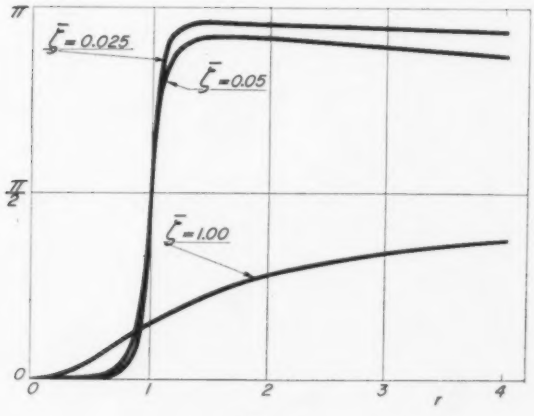

FIG. 8.

It is to be understood when using (3) and (4) that if the radicand becomes zero or negative the forms of (3) and (4) must be altered appropriately.

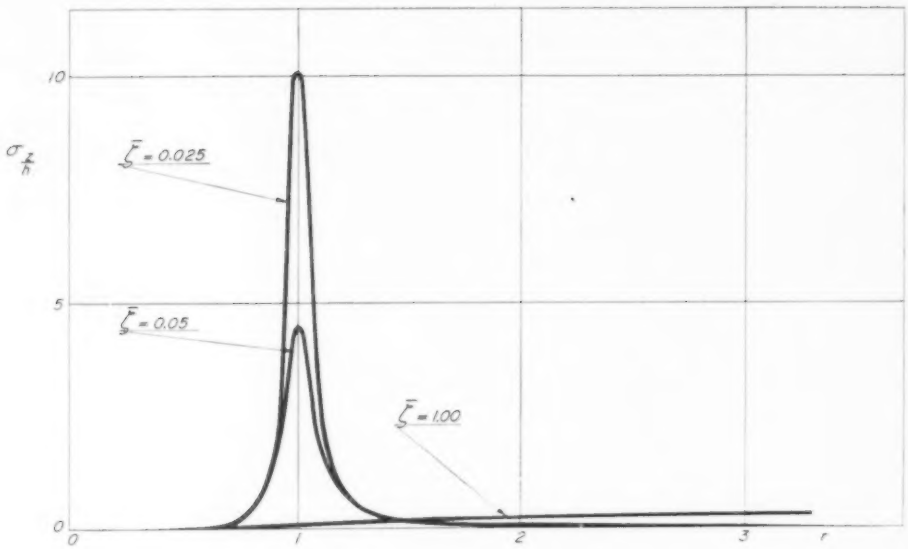
10
5
0
0
1
2
3
r
$\sigma_{\frac{r}{h}}$
$\bar{\zeta} = 0.025$
$\bar{\zeta} = 0.05$
$\bar{\zeta} = 1.00$

FIG. 9.

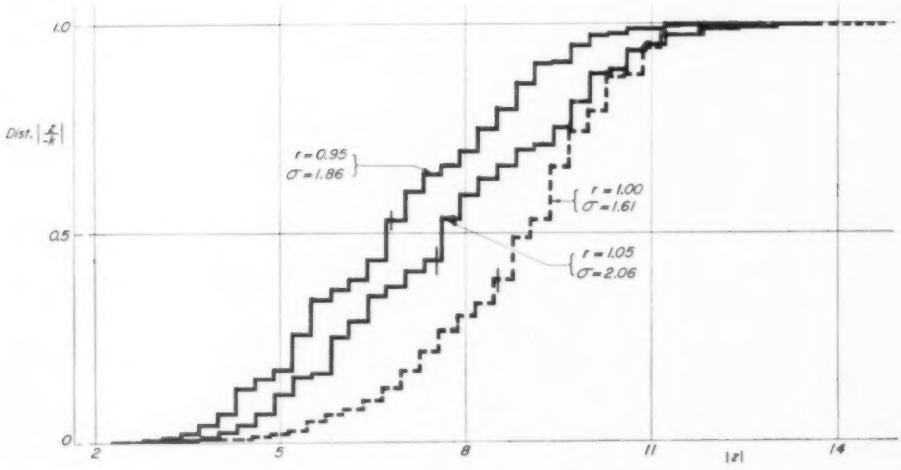
1.0
0.5
0
Dist. $\left|\frac{z}{h}\right|$
2
5
8
11
14
|z|
r = 0.95
σ = 1.86
r = 1.00
σ = 1.61
r = 1.05
σ = 2.06

FIG. 10.

Fig. 11 shows how the mean of $H(t)$, the standard deviation of $H(t)$, and $h(t)$ vary as a function of $\omega_0 t$. In this figure we again have assumed that K, M and C are independent random variables having the same discrete distribution with probabilities of taking the values $1 \pm 3\Delta_0$, $1 \pm 2\Delta_0$, $1 \pm \Delta_0$ and 1 equal to 0·0060, 0·0606, 0·2417 and 0·3834, respectively, and $\Delta_0 = 0{\cdot}050$;

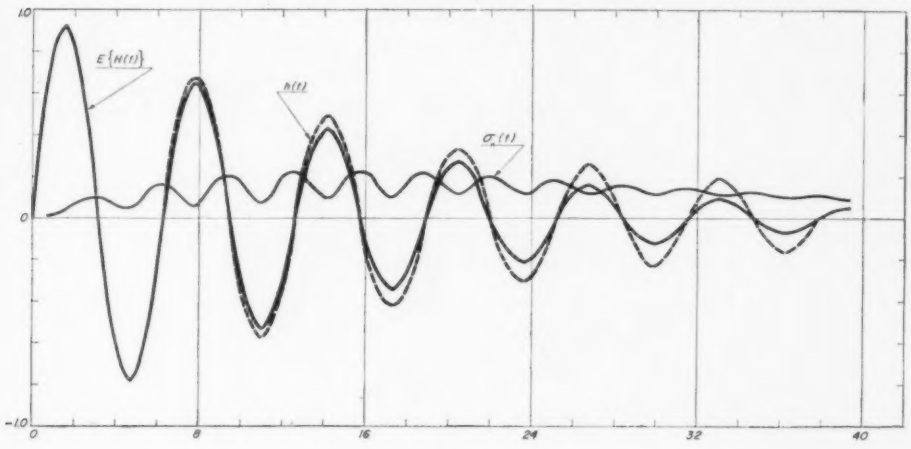

FIG. 11.

further $\zeta = 0{\cdot}050$. It is clear from this figure that $|E\{H(t)\}|$ is consistently below the function $|h(t)|$, the differences at the peaks becoming larger on a percentage basis as time increases. In addition, the standard deviation rises in an oscillatory manner until it exceeds $|E\{H(t)\}|$. Thus, if a deterministic force $\bar{m}f(t)$ acts upon the mass of Fig. 1(a) the mean response

$$E\{X(t)\} = \int_0^t E\{H(t-\tau)\} f(\tau)\, d\tau,$$

assuming rest at $t = 0$, can deviate appreciably from the deterministic response

$$x(t) = \int_0^t h(t-\tau) f(\tau)\, d\tau$$

if $f(t)$ is properly selected. Further, the scatter of

$$X(t) = \int_0^t H(t-\tau) f(\tau)\, d\tau$$

about $E\{X(t)\}$ may become appreciable.

IV. ANALYSIS

It is of interest to consider analytical means of determining either probability distributions or moments of one of the dynamical characteristics discussed in the previous Section. We shall select the impulsive admittance $H(t)$ for consideration.

Let us first consider the problem of determining the joint distribution of the displacement and velocity of $H(t)$. The pair of first-order linear differential equations which determine $H(t)$, apart from initial conditions, is

$$\left.\begin{aligned} \dot{X}_1 &= X_2 && \equiv P_1 \\ \dot{X}_2 &= -\frac{k}{m}X_1 - \frac{c}{m}X_2 && \equiv P_2 \end{aligned}\right\} \tag{7}$$

Let $f(x_1, x_2, \kappa, \mu, \gamma; t)$ denote the joint density function of displacement, velocity, spring constant, mass and damping constant, respectively. Then the partial differential equation which f must satisfy is[6,7]

$$\frac{\partial f}{\partial t} + \frac{\partial}{\partial x_1}(P_1 f) + \frac{\partial}{\partial x_2}(P_2 f) = 0$$

This equation expresses the conservation of probability. A short formal derivation, due to Kozin[6], is as follows.

The joint characteristic function of X_1, X_2, K, C, M is defined by the expression

$$\phi(u_1, u_2; v_1, v_2, v_3; t) = E\{\exp i[u_1 X_1 + u_2 X_2 + v_1 K + v_2 C + v_3 M]\}$$

$\phi(u_1, u_2; v_1, v_2, v_3)$ is thus the Fourier transform of $f(x_1, x_2, \kappa, \mu, \gamma; t)$. The differentiation of this equation with respect to time yields

$$\frac{\partial \phi}{\partial t} = E\{i(u_1 \dot{X}_1 + u_2 \dot{X}_2) \exp i[u_1 X_1 + u_2 X_2 + v_1 K + v_2 C + v_3 M]\}$$

or, with (7),

$$\begin{aligned} \frac{\partial \phi}{\partial t} = {} & iu_1 E\{P_1 \exp i[u_1 X_1 + u_2 X_2 + v_1 K + v_2 C + v_3 M]\} \\ & + iu_2 E\{P_2 \exp i[u_1 X_1 + u_2 X_2 + v_1 K + v_2 C + v_3 M]\} \end{aligned}$$

The inverse Fourier transform of this equation is just

$$\frac{\partial f}{\partial t} + \frac{\partial}{\partial x_1}(P_1 f) + \frac{\partial}{\partial x_2}(P_2 f) = 0$$

The substitution of explicit expressions from (7) yields

$$\frac{\partial f}{\partial t} + x_2 \frac{\partial f}{\partial x_1} + \left(-\frac{\kappa}{\mu}x_1 - \frac{\gamma}{\mu}x_2\right)\frac{\partial f}{\partial x_2} = \frac{\gamma}{\mu} f \tag{8}$$

Equations of this type occur repeatedly in statistical physics (see, for instance, Ref. 8). However, the parameters which define the system are not usually regarded as random variables, and we have no external disturbance.

Let $$f(x_1, x_2, \kappa, \mu, \gamma; t) = \exp\left(\frac{\gamma}{\mu} t\right) \chi(x_1, x_2, \kappa, \mu, \gamma; t) \tag{9}$$

Then (8) is replaced by

$$\frac{\partial \chi}{\partial t} + x_2 \frac{\partial \chi}{\partial x_1} + \left(-\frac{\kappa}{\mu}x_1 - \frac{\gamma}{\mu}x_2\right)\frac{\partial \chi}{\partial x_2} = 0 \tag{10}$$

The associated Lagrangian system is

$$\frac{dt}{1} = \frac{dx_1}{x_2} = \frac{dx_2}{-(\kappa/\mu)x_1 - (\gamma/\mu)x_2} = \frac{dX}{0} \tag{11}$$

The two integrals of (11) which we shall use are

$$\left.\begin{aligned} \phi_1(t) &\equiv \exp\left(\frac{\gamma t}{2\mu}\right)\left[x_1\left(\cos\omega_0' t - \frac{\gamma}{2\mu\omega_0'}\sin\omega_0' t\right) - \frac{x_2}{\omega_0'}\sin\omega_0' t\right] = \text{const.} \\ \phi_2(t) &\equiv \exp\left(\frac{\gamma t}{2\mu}\right)\left[\frac{x_1\kappa}{\omega_0'\mu}\sin\omega_0' t + x_2\left(\cos\omega_0' t + \frac{\gamma}{2\mu\omega_0'}\sin\omega_0' t\right)\right] = \text{const.} \end{aligned}\right\} \tag{12}$$

where

$$\omega_0'^2 = \frac{\kappa}{\mu} - \frac{\gamma^2}{4\mu^2} \tag{13}$$

The general solution of (8) is thus

$$f(x_1, x_2, \kappa, \mu, \gamma; t) = \psi(\phi_1, \phi_2, \kappa, \mu, \gamma)\exp\left(\frac{\gamma}{\mu}t\right) \tag{14}$$

where ψ is an arbitrary function of the indicated arguments.

Let us assume that k, m and c are independent with density functions $f_1(\kappa)$, $f_2(\mu)$ and $f_3(\gamma)$, respectively. Since at time zero the displacement must be zero and the velocity must equal unity, we have

$$f(x_1, x_2, \kappa, \mu, \gamma; 0) = \delta(x_1)\,\delta(x_2 - 1) f_1(\kappa) f_2(\mu) f_3(\gamma) \tag{15}$$

Thus, in virtue of the fact that $\phi_1(0) = x_1, \phi_2(0) = x_2$ we find that

$$\psi = \delta(\phi_1)\,\delta(\phi_2 - 1) f_1(\kappa) f_2(\mu) f_3(\gamma)\exp\left(\frac{\gamma}{\mu}t\right)$$

or

$$f(x_1, x_2, \kappa, \mu, \gamma; t) = \delta(\phi_1)\,\delta(\phi_2 - 1) f_1(\kappa) f_2(\mu) f_3(\gamma)\exp\left(\frac{\gamma}{\mu}t\right) \tag{16}$$

The joint density function of $X_1(t)$ and $X_2(t)$ is

$$f(x_1, x_2; t) = \int_{-\infty}^{\infty}\int_{-\infty}^{\infty}\int_{-\infty}^{\infty} \delta(\phi_1)\,\delta(\phi_2 - 1) f_1(\kappa) f_2(\mu) f_3(\gamma)\exp\left(\frac{\gamma}{\mu}t\right) d\kappa\, d\mu\, d\gamma \tag{17}$$

and the density function for the displacement $X_1(t)$ is

$$f(x_1; t) = \int_{-\infty}^{\infty} f(x_1, x_2; t)\, dx_2 \tag{18}$$

The integrations which occur in (17) and (18) may be difficult to evaluate if the density functions of the parameters are of the continuous type. This is not the case if they are discrete. However, in the latter case, the density functions become quite awkward to interpret. Information on moments is fairly easy to obtain for the discrete case.[6]

Let us consider for illustrative purposes a system in which $m = m_0$ (const.) and $c = c_0$ (const.) with probability 1 and k has a discrete distribution

$$f_1(\kappa) = \sum_{-n}^{n} p_i\,\delta(\kappa - \kappa_i) \tag{19}$$

Vol. 3
1961

We rewrite (12) in the form

$$\left.\begin{aligned}\phi_1'(t) &\equiv \exp(\bar{\zeta}\omega_0 t)\left[x_1\left(\cos\omega_0' t - \frac{\bar{\zeta}\omega_0}{\omega_0'}\sin\omega_0' t\right) - \frac{x_2}{\omega_0'}\sin\omega_0' t\right] \\ \phi_2'(t) &\equiv \exp(\bar{\zeta}\omega_0 t)\left[\frac{x_1\omega_0^2\kappa}{\omega_0'}\sin\omega_0' t + x_2\left(\cos\omega_0' t + \frac{\bar{\zeta}\omega_0}{\omega_0'}\sin\omega_0' t\right)\right]\end{aligned}\right\} \tag{20}$$

where

$$k = \bar{k}K, \quad \omega_0^2 = \frac{\bar{k}}{m_0}$$

$$2\bar{\zeta}\omega_0 = \frac{c_0}{m_0}, \quad \omega_0'^2 = \omega_0^2(\kappa - \bar{\zeta}^2)$$

with κ now referring to the dimensionless spring constant K. For the mean of $X_1(t)$, which is the mean of $H(t)$ for this case, we use the formula

$$\begin{aligned}E\{X_1(t)\} &= \int_{-\infty}^{\infty} x_1 f(x_1; t)\, dx_1 \\ &= \int_{-\infty}^{\infty}\int_{-\infty}^{\infty}\int_{-\infty}^{\infty} x_1 \delta(\phi_1')\,\delta(\phi_2' - 1)\exp(2\bar{\zeta}\omega_0 t) f_1(\kappa)\, dx_1\, dx_2\, d\kappa\end{aligned} \tag{21}$$

A change in the variable x_2 and an integration over this new variable gives

$$E\{X_1(t)\} = \int_{-\infty}^{\infty}\int_{-\infty}^{\infty} x_1 \frac{\omega_0'\exp(\bar{\zeta}\omega_0 t)}{\sin\omega_0' t}\,\delta\left[\frac{x_1\omega_0'\exp(\bar{\zeta}\omega_0 t)}{\sin\omega_0' t} - 1\right] f_1(\kappa)\, dx_1\, d\kappa$$

and hence

$$\begin{aligned}E\{X_1(t)\} &= \int_{-\infty}^{\infty}\int_{-\infty}^{\infty} \frac{y\exp(-\bar{\zeta}\omega_0 t)\sin\omega_0' t}{\omega_0'}\,\delta(y-1) f_1(\kappa)\, dy\, d\kappa \\ &= \int_{-\infty}^{\infty} \frac{\exp(-\bar{\zeta}\omega_0 t)\sin\omega_0' t}{\omega_0'} f_1(\kappa)\, d\kappa \\ &= \sum_{-n}^{n} p_i \frac{\exp(-\bar{\zeta}\omega_0 t)\sin[\omega_0\sqrt{(\kappa_i - \bar{\zeta}^2)}\,t]}{\omega_0\sqrt{(\kappa_i - \bar{\zeta}^2)}}\end{aligned} \tag{22}$$

An equation similar to (22) may be derived for the mean of $X_1(t)$ or $H(t)$ when each parameter has an independent discrete distribution. Of course, the results are the same as have already been employed in computing the mean of $H(t)$ which is plotted in Fig. 11. The variance of $X_1(t)$ may be obtained by evaluating $E\{X_1^2(t)\}$ and subtracting from it $[E\{X_1(t)\}]^2$.

It is of interest to point out an application of the results given in Section III for $Z(i\omega)$. Let us consider the system shown in Fig. 12. We assume that to a mass m acted upon by the force $F_0\exp(i\omega t)$ there are attached n damped linear oscillators whose system parameters are independent random variables which are also independent for different oscillators. The impedance of the mass m is

$$Z_0(i\omega) \equiv \frac{F_0}{X_0} = -\bar{k}\left(qr^2 + \sum_{1}^{n}\frac{Z_j(i\omega)}{-\bar{k}}\right) \tag{23}$$

where

$$m = q\bar{m}$$

We find that

$$E\left\{\frac{Z_0(i\omega)}{-\bar{k}}\right\} = qr^2 + nE\left\{\frac{Z(i\omega)}{-\bar{k}}\right\} = \left(qr^2 + n\left|E\left\{\frac{Z}{-\bar{k}}\right\}\right|\cos\psi\right) + in\left|E\left\{\frac{Z}{-\bar{k}}\right\}\right|\sin\psi \tag{24}$$

where $E\{Z(i\omega)/-\bar{k}\}$ is the mean of the impedance of the system shown in Fig. 1(b) and ψ is the phase angle of this mean impedance. Further,

$$\frac{\sigma^2_{Z_0}}{\bar{k}} = E\left\{\left(\frac{Z_0(i\omega) - E\{Z_0(i\omega)\}}{-\bar{k}}\right)\left(\frac{Z_0(i\omega) - E\{Z_0(i\omega)\}}{-\bar{k}}\right)^*\right\} = \frac{n\sigma^2_Z}{\bar{k}} \tag{25}$$

where the asterisk denotes complex conjugate. For appropriate conditions on the oscillator of Fig. 12, we may therefore use results given in Figs. 7–10 to evaluate mean and variance of the impedance of this system.

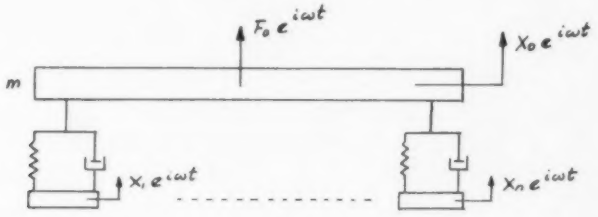

FIG. 12.

V. CONCLUSION

We have shown that by simple numerical techniques one can examine the significance of stochastic parameters on the dynamics of engineering systems. This is the first step in the quantitative treatment of the classical engineering problem of establishing rational tolerance on system components in order to achieve a given tolerance on the system performance. Thus, this transfers the tolerance problem in design from a qualitative to a quantitative level.

REFERENCES

1. E. H. KERNER, *Proc. Phys. Soc.* **A69**, 234 (1956).
2. M. BORN, *Math.-fys. Medd.* **30**, 3 (1955).
3. L. BRILLOUIN, *Inform. & Control* **2**, 45 (1959).
4. E. B. WILSON, *Ann. Math.* (2nd Series) **10**, 149 (1909).
5. P. F. CHENEA and J. L. BOGDANOFF, *Colloqium on Mechanical Impedance Methods for Mechanical Vibrations* 1958, p. 125. The American Society of Mechanical Engineers, New York (1959).
6. F. KOZIN, *J. Appl. Mech.* In press (1961).
7. M. BORN, *Math.-fys. Medd.* **30**, 1 (1955).
8. M. C. WANG and G. E. UHLENBECK, *Rev. Mod. Phys.* **18**, 323 (1945).

Int. J. Mech. Sci. Pergamon Press Ltd. 1961. Vol. 3, pp. 170–196. Printed in Great Britain

NON-UNIFORM THREE-DIMENSIONAL AND SWIRLING FLOWS THROUGH DIVERGING DUCTS AND TURBO-MACHINES

R. I. LEWIS* and J. H. HORLOCK†

(*Received* 5 *May* 1960)

Summary—An analytical study is made of incompressible inviscid, rotational and irrotational flow through cascades located in ducts of varying cross-sectional area, bounded by plane or conical surfaces. Solutions for the distribution of throughflow and transverse (or swirling) velocity are obtained, and two numerical examples are given.

1.0. NOTATION

r, θ, x; r, θ, ϕ	co-ordinates
u, v, w	velocity components
u', v', w'	velocity perturbations
ξ, ζ, η	vorticity components
p	static pressure
p_0	stagnation pressure
ψ	stream function
α	swirl angle
$A_n, B_n, a_n, c_n, p_n, K$	constants
λ	ratio of outlet area/inlet area
f, Θ, g	functions of θ
P_n, Q_n	Legendre functions
P'_n, Q'_n	associated Legendre functions
$U = C/r$	unperturbed velocity—wedge-shaped duct
$m = 2\pi C$	source strength per unit length—wedge-shaped duct
$U = C/r^2$	unperturbed velocity—conical duct
$m = 4\pi C$	source strength—conical duct

Subscripts

m	at the cascade
u	immediately upstream of cascade
d	immediately downstream of cascade

2.0. INTRODUCTION

SOLUTIONS for plane non-uniform flows through two-dimensional and conical ducts have been given in an earlier paper.[1] In turbo-machines the flows in such ducts may be deflected in the transverse or tangential direction by cascades of blades. Such blades, of arbitrary shape along their length, may impart a variety of swirling velocity distributions. The changes that occur in throughflow and swirling velocity through the duct are studied in this paper.

* Engineering Department, University of Cambridge.
† Department of Mechanical Engineering, The University, Liverpool 3.

3.0. SHEAR FLOW THROUGH A WEDGE, WITH ADDITION OF TRANSVERSE VELOCITY

A solution for the non-uniform flow through a wedge-shaped duct (Fig. 1(a)) has been given in an earlier paper.[1] A similar solution for the velocities in the r, θ plane is obtained if a velocity component w is added in the transverse x direction, provided all derivatives in this direction are zero. Patterns created by stream surfaces cutting planes normal to the x direction will be similar.

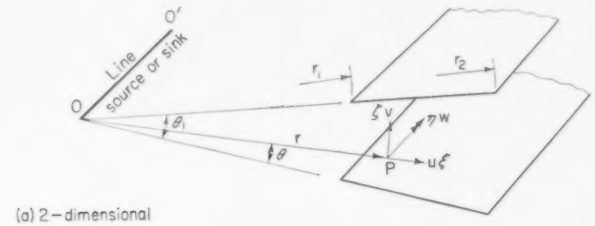

(a) 2–dimensional

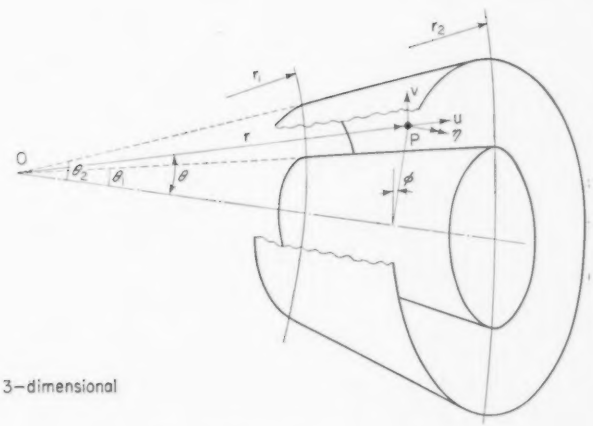

(b) 3–dimensional

FIG. 1. Co-ordinate systems.

The equations of motion for this flow are

$$u\frac{\partial w}{\partial r}+\frac{v}{r}\frac{\partial w}{\partial \theta}=-\frac{1}{\rho}\frac{\partial p}{\partial x}=0 \tag{1}$$

$$u\frac{\partial v}{\partial r}+\frac{v}{r}\frac{\partial v}{\partial \theta}+\frac{uv}{r}=-\frac{1}{\rho r}\frac{\partial p}{\partial \theta} \tag{2}$$

$$u\frac{\partial u}{\partial r}+\frac{v}{r}\frac{\partial u}{\partial \theta}-\frac{v^2}{r}=-\frac{1}{\rho}\frac{\partial p}{\partial r} \tag{3}$$

Equations (2) and (3) are identical to those describing the flow (without transverse velocity) in Ref. 1 and yield the same solution for perturbation velocities u' and v' on a potential source flow $U = C/r$.

The behaviour of the transverse velocity is governed by equation (1).

The continuity equation may be written

$$\frac{\partial(ur)}{\partial r}+\frac{\partial v}{\partial \theta}=0 \tag{4}$$

A stream function ($\psi[r,\theta]$) may be defined such that

$$u=-\frac{1}{r}\frac{\partial \psi}{\partial \theta}, \quad v=\frac{\partial \psi}{\partial r} \tag{5}$$

and

$$d\psi=\frac{\partial \psi}{\partial r}dr+\frac{\partial \psi}{\partial \theta}d\theta \tag{6}$$

Along a streamline in steady flow

$$\frac{d\psi}{dt}=0=u\frac{\partial \psi}{\partial r}+\frac{v}{r}\frac{\partial \psi}{\partial \theta} \tag{7}$$

A comparison of equations (1) and (7) shows that w is a function of ψ, and remains constant along a streamline. If the two-dimensional streamline patterns are obtained from the solutions of Ref. 1 for u' and v', then the three-dimensional motion may be obtained by superimposing specified values of w which remain constant along streamlines.

A further simplification is obtained by studying the relation between the vorticity components (ξ, ζ) in the r, θ directions.

$$\xi=\frac{1}{r}\frac{\partial w}{\partial \theta}, \quad \zeta=-\frac{\partial w}{\partial r} \tag{8}$$

From equation (1)

$$\zeta=\frac{v}{u}\xi$$

If the variation of w in the θ direction is small we may write

$$w=W+w'$$

where w' is a small perturbation of W (which is constant)

then

$$\xi=\frac{1}{r}\frac{\partial w'}{\partial \theta}$$

Since v/u is a small quantity ζ is of second order of small quantities, and we may write

$$\frac{\partial w}{\partial r}=0$$

and

$$w=f(\theta)$$

w is a function of θ only, and remains constant along radial lines. It has been shown in Ref. 1 that η is also a function of θ only.

3.1. *Flow through a cascade placed in a diverging duct*

A solution now becomes possible for the flow through a duct, diverging between r_1 and r_2 and containing an infinite cascade which introduces a sudden change in transverse velocity w and vorticity (η, ξ) at a radius r_m.

The Euler equations of motion are valid only for regions where there are no body forces. They may be applied separately to the regions upstream and downstream of the cascade, and the two solutions subsequently combined by matching the u' and v' velocity components at the cascade.

The solutions for u' and v' as given in Ref. 1 are

$$u' = -\sum_1^\infty \left\{\frac{1}{r}\left[A_n r^{p} - B_n r^{-p_n}\right] + \frac{a_n p_n r}{4-p_n^2}\right\} \cos p_n \theta \tag{9}$$

$$v' = \sum_1^\infty \left\{\frac{1}{r}\left[A_n r^{p_n} + B_n r^{-p_n}\right] + \frac{2a_n r}{4-p_n^2}\right\} \sin p_n \theta \tag{10}$$

By matching u' and v' at the cascade, where $r = r_m$, the equations

$$A_1 r_m^{p-1} - B_1 r_m^{-p-1} + \frac{a_1 p r_m}{4-p^2} = A_2 r_m^{p-1} - B_2 r_m^{-p-1} + \frac{a_2 p r_m}{4-p^2} \tag{11}$$

$$A_1 r_m^{p-1} + B_1 r_m^{-p-1} + \frac{2a_1 r_m}{4-p^2} = A_2 r_m^{p-1} + B_2 r_m^{-p-1} + \frac{2a_2 r_m}{4-p^2} \tag{12}$$

are obtained, dealing with the nth term and dropping suffix n.

The inlet and outlet boundary conditions are next considered. If the fluid enters and leaves the duct at constant pressure, then

$$\frac{1}{\rho}\frac{\partial p_1}{\partial \theta} = \frac{1}{\rho}\frac{\partial p_2}{\partial \theta} = -u\frac{\partial (vr)}{\partial r} = 0$$

and

$$A_1 r_1^{p-1} - B_1 r_1^{-p-1} + \frac{4a_1 r_1}{p(4-p^2)} = 0 \tag{13}$$

$$A_2 r_2^{p-1} - B_2 r_2^{-p-1} + \frac{4a_2 r_2}{p(4-p^2)} = 0 \tag{14}$$

Equations (11) to (14) may be written

$$\left.\begin{aligned} x_1\lambda_1 - y_1\mu_1 &= -\frac{4z_1 r_1}{p} && \text{(a)}\\ x_2\lambda_2 - y_2\mu_2 &= -\frac{4z_2 r_2}{p} && \text{(b)}\\ x_1 - y_1 + pz_1 r_m &= x_2 - y_2 + pz_2 r_m && \text{(c)}\\ x_1 + y_1 + 2z_1 r_m &= x_2 + y_2 + 2z_2 r_m && \text{(d)} \end{aligned}\right\} \tag{15}$$

Vol. 3
1961

where

$$x_1 = A_1 r_m^{p-1} \qquad x_2 = A_2 r_m^{p-1}$$

$$y_1 = B_1 r_m^{-p-1} \qquad y_2 = B_2 r_m^{-p-1}$$

$$z_1 = \frac{a_1}{4-p^2} \qquad z_2 = \frac{a_2}{4-p^2}$$

$$\lambda_1 = (r_1/r_m)^{p-1} \qquad \lambda_2 = (r_2/r_m)^{p-1}$$

$$\mu_1 = (r_1/r_m)^{-p-1} \qquad \mu_2 = (r_2/r_m)^{-p-1}$$

A simplified solution of equations (15) is obtained for small angles of divergence ($\theta \ll \pi$). Then $p \gg 1$ even for the first term in the series (e.g. if $\theta = 10^0, p_1 = 18$). Then with $r_1 < r_m < r_2$, μ_1 and λ_2 are large compared with μ_2 and λ_1 and from (15a) and (15b)

$$y_1 \doteq 0, \quad x_2 \doteq 0$$

Solving (15c) and (15d)

$$x_1 \doteq \frac{r_m}{2p}(a_1 - a_2), \quad y_2 \doteq \frac{r_m}{2p}(a_1 - a_2)$$

and

$$\left.\begin{aligned} u' &= \left\{\tfrac{1}{2}(a_2-a_1)\left(\frac{r}{r_m}\right)^{p-2} + a_1\right\}\frac{r}{p}\cos p\theta \\ v' &= \left\{-\tfrac{1}{2}(a_2-a_1)\left(\frac{r}{r_m}\right)^{p-2} - \frac{2a_1}{p}\right\}\frac{r}{p}\sin p\theta \end{aligned}\right\} \quad \text{(upstream)}$$

$$\left.\begin{aligned} u' &= \left\{-\tfrac{1}{2}(a_2-a_1)\left(\frac{r_m}{r}\right)^{p+2} + a_2\right\}\frac{r}{p}\cos p\theta \\ v' &= \left\{-\tfrac{1}{2}(a_2-a_1)\left(\frac{r_m}{r}\right)^{p+2} - \frac{2a_2}{p}\right\}\frac{r}{p}\sin p\theta \end{aligned}\right\} \quad \text{(downstream)}$$

At the radii r_1, r_2 and r_m the throughflow perturbations are

$$\left.\begin{aligned} \frac{u_1'}{r_1} &= \frac{a_1}{p}\cos p\theta, \qquad \frac{u_2'}{r_2} = \frac{a_2}{p}\cos p\theta \\ \frac{u_m'}{r_m} &= \left(\frac{a_1+a_2}{2p}\right)\cos p\theta \end{aligned}\right\} \tag{16}$$

and

$$\frac{u_m'}{r_m} = \frac{1}{2}\left(\frac{u_1'}{r_1} + \frac{u_2'}{r_2}\right) \tag{17}$$

If the angle of divergence is decreased to zero by letting r_1, r_m and $r_2 \to \infty$ while $(r_m - r_1)$ and $(r_2 - r_m)$ remain constant,

$$\frac{r_m}{r_1} \quad \text{and} \quad \frac{r_1}{r_m} \to 1$$

and

$$u_m' \to \tfrac{1}{2}(u_1' + u_2') \tag{18}$$

This represents the limiting case of a parallel-walled duct, and is the approximate relation derived by Ruden[2] for flow through a cascade in a cylindrical annulus. The expression was found to be a very close approximation to exact solutions obtained by Bragg and Hawthorne[3].

The throughflow velocity perturbations within the duct may be written in a more convenient form

$$\left.\begin{aligned} \frac{u'}{r} &= \frac{1}{2}\left(\frac{u_2'}{r_2}-\frac{u_1'}{r_1}\right)\left(\frac{r}{r_m}\right)^{p-2}+\frac{u_1'}{r_1} \quad \text{upstream of cascade} \\ \frac{u'}{r} &= -\frac{1}{2}\left(\frac{u_2'}{r_2}-\frac{u_1'}{r_1}\right)\left(\frac{r_m}{r}\right)^{p+2}+\frac{u_2'}{r_2} \quad \text{downstream of cascade} \end{aligned}\right\} \tag{19}$$

In order to relate this solution to that for the transverse components of velocity it is necessary to match the stagnation pressure at the cascade. For a stationary cascade no work is done on the fluid, and the stagnation pressure

$$p_0 = p+\tfrac{1}{2}\rho(u^2+v^2+w^2)$$

remains constant along a streamline.

Equation (2) may be written

$$\frac{1}{r}\frac{\partial p_0}{\rho\partial r} = \frac{w}{r}\frac{\partial w}{\partial\theta}-u\eta \doteq \frac{w}{r}\frac{\partial w}{\partial\theta}-\frac{C}{r}\eta \tag{20}$$

By matching $\partial p_0/\partial\theta$ at the cascade the equation

$$w_2\frac{\partial w_2}{\partial\theta}-w_1\frac{\partial w_1}{\partial\theta} = C\left(\frac{1}{r_2}\frac{\partial u_2'}{\partial\theta}-\frac{1}{r_1}\frac{\partial u_1'}{\partial\theta}\right)$$

is obtained, and upon integration

$$\frac{w_2^2-w_1^2}{2} = U_m r_m\left(\frac{u_2'}{r_2}-\frac{u_1'}{r_1}\right)+\text{constant} \tag{21}$$

Two distinct problems may be solved using (17), (19) and (21).

(a) *Direct problem.* If the inlet flow (η_1 or u_1 and w_1) to a specified cascade is given then, a solution to the outflow at radius r_2 and to the flow throughout the duct may be obtained.

The transverse velocity component w_2 will be imparted by the cascade of given outlet angle α_m such that

$$\begin{aligned} w_2 = w_m &= u_m\tan\alpha_m \\ &= \left\{U_m+\frac{r_m}{2}\left(\frac{u_1'}{r_1}+\frac{u_2'}{r_2}\right)\right\}\tan\alpha_m \end{aligned} \tag{22}$$

This equation may be used with equation (21) to give a solution for u_2' and w_2. Velocity components elsewhere are obtained from equation (19).

(b) *Indirect problem.* If an inlet flow ($u_1 w_1$) is specified, then the cascade outlet angles to produce a specified fluid outlet angle or transverse velocity w_2 can be found.

Vol. 3
1961

The equation

$$w_2 = (U_2 + u_2') \tan \alpha_2$$

and equation (21) may be solved for either u_2' and w_2 or u_2' and α_2, and then

$$\tan \alpha_m = \frac{(U_2 + u_2') \tan \alpha_2}{\{U_m + \tfrac{1}{2} r_m [(u_1'/r_1) + (u_2'/r_2)]\}} = \frac{w_2}{\{U_m + \tfrac{1}{2} r_m [(u_1'/r_1) + (u_2'/r_2)]\}} \tag{23}$$

4.0. SHEAR FLOW BETWEEN TWO CONICAL SURFACES, WITH ADDITION OF SWIRLING VELOCITY

A solution for the non-swirling shear flow through an annular passage between two cones with a common vertex [Fig. 1(b)] has been given in the first paper. The analysis may be extended to axisymmetric shear flows in which a swirling velocity component w is added in the ϕ direction. Similar solutions are obtained for the velocity components in any plane cross-section containing the axis, provided certain restrictions are imposed upon the distribution of w in the θ direction.

The equations of motion for axisymmetric flow are

$$\left.\begin{aligned} -\frac{1}{\rho r \sin\theta}\frac{\partial p}{\partial \phi} &= u\frac{\partial w}{\partial r} + \frac{v}{r}\frac{\partial w}{\partial \theta} + \frac{uw}{r} + \frac{vw\cot\theta}{r} = 0 \quad \text{(a)} \\ -\frac{1}{\rho r}\frac{\partial p}{\partial \theta} &= u\frac{\partial v}{\partial r} + \frac{v}{r}\frac{\partial v}{\partial \theta} + \frac{uv}{r} - \frac{w^2\cot\theta}{r} \quad \text{(b)} \\ -\frac{1}{\rho}\frac{\partial p}{\partial r} &= u\frac{\partial u}{\partial r} + \frac{v}{r}\frac{\partial u}{\partial \theta} - \frac{v^2}{r} - \frac{w^2}{r} \quad \text{(c)} \end{aligned}\right\} \tag{24}$$

The components of vorticity are

$$\left.\begin{aligned} \xi &= \frac{1}{r}\frac{\partial w}{\partial \theta} + \frac{w}{r}\cot\theta \\ \zeta &= -\frac{\partial w}{\partial r} - \frac{w}{r} \\ \eta &= \frac{\partial v}{\partial r} + \frac{v}{r} - \frac{1}{r}\frac{\partial u}{\partial \theta} \end{aligned}\right\} \tag{25}$$

The continuity equation is

$$\frac{\partial u}{\partial r} + \frac{2u}{r} + \frac{1}{r}\frac{\partial v}{\partial \theta} + \frac{v}{r}\cot\theta = 0 \tag{26}$$

If the solutions for u' and v' of the non-swirling flow are to be valid, the restriction on w is that the tangential equation of motion (24a) must be satisfied. This equation may be written

$$u\frac{\partial}{\partial r}(wr\sin\theta) + \frac{v}{r}\frac{\partial}{\partial \theta}(wr\sin\theta) = 0 \tag{24a}$$

From equation (26) a stream function $\psi(r, \theta)$ may be defined such that

$$u = \frac{1}{r^2 \sin\theta} \frac{\partial \psi}{\partial \theta}, \quad v = -\frac{1}{r \sin\theta} \frac{\partial \psi}{\partial r}$$

Since

$$d\psi = \frac{\partial \psi}{\partial r} dr + \frac{\partial \psi}{\partial \theta} d\theta \tag{27}$$

and $d\psi/dt = 0$ along the stream surfaces in steady flow

$$u \frac{\partial \psi}{\partial r} + \frac{v}{r} \frac{\partial \psi}{\partial \theta} = 0$$

This equation together with equation (24a) shows that

$$wr \sin\theta = f(\psi). \tag{28}$$

The quantity $(wr \sin\theta)$ remains constant along the axisymmetric stream surfaces.

Vol. 3
1961

Elimination of the pressure derivatives from (24b) and (24c) together with equation (25) yields the equation

$$\frac{\partial \eta}{\partial r} - \frac{\eta}{r} + \frac{2wr}{C} \left\{ \frac{1}{r} \frac{\partial w}{\partial \theta} - \cot\theta \frac{\partial w}{\partial r} \right\} = 0 \tag{29}$$

where $C = Ur^2$.

As in Ref. (1) the continuity equation may be differentiated to give

$$\frac{\partial^2 v'}{\partial r^2} + \frac{4}{r} \frac{\partial v'}{\partial r} + \frac{2v'}{r} + \frac{1}{r^2} \frac{\partial}{\partial \theta} (v' \cot\theta) + \frac{1}{r^2} \frac{\partial^2 v'}{\partial \theta^2} = \frac{\partial \eta}{\partial r} + 3 \frac{\eta}{r} \tag{30}$$

These two equations together with (24a) and its solution (28) describe the flow.

The solutions for u' and v' derived in Ref. 1 are valid for swirling motion when

(a) the swirl is everywhere small,

(b) the swirl has a free vortex distribution,

$$wr \sin\theta = \text{constant}$$

In each of these cases the expression containing w in (29) is eliminated.

Two other solutions may be obtained for

(c) flows with constant stagnation pressure,

(d) flows with non-uniform stagnation pressure.

These four solutions are now dealt with in greater detail.

4.1. *Small swirl perturbation*

If $w = w'$ and is of the order of u' and v', equation (29) may be written

$$\frac{\partial \eta}{\partial r} - \frac{\eta}{r} = 0$$

and

$$\eta/r = \Theta$$

The solution for u' and v' of Ref. 1 is valid, the influence of w' on these velocity perturbations being negligible.

Equation (24a) gives approximately

$$\frac{\partial(w'r)}{\partial r} = 0$$

and

$$w'r = f(\theta)$$

Constant values of $w'r$ may be superimposed upon the streamlines of the solution obtained with no swirl. The pressure gradient $\partial p/\partial\theta$ due to the swirl components of velocity is negligible.

4.2. *Free vortex swirl*

One solution of (24a) is

$$wr\sin\theta = \text{constant}$$

or

$$wR = K$$

where $R = r\sin\theta$ is the radial distance from the axis.

The flow has a "free vortex" swirl, although tangential vorticity and non-uniformity of stagnation pressure may exist, and η/r is again a function of θ only. The solution of Ref. 1 for u' and v' is valid if the boundary conditions are changed from constant static pressure to conditions of radial equilibrium at inlet and outlet radii r_1 and r_2.

Radial equilibrium is achieved when the fluid flows along cylindrical streamlines (Fig. 3) and

$$u\sin\theta + v\cos\theta = 0$$

From the continuity equation (26) it follows that

$$\frac{\partial}{\partial r}(vr) = \tan\theta\frac{\partial v}{\partial\theta} \doteqdot 0 \tag{31}$$

for small values of θ, as in the solution without swirl. At inlet and outlet

$$\frac{1}{\rho}\frac{\partial p}{\partial\theta} = w^2\cot\theta$$

from equation (24b). Thus a free vortex swirl with its associated pressure gradient may be superimposed upon the solution for non-swirling flow.

4.3. *Swirling flow with constant stagnation pressure*

The equations of motion may be written

$$\left.\begin{aligned} \frac{1}{\rho}\frac{\partial p_0}{\partial r} &= v\eta - w\zeta \\ \frac{1}{\rho r}\frac{\partial p_0}{\partial\theta} &= w\xi - u\eta \\ \frac{1}{\rho r\sin\theta}\frac{\partial p_0}{\partial\phi} &= u\zeta - v\xi \end{aligned}\right\} \tag{32}$$

If the stagnation pressure is constant

$$\xi/u = \zeta/v = \eta/w$$

and from equation (28) $\eta r \sin\theta = f(\psi)$, or approximately $\eta r = g(\theta)$ a function of θ only, for small displacements of the streamlines from the conical generators.

The solution of (30) is then

$$v' = \sum_1^\infty \left\{ A_n r^{n-1} + B_n r^{-n-2} + \frac{2a_n}{2-k_n} \right\} \left\{ P'_n(\cos\theta) + \frac{b_n}{a_n} Q'_n(\cos\theta) \right\}$$

$$u' = \sum_1^\infty \left\{ nA_n r^{n-1} - (n+1) B_n r^{-n-2} + \frac{a_n}{2-k_n} \right\} \left\{ P_n(\cos\theta) + \frac{b_n}{a_n} Q_n(\cos\theta) \right\}$$

Constant values of $(wr\sin\theta)$ may be superimposed along axisymmetric stream surfaces.

It is of interest to note the difference between the solutions for the tangential vorticity in this case and in the free vortex case.

4.4. *Flows with non-uniform stagnation pressure*

Equation (29) may be written

$$\frac{\partial\eta}{\partial r} - \frac{\eta}{r} + 2\left(\frac{w\xi}{ur}\right)\left\{1 - \frac{v}{u}\cot\theta\right\} = 0 \qquad (29a)$$

From (24a) $\quad wr\sin\theta \doteq f(\theta) \quad$ if $\quad v' \ll U$

and $$\frac{w\xi}{ur} \doteq \frac{(wr\sin\theta)}{Cr^2\sin\theta}\frac{\partial}{\partial\theta}(wr\sin\theta) \doteq \frac{f(\theta)}{r^2}$$

If $v'/u \ll \tan\theta$,* equation (29a) has the approximate solution,

$$\eta/r = f_1(\theta) + f_2(\theta)/r^2$$

The following solution of equation (30) is then obtained:

$$v' = \sum_1^\infty \left\{ A_n r^{n-1} + B_n r^{-n-2} + \frac{2a_n}{2-k_n} + \frac{4c_n r^2}{12-k_n} \right\} \left\{ P'_n(\cos\theta) + \frac{b_n}{a_n} Q'_n(\cos\theta) \right\}$$

$$u' = \sum_1^\infty \left\{ nA_n r^{n-1} - (n+1) B_n r^{-n-2} + \frac{a_n k_n}{2-k_n} + \frac{c_n k_n r^2}{12-k_n} \right\} \left\{ P_n(\cos\theta) + \frac{b_n}{a_n} Q_n(\cos\theta) \right\}$$

where $$f_1(\theta) = \sum_1^\infty \{a_n P'_n(\cos\theta) + b_n Q'_n(\cos\theta)\}$$

$$f_2(\theta) = \sum_1^\infty \{c_n P'_n(\cos\theta) + d_n Q'_n(\cos\theta)\}$$

* The order of $\dfrac{v'/u}{\tan\theta}$ may be found as follows:

$$\frac{v'/u}{\tan\theta} = \frac{v'}{u'} \cdot \frac{1}{\tan\theta} \cdot \frac{u'}{u}$$

$$= 0\left| \frac{1}{r} \cdot \frac{1}{\tan\theta} \cdot \frac{u'}{U} \right|$$

$$= 0\left| \frac{\theta_2 - \theta_1}{\tan\theta} \cdot \frac{1}{\pi} \cdot \frac{u'}{U} \right|$$

$$\doteq 0{\cdot}055$$

if $\quad \dfrac{\theta_1}{\theta_2} = 0{\cdot}4, \quad \left(\dfrac{u'}{U}\right)_{\max} = 0{\cdot}2$

and $\quad \theta = \frac{1}{2}(\theta_1 + \theta_2)$

Vol. 3
1961

and in order to satisfy the wall-boundary conditions that v' is zero at θ_1 and θ_2 for all values of r

$$\frac{b_n}{a_n} = \frac{d_n}{c_n} = -\frac{P'_n(\cos\theta_1)}{Q'_n(\cos\theta_1)} = -\frac{P'_n(\cos\theta_2)}{Q'_n(\cos\theta_2)}$$

These solutions for u' and v' contain a linear combination of the two individual solutions of Sections (4.2) and (4.3), and are valid for any type of swirl and gradient of stagnation pressure provided that u' and v' remain small perturbations and $v'/U \ll \tan\theta$.

The equation of radial equilibrium

$$\frac{1}{\rho r}\frac{\partial p_0}{\partial \theta} = \frac{w}{\sin\theta}\frac{1}{r^2}\frac{\partial}{\partial\theta}(wr\sin\theta) + \frac{u}{r}\frac{\partial u'}{\partial\theta}$$

shows this restriction upon the magnitude and distribution of w and p_0. It can be seen also that the solutions are valid for flows with very large swirling components, provided that the distribution is close to that of a free vortex,

$$w = \frac{K}{r\sin\theta} + w'$$

where w' is of the order of u'.

5.0. Flows through cascades placed in the conical annulus

It is now possible to consider the flow through an annular actuator cascade situated at radius r_m midway between inlet and outlet radii r_1 and r_2. In passing

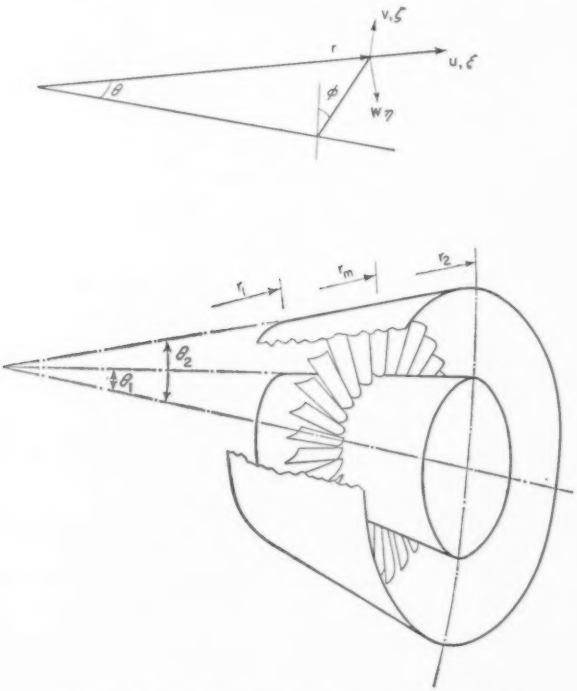

Fig. 2. Co-ordinate system for swirling flows.

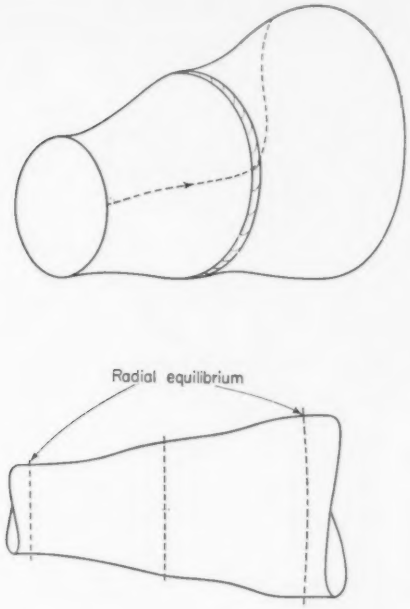

FIG. 3. Axisymmetric stream surfaces.

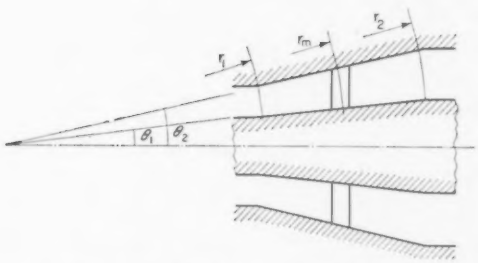

FIG. 4. Model for stator blade row.

Example 1

$$\theta_1 = 10^\circ\,43' \qquad r_2/r_m = r_m/r_1 = 1{\cdot}2$$
$$\theta_2 = 19^\circ\,37' \qquad \lambda = 1{\cdot}44$$
$$\alpha_1 = 20^\circ$$

$$\tan\alpha = \frac{\tan\alpha_1 \sin\theta}{\sin\theta_1}$$

Example 2

$$\theta_1 = 4^\circ\,50' \qquad r_2/r_m = r_m/r_1 = 1{\cdot}141$$
$$\theta_2 = 10^\circ\,12' \qquad \lambda = 1{\cdot}3$$
$$\alpha_1 = 69^\circ\,30'$$

$$\tan\alpha = \frac{\tan\alpha_1 \sin\theta_1}{\sin\theta}$$

through the cascade the fluid undergoes a sudden change in tangential velocity and vorticity, within the restrictions outlined in Section 4. As in the two-dimensional duct flow, u' and v' are matched at the cascade, and for a stationary cascade the stagnation pressure remains constant along streamlines. These two conditions along with selected inlet and outlet boundary conditions determine the flow through the duct. Cascades producing the four types of swirling flow discussed above are now considered.

5.1. *Small swirl perturbation*

The solutions for u', v' and η, being independent of w, are identical to those given in Ref. 1 for the flow through a duct with constant static pressure at inlet and outlet. For a specified cascade the distribution of w' will be

$$w' = \frac{w_1' r_1}{r} \qquad \text{upstream}$$

$$w' = \frac{u_m r_m}{r} \tan \alpha_m \qquad \text{downstream}$$

where suffix m refers to conditions at the cascade and α_m is the cascade outlet angle.

5.2. *Free vortex swirl with non-uniform stagnation pressure*

Since ξ is zero

$$\frac{1}{\rho r} \frac{\partial p_0}{\partial \theta} = -u\eta$$

and there is no change in tangential vorticity as the fluid passes through the cascade.

The solutions for u', v' and η are as in the previous case. The cascade outlet angle required to produce this free vortex swirl distribution is

$$\tan \alpha = \frac{k}{u_m r_m} \sin \theta$$

For small values of θ,

$$u_m \doteq (r_m/r_1)^2 u_1' + (r_1/r_m)^2 U_1$$

5.3. *Swirling flows with constant stagnation pressure*

If the condition of radial equilibrium exists at inlet and outlet, then equation (31) yields

$$nA_1 r_1^{n-1} - (n+1) B_1 r_1^{-n-2} + \frac{2a_1}{2-k} = 0$$

$$nA_2 r_2^{n-1} - (n+1) B_2 r_2^{-n-2} + \frac{2a_2}{2-k} = 0$$

dropping suffixes and considering the nth term. Matching u' and v' at the

cascade,

$$nA_1 r_m^{n-1} - (n+1) B_1 r_m^{-n-2} + \frac{a_1 k}{2-k} = nA_2 r_m^{n-1} - (n+1) B_2 r_m^{-n-2} + \frac{a_2 k}{2-k}$$

$$A_1 r_m^{n-1} + B_1 r_m^{-n-2} + \frac{2a_1}{2-k} = A_2 r_m^{n-1} + B_2 r_m^{-n-2} + \frac{2a_2}{2-k}$$

These equations may be written

$$nx_1 \lambda_1 - (n+1) y_1 \mu_1 + z_1 = 0$$

$$nx_2 \lambda_2 - (n+1) y_2 \mu_2 + z_2 = 0$$

$$nx_1 - (n+1) y_1 + \frac{kz_1}{2} = nx_2 - (n+1) y_2 + \frac{kz_2}{2}$$

$$x_1 + y_1 + z_1 = x_2 + y_2 + z_2$$

where

$$x_1 = A_1 r_m^{n-1} \qquad x_2 = A_2 r_m^{n-1}$$

$$y_1 = B_1 r_m^{-n-2} \qquad y_2 = B_2 r_m^{-n-2}$$

$$\lambda_1 = (r_1/r_m)^{n-1} \qquad \lambda_2 = (r_2/r_m)^{n-1}$$

$$\mu_1 = (r_1/r_m)^{-n-2} \qquad \mu_2 = (r_2/r_m)^{-n-2}$$

$$z_1 = \frac{2a_1}{2-k} \qquad z_2 = \frac{2a_2}{2-k}$$

For large values of n, z_1 and z_2 both approach zero, but μ_1 and λ_2 approach infinity. Then from the first two equations it is seen that x_2 and y_1 must approach zero. Putting them equal to zero in the second two equations yields the solution

$$x_1 = -\frac{(a_2 - a_1)}{2n}, \quad y_1 = 0$$

$$x_2 = 0, \qquad y_2 = -\frac{(a_2 - a_1)}{2n}$$

The solution for u' and v' is

$$\left.\begin{aligned} u' &= -\sum_1^\infty \left\{ \tfrac{1}{2}(a_2 - a_1) \left(\frac{r}{r_m}\right)^{n-1} + a_1 \right\} \left\{ P + \frac{b_1}{a_1} Q \right\} \\ v' &= -\sum_1^\infty \left\{ \tfrac{1}{2}(a_2 - a_1) \left(\frac{r}{r_m}\right)^{n-1} - \frac{2a_1}{n} \right\} \left\{ \frac{P' + (b_1/a_1) Q'}{n} \right\} \end{aligned}\right\} \text{ upstream of } r_m$$

$$\left.\begin{aligned} u' &= \sum_1^\infty \left\{ \tfrac{1}{2}(a_2 - a_1) \left(\frac{r}{r_m}\right)^{-n-2} - a_2 \right\} \left\{ P + \frac{b_1}{a_1} Q \right\} \\ v' &= -\sum_1^\infty \left\{ \tfrac{1}{2}(a_2 - a_1) \left(\frac{r}{r_m}\right)^{-n-2} - \frac{2a_2}{n} \right\} \left\{ \frac{P' + (b_1/a_1) Q'}{n} \right\} \end{aligned}\right\} \text{ downstream of } r_m$$

Vol. 3
1961

For purposes of calculation of the throughflow velocity profile these results may be expressed in terms of conditions at the boundaries,

$$u_1' = -a_1\left\{P + \frac{b_1}{a_1}Q\right\} \quad \text{at inlet}$$

$$u_2' = -a_2\left\{P + \frac{b_1}{a_1}Q\right\} \quad \text{at outlet}$$

$$u_m' = \tfrac{1}{2}\{u_1' + u_2'\} \quad \text{at the cascade}$$

Elsewhere
$$u' = u_1' + \tfrac{1}{2}(u_2' - u_1')\,(r/r_m)^{n-1} \quad \text{upstream}$$
$$u' = u_2' - \tfrac{1}{2}(u_2' - u_1')\,(r/r_m)^{-n-2} \quad \text{downstream}$$

The distribution of tangential velocity is found by superimposing constant values of $(wr\sin\theta)$ along axisymmetric stream surfaces. The stream surface pattern may be obtained by integration of the mass flow.

5.4. *Swirling flows with non-uniform stagnation pressure*

If the boundary conditions are the same as in the previous Section, then

$$\left.\begin{aligned} u' &= -\sum_1^\infty \left\{\left[\tfrac{1}{2}(a_2 - a_1)\left(\frac{r}{r_m}\right)^{n-1} + a_1\right] \right. \\ &\quad \left. + \left[\tfrac{1}{2}(c_2 - c_1)\left(\frac{r}{r_m}\right)^{n-1} + c_1\right] r^2\right\}\left\{P + \frac{b_1}{a_1}Q\right\} \\ v' &= -\sum_1^\infty \left\{\left[\tfrac{1}{2}(a_2 - a_1)\left(\frac{r}{r_m}\right)^{n-1} - \frac{2a_1}{n}\right] \right. \\ &\quad \left. + \left[\tfrac{1}{2}(c_2 - c_1)\left(\frac{r}{r_m}\right)^{n-1} - \frac{2c_1}{n}\right] r^2\right\}\left\{\frac{P' + (b_1/a_1)Q'}{n}\right\} \end{aligned}\right\} \text{upstream}$$

$$\left.\begin{aligned} u' &= \sum_1^\infty \left\{\left[\tfrac{1}{2}(a_2 - a_1)\left(\frac{r}{r_m}\right)^{-n-2} - a_2\right] \right. \\ &\quad \left. + \left[\tfrac{1}{2}(c_2 - c_1)\left(\frac{r}{r_m}\right)^{-n-2} - c_2\right] r^2\right\}\left\{P + \frac{b_1}{a_1}Q\right\} \\ v' &= -\sum_1^\infty \left\{\left[\tfrac{1}{2}(a_2 - a_1)\left(\frac{r}{r_m}\right)^{-n-2} - \frac{2a_2}{n}\right] \right. \\ &\quad \left. + \left[\tfrac{1}{2}(c_2 - c_1)\left(\frac{r}{r_m}\right)^{-n-2} - \frac{2c_2}{n}\right] r^2\right\}\left\{\frac{P' + (b_1/a_1)Q'}{n}\right\} \end{aligned}\right\} \text{downstream}$$

At the boundaries

$$u_1' = -\{a_1 + c_1 r_1^2\}\left\{P + \frac{b_1}{a_1}Q\right\} \quad \text{at inlet}$$

$$u_2' = -\{a_2 + c_2 r_2^2\}\left\{P + \frac{b_1}{a_1}Q\right\} \quad \text{at outlet}$$

$$u_m' = -\left\{\frac{a_1 + a_2}{2} + \frac{c_1 + c_2}{2} r_m^2\right\}\left\{P + \frac{b_1}{a_1}Q\right\} \quad \text{at the cascade}$$

It is of interest to write these perturbations as the sum of two components u'' and u''' represented by coefficients a and c. One component (u'') is induced

by the vorticity initially present. The other component (u''') is induced by vorticity created at the cascade.

Then
$$\frac{u''_m}{r_m^2} = \frac{1}{2}\left(\frac{u''_1}{r_1^2} + \frac{u''_2}{r_2^2}\right)$$
$$u'''_m = \tfrac{1}{2}(u'''_1 + u'''_2)$$

If $(r_2 - r_m)$ and $(r_m - r_1)$ remain constant as the duct angle is reduced to zero, for the limiting case of a cylindrical duct
$$u'_m \to \tfrac{1}{2}(u'_1 + u'_2)$$
which is the approximate relation derived by Ruden[2]. Elsewhere within the duct
$$u' = \left[\frac{u''_1}{r_1^2} + \frac{1}{2}\left(\frac{u''_2}{r_2^2} - \frac{u''_1}{r_1^2}\right)\left(\frac{r}{r_m}\right)^{n-1}\right] r^2 + \left[u'''_1 + \tfrac{1}{2}(u'''_2 - u'''_1)\left(\frac{r}{r_m}\right)^{n-1}\right] \quad \text{upstream of } r_m$$
$$u' = \left[\frac{u''_2}{r_2^2} - \frac{1}{2}\left(\frac{u''_2}{r_2^2} - \frac{u''_1}{r_1^2}\right)\left(\frac{r}{r_m}\right)^{-n-2}\right] r^2 + \left[u'''_2 - \tfrac{1}{2}(u'''_2 - u'''_1)\left(\frac{r}{r_m}\right)^{-n-2}\right] \quad \text{downstream of } r_m$$

The tangential velocity is superimposed as in Section 4.4, i.e.
$$wr\sin\theta = \text{constant}$$
along lines of constant θ.

CONCLUSIONS

The solution for the non-uniform flow through an actuator cascade in a two-dimensional wedge-shaped duct has been given. The throughflow velocity perturbation is given by
$$\frac{u'}{r} = \frac{1}{2}\left(\frac{u'_2}{r_2} - \frac{u'_1}{r_1}\right)\left(\frac{r}{r_m}\right)^{p-2} + \frac{u'_1}{r'_1} \quad \text{upstream}$$
$$\frac{u'}{r} = -\frac{1}{2}\left(\frac{u'_2}{r_2} - \frac{u'_1}{r_1}\right)\left(-\frac{r}{r_m}\right)^{-p-2} + \frac{u'_2}{r_2} \quad \text{downstream}$$
$$\frac{u'_m}{r_m} = \frac{1}{2}\left(\frac{u'_1}{r_1} + \frac{u'_2}{r_2}\right) \quad \text{at the cascade}$$

If $(r_2 - r_m)$, $(r_m - r_1)$ and $(r_m\theta_1 = l)$ are fixed and θ is reduced to zero, it can be shown that the solution approaches that obtained in Cartesian co-ordinates for a parallel-walled duct, provided $(r_2 - r_m)$ and $(r_m - r_1)$ are large, and
$$x = (r - r_m)$$
$$u' = \tfrac{1}{2}(u'_2 - u'_1)\exp\left(\frac{\pi x}{l}\right) + u'_1 \quad \text{upstream}$$
$$u' = -\tfrac{1}{2}(u'_2 - u'_1)\exp\left(-\frac{\pi x}{l}\right) + u'_2 \quad \text{downstream}$$
$$u'_m = \tfrac{1}{2}(u'_1 + u'_2) \quad \text{at the cascade}$$

Vol. 3
1961

The tangential components of velocity and vorticity remain constant along the stream surfaces. For flows with small variations in the tangential velocity this component remains constant along radial lines.

Four solutions for swirling flows through conical ducts have been presented. The solutions for u' and v' obtained in Ref. (1) apply to the first two of these.

(a) Flows with small swirling velocity components.

(b) Flows with a large free vortex swirl.

Two new solutions have been obtained for

(c) Flows with uniform stagnation pressure.

(d) Flows with non-uniform stagnation pressure.

These flows differ from one another in the distribution of the tangential vorticity.

In (a) and (b) as in Ref. (1)

$$\frac{\eta}{r} = f(\theta)$$

and η is attributed entirely to gradients of stagnation pressure (forming "smoke ring" vortices). There is no component of vorticity along the conical generators. In (c), where the stagnation pressure is constant,

$$\eta r = f(\theta)$$

In this case, η is the resolved component of the vorticity shed from the cascade, the vector direction of which coincides with that of the helical streamlines.

In (d)
$$\eta = r f_1(\theta) + \frac{1}{r} f_2(\theta)$$

which is a combination of the vorticity components existing in the two previous cases. One component is due to gradients of stagnation pressure ("smoke ring" vortices) and the other component is the resolved component of the streaming vorticity shed from the cascade.

Two examples of swirling flows (c) and (d) have been given. In the first example, a flow with constant stagnation pressure passes through a duct containing a "forced vortex" cascade. In the second example, a non-uniform flow passes through a duct containing a free vortex cascade.

APPENDIX I

Example 1—*Constant stagnation pressure*

The outlet angles of a stationary cascade placed at radius r_m in a divergent duct (Fig. 4) are such that solid rotation would be produced by a constant axial velocity at the cascade,

$$\tan \alpha = \tan \alpha_1 \frac{\sin \theta}{\sin \theta_1}$$

where α_1 is the outlet angle at the root section ($\theta = \theta_1$).

The flow throughout the duct may be found in three stages:

(a) by applying the radial equilibrium equation to obtain u_2' in terms of w and then α,

(b) by representing u_2' as an infinite series of Legendre polynomials,

(c) by combining (a) and (b) to obtain the flow field elsewhere in the duct.

(a) *Radial equilibrium at outlet.* If the stagnation pressure is constant

$$\frac{1}{\rho r}\frac{\partial p_0}{\partial \theta} = w\xi - u\eta = 0$$

The condition for radial equilibrium is that

$$\frac{\partial v'}{\partial r} + \frac{v'}{r} = 0$$

Vol. 3
1961

and neglecting second orders of small terms the radial equilibrium equation for constant p_0 becomes

$$\frac{w}{\sin\theta}\frac{\partial}{\partial \theta}(w\sin\theta) + \frac{C}{r^2}\frac{\partial u}{\partial \theta} = 0$$

Also $$wr\sin\theta = f(\psi)$$

but if the initial assumption is made that

$$wr\sin\theta = f(\theta)$$

then at r_2

$$w_2 = \frac{r_m}{r_2}\frac{\tan\alpha_1}{\sin\theta_1}\left(U_m + \frac{u_1' + u_2'}{2}\right)\sin\theta$$

If the fluid enters without swirl at r_1 then u_1' is zero. This expression is substituted in the radial equilibrium equation, second orders of small quantities are neglected and the equation is integrated, u_2' being obtained in terms of α

$$\frac{u_2'}{U_2} = \left[\frac{K/U_m}{\{1+(\beta\sin\theta)^2\}^2} - 1\right]\left(\frac{r_2}{r_m}\right)^2$$

where $$\beta = \frac{1}{\sqrt{2}}\frac{\tan\alpha_1}{\sin\theta_1}$$

The unknown constant K may be found by integrating the mass flow across the annulus,

$$\int_{\theta_1}^{\theta_2} u_2'\sin\theta\, d\theta = 0$$

In this example the solution becomes

$$\frac{u_2'}{U_2} = \left[\frac{1{\cdot}29766}{(1+1{\cdot}9153\sin^2\theta)^2} - 1\right]1{\cdot}44$$

which is shown in Fig. 7. The distribution of w_2/u_2 with respect to θ is given by

$$\frac{w_2}{u_2} = \left(\frac{r_2}{r_m}\right)\left[1 - \frac{1}{2}\left(\frac{r_m}{r_2}\right)^2\frac{u_2'}{U_2}\right]$$

and $\tan \alpha_2$ is given by

$$\tan \alpha_2 = \frac{w_2/U_2}{1+(u_2'/U_2)}$$

The true positions of the stream surfaces at r_1 and r_2 have been calculated by integrating the mass flow across the annulus, and are compared with the assumption of conical flow in Fig. 5.

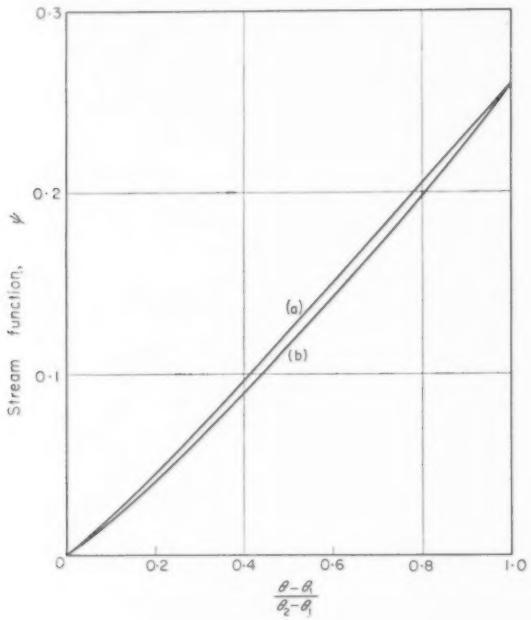

Fig. 5. Location of stream surfaces at r_m and r_2.

(a) At outlet r_2

$$\psi = \int_{\theta_1}^{\theta_2} \frac{[(u_2'/U_2)+1]\sin\theta\, d\theta}{\theta_2-\theta_1}$$

(b) At cascade r_m

$$\psi = \int_{\theta_1}^{\theta_2} \frac{[\frac{1}{2}(r_m/r_2)^2\,(u_2'/U_2)+1]\sin\theta\, d\theta}{\theta_2-\theta_1}$$

Fig. 6 shows the error in α_2 so introduced, which has a maximum value of $0°24'$.

(b) *Axial velocity throughout the duct.* In order to compute the axial velocity profile elsewhere in the duct, u_2' must be expressed as an infinite series of Legendre polynomials. The eigenvalues for a particular value of θ_1 and θ_2 are obtained from the identity

$$P_n'(\cos\theta_1)Q_n'(\cos\theta_2) - P_n'(\cos\theta_2)Q_n'(\cos\theta_1) = 0$$

This is satisfied by unique non-integer values of n. If $\theta_2-\theta_1$ is small all values of n are large, and asymptotic expressions for $P_n'(\cos\theta)$ and $Q_n'(\cos\theta)$ may be used. (For example, in this problem the smallest value of $n = 20$.)

The identity then simplifies to

$$\sin(n+\tfrac{1}{2})(\theta_2-\theta_1)=0,$$

and the eigenvalues are given by

$$n=\frac{N\pi}{\theta_2-\theta_1}-\tfrac{1}{2} \quad \text{where} \quad N=1,2,3,\ldots,\text{etc.}$$

and

$$\frac{b_n}{a_n}=\frac{2}{\pi}\left\{\frac{1-\tan[\theta_1/(\theta_2-\theta_1)]\,N\pi}{1+\tan[\theta_1/(\theta_2-\theta_1)]\,N\pi}\right\}$$

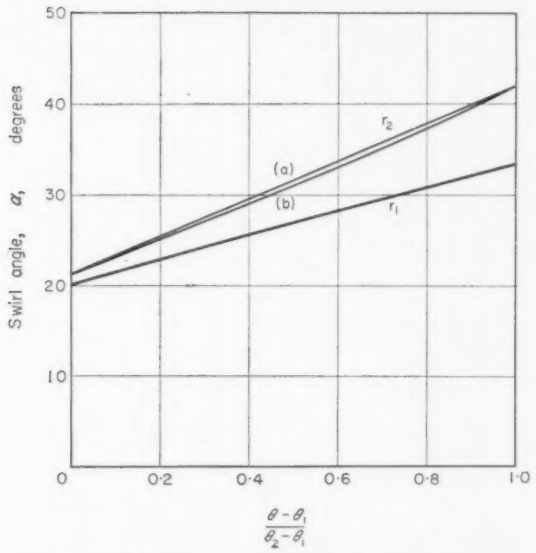

FIG. 6. Swirl angles downstream of forced vortex stator in a diverging duct (constant stagnation pressure). (a) Assuming $wr\sin\theta=f(\psi)$. (b) Assuming $wr\sin\theta=f(\theta)$.

The axial velocity profile has been fitted quite closely by a combination of the first two terms in the series (see Fig. 7)

$$\frac{u_2'}{U_2}=-0{\cdot}44\left\{\begin{matrix}P_{20}-0{\cdot}355Q_{20}\\0{\cdot}16(P_{40}-0{\cdot}347Q_{40})\end{matrix}\right\}$$

From Section (4.3), elsewhere in the duct

$$u'=\sum_1^\infty\left\{u_1'+\tfrac{1}{2}(u_2'-u_1')\left(\frac{r}{r_m}\right)^{n-1}\right\} \quad \text{upstream}$$

$$u'=\sum_1^\infty\left\{u_2'-\tfrac{1}{2}(u_2'-u_1')\left(\frac{r}{r_m}\right)^{n-2}\right\} \quad \text{downstream}$$

The higher terms in the series contribute a more rapidly changing perturbation, which causes a distortion of the axial velocity perturbation profile in the neighbourhood of the cascade. In this example, the second and higher terms are negligible compared with the first term in the series, and it is sufficiently

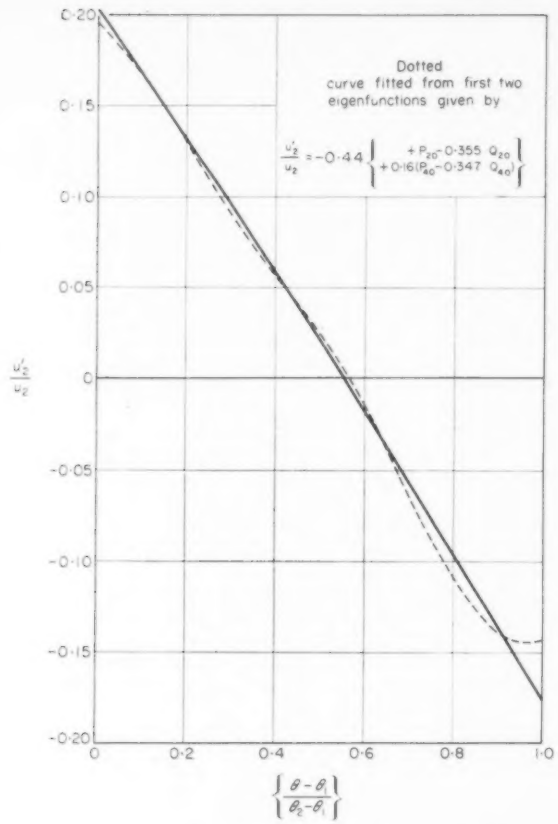

Fig. 7. Outlet axial velocity perturbation.

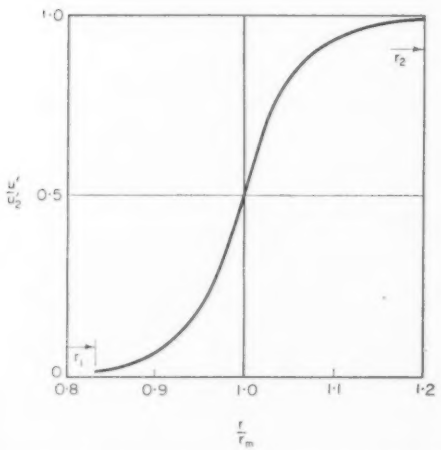

Fig. 8. Growth of axial velocity perturbation (constant stagnation pressure).

Vol. 3
1961

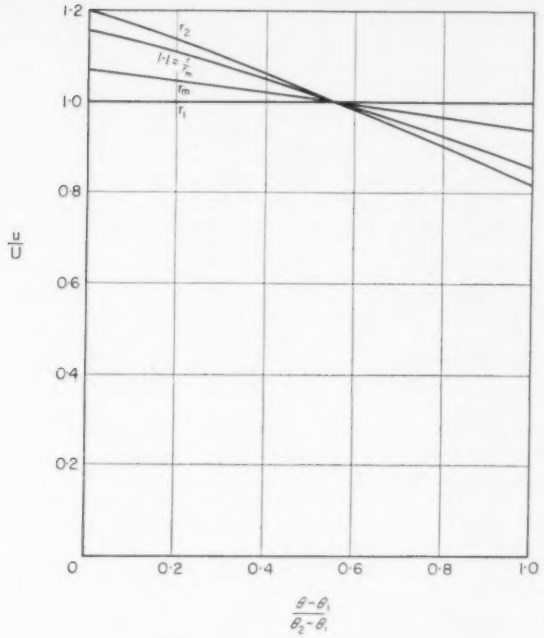

FIG. 9. Axial velocity profile with a forced vortex stator in a diverging duct.

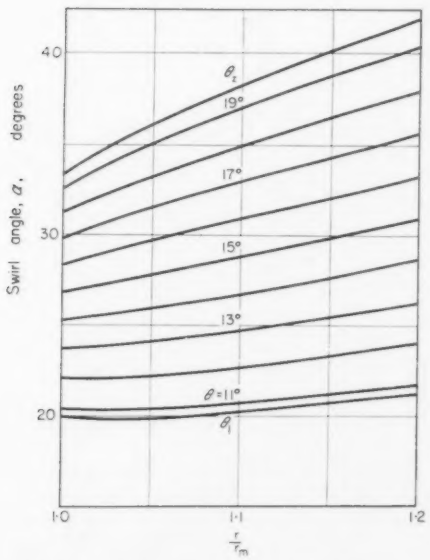

FIG. 10. Swirl angles downstream of a forced vortex stator.

accurate to write

$$\frac{u'}{u_2'} = \frac{1}{2}\left(\frac{r}{r_m}\right)^{18} \qquad \text{upstream}$$

$$\frac{u'}{u_2'} = 1 - \frac{1}{2}\left(\frac{r}{r_m}\right)^{-22} \qquad \text{downstream}$$

The growth of u'/u_2' is shown in Fig. 8.

The development of the actual velocity profile through the duct is shown in Fig. 9.

(c) *Swirl angles.* Combining (a) and (b)

$$\tan\alpha = \left(\frac{r}{r_m}\right)\left\{\frac{1+\frac{1}{2}(r_m/r_2)^2\,(u_2'/U_2)}{1+(u'/u_2')\,(r/r_2)^2\,(u_2'/U_2)}\right\}\tan\alpha_m$$

which is plotted in Fig. 10.

Example 2—Rotational flow through a free vortex cascade

In this example a free vortex cascade is located at r_m (see Fig. 4). Fluid enters the duct with non-uniform stagnation pressure and without swirl. The resulting swirl distribution downstream of the cascade differs slightly from that of a free vortex. Swirl angles may be predicted as follows.

By applying the solution obtained in Section 4.4 the problem is approached in the three stages explained in the previous example. Only the first step will be followed here, i.e. the distribution of u_2' and $wr\sin\theta$ will be calculated.

At the boundaries

$$\left.\begin{aligned} u_1' &= -\left(\frac{a_1}{2} + c_1 r_1^2\right)\Theta && \text{(a)}\\ &= -\left(\frac{a_2}{2} + c_2 r_2^2\right)\Theta && \text{(b)}\\ &= -\left\{\frac{(a_1+a_2)}{4} + \frac{(c_1+c_2)}{2} r_m^2\right\}\Theta && \text{(c)} \end{aligned}\right\} \qquad (1)$$

where

$$\Theta = P(\cos\theta) + \frac{b}{a}Q(\cos\theta)$$

Neglecting second orders of perturbation terms, equation (32b) of Section 4.3 may be written

$$\left.\begin{aligned} \frac{\partial p_0}{\rho\partial\theta} &= -U_1\eta_1 r_1 && \text{at } r_1 && && \text{(a)}\\ &= -U_m\eta_{mu} r_m && \text{at } r_m && \text{upstream} && \text{(b)}\\ &= -U_m\eta_{md} r_m + w_m\xi_m \ldots + w_m\xi_m r_m && \text{at } r_m && \text{downstream} && \text{(c)}\\ &= -U_2\eta_2 r_2 + w_2\xi_2 r_2 && \text{at } r_2 && && \text{(d)} \end{aligned}\right\} \qquad (2)$$

in which equations suffixes u and d refer to regions upstream and downstream of the cascade.

At the same locations the tangential vorticity components are

$$\left.\begin{aligned}
\eta_1 &= \frac{1}{r_1}\left(\frac{a_1}{2}+c_1 r_1^2\right)\Theta' = -\frac{1}{r_1}\frac{\partial u_1'}{\partial\theta} && \text{(a)}\\
\eta_{mu} &= \frac{1}{r_m}\left(\frac{a_1}{2}+c_1 r_m^2\right)\Theta' && \text{(b)}\\
\eta_{md} &= \frac{1}{r_m}\left(\frac{a_2}{2}+c_2 r_m^2\right)\Theta' && \text{(c)}\\
\eta_2 &= \frac{1}{r_2}\left(\frac{a_2}{2}+c_2 r_2^2\right)\Theta' = -\frac{1}{r_2}\frac{\partial u_2'}{\partial\theta} && \text{(d)}
\end{aligned}\right\} \qquad (3)$$

From (2a), (2b), (1a) and (3a) it can be shown that $a_1 = 0$, and since

$$w_2 r_2 \doteq w_m r_m$$

(2d) and (3a) may be combined to give

$$\begin{aligned}\left[1-\left(\frac{r_m}{r_2}\right)^2\right]\frac{\partial p_0}{\rho\,\partial\theta} &= -U_2[\eta_2 r_2 - \eta_{md} r_m]\\ &= -U_2 c_2 r_2^2\left[1-\left(\frac{r_m}{r_2}\right)^2\right]\Theta'\end{aligned}$$

From this equation and (2a), $\quad c_1 = c_2$

and equations (1) become

$$\left.\begin{aligned}
u_1' &= -c_1 r_1^2\,\Theta\\
u_2' &= -\left(\frac{a_2}{2}+c_1 r_2^2\right)\Theta\\
u_m' &= -\left(\frac{a_2}{4}+c_1 r_m^2\right)\Theta
\end{aligned}\right\} \qquad (4)$$

Elsewhere in the duct,

$$\begin{aligned}u' &= -\left\{\frac{a_2}{4}\left(\frac{r}{r_m}\right)^{n-1}+c_1 r^2\right\}\Theta && \text{upstream}\\ &= -\left\{-\frac{a_2}{4}\left(\frac{r}{r_m}\right)^{-n-2}+\frac{a_2}{2}+c_1 r^2\right\}\Theta && \text{downstream}\end{aligned}$$

The axial velocity perturbation has two components. One is induced by the tangential vorticity entering the duct at r_1 which develops exactly as in the absence of the cascade,

$$u'' = \left(\frac{r}{r_1}\right)^2 u_1'' = c_1 r^2\,\Theta$$

The other component is induced by the circulation shed from the cascade, and behaves in the manner of the component from the previous example.

$$\begin{aligned}\frac{u'''}{u_2'''} &= \frac{1}{2}\left(\frac{r}{r_m}\right)^{n-1} && \text{upstream}\\ &= 1-\frac{1}{2}\left(\frac{r}{r_m}\right)^{-n-2} && \text{downstream}\\ u_m''' &= \tfrac{1}{2}u_2''' && \text{at the cascade}\end{aligned}$$

Vol. 3
1961

The relation between u_1' and u_2' may be obtained from 2(b), (2c) and (4)

$$\frac{w_m \xi_m}{U_m} = \eta_{md} - \eta_{mu}$$

$$= \frac{1}{r_m}\frac{a_2}{2}\Theta'$$

$$= \frac{1}{r_m}\left(\frac{r_2}{r_1}\right)^2 \frac{\partial u_1'}{\partial \theta} - \frac{1}{r_m}\frac{\partial u_2'}{\partial \theta}$$

But

$$w_m \xi_m = \frac{w_m}{r_m \sin\theta}\frac{\partial}{\partial \theta}(w_m \sin\theta)$$

$$= \frac{U_m}{r_m}\tan^2\alpha \frac{\partial u_m'}{\partial \theta}$$

and

$$\tan^2\alpha \frac{\partial u_m'}{\partial \theta} = \left(\frac{r_2}{r_1}\right)^2 \frac{\partial u_1'}{\partial \theta} - \frac{\partial u_2'}{\partial \theta} \tag{5}$$

From (4)

$$\frac{\partial u_m'}{\partial \theta} = \left\{\left(\frac{r_m}{r_1}\right)^2 - \frac{1}{2}\left(\frac{r_2}{r_1}\right)^2\right\}\frac{\partial u_1'}{\partial \theta} + \frac{1}{2}\frac{\partial u_2'}{\partial \theta}$$

and (5) becomes

$$\frac{\partial u_2'}{\partial \theta} = \left(\frac{r_2}{r_1}\right)^2 \frac{\partial u_1'}{\partial \theta} - \left\{\frac{(r_m/r_1)^2 \tan^2\alpha}{1 + \frac{1}{2}\tan^2\alpha}\right\}\frac{\partial u_1'}{\partial \theta} \tag{6}$$

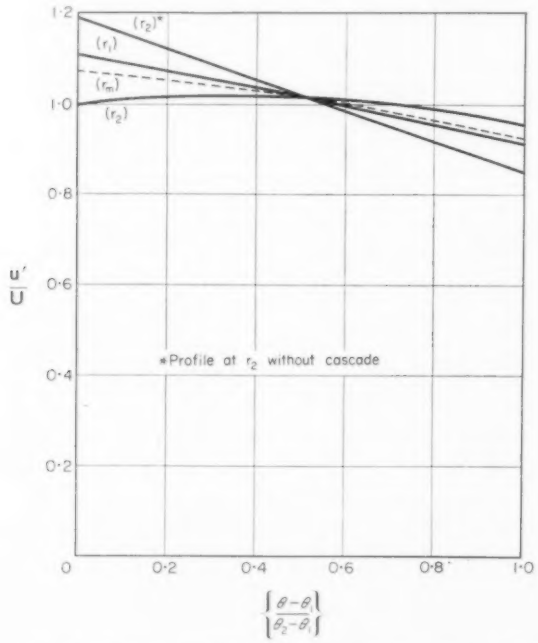

Fig. 11. Axial velocity profile with a free vortex stator in a diverging duct.

This relation between inlet and outlet axial velocity profiles shows the influence of the two superimposed vorticity fields. It is of interest to note that

the change in the outlet velocity u_2' induced by the shed circulation is opposite to that due to entering vorticity.

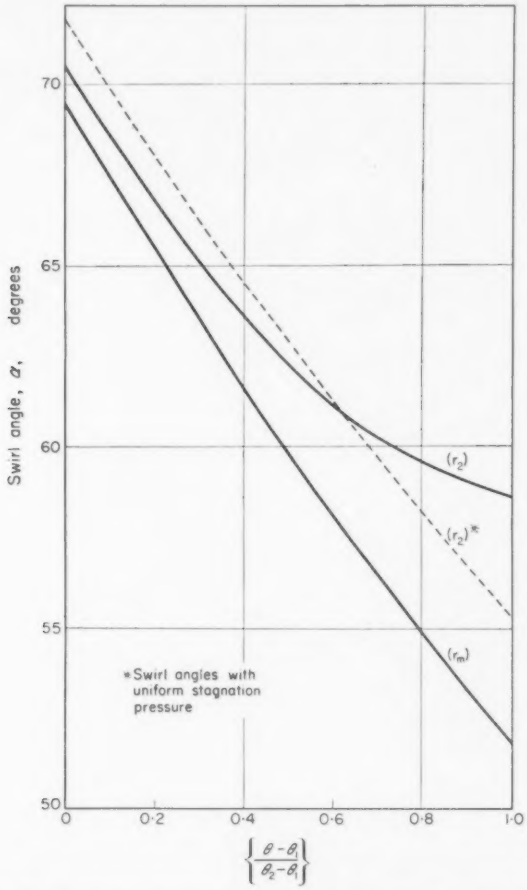

FIG. 12. Swirl angles downstream of a free vortex stator (non-uniform stagnation pressure).

A numerical example has been calculated to illustrate this effect. An irrotational flow through a free vortex cascade is first considered, and the outlet angles corresponding to this case are shown in Fig. 12. A rotational flow through the cascade is then considered, the entry axial velocity profile being

$$\frac{u_1'}{U_1} = A\sin\theta + B. \qquad \begin{matrix} A = -2{\cdot}157 \\ B = 0{\cdot}293 \end{matrix}$$

In this example the non-uniformities in the axial velocity profile are attenuated and almost reduced to zero at outlet (see Fig. 11). The growth of the same non-uniformities in the absence of a cascade is also shown in Fig. 11.

In Fig. 12 the outlet swirl angles are compared with those that would occur in the irrotational case. The inlet shear flow causes considerable departure of the swirl angles from the irrotational case, particularly at the outer casing wall.

REFERENCES

1. J. H. Horlock and R. I. Lewis, *Int. J. Mech. Sci.* **2**, 251 (1961).
2. F. Ruden, *Investigation of single stage axial flow fans.* NACA T.M. 1062 (1944).
3. S. L. Bragg and W. R. Hawthorne, *J. Aeronaut. Sci.* **17**, 243 (1950).
4. J. H. Horlock, *Some Actuator Disk Theories for the Flow of Air through an Axial Turbo-machine.* Aeronautical Research Council. R. & M. 3030 (December 1952).

Int. J. Mech. Sci. Pergamon Press Ltd. 1961. Vol. 3, pp. 197–218. Printed in Great Britain

THE INFLUENCE OF A CONCENTRATED MASS ON THE FREE VIBRATIONS OF A UNIFORM BEAM

J. C. MALTBAEK

Department of Mechanical Engineering, University of Birmingham

(*Received* 1 *September* 1960)

Summary—This paper treats the free vibrations of a uniform beam with elastic end constraints, and with a concentrated mass somewhere along the span.

The general frequency equation has been developed as a sixth-order determinant. From this determinant the frequency equations for many important cases have been derived.

Curves have been plotted for the first three roots of the frequency equations for six commonly encountered beam systems, for various mass ratios and positions of the concentrated mass.

NOTATION

a	frequency constant defined by $a^4 = \omega^2 A\gamma/EIg$ (in^{-1})
c	numerical factor
f	frequency (c/s)
g	acceleration due to gravity (in. sec^{-2})
k_1	ratio of support linear spring constant K_1 to beam stiffness K_B
k_2	ratio of support linear spring constant K_2 to beam stiffness K_B
l	length of beam (in.)
l_1, l_2	distance from end of beam to concentrated mass (in.)
m	mass of beam (lb-in^{-1} sec^2)
t_1	ratio of support rotational spring constant T_1 to beam rotational constant T_B
t_2	ratio of support rotational spring constant T_2 to beam rotational constant T_B
x, x_1, x_2	abscissa
y, y_1, y_2	ordinate
Z	frequency constant defined by $Z = al$
Z_1, Z_2	frequency constants defined by $Z_1 = Z(l_1/l)$, $Z_2 = Z(l_2/l)$
A	cross-sectional area of beam (in^2)
$C_1 \ldots C_4$ $D_1 \ldots D_4$	boundary constants (in.)
E	modulus of elasticity (lb-in^{-2})
I	second moment of area (in^4)
K, K_1, K_2	linear spring constants (lb-in^{-1})
K_B	beam stiffness constant $= EI/l^3$ (lb-in^{-1})
M	concentrated mass (lb-in^{-1} sec^2)
T_1, T_2	rotational spring constants (lb-in. rad^{-1})
T_B	beam rotational constant $= EI/l$ (lb-in.)
γ	density of beam material (lb-in^{-3})
ω	circular frequency (rad-sec^{-1})

1. FREQUENCY EQUATION

IN Fig. 1(a) is shown a beam with a concentrated mass. The beam is supported on linear and rotational springs acting in such a manner that a deflexion of the linear springs produces a force proportional to the deflexion and a rotation of the rotational springs produces a bending moment proportional to the angle of rotation.

The beam is considered uniform with a plane of symmetry in the vertical plane in which the vibrations occur.

The springs are considered massless and damping is neglected. The effects of rotatory inertia (gyroscopic effects) and deflexion due to shear force are also neglected.

The equation for the natural frequencies of the system is developed in the Appendix; the result is the following sixth-order determinant:

$$\begin{vmatrix} K_1 \sin Z_1 + Z^3 \cos Z_1 & -t_1 \cos Z_1 + Z \sin Z_1 & 0 & -1 & 0 & 0 \\ K_1 \cos Z_1 - Z^3 \sin Z_1 & t_1 \sin Z_1 + Z \cos Z_1 & -1 & -\frac{M}{2m} Z & 0 & \frac{M}{2m} Z \\ -K_1 \sinh Z_1 + Z^3 \cosh Z_1 & t_1 \cosh Z_1 + Z \sinh Z_1 & 0 & 0 & 0 & 1 \\ -K_1 \cosh Z_1 + Z^3 \sinh Z_1 & t_1 \sinh Z_1 + Z \cosh Z_1 & 0 & \frac{M}{2m} Z & 1 & -\frac{M}{2m} Z \\ 0 & 0 & K_2 \sin Z_2 + Z^3 \cos Z_2 & K_2 \cos Z_2 - Z^3 \sin Z_2 & -K_2 \sinh Z_2 + Z^3 \cosh Z_2 & -K_2 \cosh Z_2 + Z^3 \sinh Z_2 \\ 0 & 0 & -t_2 \cos Z_2 + Z \sin Z_2 & t_2 \sin Z_2 + Z \cos Z_2 & t_2 \cosh Z_2 + Z \sinh Z_2 & t_2 \sinh Z_2 + Z \cosh Z_2 \end{vmatrix} = 0 \tag{1}$$

In this determinant $Z = al$, where l = length of beam (in.), $a^4 = \omega^2 A\gamma/EIg$, ω is the natural circular frequency (rad-sec), A is the cross-sectional area of the beam (in^2), γ is the material density (lb-in^3), EI is the beam flexural rigidity (lb-in^2) and g is the acceleration due to gravity (in.-sec^2). $Z_1 = Z(l_1/l)$ and $Z_2 = Z(l_2/l)$, where l_1 is the distance from the left end point to the concentrated mass, and $l_1 + l_2 = l$, so that $Z_1 + Z_2 = Z$. M is the mass of the concentrated mass (lb-in^{-1} sec^2) and m is the mass of the beam (lb-in^{-1} sec^2).

The four constants k_1, t_1, k_2 and t_2 depend on the beam rigidity and the spring supports and are defined as follows:

$$k_1 = \frac{K_1 l^3}{EI}, \quad k_2 = \frac{K_2 l^3}{EI}, \quad t_1 = \frac{T_1 l}{EI} = \frac{T_1}{T_B}, \quad t_2 = \frac{T_2 l}{EI} = \frac{T_2}{T_B}$$

Where K_1 and K_2 are the linear spring constants of the end supports (lb-in.), T_1 and T_2 are the rotational spring constants of the end supports (lb-in. rad) and $T_B = EI/l$ (lb-in.) is the beam rotational constant. After a root Z has been

found from the frequency equation (1), the frequency is calculated from the expression

$$f = \frac{Z^2}{2\pi l^2}\sqrt{\left(\frac{EIg}{A\gamma}\right)} \quad \text{c.p.s.}$$

If the beam stiffness is defined as $K_B = EI/l^3$ (lb-in.) the frequency is $f = Z^2\sqrt{(K_B/m)}/2\pi$ c.p.s.

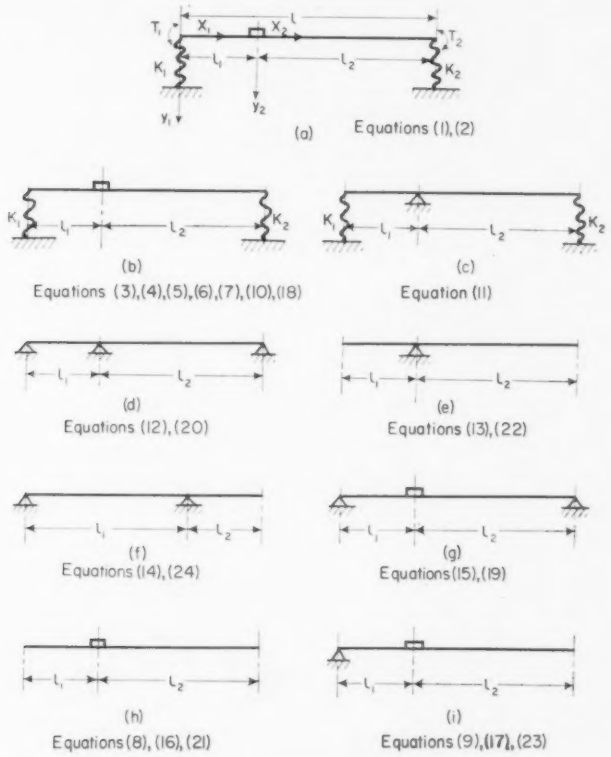

FIG. 1. (a) Uniform beam with a concentrated mass, elastically supported and elastically built-in. (b)–(i) Beam systems with no constraining moments at the ends.

In the cases where there is no concentrated mass the frequency equation is found by substituting $M = 0$, $Z_1 = 0$ and $Z_2 = Z$ in (1), when the result is

$$\begin{vmatrix} Z^3 & -k_1 & -Z^3 & -k_1 \\ t_1 & Z & t_1 & -Z \\ k_2 \sin Z & k_2 \cos Z & k_2 \sinh Z & k_2 \cosh Z \\ +Z^3 \cos Z & -Z^3 \sin Z & -Z^3 \cosh Z & -Z^3 \sinh Z \\ t_2 \operatorname{coz} Z & -t_2 \sin Z & t_2 \cosh Z & t_2 \sinh Z \\ -Z \sin Z & -Z \cos Z & +Z \sinh Z & +Z \cosh Z \end{vmatrix} = 0 \quad (2)$$

The determinant equation (2) has been discussed in Ref. 1 and will not be considered further here. The frequency equation developed from (1) is far too lengthy for practical use in the general case; it is simpler to calculate values directly from the determinant. The determinant can, however, be greatly simplified and expanded in many practical cases, some of which will be discussed in what follows.

Three classes of systems will be considered in more detail; the first class consists of beams with no restraining moments at the ends, the second class consists of beams with restraining moments but stiff supports and the third class is a combination of the first two.

2. UNIFORM BEAMS ON ELASTIC SUPPORTS

The system is shown in Fig. 1(b). Substituting the boundary conditions $t_1 = t_2 = 0$ in the determinant (1) gives the frequency equation

$$\begin{vmatrix} \cos Z_1 & \sin Z_1 & 0 & -1 & 0 & 0 \\ -\sin Z_1 & \cos Z_1 & -1 & -\frac{M}{2m}Z & 0 & \frac{M}{2m}Z \\ -\frac{2k_1}{Z^3}\sinh Z_1 + \cosh Z_1 & \sinh Z_1 & 0 & 0 & 0 & 1 \\ -\frac{2k_1}{Z^3}\cosh Z_1 + \sinh Z_1 & \cosh Z_1 & 0 & \frac{M}{2m}Z & 1 & -\frac{M}{2m}Z \\ 0 & 0 & \cos Z_2 & -\sin Z_2 & -\frac{2k_2}{Z^3}\sinh Z_2 + \cosh Z_2 & -\frac{2k_2}{Z^3}\cosh Z_2 + \sinh Z_2 \\ 0 & 0 & \sin Z_2 & \cos Z_2 & \sinh Z_2 & \cosh Z_2 \end{vmatrix} = 0 \quad (3)$$

The frequency equation from the expansion of this determinant is too lengthy for practical purposes, but in some special cases of this class of systems the equations can be found from (3) without difficulty.

A. *Systems with a concentrated mass at the end of the beam*

For the case where the concentrated mass is at the end of the beam the system is shown in Fig. 1(b) for $l_1 = l$ and $l_2 = 0$.

The frequency equation is

$$\left(\frac{M}{m}\right) = \frac{Z^6(1-\cos Z\cosh Z)+Z^3(k_1+k_2)(\cos Z\sinh Z-\sin Z\cosh Z)+2k_1k_2\sin Z\sinh Z}{Z^4[Z^3(\cos Z\sinh Z-\sin Z\cosh Z)+2k_1\sin Z\sinh Z]} \quad (4)$$

The various combined functions appearing in this and subsequent frequency equations have been tabulated by Bishop and Johnson[2]. The use of these tables greatly facilitates the solution of the frequency equations which are normally solved by a trial and error method. Using Bishop's notation, equation (4) takes the form

$$\left(\frac{M}{m}\right) = \frac{-Z^6F_3(Z)+Z^3(k_1+k_2)F_5(Z)+2k_1k_2F_1(Z)}{Z^4[Z^3F_5(Z)+2k_1F_1(Z)]} \quad (5)$$

Uniform beam with two elastic supports. If the concentrated mass $M = 0$, the result is

$$Z^6(1-\cos Z\cosh Z)+Z^3(k_1+k_2)(\cos Z\sinh Z-\sin Z\cosh Z) + 2k_1k_2\sin Z\sinh Z = 0 \qquad (6)$$

This is the frequency equation for a uniform beam on two elastic supports, which has been discussed in Ref. 1.

If the concentrated mass M is (theoretically) $= \infty$, the effect of the mass will be to enforce a node at its location, the frequency equation is

$$k_1 = \frac{Z^3(\sin Z\cosh Z-\cos Z\sinh Z)}{2\sin Z\sinh Z} = \frac{Z^3}{2}(\coth Z-\cot Z) \qquad (7)$$

(Fig. 1(b) for $M = l_2 = 0,\ K_2 = \infty$)

Free–free beam with a mass at the end. The equation is

$$\left(\frac{M}{m}\right) = \frac{(1-\cos Z\cosh Z)}{Z(\cos Z\sinh Z-\sin Z\cosh Z)} \qquad (8)$$

(Fig. 1(h) for $l_2 = 0$)

Hinged–free beam with a concentrated mass at the free end. The equation is

$$\left(\frac{M}{m}\right) = \frac{(\cos Z\sinh Z-\sin Z\cosh Z)}{2Z\sin Z\sinh Z} = \frac{\cot Z-\coth Z}{2Z} \qquad (9)$$

(Fig. 1(i) for $l_2 = 0$)

B. *Systems with a concentrated mass in the centre of the beam*

The system is shown in Fig. 1(b) for $l_1 = l_2 = l/2$. The frequency equation is

$$\left(\frac{M}{m}\right) = \frac{2Z^6(1-\cos Z\cosh Z)-2Z^3(k_1+k_2)(\sin Z\cosh Z-\cos Z\sinh Z)+4k_1k_2\sin Z\sinh Z}{2Z[Z^6(1+\cos\frac{1}{2}Z\cosh\frac{1}{2}Z)-2k_1k_2\sin\frac{1}{2}Z\sinh\frac{1}{2}Z](\cos\frac{1}{2}Z\sinh\frac{1}{2}Z-\sin\frac{1}{2}Z\cosh\frac{1}{2}Z) + (k_1+k_2)Z^4[\sin Z\sinh Z-(\sin\frac{1}{2}Z-\sinh\frac{1}{2}Z)^2]} \qquad (10)$$

Frequency equations derived from (10) are

$$2\left[Z^6\left(1+\cos\frac{Z}{2}\cosh\frac{Z}{2}\right)-2k_1k_2\sin\frac{Z}{2}\sinh\frac{Z}{2}\right]\left(\cos\frac{Z}{2}\sinh\frac{Z}{2}-\sin\frac{Z}{2}\cosh\frac{Z}{2}\right) + (k_1+k_2)Z^3\left[\sin Z\sinh Z-\left(\sin\frac{Z}{2}-\sinh\frac{Z}{2}\right)^2\right] = 0 \qquad (11)$$

(Fig. 1(c) for $l_1 = l_2$)

$$\sin\frac{Z}{2}\left(\cos\frac{Z}{2}\sinh\frac{Z}{2}-\sin\frac{Z}{2}\cosh\frac{Z}{2}\right) = 0 \qquad (12)$$

(Fig. 1(d) for $l_1 = l_2$)

The first part of this equation gives the frequencies for each span vibrating as a simply-supported beam, while the second part gives the frequencies for each span vibrating as a fixed–supported beam, that is, all modes with a horizontal tangent at the middle support.

$$\left(1+\cos\frac{Z}{2}\cosh\frac{Z}{2}\right)\left(\cos\frac{Z}{2}\sinh\frac{Z}{2}-\sin\frac{Z}{2}\cosh\frac{Z}{2}\right)=0 \tag{13}$$

(Fig. 1(e) for $l_1 = l_2$)

The first part of (13) gives the frequencies for the modes where each half of the beam vibrates as a cantilever, while the second part gives the frequencies for the modes where each half of the beam vibrates as a hinged–free beam.

$$\sin Z\sinh Z-\left(\sin\frac{Z}{2}-\sinh\frac{Z}{2}\right)^2=0 \tag{14}$$

(Fig. 1(f) for $l_1 = l_2$)

$$\left(\frac{M}{m}\right)=\frac{\sin Z\sinh Z}{Z\sin\frac{1}{2}Z\sinh\frac{1}{2}Z(\sin\frac{1}{2}Z\cosh\frac{1}{2}Z-\cos\frac{1}{2}Z\sinh\frac{1}{2}Z)}=\frac{4}{Z(\tan\frac{1}{2}Z-\tanh\frac{1}{2}Z)} \tag{15}$$

(Fig. 1(g) for $l_1 = l_2$)

All the even modes in this case have a node at the centre of the beam, so that M has no influence on these modes. The frequencies for the even modes are found from the usual equation for a simply-supported uniform beam. The frequencies from (15) are then for the odd modes only.

$$\left(\frac{M}{m}\right)=-\frac{2(\sin\frac{1}{2}Z\cosh\frac{1}{2}Z+\cos\frac{1}{2}Z\sinh\frac{1}{2}Z)}{Z(1+\cos\frac{1}{2}Z\cosh\frac{1}{2}Z)} \tag{16}$$

(Fig. 1(h) for $l_1 = l_2$)

This equation gives the frequencies for the odd modes only, since all even modes have a node in the centre of the beam. The frequencies for the even modes are the same as for a free–free beam without a concentrated mass.

$$\left(\frac{M}{m}\right)=\frac{2(\cos Z\sinh Z-\sin Z\cosh Z)}{Z[\sin Z\sinh Z-(\sin\frac{1}{2}Z-\sinh\frac{1}{2}Z)^2]} \tag{17}$$

(Fig. 1(i) for $l_1 = l_2$)

$$\left(\frac{M}{m}\right)=\frac{4\cos\frac{1}{2}Z\cosh\frac{1}{2}Z[k_1-\frac{1}{2}Z^3(\tan\frac{1}{2}Z+\tanh\frac{1}{2}Z)]}{Z[Z^3(1+\cos\frac{1}{2}Z\cosh\frac{1}{2}Z)+k_1\cos\frac{1}{2}Z\cosh\frac{1}{2}Z(\tan\frac{1}{2}Z-\tanh\frac{1}{2}Z)]} \tag{18}$$

(Fig. 1(b) for $l_1 = l_2$ and $K_1 = K_2$)

This equation gives the frequencies for the odd modes only. All the even modes have a node in the centre of the beam, so that M has no influence on these modes. The frequencies for even modes must then be found as for a uniform beam on equally elastic supports.

C. *Limiting cases of the general class 2*

There are three limiting cases of the general case of beams on elastic supports with frequency equation (3). These are a simply-supported beam, a free–free beam and a hinged–free beam.

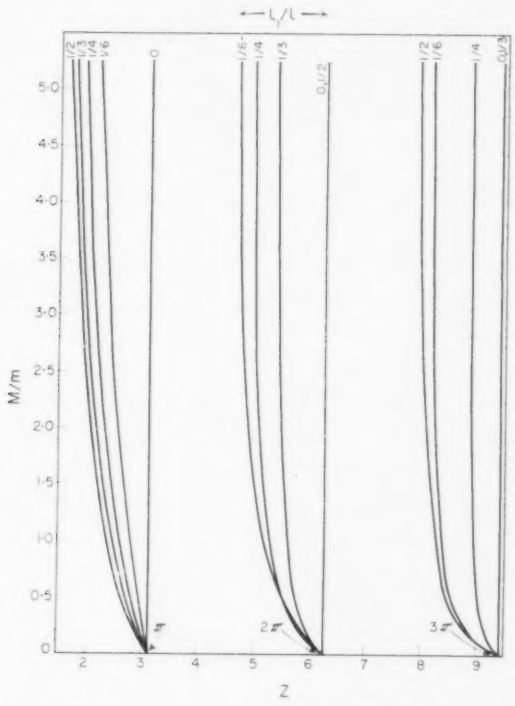

FIG. 2. Simply-supported uniform beam with a concentrated mass. First three roots of frequency equations (15) and (19).

Simply-supported beam. The system is shown in Fig. 1(g) and the frequency equation is

$$\left(\frac{M}{m}\right) = \frac{2}{Z[(\sin Z_1 \sin Z_2/\sin Z) - (\sinh Z_1 \sinh Z_2/\sinh Z)]} \tag{19}$$

The special case of the concentrated mass in the centre of the beam has already been given as equation (15).

The relation (19) has been plotted in Fig. 2 for various ratios M/m and for various positions of the mass on the beam. The first three roots of equation (19) can be taken directly from the curves on Fig. 2 for the positions given. For

intermediate positions the roots can be estimated from the curves and the exact results found from equation (19) by a trial and error method.

It is interesting to compare the exact solution given by equation (15) for the case of the mass in the centre with the simple formula for a concentrated mass on a massless spring. In the case of a beam, a certain part of the total beam mass m must be added to the concentrated mass M in the centre. This part is determined by a factor c, so that the frequency is given by

$$f = \frac{1}{2\pi}\sqrt{\left(\frac{K}{M+cm}\right)} \quad \text{c.p.s.}$$

The spring constant K for the centre of a simply-supported beam is

$$K = \frac{48EI}{l^3} \text{ (lb/in.)}$$

The exact frequency is given by

$$f = \frac{Z^2}{2\pi}\sqrt{\left(\frac{K_B}{m}\right)} = \frac{Z^2}{2\pi}\sqrt{\left(\frac{K}{48m}\right)} \quad \text{c.p.s.}$$

where Z is the fundamental root from equation (15). Equating the two expressions for the frequency gives the relation

$$c = \frac{48}{Z^4} - \left(\frac{M}{m}\right)$$

where M/m is given as a function of Z from equation (15). Calculating values of c for various values of M/m shows only a slight variation in c. For the extreme case of $M = 0$, $c = 48/\pi^4 = 0{\cdot}4928$. With this value of c, the maximum error by using the formula

$$f = \frac{1}{2\pi}\sqrt{\left(\frac{K}{M+cm}\right)}$$

is about 0·25 per cent for all ratios of M/m; Timoshenko[3] gives the value of

$$c = 17/35 = 0{\cdot}4857.$$

This value is found by using Rayleigh's method and the static deflexion of the beam. With that value of c the maximum error is about 0·75 per cent.

The following equation can be derived from (19):

$$\sin Z_1 \sin Z_2 \sinh Z - \sinh Z_1 \sinh Z_2 \sin Z = 0 \tag{20}$$

for the system in Fig. 1(d).

This equation can also be written in the form

$$(\coth Z_1 + \coth Z_2) - (\cot Z_1 + \cot Z_2) = 0$$

For $l_1 = l_2 = \frac{1}{2}l$ equation (20) takes the form of equation (12).

Free–free beam. The system consisting of a free–free beam with a concentrated mass is shown in Fig. 1(h). The frequency equation is

$$\left(\frac{M}{m}\right) = \frac{2(\cos Z \cosh Z - 1)}{Z[(\sin Z_1 \cosh Z_1 - \cos Z_1 \sinh Z_1)(1 + \cos Z_2 \cosh Z_2) + (\sin Z_2 \cosh Z_2 - \cos Z_2 \sinh Z_2)(1 + \cos Z_1 \cosh Z_1)]} \tag{21}$$

The special cases where the mass is at the end of the beam or in the centre have already been given as frequency equations (8) and (16). The relation (21) has been plotted in Fig. 3 for various ratios M/m and various positions of the mass.

The following equation is derived from (21):

$$(\sin Z_1 \cosh Z_1 - \cos Z_1 \sinh Z_1)(1 + \cos Z_2 \cosh Z_2) + (\sin Z_2 \cosh Z_2 - \cos Z_2 \sinh Z_2)(1 + \cos Z_1 \cosh Z_1) = 0 \quad (22)$$

for the system in Fig. 1(e), if $l_1 = l_2 = \frac{1}{2}l$, the equation (22) simplifies to equation (13).

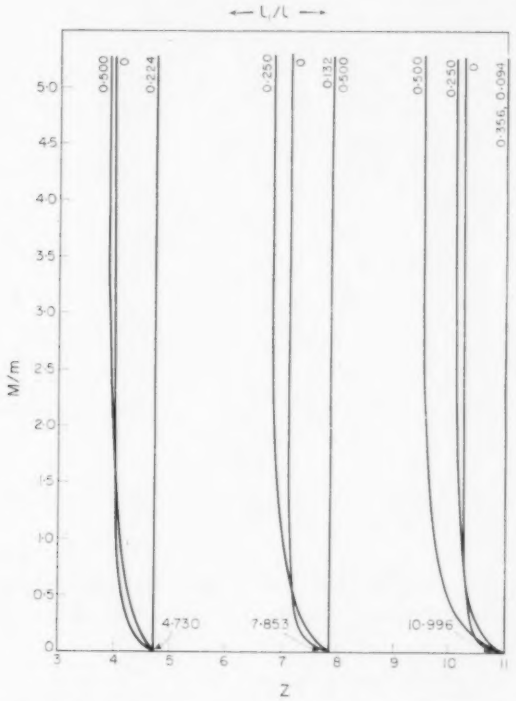

FIG. 3. Free–free uniform beam with a concentrated mass. First three roots of frequency equations (8), (16) and (21).

Hinged–free beam. The hinged–free beam with a concentrated mass is shown in Fig. 1(i). The frequency equation is

$$\left(\frac{M}{m}\right) = \frac{2(\cos Z \sinh Z - \sin Z \cosh Z)}{Z[2 \sin Z_1 \sinh Z_1 (1 + \cos Z_2 \cosh Z_2) - (\sin Z_1 \cosh Z_1 - \cos Z_1 \sinh Z_1)(\sin Z_2 \cosh Z_2 - \cos Z_2 \sinh Z_2)]} \quad (23)$$

The special case of the mass in the centre of the beam has been given before as equation (17), and for the mass at the free end, as equation (9).

The relation (23) has been plotted in Fig. 4 for various mass ratios M/m and various positions of the mass on the beam. From (23) is found the equation

$$\coth Z_1 - \cot Z_1 = \frac{2(1 + \cos Z_2 \cosh Z_2)}{(\sin Z_2 \cosh Z_2 - \cos Z_2 \sinh Z_2)} \quad (24)$$

for the system in Fig. 1(f).

Vol. 3
1961

The special case of (24), where $l_1 = l_2 = \frac{1}{2}l$, has been given before as equation (14).

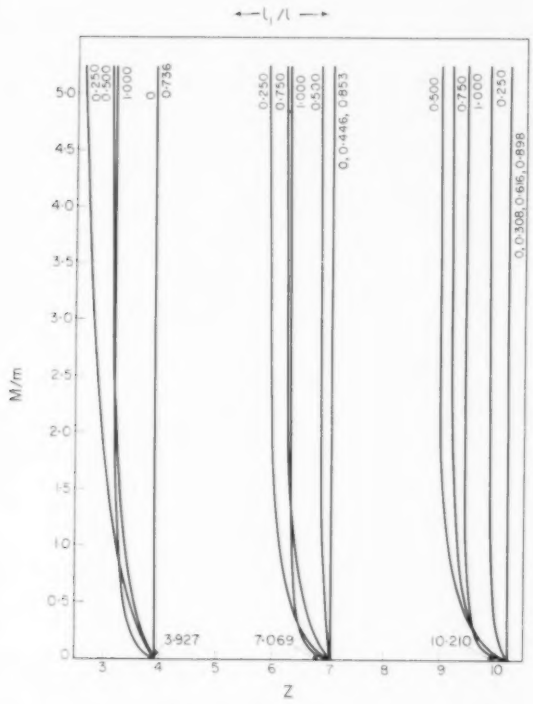

FIG. 4. Hinged–free uniform beam with a concentrated mass. First three roots of frequency equations (9), (17) and (23).

3. UNIFORM BEAMS ELASTICALLY BUILT-IN

The system is shown in Fig. 5(a). The boundary conditions are: $k_1 = k_2 = \infty$, t_1 and t_2 finite. Substituting these boundary conditions in the determinant (1) gives the following frequency determinant for the general case of this type of problems:

$$\begin{vmatrix} \sin Z_1 & -t_1 \cos Z_1 & 0 & -1 & 0 & 0 \\ \cos Z_1 & t_1 \sin Z_1 & -1 & -\dfrac{M}{2m} Z & 0 & \dfrac{M}{2m} Z \\ -\sinh Z_1 & \begin{matrix} t_1 \cosh Z_1 \\ +2Z \sinh Z_1 \end{matrix} & 0 & 0 & 0 & 1 \\ -\cosh Z_1 & \begin{matrix} t_1 \sinh Z_1 \\ +2Z \cosh Z_1 \end{matrix} & 0 & \dfrac{M}{2m} Z & 1 & -\dfrac{M}{2m} Z \\ 0 & 0 & \sin Z_2 & \cos Z_2 & -\sinh Z_2 & -\cosh Z_2 \\ 0 & 0 & -t_2 \cos Z_2 & t_2 \sin Z_2 & \begin{matrix} t_2 \cosh Z_2 \\ +2Z \sinh Z_2 \end{matrix} & \begin{matrix} t_2 \sinh Z_2 \\ +2Z \cosh Z_2 \end{matrix} \end{vmatrix} = 0 \qquad (25)$$

The general frequency equation from the expansion of the determinant (25) is too lengthy for practical purposes. It is simpler to calculate values directly from the determinant. In some special cases, however, the frequency equations can be found from (25) without much difficulty; these are the systems where the mass is in the centre of the beam.

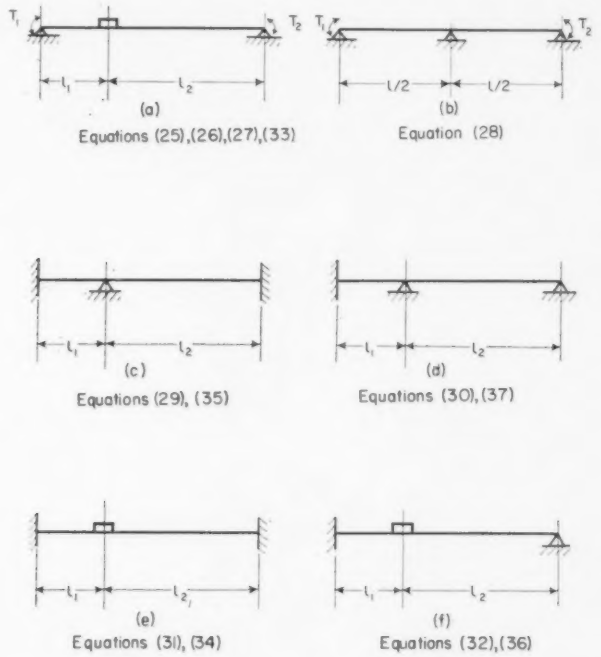

FIG. 5. Uniform beams with a constraining moment at one or both ends.

A. *Systems with a concentrated mass at the centre of the beam*

$$\left(\frac{M}{m}\right) = \frac{4Z^2 \sin Z \sinh Z + 2Z(t_1+t_2)(\sin Z \cosh Z - \cos Z \sinh Z) + 2t_1 t_2(1-\cos Z \cosh Z)}{2Z[2Z^2 \sin \tfrac{1}{2}Z \sinh \tfrac{1}{2}Z + t_1 t_2(1-\cos \tfrac{1}{2}Z \cosh \tfrac{1}{2}Z)] \times (\sin \tfrac{1}{2}Z \cosh \tfrac{1}{2}Z - \cos \tfrac{1}{2}Z \sinh \tfrac{1}{2}Z) - Z^2(t_1+t_2)[\sin Z \sinh Z - (\sin \tfrac{1}{2}Z + \sinh \tfrac{1}{2}Z)^2]} \tag{26}$$

(Fig. 5(a) for $l_1 = l_2$)

$$2Z^2 \sin Z \sinh Z + Z(t_1+t_2)(\sin Z \cosh Z - \cos Z \sinh Z) + t_1 t_2(1-\cos Z \cosh Z) = 0 \tag{27}$$

(Fig. 5(a) for $M = 0$)

This is the frequency equation for a uniform beam elastically built-in at the

ends which has been discussed by Ananeff[1].

$$\left[4Z^2\sin\frac{Z}{2}\sinh\frac{Z}{2}+2t_1t_2\left(1-\cos\frac{Z}{2}\cosh\frac{Z}{2}\right)\right]\left(\sin\frac{Z}{2}\cosh\frac{Z}{2}-\cos\frac{Z}{2}\sinh\frac{Z}{2}\right)$$
$$-Z(t_1+t_2)\left[\sin Z\sinh Z-\left(\sin\frac{Z}{2}+\sinh\frac{Z}{2}\right)^2\right]=0 \tag{28}$$

for the system in Fig. 5(b).

Fixed–fixed beam (1). For a fixed–fixed beam with a support in the centre, as shown in Fig. 5(c) for $l_1 = l_2$, the frequency equation is

$$\left(1-\cos\frac{Z}{2}\cosh\frac{Z}{2}\right)\left(\sin\frac{Z}{2}\cosh\frac{Z}{2}-\cos\frac{Z}{2}\sinh\frac{Z}{2}\right)=0 \tag{29}$$

The first part of (29) gives the frequencies for each half of the beam vibrating as a fixed–fixed beam, while the second half is the frequencies for each half of the beam vibrating as a fixed–supported beam.

The frequency equation

$$\sin Z\sinh Z-\left(\sin\frac{Z}{2}+\sinh\frac{Z}{2}\right)^2=0 \tag{30}$$

holds for the system in Fig. 5(d) for $l_1 = l_2$.

Fixed–fixed beam (2). For a fixed–fixed beam with a concentrated mass in the centre, as shown in Fig. 5(e) for $l_1 = l_2 = \frac{1}{2}l$, the frequency equation is

$$\left(\frac{M}{m}\right)=\frac{2(\sin\frac{1}{2}Z\cosh\frac{1}{2}Z+\cos\frac{1}{2}Z\sinh\frac{1}{2}Z)}{Z(1-\cos\frac{1}{2}Z\cosh\frac{1}{2}Z)} \tag{31}$$

This equation gives the frequencies for the odd modes only, since all the even modes have a node in the centre of the beam, and M thus has no influence on these modes.

Fixed–supported beam. For a fixed–supported beam with a mass in the centre, as shown in Fig. 5(f) for $l_1 = l_2 = \frac{1}{2}l$, there results

$$\left(\frac{M}{m}\right)=\frac{2(\sin Z\cosh Z-\cos Z\sinh Z)}{Z[(\sin\frac{1}{2}Z+\sinh\frac{1}{2}Z)^2-\sin Z\sinh Z]} \tag{32}$$

The general equation (26) can be somewhat simplified if the beam is equally elastically built-in. In that case

$$\left(\frac{M}{m}\right)=\frac{2t_1(\sin\frac{1}{2}Z\cosh\frac{1}{2}Z+\cos\frac{1}{2}Z\sinh\frac{1}{2}Z)+4Z\cos\frac{1}{2}Z\cosh\frac{1}{2}Z}{Z[t_1(1-\cos\frac{1}{2}Z\cosh\frac{1}{2}Z)+Z(\sin\frac{1}{2}Z\cosh\frac{1}{2}Z-\cos\frac{1}{2}Z\sinh\frac{1}{2}Z)]} \tag{33}$$

(Fig. 5(a) for $l_1 = l_2$ and $T_1 = T_2$)

This expression gives the frequencies for the odd modes only, since all the even modes for this symmetrical system have a node in the centre, so that M has no influence on the even modes.

B. *Limiting systems of the general class* 3

There are three limiting systems for the class of systems consisting of elastically built-in beams. These are the simply-supported beam with a

concentrated mass somewhere along the span, the fixed–fixed beam and the fixed–supported beam. The first of these has been treated before with the frequency equation (19).

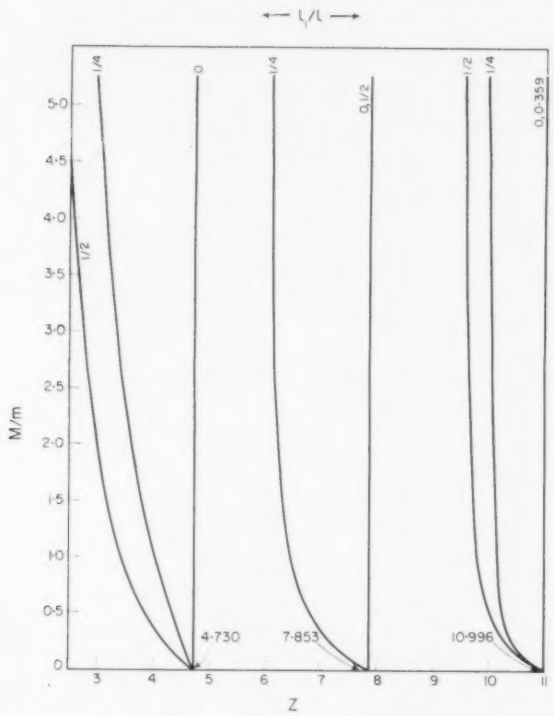

FIG. 6. Fixed–fixed uniform beam with a concentrated mass. First three roots of frequency equations (31), (34).

Fixed–fixed beam. The frequency equation for a fixed–fixed beam with a concentrated mass (Fig. 5e) is

$$\left(\frac{M}{m}\right) = \frac{2(1-\cos Z\cosh Z)}{Z[(\sin Z_1\cosh Z_1-\cos Z_1\sinh Z_1)(1-\cos Z_2\cosh Z_2) + (\sin Z_2\cosh Z_2-\cos Z_2\sinh Z_2)(1-\cos Z_1\cosh Z_1)]} \tag{34}$$

The special case where the concentrated mass is in the centre of the beam has already been given as equation (31).

The expression (34) has been plotted in Fig. 6 for various mass ratios M/m and various positions of the mass. The frequency equation

$$(\sin Z_1\cosh Z_1-\cos Z_1\sinh Z_1)(1-\cos Z_2\cosh Z_2) + (\sin Z_2\cosh Z_2-\cos Z_2\sinh Z_2)(1-\cos Z_1\cosh Z_1) = 0 \tag{35}$$

is for the system in Fig. 5(c).

If the middle support is in the centre the equation (35) simplifies to equation (29).

Vol. 3
1961

Fixed–supported beam. For the fixed–supported beam shown in Fig. 5(f) the frequency equation is

$$\left(\frac{M}{m}\right) = \frac{2(\sin Z \cosh Z - \cos Z \sinh Z)}{Z[(\sin Z_1 \cosh Z_1 - \cos Z_1 \sinh Z_1)(\sin Z_2 \cosh Z_2 - \cos Z_2 \sinh Z_2) + 2 \sin Z_2 \sinh Z_2 (1 - \cos Z_1 \cosh Z_1)]} \tag{36}$$

The special case of the concentrated mass in the centre of the beam has already been given as equation (32). The relation (36) has been plotted in Fig. 7 for various mass ratios and positions of the concentrated mass.

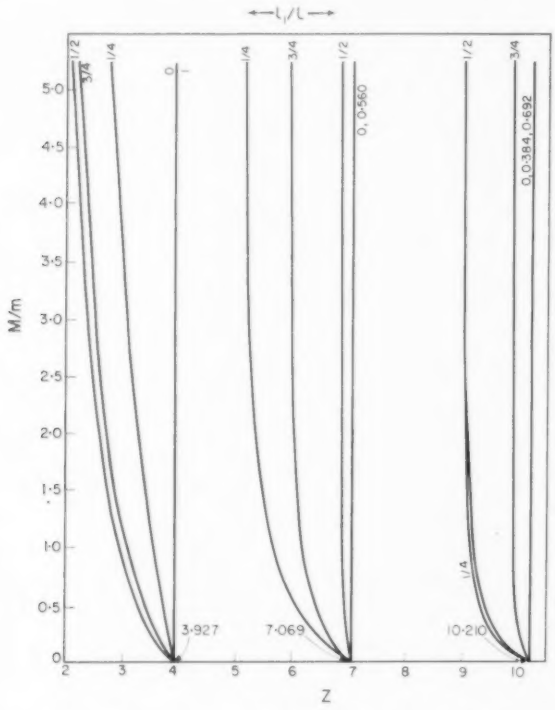

FIG. 7. Fixed–supported uniform beam with a concentrated mass. First three roots of frequency equations (32), (36).

For the system in Fig. 5(d)

$$(\sin Z_1 \cosh Z_1 - \cos Z_1 \sinh Z_1)(\sin Z_2 \cosh Z_2 - \cos Z_2 \sinh Z_2) + 2 \sin Z_2 \sinh Z_2 (1 - \cos Z_1 \cosh Z_1) = 0 \tag{37}$$

If the middle support is in the centre of the beam equation (37) simplifies to equation (30).

4. UNIFORM BEAMS ELASTICALLY BUILT-IN AT ONE END AND ELASTICALLY SUPPORTED AT THE OTHER END

The general system is shown in Fig. 8(a). The boundary conditions are: $k_1 = \infty$, $t_2 = 0$, k_2 and t_1 finite. Substituting these boundary conditions in the

determinant (1) gives the following frequency determinant for this class of problems:

$$\begin{vmatrix} \sin Z_1 & -t_1 \cos Z_1 & 0 & -1 & 0 & 0 \\ \cos Z_1 & t_1 \sin Z_1 & -1 & -\frac{M}{2m} Z & 0 & \frac{M}{2m} Z \\ -\sinh Z_1 & t_1 \cosh Z_1 + 2Z \sinh Z_1 & 0 & 0 & 0 & 1 \\ -\cosh Z_1 & t_1 \sinh Z_1 + 2Z \cosh Z_1 & 0 & \frac{M}{2m} Z & 1 & -\frac{M}{2m} Z \\ 0 & 0 & Z^3 \cos Z_2 & -Z^3 \sin Z_2 & -2k_2 \sinh Z_2 + Z^3 \cosh Z_2 & -2k_2 \cosh Z_2 + Z^3 \sinh Z_2 \\ 0 & 0 & \sin Z_2 & \cos Z_2 & \sinh Z_2 & \cosh Z_2 \end{vmatrix} = 0 \tag{38}$$

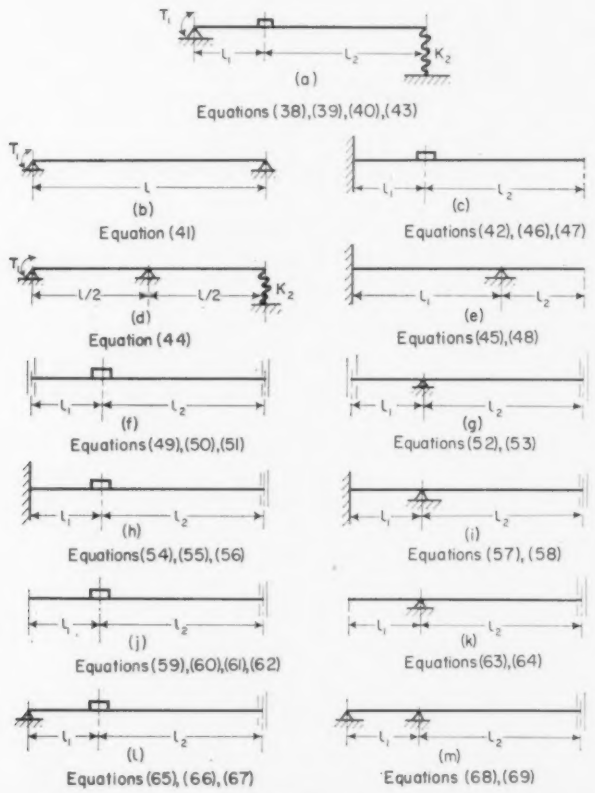

FIG. 8. Beam systems with various end constraints.

The frequency equation found by expanding this determinant is too lengthy for practical purposes. The special cases where the mass is at the elastically-supported end or in the middle of the beam will be considered in more detail.

Vol. 3
1961

A. *Systems with a concentrated mass at the elastically-supported end of the beam*

$$\left(\frac{M}{m}\right) = \frac{Z^3 t_1(1+\cos Z\cosh Z)+(k_2 t_1 - Z^4)(\sin Z\cosh Z-\cos Z\sinh Z)+2k_2 Z\sin Z\sinh Z}{Z^4[t_1(\sin Z\cosh Z-\cos Z\sinh Z)+2Z\sin Z\sinh Z]} \tag{39}$$

(Fig. 8(a) for $l_2 = 0$)

$$Z^3 t_1(1+\cos Z\cosh Z)+(k_2 t_1 - Z^4)(\sin Z\cosh Z-\cos Z\sinh Z)+2k_2 Z\sin Z\sinh Z = 0 \tag{40}$$

(Fig. 8(a) for $M = l_2 = 0$)

This is the frequency equation for a uniform beam elastically built-in at one end and elastically supported at the other end which has been discussed by Ananeff[1].

$$t_1 = \frac{2Z\sin Z\sinh Z}{(\cos Z\sinh Z-\sin Z\cosh Z)} \tag{41}$$

for the system in Fig. 8(b).

For a cantilever with a mass at the end, as shown in Fig. 8(c) for $l_1 = l$, $l_2 = 0$,

$$\left(\frac{M}{m}\right) = \frac{1+\cos Z\cosh Z}{Z(\sin Z\cosh Z-\cos Z\sinh Z)} \tag{42}$$

B. *Systems with a concentrated mass in the centre of the beam*

The system is shown in Fig. 8(a) for $l_1 = l_2 = \frac{1}{2}l$. The frequency equation is

$$\left(\frac{M}{m}\right) = \frac{2Z^3 t_1(1+\cos Z\cosh Z)+2(k_2 t_1 - Z^4)(\sin Z\cosh Z-\cos Z\sinh Z)+4k_2 Z\sin Z\sinh Z}{Z^5[\sin Z\sinh Z-(\sinh\frac{1}{2}Z-\sin\frac{1}{2}Z)^2]+2Z^2(t_1 Z^2\cos\frac{1}{2}Z\cosh\frac{1}{2}Z+2k_2\sin\frac{1}{2}Z\sinh\frac{1}{2}Z)\times(\sin\frac{1}{2}Z\cosh\frac{1}{2}Z-\cos\frac{1}{2}Z\sinh\frac{1}{2}Z)-t_1 k_2 Z[\sin Z\sinh Z-(\sinh\frac{1}{2}Z+\sin\frac{1}{2}Z)^2]} \tag{43}$$

For the system of Fig. 8(d)

$$\begin{aligned} &Z^4[\sin Z\sinh Z-(\sinh\tfrac{1}{2}Z-\sin\tfrac{1}{2}Z)^2]\\ &\quad+2Z(Z^2 t_1\cos\tfrac{1}{2}Z\cosh\tfrac{1}{2}Z+2k_2\sin\tfrac{1}{2}Z\sinh\tfrac{1}{2}Z)\\ &\quad\times(\sin\tfrac{1}{2}Z\cosh\tfrac{1}{2}Z-\cos\tfrac{1}{2}Z\sinh\tfrac{1}{2}Z)\\ &\quad-t_1 k_2[\sin Z\sinh Z-(\sinh\tfrac{1}{2}Z+\sin\tfrac{1}{2}Z)^2]=0 \end{aligned} \tag{44}$$

For the case shown in Fig. 8(e) for $l_1 = l_2 = \frac{1}{2}l$

$$\cos\frac{Z}{2}\left(\sin\frac{Z}{2}\cosh\frac{Z}{2}-\cos\frac{Z}{2}\sinh\frac{Z}{2}\right)=0 \tag{45}$$

For a cantilever beam with a mass in the centre as shown in Fig. 8(c) for $l_1 = l_2 = \frac{1}{2}l$

$$\left(\frac{M}{m}\right) = \frac{1+\cos Z\cosh Z}{Z\cos\frac{1}{2}Z\cosh\frac{1}{2}Z(\sin\frac{1}{2}Z\cosh\frac{1}{2}Z-\cos\frac{1}{2}Z\sinh\frac{1}{2}Z)} \tag{46}$$

C. *Limiting cases of the general class* 4

There are four limiting cases for this class of systems, i.e. the simply-supported, fixed–supported, hinged–free and fixed–free or cantilever beam.

The first three of these have been treated before. For the cantilever beam the system is shown in Fig. 8(c) and the frequency equation is

$$\left(\frac{M}{m}\right) = \frac{2(1+\cos Z \cosh Z)}{Z[(\sin Z_1 \cosh Z_1 - \cos Z_1 \sinh Z_1)(1+\cos Z_2 \cosh Z_2) - (\sin Z_2 \cosh Z_2 - \cos Z_2 \sinh Z_2)(1-\cos Z_1 \cosh Z_1)]} \quad (47)$$

The special cases of the concentrated mass at the free end of the beam and in the centre of the beam have already been given as frequency equations (42) and (46). The relation (47) has been plotted in Fig. 9 for various ratios of M/m and various positions of the mass on the beam.

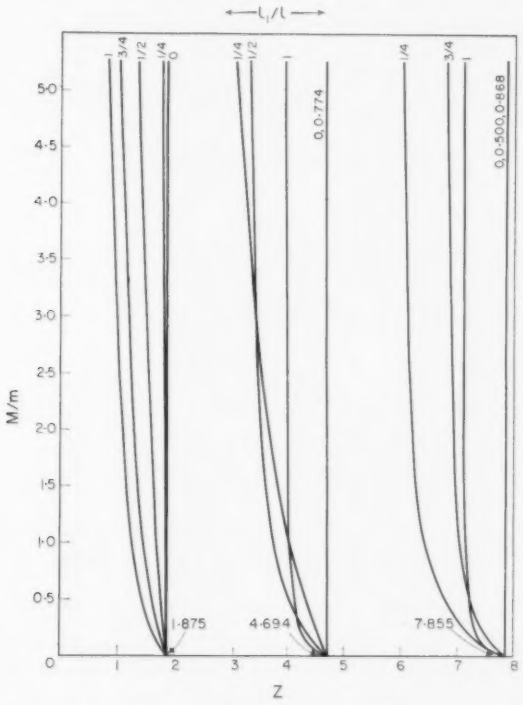

FIG. 9. Fixed–free uniform beam with a concentrated mass. First three roots of frequency equations (42), (46) and (47).

For the system shown in Fig. 8(e)

$$(\sin Z_1 \cosh Z_1 - \cos Z_1 \sinh Z_1)(1+\cos Z_2 \cosh Z_2) - (\sin Z_2 \cosh Z_2 - \cos Z_2 \sinh Z_2)(1-\cos Z_1 \cosh Z_1) = 0 \quad (48)$$

If the middle support is in the centre of the beam, equation (48) simplifies to equation (45).

It is interesting to compare the exact solution given by equation (42) for a cantilever with a mass at the end with the simple formula for a mass on a massless spring

$$f = \frac{1}{2\pi}\sqrt{\left(\frac{K}{M+cm}\right)} \quad \text{c.p.s.}$$

Vol. 3
1961

where the spring constant for the end of a cantilever is given by $K = 3EI/l^3$ (lb/in.), and c is a numerical factor to determine how big a part of the beam mass m should be added to the concentrated mass M. The exact frequency is

$$f = \frac{Z^2}{2\pi}\sqrt{\left(\frac{K_B}{m}\right)} = \frac{Z^2}{2\pi}\sqrt{\left(\frac{K}{3m}\right)} \quad \text{c.p.s.}$$

where Z is the smallest root from equation (42). Equating the two expressions for the frequency gives the following relation

$$c = \frac{3}{Z^4} - \frac{M}{m}$$

where the relation between M/m and Z is given by equation (42). Calculating values of c from this expression for various values of M/m shows only a slight variation in c. In the extreme case of $M = 0$, the result is

$$c = \frac{3}{1{\cdot}875^4} = 0{\cdot}2427$$

With this value of c in the formula

$$f = \frac{1}{2\pi}\sqrt{\left(\frac{K}{M + cm}\right)} \quad \text{c.p.s.}$$

the maximum error is about 0·5 per cent for all ratios of M/m. Timoshenko[3] gives the value of c as $c = 33/140 = 0{\cdot}2357$. This value is found by using Rayleigh's method and the static deflexion curve of the beam. With this value of c the maximum error is about 1·5 per cent.

A concentrated mass M on a vibrating beam acts with a force on the beam equal to $My\omega^2$, a linear spring with spring constant K acts with a force Ky, but in opposite direction. If a linear spring is substituted for a mass, or a mass for a spring, in any of the systems given, the frequency equation for the transferred system can be found directly by substituting $K = -M\omega^2$, or $M/m = -k/Z^4$ in the frequency equation for the original system. The modeform is determined by using the same substitution in the original modeform equations.

This substitution then greatly extends the number of systems for which the frequency equations can be found directly from the frequency equations stated here.

5. BEAMS WITH SLIDING ENDS

The limiting cases for the practical problems so far considered consisted of beams with ends that were free, fixed or simply-supported. There is, however, still another end condition for $k = 0$, $t = \infty$. This type of end is called a "guided" or "sliding end" and is sometimes encountered in practical problems. The significance of $k = 0$ is, of course, that the end of the beam is free to vibrate in a vertical direction, while $t = \infty$ means that the slope of the end must always be zero. Analytically, these conditions are expressed as $y' = y''' = 0$, or slope and shear force equals zero.

Combining a sliding end with the other three end conditions gives a further four limiting cases or a total of ten; these ten cases are the limits for all practical problems of the type discussed here.

Beam with two sliding ends. Fig. 8(f) shows a beam with two sliding ends and a concentrated mass on the beam. The frequency equation is

$$\left(\frac{M}{m}\right) = -\frac{2\sin Z \sinh Z}{Z[\sin Z \cosh Z_1 \cosh Z_2 + \sinh Z \cos Z_1 \cos Z_2]} \tag{49}$$

If the concentrated mass is in the centre

$$\left(\frac{M}{m}\right) = -\frac{4\sin Z \sinh Z}{Z[(\sin Z \cosh Z + \cos Z \sinh Z) + (\sin Z + \sinh Z)]} \tag{50}$$

If the concentrated mass is at one end

$$\left(\frac{M}{m}\right) = -\frac{2\sin Z \sinh Z}{Z(\sin Z \cosh Z + \cos Z \sinh Z)} \tag{51}$$

For the system shown in Fig. 8(g)

$$\sin Z \cosh Z_1 \cosh Z_2 + \sinh Z \cos Z_1 \cos Z_2 = 0 \tag{52}$$

With the middle support in the centre of the beam

$$(\sin Z \cosh Z + \cos Z \sinh Z) + (\sin Z + \sinh Z) = 0 \tag{53}$$

Fixed–sliding beam. Fig. 8(h) shows a fixed–sliding beam with a concentrated mass

$$\left(\frac{M}{m}\right) = \frac{2(\sin Z \cosh Z + \cos Z \sinh Z)}{Z[2(1-\cos Z_1 \cosh Z_1)\cos Z_2 \cosh Z_2 + (\sin Z_1 \cosh Z_1 - \cos Z_1 \sinh Z_1)(\sin Z_2 \cosh Z_2 + \cos Z_2 \sinh Z_2)]} \tag{54}$$

With the mass in the centre

$$\left(\frac{M}{m}\right) = \frac{4(\sin Z \cosh Z + \cos Z \sinh Z)}{Z[4(1-\cos \tfrac{1}{2}Z \cosh \tfrac{1}{2}Z)\cos \tfrac{1}{2}Z \cosh \tfrac{1}{2}Z + (1-\cos Z \cosh Z)]} \tag{55}$$

With the concentrated mass at the sliding end

$$\left(\frac{M}{m}\right) = \frac{\sin Z \cosh Z + \cos Z \sinh Z}{Z(1-\cos Z \cosh Z)} \tag{56}$$

For the system shown in Fig. 8(i)

$$2(1-\cos Z_1 \cosh Z_1)\cos Z_2 \cosh Z_2 + (\sin Z_1 \cosh Z_1 - \cos Z_1 \sinh Z_1)(\sin Z_2 \cosh Z_2 + \cos Z_2 \sinh Z_2) = 0 \tag{57}$$

If the middle support is in the centre of the span

$$4(1-\cos \tfrac{1}{2}Z \cosh \tfrac{1}{2}Z)\cos \tfrac{1}{2}Z \cosh \tfrac{1}{2}Z + (1-\cos Z \cosh Z) = 0 \tag{58}$$

Free–sliding beam. Fig. 8(j) shows a free–sliding beam with a concentrated mass. The frequency equation is

$$\left(\frac{M}{m}\right) = \frac{2(\sin Z \cosh Z + \cos Z \sinh Z)}{Z[(\sin Z_1 \cosh Z_1 - \cos Z_1 \sinh Z_1)(\sin Z_2 \cosh Z_2 + \cos Z_2 \sinh Z_2) - 2\cos Z_2 \cosh Z_2(1+\cos Z_1 \cosh Z_1)]} \tag{59}$$

If the mass is in the centre

$$\left(\frac{M}{m}\right) = \frac{4(\sin Z \cosh Z + \cos Z \sinh Z)}{Z[(1-\cos Z \cosh Z) - 4\cos \tfrac{1}{2}Z \cosh \tfrac{1}{2}Z(1+\cos \tfrac{1}{2}Z \cosh \tfrac{1}{2}Z)]} \tag{60}$$

For the case of the mass at the free end

$$\left(\frac{M}{m}\right) = -\frac{(\sin Z \cosh Z + \cos Z \sinh Z)}{2Z \cos Z \cosh Z} = -\frac{(\tan Z + \tanh Z)}{2Z} \tag{61}$$

If the mass is at the sliding end

$$\left(\frac{M}{m}\right) = -\frac{(\sin Z \cosh Z + \cos Z \sinh Z)}{Z(1+\cos Z \cosh Z)} \tag{62}$$

For the system shown in Fig. 8(k)

$$(\sin Z_1 \cosh Z_1 - \cos Z_1 \sinh Z_1)(\sin Z_2 \cosh Z_2 + \cos Z_2 \sinh Z_2) - 2\cos Z_2 \cosh Z_2(1+\cos Z_1 \cosh Z_1) = 0. \tag{63}$$

If the support is in the centre

$$(1-\cos Z \cosh Z) - 4\cos \frac{Z}{2} \cosh \frac{Z}{2}\left(1+\cos \frac{Z}{2} \cosh \frac{Z}{2}\right) = 0 \tag{64}$$

Vol. 3
1961

Simply-supported–sliding beam. Fig. 8(l) shows a simply-supported–sliding beam with a concentrated mass. The frequency equation is

$$\left(\frac{M}{m}\right) = \frac{2\cos Z\cosh Z}{Z[(\sin Z_1\cosh Z_1-\cos Z_1\sinh Z_1)\cos Z_2\cosh Z_2 + (\sin Z_2\cosh Z_2+\cos Z_2\sinh Z_2)\sin Z_1\sinh Z_1]} \tag{65}$$

With the mass in the centre

$$\left(\frac{M}{m}\right) = \frac{4\cos Z\cosh Z}{Z(\sin Z\cosh Z-\cos Z\sinh Z)} \tag{66}$$

With the mass at the sliding end

$$\left(\frac{M}{m}\right) = \frac{2\cos Z\cosh Z}{Z(\sin Z\cosh Z-\cos Z\sinh Z)} \tag{67}$$

For the system shown in Fig. 8(m), the frequency equation is

$$(\sin Z_1\cosh Z_1-\cos Z_1\sinh Z_1)\cos Z_2\cosh Z_2 + (\sin Z_2\cosh Z_2+\cos Z_2\sinh Z_2)\sin Z_1\sinh Z_1 = 0 \tag{68}$$

If the middle support is in the centre

$$\sin Z\cosh Z-\sinh Z\cos Z = 0 \tag{69}$$

6. MODEFORM EQUATIONS

The mode of vibration for a given natural frequency is given by the deflexion curve of the beam which because of the concentrated mass has to be stated as two equations:

$$\left.\begin{aligned} y_1 &= C_1\sin\frac{Z}{l}x_1+C_2\cos\frac{Z}{l}x_1+C_3\sinh\frac{Z}{l}x_1+C_4\cosh\frac{Z}{l}x_1\\ y_2 &= D_1\sin\frac{Z}{l}x_2+D_2\cos\frac{Z}{l}x_2+D_3\sinh\frac{Z}{l}x_2+D_4\cosh\frac{Z}{l}x_2 \end{aligned}\right\} \tag{70}$$

The eight constants $C_1 \dots C_4$, $D_1 \dots D_4$ are found by solving the following set of equations:

$$\left.\begin{aligned}
&\text{I.} && Z^3C_1-k_1C_2-Z^3C_3-k_1C_4 = 0\\
&\text{II.} && t_1C_1+ZC_2+t_1C_3-ZC_4 = 0\\
&\text{III.} && (k_2\sin Z_2+Z^3\cos Z_2)D_1+(k_2\cos Z_2-Z^3\sin Z_2)D_2\\
& && \quad +(k_2\sinh Z_2-Z^3\cosh Z_2)D_3\\
& && \quad +(k_2\cosh Z_2-Z^3\sinh Z_2)D_4 = 0\\
&\text{IV.} && (t_2\cos Z_2-Z\sin Z_2)D_1-(t_2\sin Z_2+Z\cos Z_2)D_2\\
& && \quad +(t_2\cosh Z_2+Z\sinh Z_2)D_3+(t_2\sinh Z_2+Z\cosh Z_2)D_4 = 0\\
&\text{V.} && (\sin Z_1)C_1+(\cos Z_1)C_2+(\sinh Z_1)C_3+(\cosh Z_1)C_4-D_2-D_4 = 0\\
&\text{VI.} && (\cos Z_1)C_1-(\sin Z_1)C_2+(\cosh Z_1)C_3+(\sinh Z_1)C_4-D_1-D_3 = 0\\
&\text{VII.} && (\sin Z_1)C_1+(\cos Z_1)C_2-(\sinh Z_1)C_3-(\cosh Z_1)C_4-D_2+D_4 = 0\\
&\text{VIII.} && (\cos Z_1)C_1-(\sin Z_1)C_2-(\cosh Z_1)C_3-(\sinh Z_1)C_4\\
& && \quad -D_1-\frac{M}{m}ZD_2+D_3-\frac{M}{m}ZD_4 = 0
\end{aligned}\right\} \tag{71}$$

For a natural frequency the determinant of this system is zero; seven of the eight constants can then be expressed as functions of the eighth constant, which means that the system of equations (71) has an infinite number of solutions. The simplest solution is found by putting one of the eight constants equal to 1 in seven of the equations and solving these seven equations for the remaining constants. The modeform equations (70) can, of course, be multiplied by the same arbitrary constant $\neq 0$.

In the special case where the mass is in the centre and the end conditions the same for each end of the beam, it is only necessary to find the modeform for half the beam, since the modeform is symmetrical around the centre of the beam. If the mass is at one end of the beam, only one equation will be found for the modeform.

APPENDIX

Development of Frequency Determinant

The system is shown in Fig. 1(a). It consists of a uniform beam supported on four springs with spring constants K_1, K_2, T_1 and T_2 as shown. A concentrated mass M is attached to the beam a distance l_1 from the left end.

The normal functions of the left-hand part of the beam are given by

$$y_1 = C_1 \sin ax_1 + C_2 \cos ax_1 + C_3 \sinh ax_1 + C_4 \cosh ax_1 \tag{72}$$

(Ref. 3, p. 325), where $a^4 = \omega^2 A\gamma/EIg$, ω is the natural circular frequency (rad/sec), A is the cross-sectional area of the beam (in^2), γ is the material density (lb/in^3), EI is the beam flexural rigidity (lb/in^2), g is the acceleration due to gravity (in./sec^2) and C_1, C_2, C_3 and C_4 are constants depending on the boundary conditions of the beam.

The consecutive derivations of (72) with respect to x_1 are

$$\left.\begin{aligned} y_1' &= C_1 a \cos ax_1 - C_2 a \sin ax_1 + C_3 a \cosh ax_1 + C_4 a \sinh ax_1 \\ y_1'' &= -C_1 a^2 \sin ax_1 - C_2 a^2 \cos ax_1 + C_3 a^2 \sinh ax_1 + C_4 a^2 \cosh ax_1 \\ y_1''' &= -C_1 a^3 \cos ax_1 + C_2 a^3 \sin ax_1 + C_3 a^3 \cosh ax_1 + C_4 a^3 \sinh ax_1 \end{aligned}\right\} \tag{73}$$

By substituting (x_2, y_2) for (x_1, y_1) and (D_1, D_2, D_3, D_4) for (C_1, C_2, C_3, C_4), the equations (72) and (73) are changed to a system of equations valid for the right-hand side of the beam.

It is assumed that the beam is supported on massless, linear and rotational springs at both ends, giving as reactions forces proportional to the deflexions at the ends and bending moments proportional to the rotation of the ends. Utilizing the well-known relations: bending moment $= -EIy''$, shear force $= -EIy'''$ and slope $= y'$, the boundary conditions for $x_1 = 0$ are

I. $$EIy'''_{10} = -K_1 y_{10}$$

II. $$EIy''_{10} = T_1 y'_{10}$$

For $x_2 = l_2$, the boundary conditions are

III. $$EIy'''_{2l_2} = K_2 y_{2l_2}$$

IV. $$EIy''_{2l_2} = -T_2 y'_{2l_2}$$

At the concentrated mass the deflexion, slope and bending moments are the same for the two parts of the beam, so that the conditions are

V. $$y_{1l_1} = y_{20}$$

VI. $$y'_{1l_1} = y'_{20}$$

VII. $$y''_{1l_1} = y''_{20}$$

The last boundary condition is found from the fact that the difference in sheer forces on either side of the concentrated mass is equal to the inertia force on the mass, or

$$EIy'''_{20} - EIy'''_{1l_1} = M\omega^2 y_{20} = M\frac{EIg}{A\gamma} a^4 y_{20}$$

from which

VIII. $$y'''_{20} - y'''_{1l_1} = \frac{Mla^4}{A(\gamma/g)\,l} y_{20} = \frac{M}{m} la^4 y_{20}$$

Vol. 3
1961

Substituting in equations (72) and (73) gives the following eight equations:

$$\text{I.} \qquad a^3 C_1 - \frac{K_1}{EI} C_2 - a^3 C_3 - \frac{K_1}{EI} C_4 = 0$$

$$\text{II.} \qquad \frac{T_1}{EI} C_1 + aC_2 + \frac{T_1}{EI} C_3 - aC_4 = 0$$

$$\text{III.} \quad \left(a^3 \cos al_2 + \frac{K_2}{EI} \sin al_2\right) D_1 - \left(a^3 \sin al_2 - \frac{K_2}{EI} \cos al_2\right) D_2 - \left(a^3 \cosh al_2 - \frac{K_2}{EI} \sinh al_2\right) D_3 - \left(a^3 \sinh al_2 - \frac{K_2}{EI} \cosh al_2\right) D_4 = 0$$

$$\text{IV.} \quad \left(a \sin al_2 - \frac{T_2}{EI} \cos al_2\right) D_1 + \left(a \cos al_2 + \frac{T_2}{EI} \sin al_2\right) D_2 - \left(a \sinh al_2 + \frac{T_2}{EI} \cosh al_2\right) D_3 - \left(a \cosh al_2 + \frac{T_2}{EI} \sinh al_2\right) D_4 = 0$$

$$\text{V.} \qquad (\sin al_1) C_1 + (\cos al_1) C_2 + (\sinh al_1) C_3 + (\cosh al_1) C_4 - D_2 - D_4 = 0$$

$$\text{VI.} \qquad (\cos al_1) C_1 - (\sin al_1) C_2 + (\cosh al_1) C_3 + (\sinh al_1) C_4 - D_1 - D_3 = 0$$

$$\text{VII.} \qquad (\sin al_1) C_1 + (\cos al_1) C_2 - (\sinh al_1) C_3 - (\cosh al_1) C_4 - D_2 + D_4 = 0$$

$$\text{VIII.} \quad (\cos al_1) C_1 - (\sin al_1) C_2 - (\cosh al_1) C_3 - (\sinh al_1) C_4 - D_1 - \frac{M}{m} alD_2 + D_3 - \frac{M}{m} alD_4 = 0$$

Multiplying equations I and III by l^3 and equations II and IV by l, and substituting

$$Z = al, \quad Z_1 = al_1, \quad Z_2 = al_2, \quad k_1 = \frac{K_1 l^3}{EI}, \quad t_1 = \frac{T_1 l}{EI}, \quad k_2 = \frac{K_2 l^3}{EI} \quad \text{and} \quad t_2 = \frac{T_2 l}{EI}$$

there results the system of equations (71).

This is a system of eight homogeneous, linear equations in eight unknowns. The condition for solutions $(C_1, \ldots, C_4, D_1, \ldots, D_4) \neq (0, 0 \ldots 0)$ is that the determinant of the coefficients is equal to zero. This gives the frequency equation in the form of an eighth-order determinant. After reduction to a sixth-order determinant and rearrangement equation (1) appears.

REFERENCES

1. I. W. ANANEFF, *Handbook on Vibrations of Elastic Bodies* (1946). (In Russian.)
2. R. E. D. BISHOP and D. C. JOHNSON, *Vibration Analysis Tables*. Cambridge University Press (1956).
3. S. TIMOSHENKO, *Vibration Problems in Engineering* (3rd ed.). Van Nostrand, New York (1955).

Int. J. Mech. Sci. Pergamon Press Ltd. 1961. Vol. 3, pp. 219–228. Printed in Great Britain

Vol. 3
1961

A NUMERICAL ANALYSIS OF LARGE DEFLECTIONS OF BEAMS

T. M. Wang, S. L. Lee and O. C. Zienkiewicz
Northwestern University, Evanston, Illinois

(*Received* 23 *January* 1961)

Summary—Numerical methods are used in this paper for calculating large deflections of beams. The success of the application of the outlined procedure to these nonlinear problems is first demonstrated on an example of a uniformly loaded cantilever beam for which an alternative solution is available. The proposed method is then applied to a simply supported beam subjected to nonsymmetrical loads. Both concentrated load and partial uniformly distributed load are considered and the results are checked by experiment. In this analysis, as indeed in all previous work, the axis of the beam is assumed to be inextensible.

INTRODUCTION

The Bernoulli–Euler equation of bending of a beam gives, for an initially straight beam,

$$\frac{d\theta}{ds} = \frac{d^2y/dx^2}{[1+(dy/dx)^2]^{\frac{3}{2}}} = -\frac{M}{EI} \tag{1}$$

in which M is the bending moment and EI the flexural rigidity of the beam. In most engineering problems the slope of the beam is considered small and its square can be neglected in comparison with unity, thus equation (1) reduces to an ordinary linear equation which is easily solved.

In the case of very flexible beams the moment M itself is in general a nonlinear function of the angle θ and the problem therefore becomes considerably more complex, and only a limited number of solutions have been presented in literature.

The case of a straight, horizontal cantilever carrying a vertical concentrated load at its free end has been solved approximately by Boyd[1] and by Gross and Lehr[2], and exactly by Barton[3] and by Bisshopp and Drucker[4]. Seames and Conway[5] also made a numerical analysis of this problem.

An initially curved cantilever with a vertical or a horizontal concentrated load had been considered and solved exactly by Conway[6]; this case was also discussed by Seames and Conway[5] and by Sato[7]. Mitchell[8] in addition considered the case in which both a vertical and a horizontal concentrated load act simultaneously.

An approximate treatment of the bending of a straight, horizontal cantilever under a uniformly distributed load was presented by Hummel and Morton[9]. The same case was treated numerically by Bickley[10] and by Seames and Conway[5]. Rohde[11] also made an approximate analysis of the problem. The same cantilever under the action of uniformly distributed normal load was considered by Truesdall[12] and Mitchell[8]. Seames and Conway[5] solved a case of an initially curved cantilever with uniformly distributed load.

For simply supported beams, only the case of a central concentrated load and a fixed distance between supports was solved by Conway[13] and Gospodnetic[14]. This scarcity of available solutions emphasizes the need for a generally applicable method of approach. It is the purpose of this paper to present such a method.

PROPOSED METHOD OF SOLUTION

If equation (1) is differentiated with respect to s we obtain the general second-order differential equation for the deflection of beams

$$\frac{d^2\theta}{ds^2} = -\frac{1}{EI}\frac{dM}{ds} = -\frac{V}{EI} \tag{2}$$

This formulation of the problem is found to be more convenient as the bending moment is in general a more complex function of θ than the shearing force. If initial approximated θ values at all points are assumed in the right-hand side of the equation, an improved solution for θ can be obtained by solving equation (2) which is thus linearized. Repetition of this process will in general lead to the final solution with improved values of θ being substituted into the right-hand side of the equation at each stage.

The solution of the linearized equation (2) is accomplished in terms of finite differences. In the finite difference form this equation becomes

$$\theta_{n+1} - 2\theta_n + \theta_{n-1} = -h^2(V/EI)_n \tag{3}$$

in which h stands for the increment of s. The numerical values of θ at the nodal points can be obtained either by a straightforward application of the well-known Southwell's relaxation technique[15] or by the inversion of the appropriate matrix. The first method was used in the calculations presented here, but if the method is programmed for a digital computer the second technique is preferable as the inverse matrix once found would be then used at each stage of the iteration.

The particular case in which θ is symmetrical, or has a zero slope condition at one end, is of some interest. It can be shown that the application of the relaxation technique provides a very simple method of obtaining the inverse of the matrix. The demonstration of this is presented in Fig. 1 which shows a systematic application of relaxation "blocks" which results in an exact reduction of all initial residuals to zero. It is easily seen that if all the θ values are initially zero, the nth initial residual is

$$R_n = (h^2\, V/EI)_n$$

With a symmetrical region divided into eight intervals only four simultaneous equations need be solved and if equations (3) are written in a matrix form as

$$[A]\,\theta + [R] = 0$$

the inverse of A is

$$[A]^{-1} = -\begin{bmatrix} 1 & 1 & 1 & \frac{1}{2} \\ 1 & 2 & 2 & 1 \\ 1 & 2 & 3 & \frac{3}{2} \\ 1 & 2 & 3 & 2 \end{bmatrix}$$

In actual numerical examples worked by hand, it is probably simpler to obtain the relaxation solutions directly in numerical terms.

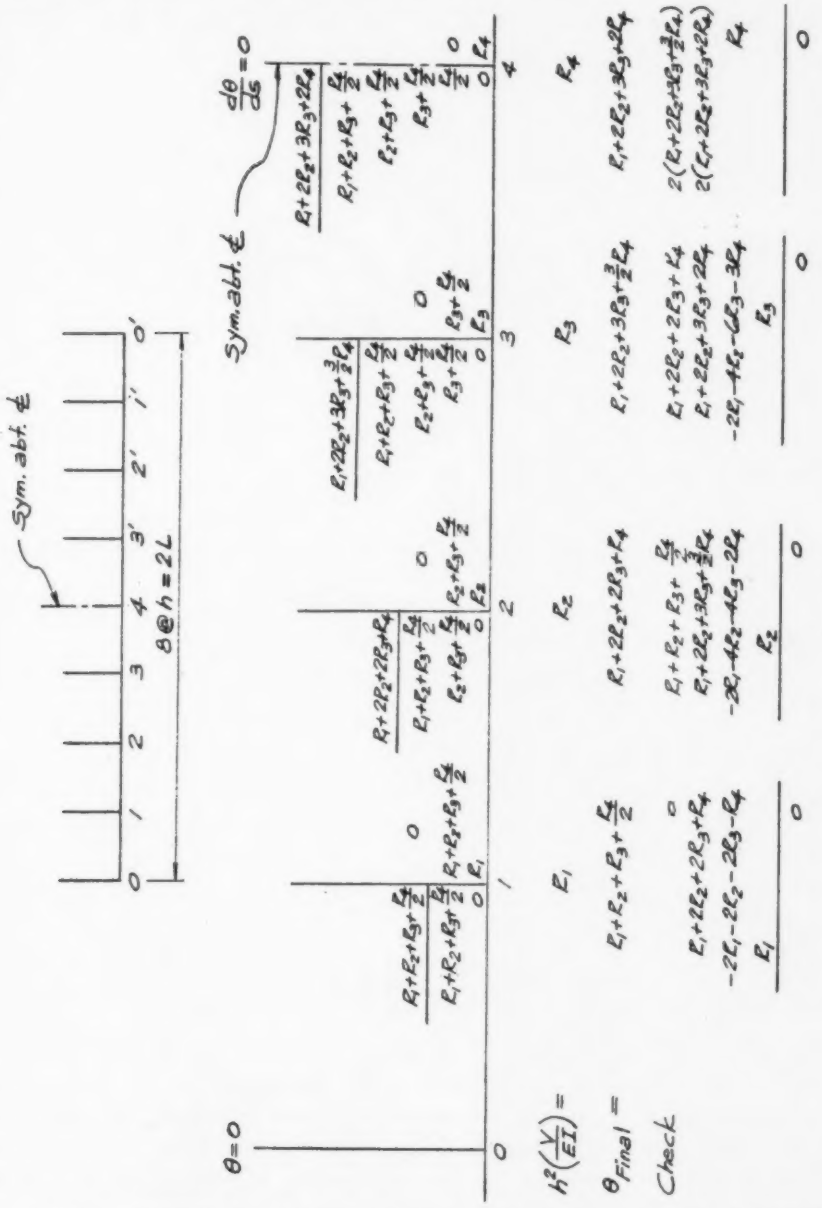

FIG. 1.

DEFLECTION OF CANTILEVER BEAM WITH UNIFORMLY DISTRIBUTED LOAD

The case considered here is shown in Fig. 2. The purpose of this example was to check the method against a known solution[11] and to illustrate the general procedure. The cross-section of the beam is assumed to be constant.

Vol. 3
1961

The shearing force at distance s along the beam from the free end is

$$V = ws\cos\theta \tag{4}$$

where w is the uniformly distributed load per unit length of the beam. Substitution in equation (3) yields

$$\theta_{n-1} - 2\theta_n + \theta_{n+1} = -(wh^2/EI)\, s\cos\theta_n \tag{5}$$

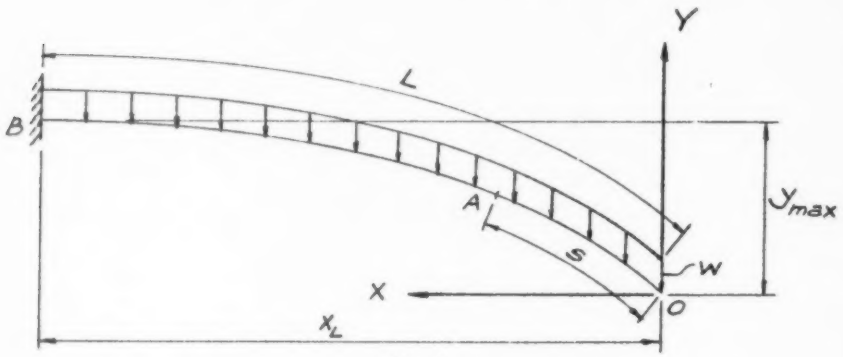

FIG. 2.

Setting $h = h'L$ and $s = s'L$, equation (5) is transformed into the nondimensional form

$$\theta_{n-1} - 2\theta_n + \theta_{n+1} = -\beta h'^2 s'\cos\theta_n \tag{6}$$

in which $\beta = wL^3/EI$. The boundary conditions are

$$d\theta/ds = 0 \text{ at } s = 0 \quad \text{and} \quad \theta = 0 \text{ at } s = L$$

In this example, $h' = 1/8$ was used and the solution obtained for values of the parameter β varying from 1 to 10.

The convergence of the process is illustrated in Table 1, where successive sets of θ values for a computation with the parameter $\beta = 1$ are shown.

TABLE 1

$s' = 1$	$\frac{7}{8}$	$\frac{3}{4}$	$\frac{5}{8}$	$\frac{1}{2}$	$\frac{3}{8}$	$\frac{1}{4}$	$\frac{1}{8}$	0
$\theta' = 0°$	0°	0°	0°	0°	0°	0°	0°	0°
$\theta'' = 0°$	3° 10′	5° 31′	7° 12′	8° 21′	9° 3′	9° 24′	9° 32′	9° 33′
$\theta''' = 0°$	3° 7′	5° 26′	7° 6′	8° 12′	8° 52′	9° 12′	9° 19′	9° 19′
$\theta^{IV} = 0°$	3° 7′	5° 26′	7° 6′	8° 13′	8° 52′	9° 12′	9° 19′	9° 19′

In the above computation θ'' obviously corresponds to the elementary solution and, in this case, the convergence is very rapid because the final solution is very close to that obtained by the elementary theory.

With θ's known at all points, the value of x_L and $y_{\max}$ (Fig. 2) can be calculated simply from the relationships

$$x_L = \int_0^L \cos\theta\, ds \tag{7}$$

and

$$y_{\max} = \int_0^L \sin\theta\, ds \tag{8}$$

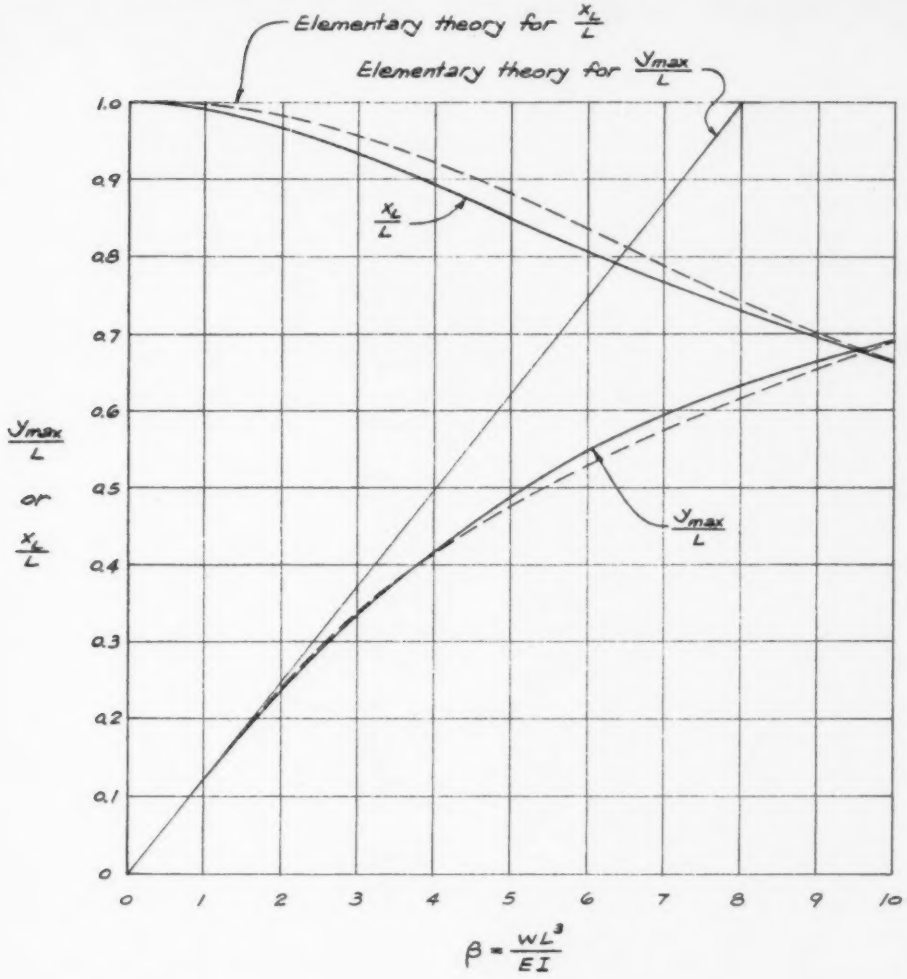

FIG. 3.

Using numerical integration, we have

$$x_L = 0{\cdot}991L \quad \text{and} \quad y_{\max} = 0{\cdot}122L$$

As β increases and the beam becomes more flexible, the speed of convergence decreases and the results may diverge if certain precautions are not taken. This divergence indicates in fact that it is necessary in the successive steps of the iteration to take an intermediate value between those obtained from the two previous steps. Thus if θ^j represents the set of values obtained from the jth step of the iteration, then the values of R_{j+1} were obtained by using an

intermediate value of θ given by

$$\theta^{j-1}+m(\theta^{j}-\theta^{j-1})$$

in which $0<m<1$. Convergence was obtained with values of m ranging from $\frac{1}{3}$ to $\frac{1}{2}$ with the lower values being somewhat more advantageous for larger values of β. In all cases, satisfactory values were obtained in not more than four cycles.

The complete results of x_L and $y_{\max}$ for $\beta = 1$ to 10 are shown in Fig. 3 and are in good agreement with those obtained by an approximate analytical solution.[11]

DEFLECTIONS OF SIMPLY SUPPORTED BEAMS

A typical example with an arbitrary loading shown in Fig. 4 is considered. It is assumed that the length of the beam between A and B remains unchanged, and that the flexural rigidity is constant. The beam is so supported that only vertical reactions exist. This problem presents some difficulties not encountered in the case of cantilevers.

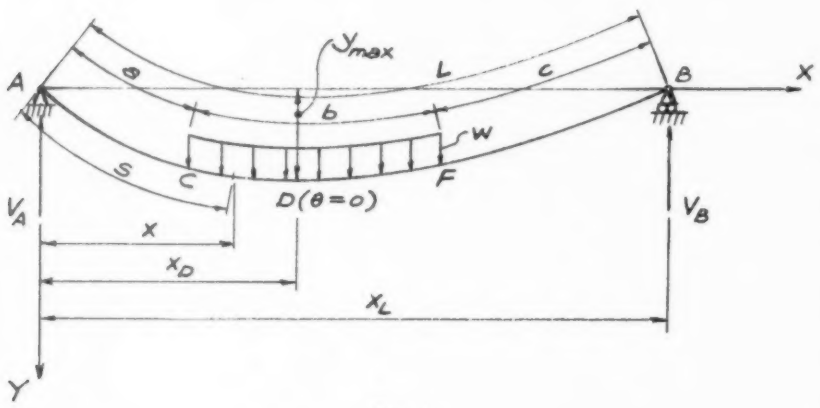

FIG. 4.

The expressions for shearing forces at any section are now given as follows:

$$V = V_A\cos\theta = w\cos\theta\left(b-\frac{1}{x_L}\int_a^{a+b} x\,ds\right) \quad \text{for} \quad 0\leqslant s\leqslant a$$

$$V = V_A\cos\theta - w(s-a)\cos\theta = w\cos\theta\left(a+b-s-\frac{1}{x_L}\int_a^{a+b} x\,ds\right) \quad \text{for} \quad a\leqslant s\leqslant a+b$$

$$V = V_A\cos\theta - wb\cos\theta = w\cos\theta\left(-\frac{1}{x_L}\int_a^{a+b} x\,ds\right) \quad \text{for} \quad a+b\leqslant s\leqslant L$$

Substituting in equation (3) and transforming into the nondimensional form lead to

$$\theta_{n-1}-2\theta_n+\theta_{n+1} = \beta h'^2\cos\theta_n(\eta_r) \tag{9}$$

where

$$\left.\begin{aligned}
\beta &= wL^3/EI \\
h' &= h/L \\
s' &= s/L \\
x &= \int_0^s \cos\theta\, ds \\
x_L &= \int_0^L \cos\theta\, ds \\
r &= 1, 2, 3 \\
\eta_1 &= b/L - \eta_3 \quad \text{for} \quad 0 \leqslant s' \leqslant a/L \\
\eta_2 &= (a+b)/L - s' + \eta_3 \quad \text{for} \quad a/L \leqslant s' \leqslant (a+b)/L \\
\eta_3 &= -\frac{1}{x_L L}\int_a^{a+b} x\, ds \quad \text{for} \quad (a+b)/L \leqslant s' \leqslant 1
\end{aligned}\right\} \tag{10}$$

The boundary conditions for the present problem are

$$d\theta/ds = 0 \quad \text{at} \quad s = 0 \quad \text{and} \quad s = L$$

Clearly a unique solution of equation (9) is not defined by these, the possible values of θ being indeterminate by a constant. To overcome this difficulty, let $\theta = \phi + k$ such that $\phi = 0$ at one end. The above boundary conditions after such transformation become

$$\phi = 0 \quad \text{at} \quad s = 0$$

$$d\phi/ds = 0 \quad \text{at} \quad s = L$$

which are similar to the previous case, thus permitting the same procedure as before to be used here. Equation (9) then becomes

$$\phi_{n-1} - 2\phi_n + \phi_{n+1} = -\beta h'^2 \cos\theta_n(\eta_r) \tag{11}$$

where β, h' and η_r are given by equations (10) and $\phi_i = \theta_i - k$ where $i = n-1, n, n+1$, k being a constant. From Fig. 4 we have

$$y = \int_0^L \sin\theta\, ds = \int_0^L \sin(\phi + k)\, ds = 0$$

which allows the value of k to be determined as

$$\tan k = -\frac{\int_0^L \sin\phi\, ds}{\int_0^L \cos\phi\, ds} \tag{12}$$

With k known, the values of θ can readily be determined.

As an example, the value of $\beta = 50$ was chosen and calculations carried out for the case in which $a = L/8$, $b = L/2$ and $c = 3L/8$. The calculation follows

Vol. 3
1961

now the same pattern as that of the previous example with each stage now involving an intermediate step of the computation of the function ϕ. Again the use of a convergence factor $m = \frac{1}{2}$ was found to be necessary and satisfactory results were achieved in six cycles. The sets of θ values are shown in Table 2.

TABLE 2

$s' = 0$	$\frac{1}{8}$	$\frac{1}{4}$	$\frac{3}{8}$	$\frac{1}{2}$	$\frac{5}{8}$	$\frac{3}{4}$	$\frac{7}{8}$	1
$\theta' = 0°$	0°	0°	0°	0°	0°	0°	0°	0°
$\theta'' = 81° 36'$	74° 36′	54° 33′	26° 7′	−5° 8′	−33° 34′	−54° 33′	−67° 9′	−71° 20′
$\theta''' = 32° 41'$	30° 46′	24° 48′	13° 11′	−2° 9′	−16° 0′	−23° 58′	−27° 51′	−28° 59′
$\theta^{IV} = 57° 19'$	52° 57′	39° 46′	19° 42′	−3° 32′	−24° 31′	−38° 24′	−46° 12′	−48° 43′
$\theta^{V} = 57° 24'$	53° 2′	39° 51′	19° 47′	−3° 29′	−24° 33′	−38° 31′	−46° 23′	−48° 56′
$\theta^{VI} = 57° 23'$	53° 1′	39° 52′	19° 48′	−3° 28′	−24° 32′	−38° 31′	−46° 25′	−49° 1′
$\theta^{VII} = 57° 24'$	53° 2′	39° 53′	19° 50′	−3° 27′	−24° 32′	−38° 32′	−46° 27′	−49° 0′
$\theta^{VIII} = 57° 24'$	53° 2′	39° 52′	19° 49′	−3° 28′	−24° 32′	−38° 32′	−46° 26′	−49° 0′

Again by equations (10) we have, on numerical integration,

$$x_L = 0{\cdot}786L$$

The value of $y_{\max}$ can be determined as

$$y_{\max} = \int_A^D \sin\theta \, ds \tag{13}$$

in which the limit of D is the point where $\theta = 0$. This results in

$$y_{\max} = 0{\cdot}272L$$

at $x_D = 0{\cdot}366L$, while the corresponding values by elementary theory gives

$$y_{\max} = 0{\cdot}429L$$

at $0{\cdot}479L$ from the left support. This large difference illustrates the need for the consideration of the nonlinearity.

SIMPLY SUPPORTED BEAM WITH ECCENTRIC LOAD

This last example presents no special difficulties and was solved by a procedure identical to that presented above. Again the total length L and the flexural rigidity of the beam are assumed constant.

A complete set of results was computed for different values of the parameter $\alpha = PL^2/EI$ with the load placed successively at distances $a = L/8$, $L/4$, $3L/8$ and $L/2$ from the left support. These results are summarized in Fig. 5 which gives the values of the maximum deflection and the horizontal projected lengths of the beam.

The values for the maximum deflections given by the elementary theory are indicated. The only analytical solution available is that for the case of $a = L/2$ (Ref. 4) and is shown for the purpose of comparison.

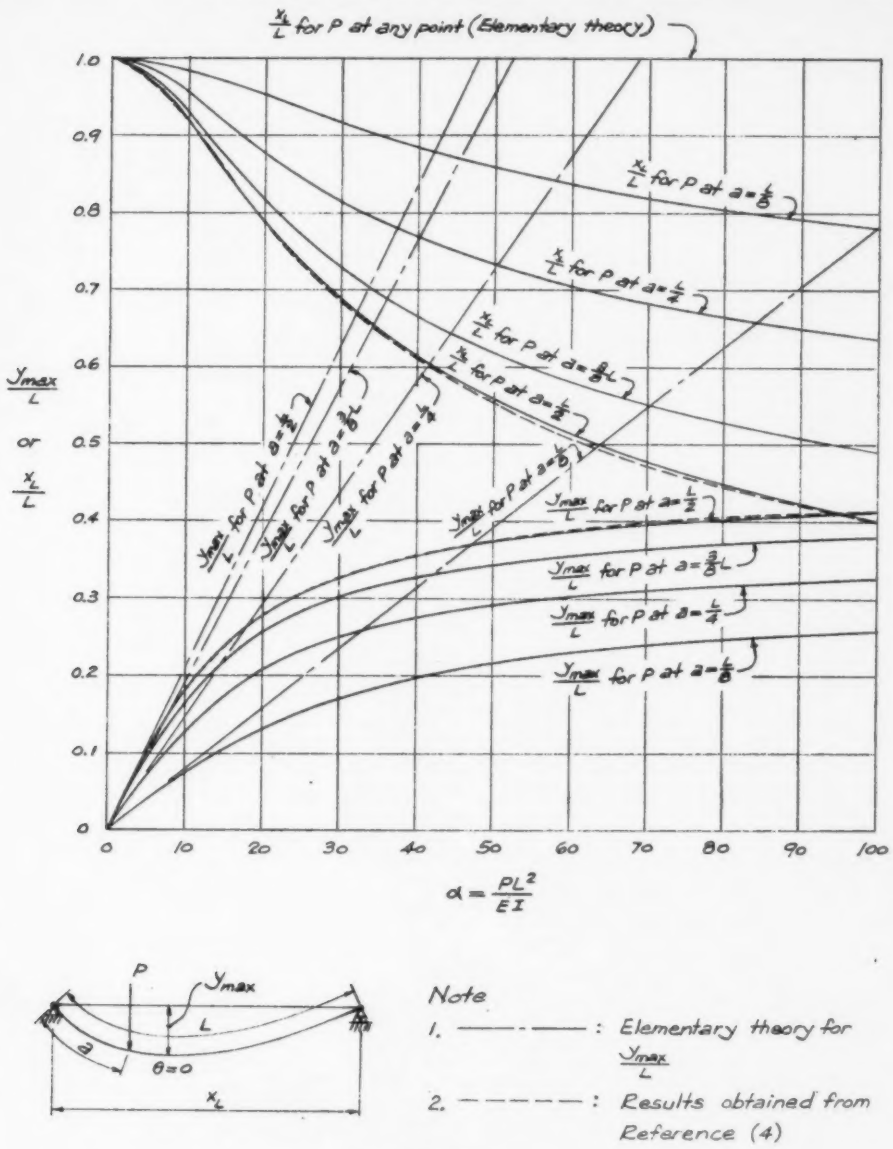
$\frac{x_L}{L}$ for P at any point (Elementary theory)
$\frac{x_L}{L}$ for P at $a=\frac{L}{8}$
$\frac{x_L}{L}$ for P at $a=\frac{L}{4}$
$\frac{x_L}{L}$ for P at $a=\frac{3}{8}L$
$\frac{x_L}{L}$ for P at $a=\frac{L}{2}$
$\frac{y_{max}}{L}$ for P at $a=\frac{L}{2}$
$\frac{y_{max}}{L}$ for P at $a=\frac{3}{8}L$
$\frac{y_{max}}{L}$ for P at $a=\frac{L}{4}$
$\frac{y_{max}}{L}$ for P at $a=\frac{L}{8}$
$\frac{y_{max}}{L}$ or $\frac{x_L}{L}$
$\alpha = \frac{PL^2}{EI}$
P
y_{max}
L
a
$\theta=0$
x_L
Note
1. ——·—— : Elementary theory for $\frac{y_{max}}{L}$
2. – – – – – : Results obtained from Reference (4)

FIG. 5.

EXPERIMENTAL VERIFICATION

The results for the simply supported beams analyzed were verified experimentally and a full description of the experimental set-up and results has been given.[16] An aluminum alloy beam 2 in. wide, $\frac{1}{16}$ in. deep and 6 ft long with $E = 10{\cdot}7 \times 10^6$ p.s.i. was used. A typical comparison is shown in Fig. 6. The possible error in the computation due to the size of the finite difference mesh and method of numerical integration (trapezoidal rule was used throughout) was investigated and found to be very small.

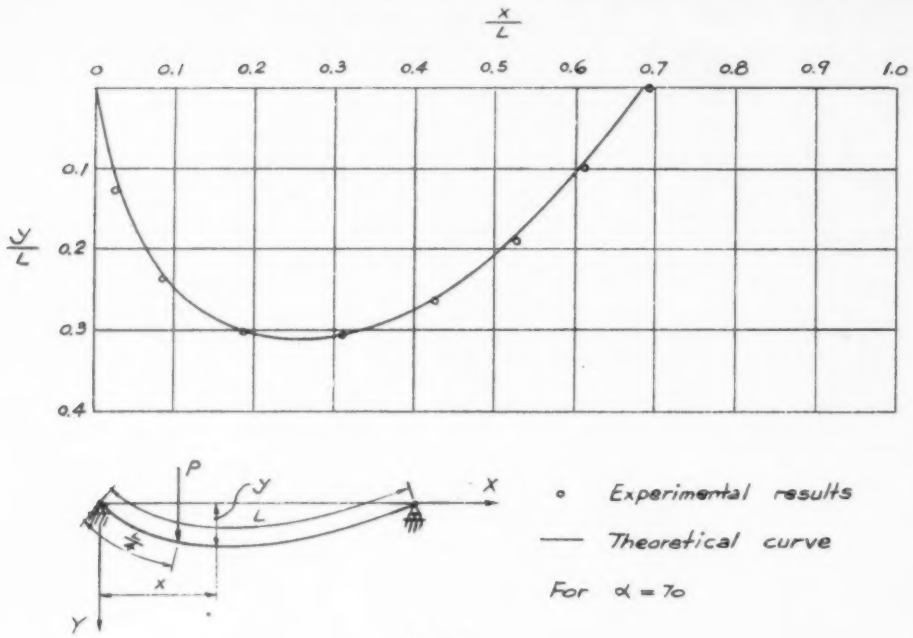

FIG. 6.

CONCLUSION

The ease with which the numerical method described here is carried out was illustrated by several examples, some of them previously unsolved. These clearly do not present the limit of applicability and little difficulty is encountered in problems involving variable flexural rigidity and complex loading condition. With some modification, the method can be extended to other support conditions.

REFERENCES

1. J. E. BOYD, *Strength of Materials.* (3rd Ed.), Appendix D. McGraw-Hill, New York (1924).
2. S. GROSS and E. LEHR, *Die Federn.* Berlin V. D. I. Verlag (1938).
3. H. J. BARTON, *Quart. Appl. Math.* **2**, 168 (1944); **3**, 275 (1945).
4. K. E. BISSHOPP and D. C. DRUCKER, *Quart. Appl. Math.* **3**, 272 (1945).
5. A. E. SEAMES and H. D. CONWAY, *J. Appl. Mech.* **24**, 289 (1957).
6. H. D. CONWAY, *J. Appl. Mech.* **23**, 7 (1956).
7. K. SATO, *J. Appl. Mech.* **25**, 294 (1958).
8. T. P. MITCHELL, *J. Appl. Mech.* **26**, 40 (1959).
9. F. H. HUMMEL and W. B. MORTON, *Phil. Mag.* **4**, 348 (1927).
10. W. C. BICKLEY, *Phil. Mag.* **17**, 603 (1934).
11. F. V. ROHDE, *Quart. Appl. Math.* **11**, 337 (1953).
12. C. TRUESDALL, *Proc. 1st Midwestern Conf. Solid Mech. Univ. Illinois, April* 1953. p. 52.
13. H. D. CONWAY, *Phil. Mag.* **38**, 905 (1947).
14. D. GOSPODNETIC, *J. Appl. Mech.* **26**, 675 (1959).
15. D. N. DE G. ALLEN, *Relaxation Methods.* McGraw-Hill, New York (1954).
16. T. M. WANG, Ph.D. Dissertation, Northwestern University, Evanston, Illinois (1960).

Int. J. Mech. Sci. Pergamon Press Ltd. 1961. Vol. 3, pp. 229–238. Printed in Great Britain

Vol. 3
1961

INDENTING WITH PYRAMIDS—I. THEORY

J. B. HADDOW* and W. JOHNSON†

(*Received* 7 *March* 1961)

Summary—Using an approximate method, expressions are obtained for the load necessary to indent a rigid–plastic non-hardening solid to a given depth with square-based and triangular-based pyramids. Experimental results will be presented in Part II.

1. INTRODUCTION

INTEREST in this subject arises from its application to measurements of the hardness of metals. The history and background to this topic are well described in the book of the same name by Tabor[1].

The theoretical "solutions" presented here are solutions of three-dimensional problems in plasticity; the methods used are described as approximate but they are, as yet, the only direct methods of predicting the loads involved. They are approximate because in seeking upper bounds[2] to the loads necessary to cause indentation the bounding surface considered is continuously altered. Intuitively one feels that the application of the Upper Bound Theorem in conjunction with the assumption of continuing geometrical similarity is a reasonably valid one. The model of deformation we assume for the purposes of calculation is based on physical observations of how the metal deforms and knowledge of the theoretical methods for investigating plane strain wedge indentation.[3] Our methods will thus be obvious to readers conversant with the latter subject.

2. INDENTING LOAD OVER-ESTIMATES

Approximate method

The approximate method presented here is a method for estimating the loads necessary to indent a rigid–plastic non-hardening solid using pyramids. A kinematically admissible velocity field is taken and the rate of work done by the load on the pyramid is equated to the rate of plastic energy dissipation in the field. As well as the usual requirements for kinematic admissibility the velocity field must be such that as the indentation proceeds the surface displaced remains geometrically similar.

(i) *Application of approximate method to square-based pyramids.* A smooth pyramid with semi-apex angle θ is shown in Fig. 1. Indentation is to depth $OE = c$; the intersection of the undisturbed surface of the indented medium and the pyramid is $ABCD$ where $AB = 2a$. During the indentation OE is normal to the undisturbed surface and geometrical similarity is preserved.

The velocity field is based on the plane-strain field for indentation with *smooth* wedges. Material displaced by the pyramid is considered to "pile up"

* Department of Mechanical Engineering, University of Alberta, Canada.
† Department of Mechanical Engineering, College of Science and Technology, Manchester, 1.

at each face of the pyramid to form a tetrahedron, e.g. *LCBH* as shown in Fig. 1. It may be deduced from the incompressibility requirement that area *LFH* = area *EOF*. Fig. 1 shows the plastically deforming region *LHQPECL* of the velocity field associated with one eighth of the pyramid. In the velocity field the stream lines are parallel to *EPQH*. *EPQHL*, which is the intersection of the plastically deforming region and the vertical plane through *OF* (Fig. 1)

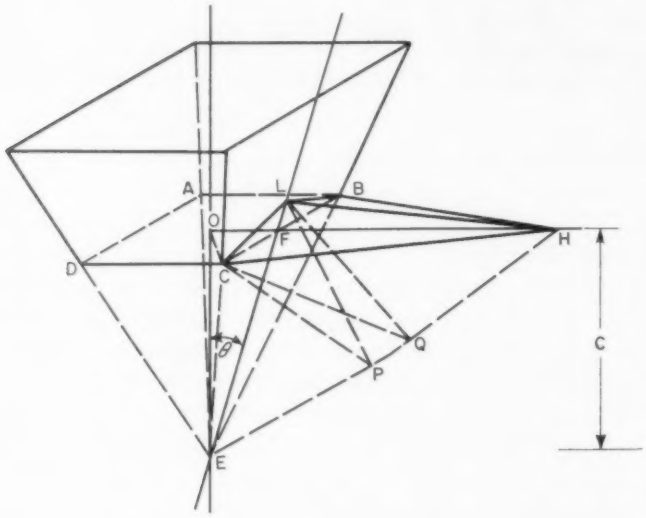

FIG. 1. Indentation with a square-based, smooth-sided pyramid of semi-apex angle θ, showing the assumed "pile-up" at the face of the wedge and (dashed) one quarter of the boundary of the plastically deforming region.

is shown in Fig. 2; *it is of the same form as the plane-strain field for indentation with a smooth wedge*. The intersection of a vertical plane, parallel to and distance x from *OF* (Fig. 1) and the deforming region, is geometrically similar to Fig. 2 and is shown in Fig. 3. Corresponding lengths are scaled down by the factor $(a-x)/a$.

Because of symmetry the downward movement of only one-quarter of the pyramid is considered. In all cases to be examined the pyramid moves vertically downward with unit speed and the velocity along the stream lines is $\sqrt{(2)}\sin\theta$. It may be shown that

$$2\theta = \psi + \cos^{-1}\tan\left(\frac{\pi}{4}-\frac{\psi}{2}\right) \tag{1}$$

and, referring to Fig. 3,

$$E'L' = L'H' = h' = c'/[\cos\theta - \sin(\theta-\psi)]$$

Considering a lamina of the deforming region contained between vertical planes distance x and $(x+dx)$ from *OF* the stream lines are parallel to *EPQH*

and the flow is a plane-strain motion; the rate of energy dissipation in the lamina is

$$d\dot{W}_p = kh' \sin\theta\{(2+\psi)\sqrt{(1+\tfrac{1}{2}\operatorname{cosec}^2\theta)}+\psi\}\,dx$$

where $h' = h(a-x)/a$. Integrating from $x = 0$ to $x = a$ gives the rate of energy

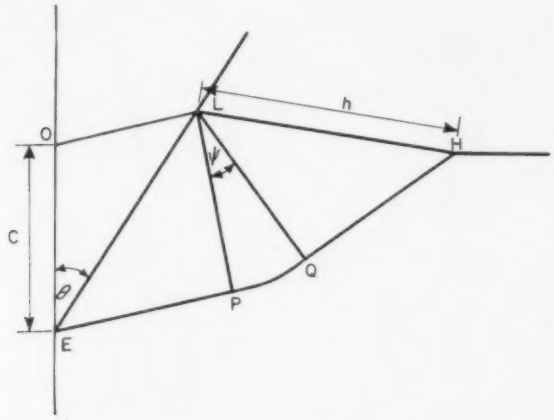

FIG. 2. Showing the intersection of a vertical plane through F (Fig. 1) with the deforming region.

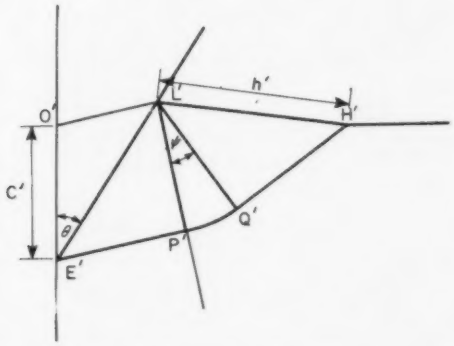

FIG. 3. Cross-section given by vertical plane parallel to, but at horizontal distance x from, that shown in Fig. 2.

dissipation in the plastically deforming region $EPQHLC$ as

$$\dot{W}_p/4 = kha\{2\sqrt{(\tfrac{1}{2}+\sin^2\theta)}+\psi[\sin\theta+\sqrt{(\tfrac{1}{2}+\sin^2\theta)}]\}$$

where $\dot{W}_p$ is the rate of energy dissipation for the whole field. By noting that

$$h[\cos\theta-\sin(\theta-\psi)] = c = a\cot\theta$$

the rate of energy dissipation may be re-written as

$$\dot{W}_p = \frac{4ka^2\cot\theta\{2\sqrt{(\tfrac{1}{2}+\sin^2\theta)}+\psi[\sin\theta+\sqrt{(\tfrac{1}{2}+\sin^2\theta)}]\}}{\cos\theta-\sin(\theta-\psi)}$$

Vol. 3
1961

The expression for F/c^2k, where F is the force required to indent, is then given by

$$\frac{F}{c^2k} = \frac{4\tan\theta\{2\sqrt{(\frac{1}{2}+\sin^2\theta)}+\psi[\sin\theta+\sqrt{(\frac{1}{2}+\sin^2\theta)}]\}}{\cos\theta-\sin(\theta-\psi)} \tag{2}$$

The values of F/c^2k, found from (2), are shown in Fig. 4 and are also given in Table 1.

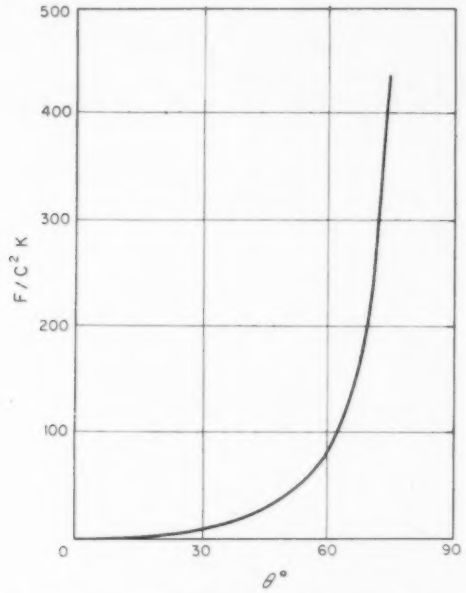

FIG. 4. Showing the variation of F/c^2k with θ for a smooth-sided square-based indenter.

TABLE 1. VALUES OF F/c^2k: SQUARE-BASED PYRAMIDS

$\theta°$	20	30	45	60	68	75
Smooth	3·4	7·6	24	81·5	177	434
Rough	—	12·5	35	109	228	490

The rates of energy dissipation for the same basic field with angles *LEP* and *LHQ* (Fig. 1) different from 45° were obtained. For some semi-apex angles the values of F/c^2k found were slightly lower than those given by equation (2) but never by more than 2 per cent.

The effect of friction between the pyramid and the deforming metal is now considered. Suppose there is a shearing stress nk ($n \leqslant 1$) on the faces of the pyramid where they make contact with the deforming metal. It seems reasonable to use the velocity field already considered if n is small. The rate of energy dissipation at the faces is then

$$\dot{W}_{pF} = 4nkah[U]$$

where $[U]$ is the tangential velocity discontinuity at the face and

$$[U] = \sin\theta + \cos\theta$$

The rate of energy dissipation at the faces is therefore

$$\dot{W}_{pF} = \frac{4nkc^2 \tan\theta(\sin\theta + \cos\theta)}{\cos\theta - \sin(\theta - \psi)}$$

and the approximate expression for F/c^2k is then

$$\frac{F}{c^2k} = \frac{4\tan\theta\{2\sqrt{(\frac{1}{2} + \sin^2\theta)} + \psi[\sin\theta + \sqrt{(\frac{1}{2} + \sin^2\theta)}] + n(\cos\theta + \sin\theta)\}}{\cos\theta - \sin(\theta - \psi)} \tag{3}$$

When the pyramid is perfectly rough it is reasonable to expect that a different plane-strain velocity field would result in a better approximation

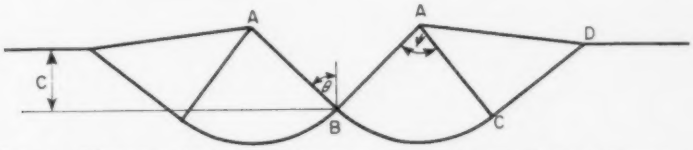

FIG. 5. Plane-strain indentation by a perfectly rough-sided pyramid.

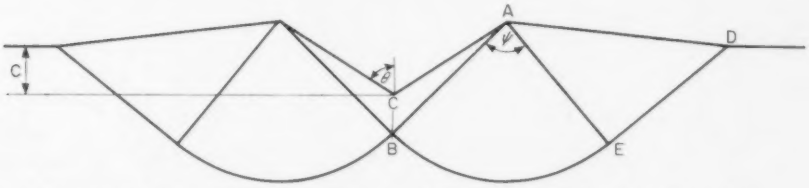

FIG. 6. Plane-strain indentation with a cap of dead metal over the head of the pyramid.

for the indenting load. Consequently a velocity field based on the field shown in Fig. 5 was tried for perfectly rough pyramids with semi-apex angles less than 45°. However, higher values of F/c^2k were obtained than were given by equation (3) with $n = 1$.

A qualitative feature of plane-strain wedge indentation indicates that a cap of dead metal may be formed over the pyramid when the semi-apex angle is greater than 45°; a velocity field for the plane-strain field for perfectly rough wedges with semi-angles greater than 45° is shown in Fig. 6. In Fig. 7 the plastically deforming region of the velocity field based on Fig. 6 is shown for one-quarter of the pyramid and the stream lines are parallel to CDE. This field gives

$$\frac{F}{c^2k} = \frac{4\sqrt{(2)}\tan\theta\sin\theta}{(\cos\theta - 2\sin\theta\cos\psi)}\left[\frac{(1+\psi)}{2}\left(1 + \frac{1}{\sin\{\tan^{-1}[1/\sqrt{(2)}]\}}\right)\right] \tag{4}$$

where ψ is given by

$$\sin\psi + \tfrac{1}{2} = \sin(\theta + \psi)/(\cos\theta - 2\sin\theta\cos\psi) \tag{5}$$

The indenting loads obtained from this are less than those given by (3) with $n = 1$, when the semi-apex angle is greater than 60°.

The same field was tried with different values of semi-angle for the dead metal cap but only very small differences from the results given by (4) were

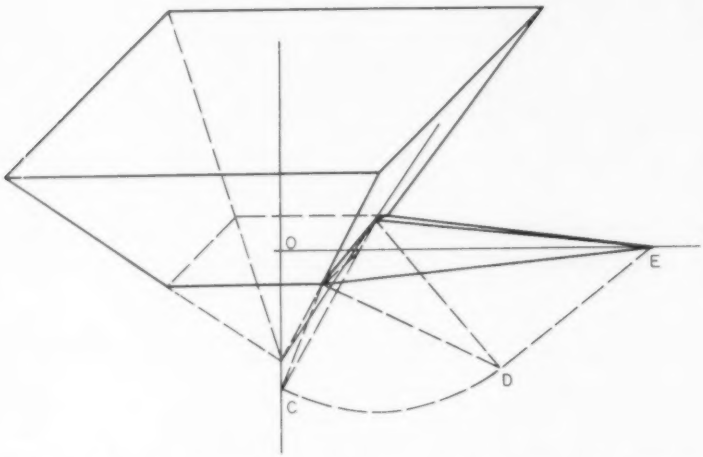

FIG. 7. Assumed plastically deforming region for a pyramid, based on the slip-line field shown in Fig. 6.

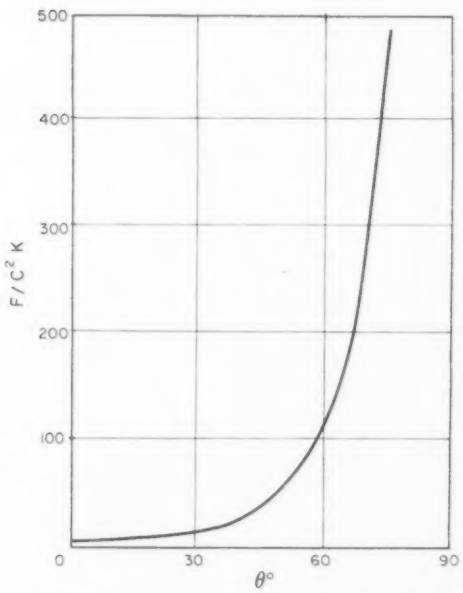

FIG. 8. Showing the variation of F/c^2k with θ for a rough-sided square-based indenter.

obtained. Approximate values of F/c^2k for perfectly rough pyramids, obtained from (3) with $n = 1$ for semi-apex angles less than 60° and from (4) for semi-apex angles greater than 60°, are shown in Fig. 8 and are also given in Table 1.

(ii) *Application of the approximate method to triangular-based pyramids.* Indentation with a right regular pyramid whose base is an equilateral triangle is now considered. For smooth triangular-based pyramids the approximate method uses a velocity field again based on the field for plane-strain indentation with smooth wedges and the procedure is similar to that for smooth square-based pyramids.

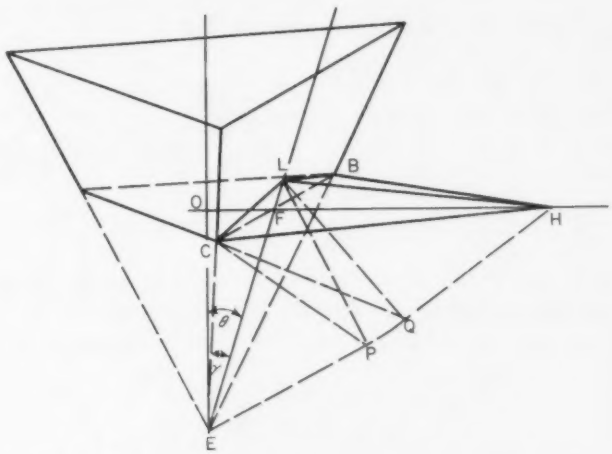

FIG. 9. Showing the plastically deforming region for a smooth-sided triangular-based pyramid.

In Fig. 9 *EPQHLC* is the plastically deforming region of the velocity field associated with one-sixth of the pyramid and the stream lines are parallel to *EPQH*. The intersection of the plastically deforming region and the vertical plane through *OF* is *EPQHL* and is shown in Fig. 2. The angle θ is the angle between the axis of the pyramid and one of the faces as shown in Fig. 9; this angle is referred to as the semi-apex angle in this Section.

It follows from the incompressibility requirement that area *EOF* = area *LFH*; also from elementary geometry

$$\sqrt{(3)}\sin\theta = \tan\gamma$$

The relationship between θ and ψ is identical with that for the square-based pyramid (Fig. 1). The intersection of a plane parallel to, and distance x from, *OFE* and the plastically deforming region is shown in Fig. 3.

When the pyramid advances with unit speed, the rate of energy dissipation in a lamina of thickness dx, distance x from, and parallel to, *OFE* is

$$d\dot{W}_p = \{(2+\psi)\sqrt{(1+\tfrac{1}{2}\cot^2\gamma)}+\psi\}\,kh'\sin\theta\,dx$$

where

$$\cot\gamma = \operatorname{cosec}\theta/\sqrt{(3)} \quad \text{and} \quad h' = h(a-x)/a$$

Integrating from $x = 0$ to $x = a$ gives the rate of energy dissipation, $\dot{W}_p/6$, in region *EPQHLCE* of Fig. 9.

Noting that

$$h = \frac{c}{\cos\theta - \sin(\theta - \psi)} = \frac{a\cot\theta}{\sqrt{(3)}\,[\cos\theta - \sin(\theta-\psi)]}$$

the approximate expression for F/c^2k derived is

$$\frac{F}{c^2k} = \frac{3\sqrt{(3)}\tan\theta\{(2+\psi)\sqrt{(\tfrac{1}{6}+\sin^2\theta)} + \psi\sin\theta\}}{\cos\theta - \sin(\theta-\psi)} \tag{6}$$

Values of F/c^2k found from (6) are given in Table 2.

Table 2. Values of F/c^2k: triangular-based pyramids

$\theta°$	30	47	50	54	64½	68	75
Smooth	7·6	32	41	57	144	208	510
Rough	13·4	45	56	74	190	—	560

When the faces of the triangular-based pyramid are rough, the same velocity field may be used but the energy dissipation at the contact area is to be included. The rate of energy dissipation at the faces when the shearing stress is nk ($n \leqslant 1$) is

$$\frac{3\sqrt{(3)}\,nkc^2\tan\theta\,(\sin\theta+\cos\theta)}{\cos\theta - \sin(\theta-\psi)}$$

and the approximate expression for F/c^2k is then

$$\frac{F}{c^2k} = \frac{3\sqrt{(3)}\tan\theta\{2\sqrt{(\tfrac{1}{6}+\sin^2\theta)} + \psi[\sin\theta + \sqrt{(\tfrac{1}{6}+\sin^2\theta)}] + n(\cos\theta+\sin\theta)\}}{\cos\theta - \sin(\theta-\psi)} \tag{7}$$

Equation (7) gives higher values of F/c^2k when $n = 1$ (i.e. for perfectly rough pyramids) than the adaptation of the fields for plane-strain indentation with perfectly rough wedges. These adapted velocity fields are shown in Figs. 10 and 11. As before, plane-strain motion is preserved and in Fig. 10 the stream lines are parallel to EPQ. It may be shown that the rate of energy dissipation associated with the field indicated in Fig. 10 is

$$\dot{W}_p = \frac{3\sqrt{(3)}\,c^2k\tan\theta\big(\cos\theta + \psi\sin\theta + \{(1+\psi)\sin\theta/\sin[\tan^{-1}\sqrt{(3)}\sin\theta]\}\big)}{\cos\theta - \sqrt{(2)}\sin(\tfrac{1}{4}\pi + \theta - \psi)}$$

when the pyramid advances with unit velocity and where ψ is given by

$$\frac{\cos(\psi - \tfrac{1}{4}\pi)}{\cos\theta - \sqrt{(2)}\sin(\tfrac{1}{4}\pi+\theta-\psi)} = \cos(\theta - \psi + \pi/4) + \frac{\sin\theta}{\sqrt{2}}$$

The expression for F/c^2k is

$$\frac{F}{c^2k} = \frac{3\sqrt{(3)}\tan\theta\big(\cos\theta + \psi\sin\theta + \{(1+\psi)\sin\theta/\sin[\tan^{-1}\sqrt{(3)}\sin\theta]\}\big)}{\cos\theta - \sqrt{(2)}\sin(\tfrac{1}{4}\pi+\theta-\psi)} \tag{8}$$

When $\theta > 50°$, of those tried the velocity field which gave the lowest value of F/c^2k is that shown in Fig. 11 and is an adaptation of the field for plane-strain indentation with rough wedges with semi-angles greater than 45°. Plane-strain motion is preserved and the stream lines are parallel to CDE in Fig. 11. It may

be shown that the rate of energy dissipation for the field shown in Fig. 11 when the pyramid moves with unit velocity is

$$\dot{W}_p = \frac{3\sqrt{(3)}\,kc^2 \sin\theta \tan\theta(1+\psi)\{1+\operatorname{cosec}\tan^{-1}\sqrt{(3/2)}\}}{\cos\theta - 2\sin\theta\cos\psi}$$

where ψ is given by (5).

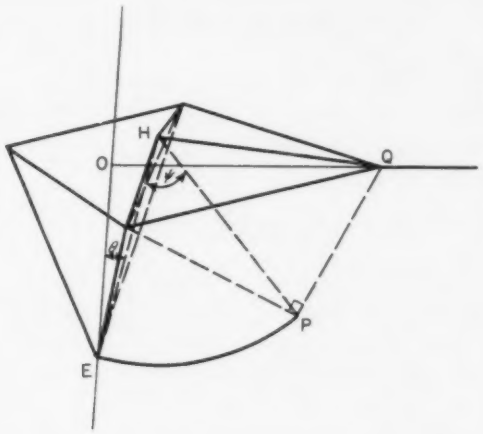

FIG. 10. Showing the plastically deforming region for a rough-sided triangular-based pyramid.

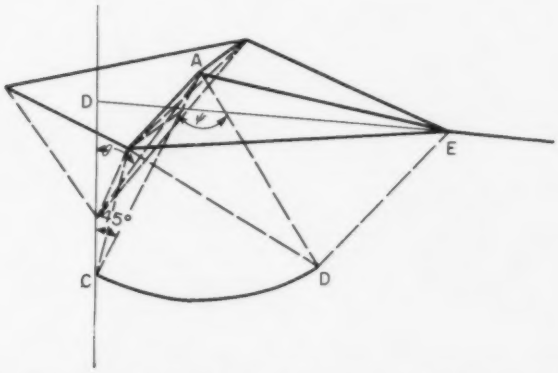

FIG. 11. Showing the plastically deforming region for a rough-sided triangular-based pyramid in which a cap of dead metal covers the pyramid apex.

The approximate expression for F/c^2k is then

$$\frac{F}{c^2k} = \frac{3\sqrt{(3)}\sin\theta\tan\theta(1+\psi)\{1+\operatorname{cosec}\tan^{-1}\sqrt{(3/2)}\}}{\cos\theta - 2\sin\theta\cos\psi} \tag{9}$$

The values of F/c^2k found from (8) when $\theta < 50°$ and from equation (9) when $\theta > 50°$ are given in Table 2.

3. OBSERVATION

In Table 3, for various values of θ, the calculated values of p'/Y and p''/Y are given for indenting with a smooth square-based pyramid. The Mises yield criterion is employed; p' is the indenting force divided by the projected area of the indentation neglecting "pile-up" and p'' includes "pile-up". The modest variation in p''/Y with θ is remarkable. Tabor[1] gives a value of about 3·2 for $\theta \simeq 68°$ as the ratio of "yield pressure" to yield stress and this compares favourably with the value of 2·8 calculated above for a *smooth* indenter.

TABLE 3. VALUES OF p'/Y AND p''/Y

$\theta°$	30	45	60	68	75
p'/Y	3·3	3·5	3·8	4·2	4·5
p''/Y	2·5	2·45	2·67	2·8	3·0

REFERENCES

1. D. TABOR, *The Hardness of Metals*, Chap. 8. Clarendon Press, Oxford (1951).
2. R. HILL, *Phil. Mag.* **42**, 900 (1951).
3. R. HILL, *Mathematical Theory of Plasticity*. Clarendon Press, Oxford (1950).

Int. J. Mech. Sci. Pergamon Press Ltd. 1961. Vol. 3, pp. 239–246. Printed in Great Britain

AN ANALOGY BETWEEN UPPER-BOUND SOLUTIONS FOR PLANE-STRAIN METAL WORKING AND MINIMUM-WEIGHT TWO-DIMENSIONAL FRAMES

W. JOHNSON
Department of Mechanical Engineering
Manchester College of Science and Technology

(*Received* 6 *February* 1961)

Summary—Slip-line fields and the method of upper bounds have been used for solving certain plane-strain metal working problems. It is demonstrated that these solutions and their associated hodographs may be used to help select the form of nearly minimum-weight frames for particular configurations and loads.

Vol. 3
1961

1. INTRODUCTION

IN A lecture in 1960 on minimum weight frames Hemp took a paper on the same subject written by Michell in 1904[1] and showed that Michell's work was, essentially, bound up with characteristic theory. Michell made nearly sixty years ago an outstanding contribution to this subject but his work seems to have been overlooked until brought to light by Hemp. In his lecture Hemp showed the similarity which exists between the now well-known characteristic solutions or slip-line fields of plane plasticity and the type of solutions Michell had suggested for minimum-weight frames. The writer was present at Hemp's lecture and this led him to re-investigate the topic using the idea of the hodograph.

This note demonstrates very simply an analogy which exists between certain solutions to plane-strain metal-working problems and the arrival at the form of some minimum-weight two-dimensional frames. To the slip-line field corresponds the least-weight space frame and with the hodograph may be identified the force diagram for the frame.

Some useful practical value can be made of techniques which are available for investigating metal-forming problems for which no slip-line fields have been found. In these cases loads may be estimated using bounding techniques and the method rests on certain Extremum Principles. These methods may be adapted to give good over-estimates for determining minimum-weight frames. They offer much flexibility in approaching this problem.

2. UPPER BOUNDS: HODOGRAPHS

We consider some upper-bound solutions to the problem of plane-strain extrusion through a rough die semi-angle 45° where the ratio $h/H = 0{\cdot}5$; see Fig. 1(a). The slip-line field solution is well known, being that of a circular quadrant and radial lines from O and O', see Fig. 1(b); the extrusion pressure in terms of the plane-strain yield-shear stress k, i.e. p, is easily shown to be[2]

$p = k(1+\pi/2)$. An upper bound using three lines of velocity discontinuity OA, AB and OB as shown in Fig. 1(c) can be obtained. This employs a theorem

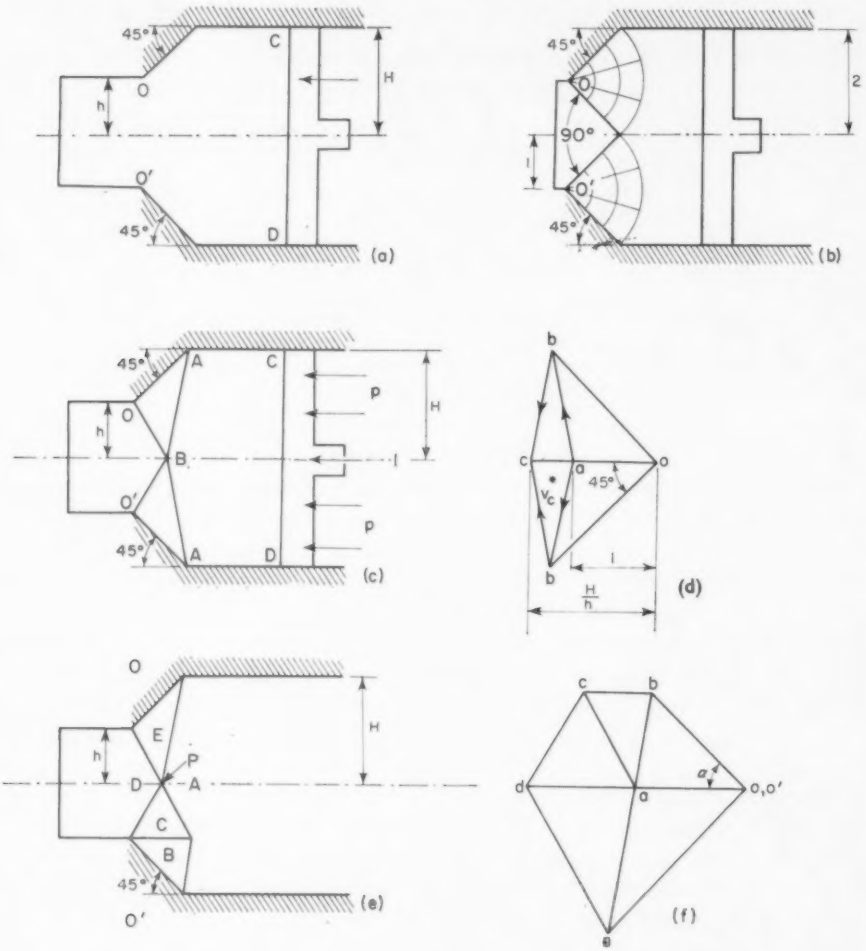

FIG. 1. (a) Plane-strain extrusion through a 45° wedge-shaped die. (b) Slip-line field as for previous case when die is perfectly rough. (c) Analysis using lines of tangential velocity discontinuity to obtain an upper bound. (d) Hodograph for (c). (e) Similar to (c), but using more lines of discontinuity in bottom half. (f) Hodograph for (e).

originally due to Hill[2], which applied to this case appears as

$$p \,.\, 1 \,.\, H = k(s_{AB}\, v^*_{AB} + s_{BO}\, v^*_{BO} + s_{OA}\, v^*_{OA}) \qquad (1)$$

s refers to the length (strictly area, but we assume unit thickness normal to the plane of flow) and v^* is the magnitude of the tangential velocity discontinuity occurring across the line designated by the double suffix to these symbols. Equation (1) states that the external work done by the ram CD of height $2H$, moving with unit speed which applies a uniform pressure p, is dissipated

plastically by shearing which takes place in infinitely thin zones OA, AB and BO. To calculate the magnitudes v^* a hodograph[3, 4] is drawn; the method of doing this for this kind of problem has been described at length elsewhere[5] and is shown in Fig. 1(d). Thus having drawn a space diagram Fig. 1(c) and a hodograph Fig. 1(d), s and v^* quantities may be read off and p calculated using equation (1).

A convenient and simple method for drawing the hodograph, not hitherto described, has been proposed by Haddow[6]. Since this is essential to the appreciation of the subject matter the hodograph of Fig. 1(d) may be re-derived as follows. The upper half of Fig. 1(c) is shown as the upper half of Fig. 1(e); the letters now refer to areas in this space diagram. Region O is stationary; region A moves to the left with unit speed, region E moves parallel to the die face and region D parallel to the centre line with speed H/h. The hodograph is now obtained by treating Fig. 1(e) as a space frame and using the lettering to facilitate the drawing of a "force" diagram, using the well-known Bow's notation. From origin o, oa is drawn parallel to OA of magnitude unity [see lower half of Fig. 1(f)]. From a draw ae parallel to AE and from o draw oe parallel to OE to determine point e. From e draw ed parallel to ED and hence locate point d. It is clear that by this means hodographs may be drawn in a more mechanical fashion than is usually the case.

Now each arbitrarily chosen position for P will yield a certain value for p. Clearly the best value of p, i.e. the value which yields the smallest over-estimate, is the "best" value of p. Accordingly after selecting a number of trial positions for P its "best" position may be decided.

Better upper bounds may be obtained by using the system of velocity discontinuities shown in the lower half of Fig. 1(e), i.e. $O'B$, BC, BA, CA, DC, where for this particular case $O'B = BC = CD$. The hodograph drawn by Haddow's method, following the lettering of the lower half of Fig. 1(e), is shown as the upper half of Fig. 1(f).

APPLICATION TO SIMPLE TWO-DIMENSIONAL FRAMES

Suppose that a pin-jointed two-dimensional framework is required to withstand certain loads, at points where two or more members meet, and consists of N rods or members all of which are stressed equally in tension or compression to a given level, σ; bending and buckling are neglected. Then the total weight of the framework W is given by

$$W = w \sum_{i=1}^{N} s_i A_i \tag{2}$$

where w is the weight per unit volume of the material of the frame, A_i the cross-sectional area and s_i the length of the ith rod.

Rewriting (2):

$$W = \frac{w}{\sigma} \sum_{i=1}^{N} s_i(\sigma A_i) = \frac{w}{\sigma} \sum_{i=1}^{N} s_i F_i \tag{3}$$

where F_i is the force in the ith member. If we are seeking a minimum weight

Vol. 3
1961

frame with w and σ given, then for W to be a minimum we require

$$\sum_{i=1}^{N} s_i F_i$$

to be a minimum. Now for any framework, s_i is found from the space diagram and F_i from the force diagram obtained by using Bow's notation in conjunction with it.

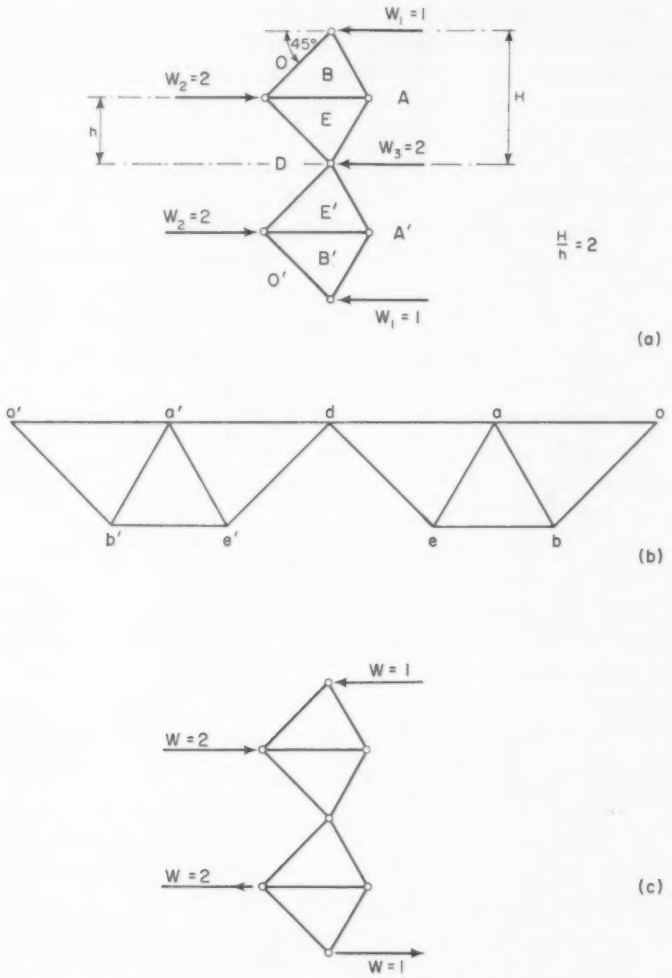

FIG. 2. (a) Space frame and loading. (b) Force diagram for (a). (c) Similar to (a), but with a different loading.

We are now in a position to see the analogy between diagrams embracing the velocity discontinuities of plane-strain problems as in Fig. 1 and certain two-dimensional structures. To a given system of velocity discontinuities in a plane-strain problem there is a corresponding two-dimensional framework; to the hodograph of the former there will be an identical force diagram for

the framework. s, a length, will be identical in both systems but F_i will correspond with v_i^* and W becomes the analogue to p of equation (1). Thus,

$$\sum_{i=1}^{N} s_i F_i$$

is least when

$$\sum_{i=1}^{N} s_i v_i^*$$

is least, i.e. least values of W will correspond with minimum values of p.

To examine the analogy more closely consider the structure shown in Fig. 2(a), adapted by reference to Fig. 1(e). If $W_1 = 1$ unit, then $W_2 = 2$ units, and thus we require $W_3 = 2$. The force diagram for this structure is shown in Fig. 2(b) and the similarity between it and the hodograph in the upper half of Fig. 1(e) is obvious. There would be complete identicality between the half hodograph of Fig. 1(f) and the force diagram of Fig. 2(b) if the system of loads to be sustained by the given frame was as shown in Fig. 2(c). The frame of least weight, to support the given loads applied at the given points, is indicated by Fig. 1(b). By the method of upper bounds as usually applied to metal-working problems we can thus see how an approach to the minimum-weight design of plane frames may be made and concurrently how some estimate of the degree of excess over a possible minimum weight as reflected in the slip-line field may be obtained.

Vol. 3
1961

FURTHER EXAMPLES

There is little need to discuss this analogy at greater length, since to readers familiar with slip-line field theory and the method of upper bounds the adaptations necessary to deal with space frames will be obvious. It will be obvious on reflexion that many simple rules could be arrived at for the purpose of exploiting the methods described. No doubt many interesting plane-frame problems can be solved simply by endeavouring to ascertain what are the analogues to the variety of known slip-line field solutions. The graphical and somewhat empirical approach to finding upper bounds for plane-strain metal-working problems for which slip-line fields are not known can readily provide a rational approach to the selection of minimum-weight plane frames.

The examples in Figs. 3–6, with the aid of the captions, are self-explanatory. It is worth noting (i) that slip-line fields having smooth boundaries [compare Fig. 3(a)] are useful only when the weight of the member corresponding to the smooth boundary is neglected, and (ii) that slip-line fields involving a perfectly rough boundary [compare Figs. 1(b), 4(a), 5(a) and 6(a)] are most useful for selecting minimum-weight frames.

Note added in proof

The Design of Michell Optimum Structures by A. S. L. Chan, College of Aeronautics, Cranfield, appeared as C.O.A. Report 142 while this article was in proof.

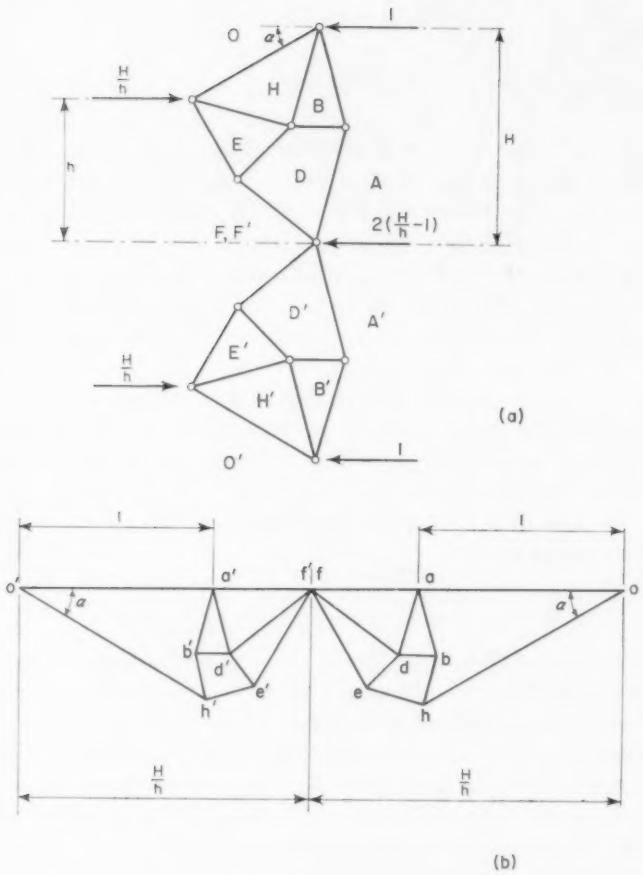

FIG. 3. Weight of rods OH and $O'H'$ negligible; most applicable when $H > h(1 + 2 \sin \alpha)$. (a) Frame. (b) Force diagram. (Based on extrusion through a perfectly smooth wedge-shaped die of small angle and for a small reduction.)

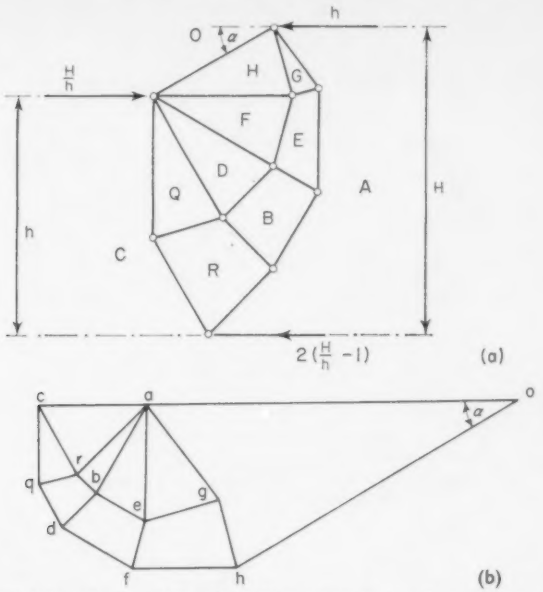

FIG. 4. Weight of rods OH and $O'H'$ included; similar to case in Fig. 3; most applicable when $H < h[1+\sqrt{(2)}\sin\alpha]$. Top half of diagram only shown. (a) Frame. (b) Force diagram. (Based on extrusion through a perfectly rough wedge-shaped die of small angle and for small reduction.)

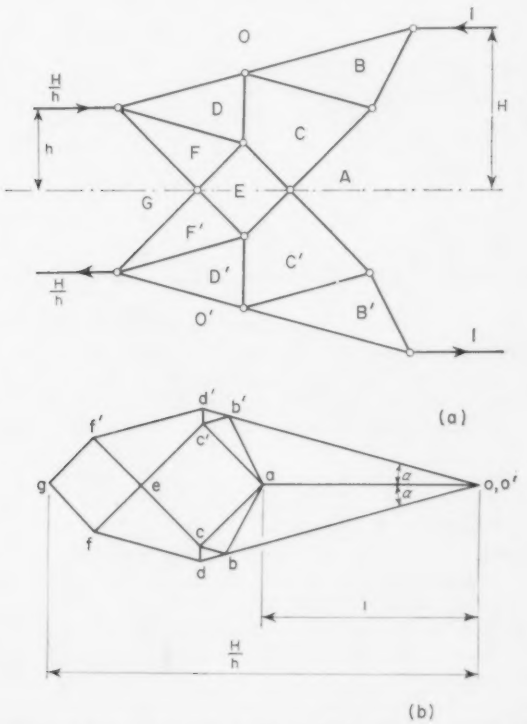

FIG. 5. Weight of rods OD, OB, $O'D'$, $O'B'$ included; most applicable when $H > h[1+\sqrt{(2)}\sin\alpha]$. (a) Frame. (b) Force diagram. (Based on extrusion through a perfectly rough wedge-shaped die, for a large reduction.)

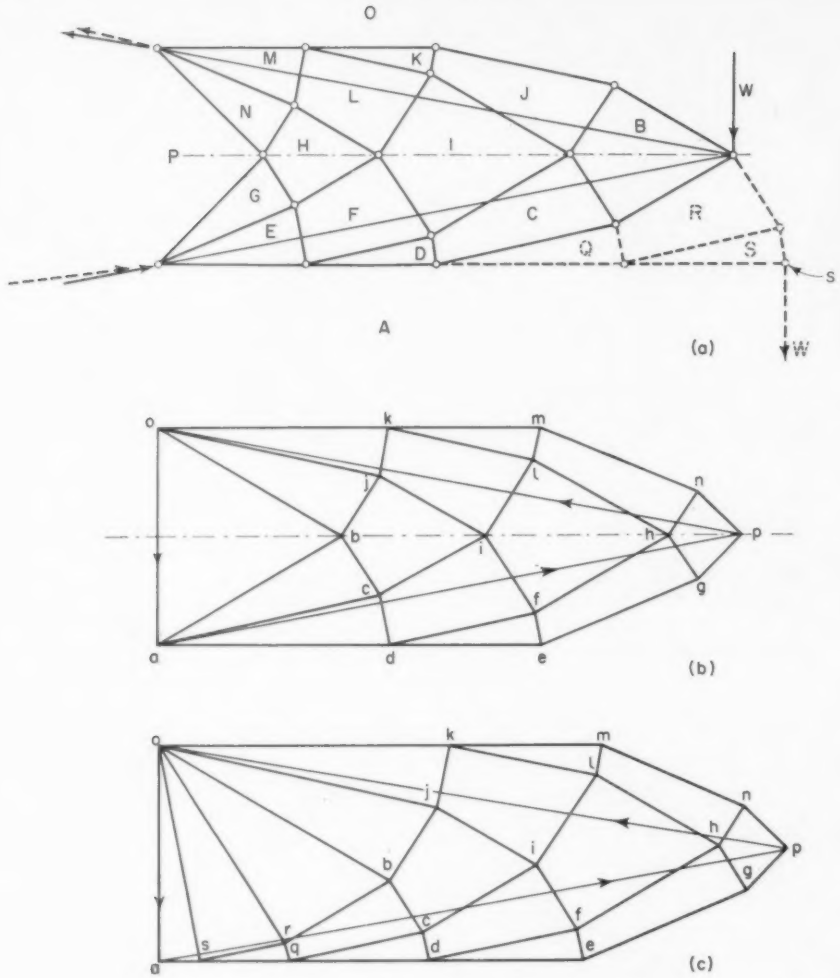

FIG. 6. Frame sustaining a transverse load and acting as a cantilever: two cases. (a) Symmetrical frame structure with (b) as the force diagram. (c) Force diagram for asymmetrical structure obtained by adding dashed lines to frame in (a) and for load acting at S. (Based on compression between perfectly rough flat plates.)

REFERENCES

1. A. G. MICHELL, *Phil. Mag.* **8**, 589 (1904).
2. R. HILL, *Mathematical Theory of Plasticity*. Clarendon Press, Oxford (1950).
3. W. PRAGER, *An Introduction to Plasticity*. Addison-Wesley, Massachusetts (1959).
4. A. P. GREEN, *J. Mech. Phys. Solids* **2**, 73 (1953).
5. W. JOHNSON, *Proc. Inst. Mech. Engrs., Lond.* **173**, 61 (1959).
6. J. B. HADDOW, "Some Indentation and Forging Problems". Ph.D. Thesis, University of Manchester (1960).

Int. J. Mech. Sci. Pergamon Press Ltd. 1961. Vol. 3, pp. 247–267. Printed in Great Britain

Vol. 3
1961

FATIGUE OF BITUMEN AND BITUMINOUS MIXES

P. S. Pell*, P. F. McCarthy† and R. R. Gardner‡

(*Received* 1 *February* 1961)

Summary—This paper gives details of an investigation into the fundamental fatigue properties of bitumen and bituminous mixes. Fatigue tests carried out under constant bending stress, at varying temperatures between $-13{\cdot}5°C$ and $+25°C$, show that the material exhibits fatigue properties over wide ranges of stress and that for a particular temperature and speed of loading the log stress–log number of cycles to failure relationship is linear between 10^4 and 10^8 cycles. The life under constant stress is highly dependent on the temperature of the test, a low temperature giving a longer life at a particular stress; it is also dependent to some extent on the speed of loading, but taking into account the stiffness of the material which depends on temperature, speed of loading, rheological characteristics and composition of the mix, it has been found that when the logarithm of the strain is plotted against the logarithm of the number of cycles to failure all experimental results at different speeds and temperatures for one mix lie with a certain amount of scatter about a straight line. It appears therefore that the factor affecting the fatigue life is one of strain rather than stress, and the effects of temperature and speed can be accounted for by their effect on the stiffness of the specimen. This has been confirmed by tests under constant torsional strain at different temperatures between $-20°C$ and $+40°C$, but at the higher temperatures under this type of loading the fatigue life includes a considerable crack-propagation time. Similar results have been obtained from mixes containing different amounts of aggregate, but as the quantity of aggregate in the mix is reduced so the life for a given strain increases, suggesting that the criterion of failure may be one of tensile strain in the bitumen present in the mix. Some tests have also been carried out on pure bitumen specimens at different temperatures.

Careful examination of the fatigue cracks and failure surfaces shows that in nearly all cases failure originates on the principal tensile plane. The effects of such factors as surface conditions, void content and rest periods have also been studied.

INTRODUCTION

In the past the design of bituminous road carpets has been based on a bitumen content determined by stability requirements, and a thickness related to static loading conditions. But roads are built to carry traffic and therefore by the very nature of the loading system are subjected to dynamic loads, and failure by fatigue has been suggested as one of the causes of the cracking of bituminous carpets in practice.[1]

A considerable amount of work on the fatigue testing of bituminous mixes has been carried out at the Royal Dutch Shell laboratories at Amsterdam and some of the results have been published.[2,3] The work described in this paper constitutes an independent investigation carried out at Nottingham University into the fundamental fatigue properties of bitumen and bituminous mixes under both bending and torsional loading. The effects of such factors as temperature, speed of loading, composition of mix, void content, surface finish

* Department of Civil Engineering, University of Nottingham.
† "Shell" Research Ltd., Thornton Research Centre, Chester.
‡ "Shell" Research Ltd., Thornton Research Centre, Chester.

and rest periods have been investigated. Part of the work has been reported earlier[3] but has been briefly included so that a complete picture may be obtained.

Although this paper is concerned with bituminous materials it is being published in the hope that it will be of interest to workers in the field of fatigue of other visco-elastic materials and may throw some light on the general phenomena of fatigue.

CONSTANT BENDING-STRESS FATIGUE TESTS ON SANDSHEET SPECIMENS

Specimens of the type shown in Fig. 1 were manufactured having a minimum diameter at the neck of $1\frac{1}{4}$ in. increasing continuously towards either end where there is a cylindrical steel end piece. Sandsheet specimens were made from a mix containing 81 per cent by volume of mineral aggregate and 19 per cent by volume of bitumen. This consisted of 85 parts by weight of sand having a consistent grading, 15 parts by weight of limestone filler and $9\frac{1}{2}$ parts by weight of a 40/50 penetration bitumen with a Ring and Ball softening point of 55·5°C. The loose hot mix was placed in split moulds vigorously tamped by hand and then finally compacted in a hydraulic press under a load of 15 tons applied for one minute. On cooling the moulds were stripped from the specimen and Fig. 2 shows a demoulded specimen ready for testing and also a broken specimen which has failed in fatigue after testing.

The specimen is clamped in a vertical position in the chuck of a rotating-type cantilever fatigue machine (Fig. 1), and the load is applied to the top bearings by stirrups and wires which run over a system of pulleys so that equal and opposite loads are applied to different points at the top of the specimen and hence a constant bending moment to the specimen. This results in the maximum stress occurring at the neck of the specimen which is situated as far as possible from probable stress concentrations at the ends. Under this system of loading there is no shear stress on the specimen. The specimen is run in a carefully controlled temperature bath and at the end of each test a portion is cut from the neck and the void content determined to control the consistency of specimen manufacture. A technique of specimen preparation was developed whereby specimens were consistently produced having a smooth surface finish and a low void content, and fatigue results were only considered from specimens having less than $3\frac{1}{2}$ per cent voids.

Following calibration tests on both machines and specimens, fatigue tests were run at different temperatures and speeds. A typical set of results under constant bending at various stress levels at a temperature of $-0{\cdot}5$°C and a speed of 2300 rev/min are shown in Fig. 3. It will be seen that when the logarithm of the stress is plotted against the logarithm of the number of cycles to failure the results are scattered about a straight line. A scatter band is also shown on this figure, the limits being determined by $\pm 2s$ (s = standard deviation of log N) as calculated from the results of sixteen tests at one stress level. Statistically this scatter width includes 95 per cent of all results, and it does appear to include the vast majority of the experimental points at all the stress

FIG. 2. Sandsheet specimen before and after testing.

Vol.
196

Vol. 3
1961

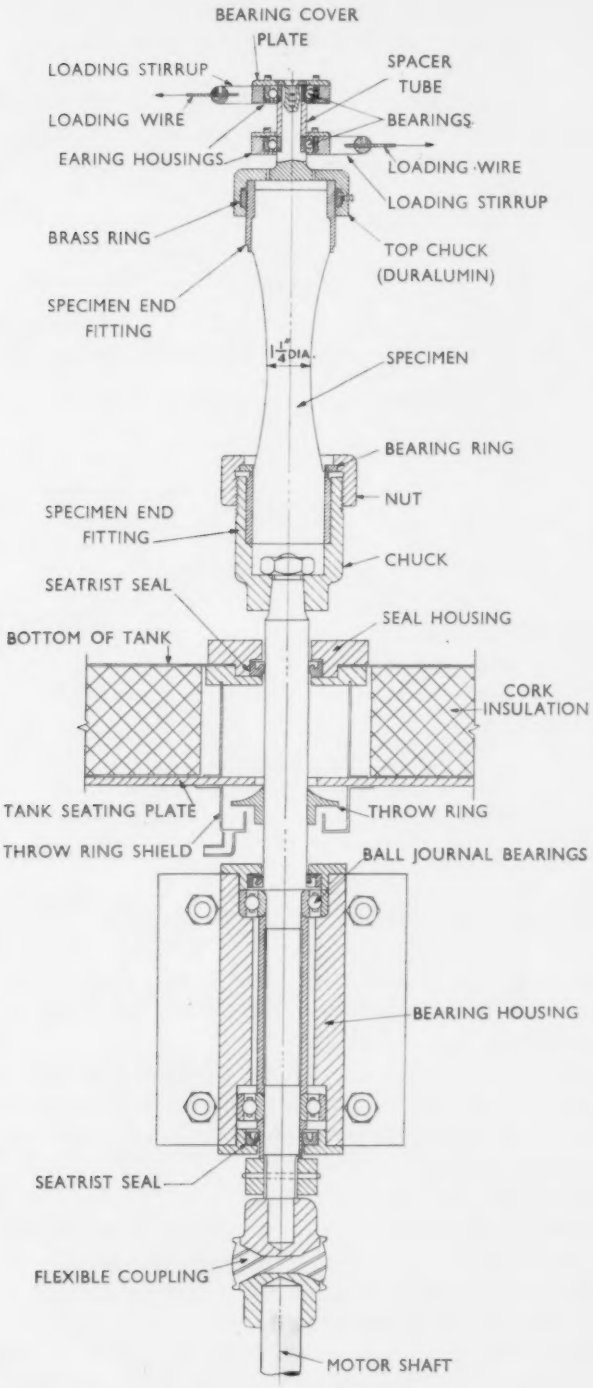

FIG. 1. Details of constant-bending fatigue machine.

levels. This scatter amounts to an overall range of 4 to 1 in life at any stress level and compares quite favourably with results obtained from similar types of fatigue tests on metals.

It is of interest to note that the actual duration of test varied from 5 min at the highest stress level to 28 days at the lowest stress, and that over the range measured there was no evidence of an endurance limit, specimens having failed after nearly 10^8 cycles.

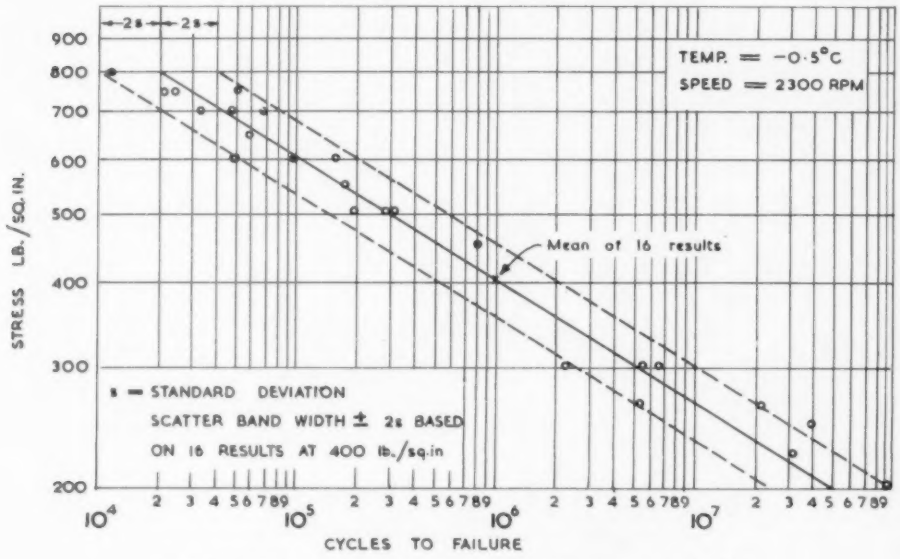

Fig. 3. Fatigue results of sandsheet specimens at −0·5°C under constant-bending stress.

Similar tests were also carried out at the following temperatures and speeds: −13·5°C/1000 rev/min; −9·5°C/3000 rev/min; +7°C/2300 rev/min; +25°C/3000 rev/min. The results of all these tests are shown in Fig. 4, where in order to avoid confusion individual experimental points are not shown but only the lines representing the mean lives.

Further tests, but at only one stress level, were also repeated at +20°C/3000 rev/min, and at 0°C at speeds varying between 800 rev/min and 3000 rev/min. These latter tests showed that the mean life at the lower speeds was significantly smaller than that at the higher speeds.

In the case of the tests at +25°C, shorter specimens 3 in. long, but still having the same neck diameter, were used in order to improve the stability of the specimen at the higher temperature. Preliminary tests at 0°C showed no significant difference between the mean lives of short and long specimens.

In all cases the specimens fractured instantaneously and without warning, the mode of failure being a brittle fracture in the region of maximum stress, with the failure plane perpendicular to the axis of the specimen and having a fairly smooth surface. Examination of these surfaces showed that generally

the failure occurred in the bitumen matrix but occasionally fracture took place through some of the larger grains of sand.

These results at the various temperatures and speeds give rise to the following comments.

(1) The fatigue life of the sandsheet mix under an alternating bending stress of constant amplitude is highly temperature dependent—the lower the temperature the longer is the life.

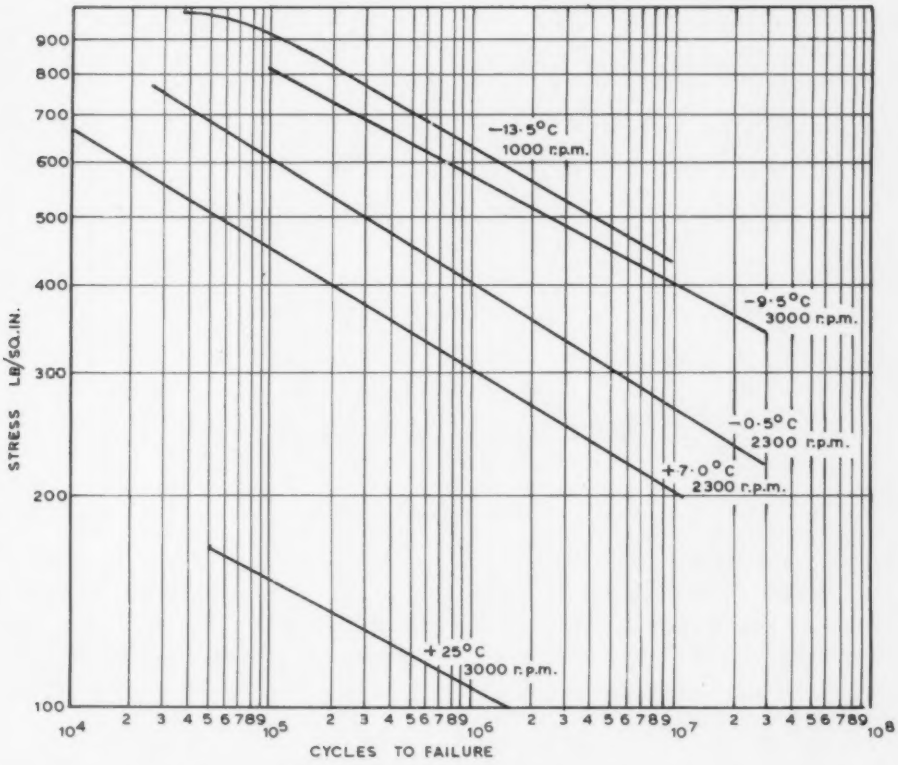

FIG. 4. Fatigue results of sandsheet specimens at various temperatures and speeds under constant-bending stress.

(2) The fatigue life is also dependent to some extent on the speed of loading —the lower the speed the shorter the life.

(3) The relationship between the logarithm of the stress and the logarithm of the number of cycles to failure appears to be linear at all temperatures and speeds over wide ranges of stress, although there is some evidence at very high stresses of non-linearity.

(4) The slope of the plot of log stress against log cycles, considering the experimental scatter present, does not appear to be dependent on the temperature or speed.

In the work reported by van der Poel[4, 5] the effects of the time of loading and temperature on the stiffness of bitumen have been clearly shown. Under a

sinusoidally varying stress the dynamic stiffness is defined as the ratio of stress amplitude to strain amplitude. Van der Poel's results were published in the form of a nomograph which enables the stiffness of a particular bitumen to be determined for any speed of loading and temperature if the Penetration Index and Ring and Ball temperature are known. From a further nomograph,

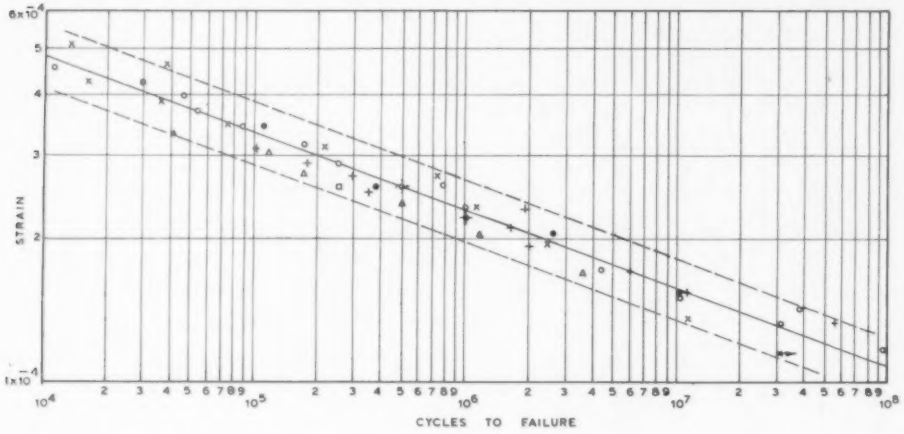

TEMP °C	+ 25	+ 20	+ 7	− 0·5	− 0·5	− 0·5	− 9·5	− 13·5
SPEED R.P.M.	3000	3000	2300	1000	2300	3000	3000	1000
KEY	●	□	×	⊕	○	✦	+	△

Fig. 5. Fatigue results of sandsheet specimens at various temperatures and speeds plotted as log strain against log cycles.

knowing the stiffness of the bitumen alone, it is possible to obtain the stiffness of a particular bitumen–aggregate mixture knowing the volume concentration of the mineral aggregate. In this way the stiffness of fatigue specimens was calculated for the various conditions of temperature and speed of testing and the results are tabulated in Table 1.

Table 1. Stiffness of sandsheet mix obtained from penetration index and ring and ball temperature

Temperature (°C)	Speed (rev/min)	Stiffness of bitumen (newtons/m²)	Stiffness of mix (lb/in²)
− 13·5	1000	$9{\cdot}60 \times 10^8$	$2{\cdot}90 \times 10^6$
− 9·5	3000	$9{\cdot}00 \times 10^8$	$2{\cdot}61 \times 10^6$
− 0·5	3000	$4{\cdot}10 \times 10^8$	$1{\cdot}81 \times 10^6$
− 0·5	2300	$3{\cdot}85 \times 10^8$	$1{\cdot}74 \times 10^6$
− 0·5	1000	$3{\cdot}00 \times 10^8$	$1{\cdot}57 \times 10^6$
+ 7·0	2300	$2{\cdot}10 \times 10^8$	$1{\cdot}28 \times 10^6$
+ 20·0	3000	$9{\cdot}0 \times 10^7$	$6{\cdot}80 \times 10^5$
+ 25·0	3000	$5{\cdot}5 \times 10^7$	$4{\cdot}65 \times 10^5$

During mixing some hardening of the bitumen takes place and in order to take account of this, the Penetration Index and Ring and Ball temperature were determined on bitumen recovered from the specimens.

The stiffness of specimens at 0°C/1000 rev/min was also measured directly from a load-deflexion curve and was found to agree closely with the nomographic value.

From these values of stiffness the strain was calculated for each fatigue test and the result of plotting the logarithm of the strain against the logarithm of the number of cycles to failure is shown in Fig. 5. From this graph it can be seen that all the results from different conditions of temperature and speed appear to lie about a straight line with only slightly more scatter (6 to 1) than that obtained from tests at one particular temperature. To prevent congestion in the figure when more than one result was obtained at any one stress level the mean result only has been plotted on the graph. Subsequent checks have shown that this scatter includes 94 per cent of the individual results and the points shown in the graph represent over one hundred and twenty individual fatigue tests. It is remarkable that the scatter is so small when one considers that the computations of stiffness involve values which themselves have been compiled from experimental results having considerable scatter.

Taking the mean line of the results shown in Fig. 5 the following expression for the relationship between stress and fatigue life is obtained:

$$N = 1{\cdot}44 \times 10^{-16}\left(\frac{S}{\sigma}\right)^6 \quad \text{for} \quad 10^4 < N < 10^8 \tag{1}$$

where N = number of cycles to failure

S = stiffness of the sandsheet mix

σ = applied bending stress.

From the above relationship it may be concluded that the fatigue life of a sandsheet mix within the ranges investigated is primarily controlled by the magnitude of the applied strain and not by the stress, and that the effects of temperature and speed of testing can be accounted for by their effect on the stiffness of the specimen.

CONSTANT TORSIONAL-STRAIN FATIGUE TESTS ON SANDSHEET SPECIMENS

The results of the tests in bending fatigue suggested that if the strain is kept constant then the fatigue life would be independent of the temperature, and in order to check this hypothesis and to investigate the behaviour of the material under torsion tests were carried out in a constant torsional-strain fatigue machine.

The general arrangement of the machine is shown in Fig. 6. A constant-speed electric motor is mounted with its shaft vertical and carries a horizontal cam with an eccentric arrangement to give a variable throw so that a torsional oscillation is imparted by means of a connecting rod to the top of a shaft to which the vertical specimen is firmly clamped. The bottom of the specimen is clamped to the base of the machine and the temperature is controlled by circulating aqueous alcohol solution round refrigeration or heating elements by means of a small pump mounted beneath the machine.

The specimens were identical to those used in the bending tests and the following system was used to stop the machine when the specimen cracked. A continuous-conducting square-wave pattern was painted in a silver solution on the specimen, wires were attached and a rubber sheath fixed over the specimen and sealed to prevent electrical leakage when the specimen was fixed in the temperature-controlled liquid. An electric current passing through this paint actuated a relay which allowed the electric motor to be started, but a crack across the paint stopped the current flowing and switched off the motor.

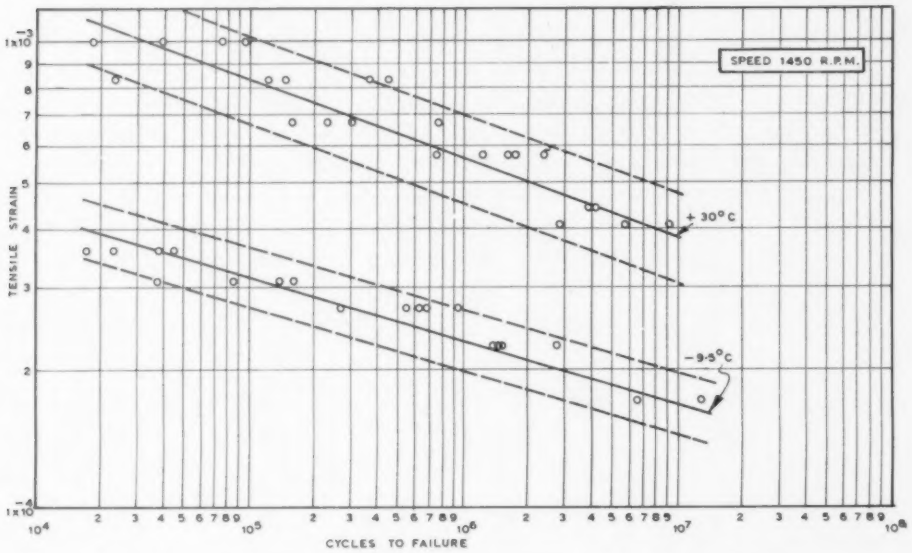

Fig. 7. Fatigue results of sandsheet specimens at −9·5°C and 30°C under constant torsional strain.

The machine was carefully calibrated to determine the deformation in the various components and consequent loss of torsional strain in the specimen.

Fatigue tests at varying strain amplitudes at temperatures of −20°C, −9·5°C, 0°C, +15°C, +30°C and +40°C were made, the speed in all cases being 1450 rev/min. Typical detailed results at temperatures −9·5°C and +30°C are shown on Fig. 7, and the mean lines for all the temperatures on Fig. 8. The results are plotted as tensile strain, which in this case of pure torsion is equal to half the torsional strain, to enable a comparison to be made with the results in bending.

It will be seen that again there is a linear relationship between the logarithm of tensile strain and the logarithm of cycles to failure at all temperatures. The lines at low temperatures of 0°C and below lie close together with no statistical significant difference between them. At these low temperatures there is reasonable agreement between the results in bending and torsion except that the slope of the torsion lines is slightly flatter. It will be remembered, however, that the torsional strain machine is stopped by the propagation of a crack

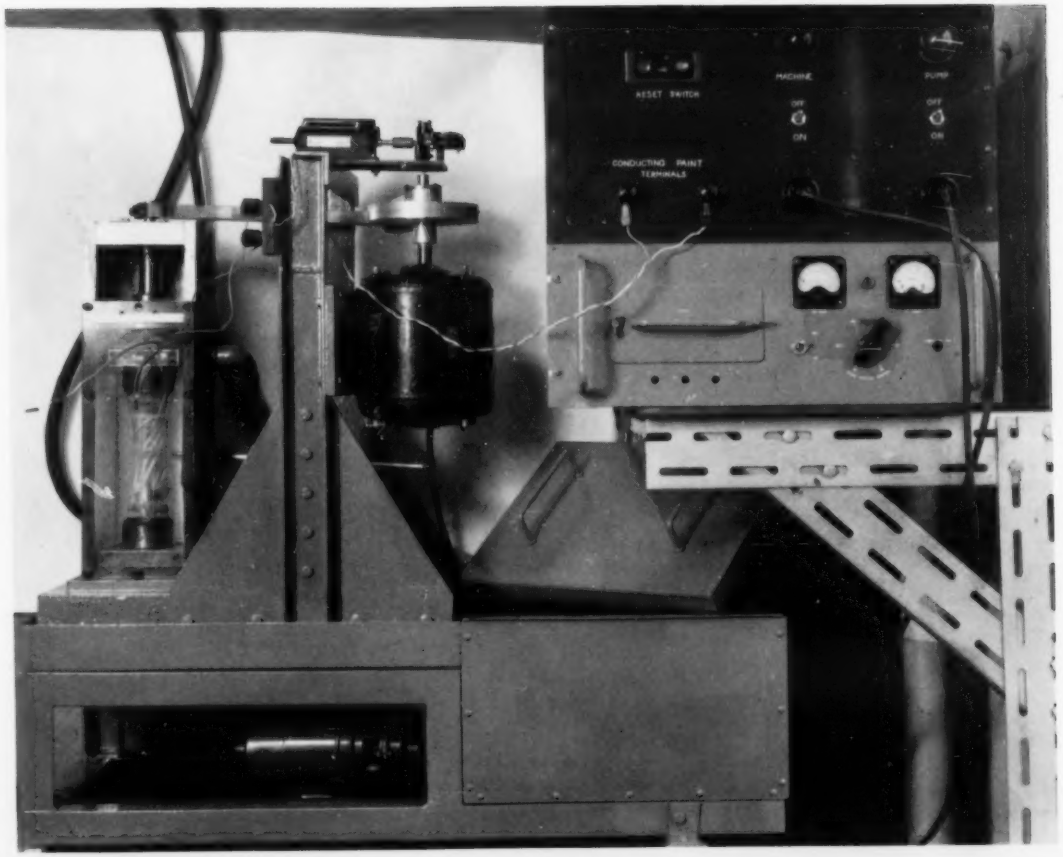

FIG. 6. Constant torsional-strain fatigue machine.

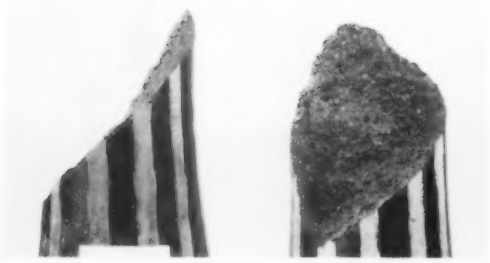

−20°C

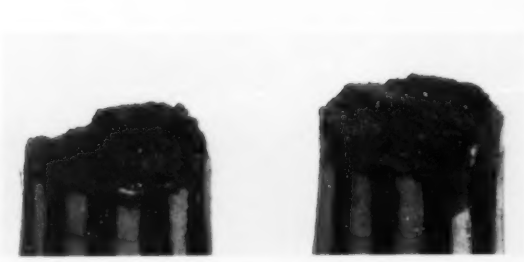

+15°C

−9·5°C

+30°C

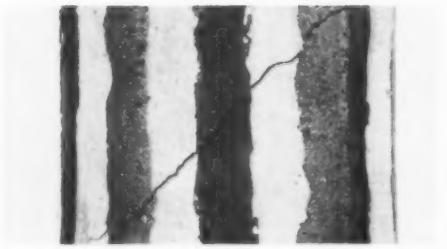

0°C

+40°C

FIG. 9. Fatigue cracks and failure surfaces of sandsheet specimens tested at various temperatures in constant torsional-strain machine.

across a strip of conducting paint and this might well cause longer apparent lines at the lower strains.

When comparing the results of the two types of test it should be remembered that the stress systems differ in both machines, that in the bending machine being a uniaxial system whilst that in the torsional-strain machine is a biaxial stress system.

A significant feature of the fatigue tests at various temperatures in the torsional-strain machine was that at $-20°C$, $-9{\cdot}5°C$ and $0°C$ failure surfaces

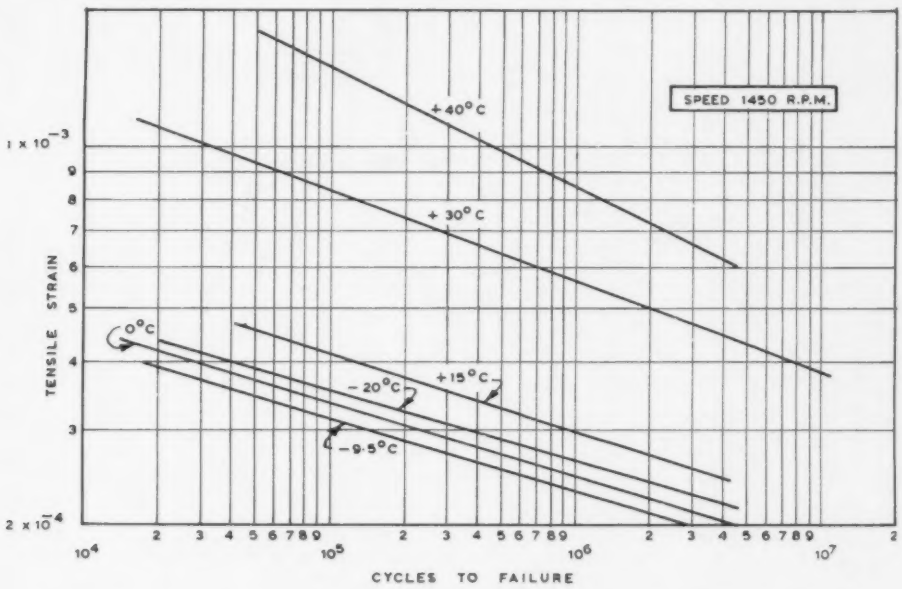

FIG. 8. Fatigue results of sandsheet specimens at various temperatures under constant torsional strain.

were inclined to the axis of the specimen at an approximate angle of 45°, whilst at $+15°C$, $+30°C$ and $+40°C$ the failure surface was more orthogonal (Fig. 9). This may indicate a brittle failure on the principal tensile plane at low temperatures, and considered in conjunction with the agreement between the low temperature constant torsional-strain fatigue results and the bending-fatigue results tends to confirm the hypothesis that the important factor anyway at low temperatures is the magnitude of the principal tensile strain.

At the temperatures above $0°C$, the fatigue results in the constant torsional-strain machine will be seen to be dependent on the temperature, the measured life being much longer at high temperatures, but the authors suggest that these apparently longer lives are due to an extremely slow rate of crack propagation as the stress on the specimen is very low due to the small value of the specimen stiffness at high temperatures.

It will be recalled that the high-temperature ($+20°C$ and $+25°C$) results in the constant-stress machine agreed with the low-temperature results on the

strain relationship, as in this type of machine the onset of cracking results in an increase in actual stress, the crack also acting as a stress concentration, hence leading to rapid propagation and catastrophic failure. In the constant-strain machine, on the other hand, cracking results in a decrease in stress and hence a very slow rate of propagation.

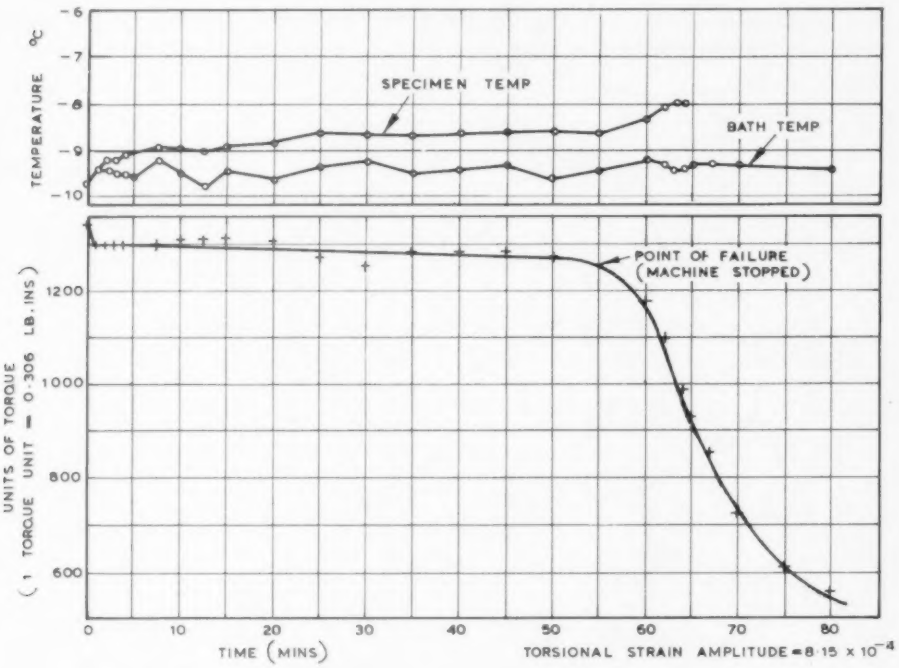

Fig. 10. Torque and temperature measurements during fatigue test on sandsheet specimen at −9·5°C.

In this connexion the results of torque and temperature measurements on the specimen during a fatigue test are of considerable interest. A strain-gauged load cell was fitted in the machine above the specimen to enable the torque acting on the specimen to be observed at any time. Also thermocouples were fixed to the neck of the specimens to measure the surface temperature.

Torque–time curves were obtained for all temperatures at which fatigue lives were measured. Typical results are shown in Figs. 10 and 11 for temperatures of −9·5°C and +30°C respectively. At all temperatures with the exception of −20°C it was found that the consistent characteristics of the curves show an initial rapid reduction in torque over the first few minutes of the test, followed by a more gradual fall-off up to the point of failure, defined by the stopping of the machine by a crack across the conducting paint. If the test is continued by short circuiting the conducting wave pattern, there is a final rapid reduction in torque due to the propagation of the fatigue crack through the specimen. The ultimate flattening of the curve is thought to be due to the fact that the effective cross-sectional area is reduced and the applied strain

is too low to fatigue the remainder of the specimen. The magnitude of the initial reduction in torque and gradual fall-off up to failure is much greater at high than at low temperatures. The ratio between initial torque and the torque at failure was found to be approximately constant at 1·5 to 1 at all temperatures of 15°C and above.

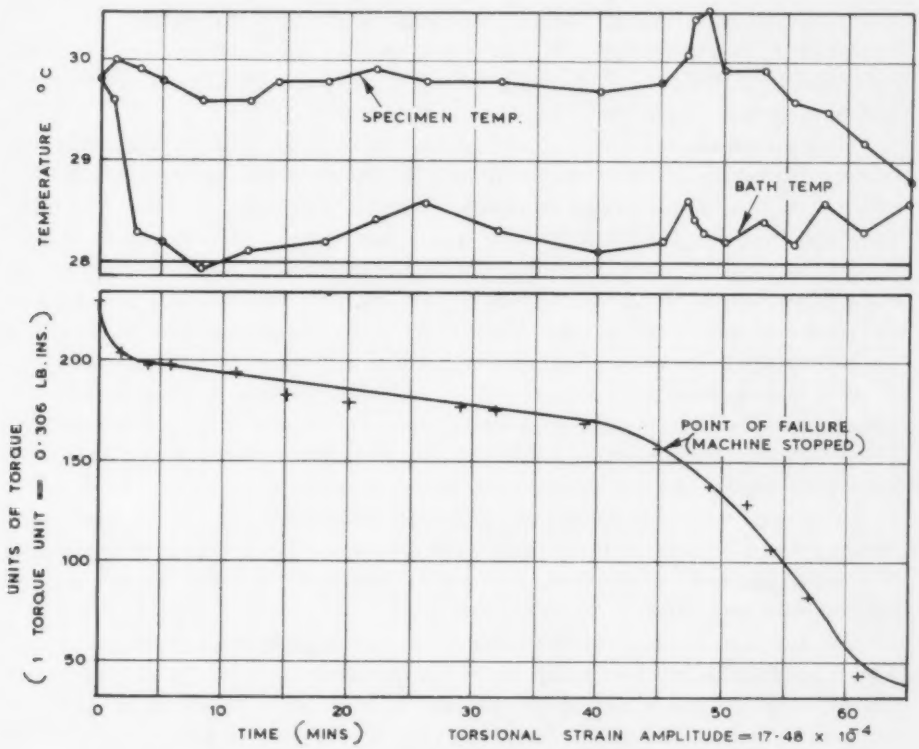

FIG. 11. Torque and temperature measurements during fatigue test on sandsheet specimen at +30°C.

At −20°C the initial torque was maintained throughout the test up to the point of failure where it suddenly drops completely indicating a catastrophic failure of the specimen at this point.

The reduction in torque might well be attributed to increase in temperature of the specimen due to hysteresis, thereby causing a reduction in stiffness. Measurements indicated that the increase in temperature of the specimen during fatigue tests varied with the magnitude of the applied strain. The increase at low strains being negligible and at high strains about 1°C at −9·5°C and 1·5°C at +30°C. The initial torque drop was much reduced at low strains indicating that this might well be partly a temperature phenomenon. A feature of the temperature–time curves is the sharp increase in specimen temperature at the point of failure; this may be due to friction of the crack surfaces before final propagation.

Vol. 3
1961

To investigate the possibility that the gradual fall-off in torque was due to increasing specimen temperature, a test was carried out at +30°C in which the temperature of the specimen was maintained as constant as possible by manually controlling the bath temperature. The result of this test is that shown in Fig. 11, where it will be seen that there is still a reduction in torque. The initial reduction may be due to the fact that a temperature gradient exists across the specimen and even though the surface temperature is at the correct level the temperature increases towards the centre of the specimen with consequent reduction of stiffness and resulting fall-off in torque. Measurements on pure bitumen specimens reported below support this view.

The gradual fall-off in torque during the greater part of life at high temperatures, however, is not thought to be due to temperature but possibly to the gradual growth of small cracks causing a reduction in rigidity of the specimen. The fact that the torque at failure at temperatures of +15°C, +30°C and +40°C was in all cases, including the temperature-controlled test, approximately two-thirds of the initial torque may indicate that the cracked area of the cross-section of the specimen has reached a certain critical size, as indicated on the surface by a crack of sufficient length to cut the conducting paint strip.

It is therefore suggested that the two different types of fracture at low and high temperatures may both be failures due to the principal tensile strain. The failure at low temperatures originates at a single nucleus and propagates relatively quickly due to the high stress whilst that at high temperatures, due to a very low rate of propagation, originates at a large number of nuclei, the cracks eventually linking up to form what appears to be an orthogonal fracture. The results of tests on specimens of pure bitumen reported in a later section support this suggestion.

The increase in slope of the fatigue lines at high temperatures as seen in Fig. 8 might possibly be explained by temperature increase in the specimen. Thus at high strains at high temperatures an increase of only 1°C in specimen temperature would correspond to a considerable increase in life due to the fact that the specimen is being tested at a higher temperature and thus at a lower stiffness and stress than is actually thought. At low temperatures, i.e. from −20°C to 0°C, a considerable change in temperature produces only a negligible change in fatigue life and thus increase in specimen temperature due to hysteresis at low temperatures will not affect the fatigue life of the specimen.

OTHER FACTORS EFFECTING FATIGUE OF SANDSHEET MIXES

It has been seen that the effect of temperature and speed on the fatigue life of sandsheet mixes has been accounted for by their effect on the stiffness, and thus, as strain appears to be the important criterion, both these variables effect the fatigue life of specimens tested in the constant-stress machine. Other variables have also been investigated such as surface finish, void content and rest periods.

In order to investigate the effect of surface finish on the fatigue life specimens having the usual void content of $1\frac{1}{2}$–$3\frac{1}{2}$ per cent were prepared, some with a smooth ironed surface and others with a surface roughened by shallow pricking

with a fine heated wire. Fatigue tests at one particular stress, temperature and speed showed no significant difference between the two sets of specimens.

On the other hand, when specimens with equal surface finishes but with increased void contents were prepared by reducing the amount of tamping and compaction during manufacture the fatigue life was found to decrease.[3] This reduction in life was more than would be expected from the increased stress due to the smaller cross-sectional area caused by the presence of the voids, and may therefore be due to a stress concentration effect of the voids.

It was thought that bituminous specimens might show some recovery if they were rested periodically during a fatigue test. Specimens were therefore given rest periods at room temperature for as long as twenty hours after approximately half the mean life before the fatigue test was continued at 0°C. As the total life showed no improvement over unrested specimens rest periods of 1 and 2 hr were also given at a higher temperature of +40°C, after intervals as short as one-sixth of the mean life. The results when compared with specimens run continuously under the same conditions again showed no increase in total life.

Vol. 3
1961

Further specimens were subjected to a process of recompaction at the original mixing temperature after approximately half the mean life but these specimens also showed no improvement in overall fatigue life.

FATIGUE TESTS ON PURE BITUMEN SPECIMENS

Specimens of bitumen alone, of the same size and shape as normal sandsheet specimens, were made by pouring hot bitumen into cold moulds and cooling to a low temperature before stripping the moulds. These specimens had to be kept at a low temperature to prevent distortion until ready for testing. In these cases the conducting-wave pattern used to stop the fatigue machine on the propagation of a crack consisted of strips of aluminium foil which were placed on the inside of the moulds and adhered successfully to the surface of the specimen.

Fatigue tests were made on pure bitumen specimens in the constant torsional-strain machine at a bath temperature of −4°C. Tests were carried out at four strain levels and the results are shown on Fig. 12.

Temperature and torque measurements were also made, a thermocouple being cast into the neck of the specimen at the surface. At high strains there was a large increase in specimen surface temperature amounting to as much as 9°C at the highest value of strain, with corresponding large reduction in torque. In view of this the bath temperature was reduced rapidly during the early stages of the fatigue tests in order to keep the specimen surface temperature at −4°C, and under these conditions fatigue tests were carried out at the same strain levels as before and the results are also shown on Fig. 12. Measurements on specimens at the lowest tensile strain level of $5{\cdot}4 \times 10^{-4}$ showed no measurable increase in temperature and no reduction in torque during a fatigue test. It will be noticed that the scatter is very low and that the results of tests where the surface temperature is controlled at −4°C show a near linear relationship between the logarithm of tensile strain and the logarithm of cycles to failure.

Further temperature and torque measurements at high strain amplitudes revealed that even though the surface temperature of the specimen was maintained at $-4°C$ there was still considerable initial torque fall-off. This was thought to be due to the increase in internal temperature of the specimen and to measure this three thermocouples were cast into the neck of a specimen in

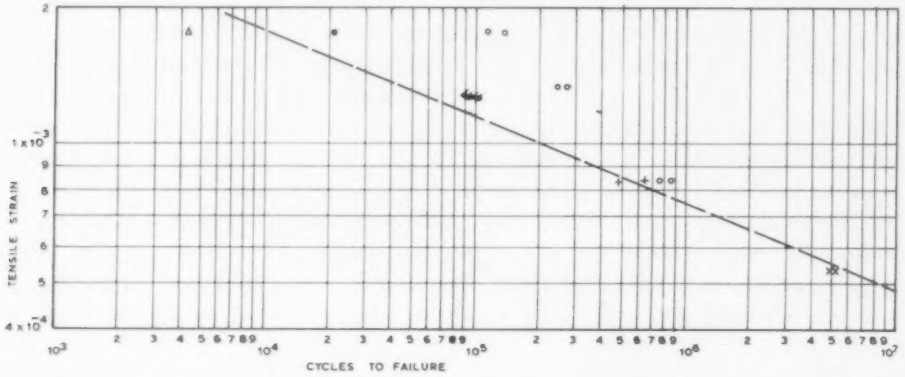

SYMBOL	○	×	+	◐	●	△
SPECIMEN SURFACE TEMPERATURE °C	varies.	−4	−4	−4	−1½	−6
BATH TEMP. °C.	−4	−4	−6	−8	−8	−11·5

FIG. 12. Fatigue results of pure bitumen specimens at $-4°C$ under constant torsional strain.

the positions shown in Fig. 13 which also gives the results of the temperature and torque measurements taken during a fatigue test. It will be seen that there is a variation in temperature over the cross-section and an initial increase in internal temperature corresponding to the reduction in torque, but after a while the temperature and torque become sensibly constant up to the point of failure.

Attempts were made at a tensile strain of $1{\cdot}74 \times 10^{-3}$ to fatigue test a pure bitumen specimen by so controlling the bath temperature that the torque remained constant up to the point of failure. This necessitated a lower surface temperature than the nominal test temperature so that despite the variation over the cross-section the overall stiffness of the specimen remained unchanged. It was found that the surface temperature of the specimen remained constant at $-6°C$ but only one fatigue result was obtained due to the brittle nature of the specimen at the low temperature. This result along with another at which the surface temperature was maintained at $-1{\cdot}5°C$ is shown on Fig. 12, and it is thought reasonable to assume that the correct fatigue life for a pure bitumen specimen at this high strain level would be approximately the mean of the two results obtained. A dotted line has been drawn through this point as well as through the experimental points at lower strain levels where little or no temperature effects were evident. This line is parallel to the strain relationship obtained for sandsheet specimens tested in the constant-stress machine.

Failure surfaces on all pure bitumen specimens tested at $-4°C$ were inclined at 45° to the axis of the specimen (Fig. 14). In all cases failure appears to have originated in a small nucleus at the surface and propagated on the maximum tensile plane through that point. At this low temperature the propagation appeared instantaneous with complete fracture of the specimen even at the low strain level.

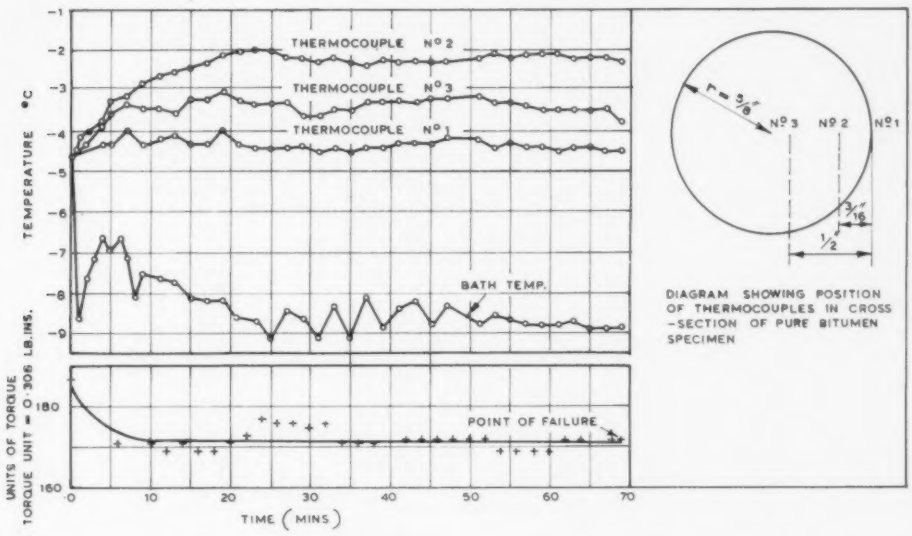

FIG. 13. Torque and temperature measurements during fatigue test on pure bitumen specimen.

Isolated fatigue tests were carried out on bitumen specimens at the higher temperatures of $+10°C$ and $+20°C$ particularly with a view to examining the failure patterns. Typical fatigue cracks and failure surfaces are shown in Fig. 14, and a close examination of the specimens showed that there is not one single nucleus of failure but many, each of which acts as the centre from which cracks propagate on the principal tensile planes and finally join up to give a "saw-tooth" fracture pattern. It also appeared that the higher the temperature the greater are the number of nuclei of failure and therefore the more plain is the appearance of the final fracture surface.

These tests at high temperatures of $+10°C$ and $+20°C$ were made at tensile strain levels of $2{\cdot}04 \times 10^{-3}$ and $3{\cdot}72 \times 10^{-3}$ respectively. The fatigue lives as indicated by a crack of sufficient length to stop the machine are shown in Fig. 15. To investigate crack propagation the machine was stopped periodically and the specimens carefully examined and photographed, some of these photographs being shown in Fig. 16. It appears that a crack forms very early in the fatigue test, before 5000 cycles at a strain of $2{\cdot}04 \times 10^{-3}$ and temperature of $+10°C$, but the subsequent rate of propagation is very low. The crack formation is on a microscopic scale, initiating generally in a small flaw on the surface which no doubt acts as a stress or strain concentration. Since, however,

Vol. 3
1961

the fatigue test is in constant strain further propagation would appear to depend on the magnitude of the stress field. This would in turn depend on the stiffness of the specimen which would ultimately be governed by the test temperature.

From results obtained it seems that fatigue tests on bitumen specimens at $-4°C$ produced virtually instantaneous rates of crack propagation. Fig. 15 shows the strain-life line for bitumen at $-4°C$ extrapolated to a fatigue life of 100 cycles. It will be seen that at a tensile strain of $2{\cdot}04 \times 10^{-3}$ this line

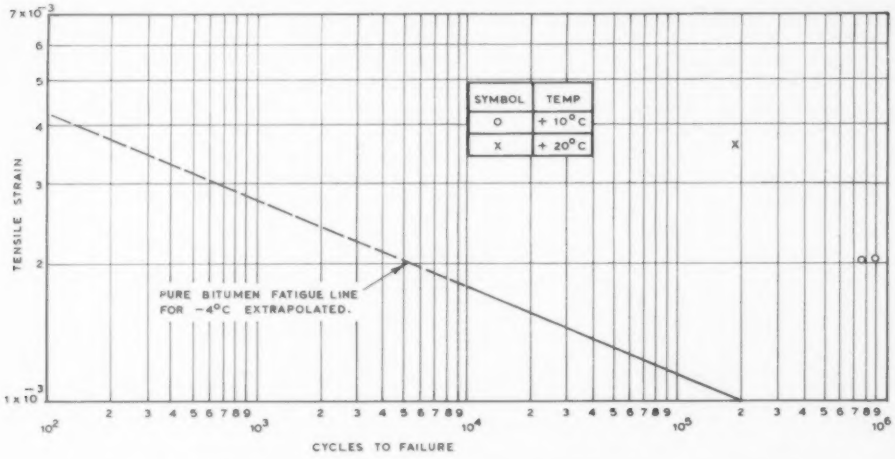

Fig. 15. Fatigue results of pure bitumen specimens at $+10°C$ and $+20°C$ under constant torsional strain.

indicates an approximate life of 5000 cycles, which is about the life at which a specimen tested at this strain level, at a temperature of $+10°C$, first showed signs of minute cracks. Failure of the specimen, however, would not be recorded in the constant-strain machine until a life of $8{\cdot}7 \times 10^5$ cycles had been reached. Similar results were obtained from the specimen tested at $+20°C$ and also from a specimen tested at room temperature (approximately $+15°C$) without coolant at a strain of $3{\cdot}72 \times 10^{-3}$ which first showed very small cracks after a mere hundred cycles or so.

Therefore, there is some evidence for the hypothesis that the fatigue of pure bitumen is also solely dependent on the magnitude of tensile strain independent of temperature, as long as the fatigue life is defined as the initiation of a crack, and that the apparent increase in fatigue life at high temperatures in the constant-strain machine may be due to a slower rate of crack propagation.

It was noted earlier that the strain-life line on a logarithmic basis of pure bitumen at $-4°C$ was parallel to that of sandsheet specimens, tested in the constant-stress machine, and this may be due to the common factor of practically instantaneous crack propagation—the flatter lines obtained from sandsheet specimens tested in the constant-strain machine being due to slower crack propagation at the lower stresses.

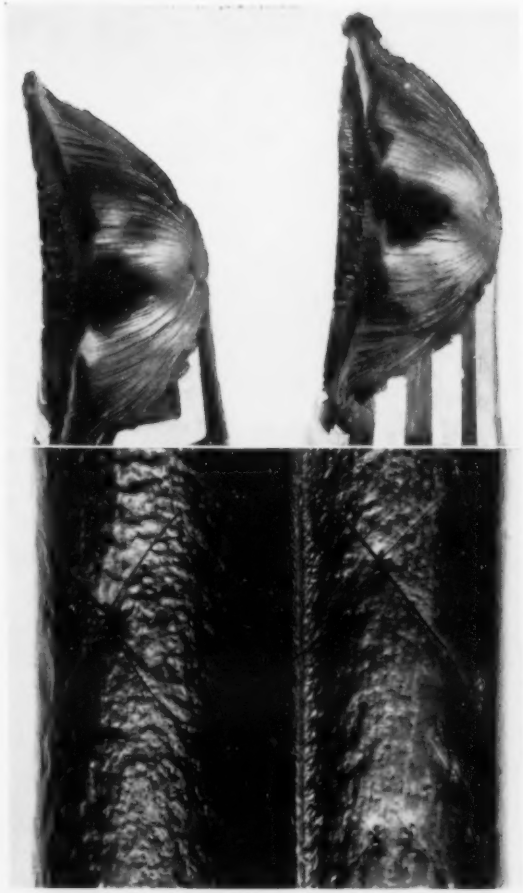

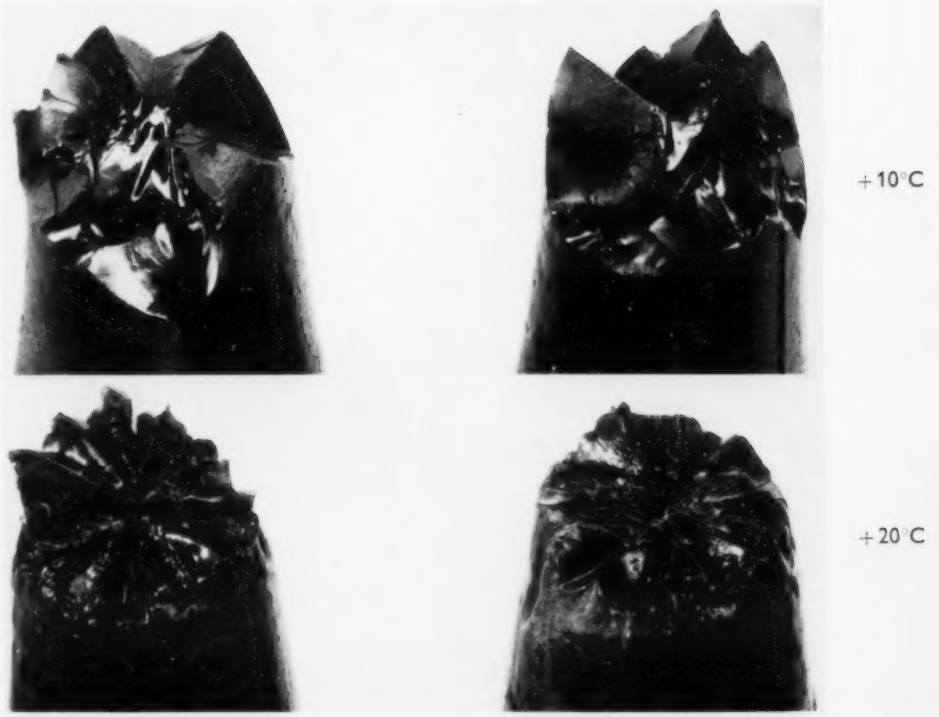

FIG. 14. Fatigue failure surfaces of pure bitumen specimens at various temperatures in constant torsional-strain machine.

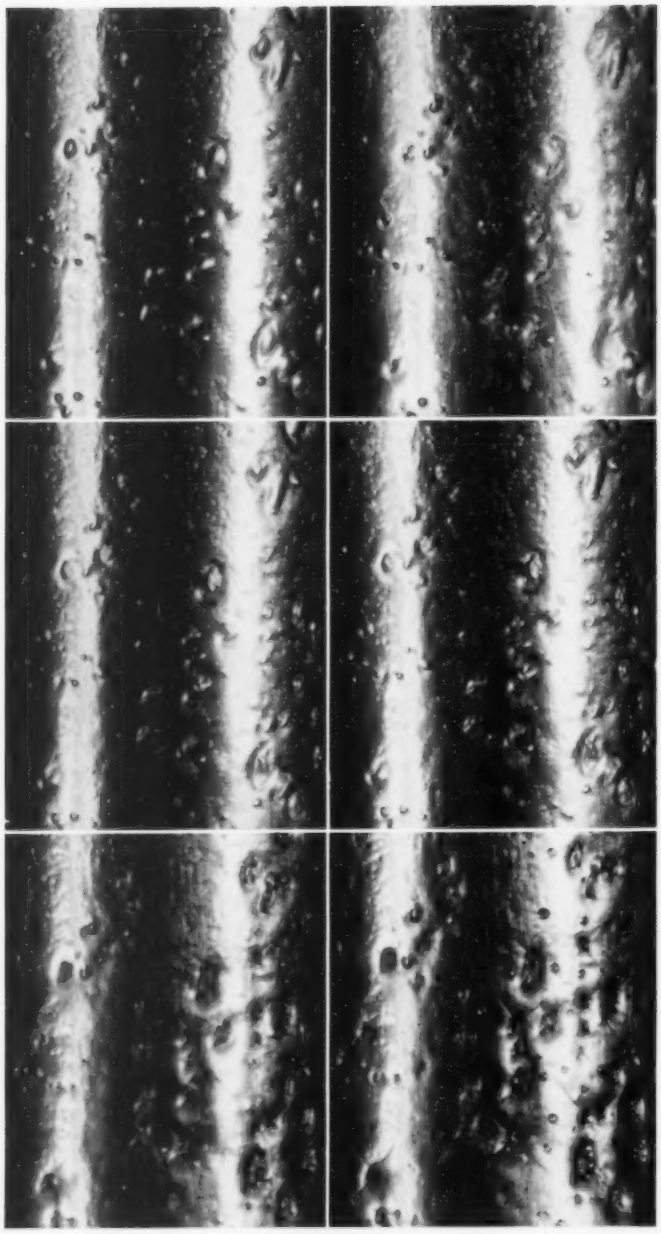

FIG. 16. Fatigue cracks in pure bitumen specimen at various stages of fatigue test at $+10^{\circ}$C. (Magnification: $\times 2$.)

(a) Before testing. (b) $5{\cdot}8 \times 10^3$ cycles. (c) $1{\cdot}16 \times 10^4$ cycles. (d) $1{\cdot}56 \times 10^5$ cycles. (e) $4{\cdot}44 \times 10^5$ cycles. (f) $8{\cdot}70 \times 10^5$ cycles.

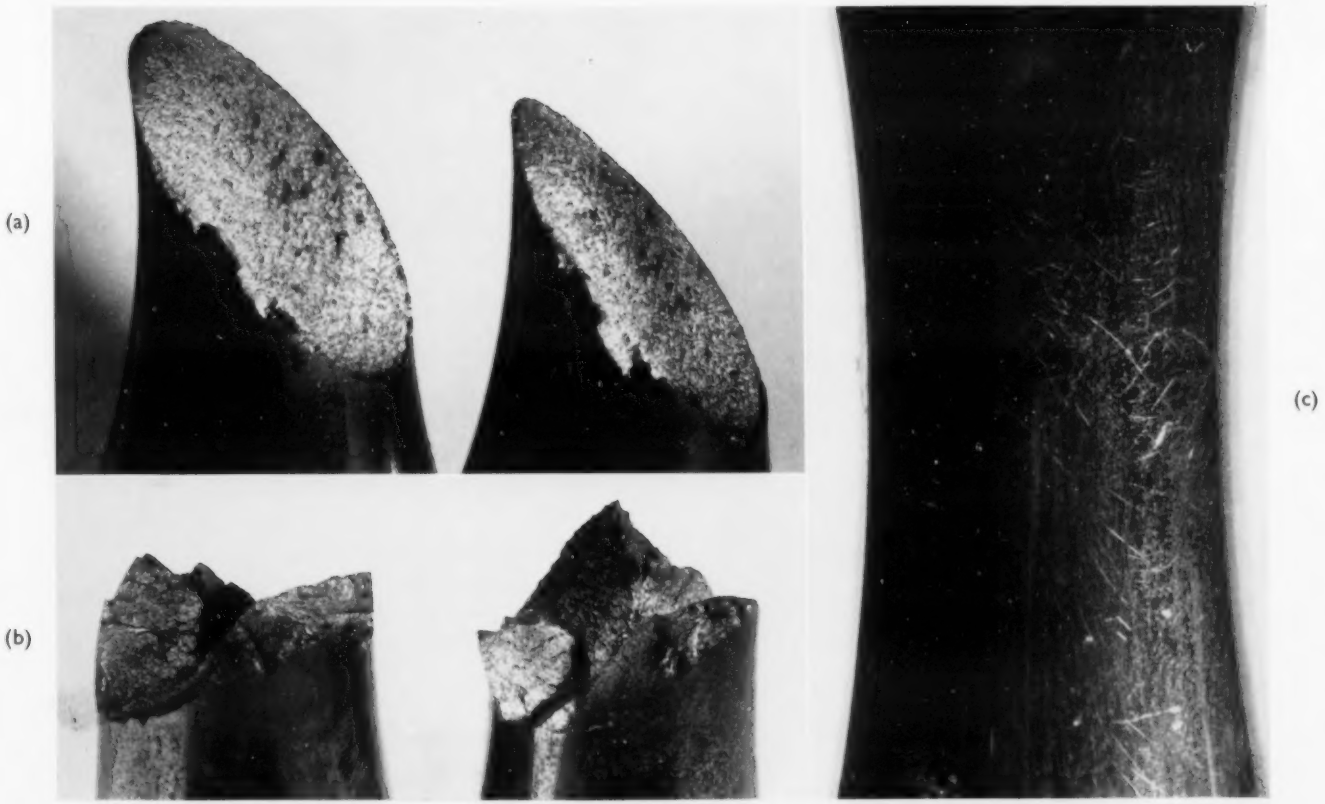

FIG. 17. Fatigue cracks and failure surfaces of steel specimens tested in constant torsional-strain machine.

(a) Sheer stress = 12·9 tons/in², N = 1,199,000 cycles. (b) Sheer stress = 14·8 tons/in², N = 301,000 cycles. (c) Sheer stress = 15·2 tons/in², N = 222,000 cycles.

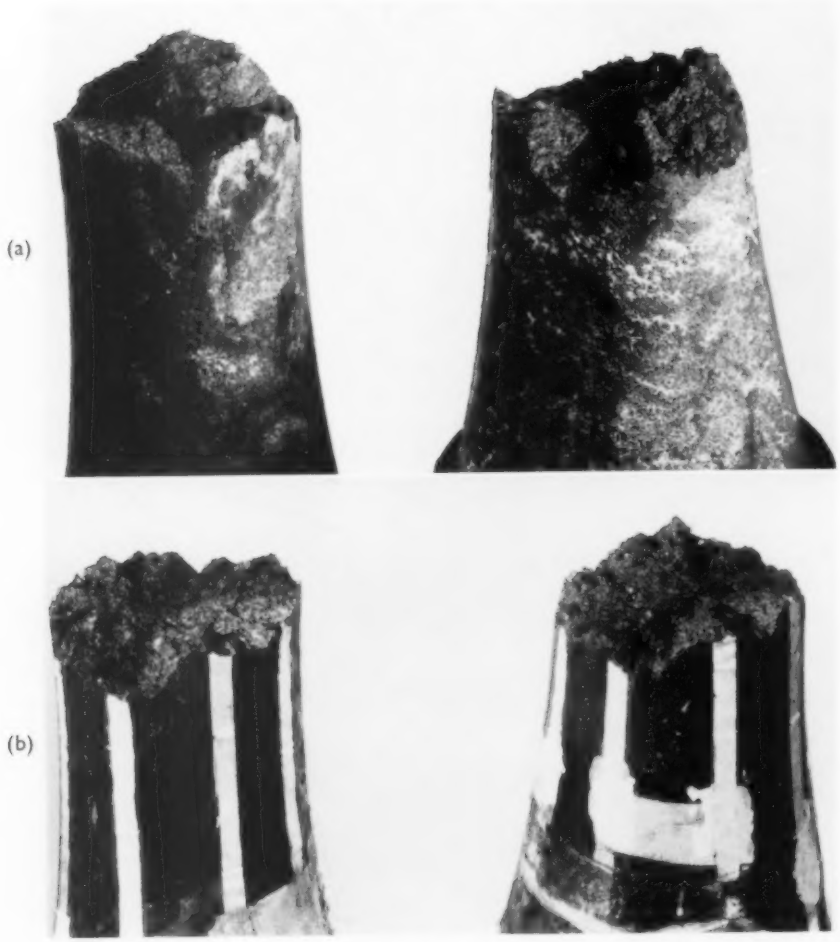

FIG. 19. Fatigue failure surfaces of mastic specimens at 0°C.
(a) 70 per cent mastic. (b) 50 per cent mastic.

In connexion with the two types of failure surface obtained in pure bitumen at high and low temperatures, the fracture surfaces of some steel specimens shown in Fig. 17 are of interest. These specimens were fatigue tested in a constant torsional-strain machine and it will be seen that whereas the highly stressed specimens result in a number of 45° cracks which eventually give a "saw-tooth" type of fracture, the lower-stressed specimen having a longer life has a single fracture at 45°.

FATIGUE TESTS ON MASTIC MIXES

In order to investigate the effect of altering the composition of the mix specimens were made with a mastic mix containing 70 per cent volume concentration of mineral aggregate and were tested at different temperatures in the constant-bending stress fatigue machine. The results of these tests reported earlier[3] showed that when plotted on a strain basis the experimental points were again scattered about a straight line, but in all cases the life was longer for a given strain than in the case of sandsheet specimens containing 81 per cent volume concentration of aggregate.

Vol. 3
1961

This result was confirmed by further tests carried out in the constant torsional-strain fatigue machine on two different mastic mixes. (1) A 70 per cent aggregate volume concentration mastic mix, the proportions being 67 parts by weight of sand, 17 parts by weight of limestone filler and 14 parts by weight of bitumen. (2) A 50 per cent aggregate volume concentration mastic mix, the proportions being 47 parts by weight of sand, 25 parts by weight of filler and 28 parts by weight of bitumen. The sand grading was the same in both cases as that used for the sandsheet specimens.

The 70 per cent mastic specimens were manufactured in the same way as sandsheet specimens except that no tamping was necessary, the average void content being 2·7 per cent. In the case of the 50 per cent mastic mix neither tamping nor compaction was necessary as the hot mix could be poured into the moulds and the resulting specimens had a very low average void content of 1·2 per cent.

Fatigue tests were made on both mixes at a temperature of 0°C and the results are shown in Fig. 18 along with the strain-life line for sandsheet at the same temperature. Although tests were carried out at only two strain levels in each case in order to define the approximate position of the line it can be clearly seen that specimens having a larger volume of bitumen give considerably longer lives for a given strain and temperature.

The failure surfaces on mastic specimens were generally on a series of planes at 45° to the axis of the specimen giving the appearance somewhat of a "saw-tooth" effect, and in the case of the 50 per cent mastic many more planes were in evidence than in the 70 per cent mastic (Fig. 19). This evidence of multiple cracks suggests considerable crack propagation taking place before the test is terminated by fracture of the conducting strip, and this is supported by the measurements of torque taken during a fatigue test on mastic specimens. Fig. 20 shows the torque–time and temperature–time curves for a 50 per cent mastic specimen, and it will be seen that there is a considerable reduction in torque during the test, the torque at failure being approximately two-thirds of

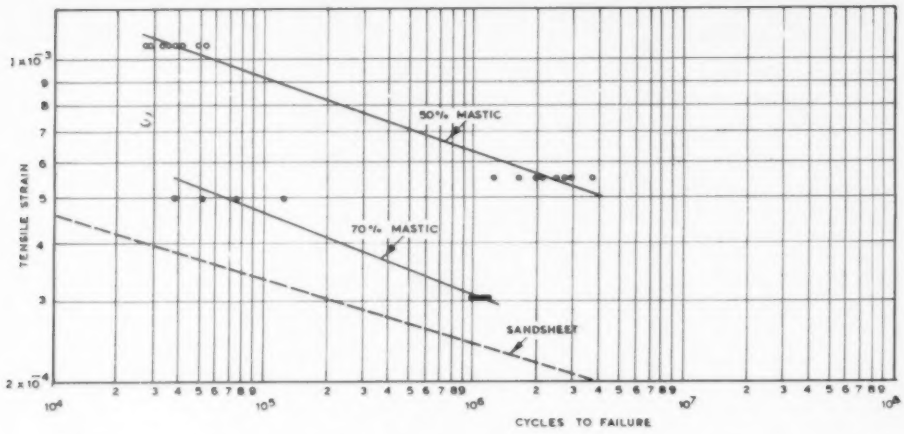

FIG. 18. Fatigue results on mastic specimens at 0°C under constant torsional strain.

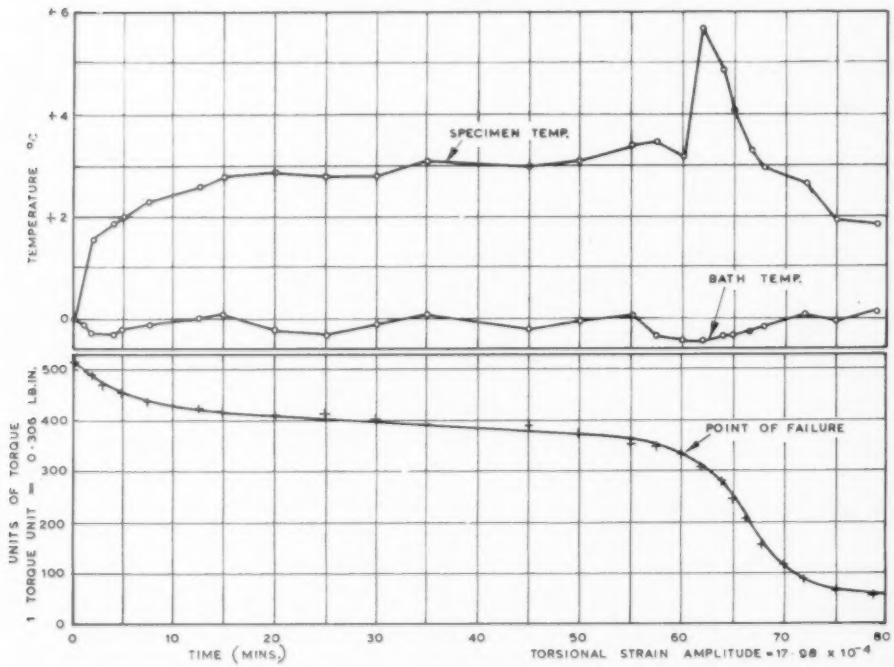

FIG. 20. Torque and temperature measurements during fatigue test on 50 per cent mastic specimen.

the initial torque, a consistent picture with the behaviour of sandsheet specimens at higher temperatures. Also the sudden increase in specimen temperature at the point of failure is again noticeable and, as suggested before, may be due to the friction of the crack surfaces.

It will be recalled that sandsheet specimens at the same temperature of 0°C showed very little reduction in torque and a single fracture plane at 45° indicating relatively rapid crack propagation. This is not surprising as the stiffness of the specimen, and hence the stress on which the rate of crack propagation depends, is dependent on the volume concentration of aggregate. The stiffness of the 70 per cent mastic specimens is approximately half that of the sandsheet specimens at 0°C and the 50 per cent mastic mix only about one-fifth the stiffness of the sandsheet mix.

CRITERION OF FATIGUE FAILURE FOR BITUMEN AND BITUMINOUS MIXES

From the work reported above it appears that the factor controlling the fatigue life of bitumen and bituminous mixes is the magnitude of the applied tensile strain. The evidence for this is not only the results of the tests at different temperatures and the nature of the resulting fractures, but also on the comparability of the results, on a basis of tensile strain, from different types of loading, both bending and torsion. However, it is clear that under certain conditions in a constant-strain test, particularly at low stresses, the measured fatigue life includes a considerable length of time necessary to propagate the crack or cracks sufficiently to terminate the test. It is important, therefore, for practical considerations, that the definition of failure as implied in a particular test should be clearly understood, since in "constant-strain" tests crack propagation may have to be taken into account, whereas in "constant-stress" tests this is not necessarily so. In the constant-stress tests reported in this paper the initiation of a crack appears to be followed by immediate and catastrophic failure of the specimen which causes the machine to stop, whereas the measurement of fatigue life in the constant-strain machine is dependent on the propagation of a crack across a conducting-wave pattern.

The results of the tests on mastic mixes indicated that a similar strain relationship to that for sandsheet specimens [see equation (1)] existed for these mixes as the strain-life lines are practically parallel but giving longer lives with increasing bitumen content for the same specimen strain. The general relationship may be written:

$$N = K_1\left(\frac{1}{\epsilon_M}\right)^6 \tag{2}$$

where N = number of cycles to failure

ϵ_M = amplitude of applied tensile strain on mix

K_1 = a constant depending on the volume concentration of the mix.

In essence all the mixes consist of particles of aggregate surrounded by bitumen. Consequently in the mastic mixes there is a thicker film of bitumen between individual grains of aggregate. Now considering a small portion of the mix, as the aggregate is infinitely harder than the bitumen all deformation takes place in the bitumen and none in the aggregate, therefore the strain in the bitumen is considerably more than the mixture or specimen strain. And

Vol. 3
1961

it follows that the greater the volume concentration, C_v, of the aggregate the smaller the volume of bitumen, and hence the greater the actual bitumen strain.

Two mixes are represented diagrammatically in Fig. 21, from which it can be seen that for a given mixture strain the actual bitumen strain is greater in

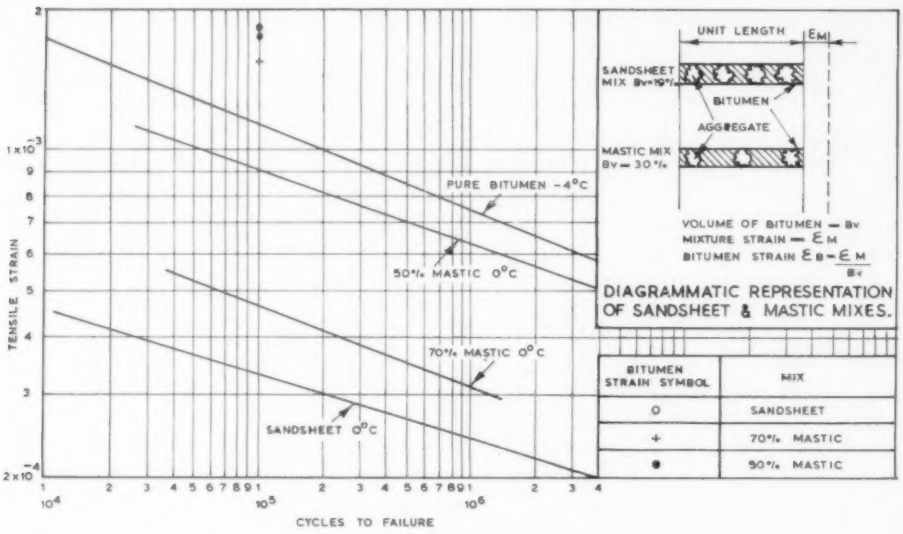

Fig. 21. Fatigue lines for different mixes showing derived bitumen strain.

the sandsheet mix than in the mastic mix. Taking this very simplified picture, the bitumen strain ϵ_B is related to the mixture strain ϵ_M in the following manner:

$$\epsilon_B = \frac{\epsilon_M}{B_v} \tag{3}$$

where B_v = volume concentration of bitumen = $1 - C_v$.

If it is postulated that the fatigue life depends on the bitumen strain, then for a given life the value of the bitumen strain should be the same for all mixes. Fig. 21 shows the experimental strain-life lines for sandsheet, 70 per cent mastic and 50 per cent mastic at 0°C and also that for pure bitumen at -4°C. The strain in the bitumen for the different mixes corresponding to a fatigue life of 10^5 cycles has been evaluated using equation (3) and is plotted on the same figure. It may be seen that these points fall close together which suggests that the original hypothesis, i.e. that the strain in the bitumen is the important factor, may well be true.

It will be noticed, however, that the points showing the derived bitumen strain do not fall on the pure bitumen fatigue line, but it must be remembered that these points have been obtained from fatigue lives which in the case of the mastics are thought to contain a considerable propagation time. Also it

is not suggested that equation (3) is exact, and the evidence is rather that the relationship should possibly be:

$$\epsilon_B = \frac{\epsilon_M}{K_2 B_v}$$

where K_2 is a term greater than unity which may well depend on the volume concentration and type of the aggregate. It should perhaps be emphasized that the much-simplified model depicted in Fig. 21 is only intended as a first step towards the relationship between strain in the bitumen and strain in the mix, and it is appreciated that it cannot be used to explain the general behaviour of bituminous mixes such as stiffness relationships.

Nevertheless it is considered that there is some evidence to support the hypothesis that the tensile strain in the bitumen is the criterion of crack initiation in bituminous mixes.

Acknowledgements—The authors wish to thank Professor R. C. Coates, Head of the Department of Civil Engineering, Nottingham University, for his help and continuing interest, and also for providing the facilities for carrying out the work. They are also indebted to Shell Research Ltd. for sponsoring the research and for permission to publish the results.

Vol. 3
1961

REFERENCES

1. L. W. Nijboer and C. van der Poel, *Proc. Assoc. Asphalt Paving Tech.* **22**, 197 (1953).
2. L. W. Nijboer, *Proc. Highw. Res. Bd., Wash.* **33**, 185 (1954).
3. R. N. J. Saal and P. S. Pell, *Kolloidzschr.* **171**, 61 (1960).
4. C. van der Poel, *J. Appl. Chem.* **4**, 221 (1954).
5. C. van der Poel, *S.P.E.J.* **11**, 1947 (1955).

Int. J. Mech. Sci. Pergamon Press Ltd. 1961. Vol. 3, pp. 268–285. Printed in Great Britain

TURBINE OPERATION WITH NONSTEADY FLOW-ANALYSIS AND EXPERIMENTS

D. F. WHITE

Department of Mechanical Engineering
The Pennsylvania State University, University Park, Pennsylvania

(*Received* 10 *February* 1961)

Summary—The paper describes a theoretical and experimental study of the internal flows in single-stage, axial-flow pulse turbine. In the theoretical analysis, based on the method of characteristics, special attention was given to the boundary condition governing the flow from the nozzles into the rotor blades under off-design conditions. The analysis showed a momentum exchange occurring across the nozzle–rotor boundary, leading to entropy generation in the rotor passages, and corresponding energy dissipation.

Experiments conducted on a test turbine, in which turbine internal work was calculated from speed change data, showed remarkably high performance figures. A comparison of predicted performance with test measurements showed good agreement in the range of turbine speeds for which the analysis was written. It was concluded that substantial improvements in pulse turbine performance through design changes involving nozzle and rotor blades are not to be expected.

NOTATION

General symbols

a = speed of sound
$A = a/a_0$, dimensionless sound speed
E = energy
F = cross-sectional area
h = enthalpy
I = mass moment of inertia
L_0 = reference length
p = pressure
$P = \frac{2}{\gamma - 1} A + U$, Riemann variable
$Q = \frac{2}{\gamma - 1} A - U$, Riemann variable
s = entropy
$S = s/s_0$, dimensionless entropy
t = time
u = particle velocity
$U = u/a_0$, dimensionless particle velocity
v_B = blade speed
$V_B = v_B/a_0$, dimensionless blade speed
x = length coordinate

Suffixes

B = rotor blade
D = exhaust duct
E = rotor exit
EA = rotor exit, absolute for velocities
N = nozzle exit
0 = reference condition
R = rotor-blade entrance, relative for velocities
RA = rotor-blade entrance, absolute for velocities

Greek symbols

β = rotor-blade entrance angle
γ = ratio of specific heats, taken as 1·4
ω = angular velocity

Vol. 3
1961

INTRODUCTION

THE pulse system of turbo-charging is used extensively by many diesel engine builders throughout the world, with both four-stroke and two-stroke cycle engines, and over a horsepower range from a few hundred to several thousand. Due principally to the extreme complexity of the flows in the internal passages of the typical pulse-turbine application, the design of these machines has in the past been based largely on steady-flow considerations. At best, an optimum configuration is arrived at by assuming a pressure and temperature variation before the turbine, and by calculating the turbine output over the period of wave motion in a series of steps, with the value of turbine efficiency at each step having been measured under steady-flow conditions. The associated problem of wave dynamics in the exhaust ducting has received considerable attention, notably by Jenny[1], and more recently by Benson and Woods[2]. In such studies the turbine is replaced by a nozzle at the end of the exhaust pipe. There seems to be little doubt that as far as the gas flow in the exhaust ducting is concerned replacing the turbine with a fixed nozzle is entirely acceptable. However, the problem of how best to design the turbine for maximum pulse-energy utilization remains in doubt.

The main purposes of the present investigation were to gain an insight into the nature of the gas flows within the passages of a representative-type pulse turbine, to develop a method for predicting turbine performance, and thereby to discover if significant improvements in performance were possible. The analytical methods used are based on the method of characteristics, a subject which has received extensive treatment in the literature (Rudinger[3], Shapiro[4]). Detailed descriptions of the basic calculation procedures are therefore omitted in the paper, although special problems involving boundary conditions are covered at some length.

ANALYSIS

I. *Flow model*

As a typical pulse-turbine type, the single stage, axial-flow machine was selected. The flow model consisted of the duct leading to the turbine proper,

the turbine nozzles and the rotor blades, all considered as a single, connected gas passage. It was recognized from the outset that the flow model would have to be highly idealized in order to limit the required calculations to a reasonable extent. Therefore, several simplifying assumptions were made, as follows. The duct leading to the turbine was assumed sufficiently long so that no wave reflexions returned to the turbine during the time of passage of a single exhaust pulse. It was assumed that the arc of admission covered the entire rotor circumference, i.e. the turbine was to operate with full admission. The rotor speed was taken to remain fixed. The latter assumption proved to be quite reasonable, at least for the conditions of the experiments described in a following section, where the rotor speed change due to the work extracted from a single pulse was less than 1 per cent of the initial rotor speed. The effects of wall friction were neglected, such that the flow in the duct was considered isentropic, and the axial clearance between the nozzle exit and the entrance to the rotor blades was assumed negligible.

Infinitely many nozzle and rotor blades of zero thickness were assumed, such that flow areas were given solely according to specified nozzle and rotor blade angles. Body forces, including centrifugal effects, were neglected. A principal assumption was made that the flow could be described in terms of a single space dimension and time, i.e. the flow was to be nonsteady, quasi-one-dimensional. With reference to the last assumption it is evident that the wave motion within the passages of the actual turbine is at least two-dimensional, and probably three-dimensional. However, the mathematical difficulties of even a two-dimensional wave analysis are of such magnitude (for example, Butler[5]) that it did not seem unreasonable to use the well-established one-dimensional theory, at least as a first approximation.

II. *Initial and boundary conditions*

The pulse form approaching the turbine was specified in terms of the flow properties at some arbitrary position in the duct upstream from the turbine as functions of time. For the purpose of simplifying the calculation procedures the maximum pulse pressure was limited to insure subsonic flow throughout the flow field. Prior to the arrival of the pulse at the turbine, it was assumed that the gas in the rotor blade passages was at rest with respect to the rotor blades and at atmospheric pressure.

The physical boundaries to be considered occur at two positions, at the nozzle exit–rotor blade entrance and the exit from the rotor blades. It is of interest to examine the general nature of the flow at the nozzle exit–rotor blade-entrance position, in the light of the assumptions which define the flow model. The wave motion produces nozzle exit gas velocities which vary continuously from zero to a value of approximately 1000 ft/sec and back to zero in a period of time of the order of 10 msec (while the rotor speed remains constant). It is, therefore, clear that a turbine with fixed geometry operates at a continuous series of off-design conditions (except for a single value of the nozzle exit velocity). For example, at a particular instant of time during the wave motion the pertinent velocities might appear as shown in Fig. 1, with a

nozzle-exit velocity far less than the design value. It is important to recognize that as a gas particle passes from the nozzle exit to the rotor entrance the stated assumptions demand that the relative velocity vector change from the direction indicated in Fig. 1 to that indicated in Fig. 2, parallel to the line which defines the rotor-blade entrance angle. The vector shown as a dashed line in Fig. 2 indicates an absolute velocity vector at the rotor blade entrance

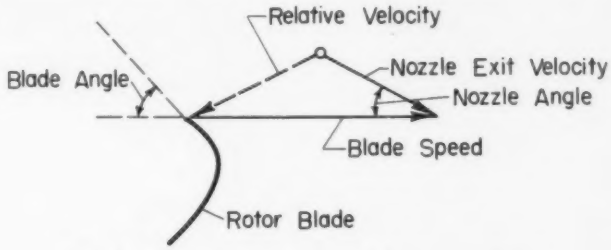

FIG. 1. Vector diagram for off-design condition.

which is larger in magnitude than the nozzle-exit velocity vector. This change in the absolute velocity vector, and the associated increase of kinetic energy of the gas, are to be interpreted as the result of work having been done on the gas by the rotor as the gas crosses the boundary between the nozzle exit and the rotor-blade entrance. From another point of view, a momentum exchange occurs across the boundary, due to the off-design condition.

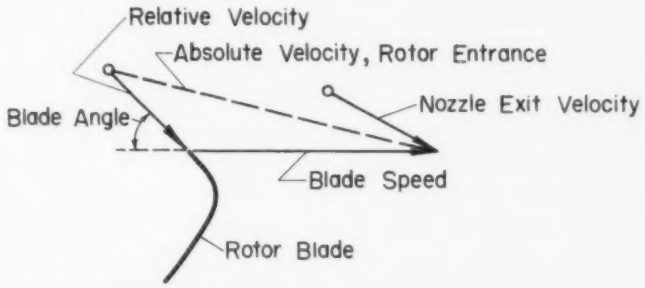

FIG. 2. Adjusted vector diagram, off-design condition.

The question arises as to whether a process of such nature, which must occur in view of the stated assumptions, is so far from reality as to cast serious doubt on the validity of the assumptions. If the situation pictured in Fig. 1 referred to a condition of steady flow, then there is little doubt that in a real machine, with a finite number of rotor blades, the flow entering the rotor would separate and that major nonuniformities in flow properties would exist across the rotor passage flow section. In short, the assumption of quasi-one-dimensional flow would not be a reasonable one. However, since the flow is nonsteady the question really is whether or not the wave form remains essentially plane as each element of the exhaust pulse traverses the boundary. It was expected that a comparison of test data with predicted performance by the one-dimensional analysis would answer this question.

Vol. 3
1961

For calculations, the boundary condition at the nozzle exit–rotor entrance station can be developed into a relatively simple form in the following manner. With conditions at the nozzle exit identified by subscript N and at the rotor-blade entrance by subscript R, at some arbitrary stage of the calculation the quantities known from the previous step are P_N, Q_R and S_N. In addition, the ratio of cross-sectional areas normal to the flow F_N/F_R and the blade speed V_B are given as initial conditions. The unknown quantities to be found are U_N, A_N, U_R, A_R and S_R. Five independent equations are therefore required for a solution. Two of these follow from the definitions of the Riemann variables:

$$P_N = \frac{2}{\gamma-1} A_N + U_N \tag{1}$$

$$Q_R = \frac{2}{\gamma-1} A_R - U_R \tag{2}$$

With the perfect gas law the entropy may be introduced by the relation

$$\frac{p_N}{p_R} = \left(\frac{A_N}{A_R}\right)^{2\gamma/(\gamma-1)} \exp\left[-\gamma(S_N - S_R)\right] \tag{3}$$

Since there was assumed no clearance between the nozzle exit and the rotor-blade entrance there exists a single value of pressure at the boundary, for subsonic flow. Thus, equation (3) becomes

$$\frac{A_R}{A_N} = \exp\left[\frac{\gamma-1}{2}(S_R - S_N)\right] \tag{4}$$

The continuity equation may be written in the form

$$U_R = U_N \frac{F_N}{F_R}\left(\frac{A_R}{A_N}\right)^2 \tag{5}$$

One additional independent equation is required to complete the specification of the boundary condition. The law of conservation of momentum is not available in this case since an additional space dimension would be required for an adequate description of the forces involved. Before writing the energy equation, it is necessary to define the absolute velocity of the gas at the rotor-blade entrance, in view of the previous discussion concerning Figs. 1 and 2. Referring to Fig. 3, the desired quantity is defined as U_{RA} and written

$$U_{RA} = (U_R^2 + 2V_B \cos\beta U_R + V_B^2)^{\frac{1}{2}} \tag{6}$$

Evidently the values U_N and U_{RA} are identical if the turbine operates at its design point. If $U_N < U_{RA}$ the energy equation becomes

$$\frac{2}{\gamma-1} A_N^2 + U_N^2 + E = \frac{2}{\gamma-1} A_R^2 + U_{RA}^2 \tag{7}$$

Equation (7) introduces an additional unknown quantity, the added energy E, so that, strictly speaking, the energy equation is not sufficient for a solution. However, it is possible to deduce an approximate relation based on energy considerations in the following manner. Before the wave arrives at the turbine the assumed condition of the gas in the rotor-blade passages is of zero relative velocity and atmospheric pressure. Thus, a starting value of entropy can be

assigned to the rotor gas, with the duct-gas entropy as a datum. The state of the gas prior to the arrival of the exhaust pulse is shown in Fig. 4. Initially then, U_{RA} is equal to V_B, according to equation (6). If, on the other hand, the turbine operates at its design point, $U_{RA} = U_N$, there being no momentum exchange as the gas crosses the nozzle exit–rotor blade entrance boundary. Then by equation (7), $A_N = A_R$, which leads to the condition $S_N = S_R$.

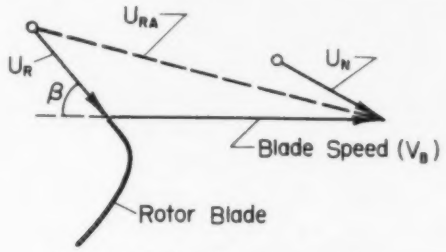

FIG. 3. Vector diagram notation.

With the two foregoing limiting values of entropy in mind, the following assumed relation is taken to describe approximately the variation of entropy of the gas at the rotor-blade entrance over the range of nozzle-exit velocities $0 \leqslant U_N \leqslant U_{RA}$:

$$S_R = \frac{U_{RA}^2 - U_N^2}{V_B^2} (S_R)_{\text{initial}} \tag{8}$$

Equation (8) states that entropy increases of the rotor gas at off-design conditions are linearly related to the kinetic energy added to the gas by the rotor, the entropy S_N being set arbitrarily equal to zero.

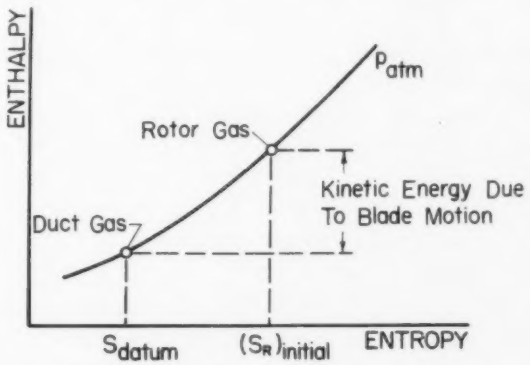

FIG. 4. Gas states prior to wave motion.

For completeness the condition $U_N > U_{RA}$ needs also to be considered. From a practical point of view it was decided that values of U_N much larger than the design magnitude would not be of interest. Furthermore, it was assumed that for U_N slightly larger than U_{RA} no appreciable entropy change would occur across the boundary. This is in line with observations of steady-flow turbine designs operating with nozzle velocities slightly higher than design values.

The boundary condition at the nozzle exit–rotor blade-entrance station may be written compactly by combining equations (1), (2), (4) and (5), resulting in the form

$$U_N = \frac{P_N \exp\{[(\gamma-1)/2](S_R - S_N)\} - Q_R}{\exp\{[(\gamma-1)/2](S_R - S_N)\} + (F_N/F_R)\exp[(\gamma-1)(S_R - S_N)]} \tag{9}$$

where

$$S_R = \frac{U_{RA}^2 - U_N^2}{V_B^2}(S_R)_{\text{initial}}; \quad 0 \leqslant U_N \leqslant U_{RA}$$

$$S_R = S_N; \qquad U_N \geqslant U_{RA}$$

The physical boundary at the rotor-blade exit results in a much simpler formulation by specifying that for subsonic outflow the exit pressure be equal to the surrounding pressure, taken as atmospheric. This results immediately in the relation

$$A_E = \exp\left[\frac{\gamma-1}{2} S_E\right] \tag{10}$$

III. *Sample solution*

In order to test the proposed analysis a wave diagram was constructed for arbitrarily assumed initial conditions. The turbine geometry was simplified to the extent that no area change was assumed from the inlet duct to the nozzle exit. In addition, there was assumed to be no change in flow area through the rotor. These assumptions do not affect materially the nature of the flow, but do provide a considerable reduction in calculation time. The wave form approaching the turbine is shown in Fig. 5, and was purposely assumed comparatively short in time, again to limit the amount of required calculation. Additional assumed data for the sample solution are as follow:

Nozzle angle = 20°
Blade entrance angle = 45°
Blade exit angle = 45°
Reference sound velocity = 1140 ft/sec
Reference length = 1 ft
Blade speed = 0·300 a_0
Duct length = 1·8 ft
Length of flow path in rotor = 0·1 ft
Reference entropy in duct = 0

The completed solution appears as the wave diagram of Fig. 6, together with an abbreviated list of gas properties as given in Table 1. The dashed lines shown between the ordinates $X/L_0 = 1{\cdot}8$ and $X/L_0 = 1{\cdot}9$ are representative particle paths in the rotor passages. It is noted that a large portion of the wave system in the rotor passages is omitted for clarity. With the mesh size selected for this problem the particle paths as shown form boundaries between regions of constant entropy. The ordinate $X/L_0 = 1{\cdot}8$ is entered twice in Fig. 6 simply for convenience in the graphical construction. Complete details of the various calculation procedures used in the wave diagram analysis are much too lengthy to be given here. A step-by-step description of the process is given by White[6].

Vol. 196

The completed wave diagram gives all of the flow properties at any section at any instant of time during the period of wave motion. Those results of interest in assessing the performance of the turbine are given in Figs. 7, 8 and 9. Fig. 7 shows sound velocity (pressure) and particle velocity against time at the nozzle exit. It can be seen that the pressure at the nozzle exit was slightly below atmospheric pressure when the calculation was stopped. This condition is caused by the generation of rarefaction waves at the nozzle exit during the latter part of the wave motion. Eventually, a series of flow reversals in the

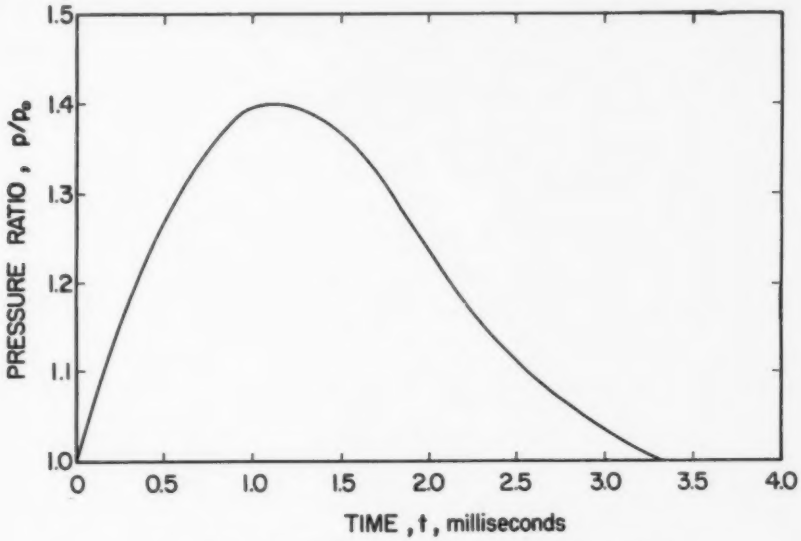

FIG. 5. Assumed incident pulse, 1·8 ft from rotor.

rotor passages probably would have occurred had the calculations been continued. However, the boundary condition at the rotor-blade exit cannot be established with any certainty should inflow occur. In addition, as far as the turbine work extracted from the pulse is concerned, it is anticipated that the net effect of such a series of flow reversals would be negligible.

Fig. 8 shows flow properties at the rotor blade entrance vs. time. It is of interest to examine the behaviour of the entropy at the rotor entrance as compared with the variation of particle velocity. The two curves are to a certain extent mirror images, save for the very beginning stages of the wave motion, and also in that the point of maximum particle velocity leads the point of minimum entropy by a small but observable time increment. The latter result is due to the fact that changes in particle velocity are propagated along the wave characteristics, while entropy changes, being propagated along particle paths, lag behind according to the magnitude of the local sound velocity.

It is to be noted that the entropy does not quite reach the abscissa, indicating that the incident wave did not produce particle velocities sufficiently large in magnitude for the turbine to reach its "design point". Fig. 9 shows flow propertics vs. time at the exit from the rotor.

Vol. 3
1961

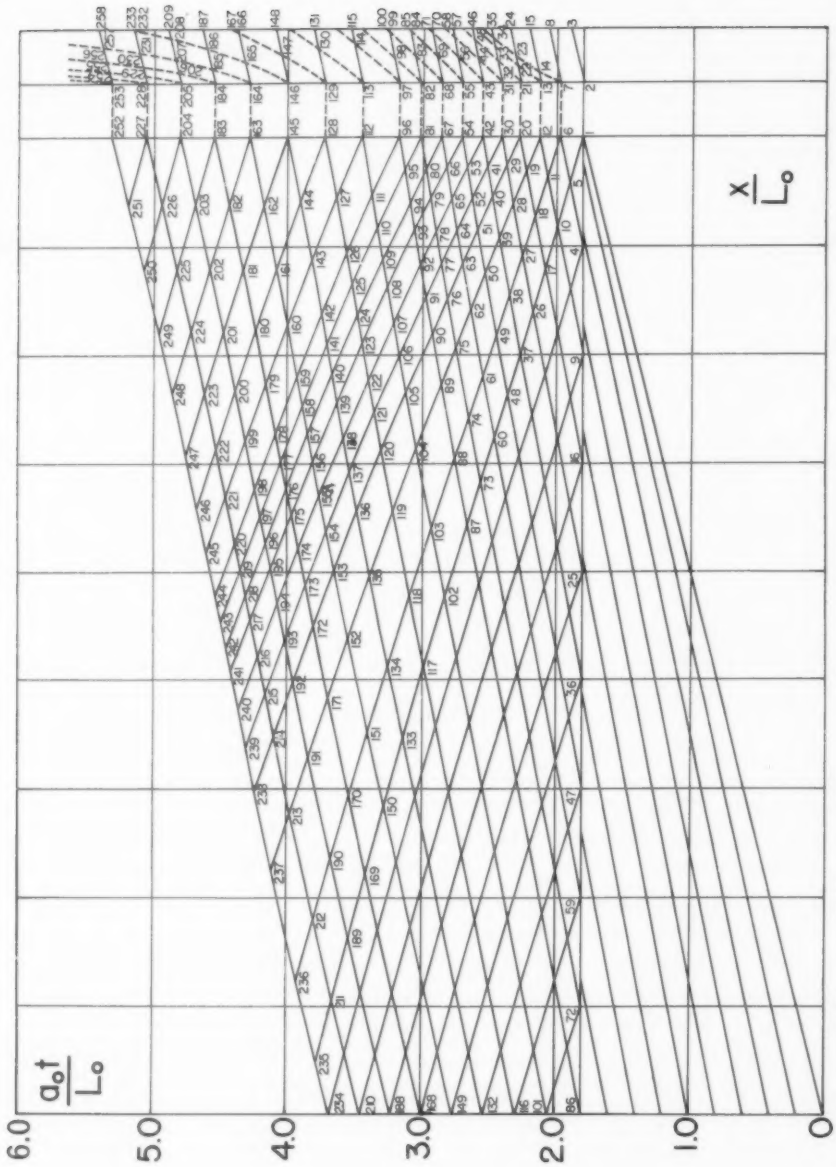

FIG. 6. Wave diagram for sample problem.

Vol. 196

The information presented in Figs. 7, 8 and 9 is sufficient to provide for a calculation of the mechanical work produced during the period of wave motion.

TABLE 1. ABRIDGED DATA FOR SAMPLE PROBLEM

Point	P	Q	A	U	S
1	5·000	5·000	1·000	0	0
2	5·045	5·045	1·009	0	0·045
3	5·045	5·045	1·009	0	0·045
12	5·378	4·698	1·008	0·340	0
13	5·258	4·921	1·018	0·168	0.051
15	5·252	4·838	1·009	0·207	0·045
30	5·478	4·544	1·002	0·467	0
31	5·258	4·804	1·006	0·227	0·020
35	5·283	4·807	1·009	0·238	0·045
54	5·492	4·497	0·999	0·500	0
55	5·250	4·754	1·000	0·248	0·005
58	5·265	4·775	1·004	0·245	0·020
81	5·465	4·525	0·999	0·470	0
82	5·228	4·772	1·000	0·228	0·005
85	5·228	4·782	1·001	0·223	0·005
112	5·382	4·590	0·997	0·396	0
113	5·193	4·807	1·000	0·193	0·014
115	5·188	4·830	1·002	0·179	0·009
145	5·235	4·741	0·997	0·247	0
146	5·149	4·905	1·005	0·122	0·039
148	5·136	4·916	1·005	0·110	0·026
183	5·126	4·856	0·998	0·135	0
184	5·109	4·975	1·008	0·067	0·051
187	5·097	4·981	1·008	0·058	0·039
252	5·012	4·948	0·996	0·032	0
253	5·046	5·014	1·006	0·016	0·050
258	5·044		1·010	−0·006	0·048

That quantity is most easily calculated by subtracting from the integrated sum of enthalpy and kinetic energy at the nozzle exit the corresponding sum leaving the rotor. The desired energy at the nozzle exit, expressed in dimensionless form is found to be

$$\frac{E_N}{a_0 p_0 F_D \Delta t} = \sum_{\text{pulse}} \frac{\gamma}{2} U_N A_N^{2\gamma/\gamma-1} \frac{F_N}{F_D} [\exp(-\gamma S_N)] \left[\frac{2}{\gamma-1} A_N^2 + U_N^2\right] \tag{11}$$

Similarly, at the rotor exit

$$\frac{E_E}{a_0 p_0 F_D \Delta t} = \sum_{\text{pulse}} \frac{\gamma}{2} U_E \frac{F_E}{F_D} \left[\frac{2}{\gamma-1} + \left(\frac{U_{EA}}{A_E}\right)^2\right] \tag{12}$$

Since the wave-diagram calculation is done in a finite series of steps the turbine work was naturally evaluated in stepwise fashion over the period of wave motion. It is interesting to note that near the beginning and the end of the pulse the calculated values of turbine work turned out to be negative. This result was expected, and is due to the fact that under far off-design conditions, which occur at the start and end of the wave motion, net work is being done on the gas by the rotor. Evidently the larger the negative work term the poorer the turbine performance will be.

Vol. 3
1961

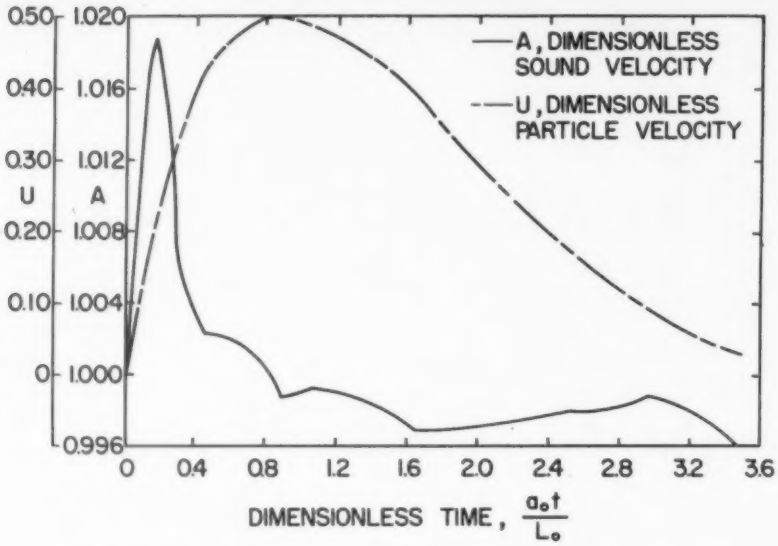

FIG. 7. Gas properties at nozzle exit over period of wave motion.

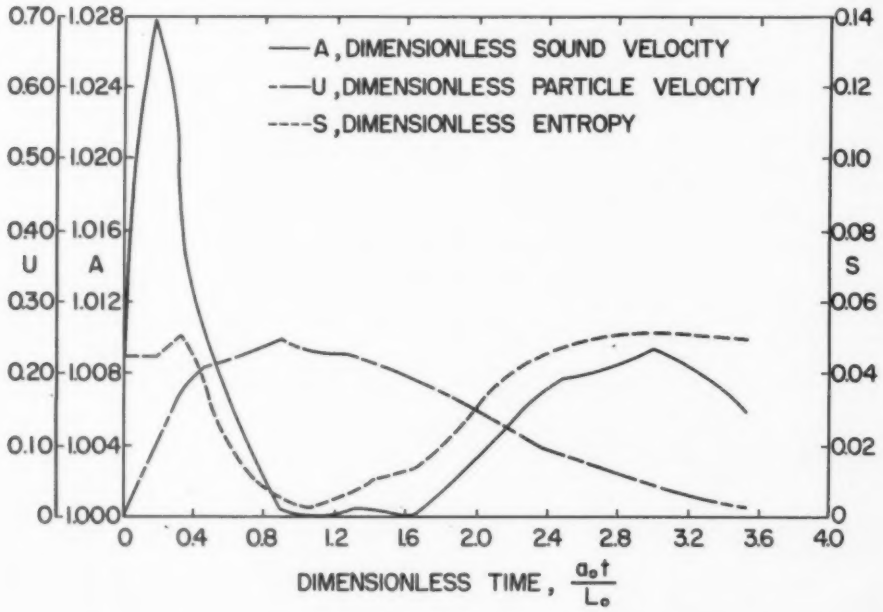

FIG. 8. Gas properties at rotor entrance over period of wave motion.

The performance of the turbine is conveniently expressed as the ratio of the work to the available energy associated with the incident pulse. The latter energy is defined as the energy resulting from isentropic expansion of each element of the incident pulse to the ambient pressure. In dimensionless

form, this quantity can be written as

$$\frac{E_{\text{available}}}{a_0 p_0 F_D \Delta t} = \sum_{\text{pulse}} \frac{\gamma}{2} U_D A_D^{2/\gamma-1}\left[\frac{2}{\gamma-1} A_D^2 + U_D^2 - \frac{2}{\gamma-1}\right] \tag{13}$$

For the conditions assumed in the sample solution the turbine efficiency as defined worked out to 16·8 per cent. This relatively poor performance figure is primarily due to the primitive turbine geometry assumed for convenience of calculation. It is reiterated that the main purpose of the sample solution was to test the proposed analysis for self-consistency. An important side result of the sample solution was the fact that it required approximately 50 hr of actual calculation time. Since the analytical solution is a numerical integration procedure, each change in initial or boundary conditions requires a

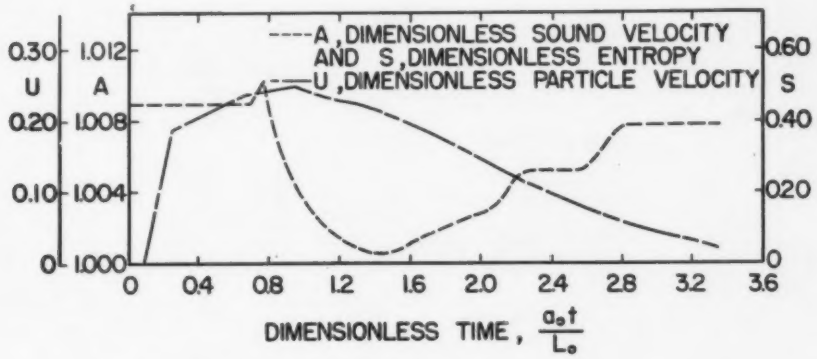

FIG. 9. Gas properties at rotor exit over period of wave motion.

separate and complete solution. It therefore became apparent that the ordinary semi-graphical solution procedure was not practical, if the flow with several sets of initial conditions was to be analysed. Accordingly the problem was programmed for machine solution, in this case for the IBM 704 EDPM. The program was written to accommodate a rather wide range of input data, and the following quantities can be adjusted at will.

(1) Area ratio, inlet duct to nozzle exit.
(2) Area ratio, rotor-blade entrance to exit.
(3) Blade speed.
(4) Area ratio, nozzle exit to rotor-blade entrance.
(5) Flow-path length through rotor.

In addition, the form of the incident wave may be selected arbitrarily, with the sole qualification that since the flow was specified to be subsonic an upper limit for incident pulse maximum pressure exists for given area ratios in the turbine proper. For representative turbine geometries this limit occurs at a pressure ratio of approximately 1·8.

The machine program is quite lengthy. A complete description of the programming problems involved and the program itself may be found in the report by White[6].

EXPERIMENTS

I. *Equipment and instrumentation*

In order to provide a direct check on the theoretical analysis a series of experiments was run on a single stage, axial-flow turbine. The experimental apparatus, shown schematically in Fig. 10, consisted of a steel cylinder containing compressed air and provided with a rapid-opening valve, the cylinder discharging into a steel pipe of 2·5 in. inside diameter leading to the turbine. The turbine, which was allowed to rotate without external loading, was equipped with two inlet ports, each serving a 180° arc of admission. The turbine was driven by means of compressed air, delivered through one admission arc.

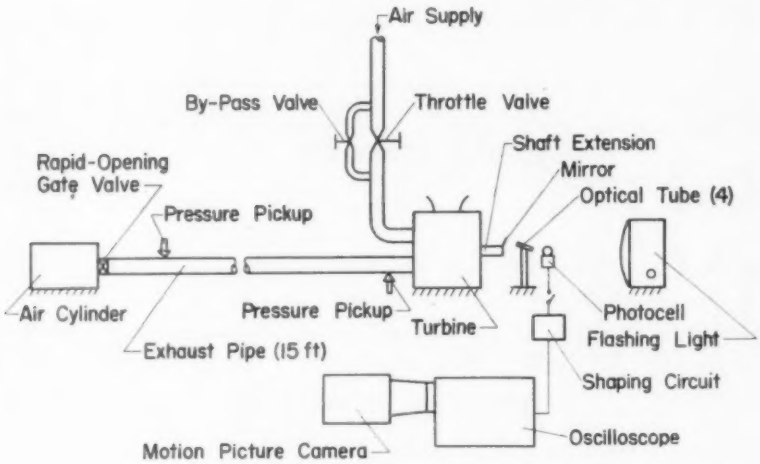

FIG. 10. Line diagram of experimental apparatus.

Its speed could be controlled closely with the pressure-control valve and air by-pass arrangement shown in Fig. 10. Pertinent specifications of the turbine are as follows.

Diameter at blade mid-height = 5·840 in.
Blade height = 0·840 in.
Area ratio, pipe to nozzle exit = 2·730
Area ratio, nozzle exit to blade entrance = 0·288
Area ratio, blade entrance to blade exit = 1·980
Blade exit angle = 24·1°

Briefly, the test procedure consisted in driving the turbine at an initial known speed, passing a pressure pulse of known form through the turbine and measuring the resulting change of turbine speed due to the work extracted from the pulse. The pressure pulse was generated by discharging the steel cylinder from an initial pressure, at a controlled valve-opening rate. This was accomplished by opening the valve by means of a massive falling weight. The cylinder was allowed to discharge completely so that a single pressure disturbance was produced in the pipe leading to the turbine. The pressure–time history at selected points in the pipe was recorded by means of piezo-electric

pressure transducers, in conjunction with a cathode-ray oscilloscope and a high-speed motion picture camera. The form of the pressure pulse could be varied by varying the initial cylinder air pressure, the cylinder volume and the rate of valve opening.

Passage of the pulse through the turbine caused the turbine speed to increase abruptly, followed by a relatively slow speed decrease toward the initial speed. The speed change was measured in the following manner. A small mirror was secured to an extension of the rotor shaft at a small radius from the shaft centerline and tilted so that the reflected light from a flashing source, focused by means of four simple two-lens optical tubes mounted at 90° intervals, fell on the sensitive element of a photocell tube. The photocell output was shaped by means of a simple electronic circuit, and then routed to an oscilloscope.

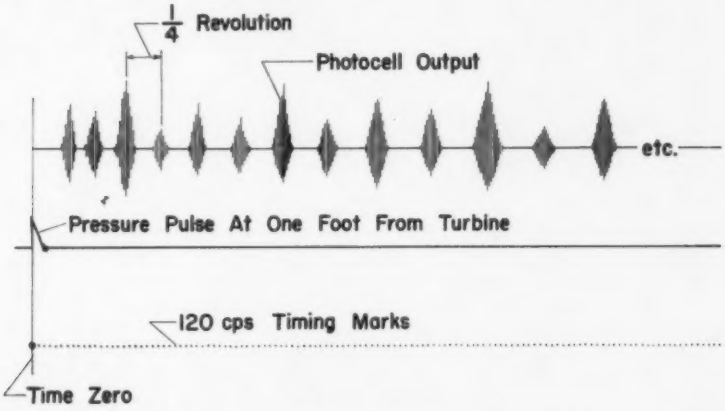

FIG. 11. Typical rotor speed-change data, reproduced from test record.

With this arrangement each time the mirror was aligned with an optical tube, and the light flashed, a pulse would appear on the oscilloscope screen. The oscilloscope screen was photographed with a high-speed camera.

During a test, the speed change instrumentation operated as follows. Initially, the light was set to a fixed flashing frequency corresponding to the desired initial turbine speed. The turbine speed was then increased until it matched the flashing rate. In this initial condition, the mirror was observed to remain stationary at some arbitrary angular position. The pressure pulse then passed through the turbine, causing an abrupt rotor speed increase. Visually, the mirror appeared to accelerate impulsively, and then to decelerate relatively slowly, eventually coming to "rest" after a period of time which varied between 2 and 6 sec, depending on test conditions.

A typical record of photocell output with time is reproduced in Fig. 11. It can be seen that the apparent mirror motion was slow enough and the mirror sufficiently wide such that several pulses appear in the vicinity of each 90° angular position. The distance between successive "peaks" evidently gives an indication of the difference between rotor speed at some time after passage of the wave and the initial rotor speed. The data thus consist of a record of the

increment of rotor speed above a known value as a function of time. These data were then plotted as shown in the example of Fig. 12. The zero of time in this graph is established by recording on the record of photocell output the pressure history just upstream of the turbine.

It was assumed that dissipative influences (viscous friction, disk friction, blade windage) were negligible during the very short interval of time of wave motion. Therefore, the energy delivered to the rotor appears wholly as an increase of kinetic energy of the rotating assembly. With a known mass moment

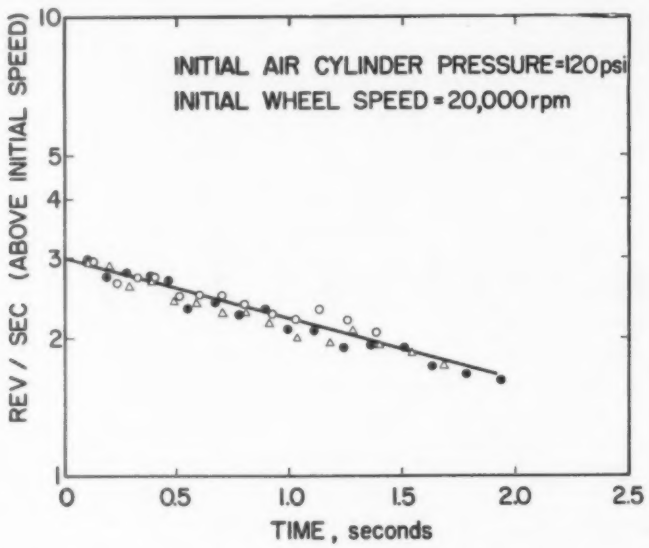

FIG. 12. Typical rotor-speed decay characteristic.

of inertia of the rotating assembly, and with the measured speed change, the work is calculated by applying the formula

$$\text{Work} = \frac{I}{2}(\omega_{\text{max}}^2 - \omega_{\text{initial}}^2) \tag{14}$$

It is to be noted that the performance figures arrived at by using equation (14) are exclusive of the afore-mentioned dissipative factors, and are based on what is usually called internal work. This point of view is, of course, in line with the assumptions used in the theoretical analysis. Therefore, the turbine work calculated from experimental data may be compared directly with predicted work by the wave diagram analysis.

II. *Test results*

Test data were obtained for two incident pulse forms, over a range of turbine speeds for both pulses. The final results are shown in Fig. 13, where turbine efficiency, as defined previously, is plotted against initial turbine speed. Several interesting features appear in Fig. 13, the most unexpected being the comparatively high peak values of turbine efficiency. It is also noted that the peak

efficiency for the weaker of the two incident pulses occurs at a lower turbine speed, a result which is in line with correspondingly lower average values of nozzle-exit gas velocities. Another interesting point is the fact that turbine efficiencies for the weaker pulse are consistently higher than those for the stronger pulse. It is quite certain that the main cause is the smaller percentage of available energy reflected from the turbine for the weaker incident pulse. From an analysis of the pressure traces it was estimated that 12 per cent of the available energy was reflected for the stronger wave, and 6 per cent for the

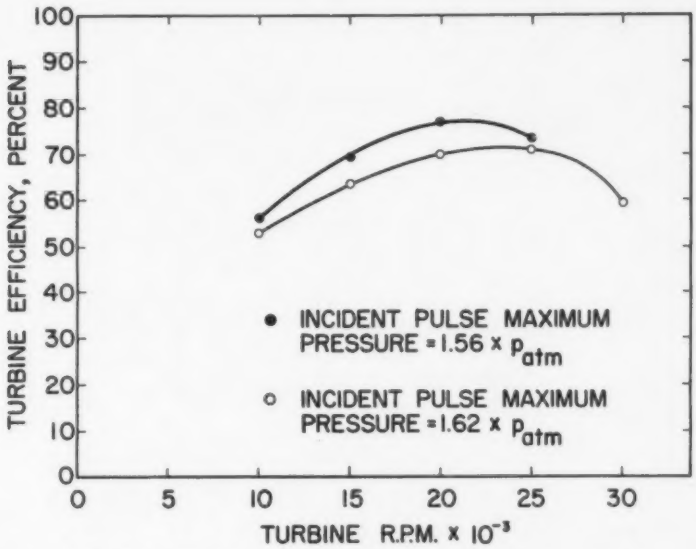

FIG. 13. Turbine performance from test measurements, for two incident pulse forms.

weaker. If an incident pulse slightly weaker than those used in the tests had been tried, it seems certain that the peak efficiency would have reached 80 per cent, a remarkably high figure, considering the wide variation of gas velocities represented in the pulse. In this connexion, it is noted that the available energies used in calculating turbine efficiencies were found by examining the incident pulses at a position in the pipe some 12 ft from the turbine. This was done in order to record the entire incident pulse before a reflexion returned from the turbine. Therefore, the effects of wall friction on the pulses over a distance of 12 ft were neglected, and the experimental values of turbine efficiency reported here are, if anything, conservative.

COMPARISON OF THEORY WITH TEST DATA

Due to the limited availability of computer time machine solutions were obtained for only one incident pulse form, that being the stronger of the two used in the test program. The incident pulse as measured in the pipe 12 ft from the turbine was given to the machine as initial data, together with necessary geometrical data, over a range of blade speeds corresponding to

Vol. 3
1961

turbine rev/min from 10,000 to 30,000. Turbine efficiency was calculated from the machine output as outlined previously. The results are shown in Fig. 14, the curve labelled "theoretical" indicating the calculated values, the curve labelled "experimental" showing test values for the same incident pulse.

At the lowest turbine speed Fig. 14 shows the theoretical efficiency approximately 20 per cent higher than the experimental, the agreement between the two curves becoming progressively better with higher turbine speeds. At 30,000 rev/min, the theoretical value is approximately 5 per cent higher than the

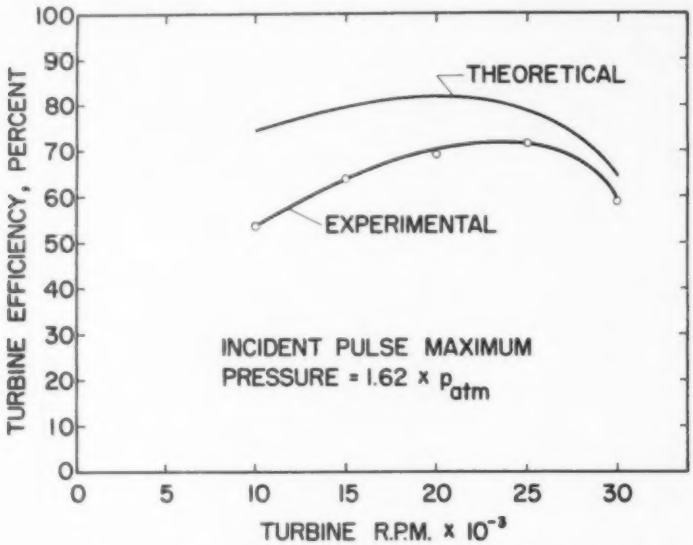

FIG. 14. Turbine performance for one incident pulse form—theoretical and test results.

experimental. The rather large discrepancy at lower turbine speeds is believed to be due primarily to one of the assumptions used in the theoretical analysis. It will be recalled that in the boundary condition statement at the nozzle exit–blade-entrance station, the quantity U_N was not to be substantially greater than U_{RA}, the absolute velocity at the rotor-blade entrance. However, at an initial turbine speed of 10,000 rev/min, the gas velocity U_N was found to be approximately twice U_{RA} for some portions of the pulse used. The boundary condition as written calls for no entropy increase as the high velocity gas issuing from the nozzles is slowed abruptly upon entering the rotor blades, i.e. the case $U_N > U_{RA}$. In short, the analysis as written cannot be expected to produce accurate results in the lower speed range of the turbine used in the tests.

The relatively close agreement shown in Fig. 14 at the higher speeds is taken to be a most encouraging result, particularly in view of the fact that wall friction in the pipe was ignored in the analysis. In other words, the theoretical curve with friction included would be shifted downwards by a small constant amount, improving the comparison over the entire speed range.

Vol. 3
1961

CONCLUSIONS

1. The one-dimensional nonsteady flow analysis developed in the paper predicts a turbine performance which is in quite good agreement with measured values, in the turbine speed range for which the analysis was intended. The principal feature of the analysis is the momentum exchange process which is assumed to occur as the gas flows from the nozzles into the rotor passages under off-design conditions. It is concluded that a momentum exchange similar to that proposed occurs in the actual machine. The calculation of entropy of the gas within the rotor passages, which follows as a result of the assumed momentum exchange, gives a clearer picture of the thermodynamic aspects of the flows in a pulse turbine, as well as indicating the source of energy "losses".

2. It appears that the assumed one-dimensional flow in the turbine passages is reasonably accurate. In particular, the assumption of no serious flow separation at the rotor-blade entrance under off-design conditions seems to be substantiated by the good agreement between test data and predicted turbine performance. If serious flow separation had occurred the accompanying entropy generation would have resulted in higher values of energy leaving the rotor, thus less turbine internal work and lower efficiency. It would therefore appear profitable in any future studies to retain the assumption of one-dimensional flow as a reasonable approximation.

3. A relatively simple, straightforward technique for measuring turbine work under nonsteady flow conditions has been developed. Unexpectedly high values of turbine efficiency were obtained from the experimental data. Whether this was the result of a fortuitous choice of experimental turbine is not known. It is, however, suggested that since the experimental turbine was in every way a standard design, and in view of the high measured values of performance, substantial improvements in pulse turbine performance through radical design changes involving the nozzles and rotor blades are not likely. Attention should rather be given to such matters as blade windage, disk friction and nonsteady partial-admission losses.

Acknowledgements—The work reported here was part of a program of research carried out in the Department of Engineering Research in The Pennsylvania State University, supported by the U.S. Navy, Office of Naval Research, under Contract No. Nonr 656(16). Thanks are due to the Elliott Company for the loan of an experimental turbine, and to the Curtiss–Wright Corporation for a generous donation of computer facilities and time.

REFERENCES

1. E. Jenny, Doctoral Thesis. Eidgenössische Technische Hochschule, Zürich. Ameba-Druck, Basel (1949).
2. R. S. Benson and W. A. Woods, *Int. J. Mech. Sci.* **1**, 253 (1960).
3. G. Rudinger, *Wave Diagrams for Nonsteady Flow in Ducts*. Van Nostrand, New York (1955).
4. A. H. Shapiro, *The Dynamics and Thermodynamics of Compressible Fluid Flow*. Ronald Press, New York (1953).
5. D. S. Butler, A.R.D.E. Report (B) 35/58 (1958).
6. D. F. White, Technical Report, ONR Contract No. Nonr 656(16) (1958).

Int. J. Mech. Sci. Pergamon Press Ltd. 1961. Vol. 3, pp. 286–311. Printed in Great Britain

THE FREE OSCILLATIONS OF CONSERVATIVE QUASILINEAR SYSTEMS WITH TWO DEGREES OF FREEDOM

A. O. GILCHRIST
Engineering Laboratory, University of Cambridge

(*Received* 8 *November* 1960)

Summary—The paper is in two parts. The first deals generally with conservative quasi-linear systems with two degrees of freedom, and describes the approximate analytical solution of their differential equations following the methods of Bogoliuboff and Mitropolski. Part I also describes a technique which facilitates a survey of the variety of motions which are possible in a non-linear system.

The second part of the paper uses these methods to analyse two particular pairs of differential equations. These apply to a number of mechanical systems, and one such system has been used to give direct experimental verification of the theory.

INTRODUCTION

A NUMBER of papers have appeared in recent years discussing the steady *forced* oscillations of mechanical systems with two degrees of freedom. Examples are Refs. 1–6, all of which take as their basic model the two-mass system of Fig. 1,

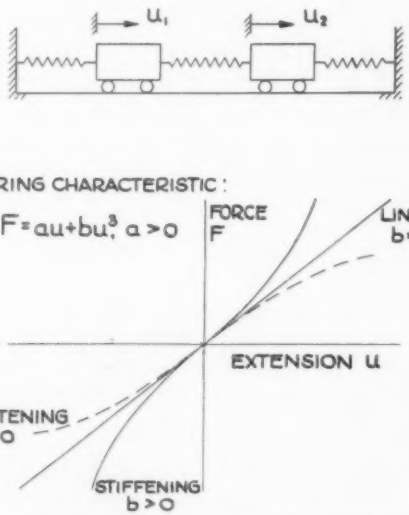

FIG. 1. Basic model of a two-degree-of-freedom system with springs of the linear + cubic type.

or a special case of this. Usually the spring forces are chosen to be linear + cubic, and the damping forces ignored. This approximation gives good accuracy in many mechanical systems, and the idealized model becomes a direct two-degree-of-freedom extension of the undamped Duffing oscillator.

The *free* oscillations of such a system may be quite complex. Assuming small non-linearity and choosing the normal coordinates of the linear terms as variables x_1 and x_2, the equations of free motion take the form:

$$\begin{aligned} \ddot{x}_1 + k_1^2 x_1 &= \epsilon(l_1 x_1^3 + m_1 x_1^2 x_2 + n_1 x_1 x_2^2 + p_1 x_2^3) \\ \ddot{x}_2 + k_2^2 x_2 &= \epsilon(l_2 x_2^3 + m_2 x_2^2 x_1 + n_2 x_2 x_1^2 + p_2 x_1^3) \end{aligned} \qquad (1)^*$$

where dots denote differentiation with respect to time, k_i, l_i, m_i, n_i, p_i, ϵ are constants, and ϵ is small. In the linear case ($\epsilon = 0$) these coordinates oscillate

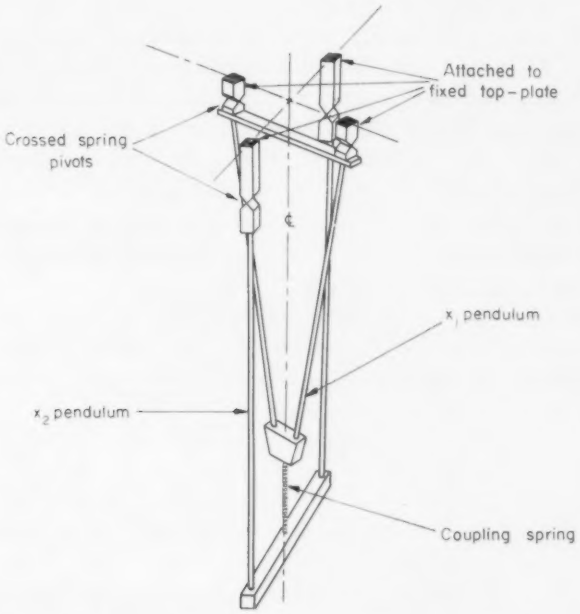

FIG. 3. Two-pendulum system used for experimental verification of solutions of equations (1).

harmonically with constant amplitude. A similar motion may also occur in the non-linear case ($\epsilon \neq 0$), but does not always do so. In particular, for certain ranges of the frequency ratio k_1/k_2,† the characteristic motion is an oscillation with periodically varying amplitude and frequency: an example of a solution with k_1/k_2 close to 1 is shown in Fig. 2.

Free motions of this type have received little attention. However, Tobias[7] and Henry and Tobias[8] do discuss some very important aspects of the behaviour of the special case of equations (1), $m_i = p_i = 0$. (These simpler equations

* With the restriction $\frac{n_1}{n_2} = \frac{3p_1}{m_2} = \frac{m_1}{3p_2}$, see p. 303.

† The forced motions also show exceptional behaviour in these regions of "internal resonance" between the degrees of freedom. These effects are usually excluded from the analyses of forced motion, although Sethna[6] discusses the point, and gives examples for the forcing of Fig. 1 when $k_1/k_2 = 3$. An example is not given for the important case $k_1/k_2 \approx 1$.

describe the symmetrical case of Fig. 1, and also have applications in the vibration of circular disks and vibration-isolating suspensions.) In particular the authors consider initial conditions which cause one normal coordinate to vibrate alone, and show that under certain conditions the other coordinate may become unstable and begin to vibrate as well. They also show that special initial conditions may result in the steady oscillation of both coordinates. These are special cases of the generally unsteady motions which result from arbitrary initial conditions, and which are analysed in Part II below both for Tobias' equations and the full set (1).

This theoretical analysis is supported by experiments made with a mechanical analogue of equations (1). This is shown schematically in Fig. 3, and consists of two pendulums free to swing in vertical planes which intersect in the centre-line of the apparatus, and which may be set to include any angle. The lower ends of the pendulums are connected by a linear spring, and in the static equilibrium position this also lies in the vertical centre-line. As suggested above, it is central to the analysis to work in terms of the linear normal coordinates: an advantage of this particular analogue is that the angular displacement of each pendulum does represent a normal coordinate, so that the characteristic beating motion between them is clearly shown.

The systems mentioned so far provide a few examples of conservative quasilinear systems with two degrees of freedom. Other examples may have different equations (e.g. the elastic pendulum of Mettler[9]). Part I defines and discusses this class of system in general.

NOTATION

x_1, x_2, x_i	coordinates of 1st, 2nd, ith normal mode
t	time
k_i	circular linear natural frequency of ith mode
ϵ	small positive parameter
l_i, m_i, n_i, p_i	constant coefficients of non-linear terms
T, V	kinetic, potential energies respectively
$T_i, V_i, U_1 \ldots U_5$	constants in energy expressions
q_1, q_2	positive integers
ω	circular frequency
Δ_i	constant measuring frequency difference
a_i	fundamental amplitude (variable)
θ_i	phase measured from $(\omega/q_i)t$ (variable)
$u_i^{(r)}$	rth term in expansion for x_i
$A_i^{(r)}$	rth term in expansion for da_i/dt
$B_i^{(r)}$	rth term in expansion for $d\theta_i/dt$
ψ_i	full phase
C	constant proportional to initial energy
χ	variable replacing a_1 and a_2
Φ	phase difference
α, β	constants, α a function of C

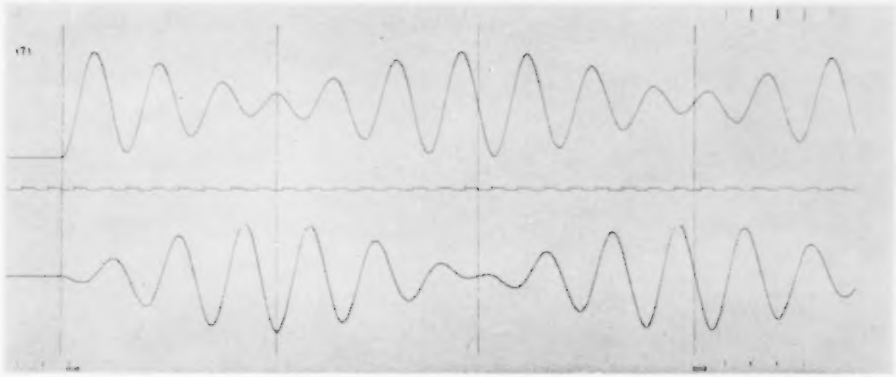

FIG. 2. Examples of solutions $x_1(t)$ and $x_2(t)$ of equations (1) when linear natural frequencies k_1 and k_2 are close. (This is an experimental trace obtained from the pendulum analogue described in the introduction. In all the illustrations of experimental solutions the upper trace gives x_1, the lower x_2, and full-scale deflexion represents a pendulum amplitude of about 7°. The time base period is 0·5 sec.)

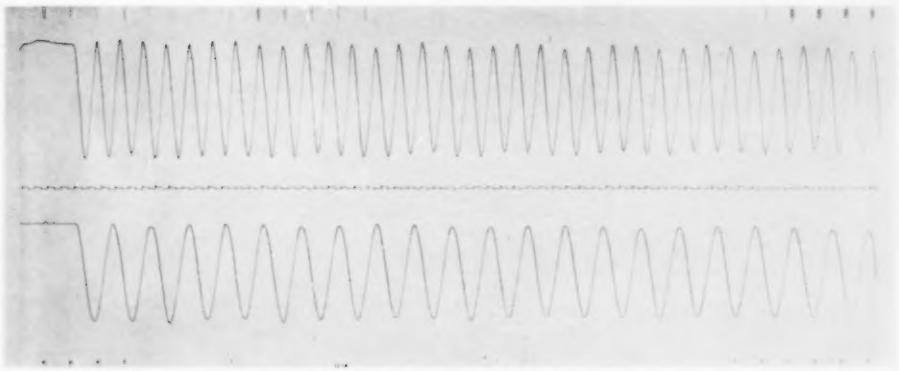

FIG. 4. Typical non-resonant solution for a conservative system with linear natural frequencies not close to an integer ratio.

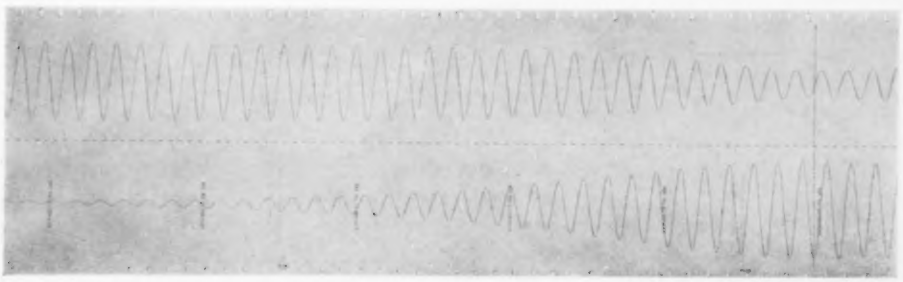

FIG. 7. Solution for Application I(a) with x_2 starting from rest, separatrix 1 of Fig. 5(a).

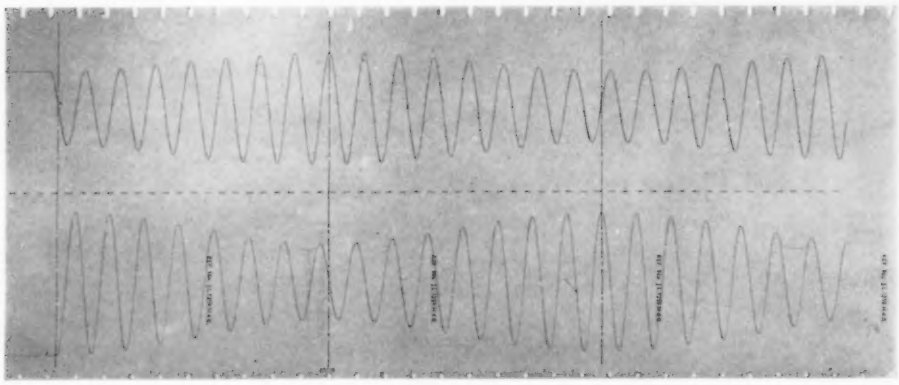

FIG. 8. Beating motion showing no net change of phase during a beat cycle. This motion appears as the oval 2 of Fig. 5(a).

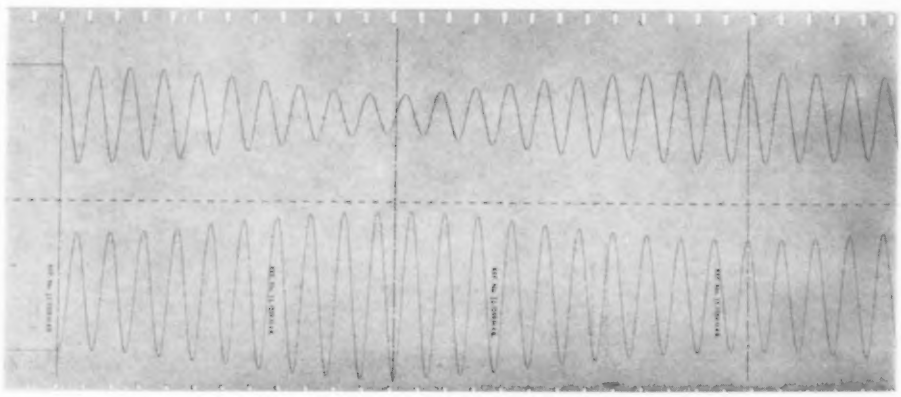

FIG. 9. Beating motion showing a phase change of π over a beat cycle. This appears as the open curve 3 of Fig. 5(a).

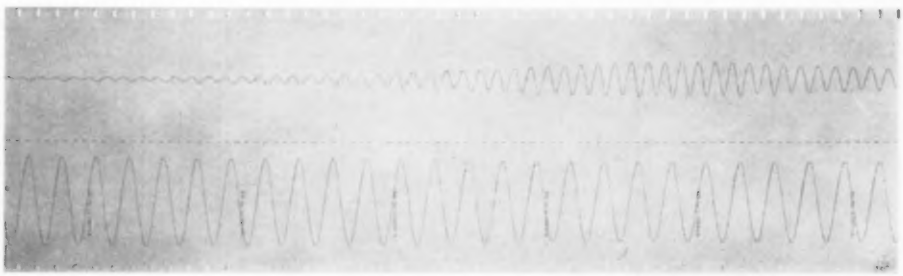

FIG. 11. Application I(b): the build-up of x_1 from rest, the separatrix of Fig. 10.

PART I. CONSERVATIVE QUASILINEAR SYSTEMS

DEFINITION

By choosing variables x_1 and x_2 proportional to the normal coordinates the kinetic and potential energies of a conservative, *linear*, two-degree-of-freedom system may always be brought to the form

$$\begin{aligned} T &= \tfrac{1}{2}T_1\dot{x}_1^2 + \tfrac{1}{2}T_2\dot{x}_2^2 \\ V &= \tfrac{1}{2}V_1x_1^2 + \tfrac{1}{2}V_2x_2^2 \end{aligned} \tag{2}$$

The potential energy V is measured from the equilibrium position $x_1 = x_2 = 0$, and for an oscillatory system this equilibrium must be stable, so that the V_i, like the T_i, are positive constants.

For a quasilinear system the dominant linear terms may be transformed to normal coordinates in the same way, and the energies now have the form

$$\begin{aligned} 2T &= T_1\dot{x}_1^2 + T_2\dot{x}_2^2 + \epsilon f_T(x_1, x_2, \dot{x}_1, \dot{x}_2) \\ 2V &= V_1x_1^2 + V_2x_2^2 + \epsilon f_V(x_1, x_2) \end{aligned} \tag{3}$$

where ϵ is a small (positive) parameter. The functions f_T and f_V are analytic functions of the displacements and velocities.

Since the system is conservative all the forces are derivable from the potential energy so that during any motion

$$T + V = \text{constant} \tag{4}$$

Equations (3) and (4) define the class of systems to be discussed in the present paper. Evidently the Lagrange equations for such systems may be written

$$\begin{aligned} \ddot{x}_1 + k_1^2x_1 &= \epsilon f_1(x_1, x_2, \dot{x}_1, \dot{x}_2) \\ \ddot{x}_2 + k_2^2x_2 &= \epsilon f_2(x_1, x_2, \dot{x}_1, \dot{x}_2) \end{aligned} \tag{5}$$

where $k_i^2 = V_i/T_i$. The problem of the free motion will be solved by setting up approximate solutions for this pair of non-linear differential equations.

CONSTRUCTION OF APPROXIMATE SOLUTIONS*

The analysis here uses the asymptotic form of solution of Bogoliuboff and Mitropolski[10]. This is particularly suited to oscillations with slowly varying phase and amplitude, being a development of the familiar Kryloff and Bogoliuboff method.[11] The new work is a considerable advance, however, giving a clear mathematical basis and continuing naturally to higher approximations. The analysis below extends to two degrees of freedom the presentation given by Bogoliuboff and Mitropolski for the forced oscillation of single-degree-of-freedom systems.

At the outset, it is necessary to distinguish between the two important cases of "resonance" and "non-resonance", since the solutions are best taken in a different form for each case. Resonance may occur between the two degrees

* The methods of this section apply to any system obeying equations (5), not necessarily conservative. Straightforward extensions are also possible to N degrees of freedom, and to forced systems having $f_i(x_1, x_2, \ldots, \dot{x}_1, \dot{x}_2, \ldots, t)$, periodic in t.

of freedom when equations (5) have linear frequencies such that

$$k_1/k_2 \approx q_2/q_1 \tag{6}$$

where q_1 and q_2 are small mutually-prime integers. This case will be treated first, and the distinction between the two discussed in more detail when proceeding to the non-resonance condition.

(a) *Resonance case*

When (6) holds, a frequency ω may be chosen so that

$$k_i^2 = \left(\frac{\omega}{q_i}\right)^2 + \epsilon\Delta_i \qquad (i = 1, 2) \tag{7}$$

where the Δ_i are constants. Equations (5) may then be written

$$\ddot{x}_i + \left(\frac{\omega}{q_i}\right)^2 x_i = \epsilon\{f_i(x_1, x_2, \dot{x}_1, \dot{x}_2) - \Delta_i x_i\} \qquad (i = 1, 2) \tag{8}$$

When $\epsilon = 0$, the solution of these equations is simply

$$x_i = a_i \cos\left(\frac{\omega}{q_i}t + \theta_i\right) \qquad (i = 1, 2) \tag{9}$$

where the a_i and θ_i are constants depending on the initial conditions. That is

$$\frac{da_i}{dt} = \frac{d\theta_i}{dt} = 0 \qquad (i = 1, 2) \tag{10}$$

However, when $\epsilon \neq 0$ (it is by definition small) (9) and (10) no longer hold. Harmonics appear in the waveforms of the x_i, and the amplitudes and phases are not in general constant but vary slowly with rates of change da_i/dt and $d\theta_i/dt$ which are functions of the amplitudes and phases a_1, a_2, θ_1, θ_2. Therefore solutions are sought in the form

$$x_i = a_i \cos\left(\frac{\omega}{q_i}t + \theta_i\right) + \epsilon u_i^{(1)}(a_1, a_2, \theta_1, \theta_2, t) + \epsilon^2 u_i^{(2)} + \ldots \tag{11}$$

where the $u_i^{(r)}$ are periodic functions in θ_1, θ_2 and t, and the a_i and θ_i are variables determined from

$$\begin{aligned} \frac{da_i}{dt} &= \epsilon A_i^{(1)}(a_1, a_2, \theta_1, \theta_2) + \epsilon^2 A_i^{(2)}(a_1, a_2, \theta_1, \theta_2) + \ldots \\ \frac{d\theta_i}{dt} &= \epsilon B_i^{(1)}(a_1, a_2, \theta_1, \theta_2) + \epsilon^2 B_i^{(2)}(a_1, a_2, \theta_1, \theta_2) + \ldots \end{aligned} \tag{12}$$

The $A_i^{(r)}$ and $B_i^{(r)}$ are periodic with period 2π in θ_1 and θ_2, since the phases θ_i are only defined within arbitrary additions of 2π.

It is seen that these solutions reduce to the known results (9) and (10) when $\epsilon = 0$, and it now remains to choose functions $u_i^{(r)}$, $A_i^{(r)}$ and $B_i^{(r)}$ for $\epsilon \neq 0$ so as to satisfy (8) to any required order of ϵ. To do this the solutions (11) and (12) are substituted into each equation (8), and the left and right sides arranged as power series in ϵ. The successive approximations are then obtained by equating terms of each order of ϵ in turn, starting with the lowest, so that the order of magnitude of the error is reduced at each step.

The left-hand sides are obtained by differentiating the series (11) for x_i as a function of the five variables a_1, a_2, θ_1, θ_2 and t, and using (12) to expand terms like da_i/dt, d^2a_i/dt^2, $(da_i/dt).(d\theta_j/dt)$, etc. The zero-order terms vanish identically, leaving

$$\begin{aligned}
&\ddot{x}_i + \left(\frac{\omega}{q_i}\right)^2 x_i \\
&\quad = \epsilon\left[-2\frac{\omega}{q_i}A_i^{(1)}\sin\left(\frac{\omega}{q_i}t+\theta_i\right) - 2a_i\frac{\omega}{q_i}B_i^{(1)}\cos\left(\frac{\omega}{q_i}t+\theta_i\right) + \frac{\partial^2 u_i^{(1)}}{\partial t^2} + \left(\frac{\omega}{q_i}\right)^2 u_i^{(1)}\right] \\
&\qquad + \epsilon^2\left[-\left\{a_i\left(A_1^{(1)}\frac{\partial B_i^{(1)}}{\partial a_1} + A_2^{(1)}\frac{\partial B_i^{(1)}}{\partial a_2} + B_1^{(1)}\frac{\partial B_i^{(1)}}{\partial \theta_1} + B_2^{(1)}\frac{\partial B_i^{(1)}}{\partial \theta_2}\right)\right.\right. \\
&\qquad\qquad \left.\left. + 2A_i^{(1)}B_i^{(1)} + 2\frac{\omega}{q_i}A_i^{(2)}\right\}\sin\left(\frac{\omega}{q_i}t+\theta_i\right)\right. \\
&\qquad\quad + \left\{A_1^{(1)}\frac{\partial A_i^{(1)}}{\partial a_1} + A_2^{(1)}\frac{\partial A_i^{(1)}}{\partial a_2} + B_1^{(1)}\frac{\partial A_i^{(1)}}{\partial \theta_1} + B_2^{(1)}\frac{\partial A_i^{(1)}}{\partial \theta_2} - a_i B_i^{(1)2} - 2a_i\frac{\omega}{q_i}B_i^{(2)}\right\} \\
&\qquad\qquad \times\cos\left(\frac{\omega}{q_i}t+\theta_i\right) + 2A_1^{(1)}\frac{\partial^2 u_i^{(1)}}{\partial a_1\,\partial t} + 2A_2^{(1)}\frac{\partial^2 u_i^{(1)}}{\partial a_2\,\partial t} \\
&\qquad + 2B_1^{(1)}\frac{\partial^2 u_i^{(1)}}{\partial \theta_1\,\partial t} + 2B_2^{(1)}\frac{\partial^2 u_i^{(1)}}{\partial \theta_2\,\partial t} + \frac{\partial^2 u_i^{(2)}}{\partial t^2} + \left(\frac{\omega}{q_i}\right)^2 u_i^{(2)}\Big] + \epsilon^3\ldots
\end{aligned}$$

The right-hand sides of equation (8) require the Taylor expansions:

$$\begin{aligned}
f_i(x_1, x_2, \dot{x}_1, \dot{x}_2) = (f_i)_0 + \epsilon\Big[&u_1^{(1)}\left(\frac{\partial f_i}{\partial x_1}\right)_0 + u_2^{(1)}\left(\frac{\partial f_i}{\partial x_2}\right)_0 \\
&+ \left\{A_1^{(1)}\cos\left(\frac{\omega}{q_1}t+\theta_1\right) - a_1B_1^{(1)}\sin\left(\frac{\omega}{q_1}t+\theta_1\right) + \frac{\partial u_1^{(1)}}{\partial t}\right\}\left(\frac{\partial f_i}{\partial \dot{x}_1}\right)_0 \\
&+ \left\{A_2^{(1)}\cos\left(\frac{\omega}{q_2}t+\theta_2\right) - a_2B_2^{(1)}\sin\left(\frac{\omega}{q_2}t+\theta_2\right) + \frac{\partial u_2^{(1)}}{\partial t}\right\}\left(\frac{\partial f_i}{\partial \dot{x}_2}\right)_0\Big] \\
&+ \epsilon^2\ldots
\end{aligned}$$

where $(\quad)_0$ are the values at

$$x_i = a_i\cos\left(\frac{\omega}{q_i}t+\theta_i\right), \quad \dot{x}_i = -a_i\frac{\omega}{q_i}\sin\left(\frac{\omega}{q_i}t+\theta_i\right)$$

The f_i are analytic, and the terms of their expansions are periodic in t.

Equating the coefficients of ϵ on the left and right sides of the ith equation gives

$$\frac{\partial^2 u_i^{(1)}}{\partial t^2} + \left(\frac{\omega}{q_i}\right)^2 u_i^{(1)} = 2\frac{\omega}{q_i}A_i^{(1)}\sin\left(\frac{\omega}{q_i}t+\theta_i\right) + \left\{2a_i\frac{\omega}{q_i}B_i^{(1)} - \Delta_i a_i\right\}\cos\left(\frac{\omega}{q_i}t+\theta_i\right) + (f_i)_0$$

$$(i = 1, 2) \qquad (13)$$

Vol. 3
1961

Dealing similarly with the coefficients of ϵ^2,

$$\frac{\partial^2 u_i^{(2)}}{\partial t^2}+\left(\frac{\omega}{q_i}\right)^2 u_i^{(2)} \qquad (i=1,2)$$

$$=\left\{a_i\left(A_1^{(1)}\frac{\partial B_i^{(1)}}{\partial a_1}+A_2^{(1)}\frac{\partial B_i^{(1)}}{\partial a_2}+B_1^{(1)}\frac{\partial B_i^{(1)}}{\partial \theta_1}+B_2^{(1)}\frac{\partial B_i^{(1)}}{\partial \theta_2}\right)\right.$$
$$\left.+2A_i^{(1)}B_i^{(1)}+2\frac{\omega}{q_i}A_i^{(2)}\right\}\sin\left(\frac{\omega}{q_i}t+\theta_i\right)$$
$$+\left\{-A_1^{(1)}\frac{\partial A_i^{(1)}}{\partial a_1}-A_2^{(1)}\frac{\partial A_i^{(1)}}{\partial a_2}-B_1^{(1)}\frac{\partial A_i^{(1)}}{\partial \theta_1}-B_2^{(1)}\frac{\partial A_i^{(1)}}{\partial \theta_2}\right.$$
$$\left.+a_i B_i^{(1)2}+2a_i\frac{\omega}{q_i}B_i^{(2)}\right\}\cos\left(\frac{\omega}{q_i}t+\theta_i\right)$$
$$-2A_1^{(1)}\frac{\partial^2 u_i^{(1)}}{\partial a_1\,\partial t}-2A_2^{(1)}\frac{\partial^2 u_i^{(1}}{\partial a_2\,\partial t}-2B_1^{(1)}\frac{\partial^2 u_i^{(1)}}{\partial \theta_1\,\partial t}-2B_2^{(1)}\frac{\partial^2 u_i^{(1)}}{\partial \theta_2\,\partial t}-\Delta_i u_i^{(1)}$$
$$+u_1^{(1)}\left(\frac{\partial f_i}{\partial x_1}\right)_0+u_2^{(1)}\left(\frac{\partial f_i}{\partial x_2}\right)_0$$
$$+\left\{A_1^{(1)}\cos\left(\frac{\omega}{q_1}t+\theta_1\right)-a_1B_1^{(1)}\sin\left(\frac{\omega}{q_1}t+\theta_1\right)+\frac{\partial u_1^{(1)}}{\partial t}\right\}\left(\frac{\partial f_i}{\partial \dot{x}_1}\right)_0$$
$$+\left\{A_2^{(1)}\cos\left(\frac{\omega}{q_2}t+\theta_2\right)-a_2B_2^{(1)}\sin\left(\frac{\omega}{q_2}t+\theta_2\right)+\frac{\partial u_2^{(1)}}{\partial t}\right\}\left(\frac{\partial f_i}{\partial \dot{x}_2}\right)_0 \qquad (14)$$

and so on (in principle) for the coefficients of ϵ^3, ϵ^4, etc.

By continuing this process up to the coefficients of ϵ^r (say), the solutions (11) are made to satisfy the original differential equations with a remainder of $0(\epsilon^{r+1})$. The solutions are therefore "asymptotic" in the sense that they approach the exact solutions for sufficiently small ϵ. The error after time t is $0(\epsilon^{r+1})t$.

At this point, a restriction must be imposed to avoid arbitrariness in the choice of the functions $a_i, u_i^{(1)}, u_i^{(2)}, \ldots, u_i^{(r)}$. For this purpose, it is convenient to make a_i the full fundamental amplitude of x_i; that is, require that $u_i^{(1)}, \ldots, u_i^{(r)}$ contain no harmonic of frequency (ω/q_i) in t.

This makes it possible to use the series of equations starting (13), (14) to determine successively the terms of expansions (11) and (12). For, since $u_1^{(1)}$ is periodic in t, the $i=1$ equation of (13) must have no term of frequency ω/q_i on its right-hand side to cause secular solutions; this determines $A_1^{(1)}$ and $B_1^{(1)}$.* Then since $u_1^{(1)}$ contains no frequency ω/q_1, equation $(13)_{i-1}$ can be solved for $u_1^{(1)}$ uniquely (the complementary function is zero). In the same way equation $(13)_{i-2}$ gives $A_2^{(1)}$, $B_2^{(1)}$ and $u_2^{(1)}$. This completes the first approximation

$$x_i=a_i\cos\left(\frac{\omega}{q_i}t+\theta_i\right)+\epsilon u_i^{(1)}$$
$$\frac{da_i}{dt}=\epsilon A_i^{(1)},\quad \frac{d\theta_i}{dt}=\epsilon B_i^{(1)} \qquad (15)\dagger$$

* $(f_1)_0$ is periodic in t. It is arranged as a Fourier series in t (with coefficients functions of $a_1, a_2, \theta_1, \theta_2$), and the terms of frequency ω/q_1 expressed as

$$g_1(a_1,a_2,\theta_1,\theta_2,)\cos(\omega t/q_1+\theta_1)+h_1(a_1,a_2,\theta_1,\theta_2)\sin(\omega t/q_1+\theta_1).$$

The unique choice of $A_1^{(1)}$ and $B_1^{(1)}$ follows directly. (See Application I(a) below.)

† These equations are a two-degree-of-freedom version of the "refined first approximation" of Kryloff and Bogoliuboff[11].

The terms $u_i^{(1)}$ represent a correction to the wave form, and are often small enough to be omitted in practice. In any case, the main features of the motion are characterized by the variations of amplitude and phase a_i and θ_i.

The effect of the first approximation, then, is to reduce the problem to four first-order equations in $a_1, a_2, \theta_1, \theta_2$. Often these equations can be integrated, as in all the applications below. But even in the worst case in which they require numerical integration the calculations are greatly shortened by working with the slowly changing envelope amplitudes a_i, rather than the actual displacements x_i.

Continuing to the second approximation the only unknowns now remaining on the right-hand side of the two equations (14) are $A_1^{(2)}$, $B_1^{(2)}$ and $A_2^{(2)}$, $B_2^{(2)}$. These are found by eliminating frequencies ω/q_1 and ω/q_2 respectively, the two equations being then solved for $u_1^{(2)}$ and $u_2^{(2)}$. In theory this procedure may be continued indefinitely, but the increasing complication of the algebra usually makes it impracticable after a few steps.

Vol. 3
1961

The reason for the appearance of internal resonances at a number of values of q_1 and q_2 can now be seen from the method of calculation. Substitution of

$$x_i = a_i \cos\left(\frac{\omega}{q_i}t + \theta_i\right), \quad \dot{x}_i = -a_i \frac{\omega}{q_i} \sin\left(\frac{\omega}{q_i}t + \theta_i\right)$$

into $f_i(x_1, x_2, \dot{x}_1, \dot{x}_2)$ to form $(f_i)_0$ on the right-hand side of (13) gives rise to a series of combination frequencies $[(m\omega/q_1) \pm (n\omega/q_2)]$ where m and n take various integer values determined by the form of $f_i(x_1, x_2, \dot{x}_1, \dot{x}_2)$. A resonance occurs if any of these coincides with (ω/q_i) so as to affect the value of $A_i^{(1)}$. The equations of the second approximation produce further combination frequencies, and therefore the possibility of resonance at other values of q_1 and q_2.

However, if q_1 and q_2 are allowed to take large values any k_1 and k_2 can be made to satisfy relation (6) to any desired accuracy. But resonances of this type will only appear in high-order approximations: their calculation is intractable, and their effect too small to be observed in practice.

(b) *Non-resonance case*

It is therefore realistic to restrict the integers q_1 and q_2 to small values (say 1, 2, 3) and consider a "non-resonance" case for which

$$k_1/k_2 \text{ is not close to } q_2/q_1 \tag{16}$$

For this case, the solutions are best taken in the form

$$x_i = a_i \cos\psi_i + \epsilon u_i^{(1)}(a_1, a_2, \psi_1, \psi_2) + \epsilon^2 \ldots \quad (i = 1, 2) \tag{17}$$

where ψ_i represents the full phase, so that

$$\frac{da_i}{dt} = \epsilon A_i^{(1)} + \epsilon^2 A_i^{(2)} + \ldots$$

$$\frac{d\psi_i}{dt} = k_i + \epsilon B_i^{(1)} + \epsilon^2 B_i^{(2)} + \ldots \qquad (i = 1, 2)$$

These solutions are substituted directly into the original equations (5) (not 8) and the successive approximations formed exactly as before. In this case, by the non-resonance assumption the combination frequencies of ψ_1 and ψ_2 produce no frequencies k_1 or k_2. From this it can be shown that the $A_i^{(r)}$ and $B_i^{(r)}$, which previously had period 2π in ψ_1 and ψ_2, are now functions of a_1 and a_2 only,

i.e.
$$\frac{da_i}{dt} = \epsilon A_i^{(1)}(a_1, a_2) + \epsilon^2 A_i^{(2)}(a_1, a_2) + \dots$$
$$\frac{d\psi_i}{dt} = k_i + \epsilon B_i^{(1)}(a_1, a_2) + \epsilon^2 B_i^{(2)}(a_1, a_2) + \dots \qquad (i = 1, 2) \qquad (18)$$

The equations giving the first approximation are

$$\begin{aligned} k_1^2 \frac{\partial^2 u_1^{(1)}}{\partial \psi_1^2} + 2k_1 k_2 \frac{\partial^2 u_1^{(1)}}{\partial \psi_1 \partial \psi_2} + k_2^2 \frac{\partial^2 u_1^{(1)}}{\partial \psi_2^2} + k_1^2 u_1^{(1)} \\ = 2k_1 A_1^{(1)} \sin\psi_1 + 2k_1 a_1 B_1^{(1)} \cos\psi_1 + (f_1)_0 \\ k_2^2 \frac{\partial^2 u_2^{(1)}}{\partial \psi_2^2} + 2k_2 k_1 \frac{\partial^2 u_2^{(1)}}{\partial \psi_2 \partial \psi_1} + k_1^2 \frac{\partial^2 u_2^{(1)}}{\partial \psi_1^2} + k_2^2 u_2^{(1)} \\ = 2k_2 A_2^{(1)} \sin\psi_2 + 2k_2 a_2 B_2^{(1)} \cos\psi_2 + (f_2)_0 \end{aligned} \qquad (19)$$

Since $u_1^{(1)}$ is periodic in the ψ_i, the right-hand side of the first equation (19) must contain no terms ψ_1. The elimination of the terms with argument $\cos\psi_1, \sin\psi_1$ is sufficient to evaluate $A_1^{(1)}$ and $B_1^{(1)}$ and the remainder of the equation can be solved for $u_1^{(1)}$. The second equation gives $A_2^{(1)}$, $B_2^{(1)}$ and $u_2^{(1)}$ in the same way.

The non-resonance analysis can be continued to higher approximations as before, but this is not normally required since its purpose is to give an idea of the general background of motions, against which the resonant motions appear as exceptional cases. More detailed investigations of particular regions will use the resonance analysis.

THE APPROXIMATE SOLUTIONS AND THE ENERGY EQUATION

The approximate solutions of the previous section apply to any differential equations of form (5), and may now be related to conservative systems by returning to the energy considerations.

Both resonance and non-resonance solutions have the form

$$x_i = a_i \cos\psi_i + 0(\epsilon)$$

where
$$\frac{da_i}{dt} = 0(\epsilon) \quad \text{and} \quad \frac{d\psi_i}{dt} = k_i + 0(\epsilon)^*$$

Differentiating,
$$\dot{x}_i = -k_i a_i \sin\psi_i + 0(\epsilon)$$

Substituting these solutions into the energy equation (4) gives

$$\begin{aligned} &\tfrac{1}{2}T_1\{k_1^2 a_1^2 \sin^2\psi_1 + \epsilon \dots\} + \tfrac{1}{2}T_2\{k_2^2 a_2^2 \sin^2\psi_2 + \epsilon \dots\} + \tfrac{1}{2}\epsilon f_T(a_1, a_2, \psi_1, \psi_2) \\ &+ \tfrac{1}{2}V_1\{a_1^2 \cos^2\psi_1 + \epsilon \dots\} + \tfrac{1}{2}V_2\{a_2^2 \cos^2\psi_2 + \epsilon \dots\} + \tfrac{1}{2}\epsilon f_V(a_1, a_2, \psi_1, \psi_2) = \text{constant} \end{aligned}$$

* For the resonance case $\frac{d\psi_i}{dt} = \frac{d}{dt}\left(\frac{\omega}{q_i}t + \theta_i\right) = \frac{\omega}{q_i} + \epsilon B_i^{(1)} + \epsilon^2 \dots = k_i + \epsilon\left(B_i^{(1)} - \frac{\Delta_i}{2k_i}\right) + \epsilon^2 \dots$

Then transferring terms of $0(\epsilon)$ to the right-hand side, and using $k_i^2 = V_i/T_i$,

$$V_1 a_1^2 + V_2 a_2^2 = \text{constant} + 0(\epsilon) \tag{20}$$

Since V_1 and V_2 are necessarily positive this equation shows that during free motion an elliptical relation holds between the two amplitudes a_1 and a_2, within an error of order ϵ. In any case where this order of accuracy is sufficient this allows a change of variable which is very helpful in visualizing the complete range of motions possible. For, discarding $0(\epsilon)$, equation (20) is satisfied by

$$a_1 = \sqrt{\left(\frac{C}{V_1}\right)} \cos\chi, \quad a_2 = \sqrt{\left(\frac{C}{V_2}\right)} \sin\chi \tag{21}$$

where $\frac{1}{2}C$ = initial energy.

Applying this first to the resonance case, a_1 and a_2 may be replaced in equations (12) by the single variable χ. Further, the right-hand sides of these equations will only contain the phase difference $\Phi = q_1\theta_1 - q_2\theta_2$ because, for an autonomous system, the rates of change of amplitude and phase cannot depend upon the choice of time datum. The two $d\theta_i/dt$ equations of (12) combine to give a single equation for $d\Phi/dt$.

With this transformation any motion is described by its initial energy $\frac{1}{2}C$ and only two time-dependent variables χ and Φ. It is therefore possible to depict all the motions with a given initial energy by solution curves in a plane with axes χ and Φ. These are the solution curves of the differential equation

$$\frac{d\chi}{d\Phi} = f(\chi, \Phi) \tag{22}$$

which results from eliminating t from the transformed equations (12), and their appearance quickly follows from a study of the singularities of this equation.

To cover all the possible motions with any initial energy a series of these (χ, Φ) planes is required for various values of C, the whole forming a three-dimensional (χ, Φ, C) space. This, too, is best analysed by studying the movement of the singularities of equation (22) with variation of C. Naturally further work is required to calculate other aspects of the solutions, in particular the period of the beating motions, but in this way the possible variations of amplitude and phase can be shown very concisely.

For the non-resonance case the same variables may be used defining $\Phi = \psi_1 - \psi_2$. However, the right-hand side of the equations for $d\chi/dt$ and $d\Phi/dt$ are now functions of χ alone, and equation (22) becomes

$$\frac{d\chi}{d\Phi} = f(\chi) \tag{23}$$

Now if χ is a function of Φ it must have period 2π, because ψ_1 and ψ_2 are defined only within arbitrary additions of 2π. But a solution

$$\chi = \sum_{n=1,2,\ldots} \alpha_n \exp(in\Phi)$$

can only satisfy equation (23) with the special form χ = constant. Therefore for any conservative quasilinear system the non-resonant first approximation

Vol. 3
1961

will predict constant-amplitude oscillations of the normal coordinates x_1 and x_2. An experimental trace of this type of motion is shown in Fig. 4.

This gives the general background of motions to be expected from quasi-linear systems, very similar to the steady oscillation of normal coordinates in linear systems, but with frequencies dependent on amplitude. However, with frequency ratios close to certain ratios of integers, this situation is interrupted by resonant motions with varying amplitudes—the "coupling of degrees of freedom" of Henry and Tobias. These resonant regions are analysed for two particular pairs of equations in the following sections.

PART II. APPLICATIONS OF THE THEORY

APPLICATION I

The theory is first used to discuss the special case $m_i = p_i = 0$ of equations (1), namely

$$\begin{aligned} \ddot{x}_1 + k_1^2 x_1 &= \epsilon(l_1 x_1^3 + n_1 x_1 x_2^2) \\ \ddot{x}_2 + k_2^2 x_2 &= \epsilon(l_2 x_2^3 + n_2 x_2 x_1^2) \end{aligned} \tag{24}$$

Various applications of these equations have already been mentioned in the Introduction. For the experimental analogue this case requires the two pendulums to swing in vertical planes at right angles to each other.

Regions of resonance

The non-resonant analysis for $k_1/k_2 \neq q_2/q_1$ gives

$$\frac{da_1}{dt} = \frac{da_2}{dt} = 0$$

which agrees with the general result of the last section.

The resonant solutions, for $k_1/k_2 \approx q_2/q_1$, have been investigated for the first three approximations. In the first approximation $A_1^{(1)} = A_2^{(1)} = 0$ unless $q_2/q_1 = 1$ when $da_i/dt = \epsilon A_i^{(1)}$ $(i = 1, 2)$. In this case of close natural frequencies the $A_i^{(1)}$ are not zero and changes in amplitude will occur.

The second approximation naturally gives improved accuracy, in this case $q_2/q_1 = 1$, but, more important, it shows an additional resonance at $q_2/q_1 = 2$ (or $\frac{1}{2}$). It is convenient to call this a "second-order resonance", defined as a resonance which first appears in the second approximation, and has

$$\frac{da_i}{dt} = \epsilon^2 A_i^{(2)} \quad (i = 1, 2)$$

A third-order resonance appears in the third approximation for $q_1/q_2 = 3$, $\frac{1}{3}$ with $da_i/dt = \epsilon^3 A_i^{(3)}$.

It is seen that the rate of amplitude change decreases by an order of ϵ with each order of resonance. For this reason the first-order resonance is much the most pronounced and the successive orders decrease rapidly in importance. Also, in a real passive system a slow decay in amplitude due to damping will inevitably be present and will be sufficient to mask any increments due to high-order resonances. The first-order resonance is also important practically for

its application to disks and other bodies with almost perfect radial symmetry which necessarily have pairs of modes with closely-equal frequencies.

Application I(a), *first-order resonance* $k_1/k_2 \approx 1$. Applying the method given above for the resonance case the first approximation is obtained from equation (13). In this case $q_1 = q_2 = 1$ and the $u_1^{(1)}$ equation is

$$\frac{\partial^2 u_1^{(1)}}{\partial t^2} + \omega^2 u_1^{(1)} = 2\omega A_1^{(1)} \sin(\omega t + \theta_1) + \{2a_1 \omega B_1^{(1)} - \Delta_1 a_1\} \cos(\omega t + \theta_1) + (f_1)_0 \quad (25)$$

where

$$(f_1)_0 = l_1\{a_1 \cos(\omega t + \theta_1)\}^3 + n_1\{a_1 \cos(\omega t + \theta_1)\}\{a_2 \cos(\omega t + \theta_2)\}^2$$

Using trigonometrical identities this term may be arranged as the following Fourier series in t:

$$\begin{aligned}(f_1)_0 = {} & \{\tfrac{1}{4} n_1 a_1 a_2^2 \sin(2\theta_1 - 2\theta_2)\} \sin(\omega t + \theta_1) \\ & + \{\tfrac{3}{4} l_1 a_1^3 + \tfrac{1}{2} n_1 a_1 a_2^2 + \tfrac{1}{4} n_1 a_1 a_2^2 \cos(2\theta_1 - 2\theta_2)\} \cos(\omega t + \theta_1) \\ & + \tfrac{1}{4} l_1 a_1^3 \cos(3\omega t + 3\theta_1) + \tfrac{1}{4} n_1 a_1 a_2^2 \cos(3\omega t + \theta_1 + 2\theta_2)\end{aligned}$$

The functions $A_1^{(1)}$ and $B_1^{(1)}$ are now chosen to eliminate the fundamental frequency ω from the right-hand side of equation (25),

i.e.

$$2\omega A_1^{(1)} = -\tfrac{1}{4} n_1 a_1 a_2^2 \sin(2\theta_1 - 2\theta_2)$$

$$2\omega B_1^{(1)} = \Delta_1 - \tfrac{3}{4} l_1 a_1^2 - \tfrac{1}{2} n_1 a_2^2 - \tfrac{1}{4} n_1 a_2^2 \cos(2\theta_1 - 2\theta_2)$$

Since $u_1^{(1)}$ is to contain no frequency ω in t the remainder of equation (25) gives the unique solution

$$u_1^{(1)} = -\frac{1}{8\omega^2}\{\tfrac{1}{4} l_1 a_1^3 \cos(3\omega t + 3\theta_1) + \tfrac{1}{4} n_1 a_1 a_2^2 \cos(3\omega t + \theta_1 + 2\theta_2)\} \quad (26)$$

The values of $A_2^{(1)}$, $B_2^{(1)}$ and $u_2^{(1)}$ follow similarly, and in this case are the same with suffices 1 and 2 interchanged. Therefore the equations of the first approximation are

$$\begin{aligned} x_1 &= a_1 \cos(\omega t + \theta_1) + \epsilon u_1^{(1)} \\ x_2 &= a_2 \cos(\omega t + \theta_2) + \epsilon u_2^{(1)} \end{aligned} \quad (27)$$

where

$$\begin{aligned} \frac{da_1}{dt} &= -\frac{\epsilon}{8\omega} n_1 a_1 a_2^2 \sin(2\theta_1 - 2\theta_2) \\ \frac{da_2}{dt} &= -\frac{\epsilon}{8\omega} n_2 a_2 a_1^2 \sin(2\theta_2 - 2\theta_1) \\ \frac{d\theta_1}{dt} &= \frac{\epsilon}{2\omega}\{\Delta_1 - \tfrac{3}{4} l_1 a_1^2 - \tfrac{1}{4} n_1 a_2^2[2 + \cos(2\theta_1 - 2\theta_2)]\} \\ \frac{d\theta_2}{dt} &= \frac{\epsilon}{2\omega}\{\Delta_2 - \tfrac{3}{4} l_2 a_2^2 - \tfrac{1}{4} n_2 a_1^2[2 + \cos(2\theta_2 - 2\theta_1)]\} \end{aligned} \quad (28)$$

The terms $u_i^{(1)}$ are given by equation (26) and the similar equation for $u_2^{(1)}$, but in practice have always proved to be negligible compared with the terms $a_i \cos(\omega t + \theta_i)$.

Vol. 3
1961

As predicted above, equations (28) only require the phase difference $\Phi = \theta_1 - \theta_2$, and the expected elliptic relation between a_1 and a_2 results from dividing the equations for da_1/dt and da_2/dt and integrating. This gives

$$\frac{a_1^2}{n_1} + \frac{a_2^2}{n_2} = C \tag{29}*$$

Then changing to the variables χ and Φ of the previous section, where

$$\begin{aligned} a_1 &= \sqrt{(Cn_1)}\cos\chi \\ a_2 &= \sqrt{(Cn_2)}\sin\chi \quad \Phi = \theta_1 - \theta_2, \end{aligned} \tag{30}$$

equations (28) become

$$\begin{aligned} \frac{d\chi}{dt} &= \frac{\epsilon}{16\omega} Cn_1 n_2 \sin 2\chi \sin 2\Phi \\ \frac{d\Phi}{dt} &= \frac{\epsilon}{2\omega}\{(\Delta_1 - \Delta_2) - \tfrac{3}{4}C(l_1 n_1 \cos^2\chi - l_2 n_2 \sin^2\chi) \\ &\qquad - \tfrac{1}{4}Cn_1 n_2(\sin^2\chi - \cos^2\chi)(2 + \cos 2\Phi)\} \end{aligned} \tag{31}$$

The (χ, Φ) curves are therefore the solution curves of the differential equation

$$\frac{d\chi}{d\Phi} = \frac{-\tfrac{1}{2}\sin 2\chi \sin 2\Phi}{\alpha + \beta\cos 2\chi - \cos 2\chi \cos 2\Phi} \tag{32}$$

where

$$\alpha = \frac{4(\Delta_2 - \Delta_1)}{Cn_1 n_2} + \frac{3}{2}\frac{l_1}{n_2} - \frac{3}{2}\frac{l_2}{n_1}, \quad \beta = \frac{3}{2}\frac{l_1}{n_2} + \frac{3}{2}\frac{l_2}{n_1} - 2$$

Before investigating the appearance of these solution curves from the singularities of equation (32) it is convenient to restrict $0 \leqslant \chi \leqslant \frac{1}{2}\pi$, so that a_1 and a_2 are positive amplitudes.† This in turn defines Φ within additions of 2π. Evidently the lines $\chi = 0$, $\chi = \frac{1}{2}\pi$ are themselves solution curves, and so attention is restricted to the strip between them. The curves in this strip are even and of period π in Φ so that only four singularities need be considered:

(i) $\Phi = 0$ $\qquad \cos 2\chi = \dfrac{\alpha}{1-\beta}$

(ii) $\Phi = \frac{1}{2}\pi$ $\qquad \cos 2\chi = \dfrac{-\alpha}{1+\beta}$

(iii) $\chi = 0$ $\qquad \cos 2\Phi = \beta + \alpha$

(iv) $\chi = \frac{1}{2}\pi$ $\qquad \cos 2\Phi = \beta - \alpha$

Two typical planes which have been verified by the mechanical analogue are shown in Fig. 5.

The nature of singularities (i) to (iv) may be tested in the usual way (e.g. Ref. 12, p. 44). This shows that (iii) and (iv) are always saddles with axes parallel to the axes of χ and Φ; that (i) is a centre or saddle according as

* Here the initial energy is proportional to C, not equal to $\frac{1}{2}C$.

† The positive square roots should be taken in equation (30) and in all subsequent equations [e.g. (37), (44) and those of Appendix II].

$\beta \lesssim +1$; and that (ii) is a centre or saddle according as $\beta \gtrless -1$. Combining this information with the conditions for the existence of the singularities, a chart can be drawn up giving the general appearance of the (χ, Φ) planes for any values of α and β (Fig. 6). Since β is a function of the system parameters only, the representative point for a particular system will move on a vertical line in this chart with varying C.

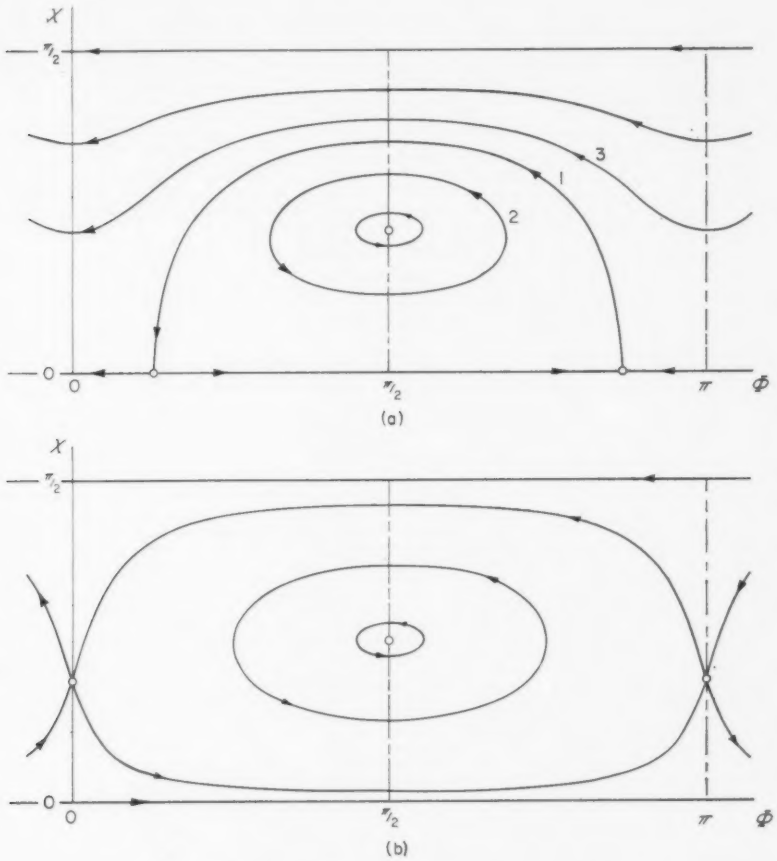

FIG. 5. Two (χ, Φ) planes for application I(a).

The features of these planes have a direct physical interpretation. A singularity of type (i) represents a steady oscillation in both normal coordinates with no phase variation. The relative phase is either 0 or π. If the singularity is a centre, its neighbouring singularities in the planes for slightly different C's will also be centres,* and any initial conditions close to the correct ones will give a motion which stays close to the singular one. A steady motion of this type has been called "stable". On the other hand, a saddle singularity represents an "unstable" motion whose neighbours do not in general lie in its

* The case where the representative point is on a boundary in the (α, β) chart is excluded.

vicinity. The criterion distinguishing between the two is $\beta \lesseqgtr +1$, and so depends on the system's parameters only. Similar remarks apply to singularity (ii) which represents a steady motion with a relative phase of $\frac{1}{2}\pi$.

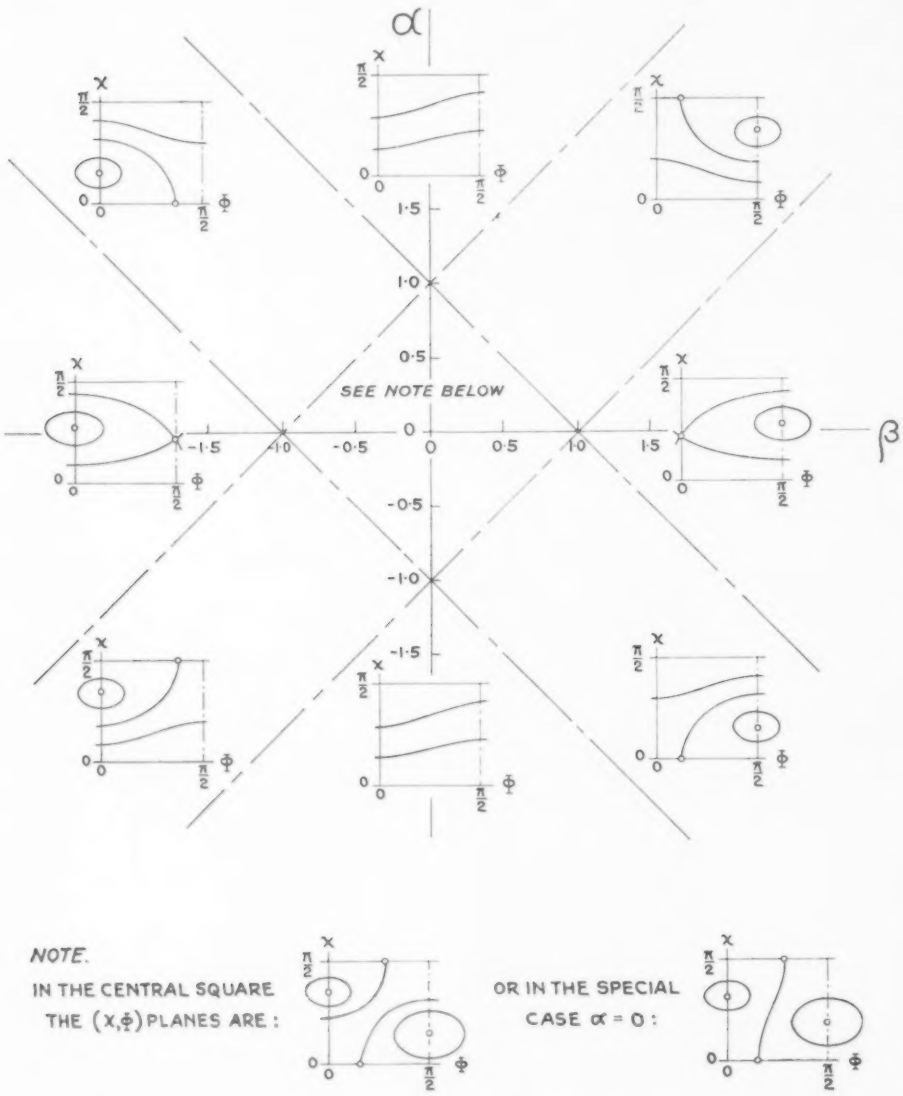

FIG. 6. Chart showing the dependence of the form of (χ, Φ) planes on the parameters α and β of equation (32).

The singularities (iii) and (iv) each represent an unstable motion with one normal coordinate oscillating while the other is at rest. The separatrix leaving the saddle point defines the subsequent motion as the stationary coordinate

builds up from its unstable rest position. A beating motion with narrow waists ensues.* The start of such a motion is shown in Fig. 7.

Finally, it is seen that just two types of beating motion can occur: in one, the ovals, there is no net change of relative phase in a beat cycle (Fig. 8); in the other, the open curves, the phase change is π in a beat cycle (Fig. 9). In all cases the maximum and minimum amplitudes occur at a relative phase of 0, $\frac{1}{2}\pi$, π, etc.

To return from the survey of solutions in general to the calculation of particular cases, equation (32) must be integrated. The resulting (χ, Φ) curve is

$$(\Delta_1-\Delta_2)\cos^2\chi-\tfrac{3}{8}Cl_1n_1\cos^4\chi-\tfrac{3}{8}Cl_2n_2\sin^4\chi \\ -\tfrac{1}{4}Cn_1n_2\cos^2\chi\sin^2\chi(2+\cos 2\Phi)=\text{constant} \qquad (33)$$

This gives the limiting values of the amplitudes and the phases associated with them. The calculation of mean frequencies and the period of the beat cycle requires numerical integration of equations (31). This is not difficult, however, since (33) is used to make the right-hand sides functions of χ only. For example,

$$\frac{d\chi}{dt}=F(\chi) \quad \text{(say)}$$

and the beat period is obtained as twice the area

$$\int_{\chi_{\min}}^{\chi_{\max}}\frac{d\chi}{F(\chi)}$$

The mean frequencies follow from the equations for $d\theta_i/d\chi$, choosing ω such that the change in θ_i over a beat cycle is zero.

Application I(b), *second-order resonance* $k_1/k_2\approx 2$. As has been seen, the second approximation is required to analyse the resonance which occurs when the ratio of natural frequencies is close to two. The results for $q_1=1$, $q_2=2$ are

$$x_1=a_1\cos(\omega t+\theta_1)+\epsilon u_1^{(1)}+\epsilon^2u_1^{(2)} \\ x_2=a_2\cos\left(\frac{\omega}{2}t+\theta_2\right)+\epsilon u_2^{(1)}+\epsilon^2u_2^{(2)} \qquad (34)$$

where

$$\frac{da_1}{dt}=\frac{\epsilon^2}{32\omega^3}n_1(l_2-n_1)a_1a_2^4\sin(2\theta_1-4\theta_2)$$

$$\frac{da_2}{dt}=\frac{\epsilon^2}{8\omega^3}n_2(n_1-l_2)a_1^2a_2^3\sin(2\theta_1-4\theta_2)$$

$$\frac{d\theta_1}{dt}=\frac{\epsilon}{2\omega}\{\Delta_1-\tfrac{3}{4}l_1a_1^2-\tfrac{1}{2}n_1a_2^2\}+\frac{\epsilon^2}{8\omega^3}\{-(\Delta_1-\tfrac{3}{4}l_1a_1^2-\tfrac{1}{2}n_1a_2^2)^2+\tfrac{3}{32}l_1^2a_1^4 \\ +\tfrac{1}{3}n_1n_2a_1^2a_2^2-\tfrac{1}{6}n_1^2a_2^4-\tfrac{1}{4}n_1(n_1-l_2)a_2^4\cos(2\theta_1-4\theta_2)\} \qquad (35)$$

$$\frac{d\theta_2}{dt}=\frac{\epsilon}{\omega}\{\Delta_2-\tfrac{3}{4}l_2a_2^2-\tfrac{1}{2}n_2a_1^2\}+\frac{\epsilon^2}{\omega^3}\{-(\Delta_2-\tfrac{3}{4}l_2a_2^2-\tfrac{1}{2}n_2a_1^2)^2+\tfrac{3}{32}l_2^2a_2^4 \\ -\tfrac{1}{12}n_2n_1a_2^2a_1^2+\tfrac{1}{24}n_2^2a_1^4+\tfrac{1}{8}n_2(l_2-n_1)a_1^2a_2^2\cos(2\theta_1-4\theta_2)\}$$

* The papers of Tobias[7] and Henry and Tobias[8] deal with the two special cases $l_1/l_2=k_1^2/k_2^2$, $n_1/l_1=n_2/l_2=1$ and $l_1/l_2=k_1^2/k_2^2$, $n_1/l_1=n_2/l_2=3$. Their results are equivalent to the conditions for the appearance of singularities (iii) and (iv) (the instability of one coordinate at rest) and the position of singularities (i) and (ii) (relations for steady oscillations, but not their stability).

Vol. 3
1961

Here the amplitude relation is

$$\frac{a_1^2}{n_1}+\frac{a_2^2}{4n_2}=C \tag{36}$$

and χ and Φ are defined by

$$\begin{aligned} a_1 &= \sqrt{(Cn_1)}\cos\chi \\ a_2 &= 2\sqrt{(Cn_2)}\sin\chi \quad \Phi=\theta_1-2\theta_2 \end{aligned} \tag{37}$$

The details of the analysis are naturally rather complicated in this case, but again the important features of the solutions are given by the singularities

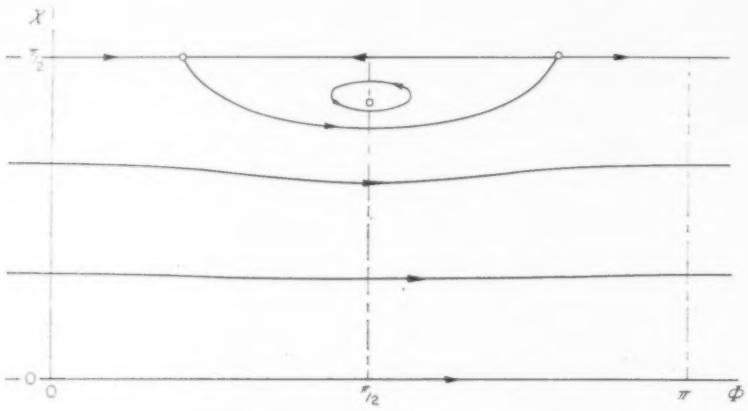

FIG. 10. (χ, Φ) plane for application I(b).

in the (χ, Φ) plane which can be listed very shortly. As before, the lines $\chi = 0$, $\chi = \frac{1}{2}\pi$ are solution curves, and the area between them is considered for $0 \leqslant \Phi \leqslant \pi$.

(i) Singularities on $\chi = 0$: none.*

(ii) Singularities on $\chi = \frac{1}{2}\pi$: one saddle point may occur. This shows that the higher frequency mode may become unstable in its rest position, but the lower frequency mode will not.

(iii) Other singularities: a number, centre or saddle, are possible on the lines $\Phi = 0, \frac{1}{2}\pi, \pi$, representing steady motions with these phases. The equations for these singularities are too complicated to solve algebraically, but they may be quickly located in a numerical case.

The evaluation of actual solution curves is again straightforward since the $d\chi/d\Phi$ equation can be integrated, although with some difficulty (Appendix I).

The only plane tested by the pendulum analogue had one singularity of type (iii) and is shown in Fig. 10. The most important feature is the build-up of the x_1 coordinate from its unstable equilibrium position; but in this case the predicted maximum amplitude a_1 was quite small, and the experimental value (Fig. 11) only some 70 per cent of it, the discrepancy being due to damping

* Actually, a singularity may occur on $\chi = 0$ for two specific values of C, but borderline cases of this sort will not have practical significance.

forces. Further calculations showed that the corresponding motion of the third-order resonance $q_2/q_1 \approx 3$ would be completely eliminated even by the very small amount of damping in the mechanical system (relative damping factor 0·0004). This emphasizes the practical insignificance of the higher-order resonances which has already been mentioned.

APPLICATION II

The second analysis is of the full equations (1):

$$\begin{aligned} \ddot{x}_1 + k_1^2 x_1 &= \epsilon(l_1 x_1^3 + m_1 x_1^2 x_2 + n_1 x_1 x_2^2 + p_1 x_2^3) \\ \ddot{x}_2 + k_2^2 x_2 &= \epsilon(l_2 x_2^3 + m_2 x_2^2 x_1 + n_2 x_2 x_1^2 + p_2 x_1^3) \end{aligned} \tag{1}$$

The application of Fig. 1 has already been mentioned: for the experimental analogue the pendulums swing in planes containing an angle less than 90°.

First it should be noticed that these equations contain more constants than may be chosen arbitrarily. For, to apply to a conservative system with cubic restoring forces, they must be the Lagrange equations for energies:

$$\begin{aligned} 2T &= T_1 \dot{x}_1^2 + T_2 \dot{x}_2^2 \\ 2V &= V_1 x_1^2 + V_2 x_2^2 + U_1 x_1^4 + U_2 x_1^3 x_2 + U_3 x_1^2 x_2^2 + U_4 x_1 x_2^3 + U_5 x_2^4 \end{aligned}$$

Whence the coefficients must always be related by

$$\frac{n_1}{n_2} = \frac{3p_1}{m_2} = \frac{m_1}{3p_2} \tag{38}$$

Regions of resonance

As before, the resonances appear against a background of uncoupled oscillations of the normal coordinates. In this case, first-order resonances occur for $q_2/q_1 = 1, 3, \frac{1}{3}$, and this appearance of an additional first-order resonance for frequency ratios close to 3:1 shows an immediate difference from the earlier case of equations (24).

Second-order resonances are also more numerous, appearing at $q_2/q_1 = 2, \frac{1}{2}, 5, \frac{1}{5}$.

A detailed discussion of the two first-order resonances is given below.

Application II(a), *first-order resonance* $k_1/k_2 \approx 1$. The equations of the first approximation give

$$\begin{aligned} x_1 &= a_1 \cos(\omega t + \theta_1) + \epsilon u_1^{(1)} \\ x_2 &= a_2 \cos(\omega t + \theta_2) + \epsilon u_2^{(1)} \end{aligned} \tag{39}$$

where

$$\begin{aligned} \frac{da_1}{dt} &= -\frac{\epsilon}{8\omega}\{m_1 a_1^2 a_2 \sin\Phi + n_1 a_1 a_2^2 \sin 2\Phi + 3p_1 a_2^3 \sin\Phi\} \\ \frac{da_2}{dt} &= +\frac{\epsilon}{8\omega}\{m_2 a_2^2 a_1 \sin\Phi + n_2 a_2 a_1^2 \sin 2\Phi + 3p_2 a_1^3 \sin\Phi\} \\ \frac{d\Phi}{dt} &= \frac{\epsilon}{2\omega}\Big\{(\Delta_1 - \Delta_2) - \tfrac{3}{4}(l_1 a_1^2 - l_2 a_2^2) - \tfrac{3}{4}a_1 a_2 (m_1 - m_2)\cos\Phi \\ &\quad - \tfrac{1}{4}(n_1 a_2^2 - n_2 a_1^2)(2 + \cos 2\Phi) - \frac{3}{4}\left(p_1 \frac{a_2^3}{a_1} - p_2 \frac{a_1^3}{a_2}\right)\cos\Phi\Big\} \quad (\Phi = \theta_1 - \theta_2) \end{aligned} \tag{40}$$

Vol. 3
1961

The amplitude relation is again (29), but in this case relation (38) is required to derive it from equations (40). The variables χ and Φ are then defined by (30).

The $d\chi/d\Phi$ equation is integrable (Appendix II), and so particular solutions can be calculated as straightforwardly as before. However, the complication of the algebra does prevent a presentation of all possible (χ, Φ) planes, but the features which may be established are listed below. Again, attention is restricted to the region between the solution curves $\chi = 0$ and $\chi = \frac{1}{2}\pi$, but the remaining solution curves are now even with period 2π in Φ.

(i) Singularities on $\chi = 0$, $\chi = \frac{1}{2}\pi$: saddle points always occur on both these lines at $\Phi = \frac{1}{2}\pi$. Therefore a steady motion with one coordinate oscillating alone is never possible. The type of motion which actually follows from these initial conditions has already been shown in Fig. 2.

(ii) Other singularities: a number may occur on the lines $\Phi = 0$ and $\Phi = \pi$, but it has not been possible to show how many may appear in any particular plane. These singularities represent stable or unstable motions with phase 0 or π, two phases which are now quite distinct (unlike the earlier case of equation 24).

One further singularity may occur inside the area $0 < \Phi < \pi$, $0 < \chi < \frac{1}{2}\pi$. This represents a steady motion with some phase intermediate between 0 and π.

Two planes depicting these features, which have been calculated for the mechanical analogue, are shown in Fig. 12.

Application II(b), *first-order resonance* $k_1/k_2 \approx 3$. The other region of first-order resonance occurs for a ratio of natural frequencies close to 3, and has solutions

$$\begin{aligned} x_1 &= a_1 \cos(\omega t + \theta_1) + \epsilon u_1^{(1)} \\ x_2 &= a_2 \cos(\tfrac{1}{3}\omega t + \theta_2) + \epsilon u_2^{(1)} \end{aligned} \tag{41}$$

where

$$\begin{aligned} \frac{da_1}{dt} &= -\frac{\epsilon}{8\omega} p_1 a_2^3 \sin\Phi \qquad (\Phi = \theta_1 - 3\theta_2) \\ \frac{da_2}{dt} &= \frac{3\epsilon}{8\omega} m_2 a_1 a_2^2 \sin\Phi \\ \frac{d\Phi}{dt} &= \frac{\epsilon}{2\omega}\left\{(\Delta_1 - 9\Delta_2) - \tfrac{3}{4}(l_1 a_1^2 - 9 l_2 a_2^2) - \tfrac{1}{2}(n_1 a_2^2 - 9 n_2 a_1^2) \right. \\ &\qquad \left. - \frac{1}{4}\left(p_1 \frac{a_2^3}{a_1} - 9 m_2 a_1 a_2\right)\cos\Phi\right\} \end{aligned} \tag{42}$$

In this case

$$\frac{a_1^2}{n_1} + \frac{a_2^2}{9n_2} = C \tag{43}$$

and χ is defined by

$$\begin{aligned} a_1 &= \sqrt{(C n_1)}\cos\chi \\ a_2 &= 3\sqrt{(C n_2)}\sin\chi, \quad 0 \leqslant \chi \leqslant \tfrac{1}{2}\pi \end{aligned} \tag{44}$$

A study of the singularities of the resulting equation for χ, Φ reveals the features listed as follows. The equation is integrable (Appendix II).

Vol. 3
1961

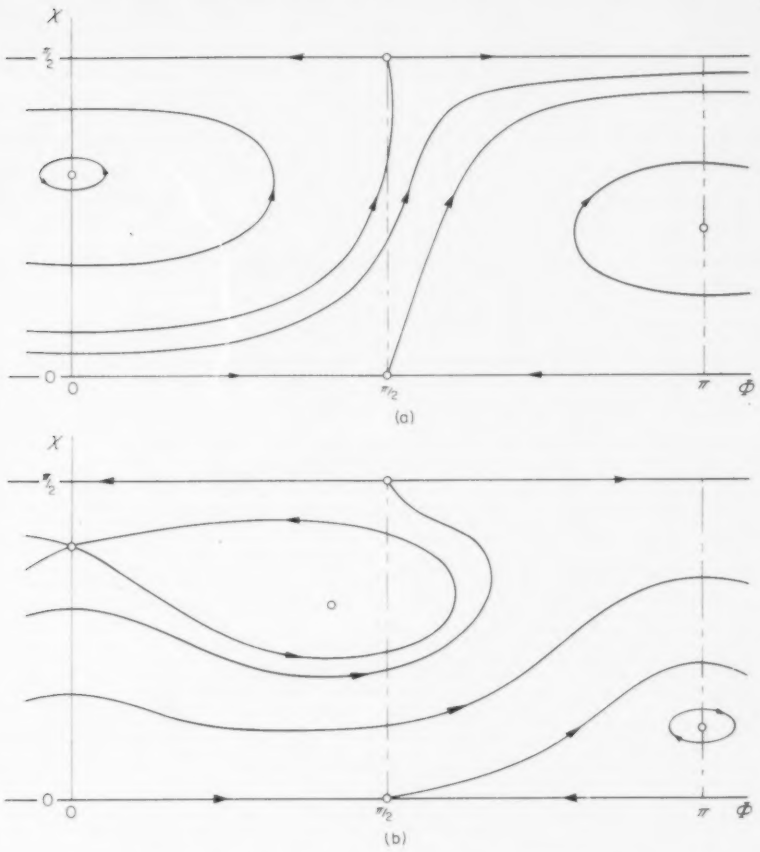

FIG. 12. Two (χ, Φ) planes for application II(a).

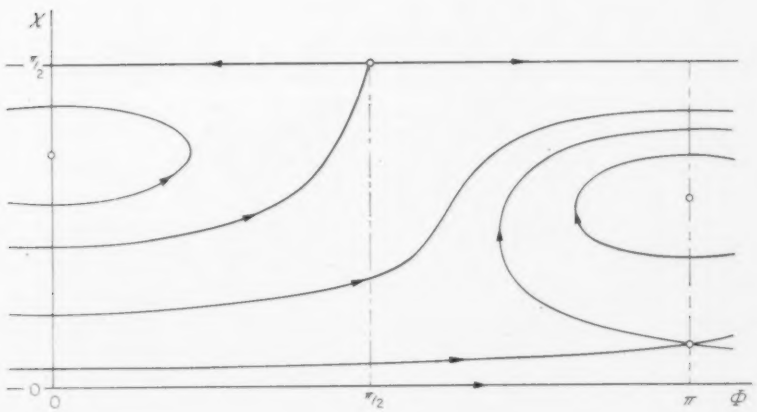

FIG. 13. (χ, Φ) plane for application II(b).

(i) Singularities on solution curve $\chi = 0$: none.* Therefore the coordinate with the lower linear frequency is not disturbed from its rest position by oscillations of the other coordinates.

(ii) Singularities on solution curve $\chi = \frac{1}{2}\pi$: a saddle always appears. That is, in this region of resonance, x_1 is always unstable at $x_1 = 0$ when x_2 is oscillating.

(iii) Other singularities: at least one, and possibly more, occur on the lines $\Phi = 0$ or π representing steady oscillations of both coordinates at particular amplitudes.

One plane, calculated for the analogue experiments, is given in Fig. 13. The experimental solutions show a strong subharmonic of order $\frac{1}{3}$ in the wave form of x_1, and in this case the values of the $u_i^{(1)}$ are not necessarily negligible. They are given, with details of the (χ, Φ) equations, in Appendix II.

EXPERIMENTAL WORK

The mechanical layout of the system used for the experimental work has already been described. To obtain records of the motions, a capacitance pick-up is fitted to each pendulum, operating through a frequency-modulated circuit to a two-channel pen-recorder. The amplitudes, frequencies and phases of the two normal coordinates are then measured directly from the resulting traces. The calibration for amplitude is taken from scales fitted to the analogue, and the time base obtained from an accurate chronometer.

For the verification of particular motions the correct initial conditions must be provided. This is done by having a solenoid to release each pendulum at the required amplitude: the initial phase is set by a trip device arranged to release the second pendulum at the required moment in the initial half-cycle of the first.

The experiments proceed by first calculating the parameters of a suitable setting of the apparatus. The coefficients of the non-linear terms can be accurately calculated from the pendulum equations of motion and measurements of length, mass and spring stiffness. (The reliability of the evaluation of these coefficients is a particular advantage of this system.) The linear natural frequencies are measured directly from the oscillations at small amplitude. A (χ, Φ) plane for a suitable initial energy is then calculated, and a series of experiments made to verify the motions defined by the various solution curves. The calculations for these motions are necessarily ill-conditioned, involving in particular a small difference between natural frequencies. However, by measuring these latter to 0·1 per cent, amplitudes and beat frequencies can be checked with an accuracy of about 10 per cent. All the (χ, Φ) planes used to illustrate the text (Figs. 5, 10, 12 and 13) have been verified in this way.

In moving from one value of initial energy to another it is particularly easy to verify the movement in the (χ, Φ) planes of singularities representing steady oscillations. This is the same as verifying the amplitude relations of the steady motions, and some results of tests of this sort are given in Fig. 14.

Two unavoidable, though not serious, limitations of the apparatus should be mentioned. Firstly, to obtain accurately linear + cubic restoring forces the

* Strictly, at one specific value of C; see footnote on p. 302.

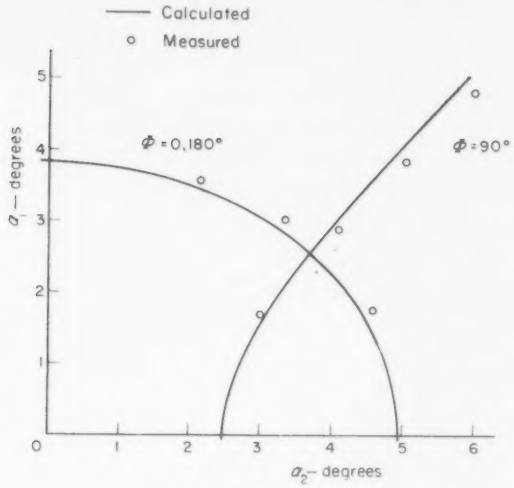

FIG. 14(a).

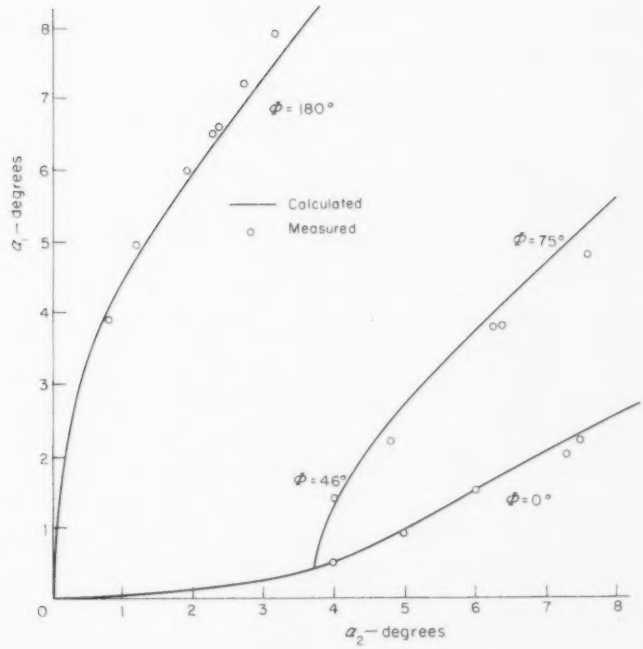

FIG. 14(b).

pendulum amplitudes must be kept small: at amplitudes of about 6°, the fifth-power terms become appreciable, particularly in their effect on frequencies. A second source of discrepancy between experiment and theory is caused by the light damping which is inevitably present in a mechanical system. But since the theory is intended for mechanical applications this has the advantage of

ensuring realistic experiments. The effect of damping forces is most noticeable in motions with a long beat period and, as has been seen, eliminates the higher-order resonances.

The mechanical system possesses several advantages particularly in comparison with the more usual electric analogues. The mechanical system is passive, and can introduce no errors due to active components. Also noteworthy are its simplicity, reliability, the stability of its parameters, and the accuracy with which these can be computed.

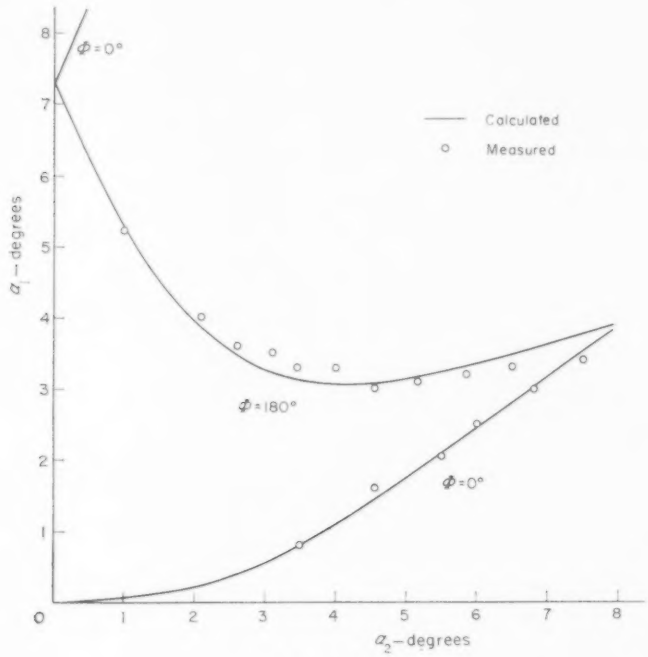

FIG. 14(c).

FIG. 14. Experimental verification of the amplitude and phase relations which give steady oscillations in both degrees of freedom.

(a) Application I(a).

(b) Application II(a). (Φ varies continuously along the centre curve, starting from 0° at the point of bifurcation.)

(c) Application II(b).

CONCLUDING REMARKS

The methods of Part I have now been used to give a rather detailed description of the behaviour of equations (24) and of the more general equations (1). These results are interesting and important in themselves, but it is expected that the general method of solution which they illustrate will also be found useful in many other quasilinear problems. It is also likely that investigation by mechanical analogues will prove equally helpful in other applications.

Acknowledgements—The work described in the present paper originally formed part of a research programme directed by Professor S. A. Tobias in the Cambridge University Engineering Department. The author wishes to record his gratitude to Professor Tobias for his suggestion of the subject and for his supervision and encouragement at this stage; also to Messrs. S. V. Dawson and R. F. Henry and Dr. J. G. Taylor for their many helpful discussions, and Mr. J. D. West for his assistance with the Russian translation. Finally, particular thanks are due to Dr. P. E. W. Grensted, who has supervised the later stages of the work.

The use of mechanical analogues was suggested to the author by Professor Tobias, and the apparatus described in the paper is developed from a demonstration model originally designed by Dr. Grensted.

The financial support of the Department of Scientific and Industrial Research is acknowledged.

APPENDIX I

Details of the (χ, Φ) *analysis for the second-order resonance of equation* (24) [*Application* I(b)]

The integration of the equation for $d\chi/d\Phi$ is equivalent to integrating equations (35) after eliminating t. This integration is not possible as they stand, but requires the approximation given below.

The equation for $d\Phi/dt$ is

$$\begin{aligned}\frac{d\Phi}{dt} = {} & \frac{\epsilon}{2\omega}\{(\Delta_1 - \tfrac{3}{4}l_1 a_1^2 - \tfrac{1}{2}n_1 a_2^2) - 4(\Delta_2 - \tfrac{3}{4}l_2 a_2^2 - \tfrac{1}{2}n_2 a_1^2)\} \\ & - \frac{\epsilon^2}{8\omega^3}\{(\Delta_1 - \tfrac{3}{4}l_1 a_1^2 - \tfrac{1}{2}n_1 a_2^2)^2 - 16(\Delta_2 - \tfrac{3}{4}l_2 a_2^2 - \tfrac{1}{2}n_2 a_1^2)^2 \\ & - (\tfrac{3}{32}l_1^2 - \tfrac{2}{3}n_2^2)\, a_1^4 - \tfrac{5}{3}n_1 n_2 a_1^2 a_2^2 + (\tfrac{1}{6}n_1^2 + \tfrac{3}{2}l_2^2)\, a_2^4 \\ & + (n_1 - l_2)\,(\tfrac{1}{4}n_1 a_2^2 - 2n_2 a_1^2)\, a_2^2 \cos 2\Phi\}\end{aligned} \tag{45}$$

If the beat period is to be long enough to allow appreciable changes in amplitude, $d\Phi/dt$ must be of the same order of magnitude as da_1/dt and da_2/dt, namely $0(\epsilon^2)$. This requires

$$(\Delta_1 - \tfrac{3}{4}l_1 a_1^2 - \tfrac{1}{2}n_1 a_2^2) - 4(\Delta_2 - \tfrac{3}{4}l_2 a_2^2 - \tfrac{1}{2}n_2 a_1^2) = 0(\epsilon) \tag{46}$$

Therefore in this case the difference of the squares of these terms may be deleted from the coefficient of ϵ^2 in equation (45).

On the other hand, if the term (46) is not small, it will dominate the other terms in equations (35). But the above approximation retains this property, and should therefore give good accuracy over the whole region of the resonances.

The simplified equations (35) may now be taken together and integrated. In terms of χ and Φ the resulting equations are:

$$\frac{d\chi}{dt} = \frac{\epsilon^2}{2\omega^3} C^2 n_1 (n_1 - l_2)\, n_2^2 \cos\chi \sin^3\chi \sin 2\Phi \tag{47}$$

$$\begin{aligned}\frac{d\Phi}{dt} = {} & \frac{\epsilon}{2\omega}\{(\Delta_1 - 4\Delta_2) - Cn_1(\tfrac{3}{4}l_1 - 2n_2)\cos^2\chi - Cn_2(2n_1 - 12l_2)\sin^2\chi\} \\ & + \frac{\epsilon^2}{8\omega^3}\{C^2 n_1^2(\tfrac{3}{32}l_1^2 - \tfrac{2}{3}n_2^2)\cos^4\chi + \tfrac{20}{3}C^2 n_1^2 n_2^2 \sin^2\chi\cos^2\chi \\ & - C^2 n_2^2(\tfrac{8}{3}n_1^2 + 24l_2^2)\sin^4\chi + 4C^2 n_1(n_1 - l_2)\, n_2^2 \sin^2\chi(2\cos^2\chi - \sin^2\chi)\cos 2\Phi\}\end{aligned} \tag{48}$$

with the integrated form:

$$(\Delta_1-4\Delta_2)\cos^2\chi-\tfrac{3}{8}Cl_1n_1\cos^4\chi-2Cn_1n_2\sin^2\chi\cos^2\chi-6Cl_2n_2\sin^4\chi$$
$$+\frac{\epsilon}{128\omega^2}C^2l_1^2n_1^2\cos^6\chi+\frac{\epsilon}{6\omega^2}C^2n_1^2n_2^2\cos^4\chi\sin^2\chi-\frac{2\epsilon}{3\omega^2}C^2n_1^2n_2^2\cos^2\chi\sin^4\chi$$
$$+\frac{2\epsilon}{\omega^2}C^2l_2^2n_2^2\sin^6\chi-\frac{\epsilon}{\omega^2}C^2n_1(n_1-l_2)n_2^2\cos^2\chi\sin^4\chi\cos 2\Phi=\text{constant} \qquad (49)$$

APPENDIX II

Some details of the analyses for Application II

Application II(a), $k_1/k_2\approx 1$. The terms $\epsilon u_i^{(1)}$ have not been found important. The (χ,Φ) equations are

$$\frac{d\chi}{dt}=\frac{\epsilon}{8\omega}\sqrt{(Cn_1)}\sqrt{(Cn_2)}\{m_1\cos^2\chi+m_2\sin^2\chi+n_1\sqrt{(n_2/n_1)}\sin 2\chi\cos\Phi\}\sin\Phi \qquad (50)$$

$$\begin{aligned}\frac{d\Phi}{dt}=\frac{\epsilon}{2\omega}\Big\{&(\Delta_1-\Delta_2)-\tfrac{3}{4}C(l_1n_1\cos^2\chi-l_2n_2\sin^2\chi)\\&-\tfrac{3}{4}\sqrt{(Cn_1)}\sqrt{(Cn_2)}\,(m_1-m_2)\sin\chi\cos\chi\cos\Phi\\&-\tfrac{1}{4}Cn_1n_2(\sin^2\chi-\cos^2\chi)(2+\cos 2\Phi)\\&-\tfrac{1}{4}\sqrt{(Cn_1)}\sqrt{(Cn_2)}\left(m_2\frac{\sin^3\chi}{\cos\chi}-m_1\frac{\cos^3\chi}{\sin\chi}\right)\cos\Phi\Big\}\end{aligned} \qquad (51)$$

with the integrated form:

$$\begin{aligned}&(\Delta_1-\Delta_2)\cos^2\chi-\tfrac{3}{8}Cl_1n_1\cos^4\chi\\&-\tfrac{3}{8}Cl_2n_2\sin^4\chi-\tfrac{1}{4}Cn_1n_2\cos^2\chi\sin^2\chi(2+\cos 2\Phi)\\&-\tfrac{1}{2}\sqrt{(Cn_1)}\sqrt{(Cn_2)}\,(m_1\cos^2\chi+m_2\sin^2\chi)\sin\chi\cos\chi\cos\Phi=\text{constant}\end{aligned} \qquad (52)$$

Application II(b), $k_1/k_2\approx 3$. In this case the terms $\epsilon u_i^{(1)}$ in equation (41) are not usually negligible. They are given by

$$\begin{aligned}u_1^{(1)}=&\frac{9}{8\omega^2}\{(\tfrac{1}{2}m_1a_1^2a_2+\tfrac{3}{4}p_1a_2^3)\cos(\tfrac{1}{3}\omega t+\theta_2)+\tfrac{1}{4}n_1a_1a_2^2\cos(\tfrac{1}{3}\omega t+\theta_1-2\theta_2)\}\\&-\frac{9}{16\omega^2}\{\tfrac{1}{4}m_1a_1^2a_2\cos(\tfrac{5}{3}\omega t+2\theta_1-\theta_2)+\tfrac{1}{4}n_1a_1a_2^2\cos(\tfrac{5}{3}\omega t+\theta_1+2\theta_2)\}\\&-\frac{9}{40\omega^2}\{\tfrac{1}{4}m_1a_1^2a_2\cos(\tfrac{7}{3}\omega t+2\theta_1+\theta_2)\}-\frac{1}{8\omega^2}\{\tfrac{1}{4}l_1a_1^3\cos(3\omega t+3\theta_1)\}\\u_2^{(1)}=&-\frac{9}{8\omega^2}\{\tfrac{1}{4}l_2a_2^3\cos(\omega t+3\theta_2)+(\tfrac{1}{2}m_2a_2^2a_1+\tfrac{3}{4}p_2a_1^3)\cos(\omega t+\theta_1)\}\\&-\frac{3}{8\omega^2}\{\tfrac{1}{4}m_2a_2^2a_1\cos(\tfrac{5}{3}\omega t+\theta_1+2\theta_2)+\tfrac{1}{4}n_2a_2a_1^2\cos(\tfrac{5}{3}\omega t+2\theta_1-\theta_2)\}\\&-\frac{3}{16\omega^2}\{\tfrac{1}{4}n_2a_2a_1^2\cos(\tfrac{7}{3}\omega t+2\theta_1+\theta_2)\}-\frac{9}{80\omega^2}\{\tfrac{1}{4}p_2a_1^3\cos(3\omega t+3\theta_1)\}\end{aligned} \qquad (53)$$

In practice, the leading terms of each expression have been found to give a significant modification to the wave form: i.e. give a $\frac{1}{3}$ subharmonic in x_1 and a third harmonic in x_2. (Compare the factor $9/8\omega^2$ of these terms with the factor $1/8\omega^2$ in equation 26.)

The (χ, Φ) equations for this case are:

$$\frac{d\chi}{dt} = \frac{\epsilon}{8\omega}\sqrt{(Cn_1)}\sqrt{(Cn_2)}\,9m_2\sin^2\chi\sin\Phi \tag{54}$$

$$\frac{d\Phi}{dt} = \frac{\epsilon}{2\omega}\{(\Delta_1 - 9\Delta_2) - Cn_1(\tfrac{3}{4}l_1 - \tfrac{9}{2}n_2)\cos^2\chi - 9Cn_2(\tfrac{1}{2}n_1 - \tfrac{27}{4}l_2)\sin^2\chi$$
$$-\tfrac{9}{4}\sqrt{(Cn_1)}\sqrt{(Cn_2)}\,m_2\sec\chi(\sin^3\chi - 3\sin\chi\cos^2\chi)\cos\Phi\} \tag{55}$$

with the integrated form:

$$(\Delta_1 - 9\Delta_2)\cos^2\chi - \tfrac{1}{2}Cn_1(\tfrac{3}{4}l_1 - \tfrac{9}{2}n_2)\cos^4\chi + \tfrac{9}{2}Cn_2(\tfrac{1}{4}n_1 - \tfrac{27}{4}l_2)\sin^4\chi$$
$$-\tfrac{9}{2}\sqrt{(Cn_1)}\sqrt{(Cn_2)}\,m_2\sin^3\chi\cos\chi\cos\Phi = \text{constant} \tag{56}$$

REFERENCES

1. R. E. Roberson, *J. Franklin Inst.* **254**, 205 (1952).
2. P. R. Sethna, *Second U.S. National Congress on Applied Mechanics*, p. 65 (1954).
3. T. C. Huang, *J. Appl. Mech.* **22**, 107 (1955).
4. T. C. Huang, *Second U.S. National Congress on Applied Mechanics*, p. 95 (1954).
5. F. R. Arnold, *J. Appl. Mech.* **22**, 487 (1955).
6. P. R. Sethna, *J. Appl. Mech.* **27**, 187 (1960).
7. S. A. Tobias, *Proc. Inst. Mech. Engng.* **171**, 691 (1957).
8. R. F. Henry and S. A. Tobias, *J. Mech. Engng. Sci.* **1**, 19 (1959).
9. E. Mettler, *Ing. Arch.* **28**, 213 (1959).
10. N. N. Bogoliuboff and I. A. Mitropolski, *Asymptotic Methods in the Theory of Non-linear Oscillations* (In Russian). State Publishers, Moscow (1958).
11. N. Kryloff and N. Bogoliuboff (Translated by S. Lefschetz), *Introduction to Non-linear Mechanics*. Princeton University Press (1947).
12. J. J. Stoker, *Non-linear Vibrations*. Interscience, New York (1951).

Vol. 3
1961

Int. J. Mech. Sci. Pergamon Press Ltd. 1961. Vol. 3, pp. 312–314. Printed in Great Britain

BOOK REVIEWS

M. M. SAVERIN (Editor): **Increasing the Loading on Gearing and Decreasing its Weight** (translated from the Russian). Pergamon Press, Oxford, 1961. 204 pp. + viii, 70s.

THERE is considerable scope for detail development of industrial gear drives by which weight and cost may be saved and life extended. The above work is a collection of papers, by various Russian authors, on particular aspects of gear design. The first paper contains an analysis of the loading carried by certain rolling mill gear drives which have been operating for some years in the U.S.S.R, together with information about how the gears have stood up to the loading. The second discusses the choice of basic parameters such as pitch, gear width and, in a two-stage gear, the individual ratios. The third deals with casing designs and includes a number of drawings showing different casing designs for housing a particular set of gears. Such matters as minimum permissible wall thickness are treated and the advantages of different designs of built-up wheel are discussed.

The fourth paper is concerned with the fatigue loading of gear teeth. It deals at some length with the problems of cumulative fatigue damage and puts forward rules for predicting the life of a gear which is subjected to a sequence of specified loading cycles. The fifth and sixth papers describe a particular variant of tooth design—that of outside-pitch-circle meshing of the second type. In gears designed in accordance with this system, the wheel teeth are all addendum and the pinion teeth all dedendum. Provided that this can be done without undue weakening of the pinion teeth in bending, it can improve the load carrying capacity by utilizing the high resistance to surface fatigue of the harder material of the pinion. As is well known, the addendum surfaces are not subject to surface failure to the same extent and the softer material of the gear wheel can therefore be used more effectively if the wheel teeth are all addendum.

The last two chapters deal with related topics, namely those of dynamic tooth loading and of tooth flexibility. These two chapters add little to the information which is general in the Western world.

The book will be useful to gear designers because much of the material is of the kind which commonly lies in the files of gear manufacturers but is rarely published so fully.

D. C. JOHNSON

J. DUCARME, M. GERSTEIN and A. H. LEFEBVRE (Editors): **Progress in Combustion Science and Technology**. Pergamon Press, Oxford, 1960. 226 pp., 70s.

THIS book is a collection of six review articles dealing with combustion science and, as stated in the Foreword, is the first of a series of annual publications of collected reviews based on aeronautical aspects of combustion and propulsion.

Of the six articles contained in this first volume, three can be described as reviewing aspects of the fundamental properties of combustion processes dealing as they do with geometric optical techniques for visual study of flames, a theoretical and experimental survey of flame quenching and considerations of delay in ignition of combustible systems with particular reference to liquid propellants for rockets.

The remaining three articles refer to gas-turbine combustion chambers. Two of these deal with the visualization of flow and the aerodynamic influence on flame stability, whilst the last summarizes the practical possibilities of following the chemical changes in the combustion zone.

Thus the field covered by each review is a fairly narrow one and it would be expected that a research worker already specializing in any one of these fields, and hence probably quite well read in the subject, would possibly gain little from reading the review. On the other hand, the remaining articles provide a convenient and effective method of keeping

abreast with other closely related topics, and hence enable a liberal outlook to be maintained. Books of this type should also be invaluable to the new graduate entering post-graduate work and searching the frontiers of various branches of research in order that he may make a reasoned choice of subject.

Whilst the review article is now generally accepted as a research "tool", a collection of reviews on related topics within a particular sphere should be even more useful than the numerical list would suggest, since with care in selection and editing it should be possible to achieve appreciable continuity of thought and even inter-relation between reviews.

In this book the various articles vary in style considerably as would be expected, but all are presented in a very direct manner without superficialities and are provided with ample references and illustrations.

One has the feeling, however, that there will be a great many technical but non-specialist readers of this book who would have appreciated the inclusion of two general non-detailed reviews in the form of preambles, one dealing with the present situation in the theory of flame propagation, the other with the progress and current problems in the development of gas-turbine combustion chambers.

G. S. CANTLE

Vol. 3
1961

G. N. SAVIN: **Stress Concentration around Holes** (translated from the Russian). Pergamon Press, Oxford, 1961. 430 pp. + xi, 84s.

THIS book is restricted to two-dimensional problems: holes in plane or plate. A further volume on three dimensions is promised. The author's approach is to solve exactly problems for various-shaped holes in infinite media subject to various distributions of stress at infinity and then to determine by experiment the accuracy of these solutions when applied to bodies of finite dimension. In its original Russian, Professor J. N. Goodier described this book as one of the most important books on elasticity published in the last decade; now translated into English, it should be in the library of anyone interested in the theory or practice of stress analysis.

Solutions are obtained by Mushkelishvili's method, which expresses the components of stress and of displacement in terms of two complex functions of the complex variables $z = x + iy$ and $\bar{z} = x - iy$ and which, by conformal transformation $z = z(\zeta)$, maps the actual boundary on to the unit circle in the ζ-plane. The method is described in chapter 1 of this book. In chapters 1–5, the state of stress is either plane strain or generalized plane stress.

In chapter 2, stresses are evaluated and shown graphically for circular, elliptical, square, rectangular and triangular holes in a sheet subject to uniaxial tension at infinity; in the latter three cases, the corners are rounded to avoid infinite stress concentrations. The stresses in biaxial tension follow by superposition. Similar results are obtained and illustrated for pure bending and flexure. The case of a circular hole in a finite width strip subject to tension at infinity can be solved exactly. This result indicates that the error in applying the solutions for infinite width to holes in strips of finite width is less than 6 per cent if the smallest dimension of the strip is at least five times that of the hole.

Chapters 3 and 5 respectively extend these results to anisotropic materials and to holes in isotropic materials strengthened by elastic rings: naturally the more complicated the physical conditions, the fewer the shapes of hole for which solutions are obtained and illustrated.

In chapter 4, it is assumed that plasticity occurs around the hole. The essential difficulty in such problems is to determine the position of the elastic–plastic boundary. In this chapter, the problems are statically determinate and the difficulty is overcome by treating the mapping $z = z(\zeta)$ as the unknown function and determining it from the equations in the elastic region (Reviewer's comment: "The yield criterion employed by Savin is valid only in plane strain and hence his results are only valid in these circumstances. However, provided the plane stress form of the criterion is adopted, his method can probably be extended to plane stress").

Chapters 6 and 7 apply similar techniques to the bending of thin plates with and without reinforcement of the holes.

In chapter 8, photoelastic and extensometer measurements are given and the stress fields plotted. From these plots, the extent of the disturbance caused by the presence of each hole can be estimated. The theoretical solution for the infinite medium can be applied to the finite specimen if the area of disturbance falls within the specimen. It would appear that the theoretical solution can be used nearly always when the diameter of the hole is less than a fifth of the width of the specimen, and frequently it can be used when the ratio is even greater. This accords with the theoretical result quoted above from chapter 2.

D. R. BLAND

P. I. ROMANOVSKII: **Mathematical Methods for Engineers and Technologists.** Edited by T. KÖVÀRY (Translated by M. SLATER). Pergamon Press, Oxford, 1961. 253 pp., 50s.

THIS is a concise but rigorous book which is designed to fill in the mathematical gaps which exist in many conventional courses of engineering and technology.

The ever-increasing demands for mathematical technique make the book a welcome volume for the third-year student and graduate of either a university engineering course or advanced technological course.

The fundamental material of Fourier series and the Fourier integral, Analytic Field Theory, the theory of analytical functions, some special functions and Operational Calculus is presented clearly and logically. Applications of the theory are omitted in this condensed volume but mathematical queries which arise in technology can be very quickly traced in the book and explained clearly. Important terms and phrases are underlined and give an obvious sense of continuity between the mathematical fundamentals and subsequent analysis.

The chapter on vector analysis includes the fundamentals, the theorems of Green, Gauss and Stokes, and vector operators in curvilinear co-ordinates. Analytic function theory takes the reader from the definition of complex numbers to conformal mapping in 70 pages. The chapter on special functions is concerned with the Gamma-Function and Bessel-Functions and the final chapter on the Laplace Transform includes a section on the solution of linear finite-difference equations with constant coefficients.

J. K. ROYLE

Vol. 3
1961